Isotopic constraints on timing of deformation and metamorphism in the Thor–Odin dome, Monashee Complex, southeastern British Columbia.

by

Yvette Dominique Kuiper

M.Sc., Utrecht University, the Netherlands, 1997

A Thesis Submitted in Partial Fulfilment of
the Requirements for the Degree of

Doctor of Philosophy

In the Graduate Academic Unit of Geology

Supervisor:	Paul F. Williams, Ph.D., Department of Geology
Co-Supervisor:	Sharon D. Carr, Ph.D., Department of Earth Sciences Carleton University, Ottawa, Ontario
Examining Board:	Jon H. Thompson, Ph.D., Department of Mathematics and Statistics, Chair Kerry MacQuarrie, Ph.D., Department of Civil Engineering David R. Lentz, Ph.D., Department of Geology
External Examiner:	Michael L. Williams, Ph.D., Department of Geosciences, University of Massachusetts, Amherst, Massachusetts, USA

This thesis is accepted

Dean of Graduate Studies

THE UNIVERSITY OF NEW BRUNSWICK

October, 2003

Yvette D. Kuiper, 2003



Frontispiece: The basement rocks of the Monashee Complex reveal parts of a complicated history of melting, transposition and various generations of folding and metamorphism, starting more than two billion years ago.

Foreword

All data presented in this thesis are original, except for the $^{40}Ar/^{39}Ar$ hornblende data presented in Chapter 3 and Appendix I, which are recalculated by P.H. Reynolds and K.A. Taylor from R.N. Spark's data, as referred to in Chapter 3. All field and laboratory work was carried out by the author; the help of other people is indicated in the Acknowledgements. The hydrogen stable isotope chemistry was performed by A. Timbal in B.E. Taylor's laboratory. M.L. Williams constructed the monazite microprobe element maps presented in Chapter 6.

This thesis is written in the form of seven papers that are either published, or submitted, or in preparation for publication. Following the University of New Brunswick School of Graduate Studies guidelines for the preparation of theses (last revised in 1999), some repetition is unavoidable.

Chapter 2 is published in Earth and Planetary Science Letters. An earlier version of Chapter 3, written in collaboration with B.E. Taylor, P.F. Williams and S.D. Carr, was submitted to Chemical Geology and is currently being revised. Chapter 3 includes, in addition to the version submitted to Chemical Geology, the $^{40}Ar/^{39}Ar$ data (Appendix I) and a scanning electron microscopy study on the presence or absence of retrograde minerals in hornblende. It does not include new stable isotope analyses that are being performed by H. Mirnejad in B.E. Taylor's laboratory, such that whole-rock and hornblende oxygen, and hornblende hydrogen stable isotope data will exist for each of the amphibolite samples presented.

An earlier version of Chapter 4 is a paper in review for American Mineralogist.

Chapters 5–7 are in preparation for publication as separate papers. Chapter 8 is a paper in preparation for publication, written in collaboration with P.F. Williams, S. Kruse and P.D. McNeill.

The name 'Tertiary' was officially abandoned by the International Union of Geological Sciences in 2001. Because (1) the name is used on the latest (1999) Geological Society of America Geologic Time Scale and (2) the term is still extensively used by the Canadian Cordilleran community and in the literature, the name 'Tertiary' is retained in this thesis.

The interpretations that Late Cretaceous–Early Eocene isotopic dates may represent the time of crustal extension (Chapter 3) and that the geology of the southern Canadian Cordillera is consistent with a channel flow model (Chapter 8) are considered to be the most reasonable explanations for existing data. However, the reader is encouraged to read with criticism, to carefully distinguish between data and interpretations, and to test the interpretations if appropriate for the reader's goals. No geological interpretation is written in stone.

Abstract

New and existing U–Pb and $^{40}Ar/^{39}Ar$ geochronological data, and oxygen and hydrogen stable isotope data, are combined with structural and metamorphic data from Thor–Odin, the southern culmination of the Monashee Complex. This leads to a new interpretation of the timing of deformation and metamorphism. Amphibolites in Thor–Odin with hornblende $^{40}Ar/^{39}Ar$ dates between ~75–70 and ~51 Ma experienced more ^{18}O- and D-depletion than amphibolites with older dates. The younger dates that were previously interpreted as cooling ages, may have resulted from complete or partial Ar loss in the presence of meteoric fluids that were introduced into the rock during extension.

Monazite crystals in pelitic schist, quartzite and orthogneiss, which have U–Pb ages younger than $^{40}Ar/^{39}Ar$ hornblende ages in amphibolite in northwest Thor–Odin, may have grown during extension in the presence of fluids. Titanite, xenotime and zircon dates may be interpreted in the same way. Thus, the U–Pb dates that were previously interpreted as representing peak of metamorphism and the hornblende $^{40}Ar/^{39}Ar$ dates that were previously interpreted as representing cooling ages, may be interpreted as reflecting meteoric fluid penetration of the crust during regional extension. This implies that the age of the thermal peak of metamorphism is older than ~75–70 Ma.

Migmatisation in a basement orthogneiss in Thor–Odin occurred at ~1.8 Ga. Dissolution rims are preserved in zircon between ~1.8 Ga domains and 52 Ma overgrowths. Because growth of new zircon (and possibly other U–Pb accessory phases) did not take place, any geological event that occurred during the ~1.8 Ga to 52 Ma time interval is not recorded. Cordilleran deformation and metamorphism may have taken place within that time interval, e.g. in the Middle Jurassic and/or mid- to Late Cretaceous,

the time of Cordilleran deformation and metamorphism in the rocks overlying the Monashee Complex.

The Joss Mountain orthogneiss, west of the Monashee Complex in the Selkirk Allochthon, is dated at 362 ± 13 Ma. F_3 folding in pelitic schist at Joss Mountain is constrained between ~73 and ~70 Ma. Existing structural, metamorphic and geochronological data in, and close to, the Shuswap Metamorphic Complex in the southern Canadian Cordillera are shown to be consistent with a channel flow model.

Acknowledgements

First of all and most of all I thank Paul Williams for intellectual and financial support, for giving me the freedom to think for myself, for his faith in me, his patience, for giving me the opportunity to see excellent rock exposures in the beautiful Monashee Mountains, and many other things. With incredible patience, Sharon Carr spent numerous hours, days, late nights and weekends with me in the laboratories to teach me every little thing there was to know about U–Pb geochronology. I am grateful for that and for many helpful and thought-provoking discussions and comments on my thesis. This project was funded by an NSERC grant to Paul Williams, except for U–Pb ID-TIMS geochronology, which was funded by an NSERC grant to Sharon Carr. Ed Ghent is acknowledged as a helpful member of my supervisory committee. Bruce Taylor encouraged me to do stable isotope analyses in his lab, and he was a great help in interpreting the data and writing it all up in a paper (Chapter 3). Adrian Timbal taught me the laboratory methods for oxygen isotope analysis, and performed the hydrogen isotope analyses and mass spectrometry. I am grateful to Paul McNeill, Brandon Cochrane and Dave Lister for very capable and pleasant field assistance. Paul, Brandon, Dave, Paul and Sharon are all thanked for helping me handle complicated rocks, steep slopes, bad weather and bears in the field.

I thank Reinoud Vissers for that push in the right direction at the right moment, that got me in touch with Paul Williams, and for his continuous help, support and enthusiasm. Brian Cousens and especially Father John (Blenkinsop) of the Mass Spectrometer, are thanked for their help with U–Pb mass spectrometry, even in the late

hours of the night, and for forgiving me my mistakes. Mike Hamilton helped me with SHRIMP preparation, data collection and interpretation of data. I thank Peter Reynolds, for talking to me about $^{40}Ar/^{39}Ar$ geochronology, showing me his lab, and discussing Bob Spark's data with me. Mike Williams made microprobe element maps of my monazites, in preparation for SHRIMP work. Bob Spark, Jim Crowley and Dennis Johnston are thanked for providing some of their samples and Dave Parkinson and Hardolph Wasteneys for making their unpublished U–Pb data available to me. These people and Paul McNeill, Stefan Kruse, Dan Gibson, Rob Scammell and other people of the Canadian Cordilleran community are thanked for good Monashee Complex discussions. Douglas Hall, Dave Lentz and James Whitehead were great help in various isotopic complexities and made me think a little deeper about those. Editorial comments by Peter Stringer greatly improved the thesis.

Carol Thompson is thanked for having her house always open to us UNB Monashee people. I am grateful to Christine Lodge, Bill and John for their friendship and for helping me with all those moves. Without having a social life, I could not write my thesis. I therefore thank my Fredericton friends: Michelle Boast, Mallory Gilliss, Ellie MacInnes, Martin de Keijzer, Jürgen Kraus, Stefan Kruse, Paul McNeill, Jim Ryan, Claudia Trepmann, Paul Wilson, Chris Wood, and my Ottawa friends: Amir (Hassan) Mirnejad, Karsten and Olga Nielsen, Niranjala Kottachchi and Steve Turgeon, and many others. I am grateful for support and friendship of family and friends in the Netherlands. I especially thank my parents, Leo and Hanneke Kuiper, for their continuous love, support, great holidays and good times together in different parts of the world.

Table of Contents

Title page i
Frontispiece ii
Abstract iii
Foreword v
Acknowledgements vii
Table of Contents ix
List of Tables xv
List of Figures xvi

Chapter 1 - Introduction 1

References 5

Chapter 2 - The interpretation of inverse isochron diagrams in $^{40}Ar/^{39}Ar$ geochronology 9

Abstract 9

2.1. Definitions and introduction 10
2.1.1. Types of argon 10
2.1.2. Introduction 11

2.2. Concepts and laboratory artifacts 12
2.2.1. Concepts 12
2.2.2. Laboratory artifacts 15

2.3. Homogeneous excess ^{40}Ar incorporation and argon loss 16

2.4. Problems and pitfalls 17
2.4.1. Heterogeneous excess ^{40}Ar distribution and argon loss 18
2.4.2. Location of data points on the inverse isochron plot 19
2.4.3. False inverse isochron plots 19

2.5. Conclusions 21

References 22

Chapter 3 - Significance of (Late Cretaceous–)Early Tertiary meteoric hydrothermal activity for the interpretation of U–Pb ages and $^{40}Ar/^{39}Ar$ (hornblende) ages in the Monashee Complex, southeastern British Columbia 28

Abstract 28

3.1. Introduction 30
3.2. Geological setting and geochronology 32

3.3. Methods and selection of samples 36
3.3.1. $^{40}Ar/^{39}Ar$ analyses 36
3.3.2. Oxygen and hydrogen isotope analyses 38
3.3.3. Hornblende chemical composition 39

3.4. Results 39
3.4.1. Oxygen and hydrogen isotopes 39
3.4.1.1. Oxygen and hydrogen isotopes in amphibolites 40
3.4.1.2. Oxygen isotopes in other rock types near faults 41
3.4.2. Argon data 42
3.4.2.1. $^{40}Ar/^{39}Ar$ spectrum disturbance 42
3.4.2.2. Excess ^{40}Ar and Ar loss 44
3.4.3. Relationships between hornblende chemical composition and (i) $^{40}Ar/^{39}Ar$ age and (ii) hydrogen isotopic composition 45
3.4.4. SEM results 47

3.5. Discussion 48
3.5.1 Extension and infiltration of meteoric fluids 48
3.5.2 Argon and hydrogen systematics in hornblende 51
3.5.2.1. Amphibolites with plateau and near-plateau spectra, and apparent ages younger than ~75–70 Ma 53
3.5.2.2. Amphibolites with disturbed spectra, and apparent ages older than ~75–70 Ma 54
3.5.2.3. Indications of pre-~75–70 Ma cooling ages in Thor–Odin 55
3.5.2.4. The influence of hornblende chemical composition on argon loss and hydrogen isotopic exchange 56
3.5.2.5. Hydrothermal alteration versus thermal overprint; interpretations of the $^{40}Ar/^{39}Ar$ hornblende dates 58
3.5.3. Ages based on U–Pb versus ages based on $^{40}Ar/^{39}Ar$ systematics 60
3.5.3.1. The monazite perspective 60

3.6. Conclusions 62

References 65

Chapter 4 - Isotopic age constraints from electron microprobe U–Th–Pb dates, using a three-dimensional concordia diagram 86

Abstract 86

4.1. Introduction 86

4.2. Methods of microprobe U–Th–Pb dating 88

4.3. Microprobe isotopic age constraints on discordant analyses 90
4.3.1. Microprobe isotopic age constraints on discordant analyses; the mathematical approach 91
4.3.2. The three-dimensional concordia diagram 94
4.3.3. Microprobe isotopic age constraints on discordant analyses; the graphical approach 95

4.4. Conclusions 98

References 98

Chapter 5 - Proterozoic (and Mesozoic?) deformation and metamorphism in basement rocks of the Thor–Odin dome in the Monashee Complex, southeastern British Columbia 104

Abstract 104

5.1. Introduction 105

5.2. Geological background 106

5.3. Methods and definitions 109
5.3.1. Isotope Dilution Thermal Ionisation Mass Spectrometry (ID-TIMS) 109
5.3.2. The Sensitive High Resolution Ion Microprobe (SHRIMP) 111
5.3.3. Discordance, reverse discordance, and assignment of errors 112

5.4. Results 113
5.4.1. U–Pb geochronology 113
5.4.1.1. Basement orthogneiss (s298-65) 113
5.4.1.2. Cranberry Valley crosscutting aplite dyke (s298-117) 118
5.4.1.3. Cranberry Valley folded pegmatite (s298-120) 120
5.4.1.4. Frigg Glacier crosscutting aplite dyke (s298-213) 122
5.4.1.5. Blanket Mountain pegmatite (RB-1-93) in F_1/F_2 boudin neck 124
5.4.2. U concentrations in zircon from the Monashee Complex 125

5.5. Discussion 128
5.5.1. Palaeoproterozoic orthogneiss formation and migmatisation 128
5.5.2. Attempts to constrain deformation by dating pegmatites; enigmatic answers to simple questions 130

5.6. Conclusions 133

References 134

Chapter 6 - Late Cretaceous to Early Eocene monazite and zircon ages in cover rocks of Thor–Odin dome of the Monashee Complex, southeastern British Columbia 161

Abstract 161

6.1. Introduction 162

6.2. Geological background 162

6.3. Methods and definitions 166
6.3.1. ID-TIMS and SHRIMP 166
6.3.2. Electron microprobe monazite geochronology 167

6.4. Results 167
6.4.1. Blanket quartzite (s298-30) 168
6.4.2. Blanket Mountain cover pelitic schist (s298-54) 170
6.4.3. Armstrong Peak cover pelitic schist (s298-70) 174
6.4.4. Three Valley Gap paragneiss (YK-TVG-97) and leucosome in paragneiss (s298-92) 177

6.5. Discussion 181
6.5.1. Late Cretaceous–Early Eocene monazite ages 181
6.5.2. Indications of Palaeoproterozoic (?) Pb in monazite 181
6.5.3. Constraining ages of metamorphism in the Monashee cover sequence, by constraining the age of the cover sequence 183
6.5.4. Indications for Mesozoic deformation and metamorphism 187

6.6. Conclusions 188

References 189

Chapter 7 - Age constraints on deformation and on deposition of (meta)sedimentary rocks of the Joss Mountain assemblage, west of the Monashee Complex, southeastern British Columbia 215

Abstract 215

7.1. Introduction 215

7.2. Geological background 216

7.3. Results 217
7.3.1. Joss Mountain orthogneiss (s279-123) 218
7.3.2. Joss Mountain pegmatite (s298-4) 220

7.4. Discussion 223
7.4.1. Late Devonian–Early Mississippian granitoids 223
7.4.2. Constraints on F_3 folding 224

7.5. Conclusions 227

References 228

Chapter 8 - Possibility of channel flow in the southern Canadian Cordillera; a new approach to explain existing data 237

Abstract 237

8.1. Introduction 238
8.1.1. Channel flow model 241
8.1.2. Fold generations 242

8.2. Deformation in the Monashee Complex explained by a channel flow model 243

8.3. The channel flow model applied to the tectonic elements of the southern Omineca Belt 244
8.3.1. Domain 1: structures and metamorphism 246
8.3.2. Domain 1: timing of deformation 248
8.3.3. Domain 2: structures and metamorphism 252
8.3.4. Domain 2: timing of deformation 254
8.3.5. Domain 3: structures and metamorphism 256
8.3.6. Domain 3: timing of deformation 260

8.4. Granitoid migration 263
8.4.1. Origin of granitoids 264
8.4.1.1. Origin of Middle–Late Jurassic granitoids 264
8.4.1.2. Origin of Cretaceous granitoids 265
8.4.1.3. Origin of Palaeocene–Eocene granitoids 266
8.4.2. Consistency with the model presented in this chapter 266

8.5. Exposure of structures in the southern Canadian Cordillera 267

8.6. Geological model 269

8.7. Conclusions 271

References 272

Chapter 9 - Conclusions 287

Appendix I. $^{40}Ar/^{39}Ar$ data, recalculated after Spark (2001) 291
Appendix II. Sample location maps (a, b) and UTM coordinates (c) 314
Appendix III. Stable isotope data 319

List of Tables

Table 3.1. Sample descriptions, oxygen, hydrogen and argon data for amphibolites in Thor–Odin. 72

Table 3.2. Whole-rock oxygen isotopic data for samples collected at various distances from the Frigg Glacier Fault and the Grizzly Flats Fault. 73

Table 3.3. Microprobe compositions for hornblende dated by $^{40}Ar/^{39}Ar$ methods (from Spark, 2001). 74

Table 3.4. Calculated values of the hydrogen isotope equilibrium fractionation factors between hornblende and water, and of δD for meteoric waters assuming equilibrium between hornblende and the waters was reached, at selected temperatures. 75

Table 3.5. Whole-rock oxygen and hydrogen data for samples with existing monazite U–Pb data. 75

Table 5.1. ID-TIMS data for samples s298-65, s298-117, s298-120, s298-120, s298-213 and RB-1-93. 140

Table 5.2. SHRIMP data for sample s298-65. 142

Table 5.3. Regressions and average age calculations for samples s298-65, s298-117, s298-120, s298-120, s298-213 and RB-1-93. 143

Table 6.1. ID-TIMS data for samples s298-30, s298-54, s298-70, s298-92 and YK-TVG-97. 194

Table 6.2. SHRIMP data for samples s298-54 and s298-70. 195

Table 6.3. Regressions and average age calculations for samples s298-30, s298-54, s298-70, s298-92 and YK-TVG-97. 197

Table 7.1. ID-TIMS data for samples s279-123 and s298-4. 230

Table 7.2. Regressions and average age calculations for samples s279-123 and s298-4. 231

Table 8.1. Overview of deformation, metamorphism, and age constraints presented by previous workers. 281

List of Figures

Fig. 1.1. Tectonic assemblage map (from Journeay and Williams, 1995). Inset: location of morphogeological belts of the Canadian Cordillera. 7

Fig. 2.1. An inverse isochron plot. The intercept with the $^{36}Ar/^{40}Ar$ axis gives the trapped argon composition. The intercept with the $^{39}Ar/^{40}Ar$ axis gives the radiogenic argon composition. 24

Fig. 2.2. The effects of an excess ^{40}Ar trapped argon component (a) and argon loss (b) on the inverse isochron plot. 25

Fig. 2.3. The development of a false near-plateau (a) and isochron (b) with the same apparent age as a result of argon loss. 26

Fig. 2.4. The development of false isochrons as a result of heterogeneous excess ^{40}Ar distribution (a, b) or heterogeneous argon loss (c). 27

Fig. 3.1. Geological map of the Monashee Complex, and the overlying Selkirk Allochthon. Inset: location of morphogeological belts of the Canadian Cordillera. 76

Fig. 3.2. Geological map of Thor–Odin and location of amphibolites with $^{40}Ar/^{39}Ar$ hornblende plateau and near-plateau spectra (a) and disturbed spectra (b). 77

Fig. 3.3. Plot of hornblende δD versus whole-rock $\delta^{18}O$ of amphibolites. 78

Fig. 3.4. Plot of whole-rock $\delta^{18}O$ and hornblende δD versus the respective $^{40}Ar/^{39}Ar$ inverse isochron age of hornblende in amphibolites. 79

Fig. 3.5. Plot of the MSWD (mean squares of weighted deviates) of the $^{40}Ar/^{39}Ar$ inverse isochron versus the inverse isochron age. 80

Fig. 3.6. Plot of initial $^{40}Ar/^{36}Ar$ ratios versus $^{40}Ar/^{39}Ar$ inverse isochron ages of hornblende. 80

Fig. 3.7. Plots of A-site occupations (Na + K) (a), Ca/K ratios (b), K-contents (c) and Fe-numbers (d) versus $^{40}Ar/^{39}Ar$ inverse isochron ages of hornblende. 81

Fig. 3.8. Plots of A-site occupations (Na + K) (a), Ca/K ratios (b), K-contents (c) and Fe-numbers (d) versus δD values for hornblende. 82

Fig. 3.9. Back scattered electron (BSE) images of sample RS24C. Hornblende grains show no alteration except some actinolite (a). No alteration is present along grain boundaries (b). 83

Fig. 3.10. BSE image of sample RS138. 84

Fig. 3.11. BSE image of sample RS241B. 84

Fig. 3.12. Plot of whole-rock $\delta^{18}O$ and δD values versus U–Pb monazite ages. 85

Fig. 4.1. Concordia diagrams, showing discordia chord between 2.80 Ga and 0 Ma, and a solid circle showing 30% Pb loss. A: U–Th–Pb concordia diagram with $^{208}Pb/^{232}Th$ versus $^{207}Pb/^{235}U$. B: U–Pb concordia diagram with $^{206}Pb/^{238}U$ versus $^{207}Pb/^{235}U$. C: U–Th–Pb concordia diagram with $^{208}Pb/^{232}Th$ versus $^{206}Pb/^{238}U$. 102

Fig. 4.2. Three dimensional U–Th–Pb concordia diagram, with three dimensional concordia curve (curve with filled circles), and its projections onto the faces of the diagram (curve with open circles). The same discordia chord and discordant point as in Fig. 1 are shown in three dimensions. 103

Fig. 5.1. Geological map of the Monashee Complex, and the overlying Selkirk Allochthon. Modified after Wheeler and McFeely (1991). Inset: location of morphogeological belts of the Canadian Cordillera. 144

Fig. 5.2. Example of transposition foliation, in calcsilicate gneiss in the Megaboudin (Fig. 4b). 145

Fig. 5.3. Folded amphibolite boudins in basement gneisses on the north slope of Blanket Mountain. 145

Fig. 5.4. (a) Map of Thor–Odin, from Spark (2001), indicating sample location s298-213, and location of (b). (b) Sample location map. 146

Fig. 5.5. Rare overprinting relationships of F_1, F_2 and F_3 in marble, in the Monashee cover sequence in the Megaboudin. 148

Fig. 5.6. Concordia diagram showing two examples of complicated systematics of monazite with excess ^{206}Pb, illustrating how the $^{207}Pb/^{235}U$ age of a monazite may not always represent the correct age of the monazite. 149

Fig. 5.7. Concordia plots for ID-TIMS data for monazites (a) and zircons (b) for a basement orthogneiss (s298-65). 150

Fig. 5.8. Concordia plot showing SHRIMP data for sample s298-65, and cathodoluminescence (CL) images with corresponding SHRIMP spots of all analysed zircons. 151

Fig. 5.9. Interpreted meanings of zonations in zircon grains H5, L2 and L4 as discussed in the text. 152

Fig. 5.10. Concordia plots for ID-TIMS data for zircons (a) and monazites (b) for a crosscutting pegmatite in Cranberry Valley (s298-117). 153

Fig. 5.11. Possible interpretations for s298-117. 154

Fig. 5.12. Concordia diagrams for a pegmatite folded by F_3 in Cranberry Valley (s298-120). (a) zircons and (b) monazites. 155

Fig. 5.13. Photographs of an aplite dyke (s298-213) near Frigg Glacier crosscutting all structures except for some of the late N–S trending shears. (a) The aplite dyke crosscuts the foliation and shears in the host orthogneiss, although locally it follows the shears. (b) Two isoclinal folds, left and right of the aplite, are crosscut by the aplite. 156

Fig. 5.14. Concordia plot for a crosscutting aplite dyke near Frigg Glacier (s298-213). 157

Fig. 5.15. (a) Photograph of a siliceous pegmatite (RB-1-93) in a boudin neck of a pelitic schist layer. 158

Fig. 5.16. Concordia plot of zircon data from a siliceous pegmatite (RB-1-93). 159

Fig. 5.17. Plot of U concentration in zircon versus $^{207}Pb/^{206}Pb$ zircon ages of near-concordant or concordant zircon data in the Monashee Complex (a) and the same without zircon from Late Cretaceous–Early Eocene pegmatite and aplite dykes, to exclude zircon of magmatic origin (b). 160

Fig. 6.1. Geological map of the Monashee Complex, and the overlying Selkirk Allochthon. Modified after Wheeler and McFeely (1991). Inset: location of morphogeological belts of the Canadian Cordillera. 198

Fig. 6.2. Sample location map. Map from Johnston (2000). 199

Fig. 6.3. Dated quartzite (s298-30; ~10m thick layers on the left part of the photograph) on north side of the Megaboudin. 200

Fig. 6.4. Concordia diagrams for monazites (a) and detrital zircons (b) for the quartzite (s298-30). BSE images in (a) show representative examples of monazites. 201

Fig. 6.5. Microprobe element maps (Y, Th, U and Pb) of monazite shown in BSE image 2 (sample s298-30, Fig. 32a), showing patchy domains. Scale shown in Fig. 32a. 202

Fig. 6.6. Concordia plot of ID-TIMS data for pelitic schist s298-54. 202

Fig. 6.7. Concordia diagrams showing SHRIMP data for sample s298-54. (a) $^{206}Pb/^{238}U$ versus $^{207}Pb/^{235}U$, also showing BSE images of representative monazites and analysed spots. (b) $^{208}Pb/^{232}Th$ versus $^{206}Pb/^{238}U$. (c) $^{208}Pb/^{232}Th$ versus $^{207}Pb/^{235}U$. 203

Fig. 6.8. Microprobe element maps of monazites 1–4 shown in Fig. 38a (sample s298-54). 205

Fig. 6.9. Photograph of pelitic schist s298-70. 207

Fig. 6.10. Concordia diagram of ID-TIMS data for pelitic schist s298-70. 207

Fig. 6.11. Concordia plots showing SHRIMP data for sample s298-70. (a) $^{206}Pb/^{238}U$ versus $^{207}Pb/^{235}U$, also showing BSE images of representative monazites and analysed spots. (b) $^{208}Pb/^{232}Th$ versus $^{206}Pb/^{238}U$. (c) $^{208}Pb/^{232}Th$ versus $^{207}Pb/^{235}U$. 208

Fig. 6.12. Microprobe element maps of monazites 1, 2 and 4 of sample s298-70 shown in Fig. 46a. 210

Fig. 6.13. Concordia plot and BSE images of zircons and monazites for the Three Valley Gap paragneiss (YK-TVG-97; labelled with capitalised letters) and its leucosome (s298-92; small letters). 212

Fig. 6.14. Microprobe element maps of monazites 1–3 of samples YK-TVG-97 and s298-92 (see Fig. 50). 212

Fig. 6.15. Zircon inclusion (indicated by the arrows) in monazite. 214

Fig. 7.1. Geological map of the Monashee Complex, and the overlying Selkirk Allochthon. Modified after Wheeler and McFeely (1991). Inset: location of morphogeological belts of the Canadian Cordillera. 232

Fig. 7.2. Example of transposition foliation, in calcsilicate gneiss in the Megaboudin (Fig. 3). 233

Fig. 7.3. Sample location map. 234

Fig. 7.4. Concordia plot for the Joss Mountain orthogneiss (sample s279-123) with two representative examples of zircon BSE images. 235

Fig. 7.5. Two E–W trending pegmatite dykes (s298-4) crosscutting the Joss Mountain orthogneiss, marble and pelitic schists at Joss Mountain. 235

Fig. 7.6. Contact of the dated pegmatite (s298-4) at Joss Mountain, crosscutting the foliation in the host paragneiss. 236

Fig. 7.7. Concordia plot and BSE images of zircons and monazites for the crosscutting pegmatite at Joss Mountain orthogneiss (sample s298-4). 236

Fig. 8.1. Tectonic assemblage map (from Journeay and Williams, 1995). Inset: location of morphogeological belts of the Canadian Cordillera. 282

Fig. 8.2. Diagrammatic representation of the history of the Monashee Complex (MC). 283

Fig. 8.3. Diagram representing different possibilities of fold overprinting relationships, developed in time. 284

Fig. 8.4. Domain division and F_3 vergence reversal zone. 285

Fig. 8.5. Location of various areas discussed in the text, with respect to the channel flow zone, changing with time. 286

Chapter 1

Introduction

The Monashee Complex, located in southeasten British Columbia, is an exposure of basement rocks and overlying supracrustal rocks of the ancestral North American continent. It is exposed within the southern Omineca Belt, which is one of five morphogeological belts forming the Canadian Cordillera (Fig. 1.1, inset; Gabrielse et al., 1991). The Omineca Belt is a polydeformed metamorphic and igneous belt that forms the hinterland to the Rocky Mountain Foreland Belt. West of the Omineca Belt, the Intermontane and Insular Belts approximately outline two superterranes that accreted onto the North American continent in the Middle Jurassic and the mid- to Late Cretaceous respectively (Monger et al., 1982; Murphy et al., 1995). The Coast Belt is a plutonic complex that lies on the boundary between the Intermontane and Insular Superterranes (Fig. 1.1; Monger et al., 1982).

The Monashee Complex has two structural culminations: Frenchman Cap in the north and Thor–Odin in the south (Fig. 1.1). It comprises a Palaeoproterozoic basement core of orthogneiss and paragneiss (Armstrong et al., 1991, and references therein; Parkinson, 1991) and a Palaeoproterozoic to Palaeozoic (?) cover of quartzite, marble, calc-silicate gneiss, pelitic schist and paragneiss (Scammell and Brown, 1990, and references therein; Parrish, 1995, and references therein). The Monashee Complex is surrounded by the overlying rocks of the Selkirk Allochthon, which consist of quartzite, marble, calc-silicate gneiss, paragneiss and orthogneiss, ages of which are Neoproterozoic or younger (Parrish, 1995, and references therein). Metamorphism

reached upper amphibolite facies in the Monashee core and cover, and lower to upper amphibolite facies at higher structural levels (e.g. Journeay, 1986; Johnston et al., 2000).

The boundary between the Monashee Complex and the Selkirk Allochthon along the western flank of the Monashee Complex was thought to be a ductile thrust termed the Monashee Décollement (e.g. Read and Brown, 1981; Brown et al., 1992, and references therein). The boundary to the east between the Monashee Complex and the Selkirk Allochthon is formed by a late brittle fault, the Columbia River Fault (Fig. 1.1). Rocks of the Selkirk Allochthon were thought to have been thrust over the Monashee Complex by transport towards the NE on the Monashee Décollement (e.g. Read and Brown, 1981; Brown et al., 1992, and references therein). Recently, Williams (1999), Johnston et al. (2000), Spark (2001) and Williams and Jiang (in review) recognised a regional transposition foliation, representing NE-directed transport throughout the Monashee Complex and Selkirk Allochthon, but no localised shear zone as the Monashee Décollement. Furthermore, rocks in the Selkirk Allochthon, directly overlying the Monashee Complex at Thor–Odin, have similar lithologies and a deformational history to rocks within the Monashee Complex. Therefore, the Selkirk Allochthon may not be allochthonous with respect to the Monashee Complex and perhaps the Monashee Complex and Selkirk Allochthon need to be redefined. A detailed study involving mapping is needed to formulate new definitions. For consistency with earlier studies, the terms Monashee Complex and Selkirk Allochthon will be used as before in this study, even though the Selkirk Allochthon is not believed to be an allochthon.

Deformation in the Monashee Complex includes transposition, tight to isoclinal F_1/F_2 folds and isoclinal to open F_3 folds that indicate transport towards the NE (e.g.

Journeay, 1986; Gibson et al., 1999; Williams, 1999; Johnston et al., 2000; Crowley et al., 2001; Spark, 2001). These structures are overprinted by gentle F_4 folds. The latest deformation event in the Monashee Complex (D_5) was crustal extension as demonstrated by ductile to brittle shear bands and brittle normal faults in and around the Monashee Complex. Widespread intrusion of Eocene pegmatite and lamprophyre dykes occurred in the Monashee Complex during extension (e.g. Lane, 1984; Johnston et al., 2000).

Carr (1992), Parrish (1995, and references therein), Crowley and Parrish (1999), Gibson et al. (1999) and Crowley et al. (2001) have attempted to constrain the timing of deformation and metamorphism related to northeastward movement in the Monashee Complex and adjacent rocks. This movement may have been related to accretion of the Intermontane and Insular Superterranes. Regional compilations of U–Pb geochronological data have been interpreted as indicating a structurally downward younging of structures and thermal peak of metamorphism, from ~170 Ma in the Selkirk and Cariboo Mountains (Fig. 1.1) to ~78 Ma in the highest structural level of the Monashee Complex and to 49 Ma in the core of the complex (Parrish,1995, and references therein; Crowley and Parrish, 1999; Gibson et al., 1999; Crowley et al., 2001).

In this study, which was aimed to constrain the ages of deformation and metamorphism in Thor–Odin, this interpretation is questioned. It is demonstrated that Late Cretaceous to Early Eocene ages in Thor–Odin as well as in Frenchman Cap may be a result of extension and the presence of fluids. Hornblende may have lost Ar due to interaction with fluids, and U–Pb accessory phases (zircon, monazite, xenotime and titanite) may have grown in the presence of fluids. The actual age of Cordilleran deformation and metamorphism in the Monashee Complex may be earlier, e.g. in the

Middle Jurassic and/or mid- to Late Cretaceous, as in the rocks that overlie the Monashee Complex. The possibility exists that certain deformation and metamorphic events (e.g. Cordilleran deformation and metamorphism) are not recorded in the minerals used for dating.

Chapter 2 discusses the use and interpretation of $^{40}Ar/^{39}Ar$ inverse isochron diagrams. Principles discussed in this chapter are fundamental to the interpretation of $^{40}Ar/^{39}Ar$ data of hornblende in amphibolites from Thor–Odin dated by Spark (2001). The amphibolites were used for an oxygen and hydrogen stable isotope study (Chapter 3), which demonstrates that $^{40}Ar/^{39}Ar$ hornblende dates younger than ~75–70 Ma may be a result of partial or complete Ar loss, due to interaction between hornblende and meteoric fluids during crustal extension in Thor–Odin.

Chapter 4 demonstrates how isotopic age constraints can be derived from electron microprobe U–Th–Pb dates. The three-dimensional concordia diagram in $^{208}Pb/^{232}Th$ - $^{207}Pb/^{235}U$ - $^{206}Pb/^{238}U$ space and its projections onto the $^{206}Pb/^{238}U$ - $^{207}Pb/^{235}U$, $^{208}Pb/^{232}Th$ - $^{207}Pb/^{235}U$ and $^{208}Pb/^{232}Th$ - $^{206}Pb/^{238}U$ planes are used. An understanding of these diagrams is essential for the interpretation of SHRIMP data presented in Chapters 5 and 6. The method of electron microprobe dating is used in Chapter 6.

In Chapters 5–7, U–Pb Isotope Dilution Thermal Ionisation Mass Spectrometry (ID-TIMS) and Sensitive High Resolution Ion Microprobe (SHRIMP) data are presented for eleven samples dated in this study. Chapter 5 concentrates on Proterozoic and Eocene deformation and metamorphism in basement rocks of Thor–Odin dome, and discusses the possibility of Mesozoic Cordilleran deformation and metamorphism in the Monashee

Complex. In Chapter 6, Late Cretaceous to Early Eocene monazite and zircon ages in cover rocks of Thor–Odin are presented. The monazites contain a component of older Pb. Age constraints on deposition and deformation at Joss Mountain, west of the Monashee Complex, are presented in Chapter 7.

In Chapter 8, a model of channel flow (cf. Beaumont et al., 2001; Williams and Jiang, in review) is demonstrated to be consistent with most of the structural, metamorphic, and geochronological data in the southern Canadian Omineca Belt, including the new data presented in the preceding chapters.

References

Armstrong, R.L., Parrish, R.R., van der Heyden, P., Scott, K., Runkle, D., 1991. Early Proterozoic basement exposures in the southern Canadian Cordillera: core gneiss of Frenchman Cap, Unit I of the Grand Forks Gneiss, and the Vaseaux Formation. Canadian Journal of Earth Sciences 28, 1169–1201.

Beaumont, C., Jamieson, R.A., Nguyen, M.H., Lee, B., 2001. Mid-crustal channel flow in large hot orogens: results from coupled thermal-mechanical models. In: Cook, F., Erdmer, P. (Compilers), 2001, Slave–Northern Cordillera Lithospheric Evolution (SNORCLE) Transect and Cordilleran Tectonics Workshop Meeting (February 22–25), Pacific Geoscience Centre, Lithoprobe Report No. 79, 112–170.

Carr, S.D., 1992. Tectonic setting and U–Pb geochronology of the early Tertiary Ladybird leucogranite suite, Thor–Odin – Pinnacles area, southern Omineca Belt, British Columbia. Tectonics 11, 258–278.

Crowley, J.L., Parrish, R.R., 1999. U–Pb isotopic constraints on diachronous metamorphism in the northern Monashee complex, southern Canadian Cordillera. Journal of Metamorphic Geology 17, 483–502.

Crowley, J.L., Brown, R.L., Parrish, R.R., 2001. Diachronous deformation and a strain gradient beneath the Selkirk allochthon, northern Monashee complex, southeastern Canadian Cordillera. Journal of Structural Geology 23, 1103–1121.

Gabrielse, H., Monger, J.W.H., Wheeler, J.O., Yorath, C.J., 1991. Part A. Morphogeological belts, tectonic assemblages, and terranes. In: Gabrielse, H., Yorath, C.J. (Editors), Chapter 2 of Geology of the Cordilleran Orogen in Canada. Geological Survey of Canada, Geology of Canada no. 4, pp.15–28.

Gibson, H.D., Brown, R.L., Parrish, R.R., 1999. Deformation-induced inverted metamorphic field gradients: an example from the southeastern Canadian Cordillera. Journal of Structural Geology 21, 751–767.

Johnston, D.H., Williams, P.F., Brown, R.L., Crowley, J.L., Carr, S.D., 2000. Northeastward extrusion and extensional exhumation of crystalline rocks of the Monashee Complex, southeastern Canadian Cordillera. Journal of Structural Geology 22, 603–625.

Journeay, J.M., 1986. Stratigraphy, internal strain, and thermo-tectonic evolution of northern Frenchman Cap dome, an exhumed basement duplex structure, Omineca hinterland, southeastern Canadian Cordillera. PhD Thesis, Queen's University, Kingston, Ontario, Canada.

Journeay, J.M., Williams, S.P., 1995. Geological Survey of Canada, Open File 2948 (v. 1.0).

Lane, L.S., 1984. Deformation history of the Monashee Decollement and Columbia River Fault zone. PhD Thesis, Carleton University, Ottawa, Ontario, Canada.

Monger, J.W.H., Price, R.A., Tempelman-Kluit, D.J., 1982. Tectonic accretion and the origin of the two major metamorphic and plutonic welts in the Canadian Cordillera. Geology 10, 70–75.

Murphy, D.C., van der Heyden, P., Parrish, R.R., Klepacki, D.W., McMillan, W., Struik, L.C., Gabites, J., 1995. New geochronological constraints on Jurassic deformation of the western edge of North America, southeastern Canadian Cordillera. In: Miller, D.M., Busby, C. (Editors), Jurassic magmatism and tectonics of the North American Cordillera. Boulder, Colorado, Geological Society of America Special Paper 299, 159–171.

Parkinson, D.L., 1991. Age and isotopic character of Early Proterozoic basement gneisses in the southern Monashee Complex, southeastern British Columbia. Canadian Journal of Earth Sciences 28, 1159–1168.

Parrish, R.R., 1995. Thermal evolution of the southeastern Canadian Cordillera. Canadian Journal of Earth Sciences 32, 1618–1642.

Read, P.B., Brown, R.L., 1981. Columbia River fault zone: southeastern margin of the Shuswap and Monashee Complexes, southern British Columbia. Canadian Journal of Earth Sciences 18, 1127–1145.

Scammell, R.J., Brown, R.L., 1990. Cover gneisses of the Monashee Terrane: a record of synsedimentary rifting in the North American Cordillera. Canadian Journal of Earth Sciences 27, 712–726.

Spark, R.N., 2001. Crustal thickening and tectonic denudation within the Thor–Odin culmination, Monashee Complex, southern Canadian Cordillera. PhD Thesis, University of New Brunswick, Fredericton, New Brunswick, Canada.

Williams, P.F., 1999. Fold Nappes and the problem of model driven interpretation. Specialist Group in Tectonics and Structural Geology Field Conference, Halls Gap, Victoria, Australia (February 14–19, 1999). Geological Society of Australia Abstracts Series #53, 267–268.

Williams, P.F., Jiang, D., in review. The relationship between thrusting, nappe formation, and channel flow. An example from the Canadian Cordillera.

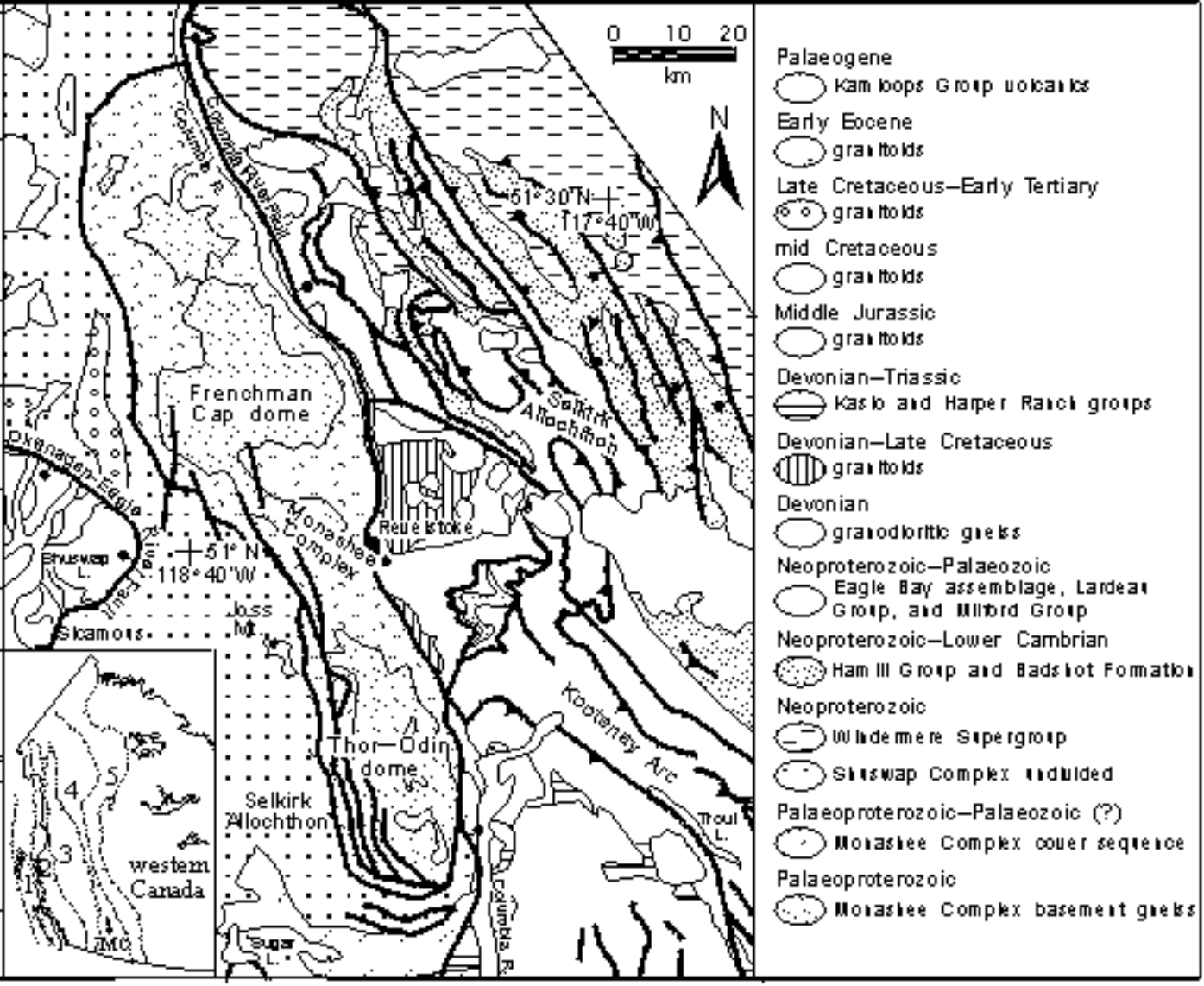

Fig. 1.1. Geological map of the Monashee Complex and surrounding geology. Modified after Wheeler and McFeely (1991). Inset: location of morphogeological belts of the Canadian Cordillera: 1. Insular Belt, 2. Coast Belt, 3. Intermontane Belt, 4. Omineca Belt, 5. Foreland Belt. MC indicates the location of the Monashee Complex.

Chapter 2

The interpretation of inverse isochron diagrams in $^{40}Ar/^{39}Ar$ geochronology[1]

Abstract

The concepts involved in the construction and interpretation of inverse isochron diagrams used in $^{40}Ar/^{39}Ar$ geochronology are reviewed. The diagrams can be useful as a means of recognising atmospheric argon and excess ^{40}Ar, incorporated in the mineral lattice, which cannot be recognised from $^{40}Ar/^{39}Ar$ spectra. The age established using an inverse isochron plot, unlike that yielded by a spectrum, is not affected by trapped argon $^{40}Ar/^{36}Ar$ ratios that are different from the atmospheric argon ratio (e.g. due to excess ^{40}Ar), and may contribute to a better age interpretation. However, a heterogeneous distribution of excess ^{40}Ar or heterogeneous argon loss can cause 'false' isochrons, with axial intercepts indicating an incorrect age and an incorrect trapped argon composition. Inconsistency between the ages from a spectrum and from the associated inverse isochron plot may indicate the degree of inaccuracy of isochrons. However, it is possible that both the spectrum and inverse isochron yield the same incorrect age. The importance of considering all possible interpretations before assigning an age to a specimen is stressed.

---

[1] Published: Kuiper, 2002, Earth and Planetary Science Letters 203, 499-506.

2.1. Definitions and introduction

2.1.1. Types of argon

In $^{40}Ar/^{39}Ar$ geochronology, there are two types of argon: radiogenic and non-radiogenic. Definitions in this section are based on those of Dalrymple and Lanphere (1969) and McDougall and Harrison (1999). *Radiogenic argon* includes ^{40}Ar accumulated from the decay of ^{40}K within the mineral or rock of interest. *Relic ^{40}Ar* is radiogenic argon that remains following a partial resetting event (e.g. by reheating), and can only in favourable cases be distinguished from radiogenic argon accumulated after re-closure (e.g. Turner et al., 1966). *Non-radiogenic argon* is argon that did not accumulate within the mineral of interest by radioactive decay of K, and comprises blank, trapped, cosmogenic and neutron-induced argon. *Blank argon* is unavoidable surficial argon introduced into the mass spectrometer with the sample. The argon ratios used in this chapter are all hypothetical, and it is assumed that they have been corrected for blank argon. *Trapped argon* is incorporated within the mineral, and can consist of atmospheric argon with or without a component of excess ^{40}Ar. *Excess ^{40}Ar* is released from older K-bearing minerals, typically during a heating event, and is subsequently trapped in the mineral of interest as it cools below its argon closure temperature. *Atmospheric argon* is argon from the Earth's atmosphere, which has an $^{40}Ar/^{36}Ar$ ratio of 295.5. In extraterrestrial samples, the 'atmospheric' argon composition commonly differs considerably. Extraterrestrial samples also contain *cosmogenic argon*, which is produced

from cosmic-ray interaction with elements such as Ca, Ti and Fe, involving spallation reactions or neutron capture (McDougall and Harrison,1999). *Neutron-induced argon* is produced during irradiation of a sample in a nuclear reactor. While ^{39}Ar is produced from ^{39}K (see Section 2.2.1), other argon isotopes are produced by neutron interactions with K, Ca and Cl (e.g. ^{40}Ar from ^{40}K, ^{36}Ar from ^{40}Ca, and ^{39}Ar from ^{42}Ca), and need to be corrected for (Roddick, 1983; McDougall and Harrison, 1999). All argon ratios used in this chapter are assumed to have been corrected. *Inherited argon* includes both radiogenic and non-radiogenic argon introduced into the mineral or rock specimen by contamination of older material (e.g. as inclusions). It involves the types of argon discussed above, and is not discussed separately in this chapter.

2.1.2. Introduction

Isochron plots and inverse isochron plots are widely used in $^{40}Ar/^{39}Ar$ geochronology. The main advantage of these plots over $^{40}Ar/^{39}Ar$ spectra is that excess ^{40}Ar, in addition to atmospheric argon, can be detected. In a step-heating spectrum, all steps are corrected for non-radiogenic ^{40}Ar, assuming that any non-radiogenic argon in the specimen has atmospheric composition. Using the atmospheric $^{40}Ar/^{36}Ar$ ratio of 295.5 (for terrestrial samples), the amount of non-radiogenic ^{40}Ar can then be calculated from the ^{36}Ar measured. The disadvantage of this method is that, where present, the additional trapped non-radiogenic ^{40}Ar (excess ^{40}Ar) cannot be detected. Consequently, after correction, all the ^{40}Ar, including the excess ^{40}Ar, is assumed to have been derived from decay of ^{40}K in the mineral, resulting in apparent ages that are too old.

Isochron plots ($^{40}Ar/^{36}Ar$ versus $^{39}Ar/^{36}Ar$) and inverse isochron plots ($^{36}Ar/^{40}Ar$ versus $^{39}Ar/^{40}Ar$) do not assume a non-radiogenic $^{40}Ar/^{36}Ar$ ratio of 295.5, and therefore they can be useful for the recognition of excess ^{40}Ar (but not relic ^{40}Ar). ^{36}Ar is the isotope present in the lowest concentrations, thus any measurement inaccuracies can introduce large errors on both axes of the isochron plot, resulting in large correlated errors (Roddick et al., 1980). Ratios calculated excluding ^{36}Ar from the nominator, as used in the inverse isochron diagram, consequently have a higher precision. Errors in the ratios also have a much smaller correlation, owing to the small fractional errors in the typically high concentrations of ^{40}Ar relative to the other isotopes (Roddick et al., 1980). The differences between isochron diagrams and inverse isochron diagrams are discussed in more detail in Roddick et al. (1980), Dalrymple et al. (1988) and McDougall and Harrison (1999). The inverse isochron diagram is generally considered more advantageous than the isochron diagram and is more commonly used. The aims of this chapter are to review the basic concepts of the inverse isochron plot and to illustrate circumstances which may lead to an erroneous interpretation of this diagram.

2.2. Concepts and laboratory artifacts

2.2.1. Concepts

In order to comprehend the inverse isochron plot, the basic concepts of $^{40}Ar/^{39}Ar$ geochronology must be understood. A detailed description of the theory and methods is

given by McDougall and Harrison (1999) and references therein. An abbreviated explanation is given here. $^{40}Ar/^{39}Ar$ geochronology is based on decay of ^{40}K to ^{40}Ar. An age can be derived from the $^{40}K/^{40}Ar$ ratio and therefore this ratio needs to be determined. In $^{40}Ar/^{39}Ar$ geochronology, ^{39}Ar is formed from ^{39}K by irradiation in a nuclear reactor. The quantity of ^{39}Ar produced is proportional to the amount of ^{39}K present in the sample. With a knowledge of the natural abundances of ^{39}K relative to ^{40}K, the amount of ^{40}K can be determined, and the $^{40}K/^{40}Ar$ ratio and age calculated. The main advantage of $^{40}Ar/^{39}Ar$ geochronology, as opposed to $^{40}K/^{40}Ar$ geochronology, is that only the argon isotopes need to be measured (as opposed to measurement of potassium and argon separately) in order to establish the $^{40}K/^{40}Ar$ ratio and age.

The data presented in an inverse isochron plot represent different temperature steps from one mineral if the step-heating method is used, or different spots within one mineral if laser-ablation techniques are used (Fig. 2.1). The locations of the data presented on this isochron depend on their ratios of trapped argon relative to radiogenic argon; measurements with a high radiogenic component plot close to the $^{39}Ar/^{40}Ar$ axis, whereas measurements with a high trapped argon component plot close to the $^{36}Ar/^{40}Ar$ axis. If the gas released is a simple two-component mixture of trapped argon and radiogenic argon, then the points are likely to be distributed along a line, and the data can be regressed and an isochron can be plotted (Fig. 2.1) (see McDougall and Harrison, 1999).

All ^{36}Ar is non-radiogenic. If the non-radiogenic argon component contains ^{36}Ar, then the age of the sample, unaffected by non-radiogenic argon, can be calculated from the intercept with the $^{39}Ar/^{40}Ar$ axis, where $^{36}Ar = 0$. However, the age can still be

affected by relic ^{40}Ar. If the ^{36}Ar concentration is very small relative to the total ^{40}Ar concentration, then data will cluster along the $^{39}Ar/^{40}Ar$ axis, and non-radiogenic ^{40}Ar cannot be distinguished from radiogenic ^{40}Ar (see also Section 2.4.2).

The intercept of the isochron with the $^{36}Ar/^{40}Ar$ axis (where $^{39}Ar = 0$) represents the hypothetical $^{36}Ar/^{40}Ar$ ratio expected in the absence of any radiogenic argon. This can be visualised as follows. In a hypothetical sample containing no K, no ^{39}Ar will be produced during irradiation and $^{39}Ar/^{40}Ar = 0$. No radiogenic ^{40}Ar will accumulate and all argon present must be non-radiogenic. This non-radiogenic argon is trapped argon, which was included in the mineral when it cooled through its argon closure temperature. Therefore, the intercept with the $^{36}Ar/^{40}Ar$ axis indicates the $^{36}Ar/^{40}Ar$ ratio of the trapped argon.

In terrestrial samples, trapped ^{40}Ar can be atmospheric and/or excess ^{40}Ar. If the intercept of the isochron with the $^{36}Ar/^{40}Ar$ axis occurs at a ratio of 1/295.5 (the composition of atmospheric argon), then all trapped ^{40}Ar has an atmospheric origin. If the $^{36}Ar/^{40}Ar$ ratio of the intercept is lower, then excess ^{40}Ar is present in addition to atmospheric argon. The presence of excess ^{40}Ar is addressed more extensively in the next section. In extraterrestrial samples, the $^{36}Ar/^{40}Ar$ ratio of 'atmospheric' argon is different from that on Earth, and cosmogenic argon may be present. The intercept of the isochron with the $^{36}Ar/^{40}Ar$ axis (unaffected by excess ^{40}Ar) may be different from the terrestrial atmospheric $^{36}Ar/^{40}Ar$ ratio. In this chapter, an atmospheric $^{40}Ar/^{36}Ar$ ratio of 295.5 is used, and absence of cosmogenic argon is assumed. For extraterrestrial samples, the intercept of the isochron with the $^{36}Ar/^{40}Ar$ axis may be different, but the principles discussed remain the same.

2.2.2. Laboratory artifacts

It is assumed that isotope ratios are correct. However, one must bear in mind that the measured isotopic ratios, and therefore the spectra and inverse isochrons, are affected by the accuracy of the applied corrections, e.g. for neutron-induced argon, recoil, and laboratory contamination (see also Harrison, 1983). For example, if only a fraction of the neutron-induced ^{36}Ar is corrected for, then the $^{36}Ar/^{40}Ar$ ratios may be systematically too high and the inverse isochron may have erroneous intercepts (an erroneously elevated initial $^{36}Ar/^{40}Ar$ ratio and lowered apparent age). Koppers et al. (2000) describe an example of recoil effects in altered seamount basalts from the western Pacific and their influence on the inverse isochron diagram. Errors in the correction for laboratory contamination may be introduced during step-heating of the sample, because the system blank is only calibrated for a certain temperature range. For the temperature steps outside this range, argon introduced from the laboratory may differ in composition from the blank correction, thus inducing systematic errors. Other artifacts may be introduced, e.g. owing to the inter-laboratory differences in error calculations and/or to uncertainties in the calculation of the value of the irradiation parameter, J (Whitehead, 1998). It is important to understand the laboratory artifacts that affect the data. However, a detailed discussion is beyond the scope of this chapter.

2.3. Homogeneous excess ^{40}Ar incorporation and argon loss

In this section the incorporation of excess ^{40}Ar and argon loss are assumed to be homogeneous within minerals, in order to simply explain the effects of these processes on data presented on inverse isochron plots. Realistic problems, including heterogeneous argon loss and excess ^{40}Ar distribution are addressed in Section 2.4.

The effect of excess ^{40}Ar on the isochron plot is depicted in Fig. 2.2a. When part of the trapped argon is excess ^{40}Ar, analyses with a component of trapped argon will have a lower ^{36}Ar/^{40}Ar ratio than when all trapped argon is atmospheric. Assuming the trapped argon/radiogenic argon ratio remains the same for all data points, all points will plot at lower ^{36}Ar/^{40}Ar values, being lowered by an amount proportional to their component of trapped argon relative to radiogenic argon (e.g. point A in Fig. 2.2a moves down farther than point B). Analyses close to the ^{36}Ar/^{40}Ar axis have a high component of trapped argon, and would therefore also contain the largest amounts of excess ^{40}Ar, if present; consequently they would be lowered more than analyses close to the ^{39}Ar/^{40}Ar axis, which contain less trapped argon. In this way, the gradient of the isochron will be lowered through the intercept, while the ^{39}Ar/^{40}Ar axis remains fixed. The intercept with the ^{36}Ar/^{40}Ar axis will become lower, and the trapped ^{40}Ar/^{36}Ar ratio higher (which reveals the presence of excess ^{40}Ar). The inverse isochron age remains unchanged despite the incorporation of excess ^{40}Ar. This is an advantage of inverse isochron plots over spectra, because the apparent ages of spectra do become older in the presence of excess ^{40}Ar. Heizler and Harrison (1988; see also McDougall and Harrison, 1999) give

examples in which the inverse isochron plot makes it possible to distinguish two compositionally distinct components of trapped argon within one mineral (i.e. by plotting two isochrons on one diagram, with the same $^{39}Ar/^{40}Ar$ intercept, but different $^{36}Ar/^{40}Ar$ intercepts). Also, they correct the spectrum steps for excess ^{40}Ar, using the trapped argon $^{36}Ar/^{40}Ar$ compositions of the isochrons on which the corresponding data points of the spectrum steps lie. In this way, uncorrected disturbed spectra can become plateaux after correction.

It is generally believed that, in nature, argon isotopes remain unfractionated during their escape from a mineral (by reheating or interaction with fluids). If this is true, then the $^{36}Ar/^{40}Ar$ ratio does not change (Fig. 2.2b) during loss. Because K is not released, the amount of ^{39}Ar that represents ^{39}K (produced in the nuclear reactor) remains unaffected by argon loss and the $^{39}Ar/^{40}Ar$ ratio increases as ^{40}Ar is lost. Consequently the gradient of the isochron will decrease while the intercept with the $^{36}Ar/^{40}Ar$ axis remains fixed. The $^{39}Ar/^{40}Ar$ axis intercept will indicate a younger apparent age. If complete argon loss occurs, then the new age indicates the timing of the end of argon loss. If argon loss is not complete, then the inverse isochron age will represent a meaningless value between that of the initial cooling event and the end of the argon loss event (see Section 2.4.3 and Fig. 2.3).

2.4. Problems and pitfalls

2.4.1. Heterogeneous excess ^{40}Ar distribution and argon loss

In this chapter, heterogeneous and homogeneous argon loss, or excess ^{40}Ar distribution, refer to changes in isotopic composition between the steps of an incremental heating spectrum. When different steps are lowered (or elevated) by various amounts, then argon loss (or excess ^{40}Ar incorporation) was heterogeneous and the spectrum is disturbed. Heterogeneity can be caused by the distribution of different argon compositions (e.g. excess ^{40}Ar, atmospheric argon and radiogenic argon) over different mineral lattice sites, which are therefore released under different conditions (during natural argon loss, or step-heating). Non-uniform relative amounts of the various types of argon in different physical locations within a mineral also cause heterogeneity. For example, a mineral rim may have more excess ^{40}Ar relative to radiogenic argon than the core, and a rim or a crack may lose a large amount of radiogenic argon relative to the core. These mechanisms result in a heterogeneous isotopic composition of the remaining argon. Heterogeneous argon loss or excess ^{40}Ar distribution do not simply refer to the variable total amounts of argon present in (or lost from) different parts of the mineral.

Phase changes take place during step-heating, which (1) affect the conditions of argon release from lattice sites, (2) can homogenise the argon isotopes within the mineral, and (3) preferentially release argon from areas in the mineral in which the phase changes take place. Therefore, the composition of the argon may be unrelated to its corresponding distribution in the original mineral, and data from temperature steps cannot simply be related to specific locations within a mineral (Lee et al., 1991; Wartho et al., 1991; Lee, 1993; Wartho, 1995).

The incorporation of excess ^{40}Ar or argon loss is commonly heterogeneous. Data points on the resulting plots usually are too scattered to define precise inverse isochrons, intercept ages or trapped argon compositions, and the spectra are commonly disturbed.

2.4.2. Location of data points on the inverse isochron plot

If all analyses from one sample have a high radiogenic argon component relative to their trapped argon component, or if the ^{36}Ar component of the trapped argon is relatively small, then the data points will cluster close to the $^{39}Ar/^{40}Ar$ intercept. In this case, although the apparent inverse isochron age will be more precisely defined, it is difficult or impossible to accurately determine the composition of the trapped argon. Furthermore, the presence of trapped argon may remain unnoticed, and the inverse isochron age may be affected by undetected excess ^{40}Ar. Conversely, if all data represent large amounts of trapped argon relative to radiogenic argon, then the points will cluster close to the $^{36}Ar/^{40}Ar$ intercept and the inverse isochron age is difficult or impossible to determine. Additionally, if the trapped argon composition is not homogenous throughout the mineral, or if argon loss occurred heterogeneously, then the data will plot with a large degree of scatter and cannot be regressed accurately. In this case, both the trapped argon composition and the intercept age become imprecise.

2.4.3. False inverse isochron plots

In some cases of argon loss or excess ^{40}Ar incorporation, data may yield 'false' plateaux and plot along a 'false' inverse isochron with meaningless intercepts. Spectra

and inverse isochron plots can even give the same incorrect age, as demonstrated below.

Argon loss within a short period of time (e.g. <20 My) after the closure of the mineral for argon could lead to false (near-)plateaux and isochron ages. For example, in Fig. 2.3, hornblende yields an apparent age from both its spectrum and its inverse isochron plot of ~61 Ma. However, the mineral may have cooled through its argon closure temperature at ~72 Ma, and subsequently lost argon at ~52 Ma. If argon loss occurs after a longer period of time after closure of the mineral for argon, false (near-) plateaux may still result if argon loss or gain is relatively homogeneous within the mineral. Similarly, excess ^{40}Ar can produce false (near-)plateaux that are older than the actual age, although generally excess ^{40}Ar does not result in older apparent inverse isochron ages, because the ^{39}Ar/^{40}Ar intercept remains the same (see also Section 2.3). False plateaux and inverse isochrons can also result from different mechanisms, e.g. mixing of two generations of minerals (Wijbrans and McDougall, 1986), or overprinting diffusion loss events (Harrison, 1983).

More complicated false isochrons can be produced in unusual cases of heterogeneous argon loss or excess ^{40}Ar incorporation. Fig. 2.4a shows a hypothetical case in which excess ^{40}Ar does not result in the expected lowering of the isochron gradient while the intercept with the ^{39}Ar/^{40}Ar axis remains fixed. Instead, regression of the disturbed data results in an ^{36}Ar/^{40}Ar intercept at the atmospheric argon composition, and in an apparent determined age from the ^{39}Ar/^{40}Ar intercept that is older than the real cooling age. In this case, the spectrum age would also be elevated. Sherlock and Arnaud (1999) describe a geological example of this from the Tavsanli Zone high-pressure metamorphic belt in northwestern Turkey.

Fig. 2.4b shows an inverse isochron plot with an apparent age younger than the real cooling age as a result of heterogeneously distributed excess ^{40}Ar. In this case, the spectrum age may still be older than the real age. However, if the excess ^{40}Ar has an excessively heterogeneous distribution within the mineral, it might not be possible to derive a (near-)plateau age and the inverse isochron age may be the only age obtainable.

Fig. 2.4c shows an inverse isochron plot displaying the effects of argon loss, but showing apparent excess ^{40}Ar. Here, the spectrum age could be the same as the isochron age, and the fact that argon loss occurred (resulting in a younger apparent age), rather than excess ^{40}Ar incorporation (which would result in an older spectrum age and an accurate isochron age), would remain unnoticed.

Examples of misleading inverse isochrons are numerous, and the interpretation of $^{40}Ar/^{39}Ar$ ages can become even more challenging when there is a complicated history with overprinting events, e.g. excess ^{40}Ar incorporation followed by argon loss. It is stressed here that the possibilities of false plateaux and inverse isochrons must always be considered carefully before a valid age interpretation can be made.

2.5. Conclusions

Inverse isochron diagrams can be useful when used in conjunction with spectra for the interpretation of $^{40}Ar/^{39}Ar$ ages. They allow the derivation of an $^{40}Ar/^{39}Ar$ age, without the assumption of a non-radiogenic $^{40}Ar/^{36}Ar$ ratio of 295.5. The $^{40}Ar/^{36}Ar$ ratio of trapped argon and the amount of excess ^{40}Ar can be determined, allowing subsequent correction of the spectra for excess ^{40}Ar. However, data can be too scattered to derive an

isochron due to heterogeneous argon loss and/or a heterogeneous non-radiogenic argon distribution. Also, if isochrons can be derived, extreme care should be taken in the interpretation of these diagrams, because false isochrons exist with erroneous intercept ages and trapped argon compositions. Comparison with spectrum ages may not indicate that the inverse isochron is false. Therefore, false isochrons may lead to incorrect age interpretations, and consequently incorrect geological interpretations. Valuable age interpretations can only be made if possibilities for false isochrons and plateaux are examined thoroughly.

Acknowledgements

I thank Paul Williams, Peter Reynolds and especially James Whitehead for critically reading earlier drafts of this chapter, and for valuable suggestions which greatly improved the manuscript. A constructive journal review by Jan Wijbrans enriched this chapter significantly. This work was supported by an NSERC grant to Paul F. Williams.

References

Dalrymple, G.B., Lanphere, M.A., 1969. Potassium–argon dating. Freeman, San Fransisco.

Dalrymple, G.B., Lanphere, M.A., Pringle, M.S., 1988. Correlation diagrams in $^{40}Ar/^{39}Ar$ dating: is there a correct choice? Geophysical Research Letters 15, 589–591.

Harrison, T.M., 1983. Some observations on the interpretation of $^{40}Ar/^{39}Ar$ age spectra. Chemical Geology 1, 319–338.

Heizler, M.T., Harrison, T.M., 1988. Multiple trapped argon isotope components revealed by $^{40}Ar/^{39}Ar$ isochron analysis. Geochimica et Cosmochimica Acta 52, 1295–1303.

Koppers, A.A.P., Staudigel, H., Wijbrans, J.R., 2000. Dating crystalline groundmass

separates of altered Cretaceous seamount basalts by the $^{40}Ar/^{39}Ar$ incremental heating technique. Chemical Geology 166, 139–158.

Lee, J.K.W., 1993. The argon release mechanisms of hornblende in vacuo. Chemical Geology 106, 133–170.

Lee, J.K.W., Onstott, T.C., Cashman, K.V., Cumbest, R.J., Johnson, D., 1991. Incremental heating of hornblende in vacuo: Implications for $^{40}Ar/^{39}Ar$ geochronology and the interpretation of thermal histories. Geology 19, 872–876.

McDougall, I., Harrison, T.M., 1999. Geochronology and thermochronology by the $^{40}Ar/^{39}Ar$ method. Oxford University Press, New York.

Roddick, J.C., 1983. High precision intercalibration of $^{40}Ar–^{39}Ar$ standards. Geochimica et Cosmochimica Acta 47, 887–898.

Roddick, J.C., Cliff, R.A., Rex, D.C., 1980. The evolution of excess argon in Alpine biotites – A $^{40}Ar–^{39}Ar$ analysis. Earth and Planetary Science Letters 48, 185–208.

Sherlock, S.C., Arnaud, N.O., 1999. Flat plateau and impossible isochrons: Apparent $^{40}Ar–^{39}Ar$ geochronology in a high-pressure terrain. Geochimica et Cosmochimica Acta 63, 2835–2838.

Spark, R.N., 2001. Crustal thickening and tectonic denudation within the Thor–Odin culmination, Monashee Complex, southern Canadian Cordillera, PhD Thesis, University of New Brunswick, Fredericton, Canada.

Turner, G., Miller, J.A., Grasty, R.L., 1966. The thermal history of the Bruderheim meteorite. Earth and Planetary Science Letters 1, 155–157.

Wartho, J.-A., 1995. Photo-emission electron microscopy (PEEM) heating investigations of a natural amphibole sample. Mineralogical Magazine 59 ,121–127.

Wartho, J.-A., Dodson, M.H., Rex, D.C., Guise P.G., 1991. Mechanisms of Ar release from Himalayan metamorphic hornblende. American Mineralogist 76, 1446–1448.

Whitehead, J., 1998. Obduction- and post-obduction-related features of the Québec Appalachian ophiolites. PhD Thesis, University of New Brunswick, Fredericton, Canada.

Wijbrans, J.R., McDougall, I., 1986. $^{40}Ar/^{39}Ar$ dating of white micas from an Alpine high-pressure metamorphic belt on Naxos (Greece): the resetting of the argon isotopic system. Contributions to Mineralogy and Petrolology 93, 187–194.

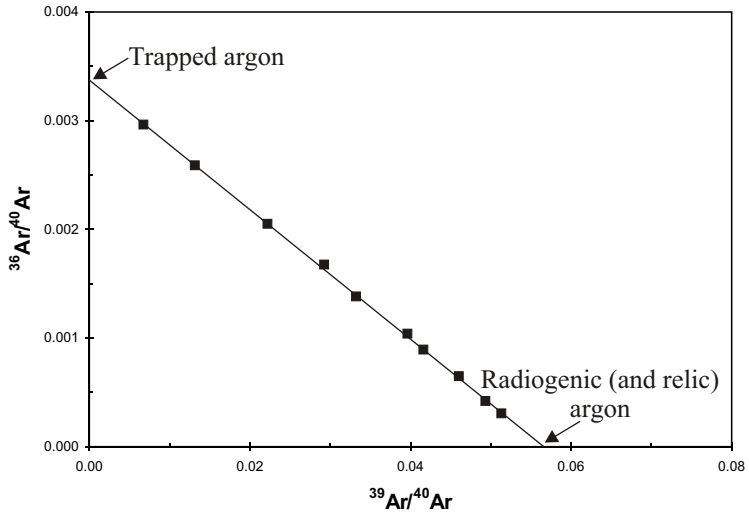

Fig. 2.1. An inverse isochron plot. The intercept with the $^{36}Ar/^{40}Ar$ axis gives the trapped argon composition. The intercept with the $^{39}Ar/^{40}Ar$ axis gives the radiogenic argon composition, from which the inverse isochron age can be calculated. All figures are corrected for blank argon.

(a)

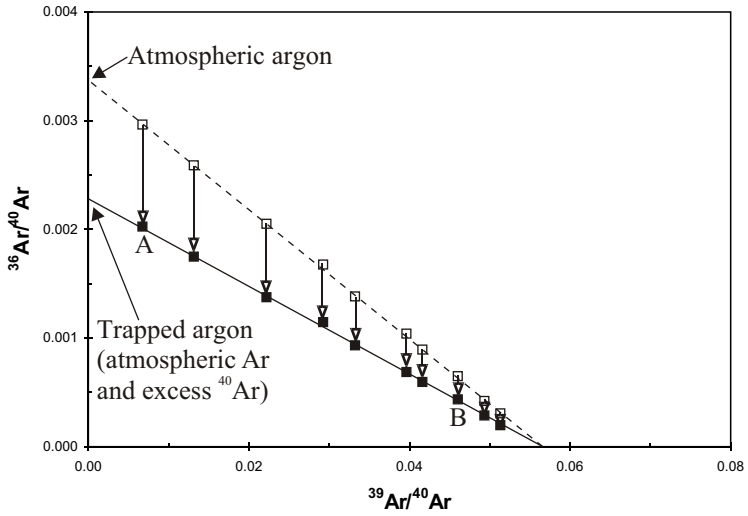

(b)

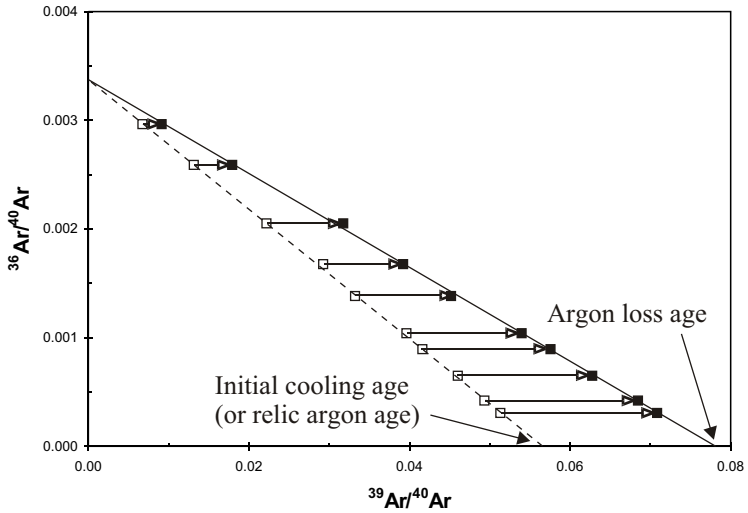

Fig. 2.2. The effects of an excess ^{40}Ar trapped argon component (a) and argon loss (b) on the inverse isochron plot. Undisturbed data are open squares and undisturbed isochrons are dashed. Solid squares and line show disturbed data and the isochron derived from those. Arrows show movement of individual data points as a result of excess ^{40}Ar (a) or argon loss (b). See text for further discussion.

(a)

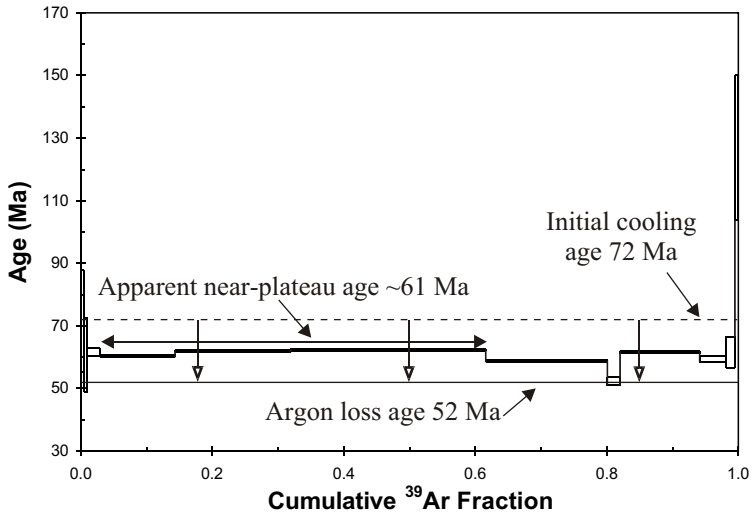

(b)

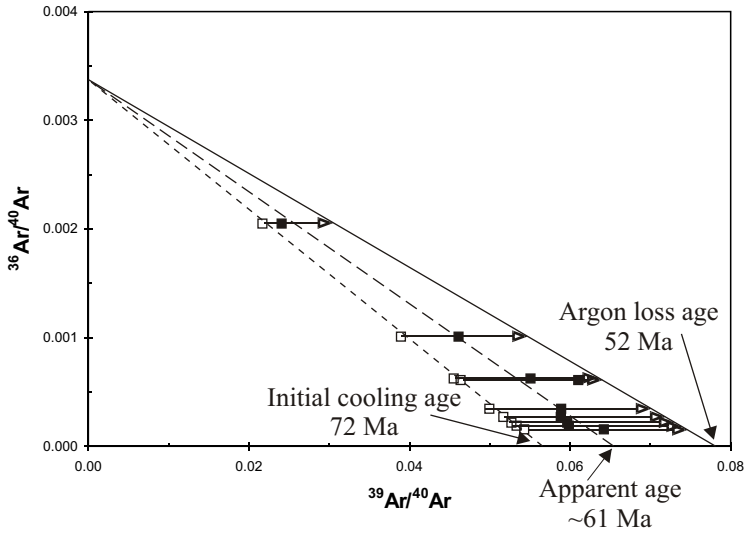

Fig. 2.3. The development of a false near-plateau (a) and isochron (b) with the same apparent age as a result of argon loss. Data from Spark (2001). The short dashed lines indicate the initial isochron and plateau as a result of cooling at 72 Ma, the long dashed line indicates the isochron as a result of partial argon loss and the solid lines indicate the isochron and plateau, which would have resulted from complete argon loss at 52 Ma. Other symbols as in Fig. 2.2.

(a)

(b)

(c)

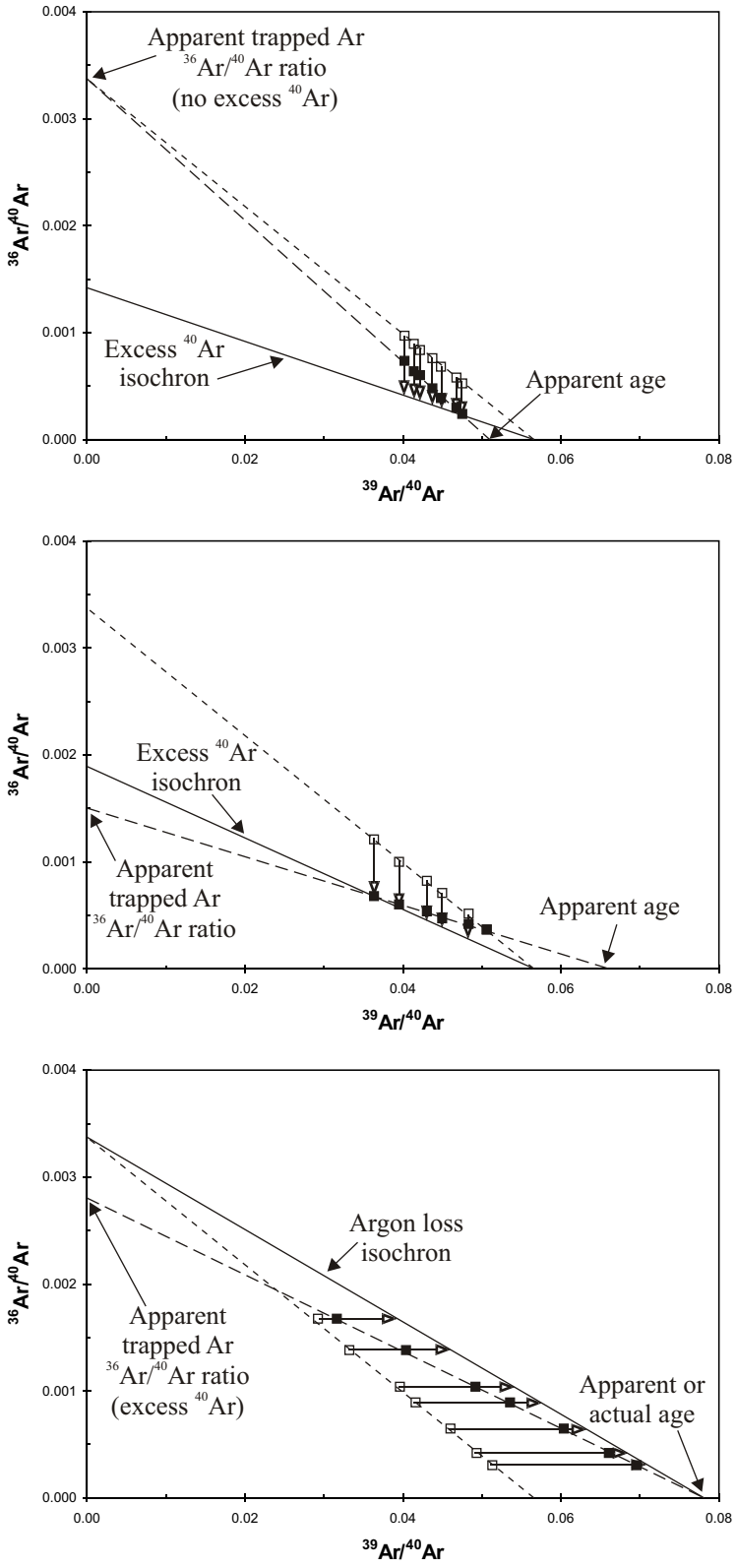

Fig. 2.4. The development of false isochrons as a result of heterogeneous excess ^{40}Ar distribution (a, b) or heterogeneous argon loss (c). Symbols as in Figs. 2.2 and 2.3.

Chapter 3

Significance of (Late Cretaceous–)Early Tertiary meteoric hydrothermal activity for the interpretation of U–Pb ages and $^{40}Ar/^{39}Ar$ (hornblende) ages in the Monashee Complex, British Columbia

Abstract

Oxygen and hydrogen isotope studies in rocks from the Monashee Complex, southeastern British Columbia, indicate water/rock interaction involving meteoric fluids, interpreted as being introduced into the rock during extension. The isotopic evidence for such interaction and the effect on $^{40}Ar/^{39}Ar$ hornblende and U–Pb monazite (and zircon, titanite and xenotime) geochronological data are evaluated in order to aid interpretation of the metamorphic and hydrothermal histories of the complex. For example, amphibolites from Thor–Odin (the southern culmination of the Monashee Complex) show a correlation between $^{40}Ar/^{39}Ar$ dates of hornblende and the amount of depletion in whole-rock ^{18}O and hornblende D. $^{40}Ar/^{39}Ar$ hornblende inverse isochron ages in Thor–Odin range between ~118 and ~51 Ma. Amphibolites with dates younger than ~75–70 Ma experienced the most ^{18}O- and D-depletion and have plateau or near-plateau $^{40}Ar/^{39}Ar$ spectra. It is argued that $^{40}Ar/^{39}Ar$ dates, younger than ~75–70 Ma, which were previously interpreted as cooling ages, resulted from complete or partial Ar loss in the presence of meteoric fluids. Because ~75–70 Ma ages are well preserved, regional cooling below the closure temperature for argon in hornblende (T_c, 530 ± 40˚C) probably happened at or before ~75–70 Ma. Amphibolites with inverse isochron ages older than ~75–70 Ma, and

generally disturbed spectra that were previously interpreted as a result of excess ^{40}Ar, are less depleted in ^{18}O and D. Hornblende inverse isochron ages of ~118 and ~51 Ma, for specimens that do not show evidence for excess ^{40}Ar, are interpreted as minimum initial cooling ages. Plateau disturbance in these samples was probably caused by Ar loss. In Thor–Odin, significant interaction with meteoric waters ended, and temperatures were below T_c, by ~51 Ma, the youngest hornblende inverse isochron age. Ar loss and hydrogen isotopic exchange in hornblende seem to be enhanced by high A-site occupancy, low Ca/K (or high K), and high Fe-number.

Monazite U–Pb ages in pelitic schist, quartzite and orthogneiss are younger than $^{40}Ar/^{39}Ar$ hornblende ages in amphibolite in northwest Thor–Odin. Therefore, monazite grew, recrystallised and/or lost Pb below the T_c of argon in hornblende. Since D-depletion was greater in samples with monazite dates younger than ~75–70 Ma than in samples with older dates, the young monazite ages probably reflect interaction between rocks and meteoric fluids below ~530˚C. Titanite, xenotime and zircon dates could possibly be interpreted the same way.

This reinterpretation of $^{40}Ar/^{39}Ar$ and U–Pb dates has major implications for the interpretation of the metamorphic and tectonic history of the Monashee Complex. U–Pb monazite (and possibly titanite, xenotime and zircon) dates previously interpreted as representing peak of metamorphism, and hornblende $^{40}Ar/^{39}Ar$ dates previously interpreted as representing cooling ages, are reinterpreted as reflecting meteoric fluid penetration of the crust during regional extension. This implies that the age of the thermal peak of metamorphism may be older than ~75–70 Ma.

This study shows that assigning a geological meaning to a geochronological data

set can be complicated, and it stresses the importance of testing various possibilities. Additional analytical methods, such as stable isotope techniques, may be helpful in determining geologically meaningful ages.

3.1. Introduction

U–Pb dating techniques have been widely used to place timing constraints on: (1) crystallisation of minerals from a magma, (2) mineral growth or Pb loss due to recrystallisation or alteration during high temperature metamorphism, and (3) maximum age of sedimentation and characterisation of provenance using detrital grains. $^{40}Ar/^{39}Ar$ and K/Ar dates are usually interpreted as reflecting the time of cooling of minerals through their respective closure temperatures of Ar. Few studies demonstrate the importance of the influence of fluids on Ar loss, Pb loss and growth of minerals used for geochronology (possibly at temperatures below the closure temperature for Pb or Ar diffusion in minerals). Criss et al. (1982) used stable isotope techniques to demonstrate that anomalously young K/Ar dates in the Idaho Batholith are mainly a result of Ar loss due to meteoric-hydrothermal alteration. Similarly, Miller et al. (1991) and Jappy et al. (2001) found, in the Dalradian rocks of Connemara in western Ireland, evidence for Ar loss related to low temperature meteoric fluid interaction and resulting K/Ar hornblende ages, younger than the youngest K/Ar muscovite and biotite ages. In the Monashee Complex, external fluids may also have had an effect on isotopic systems, and therefore on geochronological data. Stable isotope techniques are very useful for the recognition of

Tertiary to present-day meteoric waters in the Monashee Complex, because these meteoric waters have very distinct oxygen and hydrogen isotopic compositions (Taylor, 1974; Magaritz and Taylor, 1986). Magaritz and Taylor (1986) had previously shown the effect of meteoric waters on the stable isotopic compositions of rocks along major faults in southern British Columbia. The presence of metamorphic and/or magmatic and meteoric fluids, and their interaction with rocks, were demonstrated by Holk and Taylor (1997, 2000).

In this thesis, 'date' refers to the calculated result. The term 'age' is used if a meaningful interpretation of the data set is made. It may refer to: (1) a crystallisation age, (2) a cooling age representing the time the mineral passed through the closure temperature for retention of a radiogenic daughter isotope, or (3) a resetting age when the radiogenic daughter isotope was lost due to events such as recrystallisation or alteration. (See also Faure, 1986).

The aim of this study is to investigate the role of the infiltration of externally derived fluids on the $^{40}Ar/^{39}Ar$ and U–Pb geochronological systems in the Monashee Complex, and the relationship between hydrothermal meteoric alteration and geological structures. Although this study concentrates on samples from Thor–Odin, similarities exist with data from Frenchman Cap, the northern culmination of the Monashee Complex (see Section 3.2), and therefore interpretations are extrapolated throughout the Monashee Complex.

3.2. Geological setting and geochronology

The Monashee Complex (Fig. 3.1) exposes basement rocks of ancestral North America and overlying supracrustal rocks. It has two structural culminations: Frenchman Cap in the north and Thor–Odin in the south (Fig. 3.1). The Monashee Complex comprises a Palaeoproterozoic basement core of orthogneiss and paragneiss (Armstrong et al., 1991, and references therein; Parkinson, 1991) and a Palaeoproterozoic to Palaeozoic (?) cover of quartzite, marble, pelitic schist and paragneiss (Parrish, 1995, and references therein). The Monashee Complex is surrounded by the overlying rocks of the Selkirk Allochthon, which consist of quartzite, marble, paragneiss and orthogneiss, the ages of which are as old as Neoproterozoic (Parrish, 1995, and references therein). Metamorphism reached upper amphibolite facies in the Monashee core and cover, and lower to upper amphibolite facies at higher structural levels (e.g. Journeay, 1986; Johnston et al., 2000).

In earlier interpretations (cf. Brown et al., 1992, and references therein), a shear zone, the Monashee Décollement, was thought to be exposed along the western flank of the Monashee Complex, between the Monashee Complex and the Selkirk Allochthon. This shear zone was interpreted as having juxtaposed the Selkirk Allochthon and the Monashee Complex by transport of the Selkirk Allochthon towards the NE. Tight to isoclinal F_1/F_2 folds in the Monashee Complex were interpreted as being related to movement on the Monashee Décollement, and isoclinal to open F_3 and gentle F_4 folds were ascribed to separate later events. Recently, Williams (1999) and Spark (2001) recognised a regional transposition foliation, representing northeastward transport

throughout the Monashee Complex and Selkirk Allochthon, but no Monashee Décollement. Williams and Jiang (in review) propose a model of channel flow (cf. Beaumont et al., 2001) for the Monashee Complex, which explains all pre-F_4 deformation. In this model, as a result of crustal shortening, first a broad detachment zone forms in the weakest rocks of the middle crust. Subsequently, when the crust reaches a critical thickness and high temperatures are attained, the weakened rocks in this detachment zone are extruded through a horizontal channel (channel flow) (cf. Johnston et al., 2000). Detachment and channel flow, and (upper) amphibolite metamorphism, may have occurred over a long time span, perhaps between the Middle Jurassic and Late Cretaceous (cf. Kuiper et al., 2002). The latest deformation event in the Monashee Complex (D_5) was extension, as demonstrated by: (1) shear bands in and around the Monashee Complex, (2) a zone of concentrated extensional shear bands along the northwest flank of Thor–Odin (Johnston et al., 2000), and (3) brittle normal faults. Crustal extension occurred both by localised and generally large scale mechanisms (e.g. the Columbia River Fault; Fig. 3.1) and by penetrative and generally small scale mechanisms, such as shear bands and faults that occur throughout the Monashee Complex (e.g. the fault near Frigg Glacier; Section 3.4.1.2). Widespread intrusion of Eocene pegmatites occurred in the Monashee Complex during extension (e.g. Johnston et al., 2000). Additionally, some orthogneisses in the Monashee Complex have been interpreted as being Palaeocene or Eocene in age (Parkinson, 1992; Johnston et al., 2000; Carr, 2000, personal communication). Late undeformed lamprophyre dykes in the Monashee Complex are probably the same suite as Eocene lamprophyre dykes in the Kokanee Range to the south (Beaudoin et al., 1991), and are believed to be related to extension.

Two lamprophyre dykes within, and parallel to, the Columbia River Fault zone (Fig. 3.1) along the east side of the Frenchman Cap were dated at 51.1 ± 1.8 Ma and 55.3 ± 1.9 Ma (K/Ar, whole-rock; Lane, 1984). Adams et al. (in review) dated a lamprophyre dyke along the west side of the Monashee Complex, at 48.4 ± 0.3 Ma ($^{40}Ar/^{39}Ar$, muscovite in host rock).

Carr (1992), Parrish (1995, and references therein), Crowley and Parrish (1999) and Gibson et al. (1999) have attempted to constrain the timing of deformation and metamorphism related to northeastward movement in the Monashee Complex and adjacent rocks (in their models involving the supposed Monashee Décollement). Regional compilations of U–Pb geochronological data have been interpreted as indicating a younging of structures and thermal peak of metamorphism towards deeper structural levels in the Selkirk Allochthon and Monashee Complex. Monazite, zircon, titanite and xenotime dates within the Monashee Complex, which have been interpreted as metamorphic ages, range from ~78 Ma in the highest structural level (Gibson et al., 1999) to 49 Ma in the core of the complex (Crowley and Parrish, 1999). Older ages of deformation and metamorphism (as old as ~170 Ma) have been reported away from the complex, in the Selkirk and Cariboo Mountains, and are supported by interpretations based on stratigraphy and the fossil record (Parrish, 1995, and references therein). Geochronological data from western Thor–Odin could possibly be interpreted as being consistent with this same pattern (Johnson, 1994; Johnston et al., 2000; Chapters 5–7).

The Intermontane Superterrane (Fig. 3.1) has been interpreted as having accreted to the North American craton in the Middle Jurassic, and the Insular Superterrane (Fig. 3.1) in the mid-Cretaceous (Monger et al., 1982; Murphy et al., 1995). Movement

towards the NE in the Monashee Complex and surrounding areas could well have been related to accretion of the terranes (e.g. Journeay, 1986). Based on the U–Pb data described above, Carr (1992), Parrish (1995, and references therein), Crowley and Parrish (1999) and Gibson et al. (1999) interpreted deformation as having occurred diachronously, from ~170 Ma at high structural levels, to 49 Ma at the deepest levels in the Monashee Complex.

K/Ar hornblende, muscovite and biotite dates in Thor–Odin have been reported between ~105 and ~45 Ma (Lowden, 1961, 1963a, b; Wanless et al., 1978; Stevens, 1986; Armstrong et al., 1991; Hunt and Roddick, 1992), and K/Ar hornblende, muscovite, biotite, phlogopite and whole-rock dates in Frenchman Cap are between ~143 and ~40 Ma (Wanless et al., 1965, 1973, 1978, 1979; Lane, 1984; Armstrong et al., 1991). In Thor–Odin, $^{40}Ar/^{39}Ar$ hornblende dates have been recorded between ~118 and ~51 Ma (Johnson, 1994; Vanderhaeghe, 1997; Spark, 2001) and $^{40}Ar/^{39}Ar$ biotite and muscovite dates between ~55 and ~48 Ma (Vanderhaeghe, 1997). In Frenchman Cap, reported $^{40}Ar/^{39}Ar$ dates fall between ~208 and ~55 Ma for hornblende and between ~68 and ~55 Ma for biotite (Sanborn, 1996). A more extensive overview of K/Ar and $^{40}Ar/^{39}Ar$ dates in the Monashee Complex, dated prior to 1997, is given in Spark (2001). One problem, recognised by Sanborn (1996), Sanborn et al. (1999) and Spark (2001), is that $^{40}Ar/^{39}Ar$ hornblende dates, which were interpreted as representing cooling below T_c for Ar in hornblende (530 ± 40°C; McDougall and Harrison, 1999), are sometimes older than the U–Pb monazite dates from the same area, which were interpreted as representing the time of peak of metamorphism (Crowley and Parrish, 1999; Johnston et al., 2000). The interpretations of certain monazite dates in the Monashee Complex as dating the peak of

metamorphism, and of $^{40}Ar/^{39}Ar$ hornblende dates as representing cooling ages, are therefore questioned herein.

3.3. Methods and selection of samples

The amphibolites, used for stable isotope analysis (see below), occur as boudinaged, up to four metres thick, amphibolite layers throughout the Monashee Complex. During transposition, they were foliated and rotated into parallelism with the regional transposition foliation. They occur within igneous as well as metasedimentary rocks. The composition of the amphibolites varies. Some are rich in accessory biotite, garnet and/or plagioclase. Some amphibolites are isoclinally folded. In the hinge of the folds, they cut across the transposition foliation and therefore some of the amphibolites are dykes. However, generally, the origin of the amphibolites is unconstrained.

3.3.1. $^{40}Ar/^{39}Ar$ analyses

Single hornblende crystals from amphibolite samples across Thor–Odin were dated by Spark (2001) using the $^{40}Ar/^{39}Ar$ step-heating method. The data were recalculated by P.H. Reynolds and K.A. Taylor, using a revised technique for blank corrections, and are shown in Appendix I. $^{40}Ar/^{39}Ar$ spectra and inverse isochron plots were derived following standard methods (Spark, 2001). The $^{40}Ar/^{39}Ar$ amphibolite dates cannot represent igneous crystallisation ages, because the amphibolites were deformed and metamorphosed under upper amphibolite facies conditions (Spark, 2001). Sample

locations and $^{40}Ar/^{39}Ar$ spectra are shown in Fig. 3.2. To distinguish samples with different degrees of spectrum disturbance, a subdivision of the results was made based on samples with plateau-, near-plateau- and disturbed spectra. Spark (2001) used Fleck et al.'s (1977) definition of a plateau: "A plateau is that part of an age spectrum diagram composed of contiguous gas fractions that together represent more than 50% of the total ^{39}Ar released from the sample and for which no difference in age can be detected between any two fractions at the 95% confidence level." Spark (2001) used at least three fractions (or steps) to define a plateau for which each step contained more than 3% of the total ^{39}Ar released. However, there are several different definitions of a plateau (McDougall and Harrison, 1999), and different laboratories have different methods of age and error calculations. If a flat part of a spectrum, used to calculate an age, did not meet the requirements of Fleck et al. (1977), the term 'near-plateau' was used by Spark (2001), which is followed in this thesis. No age can be derived from a disturbed spectrum that is a result of excess ^{40}Ar and/or Ar loss and/or (re)crystallisation of the host grain. In this study, apparent ages from inverse isochrons are derived for samples with disturbed spectra. However, these are apparent ages rather than cooling ages, because incorporation of excess ^{40}Ar and/or Ar loss by the sample cause older and younger apparent ages, respectively. The inaccuracy of the age data is reflected in the errors in the inverse isochron ages. The dates from samples with disturbed spectra are used in this chapter, because they are older than nearly all dates derived from plateau or near-plateau spectra. Although not accurate for geochronology, incorporation of these older apparent ages in the analysis presented permits derivation of a relationship between apparent age, degree of disturbance, and interaction with fluids.

3.3.2. Oxygen and hydrogen isotope analyses

Sixteen amphibolite samples, dated by $^{40}Ar/^{39}Ar$ methods by Spark (2001), were selected for oxygen (whole-rock) and hydrogen (hornblende) isotope studies, based on a variation in apparent age, $^{40}Ar/^{39}Ar$ spectrum disturbance, and location with respect to map-scale faults and structural level (Fig. 3.2 and Table 3.1; cf. Appendix II). The purpose was to determine if fluid/rock interaction has affected $^{40}Ar/^{39}Ar$ hornblende ages. To investigate the relationship between whole-rock $\delta^{18}O$ values and distance from normal faults (which may have been the conduits for fluids), 23 samples from two orthogneisses, one quartzite and one pelitic schist, taken across normal faults, were analysed. Seven whole-rock samples from various rock-types, with known U–Pb monazite ages, were also analysed for their oxygen isotopic composition to test if externally derived fluids had affected monazite U–Pb ages. Other stable isotope data, not used for this study, are listed in Appendix III. Oxygen was extracted from whole-rock powders and from quartz and feldspar separates, using BrF_5, as described in Clayton and Mayeda (1963), and analysed as CO_2 in a Finnigan Mat 252 mass spectrometer. Hydrogen was extracted from hornblende separates (supplied by R.N. Spark) following procedures similar to those outlined by Godfrey (1962), and analysed as H_2 in a Finnigan Mat 252 mass spectrometer. Isotopic data are reported in the usual δ-notation in ‰ relative to the VSMOW standard (Coplen, 1995). Oxygen and hydrogen yields were compared to their estimated theoretical values, and some of the measurements were repeated to check for reproducibility. Whole-rock $\delta^{18}O$ analyses were routinely reproducible within 0.2‰.

The largest difference between $\delta^{18}O$ in two analyses with the same yield of one sample was 0.8‰. Hornblende δD values were reproducible within 2‰.

3.3.3. Hornblende chemical composition

The relationships between the mineral-chemical properties of hornblende (A-site occupancy, Ca/K ratio, K-content and Fe-number), and (i) hydrogen isotope exchange and (ii) Ar loss in hornblende were investigated. A-site occupancies, Ca/K ratios, K-contents, Fe-numbers and stoichiometry were calculated from Spark's (2001) microprobe analyses (averages of three analyses per sample) using the QUICK BASIC amphibole classification program 'AMPHCALC' written by James Whitehead (1997; see Whitehead, 1998). Seven amphibolite samples (RS24C, RS132A, RS133, RS138, RS212A, RS220 and RS241B) were studied in a JEOL JSM-6400 scanning electron microscope (SEM) at the University of New Brunswick for the presence of retrograde minerals within hornblende.

3.4. Results

3.4.1. Oxygen and hydrogen isotopes

3.4.1.1. Oxygen and hydrogen isotopes in amphibolites

Sample locations of amphibolites from Thor–Odin, selected for stable isotope studies, and their $^{40}Ar/^{39}Ar$ spectra are shown in Fig. 3.2. $^{40}Ar/^{39}Ar$ data, hornblende compositions and locations from Spark (2001), and $\delta^{18}O$ and δD values and thin section descriptions are given in Table 3.1. Amphibolites, selected for stable isotope studies, have hornblende inverse isochron ages that range between ~118 and ~54 Ma. The youngest hornblende $^{40}Ar/^{39}Ar$ inverse isochron age in Thor–Odin is 51.1 ± 0.7 Ma. Whole-rock $\delta^{18}O$ values are between 1.2 and 9.7‰ and hornblende δD values between -160 and -92‰.

In Fig. 3.3, δD values of hornblende separates are plotted against whole-rock $\delta^{18}O$ values of amphibolites. Also indicated, for comparison, are (1) the meteoric waterline, (2) the typical range of values for magmatic and metamorphic waters (cf. Taylor, 1974, 1986, and references therein; Sheppard, 1986, and references therein), (3) $\delta^{18}O$ and δD values of rocks that interacted with meteoric waters in the Nelson Batholith, ~60 km SSE of Thor–Odin (Magaritz and Taylor, 1986), and (4) the range of $\delta^{18}O$ values of metamorphic rocks interpreted as having equilibrated with metamorphic fluids in Thor–Odin (Holk and Taylor, 1997, 2000). The amphibolite data compare reasonably well with the δ-values of Magaritz and Taylor (1986) of rocks inferred to have interacted with meteoric waters. All amphibolites analysed in this study have been depleted in D and ^{18}O by meteoric waters, also by isotopic exchange with meteoric waters. Moreover, amphibolites with plateau and near-plateau $^{40}Ar/^{39}Ar$ spectra are generally more depleted than samples with disturbed spectra.

Whole-rock $\delta^{18}O$ values of amphibolites and δD values of hornblende separates, when plotted against the $^{40}Ar/^{39}Ar$ inverse isochron ages (Fig. 3.4), indicate that, generally, amphibolites with dates younger than ~75–70 Ma and plateau or near-plateau spectra underwent the greatest depletion of ^{18}O and D. Samples RS212A and RS131 have the oldest ages (~72 Ma) within this group. The samples with older dates and disturbed spectra, show less depletion in ^{18}O and D. Isotopic depletion does not appear to be related to present elevation, proximity to map-scale faults, or structural level (within Monashee basement, cover, or Selkirk Allochthon; see Table 3.1 and Fig. 3.2). Also, no relationship is apparent between $\delta^{18}O$, and mineralogical composition and grain size of the amphibolite or thin section-scale veins and fractures in the sample (Table 3.1).

3.4.1.2. Oxygen isotopes in other rock types near faults

Various rock types were sampled across late N–S-trending steep faults, to examine the relationship between ^{18}O depletion and the faults. Fig. 3.2a shows the location of the faults, and Table 3.2 records the $\delta^{18}O$ values and the sample distances from faults. Whole-rock analyses of a coarse-grained hornblende–biotite leucogranitic orthogneiss, collected near Frigg Glacier in southern Thor–Odin, show ^{18}O depletion within the fault zone (s298-212C, E; $\delta^{18}O \approx 5.0–5.5‰$) relative to rocks away from the fault (general values for $\delta^{18}O \approx 7.1–7.5‰$). The easternmost sample shows ^{18}O depletion (s298-212M; $\delta^{18}O = 2.3‰$) and unlike the other samples, it contains veins of chlorite (Table 3.2). Isotopic depletion of this sample was probably related to a minor fault beyond the end of the section, where the outcrop ended in a linear depression typical of

the fault lineaments. Whole-rock $\delta^{18}O$ values were also measured for samples of a quartzite, a pelitic schist and a hornblende orthogneiss, at various distances from a fault at Grizzly Flats in northwest Thor–Odin (Table 3.2). Quartz and feldspar from the hornblende orthogneiss were analysed separately, because of their different rates of oxygen isotope exchange with fluids (e.g. Criss and Taylor, 1983). In the quartzite, whole-rock depletion of ^{18}O only occurred close to the fault (s298-231A; $\delta^{18}O \approx 9.0‰$, whereas in other samples $\delta^{18}O \approx 11.8–13.2‰$). Oxygen isotope depletion in the pelitic schist and in the hornblende orthogneiss does not seem to be related to distance from the fault zone. The reason is probably that mica and feldspar in pelitic schist, and biotite and feldspar in hornblende orthogneiss, exchange oxygen isotopes more readily than quartz in quartzite (Faure, 1986, p. 467). Summarising, the data from the orthogneiss across the Frigg Glacier Fault, and from the quartzite along the Grizzly Flats Fault, indicate that ^{18}O depletion is spatially related to brittle faults.

3.4.2. Argon data

3.4.2.1. $^{40}Ar/^{39}Ar$ spectrum disturbance

The MSWD (mean squares of weighted deviates; a goodness-of-fit parameter) of an inverse isochron is a measure of the degree of scatter of data around the inverse isochron, and roughly relates to the degree of spectrum disturbance. Commonly, spectrum disturbance is also expressed as large errors in inverse isochron ages. In Fig.

3.5, the MSWD of the inverse isochron is plotted against the $^{40}Ar/^{39}Ar$ inverse isochron age (see also Spark, 2001). Amphibolites with $^{40}Ar/^{39}Ar$ inverse isochron ages younger than ~75–70 Ma all have plateau or near-plateau spectra, and the MSWD on their isochron is relatively small (<6.5). These amphibolites also underwent the most extensive oxygen and hydrogen isotope depletion (see Section 3.4.1). All amphibolites with disturbed spectra have $^{40}Ar/^{39}Ar$ inverse isochron ages older than ~75–70 Ma, and a relatively high MSWD on their inverse isochron. They are less depleted in heavy isotopes. Sample RS241B is an exception to this pattern, having a near-plateau age of 86.5 ± 0.5 Ma and an inverse isochron age of 88.9 ± 1.3 Ma. The latter is considered reliable, because of its low MSWD (2.4) on the inverse isochron. Therefore, this amphibolite is an exception in that it is older than ~75–70 Ma, but does not have a disturbed spectrum. The sample underwent marked hydrogen isotope exchange, but only a small degree of oxygen isotope exchange, with meteoric waters ($\delta D = -136‰$ and $\delta^{18}O = 5.9‰$).

In general, these results indicate that young $^{40}Ar/^{39}Ar$ dates (<~75–70 Ma) and low degrees of plateau disturbance are related to a high degree of isotopic exchange with meteoric waters, and that $^{40}Ar/^{39}Ar$ dates older than ~75–70 Ma and plateau disturbance are associated with lesser degrees of interaction with meteoric waters. $^{40}Ar/^{39}Ar$ hornblende data of Sanborn (1996) and Vanderhaeghe (1997) show similar trends; older samples have more disturbed spectra.

3.4.2.2. Excess ^{40}Ar and Ar loss

Spectrum disturbance can be caused by either excess ^{40}Ar incorporation (resulting in an older apparent inverse isochron age) or Ar loss (resulting in a younger apparent inverse isochron age). The initial $^{40}Ar/^{36}Ar$ ratio in a mineral, which can be derived from an (inverse) isochron plot, can be indicative of the presence or absence of excess ^{40}Ar (McDougall and Harrison, 1999, and references therein). Fig. 3.6 shows the relationship between the initial $^{40}Ar/^{36}Ar$ ratios and the $^{40}Ar/^{39}Ar$ inverse isochron ages. The initial $^{40}Ar/^{36}Ar$ ratio represents the isotopic ratio of argon trapped in the hornblende before the system closed to argon loss. If this ratio is 295.5, then all trapped argon was atmospheric in origin. If the ratio is higher, it means that an additional component (i.e. excess) of ^{40}Ar was trapped (McDougall and Harrison, 1999, and references therein). This excess ^{40}Ar is radiogenic in origin and is assumed to have been derived from older minerals that have degassed (e.g. during reheating). $^{40}Ar/^{36}Ar$ ratios lower than 295.5 are theoretically impossible, because ^{40}Ar cannot be lost in preference to ^{36}Ar and relatively no more ^{36}Ar than ^{40}Ar can be gained. Despite the relatively large mass differences between the Ar isotopes, fractionation between argon isotopes is generally believed not to occur, because argon is an inert gas. ^{36}Ar, which is only atmospheric in origin, cannot be gained without gaining ^{40}Ar, because there is also ^{40}Ar in atmospheric argon. Therefore, $^{40}Ar/^{36}Ar$ ratios (or error ellipses in Fig. 3.6) that are below 295.5 must indicate one or more factors (e.g. inaccuracy of the correction for neutron-induced argon, recoil effects, or fractionation during mass spectrometry) that are not, or not completely, corrected for. Since the nature of these factors is unknown, correction is not possible. However, because all of the smallest ellipses (samples RS24C, RS133, RS244, RS128, RS132C, RS212A, RS241B)

plot only slightly below 295.5 (not below 285), all $^{40}Ar/^{36}Ar$ ratios should probably be only slightly higher (by an amount that may be different for each sample). Because the difference would be small, in this chapter ratios (or error ellipses) lower than 295.5 are interpreted in the same way as ratios of ~295.5.

Fig. 3.6 shows four samples (RS120, RS218, RS220 and RS226) with disturbed spectra (see Table 3.1 and Fig. 3.2b), which have $^{40}Ar/^{36}Ar$ ratios completely or mostly above 295.5 (including their errors), suggesting the presence of excess ^{40}Ar. Two other samples (RS130 and RS138; see Table 3.1 and Fig. 3.2b) have $^{40}Ar/^{36}Ar$ ratios $\leq$295.5. Sample RS206 has yielded the youngest date in Thor–Odin (51 Ma), and has excess ^{40}Ar in the lowest two T-steps (see spectrum in Fig. 3.2a), probably derived from the outer rims of the hornblende. The sample differs from all other samples with excess ^{40}Ar in that its spectrum is not disturbed and its apparent age is younger than ~75–70 Ma. Other samples with plateau or near-plateau spectra, and dates younger than ~75–70 Ma, do not show evidence for excess ^{40}Ar (Fig. 3.6).

3.4.3. Relationships between hornblende chemical composition and (i) $^{40}Ar/^{39}Ar$ age and (ii) hydrogen isotopic composition

Hornblende (Na+K) A-site occupancies, Ca/K ratios, K-contents and Fe-numbers were plotted against δD values and $^{40}Ar/^{39}Ar$ ages (Figs. 3.7, 3.8; data in Table 3.3). A weak relationship exists between decreasing inverse isochron ages and increasing A-site occupancies (Fig. 3.7a). Inverse isochron ages also seem to decrease with lower Ca/K ratios, higher K-contents and higher Fe-numbers (Fig. 3.7b–d). A negative correlation

appears to exist for decreasing δD values with increasing A-site occupancies, and to a lesser degree with increasing Fe-numbers (Fig. 3.8a, d). Decreasing δD values may also be correlated with decreasing Ca/K ratios, and increasing K-contents (Fig. 3.8b, c), although such trends are not apparent. However, such trends are to be expected if inverse isochron ages decrease with decreasing δD values, and with decreasing Ca/K ratios and increasing K-contents. High (Na+K) A-site occupancies and low Ca/K ratios are largely a result of high K, and to a lesser extent of high Na and low Ca respectively (not shown). Relationships between any other combination of the parameters were not found, and are therefore not shown. Taking all data together, inverse isochron ages and δD values seem to decrease with increasing A-site occupancies, decreasing Ca/K ratios (or increasing K), and increasing Fe numbers (and therefore decreasing Mg numbers).

Equilibrium hydrogen isotope fractionation factors between hornblende and water (α) were calculated from fractions of Fe, Mg and Al in the octahedrally coordinated sites in hornblende, assuming certain temperatures (400, 450 and 500°C; Table 3.4), using the experimentally-determined fractionation equation of Suzuoki and Epstein (1976). The selected temperatures are below T_c of argon in hornblende, yet above the critical point of water. δD values of meteoric waters were calculated (Table 3.4) assuming equilibrium was reached. The most representative samples for equilibrium of hydrogen isotopes between hornblende and meteoric water are probably RS132A, RS133 and RS212A, which have the lowest hornblende δD values. The meteoric waters that would have equilibrated with the hornblende samples at 400°C, would have δD values of ~–110‰, which compare well with values calculated by Magaritz and Taylor (1986) for pristine

meteoric waters (δD≈−115‰) that caused D-depletion in rocks of the Nelson Batholith. The fraction of Fe in the octahedrally coordinated sites in hornblende increases and that of Mg decreases with decreasing δD values for hornblende (see average values in Table 3.4) and thus with decreasing $^{40}Ar/^{39}Ar$ inverse isochron ages, which is consistent with the trends described above. Furthermore, α increases with decreasing $^{40}Ar/^{39}Ar$ inverse isochron ages and decreasing δD values (see Tables 3.1, 3.4).

3.4.4. SEM results

No relationship has been found between the amount of retrogression of the amphibolites recognisable on the SEM, and either the $^{40}Ar/^{39}Ar$ inverse isochron ages or the oxygen and hydrogen isotopic compositions. For example, Sample RS24C, one of the samples with the lowest $^{40}Ar/^{39}Ar$ inverse isochron ages and with the most oxygen and hydrogen isotopic exchange (Table 3.1, Fig. 3.4), shows negligible alteration. The only alteration mineral present is actinolite in <2% of the grains (Fig. 3.9a). Furthermore, no alteration is present along the grain boundaries (Fig. 3.9b). The samples that show some alteration do not necessarily have lower $^{40}Ar/^{39}Ar$ inverse isochron ages and/or $\delta^{18}O$ and δD values. For example, sample RS138, the sample with the highest $^{40}Ar/^{39}Ar$ inverse isochron age and moderate depletion in ^{18}O and D, shows some retrograde chlorite and titanite along grain boundaries, and some low-Al and low-K domains (towards actinolitic composition; cf. Leake et al., 1997) within the hornblende (Fig. 3.10). Sample RS241B, the sample with the oldest age (~89 Ma) and a near-plateau spectrum, does not show alteration except for a few Al- and K-poor domains (Fig. 3.11) and a few chlorite grains

along grain boundaries. Because little alteration is present, and because no relationship is apparent between alteration and $^{40}Ar/^{39}Ar$ inverse isochron ages and/or $\delta^{18}O$ and δD values, it is considered unlikely that alteration has played a major role in Ar loss and/or oxygen and hydrogen isotopic exchange.

3.5. Discussion

Evidence from this study for the interaction between meteoric waters and rocks, and its consequent influence on $^{40}Ar/^{39}Ar$ and U–Pb ages, bears directly on the interrelationship between crustal scale extension and hydrology in the Monashee Complex. Together, the stable isotope and $^{40}Ar/^{39}Ar$ data are of significance to the timing of extension-related penetration of meteoric waters into the crust and, possibly, for the thermal history of the crust in relationship to T_c for argon in hornblende. The effect of meteoric waters both on the original hydrogen composition and on Ar loss of hornblende is evidently influenced by the chemical composition of hornblende.

3.5.1. Extension and infiltration of meteoric fluids

Magaritz and Taylor (1986) carried out an oxygen and hydrogen isotope study across the southern Canadian Cordillera, showing that δD values in batholiths are systematically lower towards the east, consistent with interaction of these rocks with fluids with a composition similar to that of present-day meteoric water. Meteoric waters are more depleted in heavy isotopes with increasing latitude, elevation and distance from the coast,

and in the Monashee Complex meteoric waters are isotopically very light (δD ≈–130‰ and $\delta^{18}O$ ≈–17.5‰, see Magaritz and Taylor, 1986). Extreme depletion of ^{18}O and D in the rocks, which typically have $\delta^{18}O$ and δD values between ca. –5 and 10‰, and –165 and –95‰, respectively (Magaritz and Taylor, 1986; Beaudoin et al., 1992b; Holk and Taylor, 1997, 2000), is diagnostic of their previous interaction with these waters. In the Monashee Complex, the lowest $\delta^{18}O$ values are found in feldspar separates from various rock types (–4.0‰, Holk and Taylor, 1997, 2000; –5.4‰, this study, Table 3.1). The lowest δD value is –160.0‰ (in hornblende, this study, Table 3.1). Magaritz and Taylor (1986) also concluded that in the Nelson Batholith depletion in D occurred either close to Tertiary (Coryell porphyry) intrusions, or along the edges of one of the large, narrow, north-trending lakes (a lineament direction known to be associated with faulting in the region). Criss et al. (1982) found a similar relationship between whole-rock depletion in ^{18}O and D in the Jurassic Idaho Batholith and sample proximity to Eocene intrusions within the batholith. Also, K/Ar dates in isotopically depleted parts of the batholith are as young as Late Eocene, presumably due to Ar loss. K/Ar dates were also dependent on elevation and location, interpreted as reflecting later cooling at deeper structural levels due to regional uplift and gentle doming of the area (Criss et al., 1982). However, rocks from lower elevations, with younger K/Ar dates, were sampled in valleys, which commonly follow major linear or ring faults (R.E. Criss, 2002, personal communication). Therefore, similar to $^{40}Ar/^{39}Ar$ dates in Thor–Odin (see below), young K/Ar dates for the Idaho Batholith could be (partly) a result of Ar loss due to meteoric hydrothermal activity along faults. In Thor–Odin, however, no relationship seems to exist between the date of a

sample and its elevation or location (see Section 3.4.1.1).

Extension is the youngest deformation event in the Monashee Complex, and postdates at least four generations of folding, and regional transposition (Section 3.2). Extension has been interpreted previously as having occurred between ~60 and 50 Ma (Parrish et al., 1988; Carr, 1992; Vanderhaeghe et al., 1999). From the previous discussion of the correlation between decreasing $\delta^{18}O$ values and decreasing distances between samples and faults (Section 3.4.1.2), it can be concluded that ^{18}O depletion, caused by water/rock interaction with isotopically light meteoric fluids, is probably related to movement along brittle normal faults in Thor–Odin (comparable to the interpretation of Magaritz and Taylor, 1986, for samples from the Nelson Batholith). If meteoric waters started interacting with the crust at or before ~75–70 Ma (see Section 3.5.2.1), then extension also started at this time, which is earlier than the ~60 Ma previously proposed (Parrish et al., 1988; Carr, 1992; Vanderhaeghe et al., 1999).

Holk and Taylor (2000) have recognised the interaction between rocks and meteoric waters in Thor–Odin. They interpreted influx of meteoric waters as having occurred along an inferred imbricate thrust zone on the SW side of Thor–Odin, which was thought to be part of the Monashee Décollement. However, it is more likely that fluid infiltration was related to regional extensional faulting than to movement on the supposed Monashee Décollement, for several reasons: (1) As explained in Section 3.2, in recent studies, the Monashee Décollement is not recognised in Thor–Odin. The interpreted position of the Monashee Décollement coincides with several lineaments (P.F. Williams, 2002, personal communication), at least one of which is known to be a major fault. (2) Depletion of ^{18}O and D does not seem to be constrained to the interpreted

position of the Monashee Décollement. Infiltration of fluids along normal faults (as interpreted above), which occur throughout the Monashee Complex, explains the wider distribution of depleted rocks. (3) Ductile thrusting would not provide the space and the downward suction for fluids, that normal faulting would accomplish. Instead, a fluid overpressure would exist and fluids would move up (Beach and Fyfe, 1972; Etheridge et al., 1983, and references therein).

The enhancement of fluid-rock interaction by regional normal faulting has been demonstrated by Singleton and Criss (2002) in the Comstock Lode mining district of Nevada. Depletion in ^{18}O occurs there within >200 m wide zones centred on normal faults. Eocene intrusions, present in the Monashee Complex (see Section 3.2), may have played a role in the circulation of fluids. Criss et al. (1982, 1991), Criss and Taylor (1983) and Magaritz and Taylor (1986) proposed that the thermal energy of the Eocene plutons drove the circulation of fluids through the Idaho and Nelson batholiths. In their models, part of the meteoric fluids, mixed with fluids derived from the upper crust and lower crust, and possibly with CO_2 from the mantle (Beaudoin et al., 1992a, b), moved upward along normal faults.

3.5.2. Argon and hydrogen systematics in hornblende

Argon is retained in a hornblende when the crystal cools below T_c (530 ± 40°C, McDougall and Harrison, 1999) and when the crystal remains a closed system. Although T_c is dependent on composition or ionic porosity (Dahl, 1996), for hornblende compositions in the Monashee Complex (cf. Johnson, 1994; Sanborn, 1996; Spark, 2001)

and reasonable cooling rates (1–100˚C/Ma), a T_c of 530 ± 40°C is an acceptable estimate (Dahl, 1996). If actinolite is present, or if the hornblende composition altered towards actinolitic composition (cf. Section 3.4.4), then the T_c is lower, which makes the conclusions of this chapter stronger. The system (hornblende) can be reopened by raising the temperature above T_c. One other mechanism of reopening the system is by exposing the crystal to fluids, even at temperatures below T_c. It is presumed that the system re-closes, and that argon starts accumulating again, when the temperature cools below T_c, or when fluid/rock interaction ceases (e.g. because the fracture, which formed the conduit for the fluid, closes). Thus $^{40}Ar/^{39}Ar$ hornblende dates may record the age of cooling below T_c (cooling age), or the age of cessation of interaction with fluids (see also Criss et al., 1982; Miller et al., 1991; Jappy et al., 2001). A meaningless intermediate age (and/or disturbed spectra) results if the system was temporarily reopened and loss of previously accumulated argon was incomplete (McDougall and Harrison, 1999, and references therein; Kuiper, 2002).

In this section, data for samples with dates older than ~75–70 Ma are discussed separately from data for samples with dates younger than ~75–70 Ma, because all plateau or near-plateau age data are ~75–70 Ma or younger (with the exception of RS241B), whereas all samples with disturbed spectra have inverse isochron ages of ~75–70 Ma and older. In general, samples younger than ~75–70 Ma underwent greater oxygen and hydrogen isotopic exchange than samples older than ~75–70 Ma.

3.5.2.1. Amphibolites with plateau and near-plateau spectra, and apparent ages younger than ~75–70 Ma

As discussed in Section 3.4.2.1, the amphibolites with plateau or near-plateau ages younger than ~75–70 Ma generally have $\delta^{18}O$ and δD values indicating interaction with meteoric waters, and they lack evidence of excess ^{40}Ar. These dates are interpreted as a result of Ar loss caused by hydrothermal alteration at temperatures below T_c, in the presence of meteoric water. Ar loss in Thor–Odin would then have started before ~75–70 Ma and continued until at least ~51 Ma, the youngest $^{40}Ar/^{39}Ar$ hornblende date (if Ar loss was incomplete, then Ar loss may have stopped after, and not at, ~51 Ma). Hornblende $^{40}Ar/^{39}Ar$ dates between ~75–70 Ma and ~51 Ma could therefore indicate the earliest ages of argon closure after interaction with fluids. It is inferred that cooling below T_c probably happened at or before ~75–70 Ma, because ~75–70 Ma dates are well preserved (samples RS212A, RS131, RS51B, RS129 and RS226). Preservation of the ~75–70 Ma dates would not be expected if the hornblende was still above T_c, or experienced reheating, after ~75–70 Ma.

Depletion of ^{18}O and D in amphibolites that show little or no disturbance of the $^{40}Ar/^{39}Ar$ spectra for hornblende can be explained either if no Ar loss, or if complete Ar loss, occurred. Assuming hydrogen and oxygen isotopic exchange in a hornblende does not occur faster or earlier than Ar loss, complete Ar loss by interaction with meteoric waters probably occurred in samples RS212A and RS131 (the samples with the oldest dates, which experienced extreme depletion in D and/or ^{18}O; see Section 3.4.1.1.) by ~75–70 Ma. Taken together, the stable isotope and $^{40}Ar/^{39}Ar$ data suggest that interaction with meteoric fluids started before ~75–70 Ma. It may have ceased locally as early as

~75–70 Ma, but continued in other places until, at least, ~51 Ma. Because interaction with meteoric fluids is probably related to normal faults (Section 3.5.1), transient fracturing and closure of fractures probably occurred at least between ~75–70 and ~51 Ma, varying randomly with locality, so that individual hornblende specimens had different water/rock reaction histories of opening and closing of the system. Significant interaction with meteoric waters had ceased, and temperatures were below T_c for hornblende, by ~51 Ma.

3.5.2.2. Amphibolites with disturbed spectra, and apparent ages older than ~75–70 Ma

Incorporation of excess ^{40}Ar was probably one of the causes of spectrum disturbance in the four samples with $^{40}Ar/^{36}Ar$ ratios above 295.5 (RS120, RS218, RS220 and RS226; see Section 3.4.2.2). Disturbance in samples with $^{40}Ar/^{36}Ar$ ratios of (or below) ~295.5 (RS130 and RS138; see Section 3.4.2.2) cannot be attributed to excess ^{40}Ar, and therefore must be a result of Ar loss only. This means that hornblende in these amphibolites accumulated radiogenic ^{40}Ar before the time indicated by their apparent ages (~86 and ~118 Ma for samples RS130 and RS138 respectively), and that therefore their apparent ages are minimum (initial) ages. These initial ages could be a result either of cooling below T_c, or of some other mechanism (e.g. fluid activity or (re)crystallisation) at temperatures below T_c, which implies that cooling below T_c occurred even earlier. Therefore, (initial) hornblende cooling ages older than ~75–70 Ma exist in Thor–Odin. Histories involving both Ar loss and incorporation of ^{40}Ar in the same specimen are also possible.

Partial Ar loss, causing plateau disturbance in samples with dates older than ~75–70 Ma, may have occurred by either of two mechanisms: (1) hornblende cooled below T_c before ~75–70 Ma, but was reheated and cooled again below T_c by ~75–70 Ma (the youngest inverse isochron age of samples with disturbed spectra), and/or (2) partial Ar loss was caused by the same meteoric fluids that caused Ar loss in the amphibolites younger than ~75–70 Ma. However, the hornblende crystals that are older than ~75–70 Ma did not lose all their argon, like some of the younger ones, and the amphibolites did not become as depleted in D and ^{18}O as the younger samples.

3.5.2.3. Indications of pre-~75–70 Ma cooling ages in Thor–Odin

Cooling in parts of Thor–Odin may have first occurred in the Early Cretaceous or earlier, and in other parts at ~89 Ma (mid-Cretaceous). Spectrum disturbance in sample RS138 was probably caused by Ar loss, because there is no evidence of excess ^{40}Ar ($^{36}Ar/^{40}Ar = 249 \pm 41$). Regardless of the mechanism of Ar loss, the apparent age of ~118 Ma would then be a minimum (initial) cooling age, because radiogenic argon must have accumulated before Ar loss could have taken place.

Three amphibolites from Thor–Odin with apparent ages of ~89 Ma suggest that this age may record an initial cooling age. Sample RS241B does not contain excess ^{40}Ar (initial $^{40}Ar/^{36}Ar = 281 \pm 5$). Its near-plateau argon spectrum, inverse isochron with a MSWD of 2.4, and similarity of inverse isochron age and near-plateau age (~89 Ma, Section 3.4.2.1) all suggest that Ar loss is unlikely. The sample is one of the two coarsest-grained samples analysed for $^{40}Ar/^{39}Ar$ geochronology (Table 3.1). It does not

show considerable retrograde metamorphism (Section 3.4.4; Fig. 3.11). Because sample RS241B does not show much alteration, the ~89 Ma date could represent a cooling age. Sample RS130 has an inverse isochron age of 86.3 ± 1.5 Ma. The MSWD on the inverse isochron is low (7.6) and the sample does not show evidence of excess ^{40}Ar ($^{40}Ar/^{36}Ar$ = 262 ± 22), although the spectrum is disturbed. This amphibolite underwent less extensive hydrogen and oxygen isotope exchange than sample RS241B (δD = –92.5‰ and $\delta^{18}O$ = 6.6‰). Sample RS218 has an inverse isochron age of 89.1 ± 3.7 Ma and a disturbed spectrum (MSWD on the inverse isochron = 58; $^{40}Ar/^{36}Ar$ = 371 ± 48; δD and $\delta^{18}O$ were not measured). These three samples suggest that apparent ages of ~89 Ma may be real and record an initial cooling age, in spite of evidence for weak water/rock interaction. If Ar loss did occur in these samples, then (initial) cooling below T_c must have happened before ~89 Ma. In any case, samples RS241B and RS130 do not show evidence for excess ^{40}Ar and therefore ~89 Ma is interpreted here as a minimum cooling age for parts of Thor–Odin.

3.5.2.4. The influence of hornblende chemical composition on argon loss and hydrogen isotopic exchange

The association of young $^{40}Ar/^{39}Ar$ inverse isochron ages and low δD values shown in this study (Fig. 3.4) indicates that processes of stable and radiogenic isotope alteration may be interrelated during water/rock interaction involving, in this case, meteoric waters. Further, the data (Figs. 3.7, 3.8; Tables 3.1, 3.3; see Section 3.4.3) suggest that Ar loss and hydrogen isotope exchange seem to be associated with high A-

site occupancy, low Ca/K (or high K) and high Fe number (=Fe^{2+}/(Fe^{2+}+Mg)) (and therefore low Mg).

Similar conclusions, based on studies of Dalradian rocks of Connemara, western Ireland, were reached by Miller et al. (1991) and Jappy et al. (2001). They also found a correlation between Ar loss in hornblende and hydrogen isotope exchange, which were both related to interaction with meteoric waters. Miller et al. (1991) concluded that hydrogen isotope exchange was related to a low A-site occupancy and to high structural water content in the hornblende, and they argued that excess water (as H_3O^+) replaced radiogenic argon in the A-site during hydrogen isotope exchange, causing Ar loss at temperatures below T_c. This was thought to explain apparent ages of hornblende younger than those of muscovite and biotite. Jappy et al. (2001) concluded that both Ar loss and hydrogen isotope exchange were facilitated by high ionic porosity in hornblende (cf. Dahl, 1996), which was related to low Mg and high Fe, Na, and especially to high K. In this study, a similar trend between Ar loss and hydrogen isotopic exchange, and high K, A-site occupancy and Fe^{2+} and low Mg is recognised.

The relationship between Ar loss and hornblende composition is a matter of debate. O'Nions et al. (1968), Onstott and Peacock (1987), and Onstott and Pringle-Goodell (1988) have suggested a correlation between Ar loss and low Mg/high Fe (and similarly, Suzuoki and Epstein (1976) suggested a relationship between hydrogen isotope exchange and low Mg/high Fe). However, Leake et al. (1988) and Cosca and O'Nions (1994) argued that the relationships found in these earlier studies between hornblende compositions and argon retentivity were actually a result of microscopically undetectable retrogression, alteration or recrystallisation. As a related example, perhaps the correlation

between hydrogen isotopic exchange and high structural water content of Miller et al. (1991) can be explained by the presence of retrograde chlorite, which contains relatively more water than hornblende and facilitates hydrogen isotope exchange (and Ar loss).

Furthermore, high K-contents and low Ca/K ratios in hornblende samples, which have experienced the most Ar loss and hydrogen isotope exchange, could indicate that microscopically undetectable phyllosilicate locally replaced hornblende, because phyllosilicate contains more K (and less Ca) than hornblende. If (part of) the K resides in these retrograde minerals, rather than in the A-site of hornblende, then the apparent trend of increasing Ar loss and hydrogen isotopic exchange with increasing A-site occupancy, as observed in this study, may not be valid. However, in this study, no phyllosilicates were found within hornblende grains (Section 3.4.4). Retrograde actinolite and chlorite that are present in some of the amphibolites (Section 3.4.4) would cause a decrease in K-content with younger age, if Ar loss was a result of retrograde metamorphism. Therefore, high K-contents in hornblende and Ar loss (and the other relationships found in this study between inverse $^{40}Ar/^{39}Ar$ isochron age, stable isotopic composition and chemical composition of hornblende) are probably not a result of retrograde mineral growth.

3.5.2.5. Hydrothermal alteration versus thermal overprint; interpretations of the $^{40}Ar/^{39}Ar$ hornblende dates

Based on his $^{40}Ar/^{39}Ar$ hornblende study (from which data and samples were used for this study), Spark (2001) inferred that heating resulted from re-equilibration of isotherms in response to their depression during thick-skinned crustal shortening.

Exhumation and cooling of these rocks below T_c would have occurred after ~70 Ma, yielding cooling ages of ~70 Ma. Continued crustal thickening by overthrusting of hot crust would have caused reheating from above and resetting of $^{40}Ar/^{39}Ar$ ages at high structural levels in Thor–Odin, prior to 50 Ma. Spark (2001) presumed that this resetting of ages at high structural levels represented the 'Cordilleran overprint' of Crowley and Parrish (1999). Tectonic denudation in the Middle Eocene cooled the rocks rapidly. According to Spark (2001), samples with excess ^{40}Ar, and resultant disturbed spectra and older apparent ages, are spatially related to heavily silicified splays associated with NNW-trending faults. This would imply that excess ^{40}Ar incorporated in hornblende was transported by fluids which moved along these faults. Alternatively, radiogenic ^{40}Ar that accumulated in older minerals at deeper structural levels was released upon reheating from above, and was incorporated in hornblende at higher structural levels (Spark, 2001). However, samples with disturbed spectra do not all show excess ^{40}Ar, and there is no indication that the samples with disturbed spectra were closer to faults than the samples with plateau or near-plateau spectra. Therefore, it seems more probable that meteoric waters moved along major or minor brittle faults (perhaps partly driven by thermal energy of intrusions, see Section 3.5.1), causing Ar loss and the resetting of ages, rather than fluids from below moving up along brittle faults, causing excess ^{40}Ar incorporation. Accordingly the youngest $^{40}Ar/^{39}Ar$ dates (< ~75–70 Ma) are interpreted as the result of Ar loss caused by interaction with meteoric waters, and not by reheating.

3.5.3. Ages based on U–Pb versus ages based on $^{40}Ar/^{39}Ar$ systematics

Peak metamorphic conditions in the Monashee Complex were at least in part coeval with transposition (e.g. Johnston et al., 2000), or according to earlier papers, with thrusting on the Monashee Décollement (e.g. Parrish, 1995). Peak metamorphic conditions were thought to have prevailed until 58–54.5 Ma (Carr, 1992, 1995; Parrish, 1995; Johnston et al., 2000), and until 49 Ma in the deepest structural levels of Frenchman Cap (Crowley and Parrish, 1999). These interpretations are based on the ages of monazite, titanite, xenotime and zircon. However, it is possible for these minerals to grow (or lose Pb) in the presence of fluids during retrograde metamorphism (see below), e.g. during extension. In the Monashee Complex, U–Pb dates from these minerals may represent the age of crustal hydrothermal activity associated with extension rather than the age of the peak of regional metamorphism.

3.5.3.1. The monazite perspective

Monazite U–Pb dates in four pelitic schists, a quartzite and two basement orthogneisses in Thor–Odin are younger than ~75–70 Ma (Parkinson, 1999, unpublished data; Johnston et al., 2000; Chapters 5, 6). With the exception of igneous crystals that grew during crystallisation of <~75–70 Ma intrusions, monazite grew, and/or lost Pb, below T_c for argon in hornblende. In northwest Thor–Odin, monazite crystals from the four pelitic schists, the quartzite and one of the orthogneisses (Johnston et al., 2000; Chapters 5, 6) give dates younger than $^{40}Ar/^{39}Ar$ hornblende dates from nearby amphibolites (Spark, 2001). Similarly, in Frenchman Cap, hornblende $^{40}Ar/^{39}Ar$ dates

from Palaeoproterozoic basement orthogneiss are older than monazite U–Pb dates from nearby pelitic schist. Even if all $^{40}Ar/^{39}Ar$ hornblende dates were cooling ages, the monazite crystals probably grew below T_c. It is also possible that monazite crystals were Mesozoic or older and recrystallised and/or lost Pb. Complete Pb loss or recrystallisation results in concordant ages, and incomplete Pb loss or recrystallisation causes discordancy and upper intercept ages older than the age of Pb loss. Monazite is known to grow in the presence of fluids at low temperatures (e.g. diagenetic monazite growth, see Evans and Zalasiewicz, 1996) and it is suggested, therefore, that monazite ages younger than ~75–70 Ma in Thor–Odin, may not represent peak metamorphic conditions, but rather growth (or recrystallisation/Pb loss) during extension and retrograde metamorphism in the presence of fluids.

Samples from the Monashee Complex with monazite dates younger than ~75–70 Ma seem to have experienced more hydrogen isotopic exchange with meteoric waters than the samples with old (Proterozoic) monazite ages (Fig. 3.12, Table 3.5). Even though only a small number of samples was analysed, this trend seems to be consistent with the interpretation that young monazite dates can be related to the activity of meteoric fluids. The apparent lack of a correlation between $\delta^{18}O$ and monazite U–Pb dates (Fig. 3.12) may be due to the fact that oxygen isotope exchange between the rock and the fluid was relatively limited.

Monazite growth, related to extension and infiltration of meteoric fluids, is further supported by the existence of more than one monazite date within single samples of rocks in, and close to, the Monashee Complex (see data in Carr, 1992; Gibson, 1997; Crowley and Parrish, 1999; Crowley et al., 2001; Chapters 6, 7). Interpreting multiple monazite

dates from single samples has previously been problematic. Crowley and Parrish (1999), for example, found two groups of monazite from an aluminous quartz-rich leucosome pod in a kyanite schist in the lower part of the cover sequence of Frenchman Cap: five single monazite grains at 65.4–63.8 Ma and two single monazite grains at 56.8–55.1 Ma (sample 223 in their Table 3.1 and Fig. 6). They interpreted the younger group of monazite as igneous (i.e. as having grown during crystallisation of the leucosome), because it is apparently coeval with igneous zircon from the same sample. They concluded that the existence of an older group of monazite is 'perplexing', and proposed the possibility of inheritance. However, inheritance in five grains to yield the same age would be very coincidental, especially when only younger monazite ages were determined in the host rock, a sillimanite–kyanite schist (sample 334; 60.8–56.2 Ma). Instead, the older monazite ages could represent leucosome formation, later metamorphism, or an alteration event, whereas the younger monazite is related to infiltration of extension-related fluids. Other minerals used for U–Pb dating in the Monashee Complex are xenotime, titanite and zircon. These minerals may also have grown below T_c in the presence of fluids.

3.6. Conclusions

Hornblende in amphibolites from Thor–Odin younger than ~75–70 Ma, with plateau or near-plateau $^{40}Ar/^{39}Ar$ spectra, occurs in rocks which underwent greater oxygen and hydrogen isotope exchange with infiltrating meteoric waters than hornblende samples yielding $^{40}Ar/^{39}Ar$ dates older than ~75–70 Ma. These 'older' samples (with one

exception) have disturbed spectra.

Infiltration of isotopically light meteoric fluids was probably related to normal faulting in Thor–Odin. $^{40}Ar/^{39}Ar$ hornblende dates younger than ~75–70 Ma are interpreted herein as being a result of partial or complete Ar loss, due to interaction between hornblende and meteoric fluids. Penetration of meteoric waters along normal faults probably continued locally at least until ~51 Ma, the youngest date determined in a sample from Thor–Odin. Because samples as old as ~75–70 Ma show plateau and near-plateau spectra and stable isotopic evidence of interaction with meteoric waters, normal faulting probably started prior to ~75–70 Ma. If so, then regional extension involving transient opening and closing of fractures occurred at least between ~75–70 and ~51 Ma. Ar loss and hydrogen isotopic exchange in hornblende seem to be facilitated by high A-site occupancy, low Ca/K (or high K), and high Fe-number.

Cooling below the closure temperature for argon in hornblende probably happened at or before ~75–70 Ma. $^{40}Ar/^{39}Ar$ inverse isochron ages of ~89 and ~118 were found for hornblende specimens with disturbed spectra, but no evidence for excess ^{40}Ar. Thus, initial cooling ages in Thor–Odin, at least as old as ~89 and ~118 Ma, may be indicated. During extension, crustal temperatures were certainly below T_c for hornblende by ~51 Ma.

In Thor–Odin, monazite probably grew, recrystallised and/or lost Pb below T_c, during the same extension-related meteoric fluid-penetration event that caused Ar loss in hornblende. Titanite, xenotime and zircon dates may be explained in the same way.

This re-evaluation of $^{40}Ar/^{39}Ar$ and U–Pb dates allows a new interpretation of the geological history of the Monashee Complex. Hornblende $^{40}Ar/^{39}Ar$ dates, and U–Pb

monazite, zircon, titanite and xenotime dates, previously interpreted as representing cooling and peak of metamorphism, respectively, are reinterpreted as being related to crustal-scale hydrothermal processes related largely to infiltration of meteoric fluids during extension. Accordingly, regional metamorphism must have occurred earlier, perhaps in the mid- to Late Cretaceous or Middle Jurassic, or between the Middle Jurassic and Late Cretaceous, as has been proposed for areas surrounding the Monashee Complex, despite the fact that such ages are not recorded within the Monashee Complex. The possibility remains to be addressed by future research.

Irrespective of the veracity of the conclusions drawn here, caution is urged in the interpretation of U–Pb and $^{40}Ar/^{39}Ar$ ages. Additional analytical methods (e.g. stable isotope techniques) may be helpful in determining the geological significance of mineral ages.

Acknowledgements

Adrian Timbal is thanked for teaching YDK the laboratory techniques of oxygen isotope geochemistry, and for performing hydrogen isotope analyses. Bob Spark graciously provided access to his amphibolite specimens and hornblende separates, and Jim Crowley to his samples from Frenchman Cap. Peter Reynolds is acknowledged for carefully reviewing and discussing Spark's (2001) $^{40}Ar/^{39}Ar$ data. James Whitehead is thanked for use of his amphibole classification program 'AMPHCALC'. This research was funded by an NSERC grant to Paul F. Williams.

References

Armstrong, R.L., Parrish, R.R., van der Heyden, P., Scott, K., Runkle, D., 1991. Early Proterozoic basement exposures in the southern Canadian Cordillera: core gneiss of Frenchman Cap, Unit I of the Grand Forks Gneiss, and the Vaseaux Formation. Canadian Journal of Earth Sciences 28, 1169–1201.

Beach, A., Fyfe, W.S., 1972. Fluid transport and shear zones at Scourie, Sutherland: Evidence of overthrusting? Contributions to Mineralogy and Petrology 36, 175–180.

Beaudoin, G., Roddick, J.C., Sangster, D.F., 1991. Eocene age for Ag–Pb–Zn–Au vein and replacement deposits of the Kokanee Range, southeastern British Columbia. Canadian Journal of Earth Sciences 29, 3–14.

Beaudoin, G., Sangster, D.F., Godwin, C.I., 1992a. Isotopic evidence for complex Pb sources in the Ag–Pb–Zn–Au veins of the Kokanee Range, southeastern British Columbia. Canadian Journal of Earth Sciences 29, 418–431.

Beaudoin, G., Taylor, B.E., Sangster, D.F., 1992b. Silver-lead-zinc veins and crustal hydrology during Eocene extension, southeastern British Columbia, Canada. Geochimica et Cosmochimica Acta 56, 3513–3529.

Beaumont, C., Jamieson, R.A., Nguyen, M.H., Lee, B., 2001. Mid-crustal channel flow in large hot orogens: results from coupled thermal-mechanical models. In: Cook, F., Erdmer, P. (Compilers), 2001, Slave–Northern Cordillera Lithospheric Evolution (SNORCLE) Transect and Cordilleran Tectonics Workshop Meeting (February 22–25), Pacific Geoscience Centre, Lithoprobe Report No. 79, 112–170.

Brown, R.L., Carr, S.D., Johnson, B.J., Coleman, V.J., Cook, F.A., Varsek, J.L., 1992. The Monashee décollement of the southern Canadian Cordillera: a crustal-scale shear zone linking the Rocky Mountain foreland belt to lower crust beneath accreted terranes. In: McClay, K.R. (Editor), Thrust Tectonics. Chapman and Hall, London, UK, pp. 357–364.

Carr, S.D., 1992. Tectonic setting and U–Pb geochronology of the early Tertiary Ladybird leucogranite suite, Thor–Odin – Pinnacles area, southern Omineca Belt, British Columbia. Tectonics 11, 258–278.

Carr, S.D., 1995. The southern Omineca Belt, British Columbia: new perspectives from the Lithoprobe Geoscience Program. Canadian Journal of Earth Sciences 32, 1720–1739.

Clayton, R.N., Mayeda, T.K., 1963. The use of bromine pentafluoride in the extraction of oxygen from oxides and silicates for isotopic analysis. Geochimica et Cosmochimica

Acta 27, 43–52.

Coplen, T.B., 1995. New guidelines for reporting stable hydrogen, carbon, and oxygen isotope-ratio data. Geochimica et Cosmochimica Acta 60, 3359–3360.

Cosca, M.A., O'Nions, R.K., 1994. A re-examination of the influence of composition on argon retentivity in metamorphic calcic amphiboles. Chemical Geology 112, 39–56.

Criss, R.E., Lanphere, M.A., Taylor, H.P., 1982. Effects of regional uplift, deformation, and meteoric-hydrothermal metamorphism on K–Ar ages of biotites in the southern half of the Idaho Batholith. Journal of Geophysical Research 87, 7029–7046.

Criss, R.E., Taylor, H.P., 1983. An $^{18}O/^{16}O$ and D/H study of Tertiary hydrothermal systems in the southern half of the Idaho Batholith. Geological Society of America Bulletin 94, 640–663.

Criss, R.E., Fleck, R.J., Taylor, H.P., 1991. Tertiary meteoric hydrothermal systems and their relation to ore deposition, northwestern United States and southern British Columbia. Journal of Geophysical Research 96, 13335–13356.

Crowley, J.L., 1999. U–Pb geochronologic constraints on Paleoproterozoic tectonism in the Monashee complex, Canadian Cordillera: elucidating an overprinted geologic history. Geological Society of America Bulletin 111, 560–577.

Crowley, J.L., Parrish, R.R., 1999. U–Pb isotopic constraints on diachronous metamorphism in the northern Monashee complex, southern Canadian Cordillera. Journal of Metamorphic Geology 17, 483–502.

Crowley, J.L., Brown, R.L., Parrish, R.R., 2001. Diachronous deformation and a strain gradient beneath the Selkirk allochthon, northern Monashee complex, southeastern Canadian Cordillera. Journal of Structural Geology 23, 1103–1121.

Dahl, P.S., 1996. The effects of composition on retentivity of argon and oxygen in hornblende and related amphiboles: A field tested empirical approach. Geochimica et Cosmochimica Acta 60, 3687–3700.

Evans, J., Zalasiewicz, J., 1996. U–Pb, Pb–Pb and Sm–Nd dating of authigenic monazite: implications for the diagenetic evolution of the Welsh Basin. Earth and Planetary Science Letters 144, 421–433.

Etheridge, M.A., Wall, V.J., Vernon, R.H., 1983. The role of fluid phase during regional metamorphism and deformation. Journal of Metamorphic Geology 1, 205–226.

Faure, G., 1986. Principles of isotope geology. John Wiley & Sons Ltd., Toronto.

Fleck R.J., Sutter, J.F., Elliott, D.H., 1977. Interpretation of discordant $^{40}Ar/^{39}Ar$ age-spectra of Mesozoic tholeiites from Antarctica. Geochimica et Cosmochimica Acta 41, 15–32.

Gibson, H.D., 1997. Thermotectonic evolution of the northern Monashee complex, southern Omineca Belt, southeastern British Columbia. MSc thesis, Carleton University, Ottawa, Ontario, Canada.

Gibson, H.D., Brown, R.L., Parrish, R.R., 1999. Deformation-induced inverted metamorphic field gradients: an example from the southeastern Canadian Cordillera. Journal of Structural Geology 21, 751–767.

Godfrey, J.D., 1962. The deuterium content of hydrous minerals from the East-Central Sierra Nevada and Yosemite National Park. Geochimica et Cosmochimica Acta 26, 1215–1245.

Holk, G.J., Taylor, H.P., 1997. $^{18}O/^{16}O$ homogenization of the middle crust during anatexis: The Thor–Odin metamorphic core complex, British Columbia. Geology 25, 31–34.

Holk, G.J., Taylor, H.P., 2000. Water as a petrologic catalyst driving $^{18}O/^{16}O$ homogenization and anatexis of the middle crust in the metamorphic core complexes of British Columbia. International Geology Review 42, 97–130.

Hunt, P.A., Roddick, J.C., 1992. A compilation of K–Ar ages: Report 21. Geological Survey of Canada, Paper 91-2, 219–220.

Jappy, T.G., Leake, B.E., Fallick, A.E., 2001. Relationship between hornblende K–Ar ages, chemical composition and hydrogen isotopes, Connemara, western Ireland; evidence for a massive extinct hydrothermal system. Journal of the Geological Society of London 158, 843–854.

Johnson, B.J., 1994. Structure and tectonic setting of the Okanagan Valley fault system in the Shuswap Lake area, southern British Columbia. PhD Thesis, Carleton University, Ottawa, Ontario, Canada.

Johnston, D.H., Williams, P.F., Brown, R.L., Crowley, J.L., Carr, S.D., 2000. Northeastward extrusion and extensional exhumation of crystalline rocks of the Monashee Complex, southeastern Canadian Cordillera. Journal of Structural Geology 22, 603–625.

Journeay, J.M., 1986. Stratigraphy, internal strain, and thermo-tectonic evolution of northern Frenchman Cap dome, an exhumed basement duplex structure, Omineca hinterland, southeastern Canadian Cordillera. PhD Thesis, Queen's University, Kingston, Ontario, Canada.

Kretz, R., 1983. Symbols for rock-forming minerals. American Mineralogist 68, 277–279.

Kuiper, Y.D., (2002). The interpretation of inverse isochron diagrams in $^{40}Ar/^{39}Ar$ geochronology. Earth and Planetary Science Letters 203, 499-506.

Kuiper, Y.D., Carr, S.D., Williams, P.F., 2000. Age constraints on penetrative structures at Joss Mountain, in the Selkirk Allochthon, southern Canadian Cordillera. In: Cook, F., Erdmer P. (Compilers), 2000, Slave–Northern Cordillera Lithospheric Evolution (SNORCLE) Transect and Cordilleran Tectonics Workshop Meeting (February 25–27), University of Calgary, Lithoprobe Report No. 72, 168.

Kuiper, Y.D., Kruse, S. Williams, P.F., McNeill, P.D., 2002. Possibility of channel flow in the southern Canadian Cordillera; a new approach to explain existing data. In: Cook, F., Erdmer, P. (Compilers), 2002, Slave–Northern Cordillera Lithospheric Evolution (SNORCLE) Transect and Cordilleran Tectonics Workshop Meeting (February 21–24), Pacific Geoscience Centre, Lithoprobe Report No. 82, 132.

Lane, L.S., 1984. Deformation history of the Monashee Decollement and Columbia River Fault zone. PhD Thesis, Carleton University, Ottawa, Ontario, Canada.

Leake, B.E., Elias, E.M., Farrow, C.M., 1988. The relationship of argon retentivity and chemical composition of hornblende. Geochimica et Cosmochimica Acta 52, 2165.

Leake, B.E. and 21 others, 1997. Nomenclature of amphiboles: report of the subcommittee on amphiboles of the international mineralogical association, commission on new minerals and mineral names. Canadian Mineralogist 35, 219–246.

Lowden, J.A., 1961. Age determinations by the Geological Survey of Canada; Report 2 - Isotopic ages. Geological Survey of Canada, Paper 61-17, 5.

Lowden, J.A., 1963a. Isotopic ages - Report 3. Geological Survey of Canada, Paper 62-17, 5–9.

Lowden, J.A., 1963b. Isotopic ages - Report 4. Geological Survey of Canada, Paper 63-17, 25–34.

Magaritz, M., Taylor, H.P., 1986. Oxygen 18/oxygen 16 studies of plutonic granitic and metamorphic rocks across the Cordilleran batholiths of southern British Columbia. Journal of Geophysical Research 91, 2193–2217.

McDougall, I., Harrison, T.M.., 1999. Geochronology and thermochronology by the $^{40}Ar/^{39}Ar$ method. Second edition, Oxford University Press, New York.

Miller, W.M., Fallick, A.E., Leake, B.E., MacIntyre, R.M., Jenkin, G.R.T., 1991. Fluid disturbed hornblende K–Ar ages from the Dalradian rocks of Connemara, Western Ireland. Journal of the Geological Society of London 148, 985–992.

Monger, J.W.H., Price, R.A., Tempelman-Kluit, D.J., 1982. Tectonic accretion and the origin of the two major metamorphic and plutonic welts in the Canadian Cordillera. Geology 10, 70–75.

Murphy, D.C., van der Heyden, P., Parrish, R.R., Klepacki, D.W., McMillan, W., Struik, L.C., Gabites, J., 1995. New geochronological constraints on Jurassic deformation of the western edge of North America, southeastern Canadian Cordillera. In: Miller, D.M., Busby, C. (Editors), Jurassic magmatism and tectonics of the North American Cordillera. Boulder, Colorado, Geological Society of America Special Paper 299, 159–171.

Onstott, T.C., Peacock, M.W., 1987. Argon retentivity of hornblende: a field experiment in a slowly cooled metamorphic terrane. Geochimica et Cosmochimica Acta 51, 2891–2903.

Onstott, T.C., Pringle-Goodell, L. 1988. The influence of microstructures on the relationship between argon retentivity and chemical composition of hornblende. Geochimica et Cosmochimica Acta 52, 2167–2168.

Parkinson, D.L., 1991. Age and isotopic character of Early Proterozoic basement gneisses in the southern Monashee Complex, southeastern British Columbia. Canadian Journal of Earth Sciences 28, 1159–1168.

Parkinson, D.L., 1992. Age and tectonic evolution of the southern Monashee complex, southeastern British Columbia: a window into the deep crust. PhD Thesis, University of Santa Barbara, Santa Barbara, California, USA.

Parrish, R.R., 1995. Thermal evolution of the southeastern Canadian Cordillera. Canadian Journal of Earth Sciences 32, 1618–1642.

Parrish, R.R., Carr, S.D., Parkinson, D.L., 1988. Eocene extensional tectonics and geochronology of the southern Omineca Belt, British Columbia and Washington. Tectonics 7, 181–212.

Sanborn, N.M., 1996. Constraints on the timing and conditions of Cordilleran tectonism in Frenchman Cap dome, Monashee complex, southeast British Columbia, from $^{40}Ar/^{39}Ar$ geochronology. BSc Thesis, Queens University, Kingston, Ontario, Canada.

Sanborn, N.M., Crowley, J.L., Archibald, D.A., 1999. Rapid Eocene cooling from peak metamorphic temperatures in the northern Monashee complex, southern Canadian Cordillera: Evidence from $^{40}Ar/^{39}Ar$ and U–Pb data. In: Cook, F., Erdmer, P.

(Compilers), 1999, Slave–Northern Cordillera Lithospheric Evolution (SNORCLE) Transect and Cordilleran Tectonics Workshop Meeting (March 5–7), University of Calgary, Lithoprobe Report No. 69, 318.

Sheppard, S.M.F., 1986. Characterization and isotopic variations in natural waters. In: Valley, J.W., Taylor, H.P., Jr., O'Neill, J.R. (Editors), Stable isotopes in high temperature geological processes. Reviews in Mineralogy 16, 165–183.

Singleton, M.J., Criss, R.E., 2002. Effects of normal faulting on fluid flow in an ore-producing hydrothermal system, Comstock Lode, Nevada. Journal of Volcanology and Geothermal Research 115, 437–450.

Spark, R.N., 2001. Crustal thickening and tectonic denudation within the Thor–Odin culmination, Monashee Complex, southern Canadian Cordillera. PhD Thesis, University of New Brunswick, Fredericton, New Brunswick, Canada.

Stevens, R.D., 1986. K–Ar isotopic ages, Report 8. Geological Survey of Canada, Paper 67-2A, 40–41.

Suzuoki, T., Epstein, S., 1976. Hydrogen isotope fractionation between OH-bearing minerals and water. Geochimica et Cosmochimica Acta 40, 1229–1240.

Taylor, H.P., 1974. The application of oxygen and hydrogen isotope studies to problems of hydrothermal alteration and ore deposition. Economic Geology 69, 843–883.

Taylor, B.E., 1986. Magmatic volatiles: isotopic variation of C, H and S. In: Valley, J.W., Taylor, H.P., Jr., O'Neill, J.R. (Editors), Stable isotopes in high temperature geological processes, Reviews in Mineralogy 16, 185–226.

Vanderhaeghe, O., 1997. Role of partial melting during late-orogenic collapse. PhD Thesis, University of Minnesota, Minneapolis, Minnesota, USA.

Vanderhaeghe, O., Teyssier, C., Wysoczanski, R., 1999. Structural and geochronological constraints on the role of partial melting during the formation of the Shuswap metamorphic core complex at the latitude of the Thor–Odin dome, British Columbia. Canadian Journal of Earth Sciences 36, 917–943.

Wanless, R.K., Stevens, R.D., Lachance, G.R., Delabio, R.N., 1973. K–Ar isotopic ages, Report 11. Geological Survey of Canada, Paper 73-2, 25.

Wanless, R.K., Stevens, R.D., Lachance, G.R., Delabio, R.N., 1978. K–Ar isotopic ages, Report 13. Geological Survey of Canada, Paper 77-2, 24–26.

Wanless, R.K., Stevens, R.D., Lachance, G.R., Delabio, R.N., 1979. K–Ar isotopic ages, Report 14. Geological Survey of Canada, Paper 79-2, 25–27.

Wanless, R.K., Stevens, R.D., Lachance, G.R., Rimsaite, R.Y.H., 1965. Part 1 - Isotopic ages, Report 5. Geological Survey of Canada, Paper 64-17, 11.

Wheeler, J.O., McFeely, P. (Compilers), 1991. Tectonic assemblage map of the Canadian Cordillera and adjacent parts of the United States of America: Geological Survey of Canada, Map 1712A, scale 1:2 000 000, 1 sheet.

Whitehead, J., 1998. Obduction- and post-obduction-related features of the Québec Appalachian ophiolites. PhD Thesis, University of New Brunswick, Fredericton, New Brunswick, Canada.

Williams, P.F., 1999. Interpretation of thrust-like structures in middle and lower crustal rocks. In: Tectonic and Magmatic Processes in Crustal Growth: a Pan-Lithoprobe Perspective. Lithoprobe report 75, 67–68.

Williams, P.F., Jiang, D., (in review). The relationship between thrusting, nappe formation, and channel flow. An example from the Canadian Cordillera. Journal of Structural Geology.

Table 3.1. Sample descriptions, oxygen, hydrogen and argon data for amphibolites in Thor–Odin. 40Ar/39Ar geochronology performed by Spark (2001).

sample	Thin section description				hornblende
number	grainsize	mineralogy	retrograde minerals	structures	composition
samples with plateau spectra					
RS-127	medium	green hbl, relict grt, pl, bt, few ttn, opq	(none)		tschermakite
RS-128	medium	green hbl, pl, bt, opq	chl, ser	vein	tschermakite
RS-132A	medium	green hbl, grt, pl, bt, opq	ttn (in fractures), chl, some scp	many fractures	ferropargasite
RS-133	medium	green hbl, pl, big ttn, bt, small ttn, opq	few scp	shear bands	pargasite
RS-212A	medium	green hbl, pl, few bt, ttn, opq	few ser	many fractures	tschermakite
RS-244	medium	brown hbl, pl, grt, ttn, opq, few bt	few chl		tschermakite
samples with near-plateau spectra					
RS-24C	medium	green hbl, relict grt, pl, pale ttn, opq	few ser		pargasite
RS-25C	medium	green hbl, grt, pl, dark ttn in grt, bt, dark and pale ttn, opq	very few scp, ser close to grt		pargasite
RS-51B	fine	green hbl, pl, bt (myrmekitic), few pale ttn	some ser		tschermakite
RS-119B	fine	green hbl, grt fragments, pl, opq + pale ttn, mostly along foliation	(none)	fractures	tschermakite
RS-125B	medium	green hbl, pl, bt, very few ttn, few opq	some ser	fractures and veins	pargasite
RS-131	medium	green hbl, grt, pl, bt, opq, very few ttn,	chl (in fractures), very few scp	fractures	magnesiohastingsite
RS-132C	fine	green hbl, grt, pl, opq	ser, some chl, some scp		tschermakite
RS-134B	fine	green hbl, pl, few opq	ser		pargasite
RS-206	fine	green hbl, pl, bt, pale ttn, opq	ser		hastingsite
RS-241B	coarse	green hbl, pl, pale ttn, opq	ser		pargasite
RS-243	fine	green hbl, pl, bt, opq, dark ttn (could be old)	ser		magnesiohornblende
samples with disturbed spectra					
RS-120	fine	green hbl, pl, bt, many pale ttn, some opq	ser		pargasite
RS-130	fine	green hbl, pl, bt, pale ttn, opq	some scp	veins	magnesiohornblende
RS-138	fine	brown hbl, grt, pl, bt, opq + small pale ttn along foliation	very few chl		tschermakite
RS-218	medium	green hbl, grt, pl, bt, opq, very few ttn	scp		ferrotschermakite
RS-220	coarse	mainly green hbl, pl, few opq, few ttn	ser	few fractures	magnesiohornblende
RS-226	medium	green hbl, pl, few opq	ser		magnesiohornblende

sample	easting	northing	elevation	δ18O (‰)	δ18O (‰)	δ18O (‰)	δD (‰)	inv isochr	error	(near-)	error	40Ar/36Ar	error	MSWD
number	(m)	(m)	(m)	whole-rock	quartz	feldspar	hornblende	age (Ma)	(Ma)	plateau age	(Ma)	ratio		
samples with plateau spectra														
RS-127	423585	5606561	2181				–122	57.7	0.5	57.0	0.6	259	28	0.36
RS-128	424051	5607004	2044					57.2	0.4	56.5	0.3	284	2	0.27
RS-132A	404708	5632318	2044	3.1			–158	56.0	1.1	55.1	0.6	248	47	1.24
RS-133	397334	5631304	2303	2.7		3.5	–160	54.4	0.4	54.2	0.3	287	2	0.53
RS-212A	427736	5615318	1220				–153	72.0	0.8	71.8	0.4	286	5	2.08
RS-244	415016	5594957	2059					57.0	0.5	56.7	0.3	286	4	1.03
samples with near-plateau spectra														
RS-24C	409054	5612881	2318	3.2		–5.4	–148	53.9	0.7	53.4	0.3	289	2	1.01
RS-25C	407939	5622363	2135	7.9			–137	67.4	0.6	67.3	0.7	295	12	0.77
RS-51B	414718	5618228	2516	9.7			–125	72.2	1.2	72.2	0.4	309	11	11.65
RS-119B	412518	5621706	2379	3.0				66.3	0.7	66.4	0.7	309	8	2.25
RS-125B	410059	5622182	2288	3.0	7.1	–1.2		61.2	0.9	61.8	0.6	303	28	3.10
RS-131	405132	5632890	2257	2.5			–136	71.8	0.8	71.7	0.4	287	7	3.05
RS-132C	404680	5632244	2028	1.2				59.3	0.5	58.1	0.3	282	3	0.54
RS-134B	397403	5642629	519	2.2			–152	65.0	2.3	65.3	1.0	327	53	5.34
RS-206	422843	5617504	1510					51.1	0.7	51.8	0.3	383	21	3.78
RS-241B	407602	5621088	1800	5.9			–136	88.9	1.2	86.8	0.5	281	5	2.39
RS-243	414329	5596427	2303					60.2	1.1	59.6	0.3	289	10	6.46
samples with disturbed spectra														
RS-120	411493	5621561	2242	5.8			–133	74.6	2.3			334	30	36.84
RS-130	412426	5624632	2379	6.6			–93	86.3	1.5			262	22	7.62
RS-138	413124	5615876	2242	6.5			–96	117.6	2.3			249	41	94.53
RS-218	424822	5621517	1449					89.1	3.7			371	48	57.87
RS-220	427129	5617936	1205					78.0	9.5			362	61	34.67
RS-226	428333	5613553	1098					72.8	7.4			352	44	35.78

Grain sizes subdivided in coarse (average grain size >2mm), medium (1–2mm) and fine (<1mm)

Mineral abbreviations after Kretz (1983), and fsp = feldspar, ser = sericite and opq = opaque minerals

Table 3.2. Whole-rock oxygen isotopic data for samples collected at various distances from the Frigg Glacier Fault and the Grizzly Flats Fault (see Fig. 3.2 for locations).

sample number	rock type	distance to fault (m) to the E/W	δ18O (‰) whole-rock	δ18O (‰) quartz	δ18O (‰) feldspar	mineralogy	other characteristics
Frigg Glacier Fault, 423600E 5600100N, 2227m							
Coarse grained (myrmekitic) hbl/bt leucogranitic orthogneiss							
s298-212I	orthogneiss	15W	6.4			fsp, qtz, hbl, bt, ttn, scp	
s298-212H	orthogneiss	10W	7.1			fsp, qtz, bt, some chl, ttn, scp	
s298-212G	orthogneiss	5W	7.5			fsp, qtz, hbl, bt, chl, some ttn, some scp	
s298-212C	orthogneiss	0	5.5			fsp, qtz, bt, some ser, some ttn, some scp	
s298-212E	orthogneiss	0	5.0			fsp, qtz, bt, some chl, many scp	
s298-212J	orthogneiss	5E	7.1			fsp, qtz, hbl, bt, some chl, ttn, scp	
s298-212K	orthogneiss	10E	7.3			fsp, qtz, bt, many chl, ttn, scp	
s298-212L	orthogneiss	15E	7.4			fsp, qtz, bt, some chl, few scp	
s298-212M	orthogneiss	20E	2.3			fsp, qtz, bt, veins with many chl, some opq	
Grizzly Flats Fault, 404400E 5629600N, 2135m							
Coarse grained quartzite							
s298-231A	quartzite	<5W	9.0			qtz, sil, chl, ttn, some ms, thin vein with chl, opq + undefined minerals	foliated
s298-231B	quartzite	10W	12.2			qtz, ms, chl, some ttn, ap?, sil, veins and cracks	strongly foliated, flattened qtz, subgrains, no CPO
s298-231C	quartzite	20W	11.8			qtz, opq, bt, ms, sil, few cracks/veins	strongly foliated, flattened qtz, subgrains, no CPO
s298-231D	quartzite	60W	13.2			qtz, ms, bt, chl, sil, opq, locally many ser, cracks, which contain ms and opq	foliated
s298-231E	quartzite	80W	12.8			qtz, bt, ms, chl, opq, ser, sil	strongly foliated, flattened qtz, subgrains, no CPO
Coarse grained pelitic schist							
s298-232A	pelitic schist	<5W	5.0			bt, sil, opq, qtz, fsp, ser	50% felsic minerals
s298-232B	pelitic schist	10W	3.1			bt, sil, many opq, some qtz and fsp, some chl, ser	40% felsic minerals
s298-232C	pelitic schist	20W	8.9			bt, sil, opq, qtz, fsp, chl, few cracks, ser	40% felsic minerals
s298-232D	pelitic schist	40W	5.9			bt, sil, opq, many qtz and fsp, some chl, ser	60% felsic minerals
s298-232E	pelitic schist	60W	11.9			bt, sil, opq, many qtz and fsp, some chl, ser	60% felsic minerals
Coarse grained hbl orthogneiss							
s298-233A	hbl orthogneiss	<5E	4.3	12.0	2.0	green hbl, many bt, ttn, few scp, fsp, qtz, chl	
s298-233B	hbl orthogneiss	30E	1.8	11.7	–5	green hbl, bt, ttn, few scp, fsp, qtz, chl	
s298-233C	hbl orthogneiss	50E	0.1	10.2	–3.2	green hbl, ttn, few scp, fsp, qtz, chl	
s298-233D	hbl orthogneiss	70E	1.6	11.2	–3	green hbl, few bt, ttn, few scp, fsp, qtz, chl	

Mineral abbreviations after Kretz (1983), and fsp = feldspar, ser = sericite and opq = opaque minerals

Table 3.3. Microprobe compositions for hornblende dated by 40Ar/39Ar methods (from Spark, 2001). Hornblende A-site occupation by Na and K (Na+K(A)), Ca/K ratio, K-content (per 23 oxygen atoms) and Fe-number (Fe2+/(Mg+Fe2+)) calculated using the QUICK BASIC amphibole classification program "AMPHCALC" (by James Whitehead, 1997; see Whitehead, 1998).

Sample	RS24C	RS25C	RS51B	RS119B	RS120	RS125B	RS127	RS128	RS130	RS131	RS132A	RS132C
SiO2	42.89	41.77	43.04	43.06	43.30	42.19	42.21	42.80	45.64	40.85	40.33	42.09
TiO2	1.34	1.56	1.04	1.17	1.27	1.49	1.45	1.38	0.96	1.10	1.67	1.42
Al2O3	12.64	14.45	12.99	12.59	11.98	12.88	13.28	13.62	9.69	14.6	13.54	12.94
MgO	12.08	12.94	10.34	8.76	12.22	10.94	9.07	9.08	14.87	11.20	7.08	9.68
CaO	11.41	11.28	11.45	11.10	11.94	11.46	10.93	10.80	11.40	11.25	10.92	10.98
Cr2O3	0.06	0.01	0	0	0.12	0.04	0	0	0.17	0.04	0	0
MnO	0.28	0.13	0.28	0.2	0.23	0.26	0.27	0.26	0.19	0.25	0.19	0.32
FeO	12.95	11.18	12.06	15.49	13.33	14.24	13.22	13.57	10.53	11.55	17.33	13.73
Fe2O3	2.92	2.39	2.94	2.44	1.42	1.91	3.74	3.78	2.23	5.66	2.86	3.29
Na2O	1.42	1.36	1.20	1.55	1.16	1.57	1.43	1.27	1.06	1.44	1.33	1.51
K2O	0.62	0.85	1.28	0.51	1	1.01	0.92	0.81	0.27	0.76	1.52	0.63
TOTAL	98.61	97.92	96.62	96.87	97.97	97.99	96.52	97.37	97.01	98.70	96.77	96.59
Na+K(A)	0.521	0.546	0.438	0.406	0.521	0.635	0.389	0.325	0.351	0.553	0.557	0.446
Ca/K	15.483	11.145	7.512	18.265	10.011	9.521	9.960	11.188	35.760	12.420	6.040	14.645
K	0.116	0.159	0.244	0.098	0.189	0.192	0.177	0.154	0.050	0.143	0.298	0.121
Fe#	0.376	0.326	0.396	0.498	0.380	0.422	0.450	0.456	0.284	0.367	0.579	0.443

Sample	RS133	RS134B	RS138	RS206	RS212A	RS218	RS220	RS226	RS241B	RS243	RS244
SiO2	40.32	42.7	41.96	40.62	43.76	42.79	45.22	46.53	41.99	44.07	43.46
TiO2	0.96	1.12	1.39	1.67	0.92	1.32	1.44	0.63	1.66	1.63	1.97
Al2O3	13.67	13.08	14.71	11.18	12.78	12.50	11.58	9.19	12.59	12.88	12.38
MgO	9.25	12.02	8.90	8.51	12.32	8.75	13.61	14.66	13.57	12.15	11.31
CaO	11.56	11.33	11.15	11.20	11.72	10.79	11	11.89	11.53	11.14	11.42
Cr2O3	0.04	0.01	0	0.07	0.01	0	0	0.11	0.08	0	0
MnO	0.41	0.22	0.02	0.33	0.26	0.25	0.21	0.22	0.14	0.25	0.09
FeO	15.00	12.15	15.45	17.95	12.69	16.40	9.27	11.08	11.14	11.14	12.25
Fe2O3	0.75	2.69	0.27	3.69	1.62	1.60	2.24	1.25	2.18	0.95	0.82
Na2O	1.31	1.38	0.99	1.69	1.21	1.44	1.48	0.86	1.83	1.25	1.23
K2O	1.18	0.95	1.51	1.20	0.73	0.55	0.32	0.20	0.10	0.85	1.39
TOTAL	94.45	97.65	96.35	98.11	98.02	96.39	96.37	96.62	96.81	96.31	96.32
Na+K(A)	0.628	0.562	0.476	0.727	0.481	0.421	0.346	0.282	0.545	0.397	0.472
Ca/K	8.214	10.022	6.196	7.821	13.453	16.528	28.733	50.514	96.368	11.013	6.887
K	0.234	0.179	0.291	0.235	0.137	0.106	0.060	0.037	0.019	0.160	0.265
Fe#	0.476	0.362	0.493	0.542	0.366	0.513	0.276	0.298	0.315	0.340	0.378

Table 3.4. Calculated values of the hydrogen isotope equilibrium fractionation factors between hornblende and water, and of δD for meteoric waters assuming, equilibrium between hornblende and the waters was reached, at selected temperatures.

sample	δD (‰)	X Mg(vi)	X Al(vi)	X Fe(vi)	1000lnα(hbl–water)			δD (‰) meteoric water		
number	hbl				400 C	450 C	500 C	400 C	450 C	500 C
samples with plateau spectra										
RS-127	–122.2	0.41	0.14	0.42	–51	–44	–42	–71	–78	–81
RS-128		0.40	0.15	0.41	–51	–44	–41			
RS-132A	–157.8	0.32	0.13	0.50	–57	–50	–47	–101	–108	–111
RS-133	–160	0.43	0.15	0.40	–50	–43	–40	–110	–117	–120
RS-212A	–153	0.54	0.13	0.31	–45	–38	–35	–108	–115	–118
RS-244		0.50	0.13	0.32	–45	–38	–35			
Average	–148	0.43	0.14	0.39	–50	–43	–40	–98	–104	–107
samples with near-plateau spectra										
RS-24C	–148.1	0.53	0.10	0.34	–46	–40	–37	–102	–108	–111
RS-25C	–136.9	0.57	0.12	0.28	–42	–35	–33	–95	–102	–104
RS-51B	–125.1	0.46	0.14	0.37	–48	–41	–38	–77	–84	–87
RS-119B		0.39	0.14	0.44	–52	–46	–43			
RS-125B		0.49	0.11	0.37	–48	–42	–39			
RS-131	–135.6	0.49	0.11	0.37	–48	–42	–39	–87	–94	–97
RS-132C		0.43	0.13	0.41	–50	–44	–41			
RS-134B	–152.3	0.53	0.12	0.33	–45	–39	–36	–107	–114	–116
RS-206		0.39	0.05	0.52	–58	–52	–49			
RS-241B	–135.9	0.60	0.09	0.28	–42	–36	–33	–94	–100	–103
RS-243		0.53	0.15	0.28	–42	–35	–33			
Average	–139	0.49	0.11	0.36	–48	–41	–38	–94	–100	–103
samples with disturbed spectra										
RS-120	–133.4	0.54	0.10	0.33	–46	–39	–36	–88	–94	–97
RS-130	–92.5	0.65	0.07	0.26	–41	–34	–32	–51	–58	–61
RS-138	–95.8	0.40	0.19	0.38	–48	–42	–39	–48	–54	–57
RS-218		0.40	0.14	0.43	–52	–45	–42			
RS-220		0.59	0.12	0.25	–41	–34	–31			
RS-226		0.64	0.08	0.26	–41	–35	–32			
Average	–107	0.54	0.12	0.32	–45	–38	–35	–62	–69	–72

Values calculated with (Suzuoki and Epstein, 1976):
1000lnα(hbl–water) = –22.4(1,000,000/(T*T)) + 28.2+(2*X Al – 4*X Mg – 68*X Fe)
1000lnα(hbl–water) = ~δD(hbl) – δD(water)
α is the hydrogen isotope equilibrium fractionation factor between hbl and water
X is the fraction of cation in the octahedrally coordinated site

Table 3.5. Whole-rock oxygen and hydrogen data for samples with existing monazite U–Pb data. Samples from Frenchman Cap sampled and dated by Crowley (1999) and from Thor–Odin by Kuiper (Chapters 5–7).

sample number	rock type	easting (m)	northing (m)	elevation (m)	δ18O (‰) whole–rock	δ18O (‰) quartz	δ18O (‰) feldspar	δD (‰) whole-rock	U–Pb mnz age (Ma)
Thor-Odin									
S298-65H	orthogneiss	416250	5625650	2135	9.4	11.1	9.3		52.5
S298-4	pegmatite	397150	5629850	2074	9.5				70, 55.5
YK-TVG-97	paragneiss	397600	5642750	488	9.4			–135	57.5
s298-54	pelitic schist	410850	5623950	2257	11.8			–120	52.5
s298-70	pelitic schist	408650	5623250	2242	16.3			–136	65, 55
Frenchman Cap									
PCA-305B-83	orthogneiss	389330	5688340	1861	7.5	8.9	7.9	–79	1848
JC-85	pelitic schist	390130	5687830	1882	11.1			–56	2057

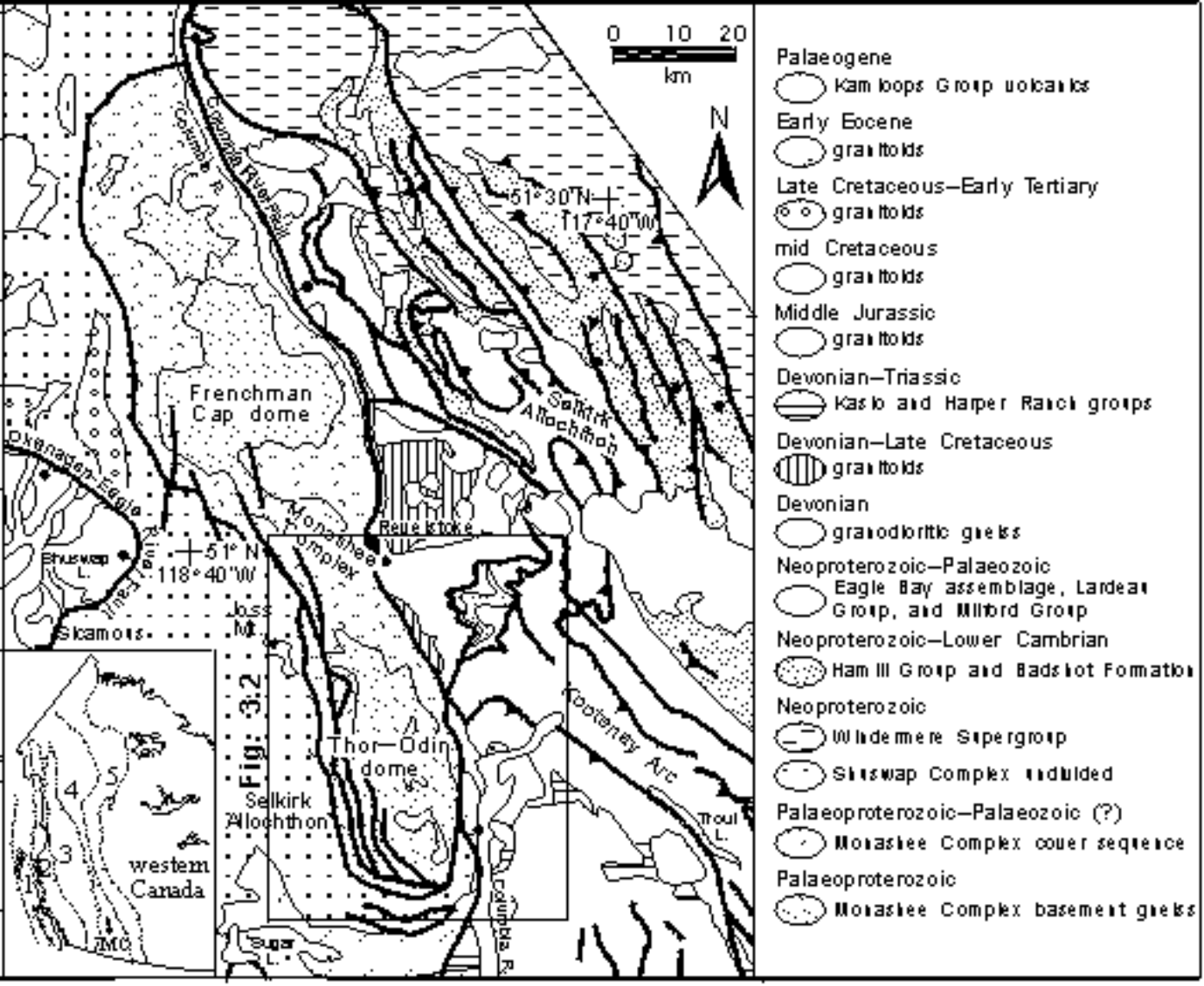

Fig. 3.1. Geological map of the Monashee Complex and surrounding geology. Modified after Wheeler and McFeely (1991). Inset: location of morphogeological belts of the Canadian Cordillera: 1. Insular Belt, 2. Coast Belt, 3. Intermontane Belt, 4. Omineca Belt, 5. Foreland Belt. MC indicates the location of the Monashee Complex.

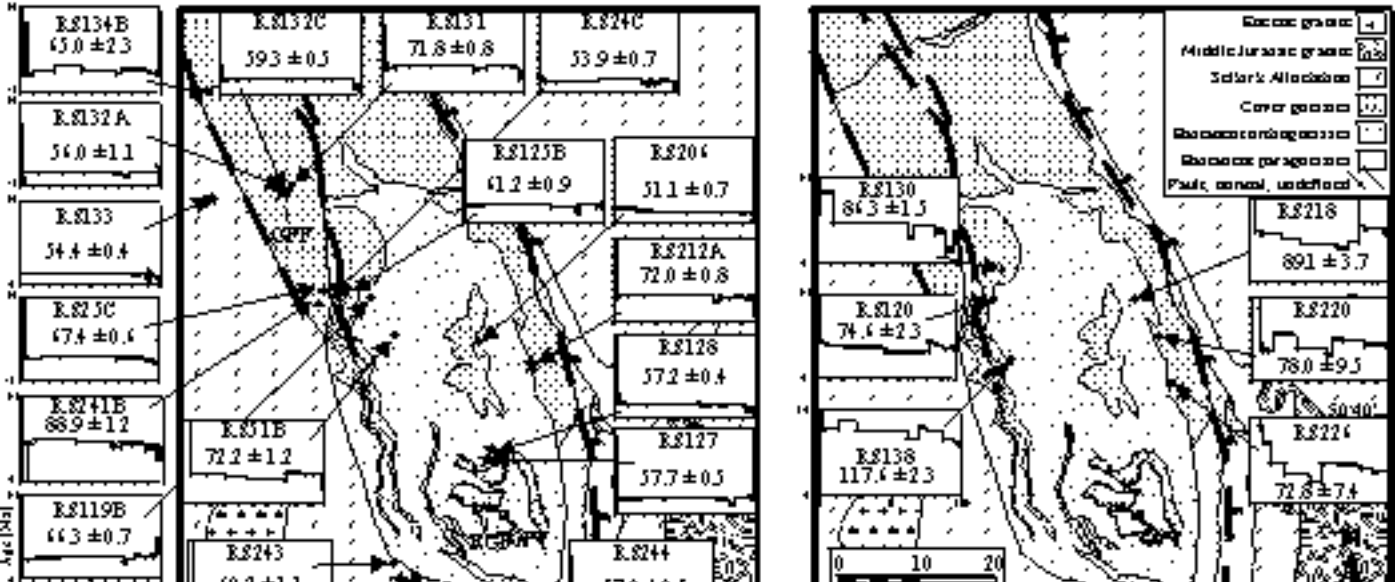

Fig. 3.2. Geological map of Thor–Odin and location of amphibolites with $^{40}Ar/^{39}Ar$ hornblende plateau and near-plateau spectra (★ and ● respectively, in a) and disturbed spectra (b). Horizontal and vertical axes are the same in all diagrams. Inverse isochron ages are indicated in Ma (see Appendix I). In (a) also indicated: Grizzly Flats Fault (GFF) and Frigg Glacier Fault (FGF); see section 4.1.2 and Table 4.2.

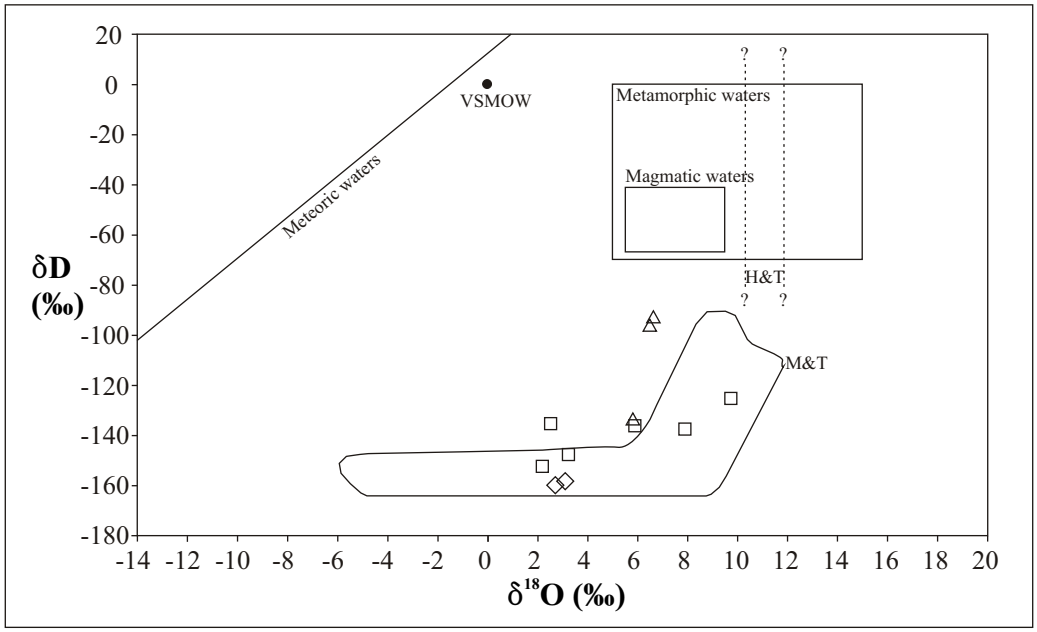

Fig. 3.3. Plot of hornblende δD versus whole-rock $\delta^{18}O$ of amphibolites. Diamonds, squares and triangles represent data from amphibolites with plateau-, near-plateau- and disturbed spectra respectively. For comparison, fields are indicated for typical metamorphic and magmatic waters (cf., Taylor, 1974; Taylor, 1986; Sheppard, 1986; and references therein), for rocks that interacted with meteoric waters in the Nelson Batholith, ~60 km SSE of Thor–Odin (M&T; Magaritz and Taylor, 1986), and the range of oxygen isotope composition, homogenised by metamorphism without interaction with meteoric fluids, for rocks from Thor–Odin (dashed lines, H&T; Holk and Taylor, 1997, 2000).

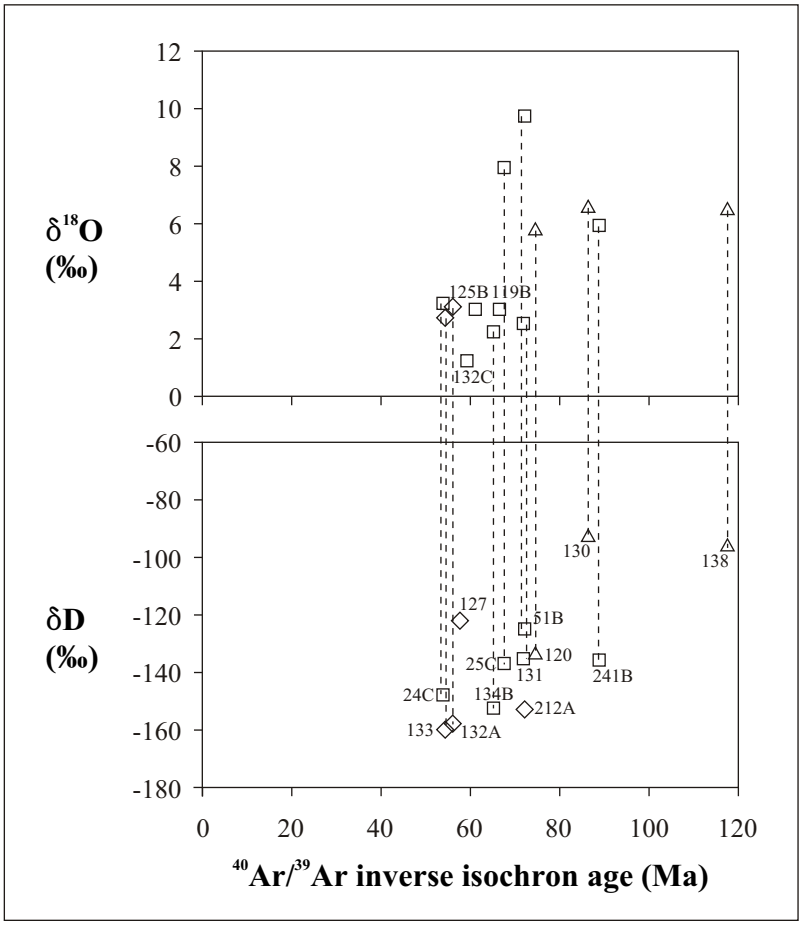

Fig. 3.4. Plot of whole-rock $\delta^{18}O$ and hornblende δD versus the respective $^{40}Ar/^{39}Ar$ inverse isochron age of hornblende in amphibolites. Symbols as in Fig. 3.3. 'RS' is omitted from sample numbers. Data from one sample are connected by dashed lines. Amphibolites with younger dates and plateau or near-plateau spectra underwent the greatest depletion of ^{18}O and D.

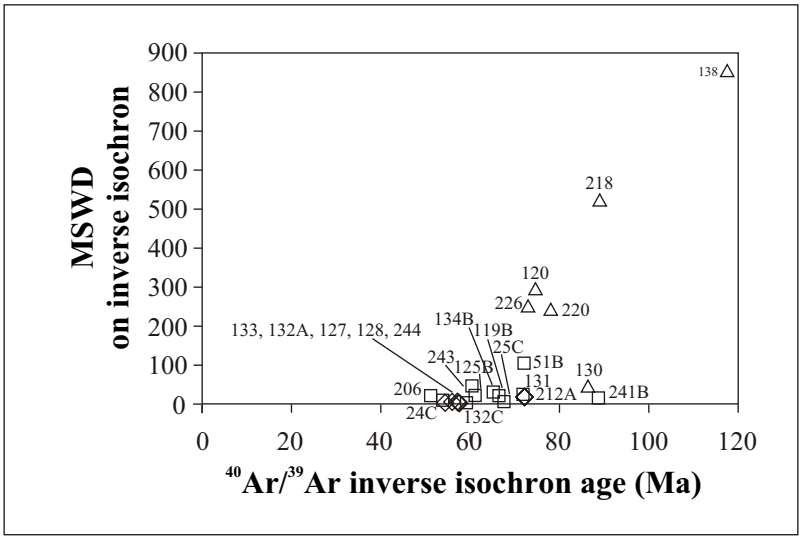

Fig. 3.5. Plot of the MSWD (mean squares of weighted deviates) of the $^{40}Ar/^{39}Ar$ inverse isochron versus the inverse isochron age. Symbols and sample numbers as in Figs. 5.3 and 5.4. Amphibolites with $^{40}Ar/^{39}Ar$ inverse isochron ages younger than ~75–70 Ma all have plateau or near-plateau spectra, and a relatively small (<6.5) MSWD for the isochron. Older amphibolites mostly have disturbed spectra and greater MSWD values.

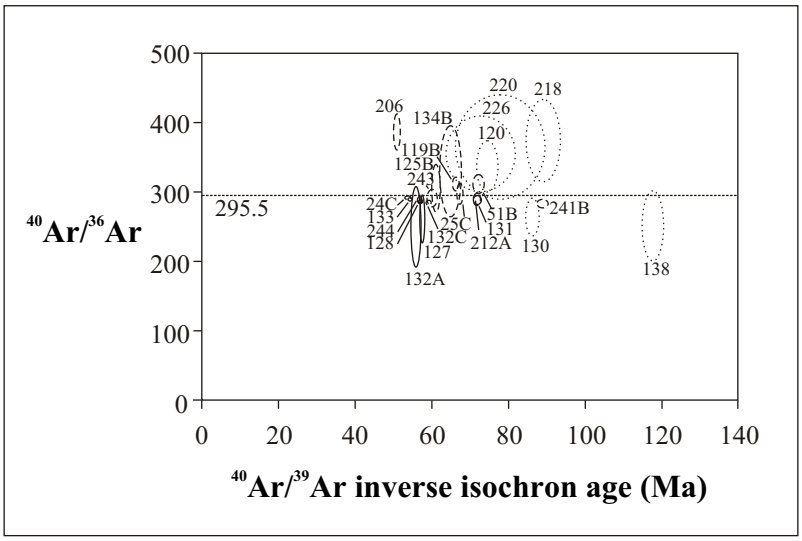

Fig. 3.6. Plot of initial $^{40}Ar/^{36}Ar$ ratios versus $^{40}Ar/^{39}Ar$ inverse isochron ages of hornblende. An $^{40}Ar/^{36}Ar$ ratio of 295.5 represents the composition of atmospheric argon. Ellipses represent a 2σ uncertainty. Solid, dashed and dotted ellipses are data from amphibolites with plateau-, near-plateau- and disturbed spectra respectively. Sample numbers as in Fig. 5.4.

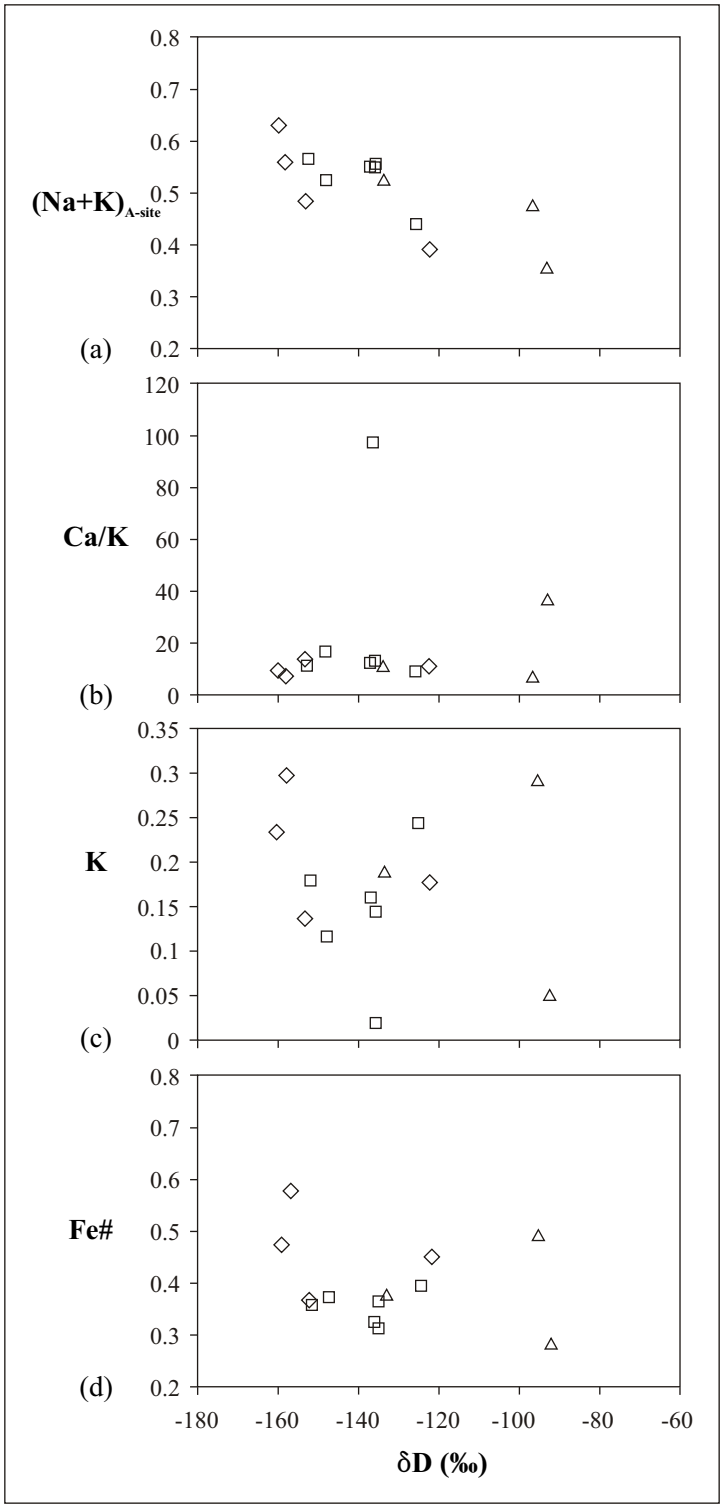

Fig. 3.7. Plots of A-site occupations (Na+K) (a), Ca/K ratios (b), K-contents (c) and Fe-numbers (d) versus $^{40}Ar/^{39}Ar$ inverse isochron ages of hornblende. Symbols and sample numbers as in Figs. 3.3 and 3.4. Inverse isochron ages decrease with higher A-site occupancies, lower Ca/K ratios, higher K-contents and higher Fe-numbers.

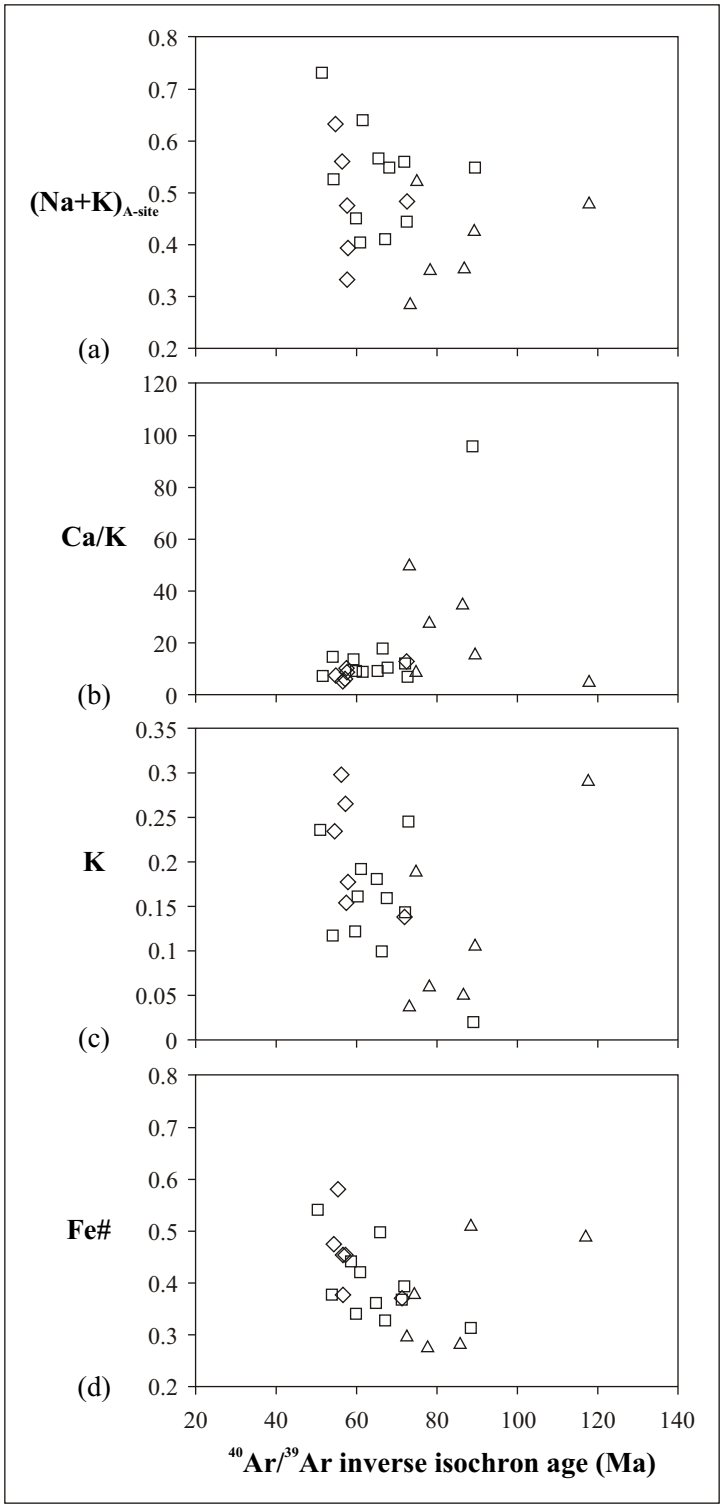

Fig. 3.8. Plots of A-site occupations (Na+K) (a), Ca/K ratios (b), K-contents (c) and Fe-numbers (d) versus δD values for hornblende. Symbols as in Fig. 3.3. Decreasing δD values are related to increasing A-site occupancies, and less clearly to decreasing Ca/K ratios, increasing K-contents, and increasing Fe-numbers.

(a)

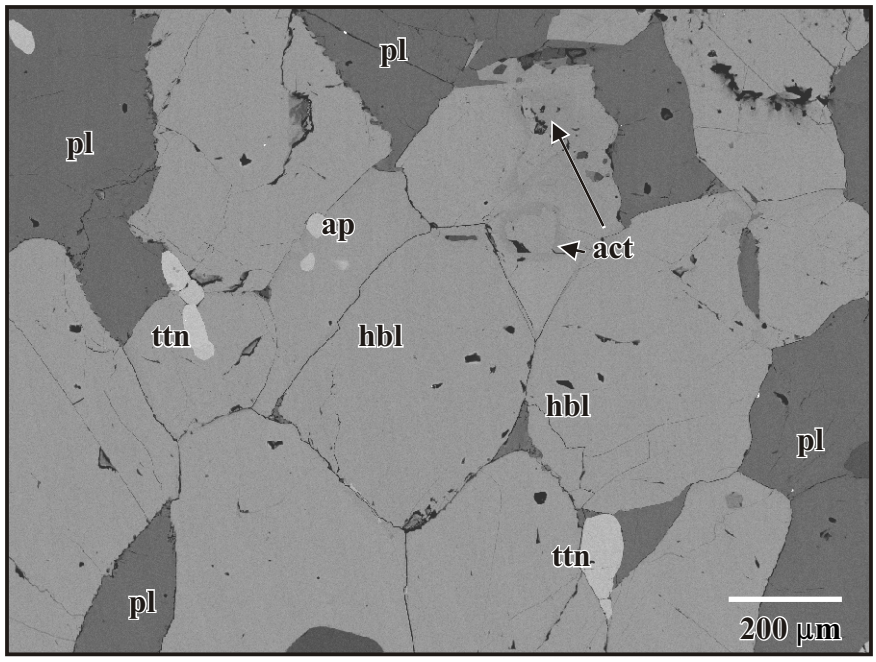

(b)

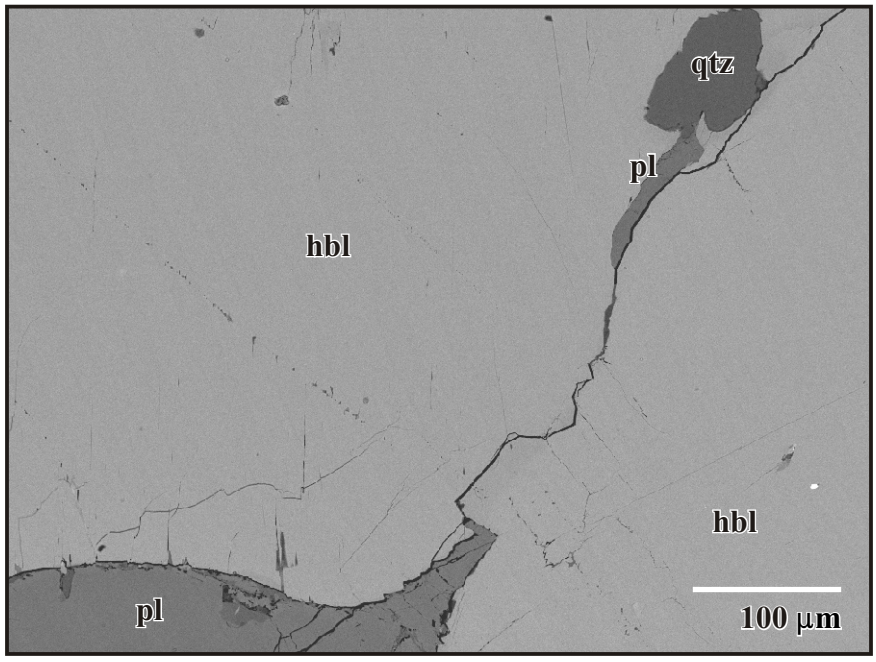

Fig. 3.9. Back scattered electron (BSE) images of sample RS24C. Mineral abbreviations after Kretz (1983). Hornblende grains show no alteration except to some actinolite (a). No alteration is present along grain boundaries (b).

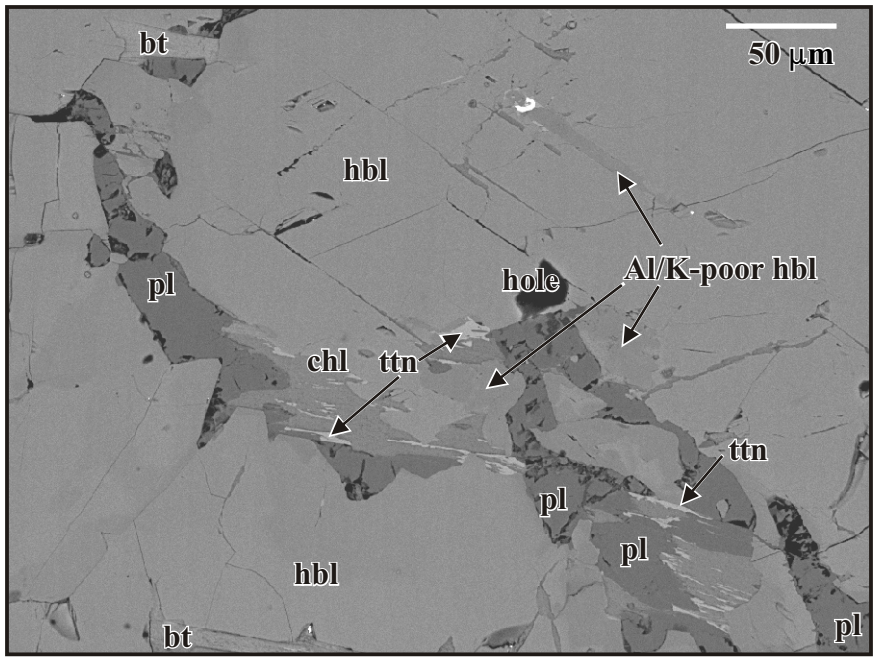

Fig. 3.10. BSE image of sample RS138. Retrograde chlorite and titanite grows along hornblende grain boundaries and Al/K-poor hornblende occurs along grain boundaries and cleavage planes.

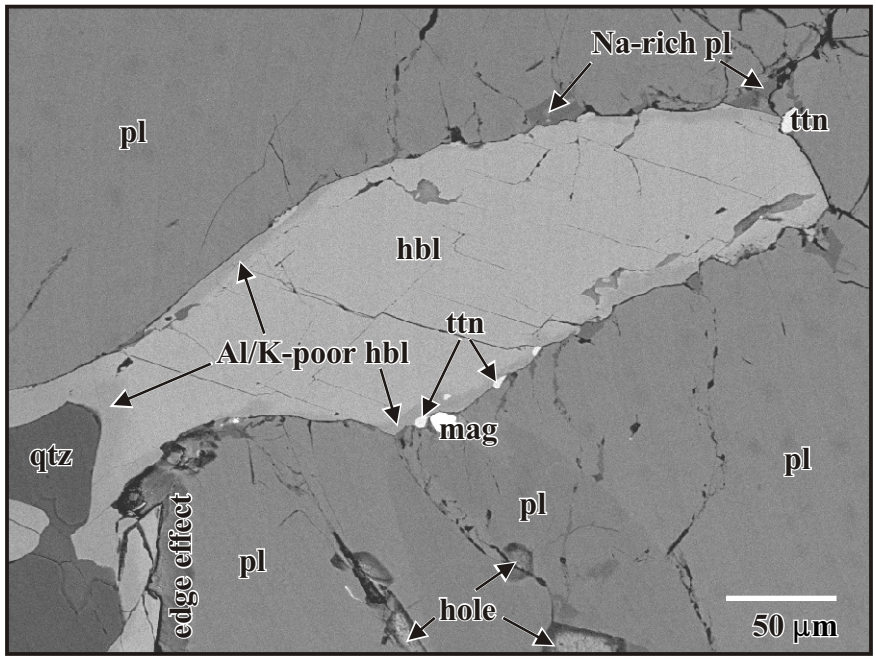

Fig. 3.11. BSE image of sample RS241B. Al/K-poor hornblende grows along the edge of the hornblende crystal.

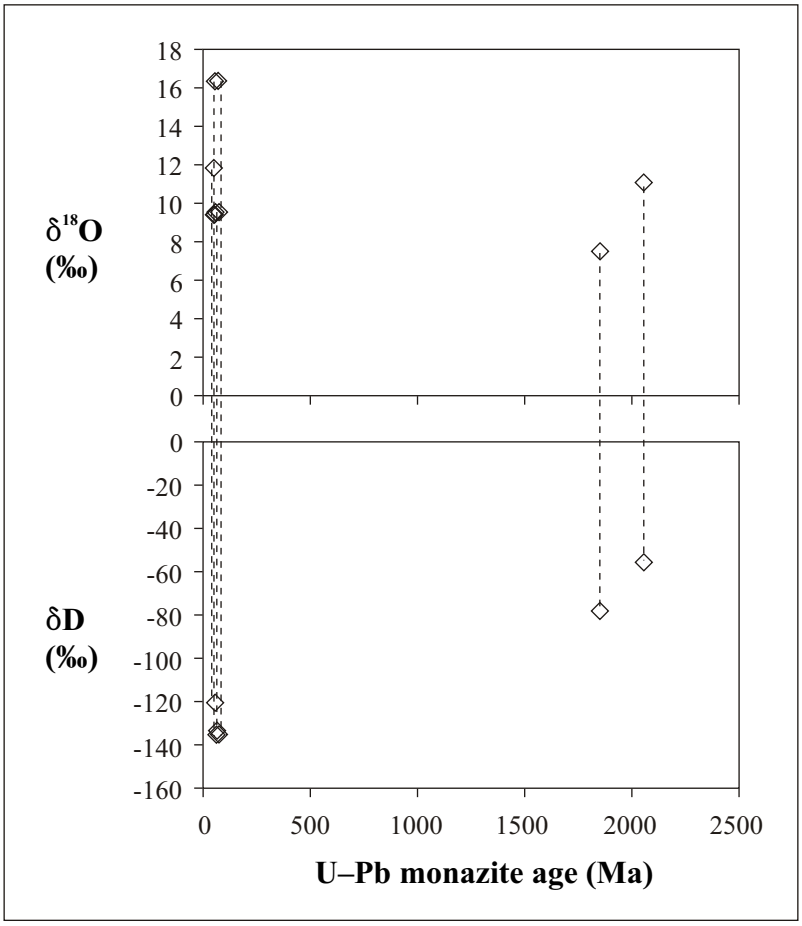

Fig. 3.12. Plot of whole-rock $\delta^{18}O$ and δD values versus U–Pb monazite ages. Data from one sample are connected by dashed lines. The Proterozoic ages were derived from samples of an orthogneiss and a pelitic schist from Frenchman Cap. The young ages are from samples of orthogneiss, paragneiss, pelitic schist and pegmatite from Thor–Odin (see Table 5).

Chapter 4

Isotopic age constraints from electron microprobe U–Th–Pb dates, using a three-dimensional concordia diagram[1]

Abstract

This chapter demonstrates with the use of a three-dimensional U–Th–Pb concordia diagram that electron microprobe U–Th–Pb analyses yield isotopic age constraints on isotopically concordant and discordant data that have not previously been recognised. The three-dimensional U–Th–Pb concordia diagram is discussed. It is proven that a date obtained from a microprobe analysis is as old as or younger than the $^{207}Pb/^{235}U$ and $^{207}Pb/^{206}Pb$ ages and as old as or older than the $^{208}Pb/^{232}Th$ age. Microprobe analyses always yield a minimum age for the oldest Pb component.

4.1. Introduction

The technique of microprobe U–Th–Pb dating of minerals that are rich in Th, U and radiogenic Pb, especially monazite, has been developed over the past decade (e.g. Suzuki and Adachi, 1991; Montel et al., 1996; Williams and Jercinovic, 2002, and references therein) and is now widely used. Because, in the spot analysis, element concentrations are measured rather than isotopes, two major assumptions need to be

[1] In review: Kuiper, 2003, Geology.

made: (1) no common Pb is present and (2) the system has remained closed and the analysed volume is homogeneous, and therefore isotopic data would yield concordant ages (Montel et al., 1996; Williams and Jercinovic, 2002). The first assumption is thought to be reasonable, because the common Pb concentration in minerals is much less than the detection limit, and less than the measurement error, for Pb on the microprobe (cf. Montel et al., 1996, and references therein). The second assumption has been considered reasonable, because the microprobe spots are as small as 2 μm, and microprobe element maps may be utilized to identify compositional domains that may correspond with possible age domains (Williams et al., 1999; Williams and Jercinovic, 2002). Therefore, the chance that two age domains overlap within the analysed volume is small. Furthermore, for monazite, the mineral used most often for microprobe dating (cf. Cocherie and Albarede, 2001; Williams and Jercinovic, 2002), Pb loss by volume diffusion is negligible (Braun et al., 1998; Cocherie et al., 1998; Crowley and Ghent, 1999; Cocherie and Albarede, 2001).

However, monazite can lose Pb by recrystallisation (Teufel and Heinrich, 1996; Hawkins and Bowring, 1997; Ayers et al., 1999; Crowley and Ghent, 1999), alteration (Hawkins and Bowring, 1997; Braun et al., 1998; Poitrasson et al., 2000) or partial dissolution and precipitation (Teufel and Heinrich, 1996; Ayers et al., 1999; Poitrasson et al., 2000). Furthermore, the method has been extended to other minerals (e.g. zircon) that are more susceptible to Pb loss (e.g. Gebauer and Grünenfelder, 1976; Mezger and Krogstad, 1997). Therefore, the possibility exists that the mineral analysed lost Pb. Also, a small possibility exists that two age domains within a mineral are probed, in which case the assumption that the analysed volume is homogeneous (see above) is

invalid. This may occur if the spot analysis intersects a second age domain at depth, or if the age domains are not coincident with the compositional domains (e.g. Catlos et al., 2002), or if small grains are analysed.

If Pb loss occurred, then the Pb/(Th+U) ratio is lowered with respect to the original ratio. If more than one age domain is probed by the microprobe beam, then the total Pb/(Th+U) ratio is lower than that of the oldest age domain. Therefore, a microprobe analysis of a discordant analysis always has a lower Pb/(Th+U) ratio and therefore yields a younger apparent age than the age of oldest Pb component, and isotopic discordance cannot be recognised by electron microprobe methods. This chapter shows more specifically that microprobe U–Th–Pb dates are minimum $^{207}Pb/^{235}U$ ages and $^{207}Pb/^{206}Pb$ ages, and maximum $^{208}Pb/^{232}Th$ ages. A hypothetical example is used to illustrate this. It is assumed that no common Pb is present, and that no excess amounts of ^{206}Pb or ^{207}Pb, as a result of decay of excess ^{230}Th and ^{231}Pa, respectively, are present (cf. Schärer, 1984). Because the purpose of this paper is theoretical, to establish a link between U–Th–Pb dates from microprobe and from isotopic analysis, analytical errors are not taken into consideration.

4.2. Methods of microprobe U–Th–Pb dating

A detailed description of the theory and methods of microprobe U–Th–Pb dating is given by Montel et al. (1996) and Cocherie and Albarede (2001). Only concepts necessary for discussion in this chapter are explained here. One main disadvantage of

microprobe dating, as opposed to U–Th–Pb isotopic dating, is that concentrations of the three elements in the minerals are measured instead of isotopic compositions. Three isotopic systems are of interest: ^{232}Th–^{208}Pb, ^{238}U–^{206}Pb and ^{235}U–^{207}Pb. Because ^{232}Th is the only principal naturally occurring isotope of Th (Faure, 1986), the ^{232}Th concentration is taken to be the same as the total Th concentration. The ^{235}U and ^{238}U concentrations are derived from the total U concentration and the abundances of the naturally occurring isotopes (0.0072 and 0.9928 respectively; Faure, 1986; cf. Montel et al., 1996). The Pb concentration is the sum of the ^{206}Pb, ^{207}Pb and ^{208}Pb concentrations. The concentrations of the individual Pb isotopes cannot be determined by microprobe methods. An age can be calculated from the element concentrations using the formula

$$Pb = Th*208/232*(\exp(\lambda^{232}t_{1m})-1) + U*206/238.04*0.9928*(\exp(\lambda^{238}t_{2m})-1) + U*207/238.04*0.0072*(\exp(\lambda^{235}t_{3m})-1) \quad (1)$$

in which Pb, Th and U are the concentrations of the three elements in ppm, λ^{232}, λ^{238} and λ^{235} are the decay constants of ^{232}Th, ^{238}U and ^{235}U respectively (per m.y.) and t is the age in Ma (cf. Montel et al., 1996). By assuming that the isotopic data are concordant, the age derived from each isotope system is the same ($t_{1m} = t_{2m} = t_{3m}$; t_m represents microprobe age) and a unique solution exists for t_m when the element concentrations are known. However, if data are discordant, e.g. because of Pb loss, the age derived from each of the three isotope systems is different and the age calculated by assuming $t_{1m} = t_{2m} = t_{3m}$ does not represent the age of the mineral of interest. Rhede et al. (1996) and

Cocherie and Albarede (2001) developed methods to calculate Th/Pb and U/Pb ages independently, whereby discordance between the Th/Pb age and the U/Pb age can be recognised, but not discordance between the $^{206}Pb/^{238}U$ and $^{207}Pb/^{235}U$ ages (i.e. $t_{1m} \neq t_{2m} = t_{3m}$).

4.3. Microprobe isotopic age constraints on discordant analyses

In microprobe dating, the total Pb concentration is measured, which is the same as the total of ^{206}Pb, ^{207}Pb and ^{208}Pb concentrations. By assuming that a microprobe analysis yields a concordant age, for discordant data one or two of the three Pb isotope concentrations have to be overestimated and one or two underestimated. They cannot all be overestimated or underestimated, because the total measured Pb concentration would be higher or lower than total of ^{206}Pb, ^{207}Pb and ^{208}Pb concentrations of the discordant data point. Whether the Pb isotopes are over- or underestimated depends on the decay rates of their parent isotopes. Of the three isotope systems of interest, ^{235}U decays fastest (half life is 0.70381 Gy), ^{238}U decays more slowly (half life is 4.4683 Gy) and ^{232}Th is the slowest (half life is 14.010 Gy) (decay constants from Steiger and Jäger, 1977). In microprobe dating of isotopically discordant material, the Pb isotope concentration of the fastest decay system (^{207}Pb) is underestimated and the Pb isotope concentration of the slowest decay system (^{208}Pb) overestimated, such that the total Pb concentration of the actual discordant analysis and the concordant microprobe analysis remain the same. ^{206}Pb may be over- or underestimated.

4.3.1. Microprobe isotopic age constraints on discordant analyses; the mathematical approach

In this section, the range of possible microprobe ages is calculated for a given isotopically discordant data point. In isotopic dating, under the assumption that no common Pb is present, the isotopic composition of Pb can be expressed by three equations (cf. Faure, 1986):

$$^{208}Pb = {}^{232}Th(\exp(\lambda^{232}t_1)-1) \quad (2)$$

$$^{206}Pb = {}^{238}U(\exp(\lambda^{238}t_2)-1) \quad (3)$$

$$^{207}Pb = {}^{235}U(\exp(\lambda^{235}t_3)-1) \quad (4)$$

The total amount of radiogenic Pb is:

$$Pb = {}^{232}Th(\exp(\lambda^{232}t_1)-1) + {}^{238}U(\exp(\lambda^{238}t_2)-1) + {}^{235}U(\exp(\lambda^{235}t_3)-1) \quad (5)$$

Formula (5) is similar to a modified version of formula (1):

$$Pb = Th(\exp(\lambda^{232}t_{1m})-1) + 0.9928U(\exp(\lambda^{238}t_{2m})-1) + 0.0072U(\exp(\lambda^{235}t_{3m})-1) \quad (6)$$

in which Pb, Th and U are atomic amounts instead of concentrations in ppm as in formula (1). Because Pb in equation (6) must be equal to Pb in equation (5), the equations can be

resolved as follows:

$$^{232}Th(\exp(\lambda^{232}t_1)-1) + {}^{238}U(\exp(\lambda^{238}t_2)-1) + {}^{235}U(\exp(\lambda^{235}t_3)-1) = Th(\exp(\lambda^{232}t_{1m})-1) + 0.9928U(\exp(\lambda^{238}t_{2m})-1) + 0.0072U(\exp(\lambda^{235}t_{3m})-1) \quad (7)$$

Because in microprobe dating $t_{1m} = t_{2m} = t_{3m}$, the microprobe age (t_m) can be resolved in this equation if the Th and U concentrations, and the isotopic ages (t_1, t_2 and t_3) of an analysis, are known. If the Th and U concentrations are not known, a range of possible ages for t_m can be calculated for a given set of isotopic ages. Equation (7) can be rewritten as:

$$Th(\exp(\lambda^{232}t_1)-1) + 0.9928U(\exp(\lambda^{238}t_2)-1) + 0.0072U(\exp(\lambda^{235}t_3)-1) = Th(\exp(\lambda^{232}t_m)-1) + 0.9928U(\exp(\lambda^{238}t_m)-1) + 0.0072U(\exp(\lambda^{235}t_m)-1) \quad (8)$$

The minimum and maximum possible ages for t_m are for the conditions where the U and Th concentrations are 0, respectively, because the concentrations cannot be negative. If U=0:

$$Th(\exp(\lambda^{232}t_1)-1) = Th(\exp(\lambda^{232}t_m)-1);\ t_m = t_1\ (= {}^{208}Pb/{}^{232}Th \text{ age}) \quad (9)$$

If Th=0:

$$0.9928U(\exp(\lambda^{238}t_2)-1) + 0.0072U(\exp(\lambda^{235}t_3)-1) = 0.9928U(\exp(\lambda^{238}t_m)-1) + 0.0072U(\exp(\lambda^{235}t_m)-1) \quad (10)$$

or

$$0.9928\exp(\lambda^{238}t_2) + 0.0072\exp(\lambda^{235}t_3) = 0.9928\exp(\lambda^{238}t_m) + 0.0072\exp(\lambda^{235}t_m) \quad (11)$$

The youngest age constraint is therefore the $^{208}Pb/^{232}Th$ age, and the oldest age constraint is between the $^{206}Pb/^{238}U$ age and the $^{207}Pb/^{235}U$ age, according to equation (11).

To illustrate the point, a hypothetical mineral that grew at 2.80 Ga and experienced 30% Pb loss at 0 Ma is considered. This example is solely chosen because it well illustrates the relationship between an isotopically discordant data point and its range of potential microprobe dates (especially for the graphical approach discussed in Section 4.3.3 and Figs. 4.1 and 4.2), not because it is necessarily a common scenario for mineral domains analysed on the microprobe. A mineral with an age of 2.80 Ga would have isotopic ratios of $^{208}Pb/^{232}Th = 0.149$, $^{206}Pb/^{238}U = 0.544$ and $^{207}Pb/^{235}U = 14.8$ according to formulae (2), (3) and (4) respectively. If the same mineral lost 30% of its Pb, then the ratios become 0.104, 0.381 and 10.3 respectively. The isotopic ages of the now discordant point would be: $^{208}Pb/^{232}Th$ age = 2.00 Ga, $^{206}Pb/^{238}U$ age = 2.08 Ga and $^{207}Pb/^{235}U$ age = 2.47 Ga according to formulae (2), (3) and (4). Equations (9) and (11) can be resolved as follows:

$$(\exp(\lambda^{232}2000)-1) = (\exp(\lambda^{232}t_m)-1);\ t_m = 2000\ \text{Ma} \quad (12)$$

and

$$0.9928\exp(\lambda^{238}2080) + 0.0072\exp(\lambda^{235}2470) = 0.9928\exp(\lambda^{238}t_m) + 0.0072\exp(\lambda^{235}t_m);$$

$$t_m = 2176\ \text{Ma} \quad (13)$$

In the hypothetical example, t_m is, therefore, between 2.00 and 2.18 Ga.

4.3.2. The three-dimensional concordia diagram

In Fig. 4.1a–c, concordia plots of the three pairs of isotope systems are shown. In this thesis, the isotope system with the shorter half life is always plotted on the x-axis. The curvature in the concordia curve is dependent on the difference in half lives between the two isotopic decay schemes. Fig. 4.2 shows the three-dimensional concordia diagram of the three isotope systems, and clarifies the relationship between the three systems. The concordia curve does not lie in a plane and can therefore not be plotted in two dimensions.

The combination of the three isotopic systems (^{232}Th–^{208}Pb, ^{238}U–^{206}Pb and ^{235}U–^{207}Pb) was first used by Ahrens (1955). Steiger and Wasserburg (1966) and Allègre (1967) introduced the concordia curve in ^{208}Pb/^{232}Th - ^{207}Pb/^{235}U - ^{206}Pb/^{238}U space and used projections onto the ^{208}Pb/^{232}Th - ^{207}Pb/^{235}U and ^{206}Pb/^{238}U - ^{207}Pb/^{235}U planes (cf.

Fig. 4.1a, b), but not onto the $^{208}Pb/^{232}Th$ - $^{206}Pb/^{238}U$ plane (cf. Fig. 4.1c). The latter projection, with the $^{206}Pb/^{238}U$ ratio on the y-axis and the $^{208}Pb/^{232}Th$ ratio on the x-axis, is now frequently used in U–Th–Pb dating (e.g. Gibson, 1997; Crowley et al., 2000; Foster et al., 2000). Because it is mostly used for young data, in order to avoid the large errors on the $^{207}Pb/^{235}U$ ratio due to the low concentration of ^{207}Pb in young minerals, the part of the concordia curve that is enlarged to show young ages is nearly a straight line. However, one must bear in mind that, with the $^{206}Pb/^{238}U$ ratio on the y-axis and the $^{208}Pb/^{232}Th$ ratio on the x-axis, the concordia curve is concave upward due to the shorter half life of ^{238}U than that of ^{232}Th. Data that are discordant as a result of Pb loss or mixing of ages are 'normally' discordant in the sense used by Wetherill (1956) and Tilton (1960) (not reversely discordant as a result of excess ^{206}Pb; cf. Schärer, 1984) and therefore they plot above the concordia curve, on the side of the $^{206}Pb/^{238}U$ axis (cf. Figs. 4.1c, 4.2). In this thesis, the $^{208}Pb/^{232}Th$ ratio is plotted on the y-axis and the $^{206}Pb/^{238}U$ ratio on the x-axis (Fig. 4.1c), such that the concordia curve is concave downward, and discordant data plot below the concordia curve, in all three projections (Fig. 4.1a–c). In Fig. 4.2, the concordia curve projected on the $^{208}Pb/^{232}Th$ - $^{206}Pb/^{238}U$ plane is concave upward, such that the conventional U/Pb concordia curve (on the $^{206}Pb/^{238}U$ - $^{207}Pb/^{235}U$ plane) could be plotted on the back plane of the diagram.

4.3.3. Microprobe isotopic age constraints on discordant analyses; the graphical approach

For the following discussion, the projections shown in Fig. 4.1 are used, but the

example is also shown in Fig. 4.2. The same hypothetical example is used as in Section 4.3.1, in which a mineral grew at 2800 Ma and experienced 30% Pb loss at 0 Ma. The solid circle in Fig. 4.1a–c shows the data point on the discordia chord after 30% Pb loss. Dashed lines represent isotope ratios and the ages (as indicated) of the discordant point.

If the microprobe age is plotted on the concordia curve between 2.00 and 2.18 Ga, the $^{207}Pb/^{235}U$ ratio is underestimated and the $^{208}Pb/^{232}Th$ ratio overestimated with respect to the discordant point. If the microprobe age were younger than 2.00 Ga (the $^{208}Pb/^{232}Th$ age), all three isotope ratios would have to be underestimated, because the $^{206}Pb/^{238}U$, $^{207}Pb/^{235}U$ and $^{208}Pb/^{232}Th$ ratios along the concordia curve for ages younger than 2.00 Ga are never higher than the respective ratios of the discordant point (Fig. 4.1a–c). Therefore, all three Pb isotope concentrations would be underestimated because the Th and U isotope concentrations are known. Consequently the total Pb concentration of the microprobe data point would be lower than that of the discordant point, which is impossible. Therefore the $^{208}Pb/^{232}Th$ age is the youngest age constraint for t_m (for U = 0). The oldest age constraint (if Th = 0) is not simply the $^{207}Pb/^{235}U$ age, because the $^{207}Pb/^{235}U$ and $^{206}Pb/^{238}U$ isotopic systems are coupled and ^{238}U cannot be 0 without ^{235}U being 0. Therefore the oldest age constraint is between the $^{206}Pb/^{238}U$ and $^{207}Pb/^{235}U$ ages (2.18 Ga; equation (13)). The oldest age constraint can be calculated using equation (11), but cannot simply be derived from the concordia plots (Figs. 4.1, 4.2). For a concordant analysis, the microprobe age and the $^{206}Pb/^{238}U$, $^{207}Pb/^{235}U$ and $^{208}Pb/^{232}Th$ ages are the same. For these reasons, microprobe dates are always the same as or higher than the $^{208}Pb/^{232}Th$ age and the same as or lower than the $^{207}Pb/^{235}U$ age. The $^{206}Pb/^{238}U$ ratio may be higher than, lower than, or the same as, the one derived from microprobe dating

(Fig. 4.1b, c). The amount of under- or overestimation of the isotope ratios cannot be resolved by microprobe methods. In order to know exactly where an analysis plots on the concordia diagrams, the isotopes need to be measured. For a typical monazite, with a high Th/U ratio, the microprobe age will be close to, but greater than, the $^{208}Pb/^{232}Th$ age. If, in the hypothetical example, Th = 100000 ppm and U = 5000 ppm, then t_m = 2.034 Ga. However, for monazites with lower Th/U ratios and for other minerals, t_m may be much greater than the $^{208}Pb/^{232}Th$ age. If a mineral would contain Th but no U, the microprobe age would be equal to the $^{208}Pb/^{232}Th$ age, but Pb loss would be undetectable.

Cocherie and Albrede (2001; cf. Rhede et al., 1996) use a Th/Pb versus U/Pb isochron diagram to represent their data and to derive independent Th/Pb and U/Pb ages. In this method, the Th/Pb age is not overestimated and the U/Pb age not underestimated, for discordant data, as in other microprobe dating methods as outlined above. Although a disadvantage of this method is that a number of analyses in a homogeneous domain is necessary to derive one Th/Pb age and one U/Pb age, the Th/Pb age would be the correct Th/Pb age or ratio of the discordant set. This age would be lower than the Th/Pb age as derived by the methods of Suzuki and Adachi (1991) and Montel et al. (1996). The U/Pb age would be higher than the U/Pb age derived by the methods of Montel et al. (1996) and Suzuki and Adachi (1991). However, discordance between $^{206}Pb/^{238}U$ and $^{207}Pb/^{235}U$ ages can still not be specified. Also, a Th/Pb age of a discordant analysis does not yield more information on the age of a domain or the age of Pb loss in a mineral than a U–Th–Pb microprobe date.

The fact that microprobe dates are minimum $^{207}Pb/^{235}U$ ages implies that they are also minimum $^{207}Pb/^{206}Pb$ ages, assuming data are not reversely discordant. $^{207}Pb/^{206}Pb$

ages are minimum ages for the oldest Pb component in the dated mineral, or spot analysis in the case of microprobe dating. Therefore a microprobe analysis yields a minimum age for the oldest Pb component in the spot analysed. If the analysis is concordant, then the microprobe age represents the age of the mineral or age domain within the mineral. If the analysis is discordant due to Pb loss, the mineral or age domain is older than the age derived from microprobe analysis. A small chance exists that the spot includes more than one age domain, in which case the oldest domain is older than the microprobe date and may or may not have experienced Pb loss.

4.4. Conclusions

Although ages derived from microprobe analysis do not indicate whether the analysis is discordant or not, it can be concluded that they are minimum age constraints on $^{207}Pb/^{235}U$ and $^{207}Pb/^{206}Pb$ ages and maximum age constraints on $^{208}Pb/^{232}Th$ ages. A microprobe date is always a minimum age constraint on the oldest Pb component.

Acknowledgements

I thank Douglas Hall, Paul Williams and Sharon Carr for their constructive comments. This work was supported by an NSERC grant to Paul F. Williams.

References

Ahrens, L.H., 1955. The convergent lead ages of the oldest monazites and uraninites

(Rhodesia, Manitoba, Madagascar, and Transvaal). Geochimica et Cosmochimica Acta 7, 294–300.

Allègre, C.J., 1966. Méthode de discussion géochronologique concordia generalisée: Application à la discussion des âges uranium–thorium–plomb discordants. Earth and Planetary Science Letters 2, 57–66.

Ayers, J.J., Miller, C., Gorisch, B., Milleman, J., 1999. Textural development of monazite during high grade metamorphism: Hydrothermal growth kinetics, with implications for U,Th–Pb geochronology. American Mineralogist 84, 1766–1780.

Braun, J., Montel, J.M., Nicollet, C., 1998. Electron microprobe dating of monazite from high-grade gneisses and pegmatites of the Kerala Khondalite Belt, southern India. Chemical Geology 146, 65–85.

Catlos, E.J., Gilley, L.D., Harrison, T.M., 2002. Interpretation of monazite ages obtained via in situ analysis. Chemical Geology 188, 193–215.

Cocherie, A., Legendre, O., Peucat, J.J., Kouamelan, A.N., 1998. Geochronology of polygenetic monazites constrained by in situ electron microprobe Th–U–total Pb determination: Implications for lead behaviour in monazite. Geochimica et Cosmochimica Acta 62, 2475–2497.

Cocherie, A., Albrede, F., 2001. An improved U–Th–Pb age calculation for electron microprobe dating of monazite. Geochimica et Cosmochimica Acta 65, 4509–4522.

Crowley, J.L., Ghent, E.D., 1999. An electron microprobe study of the U–Th–Pb systematics of metamorphosed monazite: The role of Pb diffusion versus overgrowth and recrystallization. Chemical Geology 157, 285–302.

Crowley, J.L., Ghent, E.D., Carr, S.D., Simony, P.S., Hamilton, M.A., 2000. Multiple thermotectonic events in a continuous metamorphic sequence, Mica Creek area, southeastern Canadian Cordillera. Geological Materials Research 2, 1–45.

Faure, G., 1986. Principles of isotope geology. John Wiley & Sons Ltd., Toronto.

Foster, G., Kinny, P., Vance, D., Prince, C., Harris, N., 2000. The significance of monazite U–Th–Pb age data in metamorphic assemblages; a combined study of monazite and garnet chronometry. Earth and Planetary Science Letters 181, 327–340.

Gebauer, D., Grünenfelder, M., 1976. U–Pb zircon and Rb–Sr whole-rock dating of low-grade metasediments example: Montagne Noir (Southern France). Contributions to Mineralogy and Petrology 59, 13–32.

Gibson, H.D., 1997. Thermotectonic evolution of the northern Monashee complex, southern Omineca Belt, southeastern British Columbia. MSc Thesis, Ottawa, Ontario,

Canada, Carleton University.

Hawkins, D.P., Bowring, S.A., 1997. U–Pb systematics of monazite and xenotime: case studies from the Paleoproterozoic of the Grand Canyon, Arizona. Contributions to Mineralogy and Petrology 127, 87–103.

Mezger, K., Krogstad, E.J., 1997. Interpretation of discordant U–Pb zircon ages: An evaluation. Journal of Metamorphic Petrology 15, 127–140.

Montel, J.-M., Foret, S., Veschambre, M., Nicollet, C., Provost, A., 1996. Electron microprobe dating of monazite. Chemical Geology 131, 37–53.

Poitrasson, F., Chenery, S., Shepherd, T.J., 2000. Electron microprobe and LA-ICP-MS study of monazite hydrothermal alteration: Implications for U–Th–Pb geochronology and nuclear ceramics. Geochimica et Cosmochimica Acta 64, 3283–3297.

Rhede, D., Wendt, I., Förster, H.-J., 1996. A three-dimensional method for calculating independent chemical U/Pb- and Th/Pb-ages of accessory minerals. Chemical Geology 130, 247–253.

Schärer, U., 1984. The effect of initial ^{230}Th disequilibrium on young U–Pb ages: the Makalu case, Himalaya. Earth and Planetary Science Letters 67, 191–204.

Steiger, R.H., Jäger, E., 1977. Subcommission on geochronology: convention on the use of decay constants in geo- and cosmochronology. Earth and Planetary Science Letters 36, 359–362.

Steiger, R.H., Wasserburg, G.J., 1966. Systematics in the Pb^{208}–Th^{232}, Pb^{207}–U^{235}, and Pb^{206}–U^{238} systems. Journal of Geophysical Research 71, 6065–6090.

Suzuki, K., Adachi, M., 1991. Precambrian provenance and Silurian metamorphism of the Tsubonosawa paragneiss in the South Kitakami terrane, Northeast Japan, revealed by the chemical Th–U–total Pb isochron ages of monazite, zircon and xenotime. Geochemical Journal 25, 357–376.

Teufel, S., Heinrich, W., 1997. Partial resetting of the U–Pb isotope system in monazite through hydrothermal experiments: An SEM and U–Pb isotope study. Chemical Geology 137, 273–281.

Tilton, G.R., 1960. Volume diffusion as a mechanism for discordant lead ages. Journal of Geophysical Research 65, 2933–2945.

Wetherill, G.W., 1956. Discordant uranium–lead ages. Transactions, American Geophysical Union 37, 320–326.

Williams, M.L., Jercinovic, M.J., Terry, M.P., 1999. Age mapping and dating of

monazite on the electron microprobe: Deconvoluting multistage tectonic histories. Geology 27, 1023–1026.

Williams, M.L., Jercinovic, M.J., 2002. Microprobe monazite geochronology: putting absolute time into microstructural analysis. Journal of Structural Geology 24, 1013–1028.

(a)

(b)

(c)

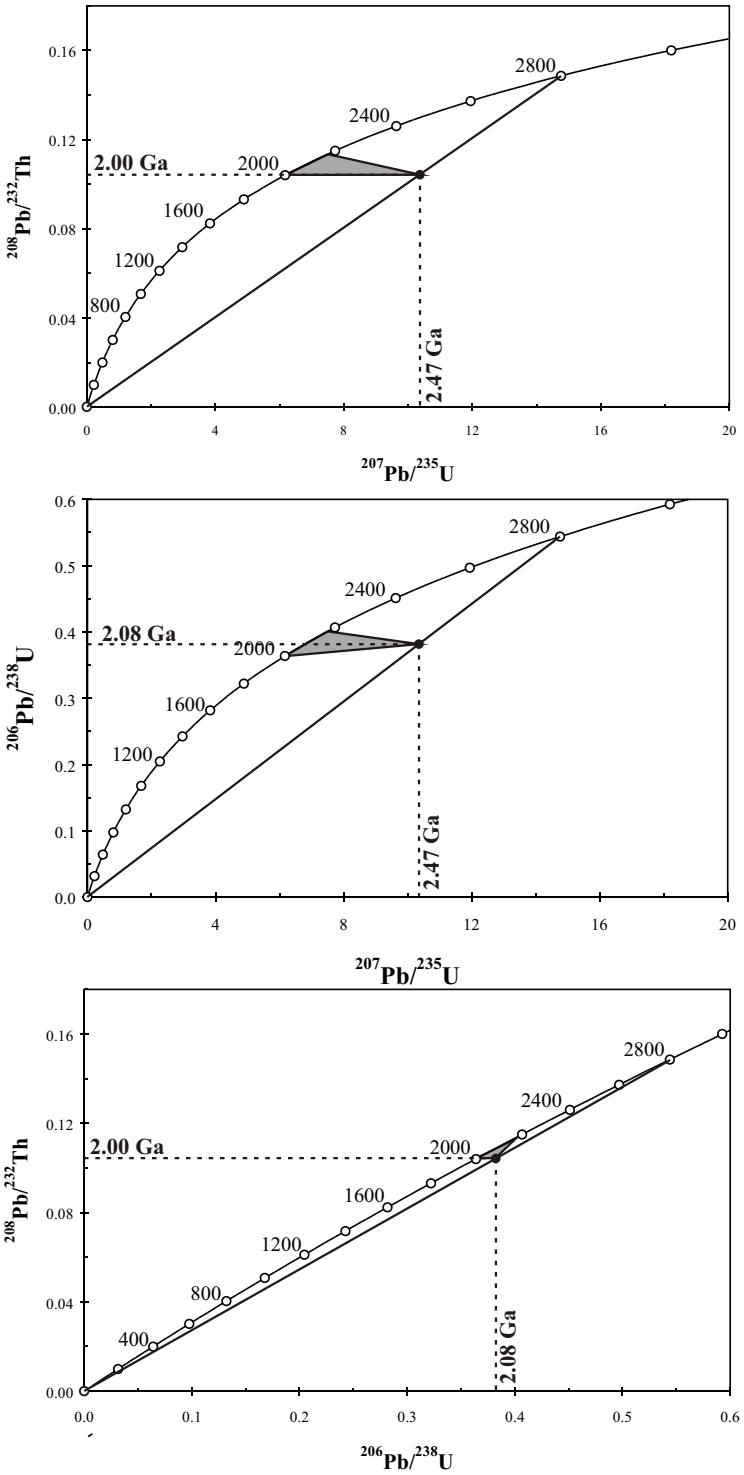

Fig. 4.1. Concordia diagrams, showing discordia chord between 2.80 Ga and 0 Ma, and a solid circle representing a point with 30% Pb loss. (a) U–Th–Pb concordia diagram with $^{208}Pb/^{232}Th$ versus $^{207}Pb/^{235}U$. (b) U–Pb concordia diagram with $^{206}Pb/^{238}U$ versus $^{207}Pb/^{235}U$. (c) U–Th–Pb concordia diagram with $^{208}Pb/^{232}Th$ versus $^{206}Pb/^{238}U$. Dashed lines indicate isotope ratios and corresponding ages of the discordant point (solid circle). Shaded areas show the connection between the discordant point and the range of possible microprobe ages.

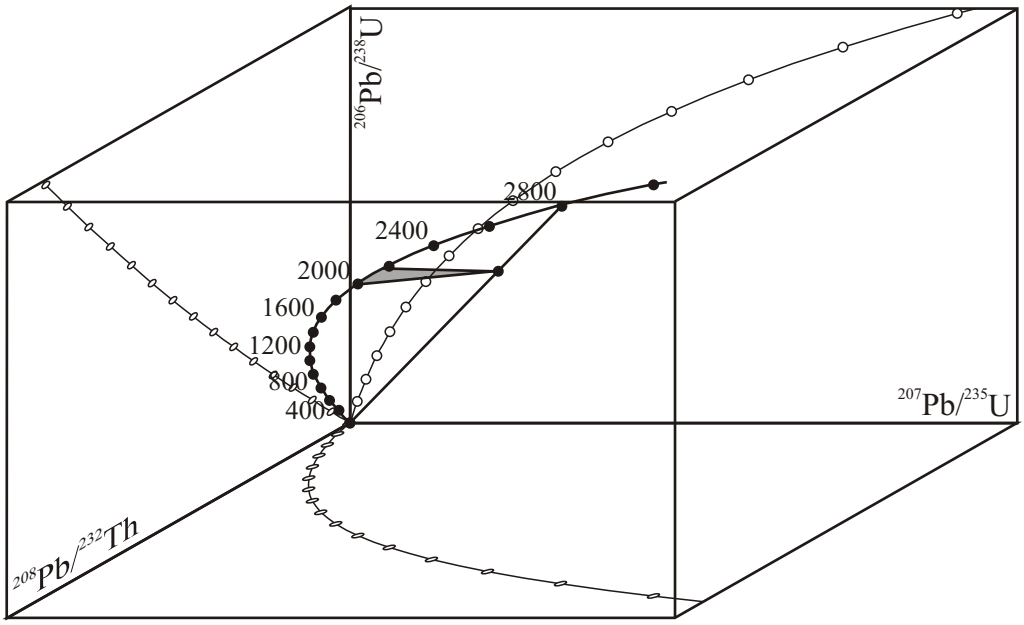

Fig. 4.2. Three-dimensional U–Th–Pb concordia diagram, with three-dimensional concordia curve (curve with filled circles), and its projections onto the faces of the diagram (curve with open circles). The same discordia chord and discordant point as in Fig. 4.1 are shown in three dimensions. Also indicated is the shaded surface between the discordant point and the possible microprobe ages that can be derived (2.00–2.18 Ga) ages). Note that the concordia curve does not lie in a plane and cannot be shown in a two dimensional plot without projecting it on one of the sides of the diagram.

Chapter 5

Proterozoic (and Mesozoic?) deformation and metamorphism in basement rocks of Thor–Odin dome of the Monashee Complex, southeastern British Columbia

Abstract

Palaeoproterozoic deformation and metamorphism in the Monashee Complex has previously only been recognised in the Frenchman Cap dome, the northern dome of the Monashee Complex. This chapter presents evidence for Palaeoproterozoic migmatisation, and discusses the possibility of other Palaeoproterozoic deformation and metamorphism in basement rocks of the Thor–Odin dome, the southern dome of the Monashee Complex. Sensitive High Resolution Ion Microprobe (SHRIMP) and Isotope Dilution Thermal Ionisation Mass Spectrometry (ID-TIMS) geochronological studies were carried out on a basement migmatitic orthogneiss in Thor–Odin. The protolith age is interpreted as ~2.1 Ga and the migmatisation age as ~1.8 Ga. Zircon overgrowth and monazite growth occurred at ~52 Ma. ID-TIMS discordia chords of four felsic intrusive dykes in the basement have Palaeoproterozoic upper intercept ages and Early Eocene lower intercept ages. A crosscutting aplite dyke, near Frigg Glacier in Thor–Odin, may indicate pre-1792 ± 49 Ma deformation (its upper intercept age, which may represent the crystallisation age), but possibly the 47.9 ± 11 Ma lower intercept age is the crystallisation age of the aplite dyke. A pegmatite in an F_1/F_2 boudin neck at Blanket

Mountain in northern Thor–Odin has an upper intercept of 1939 ± 6 Ma and a lower intercept of 52.5 ± 3.0 Ma. Again, it is unclear which age is the crystallisation age of the pegmatite. A folded pegmatite and a crosscutting aplite dyke were dated at Cranberry Valley in northern Thor–Odin, in order to constrain F_3 folding. However, all zircon data are discordant and the monazite ages are Early Eocene, and the crystallisation ages of the pegmatite and aplite dyke cannot be determined. Lower intercept and/or monazite ages in all samples are Early Eocene, and may be interpreted as a result of extension (cf. Chapter 3).

It is shown how deformation and metamorphism could have happened at times not recorded by zircon and monazite. Cordilleran deformation may well have occurred in the Middle Jurassic and/or mid-Cretaceous, as in surrounding rocks of the Monashee Complex despite the lack of evidence within the Monashee Complex. If dissolution rather than growth of minerals used for U–Pb dating occurred during deformation and metamorphism, and if Pb loss was incomplete or absent, a deformation and/or metamorphic event may not be recorded. Evidence for dissolution of zircon between ~1.8 Ga and 52 Ma is presented for the migmatitic basement orthogneiss.

5.1. Introduction

U–Pb geochronology is used to determine the protolith age, age of migmatisation and the age of a later event, in a migmatitic basement orthogneiss in Thor–Odin. ID-TIMS zircon analyses resulted in discordant data. SHRIMP data resulted in concordant

ages, which are related to particular domains within the zircon with the use of cathodoluminescence (CL) images. Four felsic dykes were dated by ID-TIMS methods in order to constrain specific deformation events. Their data can be interpreted in several ways.

5.2. Geological background

The Monashee Complex is an exposure of ancestral North American rocks within the southern Omineca Belt in southeastern British Columbia (Fig. 5.1). It has a Palaeoproterozoic basement of orthogneiss and paragneiss (Armstrong et al., 1991, and references therein; Parkinson, 1991) and a Palaeoproterozoic to Palaeozoic (?) cover of quartzite, marble, calc-silicate gneiss, pelitic schist and paragneiss (Parrish, 1995, and references therein). The Monashee Complex has two structural culminations: Frenchman Cap in the north and Thor–Odin in the south (Fig. 5.1).

Previously recognised orthogneiss protolith ages in the basement of Frenchman Cap are 2.08, 1.86, 1.85, and possibly 2.27 and 2.10 Ga (Crowley, 1999) and in Thor–Odin they are 1.87 and 1.93 (Parkinson, 1991) and 1.96 (Wanless and Reesor, 1974). Palaeoproterozoic metamorphism has previously been dated at deep structural levels in Frenchman Cap at 2.06 Ga (Crowley, 1999) and ~1.85 Ga (Armstrong et al., 1991; Crowley, 1999), but not in Thor–Odin. Crowley (1999) proposed that at the deepest structural levels no significant deformation occurred after intrusion of the mostly undeformed 1852–1832 Ma Pettipiece pegmatite suite.

After deposition of the Monashee cover sequence, penetrative deformation occurred throughout the Monashee Complex. F_1/F_2 folds are tight to isoclinal and NE verging, with generally SW-dipping axial planes. Overprinting relationships between F_1 and F_2 folds can rarely be seen, and therefore the folds are commonly referred to as F_1/F_2 folds. The entire Monashee basement and cover sequence is strongly transposed (Williams, 1999; Spark, 2001), indicating that it is part of a regional NE-directed subhorizontal shear zone (Williams, 1999). Transposition caused dismembering of folds (e.g. Fig. 5.2) and lithological units, and therefore lithological units cannot always be correlated on a regional scale. Competent layers formed cm- to km-scale boudins (e.g., Johnston et al., 2000) during transposition, and were later folded (e.g. the amphibolite layer in Fig. 5.3). An example of a km-scale boudin is the 'Megaboudin', containing various cover lithologies and rimmed by quartzite, located at Blanket Mountain (Fig. 5.4b). F_3 folds are isoclinal to open and verge predominantly to the NE within the Monashee Complex. An example of overprinting of F_1 by F_2 and F_3 folds in marble is shown in Fig. 5.5. F_3 folds have been interpreted as a product of the same shear zone that was responsible for transposition (Williams and Jiang, in review). They are overprinted by gentle upright F_4 folds. Shear bands in and around the Monashee Complex, a zone of concentrated extension along the NW flank of Thor–Odin (Johnston et al., 2000) and later brittle normal faults, indicate extension (D_5). Shear bands and faults occurred both at large scales (e.g. localised faults such as the Columbia River Fault; Fig. 5.1) and at small scales in a penetrative way. Eocene (sub)vertical pegmatites (e.g. Johnston et al., 2000) and lamprophyres (e.g. Lane, 1984) intruded during late extension and are undeformed.

Peak of metamorphism in most of the Monashee Complex, related to transposition, occurred under upper amphibolite facies conditions (e.g. Journeay, 1986).

Based on regional correlations, Brown et al. (1986) inferred penetrative deformation, related to the NE movement described above (Cordilleran deformation), and deep burial of the Monashee Complex, to have taken place in the Jurassic. Journeay (1986) recognised two pulses of deformation and metamorphism in Frenchman Cap dome. He interpreted metamorphism related to F_2 folding as having been between upper amphibolite–lower granulite in the deepest structural levels of Frenchman Cap and middle amphibolite along the flanks of the dome, and as having occurred in the Middle Jurassic. Metamorphism related to F_3 folding was middle greenschist in the deepest structural levels of the complex, and upper amphibolite–lower granulite at higher structural levels and was related to mid-Cretaceous regional deformation (Journeay, 1986).

More recently, Carr (1992), Parrish (1995, and references therein), Crowley and Parrish (1999) and Gibson et al. (1999) have tried to constrain the timing of Cordilleran deformation and metamorphism. Monazite, zircon, titanite and xenotime dates in Frenchman Cap, which range from ~78 Ma at the highest structural levels (Gibson et al., 1999) to 49 Ma at the deepest structural levels of the complex (Crowley and Parrish, 1999), were interpreted as metamorphic ages. Older ages of deformation and metamorphism (as old as ~170 Ma) have been reported away from the complex, in the Selkirk and Cariboo Mountains, and are supported by interpretations based on stratigraphy and the fossil record (Parrish, 1995, and references therein). All data together were interpreted as indicating a younging of structures and thermal peak of

metamorphism towards deeper structural levels in the Selkirk Allochthon and Monashee Complex. U–Pb data from western Thor–Odin fit the same pattern (Johnson, 1994; Johnston et al., 2000).

Cordilleran deformation and metamorphism can be related to accretion of terranes to the west of the Monashee Complex. The Intermontane Superterrane (Fig. 5.1) has been interpreted as having accreted onto the North American craton in the Middle Jurassic, and the Insular Superterrane (Fig. 5.1) in the mid-Cretaceous (Monger et al., 1982; Murphy et al., 1995). Movement towards the NE in the Monashee Complex and surrounding areas could well have been related to accretion of the terranes (e.g. Journeay, 1986). Based on the U–Pb data outlined above, Carr (1992), Parrish (1995, and references therein), Crowley and Parrish (1999) and Gibson et al. (1999) interpreted deformation as a result of crustal shortening taking place diachronously, from ~170 Ma at high structural levels to 49 Ma at the deepest levels in the Monashee Complex.

5.3. Methods and definitions

5.3.1. Isotope Dilution Thermal Ionisation Mass Spectrometry (ID-TIMS)

U–Pb geochronology was carried out at Carleton University under the supervision of S.D. Carr. Heavy minerals were separated from ~10–25 kg rock samples by standard crushing, grinding, Rogers Gold™ table separation, sieving through a 250 μm screen and heavy liquid separation. Mineral separates containing the least magnetic zircon and monazite were separated by Frantz™ magnetic separation techniques, following removal

of the most magnetic minerals, using a rare earth magnet. The separates were sieved in alcohol into various size fractions. Minerals with the least amount of inclusions and fractures, the best clarity and no visible cores and overgrowths were selected for dating by handpicking under an optical microscope. Where zircon tips were used, these were either cut by hand, or tips broken during crushing and grinding were selected. Therefore, some of the tips may contain core material. Grains that were not dated were selected for backscattered electron (BSE) imaging, in order to obtain a better understanding of their internal morphologies. All zircon fractions were abraded with pyrite (Krogh, 1982), and washed in warm HNO_3 to remove abrasion residues.

Minerals selected for dating were spiked with a mixed ^{205}Pb–^{233}U–^{235}U tracer (Parrish and Krogh, 1987) and dissolved in HF (zircon) or HCl (monazite) in Teflon^{TM} microcapsules (Parrish, 1987). U and Pb were separated using anion exchange column chemistry procedures described by Parrish et al. (1987) (cf. Krogh, 1973; Roddick et al., 1987) and their isotopic compositions were measured on a Finnigan-MAT 261 variable multicollector mass spectrometer (Roddick et al., 1987). Procedural blanks were generally less than 5 pg for U and 6–60 pg for Pb. For monazite fractions M1–M3 of sample s298-117 and M1–M4 of s298-120, Pb blanks were up to 386 pg due to contamination from an unknown source. Common-Pb corrections were made using Pb compositions derived from Stacey and Kramers (1975). Decay constants recommended by Steiger and Jäger (1977) were used. Errors on isotope ratios were estimated using numerical error propagation (Roddick, 1987). All errors on ages are reported at the 2σ level. Discordia chords through data were calculated using a modified York (1969)

regression (Parrish et al., 1987). All data, including SHRIMP data (see below), were plotted using Isoplot/Ex v. 2.49 (Ludwig, 2001).

5.3.2. The Sensitive High Resolution Ion Microprobe (SHRIMP)

Zircon from sample s298-65 was analysed on the SHRIMP II at the Geological Survey of Canada (GSC) in Ottawa, in collaboration with M.A. Hamilton, following methods described by Stern (1997) and Stern and Sanborn (1998). Minerals that had been separated for the ID-TIMS study were mounted in epoxy and polished to reveal the internal structures of the grains. Spots were selected for analysis based on CL images taken on a Cambridge Instruments S360 scanning electron microscope (SEM) at the GSC in Ottawa. The grain mount was repolished and coated with conductive high purity Au (99.9999%). Spot sizes were ~17*21 μm. GSC zircon standard BR266 was used for calibrations of the Pb/U and Pb/Th ratios (Stern, 1997). Pb/U and Pb/Th ratios were calibrated using GSC monazite standards 2908, 3345 and 4170 (Stern, 1997). Common-Pb corrections for all isotope ratios were made using the ^{204}Pb method (Stern, 1997). ^{206}Pb/^{238}U ages corrected for common Pb using the ^{207}Pb method (Stern, 1997) are discussed in Section 6.4.2. Errors on ages and error ellipses in concordia diagrams are 1σ, in order to avoid large overlaps of error ellipses, which makes it hard to distinguish data from different spots. Note that all errors for ID-TIMS ages are reported at the 2σ level.

5.3.3. Discordance, reverse discordance, and assignment of errors

A fraction is considered to be concordant if it is less than 0.3% discordant or reversely discordant (S.D. Carr, 2002, personal communication) and if its error ellipse overlaps concordia. A fraction that plots below concordia is considered to be discordant and a fraction that plots above concordia is reversely discordant. Th-rich minerals, e.g. monazites, may contain radiogenic ^{206}Pb in addition to that produced by decay of ^{238}U, resulting from decay of ^{230}Th (Schärer, 1984). This excess ^{206}Pb may result in reversely discordant data. This is especially obvious in young minerals, because of the much faster decay rate of ^{230}Th compared to ^{238}U. In 'old' (e.g. Late Cretaceous and older in this study) minerals, the amount of radiogenic Pb from U will be large enough that the amount of ^{206}Pb produced by ^{230}Th is negligible. Zircon is not Th-rich and therefore does not contain significant amounts of excess ^{206}Pb. To circumvent the problem of excess ^{206}Pb for reversely discordant ID-TIMS monazite data, the $^{207}Pb/^{235}U$ age is taken as the monazite age. However, one must bear in mind that this is only a best approximation, as the monazite systematics may be more complicated. For example, Fig. 5.6 shows two examples of how a reversely discordant data point can have been influenced by the presence of a component of older Pb, or by recent Pb loss (cf. Parrish, 1990). In these cases the $^{207}Pb/^{235}U$ age would not represent the true age of the monazite. In the case of a cluster of reversely discordant analyses, it is reasonable to use the $^{207}Pb/^{235}U$ age, as it is unlikely that all analyses contain the same mixture of two or more Pb components.

Errors on interpreted ages are the 2σ errors on upper and lower intercept ages of discordia chords. Where an average age is used (e.g. average $^{207}Pb/^{235}U$ age for reversely

discordant monazite data), the envelope of the errors of the data used is taken as the error on the average age.

5.4. Results

5.4.1. U–Pb geochronology

5.4.1.1. Basement orthogneiss (s298-65)

Sample s298-65 is a migmatitic basement orthogneiss on the NE slope of Blanket Mountain (Fig. 5.4b). The grey, granitic to granodioritic host orthogneiss is fine to medium grained and homogeneous, and contains (minerals given in order of decreasing content) feldspar, quartz and biotite and traces of sillimanite and unstable muscovite (reacting to biotite). Leucocratic leucosome has approximately the same composition, but is slightly coarser grained and contains less biotite. Both host rock and leucosome contain accessory zircon, rutile and monazite, and retrograde or late chlorite and scapolite. Host orthogneiss and leucosome are foliated and folded by F_1/F_2 and F_3. Leucosome is disposed in veins that are generally parallel to the foliation, but crosscut it in fold hinges. Leucosome is rimmed by biotite, and is interpreted as being a result of anatexis.

Zircons from the host orthogneiss and leucosome were analysed to constrain the protolith age and ages of later migmatisation and/or metamorphism. Both host rock and

leucosome are folded by F_1/F_2, and therefore the age of the host rock and of leucosomes would give a lower age constraint on F_1/F_2. Monazite crystals were dated to determine the age of metamorphism. Questions were whether Proterozoic metamorphic events occurred in Thor–Odin as in Frenchman Cap (2.06 and ~1.85 Ga; Crowley, 1999) and whether or not metamorphic events took place in the Mesozoic–Tertiary. Zircon and monazite fractions from the leucosome (c, d, g, h and m3, m4, m6 respectively) and from the host orthogneiss (A, B, E, F and M1, M2, M5 respectively) were analysed separately by ID-TIMS and SHRIMP methods. ID-TIMS data are discussed first (Fig. 5.7, Table 5.1). All grains are 149–250 μm in size. Zircon grains in the host orthogneiss are faceted bipyramidal prisms with aspect ratios between 1:1.5 and 1:2.5. The general population includes metamict, broken, and colourless to light yellow grains, interpreted as high-U grains. However, the dated crystals are colourless and have no fractures. Fraction A is a single crystal, with good clarity and an indentation. Fraction B consists of five clear zircons which have a few colourless inclusions. Fractions E and F are single zircon fractions with colourless inclusions. Fraction E has excellent clarity, and F is foggy and has a thin overgrowth. Zircon crystals in the leucosome are prismatic with aspect ratios between 1:1.5 and 1:4. All fractions have good clarity and a few colourless inclusions. Grain H has a colourless inclusion with a red rim. Fraction D consists of five zircons and fractions C, G and H are single grains. Fraction G seems to have an overgrowth on one tip. BSE images for grains of the host orthogneiss and the leucosomes reveal different internal structures. The zircons of the host orthogneiss show no internal structures, except for overgrowths and alteration (some are patchy). The zircons of the leucosomes have well developed oscillatory zonations, and they have cores and overgrowths. CL

images are described in the SHRIMP section below. Monazite crystals are yellow (M1, M2, m3) or pale yellow (m4, M5, m6), and have bad (M1), good (M2–M5) or excellent (m6) clarity. Monazites M1, M2, m4 and M5 are rounded or subrounded and have indentations. Fraction m3 is subhedral and m6 is euhedral. Monazites M1, M2, M5 and m6 have one colourless inclusion each. None has fractures. Some of the BSE images show patchy domains with curved boundaries (Fig. 5.7a shows an example of a monazite from the leucosome).

The monazite age is interpreted as 51.6 ± 0.7 Ma, the $^{207}Pb/^{235}U$ age of m3, the only reversely discordant fraction. Data from the monazites from leucosome and from host orthogneiss are consistent with each other and therefore they are considered together. Fractions M1 and m6 are discordant. Fraction M2 has poor U data, M4 has a high blank and M5 has poor Pb data and therefore all have large errors (Table 5.1) and are not plotted in Fig. 5.7a. The error ellipses of M4 and M5 overlap m3. The 51.6 ± 0.7 Ma monazite age may represent new growth and/or recrystallisation. Discordance is thought to be a result of the presence of older Pb. All zircon fractions are discordant (Fig. 5.7b, Table 5.1). All zircon fractions from the leucosomes have younger $^{207}Pb/^{206}Pb$ ages than those from the host orthogneiss (Table 5.1). Better zircon age constraints have been derived from SHRIMP data, and therefore ID-TIMS zircon data are not further discussed.

Zircon grains from host orthogneiss and leucosome have been analysed on the SHRIMP (Fig. 5.8, Table 5.2). In general, CL images of the zircons show Palaeoproterozoic cores, and two overgrowths correlating with ~1.8 Ga and ~52 Ma age domains. Age domains are separated by dissolution rims. A detailed discussion follows,

beginning with the youngest age domains. A discordia chord through the spots with the lowest $^{207}Pb/^{206}Pb$ ages, L2.3, L2.4, L4.1 (outer overgrowths) and L2.5 (inner overgrowth), yields an upper intercept age at 1814 ± 11 Ma and a lower intercept at 52.3 ±1.8 Ma (MSWD = 0.3; Table 5.3). A discordia chord also including L1.2 (outer overgrowth) and H5.2 (inner overgrowth), or only including L2.3, L2.4 and L2.5, gives similar results (Table 5.3). Spot L4.1 is concordant with a $^{206}Pb/^{238}U$ age of 51.1 ± 0.7 Ma at the lower intercept of the discordia chord. Because the 52.3 ± 1.8 SHRIMP lower intercept age is consistent with this 51.1 ± 0.7 Ma age and with the 51.6 ± 0.7 ID-TIMS monazite age, the lower intercept age is interpreted as being 52.0 ± 2.0 Ma. The youngest spots, L4.1, L2.3 and L2.4, are thin irregular dark outer rims of leucosome zircons (Figs. 5.8, 5.9). These rims are separated from the internal parts of the grain by bright, probably low U, irregular boundaries that may well be resorption or dissolution rims (Fig. 5.9, all grains). Dissolution would explain the irregularity of the boundary, and the low U content. Spots L2.5, L1.2 and H5.2 are located in dark interior rims that lie inside the dissolution rims. The dark interior rims are interpreted as having grown at ~1.8 Ga and as having lost Pb during dissolution after ~1.8 Ga (Figs. 5.8, 5.9). Discordance of spots L1.2, L2.3 and L2.4 may have been caused by inclusion of inner overgrowth material in the analyses. Similarly, discordance of spots L2.5 and H5.2 may have been (partly) caused by inclusion of outer overgrowth material.

Another discordia chord is plotted through H2.1, H4.1, H4.2, H6.1 and L1.1, because they seem to form a linear array with an upper intercept of ~2.1 Ga, which may therefore be meaningful. The upper intercept is 2100 ± 21 Ma, and the lower intercept is 530 ± 173 Ma (MSWD = 2.8; Table 5.3). The lower intercept is probably meaningless

because data may have been affected by multiple events after 2.1 Ga. The upper intercept is supported by the 2081 ± 17 Ma weighted mean of $^{207}Pb/^{206}Pb$ ages (MSWD = 3.8; Table 5.3). The concentric zonation of zircon H4 and H6 (see upper right part of grain H6 in Fig. 5.8) and the sector zonation of the core of L1 (Fig. 5.8) suggest magmatic zircon growth at ~2.1 Ga. Spot H2.1 is a bright rim, which may be a recrystallised rim on an older, perhaps ~2.1 Ga, zircon. Spots L3.1, L3.2, L4.2, H1.1 and H3.1 plot in a scattered array between the discordia chords with upper intercept ages at ~1.8 and ~2.1 Ga (Table 5.3; see above). All data, except for spot L3.1, are from zircon domains with concentric oscillatory or herringbone zonation (Fig. 5.8), and may therefore be interpreted as having grown at ~2.1 Ga (or earlier) and as having lost Pb, e.g. at ~1.8 Ga. The interpretation that recrystallisation occurred at ~1.8 Ga and that older Pb is preserved in the grains is considered unlikely, because regular zonations are preserved, which is not likely after recrystallisation. Within grain L3, a bright irregular domain exists which is more discordant and has a younger $^{207}Pb/^{206}Pb$ age (1946 ± 7 Ma; L3.1) than the rest of the grain (1970 ± 6 Ma; L3.2; Fig. 5.8, Table 5.2). This domain may be a recrystallisation domain.

Spots H5.1, L2.1 and L2.2 from within cores of zircons and H7.1 from a clear euhedral grain have $^{207}Pb/^{206}Pb$ ages between 2.28 and 2.42 Ga. They are interpreted as xenocrysts in the orthogneiss, although the possibility of protolith crystallisation of the orthogneiss prior to ~2.1 Ga cannot be ruled out. Alternatively the orthogneiss may have been a composite granitoid as a result of several generations of magmatism between ~2.4 and 2.1 Ga or slightly younger. The reverse discordance of H3.1 and H7.1 is probably an

artifact of the correction of the fractionation between Pb and U. Grain L2 in Fig. 5.9 also shows a dissolution rim around the inherited core, located inside the 1.8 Ga overgrowth.

In summary (cf. Fig. 5.9), zircon grains with $^{207}Pb/^{206}Pb$ ages older than ~2.1 Ga are interpreted as being xenocrystic. Magmatic zircon growth and igneous crystallisation are interpreted as having occurred at ~2.1 Ga, based on the concentric and sector zonations of zircon domains of that age. Possibly, the granitic to granodioritic protolith formed during several pulses of magmatism between ~2.4 and ~2.1 Ga. At ~1.8 Ga, zircon overgrowth, and Pb loss and recrystallisation, of older grains occurred, perhaps during migmatisation. Dissolution occurred between ~1.8 Ga and 52.0 Ma. At 52.0 Ma, new overgrowths formed, either during metamorphism, or during an extension-related fluid event (see Chapter 3)

5.4.1.2. Cranberry Valley crosscutting aplite dyke (s298-117)

Sample s298-117 is a ca. 15 cm wide, white to light orange aplite dyke from Cranberry Valley (Fig. 5.4b), north of Cranberry Mountain, that intruded a biotite quartz feldspar basement orthogneiss with sillimanite–feldspar faserkiesel (sample s298-123). The aplite dyke consists of feldspar, quartz, unstable muscovite, accessory pyrite, monazite and zircon, and retrograde sericite and chlorite. The dyke dips 60° to 100°. It is interpreted as crosscutting F_3, because it crosscuts the transposition foliation and F_1/F_2 in the host rock, and its orientation is approximately perpendicular to the axial planar foliation of F_3, which dips 50–70° to the west. Furthermore, it is nearly undeformed and can be traced over tens of metres. A weak foliation parallels the foliation in the host rock. Recrystallisation occurred along grain boundaries, and some grain boundary

migration or bulging is visible. Some feldspar crystals show deformation lamellae but also concentric zonation. The aplite dyke does not have chilled margins.

Six zircon fractions and seven single monazite fractions were dated, using ID-TIMS merthods (Fig. 5.10, Table 5.1), to determine the crystallisation age of the aplite in order to find an upper constraint on F_3 deformation. Fractions A, B, C and D are 74–105 μm, and consist of 39, seven, six and six crystals, respectively. Fraction E consists of seven 74–250 μm crystals and fraction F of three 105–149 μm crystals. In fraction B, zircon crystals are bipyramidal prisms and sub- to euhedral, and in all other fractions they are stubby and subhedral. All zircon crystals are colourless, of good clarity and with inclusions, except for fraction F, in which no inclusions were present. BSE images show concentric oscillatory zonations, truncated by overgrowths (Fig. 5.10a, grains 1,2), but no evidence for clear cores, although one might be present in grain 1. All monazite crystals are subhedral and of excellent clarity, except for M4, which is subrounded and with good clarity. Grains M1–M4 are 149–250 μm and M5–M7 are 105–149 μm. Monazites M1–M4 have indentations. Grains M1, M2, M3 and M5 have a few colourless inclusions. None has fractures, although a piece is broken off M1. Some BSE images show vague concentric zonation, and they generally show irregular patchy domains (Fig. 5.10b, grains 1 and 2 respectively). The monazite age is interpreted as being 52.3 ± 3.0 Ma, based on the average $^{207}Pb/^{235}U$ age of reversely discordant fractions M1, M2 and M4. The error includes the errors of the three fractions, and that of the weighted average of 53.0 ± 2.0 (Table 5.3). Fraction M3 has a large error due to poor U analyses on the mass spectrometer. Fractions M3, M5 and M7 are discordant with $^{207}Pb/^{206}Pb$ ages between ~67 and ~100 Ma, probably because they contain older Pb.

All zircon fractions are discordant and do not plot on a discordia chord (see regressions involving all or nearly all data, Table 5.3), indicating that multiple events took place, starting in the Palaeoproterozoic. A discordia chord through M1 and D gives a youngest upper intercept of 1952 ± 4 Ma, and one through M1 and F gives an oldest upper intercept of 2087 ± 2 Ma (Table 5.3). The lower intercept age from both discordia chords is 52.7 ± 0.6 Ma, in accordance with the 52.3 ± 3.0 Ma monazite age (see above). The use of upper intercept ages is preferred over $^{207}Pb/^{206}Pb$ ages in the age interpretation, because discordance in zircon is more likely to be a result of the 52.3 ± 3.0 Ma event than of recent Pb loss. Assuming that no zircon overgrowth or Pb loss occurred between the crystallisation age and 52.3 ± 3.0 Ma, in this interpretation the aplite dyke crystallised at 1952 ± 4 Ma (Fig. 5.11a) or after (e.g. Fig. 5.11b, interpretation A). Older upper intercept ages are then a result of inheritance. Alternatively, the aplite dyke could be older than 2087 ± 2 Ma, the oldest upper intercept, in which case younger upper intercept ages are a result of two or more events of Pb loss and/or recrystallisation and/or overgrowth (e.g. Fig. 5.11b, interpretation B). Another alternative is that the monazite age 52.3 ± 3.0 Ma reflects aplite dyke crystallisation, and that older zircon ages result from inheritance.

5.4.1.3. Cranberry Valley folded pegmatite (s298-120)

Sample s298-120 is a ca. 20 cm wide, white to light orange granitic pegmatite from Cranberry Valley (Fig. 5.4b) in a biotite–sillimanite(+kyanite)–feldspar–quartz paragneiss (samples s298-113 and s298-121). The pegmatite consists of feldspar, quartz, biotite, sillimanite and muscovite, accessory pyrite, monazite and zircon, and retrograde

sericite. The pegmatite and its host rock are folded by approximately N–S-trending open F_3 folds, and contain an axial planar foliation that dips 60°, or 50–70° regionally, to the west. No chilled margins were observed.

Six zircon fractions and seven single monazite fractions were dated to establish a lower age constraint on F_3 folding (Fig. 5.12, Table 5.1). Fractions A and B are 74–105 μm and consist of 30 and five crystals respectively. Fractions C and D, six tips and three grains respectively, are 105–250 μm and E and F are 149–250 μm single crystals. All zircon crystals are colourless faceted bipyramidal prisms. Fractions A–D have colourless inclusions. Fraction E has four red inclusions and F has no inclusions, but is cloudy. All other fractions have excellent (fractions A, B, D and E), or good (C) clarity. Fractions C, E and F seem to have overgrowths. BSE images show concentric zonations (Fig. 5.12a, grain 1), cores and overgrowths (also visible in grain 1?), and alteration (Fig. 5.12a, grain 2). Monazite crystals are subhedral (M1 and M5) or subrounded (M2, M3, M4, M6 and M7), have excellent clarity, and indentations. Grains M1 and M2 are 149–250 μm and M3–M7 are 105–149 μm. Grain M2 is half a crystal. Monazites M5–M7 have a few colourless inclusions. None has fractures. Fractions M5 and M7 may have overgrowths. BSE images are patchy (Fig. 5.12b, grain 1), and some show large bright cores (grain 2).

M6 is the only reversely discordant fraction and has a $^{207}Pb/^{235}U$ age of 51.0 ±1.0, which is taken as the monazite age of the sample. Fractions M1–M4 had poor U and/or Pb analyses, probably due to problems with the silica-gel, and therefore have large errors (Table 5.1). Fractions M2 and M3 are not plotted for that reason, but are consistent with a ~51 Ma age. Fractions M5 and M7 are discordant and probably contain older Pb.

All zircon fractions are discordant and scattered within an elongate array (Fig. 5.12a; see various regressions of all or most data in Table 5.3), indicating that multiple events took place. A discordia chord through M6 and D yields a youngest upper intercept of 1949 ± 2 Ma. A chord through M6 and B gives an oldest upper intercept of 2013 ± 2 Ma (Table 5.3). The lower intercept age from both discordia chords is 51.8 ± 0.7 Ma, consistent with the 51.0 ± 1.0 Ma monazite age. If no zircon overgrowth or Pb loss occurred between the age of crystallisation and 51.0 ± 1.0 Ma, the pegmatite crystallised at or after 1949 ± 2 Ma (see explanation for s298-117). Older upper intercept ages are then a result of inheritance. Alternatively, as for s298-117, the aplite dyke could be older than 2013 ± 2 Ma, in which case younger upper intercept ages are a result of younger events. Possibly, the monazite age of 51.0 ± 1.0 Ma could represent pegmatite crystallisation, and older zircon ages inheritance.

5.4.1.4. Frigg Glacier crosscutting aplite dyke (s298-213)

Sample s298-213 is a SE-trending, shallowly SW-dipping ca. 10 cm wide, orange stained white aplite dyke (Fig. 5.13a, b), sampled W of Frigg Glacier (Fig. 5.4a). It consists of feldspar, quartz and concentrations of randomly orientated biotite. Alteration is indicated by sericite, orange coloured cracks and the presence of some rutile. Other accessory minerals are pyrite and zircon. The aplite dyke intruded a variety of basement orthogneisses, which are also intruded by amphibolites. It does not have chilled margins. The aplite dyke crosscuts all ductile structures in the host rock, such as the transposition foliation and isoclinal folds (Fig. 5.13a, b). Only some of the late N–S-trending dextral and sinistral shears, that are present in that area, offset the aplite. A very weak foliation

exists at an angle to the margins of the aplite dyke. Minor deformation is also indicated by bent cracks in feldspar, and by undulose extinction, grain boundary migration/bulging, and subgrain formation in both feldspar and quartz. Quartz and feldspar are partly recrystallised along their grain boundaries.

Six zircon fractions were dated (Fig. 5.14, Table 5.1). Fraction A consists of 35 crystals, B of five crystals, C of five tips, D of two crystals, and E and F of single crystals. Fractions A and B are 74–105 μm, C and D are 105–149 μm, and E and F are 149–250 μm. All grains are sharply faceted and have a few (B, C, D) or many (A, E, F) inclusions. Fractions E and F are turbid and metamict. A, B and C have excellent clarity and D has good clarity. BSE images show strong alteration and metamictisation, presumably as a result of high U (Fig. 5.14, grain 1). This supports Pb loss as a cause for discordance. One image shows either a core or a concentric zonation, and an overgrowth (grain 2).

All fractions are discordant (Fig. 5.14, Table 5.1). A linear regression through all fractions results in a discordia chord with an upper intercept of 1792 ± 49 Ma, and a lower intercept of 47.9 ± 11 Ma (MSWD = 315; Table 5.3). Although the chord has a high MSWD, the intercept ages are considered meaningful, because discordia chords through fewer fractions with better MSWDs (e.g. E, D and F or A, B, D and F) give similar results (Table 5.3). The crystallisation age of the aplite could be 47.9 ± 11 Ma, in which case the upper intercept is a result of inheritance. However, the host migmatitic orthogneiss is 1.96 Ga (Wanless and Reesor, 1974), and therefore not a likely source for ~1.8 Ga inheritance for the aplite dyke. Alternatively the aplite dyke could have intruded

at ~1.8 Ga, the age of migmatisation at other locations in Thor–Odin (Sections 5.4.1.1 and 5.5.1). The lower intercept age would then represent a younger event.

5.4.1.5. Blanket Mountain pegmatite (RB-1-93) in F_1/F_2 boudin neck

Sample RB-1-93 is a metre-scale (example in Fig. 5.15 is only 50 cm) yellow-orange siliceous pegmatite or in situ melt in a boudin neck on the limb of an F_1/F_2 fold, south of the Megaboudin on the northern slope of Blanket Mountain (Fig. 5.4b). The host rock is a boudinaged quartz-depleted, aluminium-rich pelitic schist layer (samples 45–47, 155–160), which occurs at different locations throughout the Monashee Basement sequence (see detailed descriptions by Norlander et al., 2002). At this location, the schist layer dips to the north, but more generally in northwest Thor–Odin it dips NW. The pegmatite mainly consists of quartz. Relict kyanite, corundum and cordierite coexist within sillimanite, and kyanite is replaced by sillimanite and K-feldspar and/or quartz. Accessory zircon, monazite and rutile, and late scapolite are present. The fact that both the pegmatite and the pelitic schist contain aluminosilicates and corundum may indicate that the pegmatite was derived from the pelitic schist. Irregular cracks and palisade growth of sillimanite are present perpendicular to the contact (Fig. 5.15). No penetrative foliation is present, but the pegmatite may be deformed. Quartz grains have subgrains and show undulose extinction and are flattened. A weak lattice preferred orientation and flattening of grains could be associated with palisade growth or with deformation. Recrystallisation is not visible.

Seven zircon fractions were analysed (Fig. 5.16, Table 5.1). Fraction A consists of 32 <105 μm grains. Fraction B and C are 74–105 μm and consist of five and six

grains respectively. Fractions D consisting of four tips, and E, a single half crystal or tip, are <149 μm and fractions F and G are single crystals that are >149 μm. All crystals are sharply faceted bipyramidal prisms. Clarity is excellent for fractions B, C, E and G, and good for A, D and F. A–D have small inclusions. Zircon G has a zircon inclusion and perhaps a rutile and a few other inclusions. None has fractures. Crystals in fraction A seem to have cores, although they could be a result of initial high-U growth. No BSE images were made, to preserve crystals for analysis.

A linear regression through fractions B–G gives a discordia chord with upper and lower intercept ages of 1939 ± 6 Ma and 51.8 ± 0.9 Ma respectively (MSWD = 15.2; Table 5.3). Fraction A has a high blank and is therefore omitted in the regression. A regression including fraction A gives similar results and a higher MSWD (Table 5.3). From near-concordant fraction F, the lower intercept age and the monazite age of 54.5 ± 1.0 Ma, determined by Johnston et al. (2000), the lower intercept and monazite age is here interpreted as being 52.5 ± 3.0 Ma. If the crystallisation of the pegmatite is 52.5 ± 3.0 Ma, then the fact that all data fit on a discordia chord would be very coincidental. Where exposed, the pegmatite is surrounded by a pelitic schist. It is unlikely that all inherited grains from a metasedimentary rock would have the same age.

5.4.2. U concentrations in zircon from the Monashee Complex

U concentrations in zircons and zircon overgrowths from the Monashee Complex that are younger than ~75–70 Ma, are higher, and Th/U ratios lower, than those in older igneous or metamorphic zircons (see data of Wanless and Reesor, 1974; Parrish and Scammell, 1988; Parrish et al., 1988; Coleman, 1990; Parkinson, 1991, 1992; Armstrong

et al., 1991; Parrish, 1992; Carr, 1992, 1995; Parrish, 1995; Crowley, 1997, 1999; Crowley and Parrish, 1999; Crowley et al., 2001; Johnston et al., 2000; Wasteneys, unpublished; this chapter). In Fig. 5.17a, U concentrations are plotted against $^{207}Pb/^{206}Pb$ dates, for samples with (near-)concordant ID-TIMS data from the Monashee Complex, for which both U concentrations and $^{207}Pb/^{206}Pb$ dates were available (Coleman, 1990; Parkinson, 1992; Carr, 1992; Parrish, 1995; Crowley, 1997; Johnston et al., 2000; this thesis). Fig. 5.17b is similar, but excludes data from Late Cretaceous–Early Eocene pegmatite and aplite dykes, in order to exclude zircon with igneous origin. Samples with interpreted ages younger than ~75–70 Ma (and $^{207}Pb/^{206}Pb$ dates less than ~100 Ma) have generally high U concentrations that are up to 21400 ppm (Fig. 5.17a) or up to 4150 ppm if zircon of igneous origin is excluded (Fig. 5.17b). Samples with interpreted ages and $^{207}Pb/^{206}Pb$ dates older than 1200 Ma have low U concentrations (less than 360 ppm).

High U concentrations in zircon are thought by some workers to be a characteristic of zircons of magmatic origin only. Igneous zircon may contain several 100 to several 1000 ppm U and metamorphic zircon a few 100 ppm (Williams and Claessons, 1987; Mezger and Krogstad, 1992; Pidgeon, 1992; Gibson and Ireland, 1995; Nemchin and Pidgeon, 1997; Pidgeon et al., 1998; Mueller and McNaughton, 2000). A principal reason proposed for this difference is the fact that the partition coefficients seem to favour lower U concentrations in zircon that grows in metamorphic rocks compared to zircon that grows in magmatic rocks, due to the generally lower temperatures of metamorphism (Mezger and Krogstad, 1992). In addition, during metamorphism not all the U in the rock may be available for reaction with newly growing zircon (Mezger and Krogstad, 1992). Furthermore, U and Th loss may occur during metamorphism. Pidgeon

et al. (1966) and Sinha et al. (1992) demonstrate the loss of Pb, and to a lesser extent U and Th (and other REE), during hydrothermal experiments at amphibolite facies. Initial fast loss due to leaching from a metamict zircon is followed by slow loss, possibly during recrystallisation. Pidgeon (1992) shows recrystallisation of oscillatory zones in zircon accompanied by loss of U, Th and Pb. Geisler et al. (2002) demonstrate significant loss of U, Th and especially Pb in metamict zircon at temperatures as low as 175°C.

However, zircon is also known to grow at low temperatures (e.g. greenschist facies conditions) in the presence of fluids (Rubin et al., 1989, 1993: Schmitz and Bowring, 2000). High U concentrations in zircon that crystallised from fluids are recorded by Sinha and Glover (1978), Rubin et al. (1989, 1993) and Wayne et al. (1992). For Zr dissolution and transportation, a fluid needs to be undersaturated in Zr (Schmitz and Bowring, 2000) and rich either in F (Rubin et al., 1989, 1993; Wayne et al., 1992) or in Cl (Sinha et al., 1992). U dissolves well in water, U (and Th) partitions in F-rich solutions, and U partitions in Cl- or CO_2-rich fluids (Rubin et al., 1993). Therefore, zircon dissolution, transportation and high-U zircon growth at low temperature require fluids (water) high in F, Cl or CO_2, for example F- or Cl-rich igneous fluids. Metamorphic fluids would not produce such high-U zircon, and meteoric fluids would not carry much Zr or U (unless they mixed with other fluids and interacted with the rocks).

In previous research, high U concentrations and low Th/U ratios in zircons from the Monashee Complex have been interpreted as being characteristic of igneous zircon (Crowley and Parrish, 1999; Gilley, 1999; Johnston et al., 2000). Similarly, the ~52 Ma ages of zircon and zircon overgrowths with high U concentrations and low Th/U ratios in

this chapter (spots L2.3, L2.4 and L4.1 of sample s298-65 and fractions E and F of sample RB-1-93; Tables 5.1 and 5.2) may be interpreted as crystallisation ages of the igneous host rock. However, the Eocene zircons do not need to have crystallised from a melt. Zircon growth may be a result of the presence of igneous fluids, possibly mixed with meteoric fluids that were present at that time (Chapter 3). Igneous fluids could be derived from Late Cretaceous–Early Eocene pegmatites that intruded during crustal extension in the Monashee Complex. Low U concentrations in <~75–70 Ma zircon (Fig. 5.17a) may be explained by Pb loss in older zircon, rather than by zircon growth during fluid activity. Using these arguments, young zircon dates may be interpreted as representing extension-related igneous and meteoric fluids rather than peak of metamorphism.

5.5. Discussion

5.5.1. Palaeoproterozoic orthogneiss formation and migmatisation

The protolith age of the migmatitic basement orthogneiss (s298-65) is interpreted as being 2100 ± 21 Ma (or possibly earlier) and older ages are attributed to the presence of xenocrystic grains. Migmatisation is interpreted as having taken place at 1814 ± 11 Ma. It is not interpreted as having occurred between 1814 Ma and 52.0 Ma, because there is no evidence for migmatisation in that time range and no zircon data plot above the discordia chord with the upper intercept of 1814 Ma. At 52.0 Ma, zircon overgrowths

formed and zircon possibly lost Pb, either during metamorphism or during an extension-related fluid event (see Chapter 3).

A ~2.1 Ga crystallisation is reasonable, because, in Frenchman Cap, orthogneiss protoliths of 2.08 and 2.1 Ga exist (Crowley, 1999). The ~1.8 Ga age is a commonly occurring age; ~1.85 Ga is an age of metamorphism at Frenchman Cap (Armstrong et al., 1991; Crowley, 1999) and ~1.8 Ga is a commonly occurring zircon $^{207}Pb/^{206}Pb$ age in two basement migmatitic orthogneisses in Thor–Odin, dated by SHRIMP methods (Vanderhaeghe et al., 1999). The latter zircon crystals have cores with ~2.2–2.4 Ga $^{207}Pb/^{206}Pb$ age, and overgrowths with ~56 Ma concordant ages, similar to basement orthogneiss (s298-65). Vanderhaeghe et al. (1999) interpret the lower intercept ages (~56 Ma) as the migmatisation age and all older ages as inheritance. However, the ~56 Ma ages seem to come from overgrowths only (their Fig. 5.11a, b; cf. ~52 Ma overgrowths in s298-65; Figs. 5.8, 5.9). Furthermore, most data from both samples seem to fit well on discordia chords between ~1.8 and ~56 Ga. This argues for ~1.8 Ga as an igneous or migmatisation age, as inherited grains commonly have different origins and therefore different $^{207}Pb/^{206}Pb$ ages. Some spots have ages $^{207}Pb/^{206}Pb$ ages older than ~1.8 Ga, up to ~2.4 Ga, which may indicate inheritance of older grains, or the granitoid crystallisation age, if ~1.8 Ga is the age of migmatisation. ~1.8 Ga spots seem to come from areas that, in CL images (Fig. 11a, b of Vanderhaeghe et al., 1999), are between older cores and younger, ~56 Ma, dark overgrowths, similar to the ~1.8 Ga domains in s298-65 (Figs. 5.8, 5.9). Therefore, it seems more likely that ~1.8 Ga is the age either of migmatisation, as interpreted for s298-65, or perhaps of granite crystallisation, and that ~56 Ma represents a younger event.

5.5.2. Attempts to constrain deformation by dating pegmatites; enigmatic answers to simple questions

Various interpretations can be made for the crosscutting aplite dyke (s298-117) and the folded pegmatite (s298-120) in Cranberry Valley (Sections 5.4.1.2 and 5.4.1.3). If the 52.3 ± 3.0 Ma and 51.0 ± 1.0 Ma lower intercept ages of the aplite and pegmatite, respectively, are taken as crystallisation ages, then the crosscutting aplite would be older than the folded pegmatite. The possibility exists that s298-117 is the same age or younger than s298-120, because the lower intercept ages overlap, and also monazite systematics may be complicated as exemplified in Fig. 5.6. For example, the reversely discordant monazites in s298-117 may be younger than the age indicated by their $^{207}Pb/^{235}U$ ages, as for example A in Fig. 5.6. The problem remains, however, that no evidence exists for s298-117 being younger than s298-120.

Another (preferred) interpretation is that the lower intercept ages are a result of extension-related fluids (cf. Chapters 3 and 6), or possibly a metamorphic event, and that the crystallisation ages are older. However, realistic arguments can be made for any crystallisation age for both samples, as long as it is as old as or older than the monazite age (cf. Sections 5.4.1.2 and 5.4.1.3). Therefore, F_3 folding at Cranberry Valley cannot be constrained by these pegmatites.

The crystallisation age of the crosscutting aplite dyke near Frigg Glacier, sample s298-213, may be 47.9 ± 11 Ma or 1792 ± 49 Ma (Section 5.4.1.4). If 1792 ± 49 Ma represents the crystallisation age of the aplite dyke, it is slightly younger than the 1852–1832 Ma age of the Pettipiece pegmatite suite that is interpreted as mostly undeformed

(Crowley, 1999) and may be related to it. As outlined in Section 5.5.1, ~1.8 Ga is interpreted as an age of migmatisation in Thor–Odin. The aplite dyke may therefore represent an anatectic melt. The aplite dyke postdates all ductile deformation in the host rocks and therefore deformation is older than 1792 ± 49 Ma (if this is the crystallisation age of the aplite dyke). This would imply that evidence for Palaeoproterozoic (pre-Cordilleran) deformation is preserved at this deep structural level in Thor–Odin, similar to preservation of Palaeoproterozoic deformation in Frenchman Cap (Crowley, 1999).

However, the possibility that 47.9 ± 11 Ma is the crystallisation age of the aplite cannot be ruled out. For the same reason, the Pettipiece pegmatite suite can be interpreted as being Late Cretaceous (?)–Early Eocene, because all three samples (84, 91 and 308 of Crowley, 1999) have lower intercept ages within that age range. In that case, at least part of the deformation in the host rocks may be as young as Late Cretaceous. Furthermore, sample 84 is folded and foliated, and sample 308 is weakly foliated (Crowley, 1999). Samples 308 and 91 appear to be folded, and deformed at their contacts, in Fig. 9 of Crowley (1999). Therefore, the possibility exists that some deformation occurred after intrusion of the Pettipiece pegmatite suite.

The siliceous pegmatite, RB-1-93, in a boudin neck on the limb of an F_1/F_2 fold, south of the Megaboudin, may have crystallised at 1939 ± 6 Ma because all fractions plot on one discordia chord, which is unlikely if the Palaeoproterozoic cores are a result of inheritance (Section 5.4.1.5). If the host pelitic schist is the regolith below the basal quartzite of the Monashee cover sequence (McMillan, 1973; Journeay, 1986; Crowley, 1997; Johnston et al., 2000), then the pelitic schist is also part of the cover sequence, and was deposited between ~1.99 and ~1.85 Ga (cf. Crowley, 1997). In that case, folding and

boudinaging of the pelitic schist and crystallisation of the pegmatite at 1.93 Ga seems unlikely. If the pelitic schist is the schist that occurs in boudins throughout the basement (Norlander et al., 2001; this study), an interpretation which is preferred herein, then deformation and crystallisation of the pegmatite could have happened at 1.93 Ga. Pegmatites of this age have not been recognised elsewhere in the Monashee Complex. Orthogneisses of similar age exist in Thor–Odin at 1.93 Ga (Parkinson, 1991) and 1.96 Ga (Wanless and Reesor, 1974), but not in Frenchman Cap. If the pegmatite is 1.93 Ga, then boudinaging of the pelitic schist occurred at that time. If true, then boudinaging of the pelitic schist was probably earlier than and not related to F_1/F_2 folding, which was probably related to Cordilleran deformation. However, it is possible that the pegmatite crystallised at 52.5 ± 3.0 Ma, and postdated Cordilleran deformation.

Alternative interpretations, e.g. with events in the Mesozoic (as for s298-117 and s298-120), can be made for both samples s298-213 and RB-1-93. This would also explain the imperfect fit, if all fractions are incorporated in one discordia (MSWD = 315 for s298-213 and 112 for RB-1-93). A reason that events between 1.8 Ga and ~75–70 Ma have not been recorded within the Monashee Complex may be that the rocks were too hot and that melting of rocks and dissolution of minerals such as zircon and monazite occurred during those events. Crystallisation of melts and precipitation of zircon and monazite then occurred in the overlying rocks of the Selkirk Allochthon (Chapter 8). Dissolution rims of old cores, which are overgrown by Eocene zircon rims in s298-65 (Fig. 5.9), are evidence for dissolution of zircon. Dissolution rims in other samples have not been observed, perhaps because dissolution rims may be visible on CL images only, and for all other samples only BSE images were taken. Lower intercept ages of discordia

chords in the Palaeozoic/Mesozoic (Wanless and Reesor, 1974; Armstrong et al., 1991; Parkinson, 1991; Crowley, 1997, 1999) may be a result of Pb loss in Proterozoic cores. In the future, detailed CL imaging and in situ U–Pb geochronology may help to unravel the internal structures and age domains of zircons of samples discussed in this section.

5.6. Conclusions

(1) A migmatitic orthogneiss in the basement sequence of Thor–Odin has a protolith age of ~2.1 Ga, or a composite age between ~2.4 and ~2.1 Ga, and a migmatisation age of ~1.8 Ga. Overgrowth occurred at 52 Ma.

(2) A number of interpretations can be made for the ages of the pegmatite and aplite dykes (s298-117, s298-120, s298-213 and RB-1-93), dated to constrain deformation. This shows that ID-TIMS work does not always give conclusive results, especially if multiple events of overgrowth and/or Pb loss occurred, and if data are discordant. In situ geochronology is required to resolve ID-TIMS data. Unfortunately, for that reason, the data presented here do not give any constraints on Palaeoproterozoic and/or Cordilleran deformation. The latest event occurred in the Early Eocene, which may be extension (cf. Chapter 3).

(3) Deformation and/or metamorphic events may not be recorded by minerals used for U–Pb dating, if these dissolved rather than grew during these events. Dissolution rims are visible in the migmatitic basement orthogneiss. Pb loss of older cores during an unrecorded metamorphic event may have occurred, but was not complete, as completion would result in concordant ages indicating the time of metamorphism.

References

Armstrong, R.L., Parrish, R.R., van der Heyden, P., Scott, K., Runkle, D., 1991. Early Proterozoic basement exposures in the southern Canadian Cordillera: core gneiss of Frenchman Cap, Unit I of the Grand Forks Gneiss, and the Vaseaux Formation. Canadian Journal of Earth Sciences 28, 1169–1201.

Brown, R.L., Journeay, J.M., Lane, L.S., Murphy, D.C., Rees, C.J., 1986. Obduction, backfolding, and piggyback thrusting in the metamorphic hinterland of the southeastern Canadian Cordillera. Journal of Structural Geology 8, 255–268.

Carr, S.D., 1992. Tectonic setting and U–Pb geochronology of the early Tertiary Ladybird leucogranite suite, Thor–Odin – Pinnacles area, southern Omineca Belt, British Columbia. Tectonics 11, 258–278.

Carr, S.D., 1995. The southern Omineca Belt, British Columbia: new perspectives from the Lithoprobe Geoscience Program. Canadian Journal of Earth Sciences 32, 1720–1739.

Coleman, V.J., 1990. The Monashee décollement at Cariboo Alp and regional kinematic indicators, southeastern British Columbia. MSc Thesis, Carleton University, Ottawa, Ontario, Canada.

Crowley, J.L., 1997. U–Pb geochronologic constraints on the cover sequence of the Monashee complex, Canadian Cordillera: Paleoproterozoic deposition on basement. Canadian Journal of Earth Sciences 34, 1008–1022.

Crowley, J.L., 1999. U–Pb geochronologic constraints on Paleoproterozoic tectonism in the Monashee complex, Canadian Cordillera: elucidating an overprinted geologic history. Geological Society of America Bulletin 111, 560–577.

Crowley, J.L., Parrish, R.R., 1999. U–Pb isotopic constraints on diachronous metamorphism in the northern Monashee complex, southern Canadian Cordillera. Journal of Metamorphic Geology 17, 483–502.

Crowley, J.L., Brown, R.L., Parrish, R.R., 2001. Diachronous deformation and a strain gradient beneath the Selkirk allochthon, northern Monashee complex, southeastern Canadian Cordillera. Journal of Structural Geology 23, 1103–1121.

Geisler, T., Pidgeon, R.T., van Bronswijk, W., Kurtz, R., 2002. Transport of uranium, thorium, and lead in metamict zircon under low-temperature hydrothermal conditions. Chemical Geology 191, 141–154.

Gibson, G.M., Ireland, T.R., 1995. Granulite formation during continental extension in Fiordland, New Zealand. Nature 375, 479–482.

Gibson, H.D., Brown, R.L., Parrish, R.R., 1999. Deformation-induced inverted metamorphic field gradients: an example from the southeastern Canadian Cordillera. Journal of Structural Geology 21, 751–767.

Gilley, L.D., 1999. The nature and timing of partial melting in the Shuswap metamorphic core complex: a SHRIMP U–Pb geochronologic investigation. BSc Thesis, Stanford University, Stanford, California, USA.

Johnson, B.J., 1994. Structure and tectonic setting of the Okanagan Valley fault system in the Shuswap Lake area, southern British Columbia. PhD Thesis, Carleton University, Ottawa, Ontario, Canada.

Johnston, D.H., Williams, P.F., Brown, R.L., Crowley, J.L., Carr, S.D., 2000. Northeastward extrusion and extensional exhumation of crystalline rocks of the Monashee Complex, southeastern Canadian Cordillera. Journal of Structural Geology 22, 603–625.

Journeay, J.M., 1986. Stratigraphy, internal strain, and thermo-tectonic evolution of northern Frenchman Cap dome, an exhumed basement duplex structure, Omineca hinterland, southeastern Canadian Cordillera. PhD Thesis, Queen's University, Kingston, Ontario, Canada.

Krogh, T.E., 1973. A low contamination method for hydrothermal decomposition of zircon and extraction of U and Pb for isotopic age determinations. Geochimica et Cosmochimica Acta 37, 485–494.

Krogh, T.E., 1982. Improved accuracy of U–Pb zircon ages by the creation of more concordant systems using an air abrasion technique. Geochimica et Cosmochimica Acta 46, 637–649.

Lane, L.S., 1984. Deformation history of the Monashee Decollement and Columbia River Fault zone. PhD Thesis, Carleton University, Ottawa, Ontario, Canada.

Ludwig, K.R., 2001. Users manual for Isoplot/Ex v.2.49. A geochronological toolkit for Microsoft Excel. Berkeley Geochronology Center Special Publication no. 1a, Berkeley, California.

McMillan, W.J., 1973. Petrology and structure of the west flank, Frenchman's Cap dome, near Revelstoke, British Columbia. Geological Survey of Canada, Paper, 71–29.

Mezger, K., Krogstad, E.J., 1992. Interpretation of discordant U–Pb ages: An evaluation. Journal of Metamorphic Geology 15, 127–140.

Monger, J.W.H., Price, R.A., Tempelman-Kluit, D.J., 1982. Tectonic accretion and the origin of the two major metamorphic and plutonic welts in the Canadian Cordillera. Geology 10, 70–75.

Montel, J.-M., Foret, S., Veschambre, M., Nicollet, C., Provost, A., 1996. Electron microprobe dating of monazite. Chemical Geology 131, 37–53.

Mueller, A.G., McNaughton, N.J., 2000. U–Pb ages constraining batholith emplacement, contact metamorphism, and the formation of gold and W-Mo skarns in the Southern Cross area, Yilgarn craton, Western Australia. Economic Geology 95, 1231–1257.

Murphy, D.C., van der Heyden, P., Parrish, R.R., Klepacki, D.W., McMillan, W., Struik, L.C., Gabites, J., 1995. New geochronological constraints on Jurassic deformation of the western edge of North America, southeastern Canadian Cordillera. In: Miller, D.M., Busby, C. (Editors), Jurassic magmatism and tectonics of the North American Cordillera. Boulder, Colorado, Geological Society of America Special Paper 299, 159–171.

Nemchin, A.A., Pidgeon, R.T., 1997. Evolution of the Darling Range Batholith, Yilgarn craton, Western Australia: a SHRIMP zircon study. Journal of Petrology 38, 625–649.

Norlander, B.H., Whitney, D.L., Teyssier, C., Vanderhaeghe, O., 2002. Partial melting and decompression of the Thor–Odin dome, Shuswap metamorphic core complex, Canadian Cordillera. Lithos 61, 103–125.

Parkinson, D.L., 1991. Age and isotopic character of Early Proterozoic basement gneisses in the southern Monashee Complex, southeastern British Columbia. Canadian Journal of Earth Sciences 28, 1159–1168.

Parkinson, D.L., 1992. Age and tectonic evolution of the southern Monashee complex, southeastern British Columbia: a window into the deep crust. PhD Thesis, University of Santa Barbara, Santa Barbara, California, USA.

Parrish, R.R., 1987. An improved micro-capsule for zircon dissolution in U–Pb geochronology. Chemical Geology 66, 99–102.

Parrish, R.R., 1992. Miscellaneous U–Pb zircon dates from southeast British Columbia. Geological Survey of Canada, Paper 91-2, 143–153.

Parrish, R.R., 1995. Thermal evolution of the southeastern Canadian Cordillera. Canadian Journal of Earth Sciences 32, 1618–1642.

Parrish, R.R., Krogh, T.E., 1987. Synthesis and purification of ^{205}Pb for U–Pb geochronology. Chemical Geology 66, 103–110.

Parrish, R.R., Scammell, R.J., 1988. The age of the Mount Copeland syenite gneiss and its metamorphic zircons, Monashee Complex, southeastern British Columbia. Geological Survey of Canada, Paper 88-2, 21–28.

Parrish, R.R., Carr, S.D., Parkinson, D.L., 1988. Eocene extensional tectonics and geochronology of the southern Omineca Belt, British Columbia and Washington. Tectonics, 7, 181–212.

Parrish, R.R., Roddick, J.C., Loveridge, W.D., Sullivan, R.W., 1987. Uranium–lead analytical techniques at the geochronology laboratory, Geological Survey of Canada. Geological Survey of Canada, Paper 87-2, 3–7.

Pidgeon, R.T., 1992. Recrystallization of oscillatory zoned zircon: some geochronological and petrological implications. Contributions to Mineralogy and Petrology 110, 463–472.

Pidgeon, R.T., O'Neil, J.R., Silver, L.T., 1966. Uranium and lead isotopic stability in a metamict zircon under experimental hydrothermal conditions. Science 154, 1538–1540.

Pidgeon, R.T., Nemchin, A.A., Hitchen, G.J., 1998. Internal structures of zircons from Archean granites from the Darling Range batholith: implications for zircon stability and the interpretation of zircon U–Pb ages. Contributions to Mineralogy and Petrology 132, 288–299.

Roddick, J.C., 1987. Generalized numerical error analysis with applications to geochronology and thermodynamics. Geochimica et Cosmochimica Acta 51, 2129–2135.

Roddick, J.C., Loveridge, W.D., Parrish, R.R., 1987. Precise U/Pb dating of zircon at the sub-nanogram Pb level. Chemical Geology 66, 111–121.

Rubin, J.N., Henry, C.D., Price, J.G., 1989. Hydrothermal zircons and zircon overgrowths, Sierra Blanca Peaks, Texas. American Mineralogist 74, 865–869.

Rubin, J.N., Henry, C.D., Price, J.G., 1993. The mobility of zirconium and other "immobile" elements during hydrothermal alteration. Chemical Geology 110, 29–47.

Schärer, U., 1984. The effect of initial ^{230}Th disequilibrium on young U–Pb ages: the Makalu case, Himalaya. Earth and Planetary Science Letters 67, 191–204.

Schmitz, M.D., Bowring, S.A., 2000. The significance of U–Pb zircon dates in lower crustal xenoliths from the southwestern margin of the Kaapvaal craton, southern Africa. Chemical Geology 172, 59–76.

Sinha, A.K., Glover, L., 1978. U/Pb systematics of zircons during dynamic metamorphism. A study from the Brevard fault zone. Contributions to Mineralogy and Petrology 66, 305–310.

Sinha, A.K., Wayne, D.M., Hewitt, D.A., 1992. The hydrothermal stability of zircon: Preliminary experimental and isotopic studies. Geochimica et Cosmochimica Acta 56, 3551–3560.

Spark, R.N., 2001. Crustal thickening and tectonic denudation within the Thor–Odin culmination, Monashee Complex, southern Canadian Cordillera. PhD Thesis, University of New Brunswick, Fredericton, New Brunswick, Canada.

Stacey, J.S., Kramers, J.D., 1975. Approximation of terrestrial lead isotope evolution by a two-stage model. Earth and Planetary Science Letters 26, 207–221.

Steiger, R.H., Jäger, E., 1977. Subcommission on geochronology: convention on the use of decay constants in geo- and cosmochronology. Earth and Planetary Science Letters 36, 359–362.

Stern, R.A., 1997. The GSC Sensitive High Resolution Ion Microprobe (SHRIMP): analytical techniques of zircon U–Th–Pb age determination and performance evaluation. Geological urvey of Canada, Current Research 1997-F, Radiogenic Age and Isotopic Studies 10, 1–31.

Stern R.A., Sanborn, N.M., 1998. Monazite U–Pb and Th–Pb geochronology by high-resolution secondary ion mass spectrometry. Geological Survey of Canada, Current Research 1998-F, Radiogenic Age and Isotopic Studies 11, 1–18.

Vanderhaeghe, O., Teyssier, C., Wysoczanski, R., 1999. Structural and geochronological constraints on the role of partial melting during the formation of the Shuswap metamorphic core complex at the latitude of the Thor–Odin dome, British Columbia. Canadian Journal of Earth Sciences 36, 917–943.

Wanless, R.K., Reesor, J.E., 1974. Precambrian zircon age of orthogneiss in the Shuswap Metamorphic Complex, British Columbia. Canadian Journal of Earth Sciences 12, 326–332.

Wayne, D.M., Sinha, A.K., Hewitt, D.A., 1992. Differential response of zircon U–Pb isotopic systematics to metamorphism across a lithologic boundary: an example from the Hope Valley Shear Zone, southeastern Massachusetts, USA. Contributions to Mineralogy and Petrology 109, 408–420.

Wheeler, J.O., McFeely, P. (Compilers), 1991. Tectonic assemblage map of the Canadian Cordillera and adjacent parts of the United States of America: Geological Survey of Canada, Map 1712A, scale 1:2 000 000, 1 sheet.

Williams, I.S., Claesson, S., 1987. Isotopic evidence for the Precambrian provenance and Caledonian metamorphism of high grade paragneisses from the Seve Nappes, Scandinavian Caledonides. Contributions to Mineralogy and Petrology 97, 205–217.

Williams, M.L., Jercinovic, M.J., Terry, M.P., 1999. Age mapping and dating of monazite on the electron microprobe: Deconvoluting multistage tectonic histories. Geology 27, 1023–1026.

Williams, P.F., 1999. Fold Nappes and the problem of model driven interpretation. Specialist Group in Tectonics and Structural Geology Field Conference, Halls Gap, Victoria, Australia (February 14–19, 1999). Geological Society of Australia Abstracts Series #53, 267–268.

Williams, P.F., Jiang, D., in review. The relationship between thrusting, nappe formation, and channel flow. An example from the Canadian Cordillera.

York, D., 1969. Least squares fitting of a straight line with correlated errrors. Earth and Planetary Science Letters 5, 320–324.

Table 5.1. ID-TIMS data for samples s298-65, s298-117, s298-120, s298-120, s298-213 and RB-1-93.

Fraction size [a]	Wt. (µg) [b]	U (ppm) [b]	Pb* (ppm) [b]	$^{206}Pb/^{204}Pb$	Pb (pg) [c]	^{208}Pb (%)	Th/U [d]	$^{206}Pb/^{238}U$	$^{207}Pb/^{235}U$	$^{207}Pb/^{206}Pb$	$^{206}Pb/^{238}U$ Age (Ma)	$^{207}Pb/^{235}U$ Age (Ma)	Correlation coefficient	$^{207}Pb/^{206}Pb$ Age (Ma)	Discordance (%) [e]
S298-65 Basement orthogneiss host rock (capitalised letters) and leucosome (small letters), UTM 415050E, 5624650N															
A (s,149–250)	13	154	49	3153	11	16.6	0.77	0.273838 ± .96%	4.52125 ± .96%	0.11975 ± .12%	1560.3 ± 26.6	1734.9 ± 15.9	0.9927	1952.4 ± 4.1	22.6
B (m,149–250)	38	155	53	7381	16	8	0.34	0.327310 ± .99%	5.58778 ± .99%	0.12382 ± .04%	1825.3 ± 31.5	1914.2 ± 17.1	0.9994	2011.9 ± 1.3	10.6
c (s,149–250)	18	217	48	4257	12	8.7	0.37	0.208649 ± .33%	3.38788 ± .34%	0.11776 ± .07%	1221.6 ± 7.3	1501.6 ± 5.3	0.9782	1922.6 ± 2.5	40.0
d (m,149–250)	41	356	92	11852	20	6.4	0.26	0.251232 ± .40%	4.02776 ± .40%	0.11628 ± .06%	1444.8 ± 10.4	1639.8 ± 6.5	0.9905	1899.7 ± 2.0	26.7
E (s,149–250)	23	25	9	3229	4	10	0.43	0.318848 ± .29%	5.48786 ± .29%	0.12483 ± .09%	1784.1 ± 9.1	1898.7 ± 5.0	0.9569	2026.4 ± 3.0	13.7
F (s,149–250)	13	198	43	1225	28	7.8	0.33	0.207156 ± 2.3%	3.56685 ± 2.3%	0.12488 ± .09%	1213.6 ± 50.6	1542 ± 36.3	0.9992	2027.1 ± 3.3	43.9
g (s,149–250)	18	339	78	1688	53	2.9	0.11	0.233069 ± .16%	3.83522 ± .18%	0.11935 ± .08%	1350.6 ± 3.9	1600.2 ± 2.8	0.8906	1946.4 ± 2.9	33.9
h (s,149–250)	18	251	33	5686	6	5.9	0.24	0.128706 ± .13%	2.02496 ± .14%	0.11411 ± .05%	780.5 ± 1.9	1123.9 ± 1.9	0.9384	1865.8 ± 1.7	61.7
M1 (s,149–250)	19	5201	115	665	80	66	6.36	0.008258 ± .20%	0.05399 ± .49%	0.04742 ± .41%	53.0 ± 0.2	53.4 ± 0.5	0.5850	70.3 ± 19.4	24.7
M2 (s,149–250)	*24*	*6141*	*112*	*1699*	*39*	*65.7*	*6.25*	*0.006940 ± 30.3%*	*0.04504 ± 30.3%*	*0.04707 ± .24%*	*44.6 ± 26.9*	*44.7 ± 26.5*	*1.0000*	*53.0 ± 11.6*	*16.0*
m3 (s,149–250)	46	6331	142	1849	83	67.2	6.67	0.008164 ± .93%	0.05212 ± .73%	0.04630 ± .79%	52.4 ± 1.0	51.6 ± 0.7	0.5702	13.3 ± 38.0	–295.44
m4 (s,149–250)	*33*	*4571*	*107*	*172*	*506*	*68.4*	*7.08*	*0.008137 ± 1.5%*	*0.05149 ± 5.0%*	*0.04589 ± 4.4%*	*52.2 ± 1.6*	*51.0 ± 5.0*	*0.5031*	*–8 +201.7/–229.8*	*–295.44*
M5 (s,149–250)	*13*	*4171*	*123*	*771*	*37*	*74.9*	*9.80*	*0.008153 ± 1.2%*	*0.05520 ± 5.5%*	*0.04910 ± 5.2%*	*52.3 ± 1.2*	*54.6 ± 5.8*	*0.3429*	*152.8 +227.8/–264.7*	*66.0*
m6 (s,149–250)	10	11945	279	2441	26	67.7	6.85	0.008321 ± .37%	0.05415 ± .37%	0.04720 ± .12%	53.4 ± 0.4	53.5 ± 0.4	0.9517	59.3 ± 5.5	9.9
S298-117 Cranberry Valley crosscutting aplite, UTM 415925E, 5620400N															
A (m, 74–105)	83	639	137	11110	62	6.9	0.29	0.206944 ± 1.3%	3.50532 ± 1.3%	0.12285 ± .05%	1212.5 ± 28.8	1528.4 ± 20.6	0.9993	1998.0 ± 1.8	43.1
B (m, 74–105)	14	619	171	16335	9	10	0.43	0.257849 ± .27%	4.30039 ± .25%	0.12096 ± .11%	1478.8 ± 7.2	1693.4 ± 4.2	0.9087	1970.4 ± 4.1	27.9
C (m, 74–105)	19	295	75	7052	12	7.7	0.33	0.242432 ± .42%	4.20964 ± .43%	0.12594 ± .06%	1399.3 ± 10.6	1675.9 ± 7.0	0.9886	2042.0 ± 2.3	35.0
D (m, 74–105)	14	431	116	14665	7	5.8	0.24	0.262978 ± .91%	4.32034 ± .90%	0.11915 ± .09%	1505.1 ± 24.3	1697.2 ± 14.9	0.9949	1943.5 ± 3.3	25.3
E (m, 74–2505)	15	457	104	7890	11	8.8	0.38	0.214024 ± .59%	3.67729 ± .60%	0.12461 ± .07%	1250.2 ± 13.5	1566.5 ± 9.5	0.9924	2023.3 ± 2.6	42.0
F (m, 105–149)	15	336	81	8102	9	10.1	0.44	0.223271 ± .72%	3.89769 ± .72%	0.12661 ± .04%	1299.1 ± 16.9	1613.2 ± 11.6	0.9988	2051.4 ± 1.2	40.4
M1 (s, 149–250)	16	6019	178	371	141	74.9	9.76	0.008172 ± .29%	0.05271 ± .87%	0.04678 ± .75%	52.5 ± 0.3	52.2 ± 0.9	0.5505	37.9 ± 35.9	–38.5
M2 (s, 149–250)	19	4500	133	210	224	75	9.80	0.008178 ± .39%	0.05185 ± 2.0%	0.04598 ± 1.9%	52.5 ± 0.4	51.3 ± 2.0	0.5355	–3.3 ± 89.9	–38.5
M3 (s, 149–250)	10	4710	144	200	136	76.2	10.45	0.008021 ± 1.5%	0.05238 ± 2.4%	0.04736 ± 1.7%	51.5 ± 1.5	51.8 ± 2.5	0.6989	67.4 ± 83.2	23.7
M4 (s, 149–250)	22	3193	104	871	43	76.7	10.75	0.008347 ± .25%	0.05409 ± .49%	0.04700 ± .38%	53.6 ± 0.3	53.5 ± 0.5	0.6273	49.0 ± 18.3	–9.32
M5 (s, 105–149)	8	3976	127	1595	10	76.4	10.61	0.008290 ± .85%	0.05488 ± 1.5%	0.04801 ± 1.3%	53.2 ± 0.9	54.2 ± 1.6	0.5002	99.9 ± 61.4	46.9
M6 (s, 105–149)	4	4442	146	776	13	76.1	10.44	0.008629 ± .54%	0.05630 ± 1.3%	0.04732 ± 1.1%	55.4 ± 0.6	55.6 ± 1.4	0.5038	65.5 ± 54.0	15.5
M7 (s, 105–149)	4	4618	144	836	12	76	10.36	0.008251 ± .53%	0.05423 ± .91%	0.04766 ± .74%	53.0 ± 0.6	53.6 ± 1.0	0.5848	82.6 ± 35.1	36.0
S298-120 Cranberry Valley pegmatite folded by F3 folds, UTM 415900E, 5620525N															
A (m, 74–105)	4	17055	4014	8224	112	8	0.34	0.224307 ± 3.2%	3.77040 ± 3.2%	0.12191 ± .04%	1304.6 ± 75.1	1586.5 ± 51.0	0.9999	1984.4 ± 1.4	37.8
B (m, 74–105)	13	555	85	8238	8	6.7	0.28	0.149024 ± .37%	2.49378 ± .37%	0.12137 ± .04%	895.5 ± 6.2	1270.2 ± 5.4	0.9939	1976.4 ± 1.5	58.5
C (m, 105–250)	22	991	85	11439	10	5.3	0.22	0.084489 ± .41%	1.33386 ± .41%	0.11450 ± .03%	522.9 ± 4.1	860.6 ± 4.8	0.9964	1872.0 ± 1.3	74.9
D (m, 105–250)	21	427	111	15946	9	8.8	0.38	0.246206 ± .23%	4.03164 ± .23%	0.11876 ± .03%	1418.9 ± 5.8	1640 ± 3.8	0.9915	1937.7 ± 1.1	29.8
E (s, 105–149)	23	320	80	3802	27	8.9	0.38	0.237380 ± .69%	3.91251 ± .70%	0.11954 ± .10%	1373.1 ± 17.1	1616.3 ± 11.4	0.9903	1949.3 ± 3.5	32.8
F (s, 105–149)	21	285	65	3910	20	8.2	0.35	0.218129 ± .59%	3.63691 ± .60%	0.12093 ± .08%	1272.0 ± 13.5	1557.6 ± 9.5	0.9909	1969.9 ± 2.9	39.0
M1 (s, 149–250)	12	8615	264	313	164	77	11.17	0.007715 ± 1.1%	0.05592 ± 1.5%	0.05257 ± .86%	49.5 ± 1.1	55.3 ± 1.6	0.8086	310.3 ± 39.1	84.4
M2 (s, 149–250)	*12*	*5458*	*175*	*168*	*228*	*77.1*	*11.02*	*0.008074 ± 2.1%*	*0.05251 ± 6.9%*	*0.04717 ± 6.1%*	*51.8 ± 2.2*	*52.0 ± 7.0*	*0.5098*	*57.8 +266.5/–318.0*	*10.4*
M3 (s, 105–149)	*2*	*18510*	*481*	*56*	*386*	*72.9*	*8.81*	*0.007775 ± 1.2%*	*0.05146 ± 9.1%*	*0.04801 ± 8.3%*	*49.9 ± 1.2*	*51.0 ± 9.1*	*0.6956*	*99.7 +352.8/–449.7*	*50.1*
M4 (s, 105–149)	4	6159	231	98	155	79.7	12.88	0.008370 ± .59%	0.05471 ± 4.2%	0.04741 ± 3.8%	53.7 ± 0.6	54.1 ± 4.4	0.6500	70.1 +172.2/–192.3	23.4
M5 (s, 105–149)	14	3360	102	1567	15	75.6	10.17	0.008158 ± .35%	0.05447 ± 1.1%	0.04843 ± .99%	52.4 ± 0.4	53.9 ± 1.1	0.4304	120.1 ± 46.5	56.6
M6 (s, 105–149)	11	2910	97	885	19	78.1	11.67	0.008020 ± .32%	0.05154 ± .96%	0.04661 ± .89%	51.5 ± 0.3	51.0 ± 1.0	0.3679	29.1 ± 42.8	–77.44
M7 (s, 105–149)	4	6188	228	817	18	79.3	12.49	0.008443 ± .19%	0.05493 ± .37%	0.04719 ± .32%	54.2 ± 0.2	54.3 ± 0.4	0.5046	58.8 ± 15.1	7.9

Table 5.1. (continued)

Fraction size [a]	Wt. (µg) [b]	U (ppm) [b]	Pb* (ppm) [b]	$^{206}Pb/^{204}Pb$	Pb (pg) [c]	^{208}Pb (%)	Th/U [d]	$^{206}Pb/^{238}U$	$^{207}Pb/^{235}U$	$^{207}Pb/^{206}Pb$	$^{206}Pb/^{238}U$ Age (Ma)	$^{207}Pb/^{235}U$ Age (Ma)	Correlation coefficient	$^{207}Pb/^{206}Pb$ Age (Ma)	Discordance (%) [e]
S298-213 Frigg Glacier crosscutting aplite, UTM 423625E, 5600025N															
A (m, 74–105)	110	2447	104	4196	176	2.2	0.083	0.04402 ± 2.2%	0.6097 ± 2.2%	0.10046 ± .06%	277.7 ± 12.0	483.3 ± 17.0	0.9997	1632.6 ± 2.1	84.7
B (m, 74–105)	14	5110	85	5443	13	6.8	0.27	0.01658 ± .50%	0.1924 ± .51%	0.08416 ± .10%	106.0 ± 1.1	178.7 ± 1.7	0.9795	1296.3 ± 4.0	92.6
C (mt, 104–149)	31	1569	80	9525	16	2.6	0.10	0.05239 ± .55%	0.7626 ± .54%	0.10559 ± .14%	329.2 ± 3.5	575.5 ± 4.8	0.9676	1724.5 ± 5.1	82.9
D (m, 105–149)	16	1291	77	3121	24	1.3	0.051	0.06231 ± .83%	0.8898 ± .85%	0.10357 ± .17%	389.6 ± 6.3	646.2 ± 8.1	0.9806	1689.1 ± 6.1	79.2
E (s, 149–250)	43	1432	51	1955	71	1.2	0.046	0.03757 ± .14%	0.5006 ± .16%	0.09664 ± .07%	237.8 ± 0.6	412.1 ± 1.1	0.8929	1560.2 ± 2.8	86.3
F (s, 149–250)	22	2318	151	5897	35	0.7	0.028	0.06803 ± .70%	0.9781 ± .72%	0.10428 ± .05%	424.3 ± 5.8	692.6 ± 7.2	0.9976	1701.6 ± 1.9	77.5
RB-1-93 Blanket Mountain siliceous pegmatite in boudin neck, UTM 412600E, 5625330N															
A (m, <105)	74	1544	64	2154	141	4	0.16	0.04182 ± .95%	0.5852 ± .96%	0.10149 ± .11%	264.1 ± 4.9	467.8 ± 7.2	0.9937	1651.6 ± 4.0	85.7
B (m, 74–105)	9	1206	68	1612	22	6.4	0.26	0.05514 ± .34%	0.8255 ± .35%	0.10859 ± .14%	346.0 ± 2.3	611.1 ± 3.2	0.9199	1775.8 ± 5.0	82.6
C (m, 74–105)	6	1944	103	4250	9	5.1	0.20	0.05289 ± .34%	0.7983 ± .30%	0.10947 ± .16%	332.2 ± 2.2	595.8 ± 2.7	0.8783	1790.5 ± 5.8	83.5
D (mt, <149)	9	4748	66	4784	8	2.2	0.080	0.01456 ± .23%	0.1605 ± .24%	0.07991 ± .06%	93.2 ± 0.4	151.1 ± 0.7	0.9677	1194.8 ± 2.4	92.9
E (st, <149)	4	9575	72	2246	8	0.2	0.0056	0.00830 ± .86%	0.0554 ± .74%	0.04839 ± .58%	53.3 ± 0.9	54.7 ± 0.8	0.7469	118.4 ± 27.5	55.2
F (s, 149–250)	7	12602	92	4690	9	0.1	0.0037	0.00810 ± .27%	0.0530 ± .27%	0.04739 ± .13%	52.0 ± 0.3	52.4 ± 0.3	0.8894	68.9 ± 6.1	24.6
G (s, 149–250)	12	502	80	8370	7	7.2	0.30	0.15432 ± .27%	2.4844 ± .28%	0.11676 ± .04%	925.1 ± 4.7	1267.5 ± 4.0	0.9906	1907.3 ± 1.4	55.2

Errors are 1 std. error of mean in % except for age errors which are 2 std. errors in Ma

* = Radiogenic Pb

a = Single grain (s), multiple grains (m), single tip (st) or multiple tips (mt); sizes in micrometres

b = Include sample weight error of ± 0.001 mg in concentration uncertainty

c = Total common Pb in analysis

d = Th/U from 208*/206* and 207*/206* age

e = Discordance on chord to origin

Fractions dispayed in italics have large errors and are not shown in concordia plots

Table 5.2. SHRIMP data for sample s298-65.

Spot	U(ppm)	Th(ppm)	Th/U	± Th/U	Pb*(ppm)	204/206	± 204/206	f206	± f206	208/206	± 208/206	208/232	± 208/232	207/235	± 207/235	206/238	± 206/238	R	207/206	± 207/206
s298-65 Basement migmatitic orthogneiss, UTM 415050E, 5624650N																				
Host orthogneiss																				
H-1.1	209.2	180.2	0.8900	0.0036	85	1.00E-05	1.11E-05	0.0002	0.0002	0.25576	0.00149	0.09849	0.00145	5.8575	0.0863	0.34272	0.00443	0.9248	0.12396	0.00070
H-2.1	157.5	68.0	0.4462	0.0090	50	2.60E-06	8.89E-06	0.0001	0.0002	0.14981	0.00077	0.09732	0.00238	4.9227	0.0706	0.28983	0.00377	0.9478	0.12319	0.00057
H-3.1	50.1	57.1	1.1770	0.0497	24	2.53E-05	4.74E-05	0.0004	0.0008	0.35065	0.00501	0.11038	0.00523	6.1441	0.1388	0.37051	0.00593	0.7858	0.12027	0.00169
H-4.1	78.4	75.8	1.0000	0.0062	37	5.47E-05	3.41E-05	0.0010	0.0006	0.28456	0.00215	0.10893	0.00171	6.8667	0.0981	0.38279	0.00474	0.9163	0.13010	0.00075
H-4.2	130.3	76.3	0.6052	0.0082	50	3.40E-05	1.82E-05	0.0006	0.0003	0.17224	0.00212	0.09726	0.00216	6.0737	0.0894	0.34175	0.00429	0.9063	0.12890	0.00081
H-5.1	204.6	91.6	0.4624	0.0038	91	1.00E-05	1.00E-05	0.0002	0.0002	0.13058	0.00146	0.11426	0.00223	8.2073	0.1347	0.40460	0.00556	0.8935	0.14712	0.00109
H-5.2	729.1	3.5	0.0050	0.0001	211	5.27E-06	5.92E-06	0.0001	0.0001	0.00177	0.00023	0.10772	0.01399	4.7419	0.0593	0.30216	0.00368	0.9911	0.11382	0.00019
H-6.1	208.5	98.5	0.4879	0.0019	84	3.02E-05	1.75E-05	0.0005	0.0003	0.14046	0.00147	0.10661	0.00179	6.5586	0.0864	0.37032	0.00462	0.9743	0.12845	0.00038
H-7.1	152.4	45.0	0.3049	0.0028	71	4.11E-05	6.97E-06	0.0007	0.0001	0.08407	0.00468	0.12185	0.00706	8.8055	0.2259	0.44191	0.00592	0.6207	0.14452	0.00293
Leucosome																				
L-1.1	683.8	487.7	0.7369	0.0097	289	1.00E-05	2.15E-06	0.0002	0.0000	0.21548	0.00060	0.10675	0.00219	6.5279	0.1063	0.36507	0.00564	0.9763	0.12969	0.00046
L-1.2	1130.3	17.4	0.0159	0.0006	279	1.01E-05	2.55E-06	0.0002	0.0000	0.00488	0.00013	0.07895	0.00372	3.9677	0.0509	0.25704	0.00313	0.9775	0.11195	0.00030
L-2.1	266.4	115.4	0.4477	0.0150	133	1.76E-05	4.87E-06	0.0003	0.0001	0.12451	0.00055	0.12632	0.00454	9.8288	0.1269	0.45426	0.00554	0.9737	0.15693	0.00046
L-2.2	173.5	56.4	0.3358	0.0012	81	1.00E-05	1.00E-05	0.0002	0.0002	0.09477	0.00133	0.12184	0.00231	9.2589	0.1181	0.43173	0.00525	0.9789	0.15554	0.00041
L-2.3	1267.1	7.7	0.0063	0.0001	15	1.00E-05	1.00E-05	0.0002	0.0002	0.00923	0.00206	0.01822	0.00409	0.1207	0.0040	0.01241	0.00026	0.7190	0.07051	0.00163
L-2.4	1421.0	7.8	0.0057	0.0001	17	5.50E-05	3.83E-05	0.0010	0.0007	0.00121	0.00145	0.00275	0.00329	0.1253	0.0022	0.01286	0.00016	0.7882	0.07069	0.00076
L-2.5	1328.5	10.2	0.0079	0.0002	181	2.38E-05	5.39E-06	0.0004	0.0001	0.00242	0.00025	0.04350	0.00455	2.1445	0.0276	0.14297	0.00174	0.9746	0.10879	0.00032
L-3.1	350.1	54.2	0.1599	0.0006	112	2.65E-05	1.25E-05	0.0005	0.0002	0.04587	0.00070	0.09188	0.00183	5.2700	0.0703	0.32026	0.00396	0.9617	0.11934	0.00044
L-3.2	931.7	523.6	0.5805	0.0089	355	6.30E-07	9.00E-07	0.0000	0.0000	0.16903	0.00054	0.09992	0.00198	5.7218	0.0734	0.34318	0.00414	0.9707	0.12092	0.00038
L-4.1	1154.9	3.9	0.0035	0.0000	8	3.15E-04	1.49E-04	0.0055	0.0026	–0.00452	0.00556	–0.01042	–0.01283	0.0507	0.0028	0.00796	0.00011	0.3599	0.04621	0.00239
L-4.2	121.2	59.2	0.5046	0.0023	47	1.00E-05	1.00E-05	0.0002	0.0002	0.14335	0.00127	0.10183	0.00161	6.2913	0.0848	0.35842	0.00441	0.9514	0.12731	0.00053

	204 corrected ages (Ma)								
Spot	208/232	±	206/238	±	207/235	±	207/206	±	% conc
s298-65 Basement migmatitic orthogneiss, UTM 415050E, 5624650N									
Host orthogneiss									
H-1.1	1898.7	26.7	1899.7	21.3	1955.0	12.9	2013.9	10.1	94.3
H-2.1	1877.1	43.9	1640.7	18.9	1806.2	12.2	2002.9	8.2	81.9
H-3.1	2116.2	95.4	2031.8	27.9	1996.5	19.9	1960.2	25.4	103.6
H-4.1	2089.8	31.3	2089.3	22.1	2094.4	12.7	2099.4	10.2	99.5
H-4.2	1876.1	39.9	1895.1	20.7	1986.5	12.9	2083.0	11.1	91.0
H-5.1	2186.8	40.6	2190.2	25.6	2254.2	15.0	2312.7	12.8	94.7
H-5.2	2067.9	256.9	1702.0	18.3	1774.7	10.5	1861.3	3.0	91.4
H-6.1	2047.5	32.7	2030.9	21.8	2053.8	11.7	2076.8	5.3	97.8
H-7.1	2324.0	127.6	2359.2	26.5	2318.1	23.7	2282.0	35.3	103.4
Leucosome									
L-1.1	2050.2	40.0	2006.1	26.7	2049.7	14.4	2093.7	6.3	95.8
L-1.2	1536.0	69.8	1474.7	16.1	1627.6	10.5	1831.4	5.0	80.5
L-2.1	2404.5	81.7	2414.2	24.6	2418.9	12.0	2422.8	5.0	99.6
L-2.2	2323.8	41.6	2313.5	23.7	2364.0	11.8	2407.8	4.5	96.1
L-2.3	365.0	81.3	79.5	1.7	115.7	3.6	943.3	48.2	8.4
L-2.4	55.5	66.1	82.3	1.0	119.9	2.0	948.5	22.1	8.7
L-2.5	860.7	88.2	861.4	9.8	1163.3	9.0	1779.2	5.3	48.4
L-3.1	1776.6	33.9	1791.0	19.4	1864.0	11.5	1946.4	6.6	92.0
L-3.2	1925.0	36.4	1902.0	19.9	1934.7	11.2	1969.9	5.6	96.6
L-4.1	0.0	0.0	51.1	0.7	50.3	2.7	11.0	117.7	463.3
L-4.2	1960.1	29.6	1974.7	21.0	2017.3	11.9	2061.1	7.4	95.8

Errors are 1 std. error of mean
isotopes indicated by their masses: 204–208 = Pb; 232 = Th; 235 and 238 = U
* = Radiogenic Pb
f206 = fraction of 206Pb that is common Pb
%conc = concordance on chord from origin
Sample s298-70 spot 1.2 (dispayed in italics) has large errors and is not shown in concordia plots

Table 5.3. Regressions and average age calculations for samples s298-65, s298-117, s298-120, s298-120, s298-213 and RB-1-93.

sample	fractions	upper intercept	error (Ma)	lower intercept	error (Ma)	average age (Ma)	error (Ma) *	MSWD	comments
S298-65	M1,5,m3,4,6,d,h	1910	2	53	0.3			1.34	youngest upper intercept
IDTIMS	M1,5,m3,4,6,F	2047	5	53	0.3			1.52	oldest upper intercept
SHRIMP	**L:2.3,2.4,2.5,4.1**	**1814**	**11**	**52.3**	**1.8**			**0.3**	best lower and youngest upper intercept
	L:1.2,2.3,2.4,2.5,4.1	1828	15	52.8	3.5			4.1	(support)
	L:2.3,2.4,2.5	1814	11	52.4	2			0.5	(support) one grain
	H:2.1,4.1,4.2,6.1;L:1.1	**2100**	**21**	**530**	**173**			**2.8**	best upper intercept
	H:2.1,4.1,4.2; L:1.1	2112	17	571	110			1	(support)
	H:4.1,4.2,6.1; L:1.1	2087	+36/–16	80	855			3.2	(support)
	H:4.1,4.2	2100	29	274	454			0	(support) one grain
	H:2.1,4.1,4.2,6.1;L:1.1					2081	17	3.8	wtd. 207Pb/206Pb average
S298-117	M1,M2,M4					53.0	2.0	4.9	wtd. 207Pb/235U average
	M1,M2,M4					**52.3**	**3.0**		207Pb/235U average (error includes all errorbars)
	M1,A–F	2050	29	53.1	14.4			932	
	M1,A,D	2005	55	52.6	15			948	
	A–F	1830	+134/–58	–1411	+1230/–411			152	
	B–F	1831	+153/–59	–1439	+1360/–439			140	
	M1,D	**1952**	**4**	**52.7**	**0.6**			**0**	youngest upper intercept
	M1,F	**2087**	**2**	**52.7**	**0.5**			**0**	oldest upper intercept
S298-120	M1–7,A–F	1976	17	53.3	5.8			579	
	M6,B–F	1968	30	51.2	20.3			1274	
	A–F	data did not converge							
	M6,A–F	data did not converge							
	M6,B	**2013**	**2**	**51.8**	**0.7**			**0**	oldest upper intercept
	M6,A,B	2011	10	51.7	4.1			43.16	
	M6,D	**1949**	**2**	**51.8**	**0.7**			**0**	youngest upper intercept
	M6,C,D,E	1951	6	51.1	3.5			37.07	
s298-213	**A–F**	**1792**	**49**	**47.9**	**11**			**315**	
	E,D,F	1829	6	62	1.4			0.6	
	A,B,D,F	1789	3	44.4	0.7			0.83	
	B,C	1864	8	48.7	0.9			0	
RB-1-93	A–G	1938	15	52.0	2.2			112	all
	B–G	**1939**	**6**	**51.8**	**0.9**			**15.15**	all but one
	C–G	1940	2	51.8	0.3			0.35	all but two
	A,B,C,G	1949	20	64.4	14.2			1.6	
	D,E,F	1942	11	51.8	0.4			0.75	

* errors between brackets include all errorbars

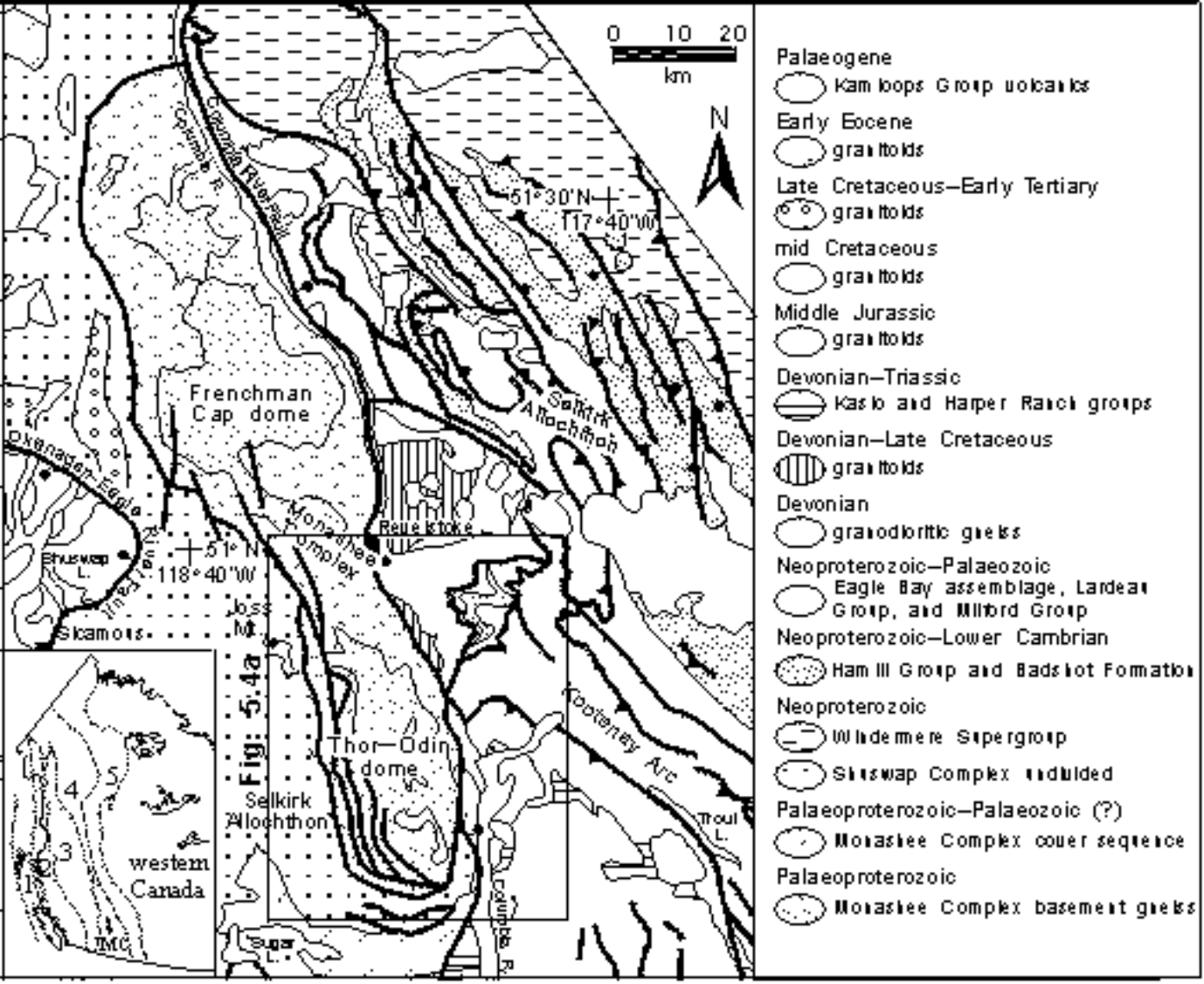

Fig. 5.1. Geological map of the Monashee Complex and surrounding geology. Modified after Wheeler and McFeely (1991). Inset: location of morphogeological belts of the Canadian Cordillera: 1. Insular Belt, 2. Coast Belt, 3. Intermontane Belt, 4. Omineca Belt, 5. Foreland Belt. MC indicates the location of the Monashee Complex.

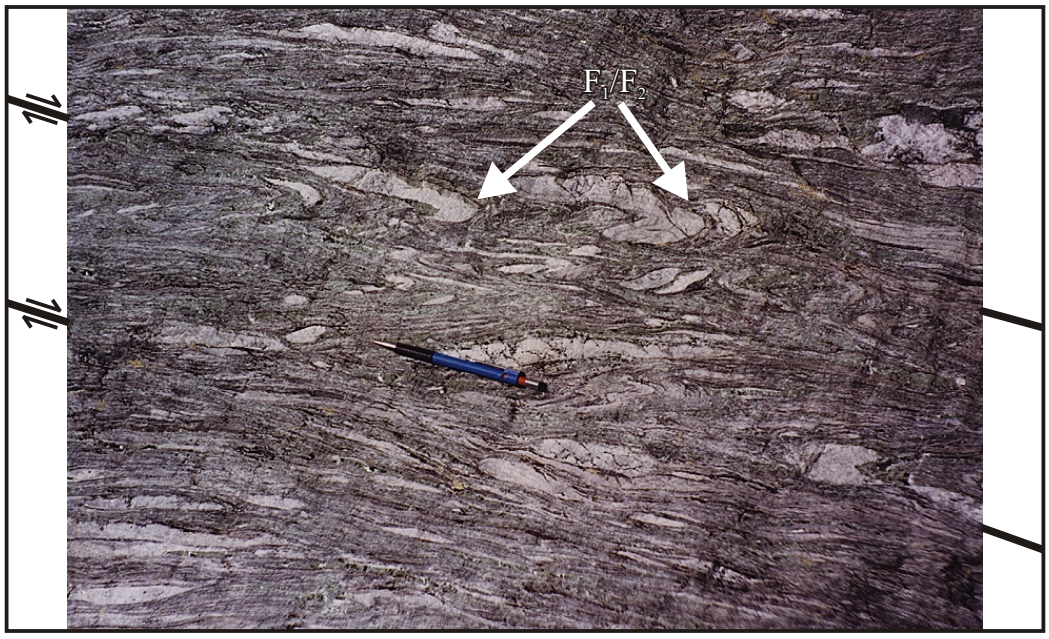

Fig. 5.2. Transposition foliation, in calc-silicate gneiss in the Megaboudin (Fig. 5.4b), looking down towards the NW. F_1/F_2 folds are dismembered by local shears. Pencil for scale.

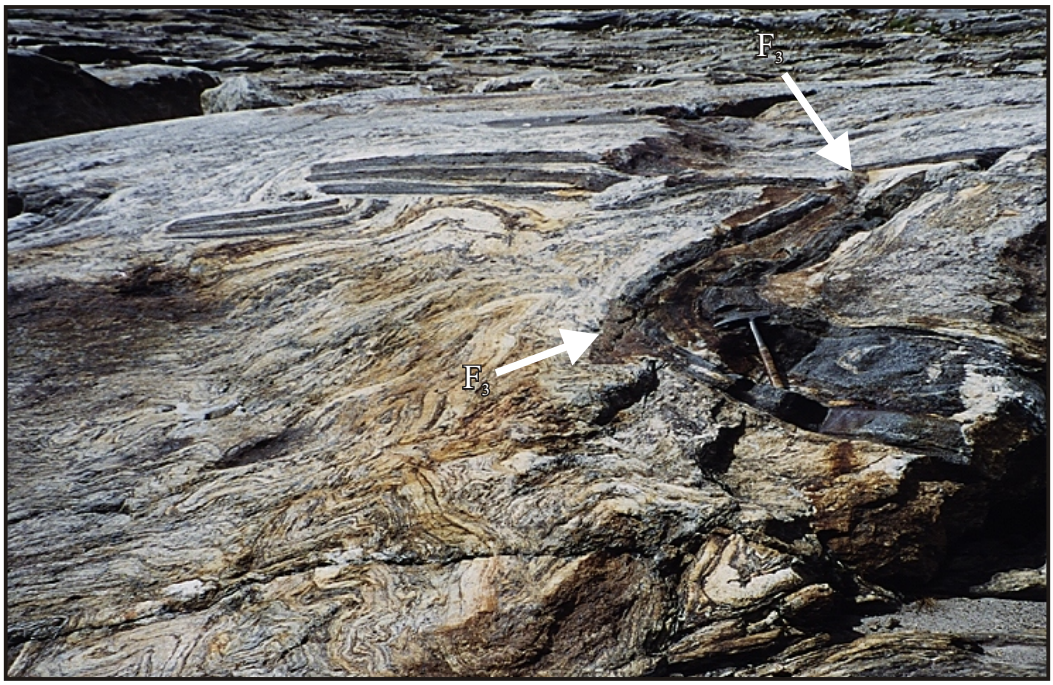

Fig. 5.3. Folded amphibolite boudins in basement gneisses on the north slope of Blanket Mountain. Boudins formed during F_1/F_2 folding and transposition and were folded during F_3 folding. Viewing direction is towards the W and the hammer is for scale.

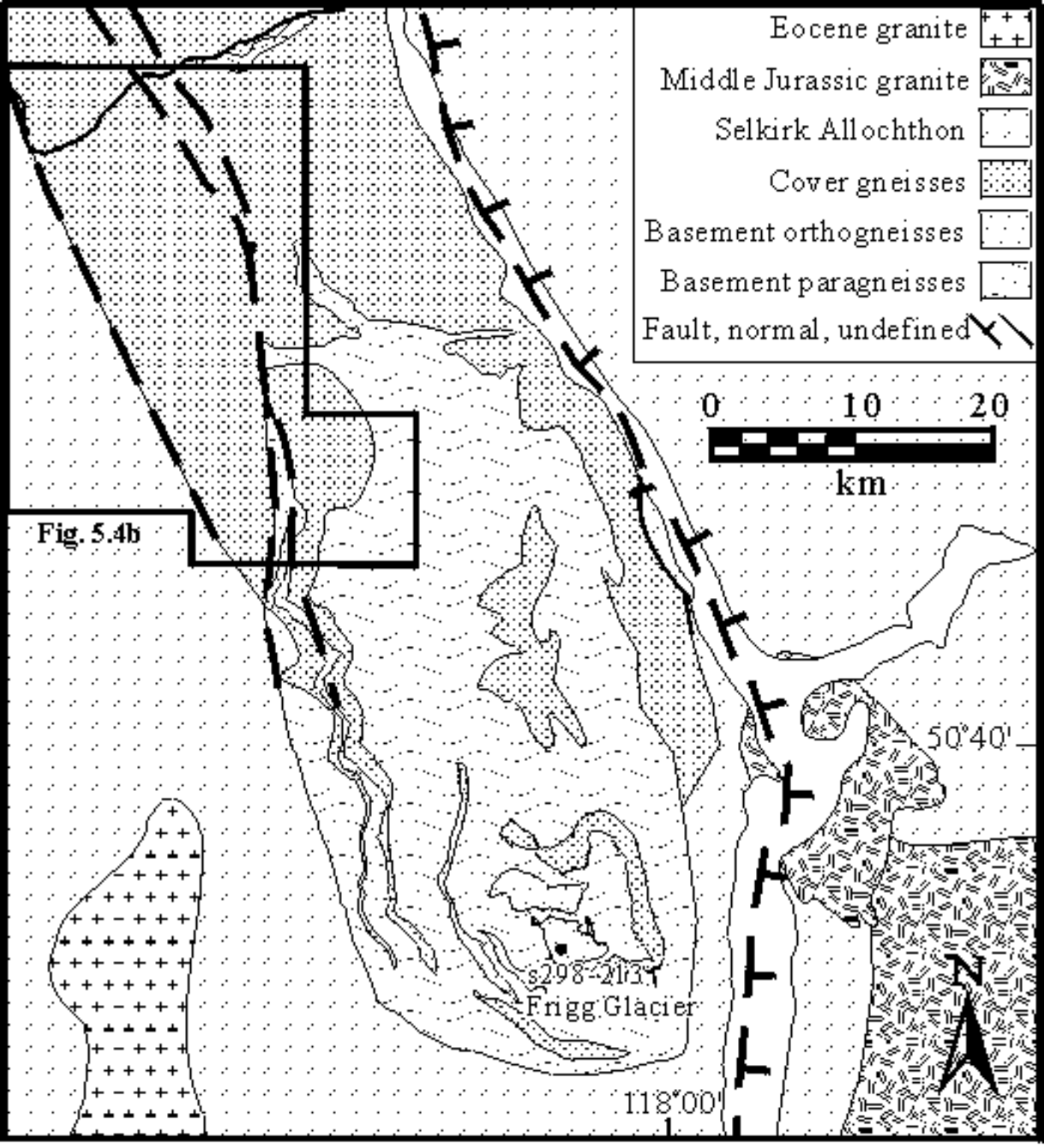

Fig. 5.4a. Geological map of Thor–Odin, after Spark (2001), indicating location of sample s298-213.

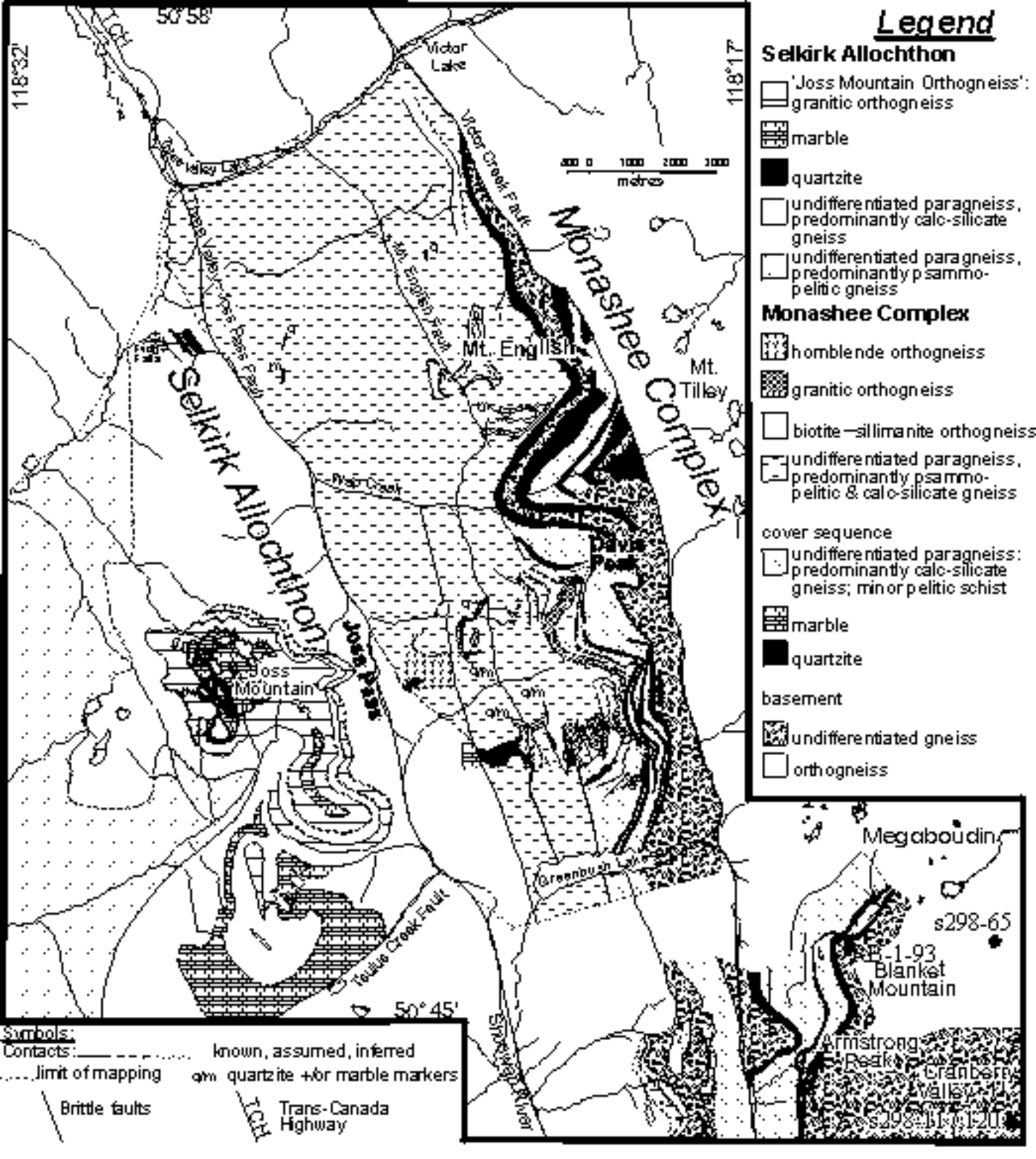

Fig. 5.4b. Geological map of northwest Thor–Odin, after Johnston et al. (2000). Locations are shown for samples *s298-65*, *s298-117*, *s298-120* and RB-1-93.

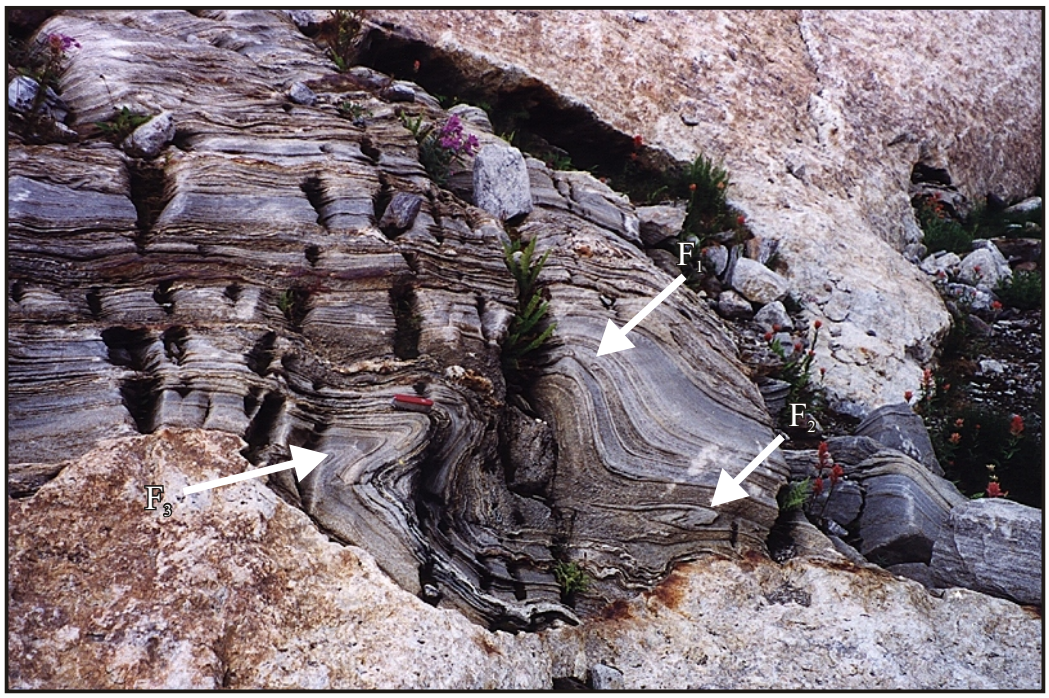

Fig. 5.5. Rare overprinting relationships of F_1 by F_2 and F_3 folds in marble, in the Megaboudin in the Monashee cover sequence. Viewing direction is towards the W. Pocket knife (on top of F_3 fold) for scale. F_1 fold indicated plunges 128°/12° and the F_3 fold plunges 300°/31°. F_2 could not be measured.

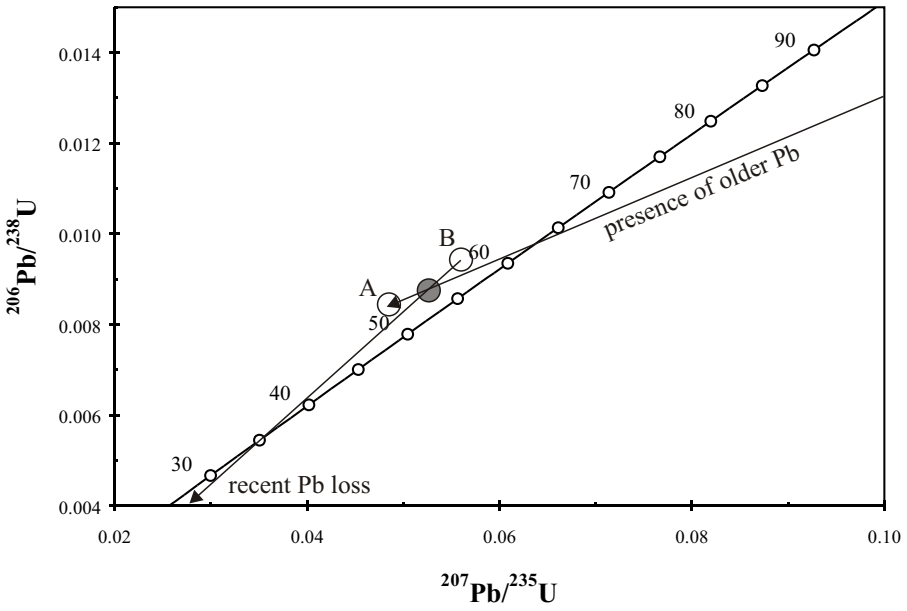

Fig. 5.6. Concordia diagram showing two examples of complicated systematics of monazite with excess ^{206}Pb, illustrating how the $^{207}Pb/^{235}U$ age of a monazite may not always represent the correct age of the monazite. The grey filled circle represents the monazite analysis. It may be a point on a mixing line between a younger reversely discordant monazite (open circle A) with more excess ^{206}Pb than shown by the grey circle, and inherited Pb. The true monazite age would then be younger than the $^{207}Pb/^{235}U$ age of the analysis (grey circle). The analysis may also plot as a point on a mixing line between an older reversely discordant monazite with more excess ^{206}Pb (open circle B) and the age of recent Pb loss in which case the monazite age would be older than the $^{207}Pb/^{235}U$ age of the analysis (grey circle).

(a)

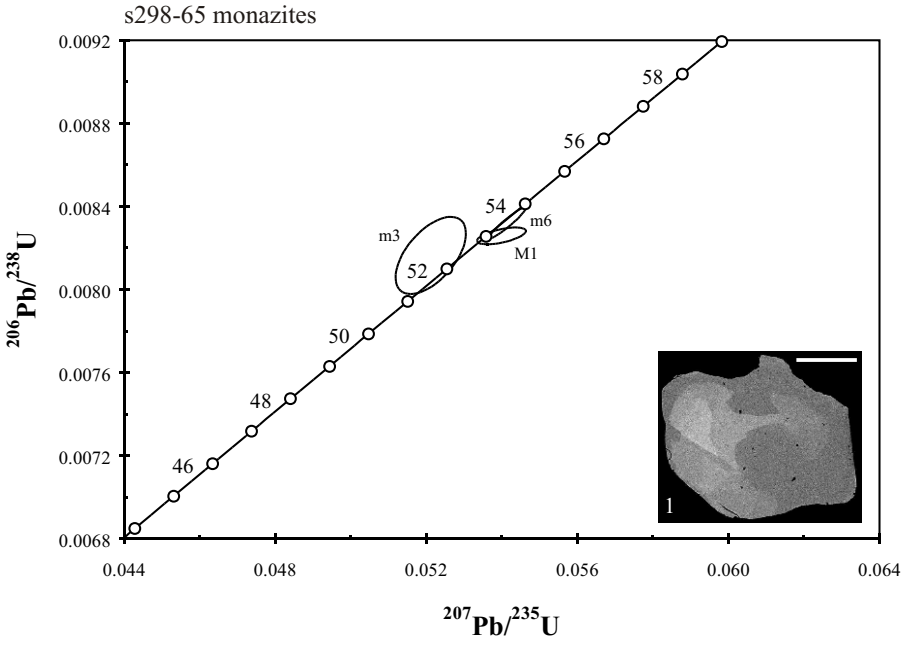

(b)

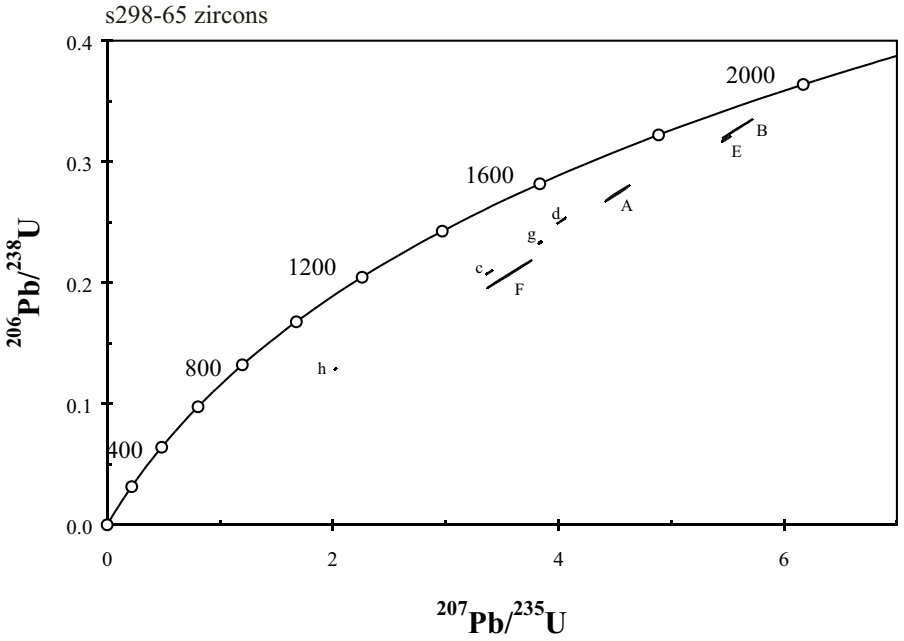

Fig. 5.7. Concordia plots for ID-TIMS data for monazites (a) and zircons (b) for a basement orthogneiss (s298-65). Grains for the host orthogneiss are labelled with capitalised letters and those of the leucosome with small letters. BSE image in (a) is a monazite (scale bar is 50 μm). See text for discussion.

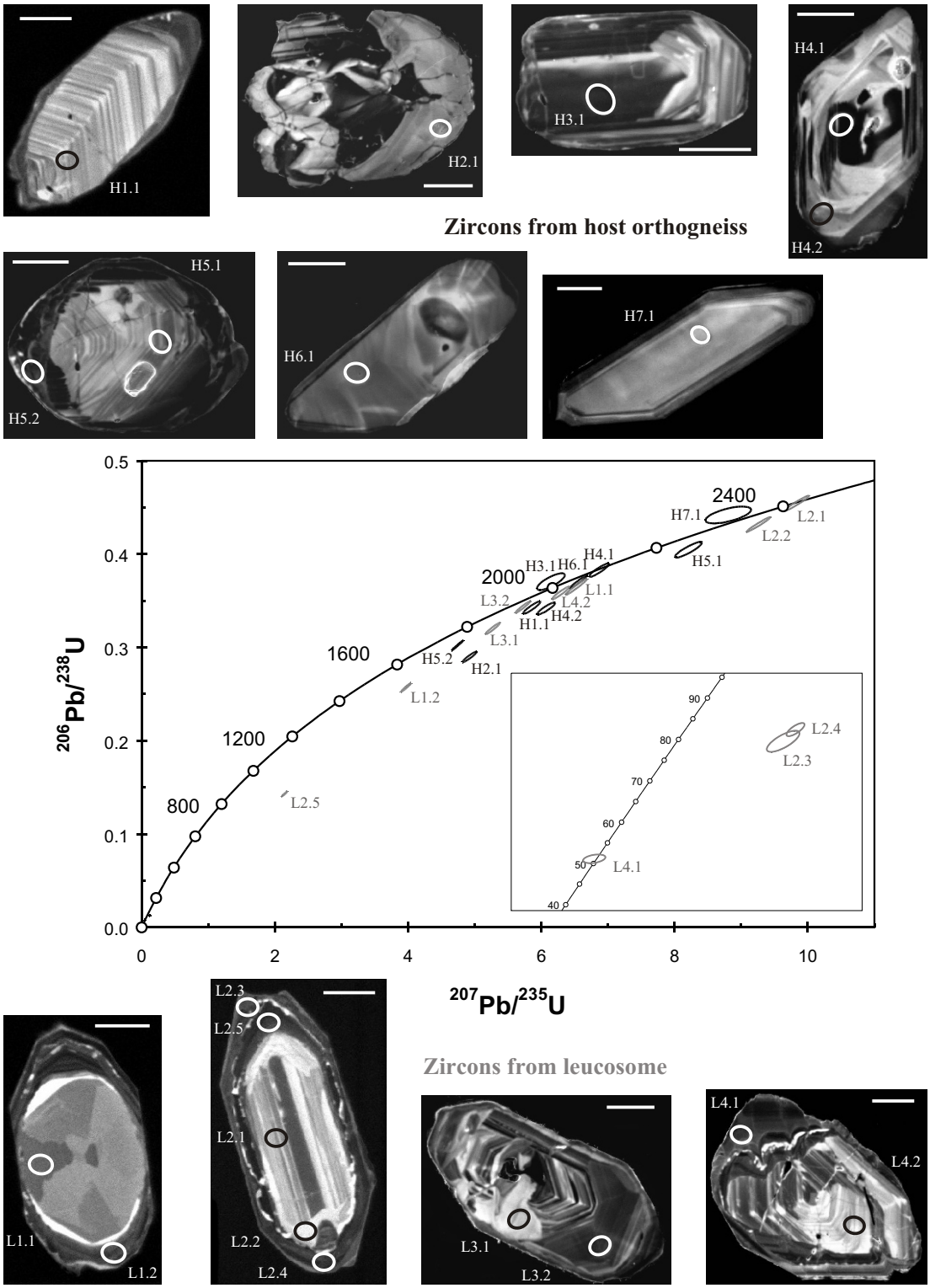

Fig. 5.8. Concordia plot showing SHRIMP data for sample s298-65. Host orthogneiss data are plotted in black, and leucosome data in grey. Cathodoluminescence images show corresponding SHRIMP spots of all analysed zircons. Scale bars are 50 μm.

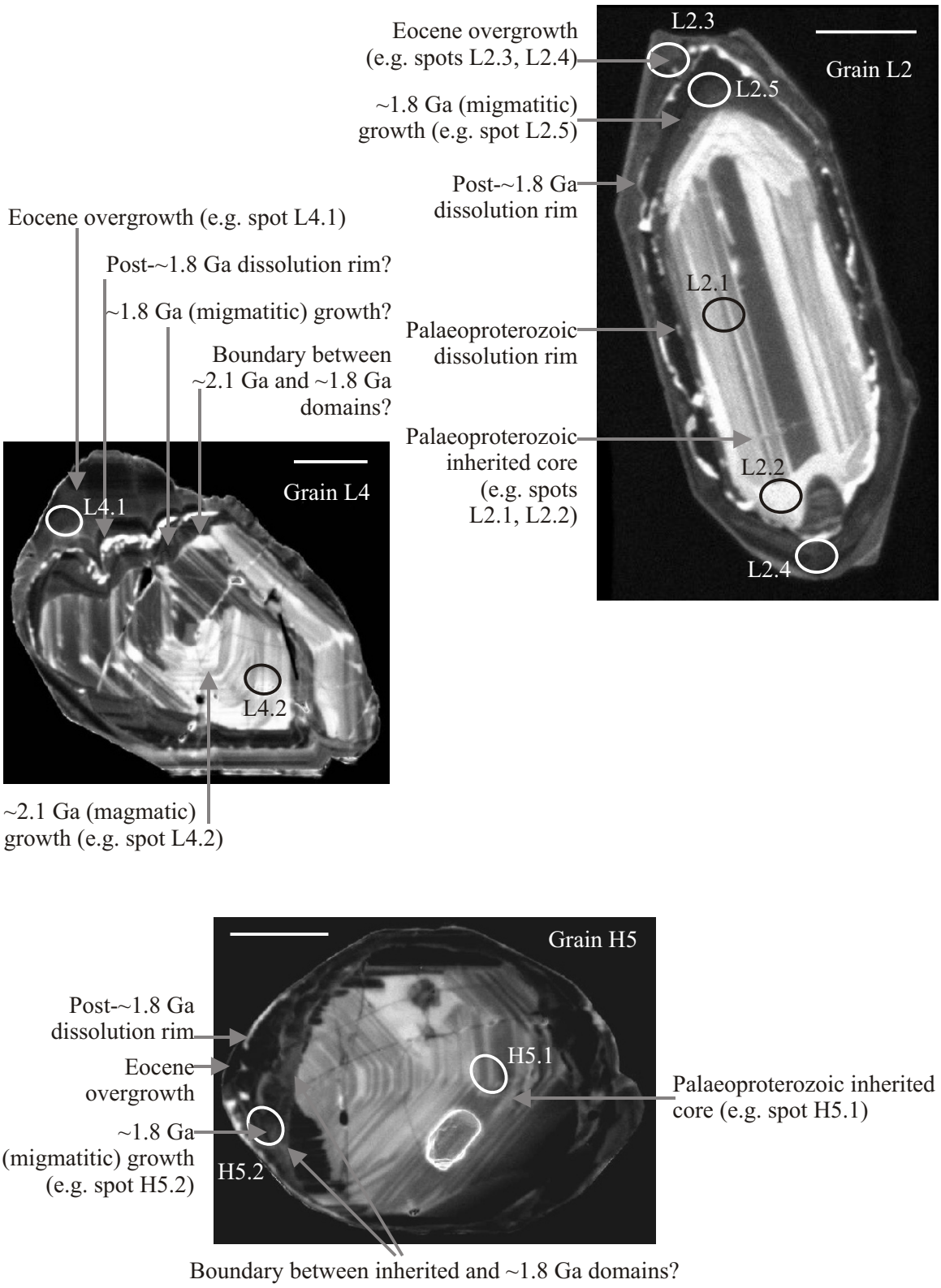

Fig. 5.9. Interpreted significance of zonations in zircon grains H5, L2 and L4 (see text for discussion). Scale bars are 50 μm.

(a)

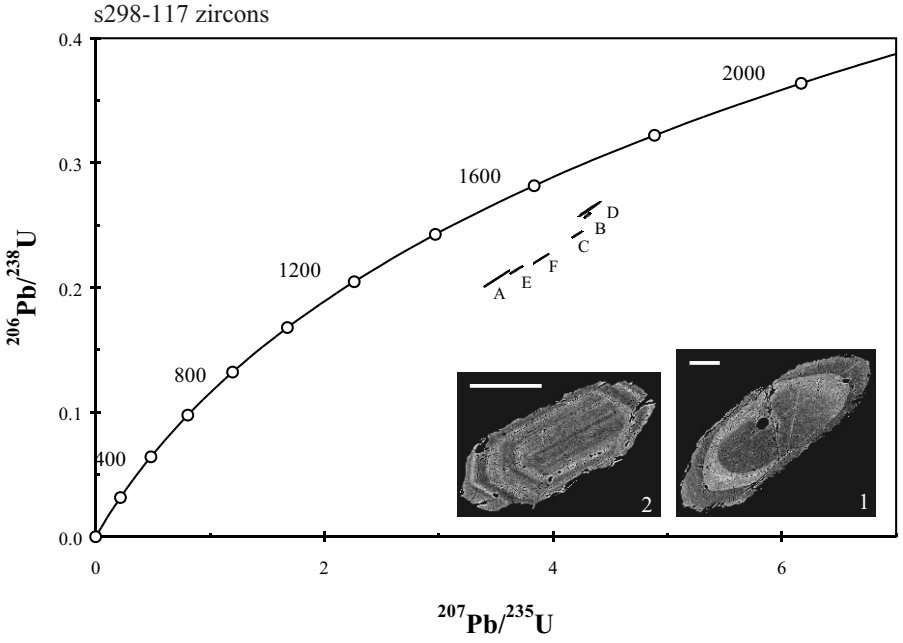

(b)

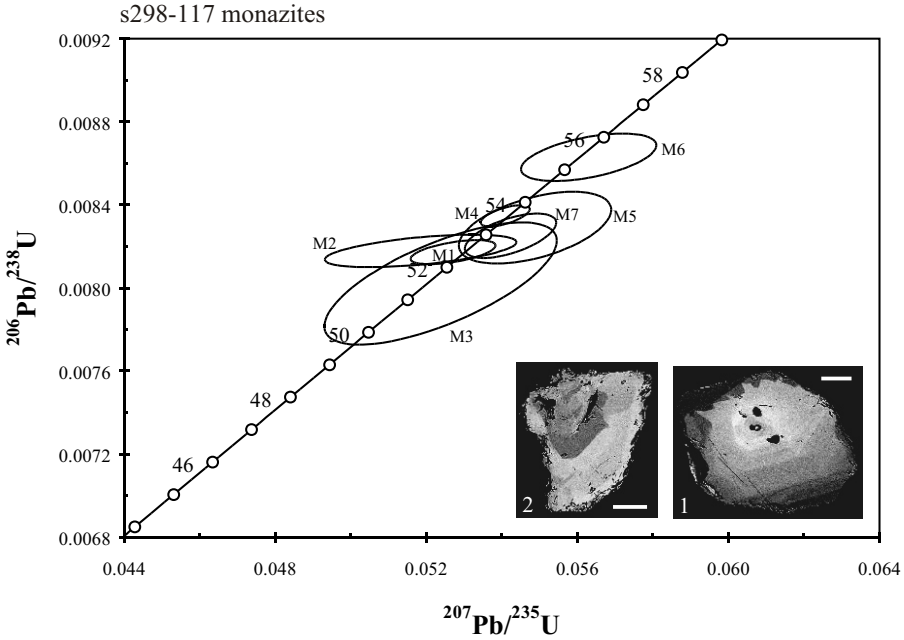

Fig. 5.10. Concordia plots for ID-TIMS data for zircons (a) and monazites (b) for a crosscutting aplite dyke in Cranberry Valley (s298-117). BSE images from zircons and monazites shown as insets with 50 μm scale bars.

(a)

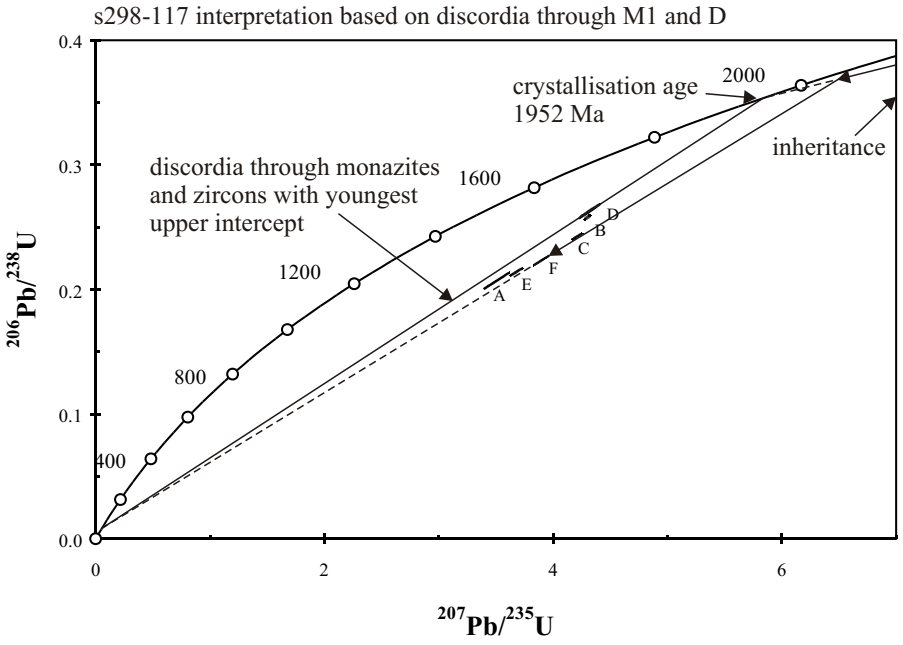

(b)

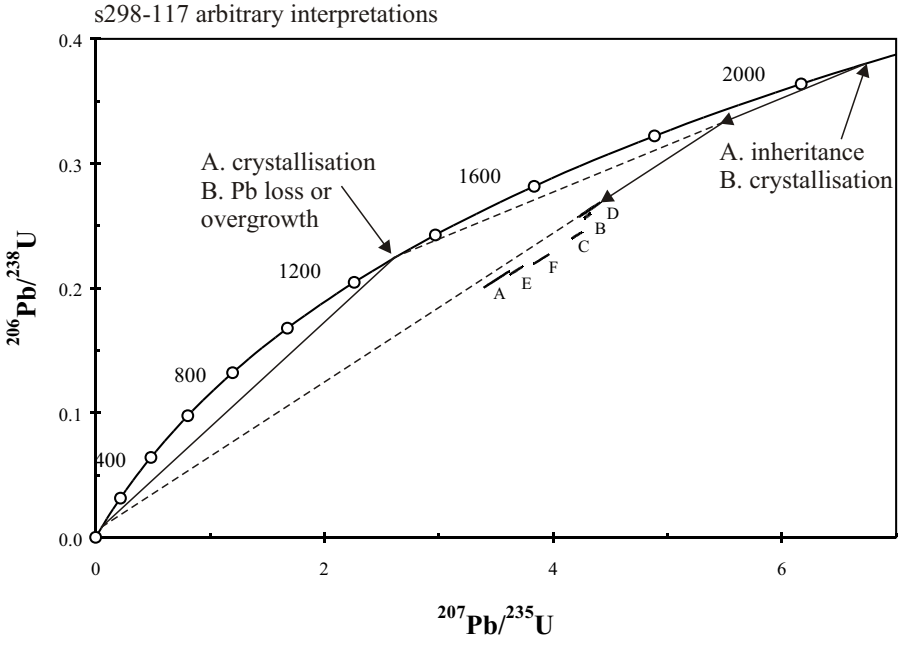

Fig. 5.11. Possible interpretations for s298-117. (a) Interpretation based on discordia chord drawn through M1 and D, with the youngest upper intercept. Crystallisation of the aplite occurred at 1952 Ma and zircons have inheritance. Pb loss or overgrowth occurred at 52.3 Ma (monazite age). Trajectory of fraction F is indicated by arrows along discordia chords. (b) Arbitrary interpretations to exemplify that a number of of interpretations can be made based on a data set with discordant zircon fractions. In interpretation (A), 1.3 Ga represents the age of crystallisation and 2.1 Ga the age of an inherited core. In interpretation (B), crystallisation occurred at 2.1 Ga and Pb loss or overgrowth at 1.3 Ga.

(a)

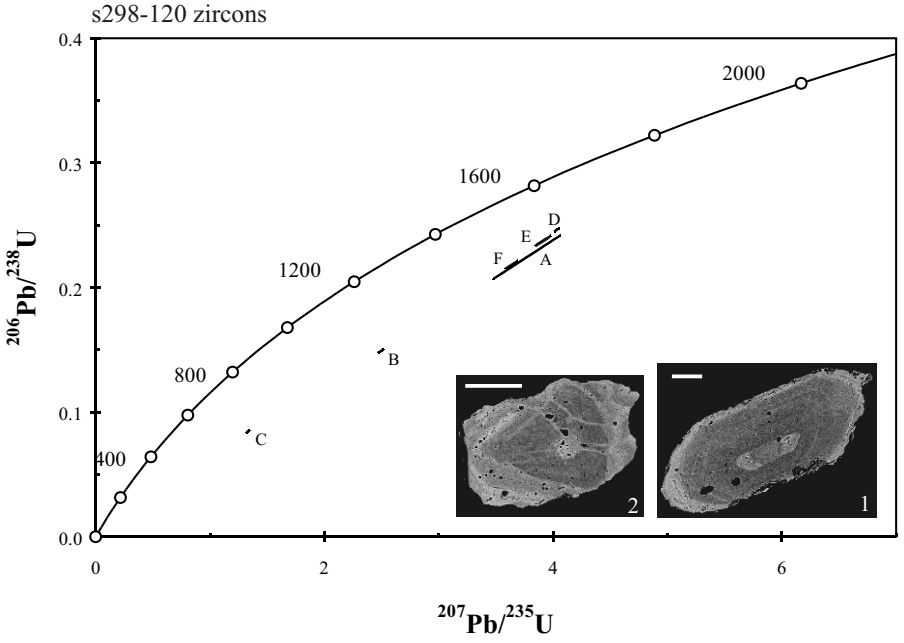

(b)

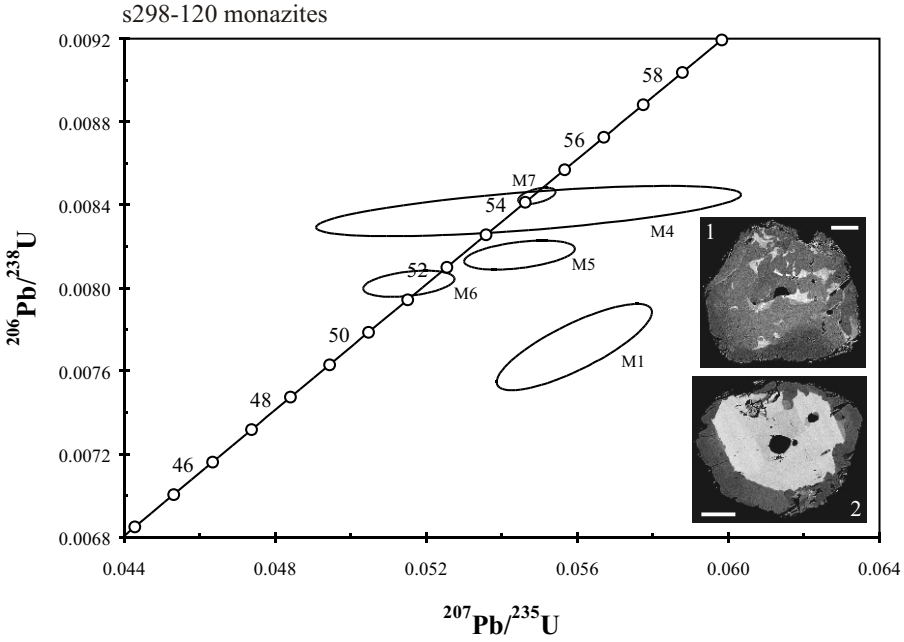

Fig. 5.12. Concordia diagrams for a pegmatite folded by F_3 in Cranberry Valley (s298-120): (a) zircons and (b) monazites. The BSE images have 50 μm scale bars.

(a)



(b)

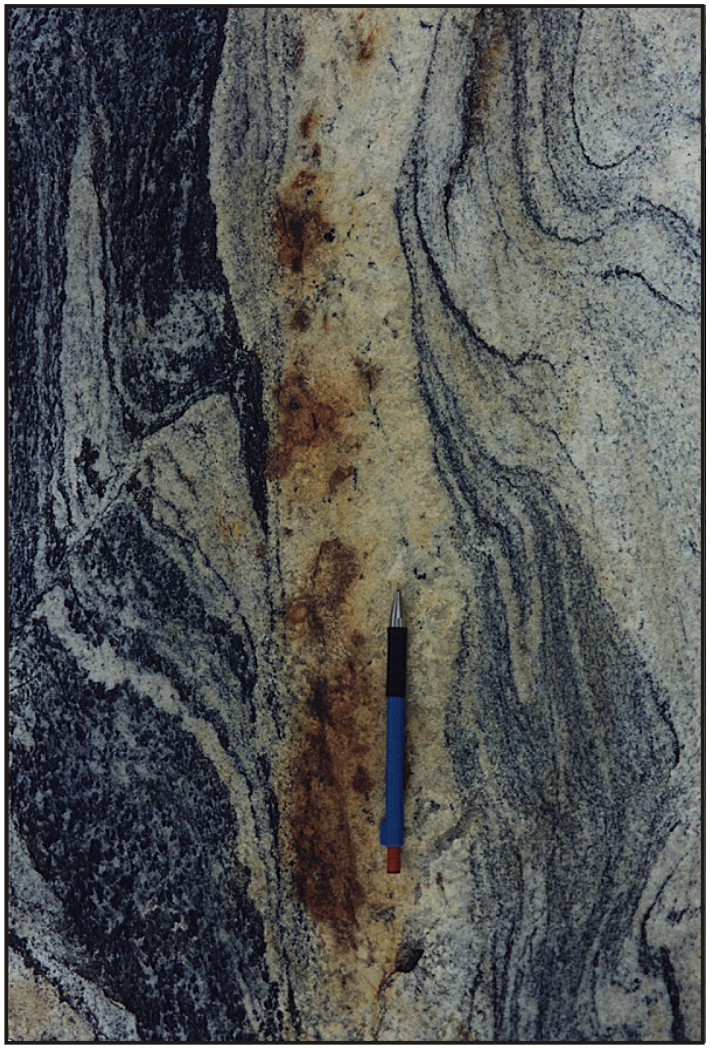

Fig. 5.13. Photographs of an aplite dyke (s298-213) near Frigg Glacier crosscutting all structures except for some of the late N–S-trending shears, looking towards the SE. Pencil for scale. (a) The aplite dyke crosscuts the foliation and shears in the host orthogneiss, although locally it follows the shears (top of photo). (b) Two isoclinal folds, left and right of the aplite, are crosscut by the aplite dyke.

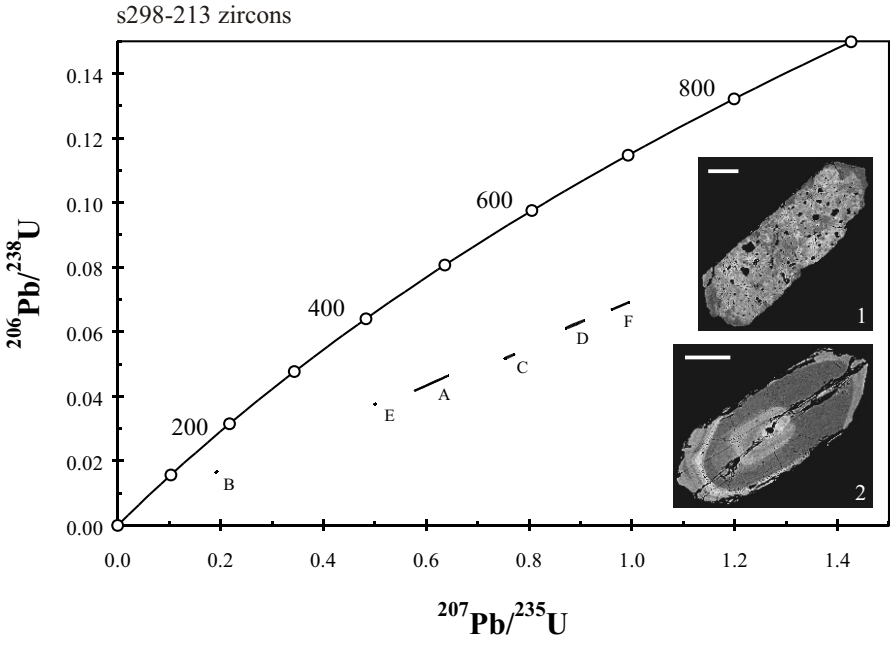

Fig. 5.14. Concordia plot for a crosscutting aplite dyke near Frigg Glacier (s298-213). Scale bars for the BSE images for representative zircon grains are 50 μm.

(a)



(b)



Fig. 5.15. (a) Photograph of a siliceous pegmatite (RB-1-93) in a boudin neck of a pelitic schist layer. Sillimanite crystals show palisade growth perpendicular to the contact with the pelitic schist boudin. (b) close-up of (a). Pencil and hand lens for scale.

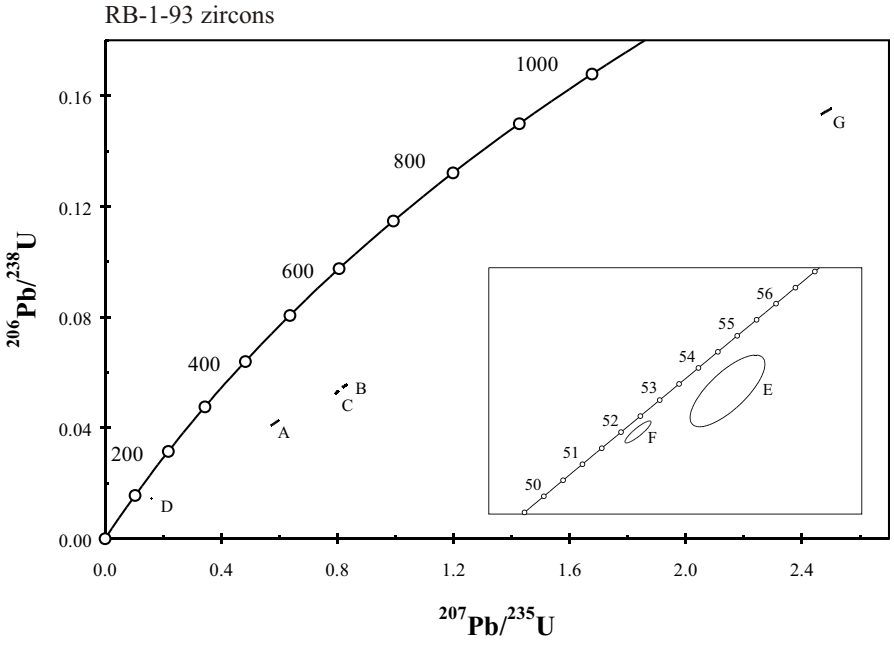

Fig. 5.16. Concordia plot of zircon data from a siliceous pegmatite (RB-1-93).

(a)

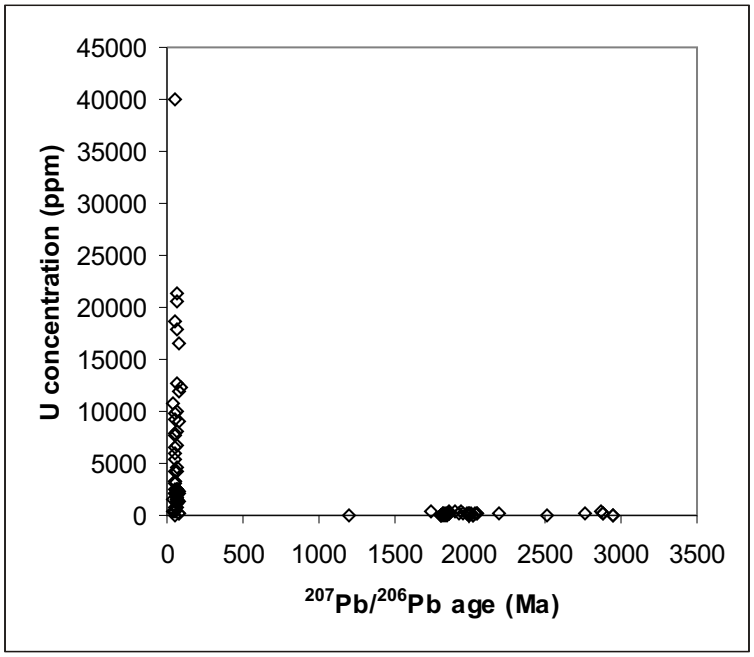

(b)

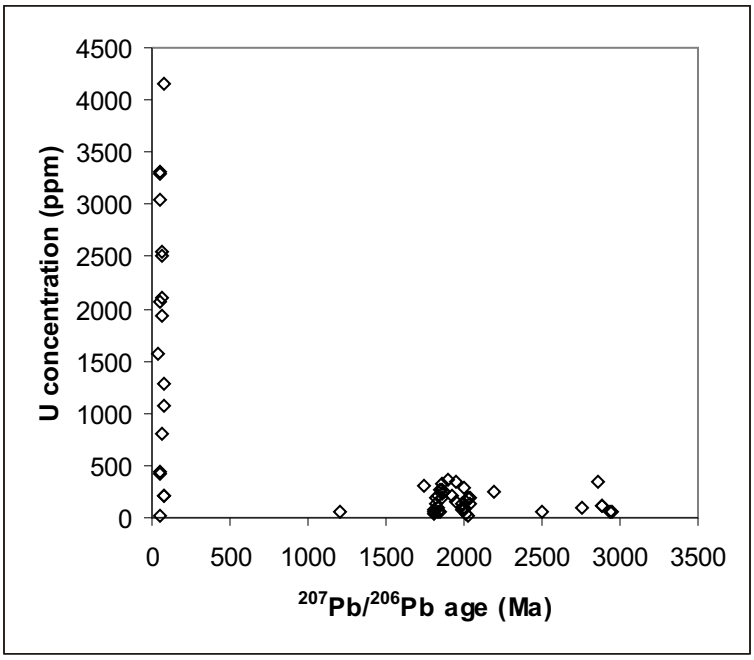

Fig. 5.17. (a) Plot of U concentration in zircon versus $^{207}Pb/^{206}Pb$ zircon ages of near-concordant or concordant zircon data in the Monashee Complex. (b) As (a), but without zircon from Late Cretaceous–Early Eocene pegmatite and aplite dykes, to exclude zircon of magmatic origin. Only data less than 10% discordant were used to avoid mixture of U concentrations of different age domains. Discordance was estimated from concordia plots, where data were not discordant towards the origin. Data from Coleman (1990), Parkinson (1992), Carr (1992), Parrish (1995), Crowley (1997), Johnston et al. (2000) and Kuiper (this chapter).

Chapter 6

Late Cretaceous to Early Eocene monazite and zircon ages in cover rocks of Thor–Odin dome of the Monashee Complex, southeastern British Columbia

Abstract

Monazite from four samples of upper amphibolite facies metasedimentary rocks, and zircon of one of these samples has been dated by U–Pb ID-TIMS and SHRIMP methods in order to constrain the age of metamorphism in Thor–Odin, the southern dome of the Monashee Complex. Monazite ages are between ~72 and 50 Ma, and indicate secondary growth (perhaps as a result of extension; cf. Chapter 3), because all samples show indications of older, Palaeoproterozoic (?), Pb. This may indicate the presence of older cores. However, these could not be found by electron microprobe or SHRIMP methods. Alternatively, old radiogenic Pb may be present that remained in the monazite after nearly complete Pb loss, e.g. by recrystallisation of an old monazite.

The older Pb component may indicate either an earlier, Palaeoproterozoic (?), metamorphic event or the age of detrital monazites. Metamorphism could possibly have taken place later in the Proterozoic, or in the Palaeozoic or Mesozoic, even though no definitive evidence exists for that in dated samples from the Monashee Complex. If true, the absence of concordant data within that time range can be explained by the lack of growth of monazite and metamorphic zircon. If Pb loss occurred, it was incomplete, so

that the timing of metamorphism was not revealed by Pb loss ages. Possibly, dissolution of monazite and other minerals used for U–Pb dating occurred during metamorphism.

6.1. Introduction

U–Pb geochronology was carried out on four samples in order to constrain timing of metamorphism and deformation in Thor–Odin. ID-TIMS work revealed <~72 Ma monazite ages as well as discordant monazite data with older $^{207}Pb/^{206}Pb$ ages. Electron microprobe dating and SHRIMP work were performed in order to find possible pre-~72 Ma age domains in samples containing discordant monazite.

6.2. Geological background

The Monashee Complex, of the southern Omineca Belt in southeastern British Columbia, is an exposure of ancestral North American rocks (Fig. 6.1). Its Palaeoproterozoic basement consists of orthogneiss and paragneiss (Armstrong et al., 1991, and references therein; Parkinson, 1991) and its Palaeoproterozoic to Palaeozoic (?) cover of quartzite, marble, calc-silicate gneiss, pelitic schist and paragneiss (Parrish, 1995, and references therein). Rocks of the Selkirk Allochthon, that presently surround the Monashee Complex, structurally overlie the Monashee Complex. They comprise Neoproterozoic and younger quartzite, marble, paragneiss and orthogneiss (Parrish, 1995,

and references therein). The Monashee Complex has two structural culminations: Frenchman Cap in the north and Thor–Odin in the south (Fig. 6.1).

The earliest deformation and metamorphism has been recognised in deep basement rocks of Frenchman Cap at 2.06 Ga (Crowley, 1999) and ~1.85 Ga (Armstrong et al., 1991; Crowley, 1999). Later deformation and metamorphism occurred throughout rocks of the Monashee Complex and the Selkirk Allochthon. Tight to isoclinal NE-verging F_1/F_2 folds have generally SW-dipping axial planes. Because overprinting relationships are rarely seen, the folds are often referred to as F_1/F_2 folds rather than F_1 and F_2. The entire Monashee basement and cover sequence is strongly transposed (Williams, 1999; Spark, 2001), indicating that it is part of a regional NE-directed subhorizontal shear zone (Williams, 1999). Folds and lithological units are dismembered by transposition (cf. Section 5.2). F_3 folds are isoclinal to open and verge predominantly to the NE within the Monashee Complex. They are overprinted by gentle upright F_4 folds. The latest deformation event was extension (D_5), indicated by shear bands in and around the Monashee Complex, a zone of concentrated extension along the NW flank of Thor–Odin (Johnston et al., 2000), and later brittle normal faults. Shear bands and faults occurred both at large scales in a localised way and at small scales in a penetrative manner. Undeformed (sub)vertical Eocene pegmatites (e.g. Johnston et al., 2000) and lamprophyres (e.g. Lane, 1984) intruded during extension. Metamorphism, related to transposition, reached upper amphibolite facies conditions in the Monashee basement and cover, and lower to upper amphibolite facies at higher structural levels (e.g. Journeay, 1986; Johnston et al., 2000).

Based on regional correlations, Brown et al. (1986) inferred deformation related to the NE movement described above (Cordilleran deformation) and deep burial of the MC to have taken place in the Jurassic. Journeay (1986) recognised two pulses of deformation and associated metamorphism in Frenchman Cap dome. He interpreted metamorphism related to F_2 folding as having ranged from upper amphibolite–lower granulite in the deepest structural levels of Frenchman Cap to middle amphibolite along the flanks of the dome, and as having occurred in the Middle Jurassic. Metamorphism related to F_3 folding was middle greenschist at the deepest structural levels of the complex and upper amphibolite–lower granulite at higher structural levels and was related to mid-Cretaceous regional deformation (Journeay, 1986).

More recently, Carr (1992), Parrish (1995, and references therein), Crowley and Parrish (1999) and Gibson et al. (1999) have attempted to constrain the timing of Cordilleran deformation and metamorphism. Monazite, zircon, titanite and xenotime dates in Frenchman Cap, that range from ~78 Ma at the highest structural levels (Gibson et al., 1999) to 49 Ma at the deepest structural levels of the complex (Crowley and Parrish, 1999) were interpreted as metamorphic ages. Older ages of deformation and metamorphism, as old as ~170 Ma, have been reported away from the complex, in the Selkirk and Cariboo Mountains, and are supported by interpretations based on stratigraphy and the fossil record (Parrish, 1995, and references therein). All data together were interpreted as indicating a younging of structures and thermal peak of metamorphism towards deeper structural levels in the Selkirk Allochthon and Monashee Complex. U–Pb data from western Thor–Odin fit the same pattern (Johnson, 1994; Johnston et al., 2000).

Cordilleran deformation and metamorphism can be related to accretion of terranes to the west. The Intermontane Superterrane (Fig. 6.1) has been interpreted as having accreted onto the North American craton in the Middle Jurassic, and the Insular Superterrane (Fig. 6.1) in the mid-Cretaceous (Monger et al., 1982; Murphy et al., 1995). Movement towards the NE in the Monashee Complex and surrounding areas could well have been related to accretion of the terranes (e.g. Journeay, 1986). Based on the U–Pb data described above, Carr (1992), Parrish (1995, and references therein), Crowley and Parrish (1999) and Gibson et al. (1999) interpreted the deformation resulting from crustal shortening as having occurred diachronously, from ~170 Ma at high structural levels to 49 Ma at the deepest levels in the Monashee Complex.

In Chapter 3, monazite younger than ~75–70 Ma is proposed to have grown during extension in the presence of fluids. It is demonstrated that amphibolites in Thor–Odin, dated by Spark (2001) by $^{40}Ar/^{39}Ar$ methods, with dates younger than ~75–70 Ma, experienced the most ^{18}O- and D-depletion and had plateau or near-plateau $^{40}Ar/^{39}Ar$ spectra. Amphibolites with inverse isochron ages older than ~75–70 Ma, and generally disturbed spectra, were less depleted in ^{18}O and D. It is argued that $^{40}Ar/^{39}Ar$ dates younger than ~75–70 Ma resulted from complete or partial Ar loss in the presence of meteoric fluids, which were penetrating the rocks during extension. Monazite U–Pb ages in pelitic schist, quartzite and orthogneiss are younger than $^{40}Ar/^{39}Ar$ hornblende ages in amphibolite in northwest Thor–Odin. Therefore, in Chapter 3 it is argued that monazite grew, recrystallised and/or lost Pb below T_c of argon in hornblende (530 ± 40˚C), in the presence of meteoric fluids, during extension. If true, the age of metamorphism is older than ~75–70 Ma.

6.3. Methods and definitions

6.3.1. ID-TIMS and SHRIMP

ID-TIMS methods are the same as described in Section 5.3.1. Concordance and discordance are as defined in Section 5.3.3. Monazite of samples s298-54 and s298-70 was analysed on the SHRIMP II at the Geological Survey of Canada (GSC) in Ottawa, in collaboration with M.A. Hamilton, following the same methods as described in Section 5.3.2.

BSE images were taken of the monazites on a Cambridge Instruments S360 scanning electron microscope (SEM) at the GSC in Ottawa. Selected monazite crystals in the grain mount were mapped at high resolution for Y, Th, U, and Pb on a four-spectrometer Cameca SX50 electron microprobe at the University of Massachusetts by M.L. Williams and M.J. Jercinovic (cf. Williams et al., 1999). In the resulting maps, domains that are rich in the element mapped are bright and domains that are poor in the element mapped are dark.

The grain mount was repolished and coated with conductive high purity Au (99.9999%). Spots were selected for analysis based on their SEM images and microprobe element maps. Spot sizes were ~10*13 μm (s298-54 spots 1.2, 1.3, 3.3, 6.1 and s298-70 spots 2.2, 7.1) and 17*21 μm (all other spots). Pb/U and Pb/Th ratios were calibrated using GSC monazite standards 2908, 3345 and 4170 (Stern, 1997). Errors on ages, and error ellipses in concordia diagrams are 1σ, to avoid too large overlaps of error

ellipses, which makes it hard to distinguish data from different spots. It should be noted that all errors for ID-TIMS ages are reported at the 2σ level. Where an average age is used, e.g. average $^{207}Pb/^{235}U$ age for reversely discordant monazite data, the envelope of the errors of the used data is taken as the error of the average age.

6.3.2. Electron microprobe monazite geochronology

Monazite crystals of samples with discordant ID-TIMS monazite data were analysed on a JEOL-733 electron microprobe at the University of New Brunswick, in collaboration with D.C. Hall, for U, Th and Pb, following the methods described in Montel et al. (1996) and Williams et al. (1999). Crystals were selected that showed cores or patches on BSE images. The main disadvantage of electron microprobe dating over ID-TIMS and SHRIMP methods is that elements are measured rather than isotopes, and in the age calculation it is assumed that data are concordant. Microprobe ages of the monazites are not reliable, because the assumption that data are concordant is probably invalid for the samples analysed in this study. However, old age domains may be revealed by microprobe methods if enough Pb is present to detect on the microprobe. These potential old age domains can then be dated by other methods, e.g. SHRIMP. Five spots were analysed in two crystals from a quartzite (s298-30), six in three grains from a pelitic schist (s298-54) and six spots in two grains from another pelitic schist (s298-70).

6.4. Results

Results of the four samples analysed are given from lower to higher structural levels. Discordant monazite fractions, present in all the samples discussed in this section, are discussed in Section 6.5.

6.4.1. Blanket quartzite (s298-30)

Sample s298-30 is a quartzite forming the NW boundary of the 'Megaboudin' (Section 5.2) on the northern slope of Blanket Mountain (Figs. 6.2, 6.3). The quartzite is bounded on both sides by metasedimentary rocks of the Monashee cover sequence. It may be the same quartzite that forms the base of the cover sequence (Reesor and Moore, 1971). The lack of basement rocks below the quartzite (as is characteristic for the basal quartzite; Reesor and Moore, 1971) may be a result of transposition and juxtaposition of the base of the quartzite with cover sequence rocks. Along the south side of the Megaboudin, a quartzite exists on top of basement rocks (south of the Megaboudin). Both quartzites join up to the SW and can be traced southward to the Gunnarsen fold (Reesor and Moore, 1971; Spark, 2001). At the sample location site, the quartzite is only ca. 10 m thick, but elsewhere in the Monashee Complex quartzites have thicknesses up to several hundreds of metres (Read and Klepacki, 1981). The quartzite is medium grained and contains quartz, biotite, sillimanite, K-feldspar (minerals given in order of decreasing content), accessory titanite (especially in sillimanite-rich layers), zircon, monazite, rutile, ilmenite and sphalerite, and late scapolite. Locally tourmaline, and sillimanite faserkiesel are present. A foliation in the quartzite dips moderately to the NW, consistent with the S_2 foliation in and around the Megaboudin (Fig. 6.2) and a sillimanite lineation plunges to

the SW. Sillimanite is oriented parallel to the foliation, between quartz grain boundaries, and may be related to extension.

U–Pb data for the quartzite are shown in Fig. 6.4 and Table 6.1. The analysed monazite crystals are subrounded to euhedral, with indentations. This morphology suggests growth or modifications during solid state metamorphism. Dated single crystals (149–250 μm) are pale yellow and have good (M3, M4 and M5) or excellent (M2) clarity. They have no inclusions or fractures. Fractions M2 and M4 seem to have small overgrowths. On the BSE images, some of the monazites show cores (Fig. 6.4a, grain 1) and some show patchy domains (Fig. 6.4a, grain 2). Patchy domains, and perhaps cores are also visible on Th, Y, and vaguely on U microprobe element maps (Fig. 6.5). Fraction M4 is reversely discordant and M2 and M3 are (normally) discordant. Monazite M5 gives very large errors (Table 6.1) due to poor U data, and is therefore not shown in Fig. 6.4a. The interpreted monazite age is taken to be the $^{207}Pb/^{235}U$ age of reversely discordant fraction M4, which is 54.2 ± 0.3 Ma. However, the actual age may be slightly younger, if an older Pb component is present, or older, if the monazite suffered recent Pb loss (cf. Fig. 5.6).

Based on morphology, four detrital zircon populations were recognised: abraded rounded, abraded indented, faceted, and abraded metamict. One zircon (149–250 μm) of each of the first three populations was dated (Fig. 6.4b) as a preliminary study to constrain the depositional age of the quartzite, and compare it to the 1.99–1.85 Ga quartzite in Frenchman Cap (Crowley, 1997). The age of the quartzite is younger than the youngest detrital zircon. Data were 2.8–19.1% discordant. $^{207}Pb/^{206}Pb$ ages are 2763 ± 2, 2506 ± 4 and 1825 ± 6 Ma, of which the youngest is reasonably consistent with the

age of Crowley (1997). The study seemed a repetition of Crowley (1997) and because samples with higher priority were to be dated, the detrital study was not continued.

6.4.2. Blanket Mountain cover pelitic schist (s298-54)

Sample s298-54 is a pelitic schist from the Monashee cover sequence on the western slope of Blanket Mountain (Fig. 6.2). The pelitic schist is fine to medium grained, and consists of biotite, sillimanite, K-feldspar, quartz, garnet, accessory zircon, monazite and rutile, and retrograde or late muscovite, chlorite, scapolite and sericite. Poikiloblastic 0.5 cm garnets include an old foliation formed by biotite, quartz and feldspar inclusion trails. High relief inclusions (monazite and/or zircon) in garnet are smaller than 0.15 mm. The foliation dips to the W. Sillimanite forms a weak southwesterly-plunging lineation. Down-to-the-west shear bands can be distinguished in thin section.

The four 149–250 μm single monazite grains dated by ID-TIMS methods (Fig. 6.6, Table 6.1) are subhedral and pale yellow. Fractions M1–M3 have good, and M4 excellent clarity. Monazites M1 and M2 have colourless inclusions, and M2 and M3 have fractures. Fraction M3 has a local overgrowth. On the BSE images, some of the monazites show cores and/or patches (see descriptions and Figs. 6.7 and 6.8 for SHRIMP section below). The monazite growth age is taken to be the $^{207}Pb/^{235}U$ age of reversely discordant fraction M2, which is 54.5 ± 1.2 Ma (Table 6.1, Fig. 6.6). Fractions M1, M3 and M4 are discordant. However, the error ellipse of M1 is included in the ellipse of M2, and is thought to support the age of M2. The 54.5 ± 1.2 Ma monazite age is consistent

with monazite ages in pelitic schists and basement orthogneisses in the region (Parkinson, 1999, unpublished data; Johnston et al., 2000; this thesis).

SHRIMP data are generally concordant, with no good evidence for older cores, and indicate an age similar to the 54.5 ± 1.2 Ma ID-TIMS age (Table 6.2, Figs. 6.7, 6.8). The SHRIMP monazite age is taken to be 52.6 ± 6.3 Ma, the weighted average of $^{206}Pb/^{238}U$ ages, corrected for common Pb using the ^{204}Pb method (MSWD = 2.5; Table 6.3). The error is taken to include all error bars at the 2σ level, which is considered to be more accurate than the 1.0 Ma 2σ error that results from the weighted average. All data are included in this calculation, because most ellipses overlap concordia, and exclusion of the three ellipses that do not overlap concordia at the 1σ level, 1.1, 1.3 and 6.1, yields similar ages (not shown). The weighted average of $^{206}Pb/^{238}U$ ages, corrected for common Pb using the ^{207}Pb method, is similar (53.0 ± 1.0 Ma; Table 6.3), but is not preferred. The common-Pb correction based on ^{207}Pb assumes that normal and reverse discordance are solely an artifact of under- or overcorrection of common Pb. The weighted average of $^{206}Pb/^{238}U$ ages is calculated after projection of the uncorrected data onto the concordia from the common-Pb composition (Stern, 1997). Thereby, the $^{207}Pb/^{206}Pb$ ages of the data are assumed, which also implies the assumption that all data are concordant. However, in this sample, SHRIMP data may actually be normally and/or reversely discordant, as the ID-TIMS data, and therefore the common-Pb correction using ^{204}Pb is preferred here.

As explained above, $^{206}Pb/^{238}U$ ages may be inaccurate because of excess ^{206}Pb. Therefore, for reversely discordant ID-TIMS monazite data, the $^{207}Pb/^{235}U$ age is used. For the same reason, the $^{207}Pb/^{235}U$ ages of reversely discordant data, corrected for

common Pb using the ^{204}Pb method, could be used herein. This is not preferred for two reasons: (1) the error on ^{207}Pb is relatively large for SHRIMP data for young samples, due to its low concentration, and therefore ^{207}Pb/^{235}U ratios are not as precise as ^{206}Pb/^{238}U ratios (note how the ^{208}Pb/^{232}Th - ^{206}Pb/^{238}U concordia plot (Fig. 6.7b) yields much smaller error ellipses than the concordia plots involving ^{207}Pb (Fig. 6.7a, c)); (2) reverse discordance may be a result of overcorrection for common Pb, rather than of excess ^{206}Pb. Over- (or under-) correction of common Pb may occur when the ^{204}Pb method is used, as for the ^{207}Pb method, because ^{204}Pb concentrations are small. All reversely discordant data, except for spot 3.1, have high common-Pb concentrations (spots 3.3, 4.1, 5.1; see ^{204}Pb/^{206}Pb ratios in Table 6.2) relative to other spots in the same sample, and therefore errors in the common-Pb corrections have relatively large effects on the ^{207}Pb/^{235}U ages. Reverse discordance may therefore be a result of a ^{207}Pb/^{235}U ratio that is too low due to overcorrection of common Pb, rather than a ^{206}Pb/^{238}U ratio that is too high due to excess ^{206}Pb. The ^{206}Pb/^{238}U ages are less influenced by common-Pb corrections, because the radiogenic ^{206}Pb concentration is much higher than the radiogenic ^{207}Pb concentration. High common Pb, and an undercorrection for common Pb, may explain the discordance of spot 1.2. Spots 6.1 and 1.3 are discordant and their 1σ error ellipses do not overlap concordia. They have very low common-Pb concentrations and therefore their discordance may be a result of the presence of older radiogenic Pb, e.g. older radiogenic Pb that remained after recrystallisation of the monazite. Old age domains were not found in this sample. An argument against the presence of excess ^{206}Pb is that all spots except spot 3.2 have ^{208}Pb/^{232}Th ages older than the ^{206}Pb/^{238}U ages (Table 6.2, Fig. 6.7b). However, the fact that the ^{208}Pb/^{232}Th ages are

systematically older than the $^{206}Pb/^{238}U$ ages may be partly an artifact of the correction for fractionation between Th and Pb, which is probably not as good as the U–Pb fractionation correction (M.A. Hamilton, 2002, personal communication). The ID-TIMS data also do not show evidence for excess ^{206}Pb. Only M2 is slightly reversely discordant, but the error ellipse overlaps concordia. For the reasons presented above, the 52.6 ± 6.3 Ma weighted average of $^{206}Pb/^{238}U$ ages (which includes the 54.5 ± 1.2 Ma ID-TIMS age), corrected for common Pb using the ^{204}Pb method, is considered to represent the age of monazite growth.

No clear separate age domains are present in this sample. Only small age differences exist within the monazite data cluster, sometimes within single grains. Grain 2 has a low Th, low Y domain (spot 2.1, Fig. 8b, Table 6.2) that is slightly younger than the rest of the grain (spot 2.2). This may be a recrystallisation domain that formed after growth of the monazite. Grain 4 has a low Y, low Th (and high U) domain (spot 4.1; Fig. 6.8d, Table 6.2) that is slightly older than spot 4.2 in a high Y, high Th domain. However, at the 2σ level, error ellipses of spots within each of the grains overlap. Grains 1 and 3 are examples of monazites with complicated Y, Th and U domains (Fig. 6.8a, c). It should be noted that the domains are visible in Y, Th and/or U maps, but not in the BSE images. However, in each grain, three spots have similar ages (Table 6.2). Therefore, compositional domains do not always represent age domains. No relationship was found between age and (1) U concentration, (2) Th concentration and/or (3) Th/U ratios, from Table 6.2.

6.4.3. Armstrong Peak cover pelitic schist (s298-70)

Sample s298-70 is a pelitic schist from the cover sequence of the Monashee Complex on the N–S-trending ridge on the NW side of Armstrong Peak (Fig. 6.2). It is a medium- to coarse-grained pelitic schist (Fig. 6.9) with coarse, up to 2 cm, anhedral to subhedral garnets, and with biotite, sillimanite, K-feldspar, quartz, kyanite, corundum, cordierite, and relict staurolite. Blue kyanite is visible in hand specimen, and thin sections reveal the presence of stable kyanite and relict kyanite overgrown by sillimanite. Staurolite is replaced by corundum and sillimanite or zoisite. Garnet has inclusions of rutile and quartz or feldspar, which preserve an old foliation, and of ilmenite and staurolite. A few <0.01 mm high relief inclusions exist in garnet. Accessory zircon, rutile, ilmenite, and monazite, and retrograde sericite and chlorite are present. The schist has a W-dipping foliation and a WSW-plunging sillimanite lineation.

Five single monazite fractions, M1–M5, 149–250 μm in size, were dated (Fig. 6.10, Table 6.1). All are pale yellow, of good clarity and without fractures, inclusions or cores. Fraction M2 has excellent clarity. The grains are rounded, and except for M5 have indentations. Fraction M1 is strongly indented and M2 is disc shaped. On the BSE images there are patches with two different grey tones (see SHRIMP section below).

All fractions are discordant. Fraction M1 (Table 6.1) is not shown in Fig. 6.10 because it has very large errors due to poor Pb and U analyses on the mass spectrometer. Grain M2 is near-concordant at 63.6 ± 2.5 Ma, based on its equal $^{206}Pb/^{238}U$ and $^{207}Pb/^{235}U$ ages (Table 6.1).

SHRIMP data are presented in Table 6.2 and Fig. 6.11a–c. The weighted average of $^{206}Pb/^{238}U$ ages, corrected for common Pb using the ^{204}Pb method, is 60.7 ± 12.4 Ma

(MSWD = 15). The error includes all error bars at the 2σ level (Table 6.3; cf. s298-54). All data are included in this calculation, because most ellipses overlap concordia (Fig. 6.11a), and excluding the data of spots 1.1, 4.3 and 5.1 that do not overlap concordia at the 1σ level does not make a significant difference in ages calculated (not shown). Alternatively, two periods of monazite growth may have existed at 64.8 ± 7.1 Ma (MSWD = 15) and 54.2 ± 6.8 Ma (MSWD = 1.4) (Table 6.3). For the same reasons as outlined for sample s298-54, the $^{206}Pb/^{238}U$ ages corrected for common Pb using the ^{204}Pb method are preferred over both $^{206}Pb/^{238}U$ ages corrected for common Pb using the ^{207}Pb method and $^{207}Pb/^{235}U$ ages corrected for common Pb using the ^{204}Pb method. Not all reversely discordant data have high common-Pb compositions. Spots 3.1, 5.2 and 6.1, for example, have low $^{204}Pb/^{206}Pb$ ratios (Table 6.2), which means that inaccuracies in the common-Pb correction may not necessarily account for reverse discordance. However, all data, except for 3.1 have higher $^{208}Pb/^{232}Th$ ages than $^{206}Pb/^{238}U$ ages, which argues against the presence of excess ^{206}Pb, and also ID-TIMS data do not show evidence for excess ^{206}Pb. Therefore, there is no clear evidence for excess ^{206}Pb, but it may be present. Spots 1.1, 4.3 and 5.1 are normally discordant and their 1σ error ellipses do not overlap concordia. Spots 1.1 and 5.1 have low common-Pb concentrations (Table 6.2) and therefore discordance may be real.

Two monazite ages may be present in this sample, as is exemplified most clearly in grain 5 (Fig. 6.11, Table 6.2). A brighter patch (spot 5.1), which may be a result of recrystallisation or alteration, has younger $^{206}Pb/^{238}U$, $^{207}Pb/^{235}U$ and $^{208}Pb/^{232}Th$ ages than spot 5.2 in the main darker part of the grain. Microprobe element maps are not available. These spots also show that the data ellipses are probably not exactly in the

right location on the concordia diagram (Fig. 6.11a) because a discordia chord through both points would have a lower intercept in the distant future, which is impossible. Possible explanations are that spot 5.2 contains excess ^{206}Pb or that one or both of the points are under- or overcorrected for common Pb. Grain 6 may show a bright core (spot 6.1) in a slightly darker and younger grain (spot 6.2), but the $^{206}Pb/^{238}U$ and $^{207}Pb/^{235}U$ ages overlap each other, and the $^{208}Pb/^{232}Th$ age of spot 6.1 is younger than that of spot 6.2 (Fig. 6.11, Table 6.2). Grain 2 (Figs. 6.11a, 6.12b) has a slightly older high Y, low Th, low U core (spot 2.2) in a relatively lower Y, higher Th and U grain (spot 2.1). However, $^{206}Pb/^{238}U$ and $^{207}Pb/^{235}U$ ages of the two analyses overlap each other, and only the $^{208}Pb/^{232}Th$ age of spot 2.2 is clearly older than spot 2.1 (Table 6.2). The age of the two compositionally different domains is not that different, e.g. the difference in $^{206}Pb/^{238}U$ ages is 3 Ma, which shows that different domains may form over a short time period. Grain 4 shows a high Y, low Th domain, with fluid (?) inclusions, which may represent an alteration or recrystallisation zone (Figs. 6.11a, 6.12a). However, $^{206}Pb/^{238}U$ ages from this zone (spots 4.1 and 4.2) are the same as spot 4.3, in the unaltered part of the crystal (Fig. 6.11, Table 6.2). $^{207}Pb/^{235}U$ ages are not compared due to the high common-Pb concentration, and therefore possible error on ^{207}Pb, of spot 4.3. $^{208}Pb/^{232}Th$ ages increase from spot 4.3 to spot 4.2 via spot 4.1. Grain 1 (Figs. 6.11a, 6.12c) shows a similar domain pattern as grain 4. It also shows an irregularly-shaped high Y, low Th zone, with inclusions. Spot 1.1, within this zone has $^{206}Pb/^{238}U$, $^{207}Pb/^{235}U$ and $^{208}Pb/^{232}Th$ ages very similar to spots 4.1 and 4.2. Spot 1.2 has high common Pb, as spot 4.3. Ages seem similar to spot 1.1 and spots in grain 4, but the errors are so large that the analysis is not plotted and the data cannot be considered reliable (Table 6.2). If alteration

or recrystallisation occurred in grains 4 and 1, it probably occurred very shortly after monazite growth. Alternatively, alteration or recrystallisation did not significantly affect the amount of Pb. A relationship between age, and (1) U concentration, (2) Th concentration and/or (3) Th/U ratios was not recognised (cf. Table 6.2).

Summarising, SHRIMP data do not show clear evidence for older cores or discordance. Age domains within grains may exist, but are not conclusive. The monazites probably grew during one continuous period around 60.7 ± 12.4 Ma, although the possibility exists that spots 5.1, 6.1 and perhaps 6.2 indicate a 54.2 ± 6.8 Ma monazite growth event that is later than the 64.8 ± 7.1 Ma growth event, indicated by all other spots.

6.4.4. Three Valley Gap paragneiss (YK-TVG-97) and leucosome in paragneiss (s298-92)

The Three Valley paragneiss (YK-TVG-97) was sampled along the Trans-Canada Highway at Three Valley Lake in the WSW-trending valley between Frenchman Cap and Thor–Odin, east of the Three Valley–Joss Pass fault (Fig. 6.2). The paragneiss is the upper member of the Three Valley assemblage (unit 14 of Johnston, 1997). It is a migmatitic semi-pelitic gneiss with quartz- and feldspar-bearing leucosomes (sample s298-92; see below). It consists of biotite, sillimanite, K-feldspar, quartz, inequant garnet and retrograde sericite. Accessory minerals are zircon, monazite, ilmenite and rutile. The foliation dips to the W and a W-plunging sillimanite lineation is present.

Zircon crystals, used for dating (Fig. 6.13, Table 6.1), are colourless, stubby (aspect ratios between 1:1 and 1:2) and subrounded with crystal facets. They have

excellent clarity. Some show small colourless inclusions (B, D) and none has fractures. Fractions A and D each consist of one crystal, B of nine, F of three, G of four and H of 25 crystals. The five dated single monazite fractions are yellow and have no inclusions, fractures or cores and overgrowths. All grains are 149–250 μm, except for zircon fraction H, in which grains are 105–149 μm. BSE images show cores and overgrowths in some of the grains, which are also visible in the Y and Th microprobe element maps (Figs. 6.13a, 6.14). Grain 2 shows a patchy core, and an overgrowth in its Y (and Th) map (Figs. 6.13, 6.14b). BSE images of zircon crystals show irregularly-shaped cores, and overgrowths (Fig. 6.13, grains 1, 2). In some crystals vague concentric zonation is visible (grain 1).

Sample s298-92 is leucosome from a paragneiss from Three Valley Gap (YK-TVG-97). It contains quartz, feldspar, biotite, garnet, sillimanite, accessory zircon, monazite, rutile and ilmenite, and retrograde or late sericite, chlorite and epidote. Garnets are euhedral and inequant, with grain sizes up to 4 mm, and with a few inclusions of zircon and/or monazite (0.01–0.02 mm).

Zircon crystals are colourless bipyramidal prisms with aspect ratios between 1:1.5 and 1:8, and excellent clarity. All fractions have small colourless inclusions. Fraction a, c, d and e are single tips, fraction b consists of ten zircon tips. Fractions in this sample are designated in lower case to distinguish them from the fractions of the host paragneiss, sample YK-TVG-97, designated in capitals. None shows cores, overgrowths, or fractures. Monazite crystals are pale yellow, and have excellent clarity, except for m3, which has good clarity. All fractions consist of one monazite. Fraction m1 is discoid, m2 and m3 are rounded and m4 is euhedral. Monazite m1 has a fracture and all but m2

have a few colourless inclusions. All zircon and monazite grains were 149–250 μm. On BSE images (Fig. 6.13), the monazite grains have patchy domains. This is also visible in the Y (and Th) microprobe element maps (Figs. 6.13, 6.14c). Zircon crystals have cores and overgrowths, and sometimes concentric oscillatory zonation is visible in the main domain of the zircon (Fig. 6.13, grain 3).

Data from samples YK-TVG-97 and s298-92 are presented together (Fig. 6.13, Table 6.1), because no great differences appear to exist between the data of the two samples. The zircon fractions form an array of discordant data with $^{206}Pb/^{238}U$ and $^{207}Pb/^{235}U$ ages between ~73 and ~100 Ma and $^{207}Pb/^{206}Pb$ ages between ~79 and ~230 Ma (Fig. 6.13, Table 6.1). Fractions b, d and e have very large errors (Table 6.1) due to poor U mass spectrometer analyses, and are therefore not shown in Fig. 6.13. Fraction F is considered concordant at 79.5 ± 2 Ma. It is actually –1.1% discordant (Table 6.1), but its error ellipse overlaps concordia and reverse discordance is not common for zircons (Section 5.3.3). Therefore, reverse discordance is attributed to a small analytical error. However, concordance seems improbable, because the fraction consists of three zircons which increases the probability of inheritance, overgrowths or Pb loss, relative to single zircon fractions.

The monazites form two clusters: three monazites (M1, M2, m2) have an average $^{207}Pb/^{235}U$ age of 71.7 ± 1.5 Ma, and three others (m1, M5, M6) have an average age of 57.5 ± 5 Ma (Fig. 6.13, Table 6.1). Normal averages are preferred over averages that are weighted according to errors, because ages with different errors are considered to be of equal importance. The errors include errors of all analysed fractions, and also include the weighted averages and their errors (Table 6.3). Fraction m3 is near-concordant at 75.7 ±

0.3 Ma (1.8% discordant, Table 6.1). The lack of excess ^{206}Pb in m3, may indicate that m3 is actually a slightly younger monazite (as M1, M2, m2) with excess ^{206}Pb, and with some older radiogenic Pb (Section 5.3.3). Fractions M4 and m4 are discordant.

U–Pb geochronology on the Three Valley paragneiss has been conducted previously by Wasteneys (unpublished data, 1998) on five zircon fractions. His data revealed a zircon growth event at 89.5 Ma, based on one single and one multiple zircon fraction, which may be interpreted as being related to a metamorphic event. The age is supported by apparent $^{40}Ar/^{39}Ar$ ages of ~89 Ma for three amphibolites from Thor–Odin, which may suggest an initial cooling age (Chapter 3; Spark, 2001). Another fraction of Wasteneys (unpublished data, 1998) of 2 zircon crystals is near-concordant and overlaps concordia at 73 Ma. Gilley (1999) dated zircon from a leucosome in the same paragneiss on the SHRIMP. Zircons and zircon rims yielded concordant ages at ~74 Ma. The spread of discordant and concordant ages of cores is ~1.3 Ga. Parkinson (1992) analysed six zircon fractions from an amphibolite boudin in the paragneiss. The analyses plot along a discordia chord with a ~1.5–1.6 Ga upper intercept, which is interpreted as the protolith age, and a lower intercept near 73.4 ± 1.7 Ma, which is interpreted as an age of metamorphism (Parkinson, 1992). The 71.7 ± 1.5 monazite age obtained here is consistent with Parkinson's (1992) lower intercept age at 73.4 ± 1.7 Ma in an amphibolite boudin in the paragneiss, Wasteneys' (unpublished data, 1998) near-concordant zircon at 73 Ma, and with Gilley's (1999) concordant ages at ~74 Ma.

Linear regressions through combinations of concordant and discordant data were not performed, because multiple events occurred between ~89 and ~57.5 Ma and

discordant data may be influenced by more than one event. Therefore, discordia chords based on any of the concordant lower intercept ages would be meaningless.

6.5. Discussion

6.5.1. Late Cretaceous–Early Eocene monazite ages

The four samples described in Section 6.4 show ~72–52 Ma monazite growth and/or recrystallisation, which is consistent with monazite ages in pelitic schists and basement orthogneisses in the region (Parkinson, 1999, unpublished data; Johnston et al., 2000; this study). These ages could represent metamorphism. However, they may well represent a time of crustal extension. Fluids related to extension may have caused monazite growth and/or recrystallisation, as proposed in Chapter 3 (see Section 3.2). If true, the age of metamorphism must be older.

6.5.2. Indications of Palaeoproterozoic (?) Pb in monazite

All four samples described above have discordant monazite fractions. Discordia chords through concordant and discordant fractions for all samples are Palaeoproterozoic or older, and poorly constrained (Table 6.3). Discordia chords for sample s298-92 involving m4 have upper intercept ages at ~600–500 Ma (Table 6.3). Two possible explanations exist for the cause of discordant monazite fractions: (1) Old zircon inclusions in monazite (e.g. visible in Fig. 6.15) may cause discordance in monazite. However, no zircon inclusions were observed in any of the crystals dated. Furthermore,

taking reasonable radiogenic Pb concentrations for Palaeoproterozoic zircon and Eocene monazite (150 and 100 ppm respectively; cf. Table 5.2, 6.1 and 6.2), even zircons of the sizes shown in Fig. 6.15 do not cause considerable discordance (<1.5%) in those monazites. Zircon grains that are too small to be visible under an optical microscope would therefore not cause discordance. (2) Discordance may be a result of the presence of older cores, or of older Pb (that remained in the monazite after recrystallisation of an older monazite). The presence of older cores was checked by microprobe methods (below) and on the SHRIMP (Section 6.4).

Monazite crystals of samples with discordant ID-TIMS monazite data were analysed on an electron microprobe for U, Th and Pb (see Section 6.3.2), to investigate the presence or absence of old age domains. The Pb concentration in radiogenic minerals increases with age of the mineral, as radiogenic Pb accumulates with time. The Pb concentration in all seventeen monazite spots analysed was below the detection limit of the microprobe (160 ppm; Douglas Hall, 1999, personal communication). This may be explained by one or more of the following: (1) no old age domains are present in the monazite grains analysed on the microprobe, (2) the old age domains lost Pb, (3) old Pb was present in the entire monazite, but was partly lost, e.g. during recrystallisation at the time indicated by the concordant monazite ages, (4) old age domains are present, but are smaller than the microprobe beam spot, and therefore only part of the measured area is an old age domain, and still may not yield enough Pb and (5) the old age domains are not old enough to yield enough Pb. This last possibility is considered unlikely, because discordia chords through the monazite fractions in all samples have upper intercept ages in the Proterozoic (or older; Table 6.3). Using SHRIMP methods, no old age domains were

found for samples s298-54 and s298-70. This may be explained by the same reasons as the first four explanations proposed above.

Palaeoproterozoic upper intercept ages may indicate metamorphism and deformation, or ages of detrital grains. If they indicate metamorphism and deformation, then the protolith ages must be older than these upper intercept ages. If they indicate ages of detrital grains, the age of deformation and metamorphism must be younger. If the latter is true, and if the interpretation that monazite ages younger than ~75–70 Ma represent extension is correct, then neither the upper intercepts nor the lower intercepts represent the age of deformation and metamorphism. Possibly, the Palaeoproterozoic upper intercept ages are meaningless, due to their large errors and the proximity of all data to the lower intercept ages.

6.5.3. Constraining ages of metamorphism in the Monashee cover sequence, by constraining the age of the cover sequence

The age of any metamorphism and deformation, e.g. transposition, that affected the entire Monashee Complex, is constrained by the youngest Monashee cover rocks that underwent all the deformation events. Rocks of the Monashee cover sequence have been tentatively correlated with the ~1.7–1.2 Ga Purcell Supergroup and the ~780–570 Ma Windermere Supergroup (Scammell and Brown, 1990; Aitken and McMechan, 1991; Parkinson, 1992) and partly with the Lower Cambrian Hamill Group and Badshot Formation (Reesor and Moore, 1971). Whether these correlations are correct or not (see discussion below), folding, transposition and metamorphism are unlikely to have

occurred during these periods, as sedimentation and rifting were ongoing then (Aitken and McMechan, 1991).

The age of the oldest cover rock, or the base of the Monashee cover sequence, is interpreted as being between 1.99 (or 1.86) and 1.85 Ga. It is younger than the youngest basement rocks on which it was deposited, which is presumably the 1862 ± 1 Ma Kirbyville orthogneiss (Crowley, 1997), and younger than the youngest 1.99 Ga detrital zircons of basal units of the Monashee cover sequence (Ross and Parrish, 1991; Crowley, 1997). One basal unit is crosscut by a pegmatite, the age of which has been interpreted as 1852 ± 4 Ma (Crowley, 1997), the upper intercept of five zircon analyses. Alternatively, the crystallisation age of the pegmatite could be the lower intercept age (149 ± 20 Ma), or the age of Early Eocene xenotime and monazite in the same sample.

The potentially youngest depositional age in the Monashee Complex is constrained by a ~388 Ma or younger metamorphic felsic volcaniclastic rock (Scammell and Parrish, 1993), an amphibolite with 540 Ma zircons (Parrish, 1995) and an Early Cambrian stratiform Pb-Zn horizon (Höy and Godwin, 1988). However, none of these rocks is conclusively depositional; they could be intrusive or hydrothermal, and younger than their host rocks. Furthermore, the age of the felsic volcaniclastic rock is based on one concordant 388.1 ± 0.7 Ma zircon, and all other zircons are Proterozoic, or discordant with Proterozoic 207/206 ages. Therefore, ~388 Ma could be a metamorphic age and the rock could be Proterozoic. Scammell and Brown (1990) infer deposition of part of the Monashee cover sequence during Windermere rifting, based on the age and alkaline chemistry of the 740 ± 36 Ma Mount Copeland intrusion (Okulitch et al., 1981; Parrish and Scammell, 1988) and on the presence of a stratiform pyroclastic carbonatite

that is presumed to have the same age. However, this is not a unique interpretation (Scammell and Brown, 1990).

Other age constraints are detrital zircons in sedimentary rocks dated by Ross and Parrish (1991), Crowley (1997) and this study, which have $^{207}Pb/^{206}Pb$ ages older than 1.75 Ga, except for one discordant zircon which has a $^{207}Pb/^{206}Pb$ age of 1.21 Ga (Crowley, 1997). Gilley (1999) recorded discordant and concordant data of cores of zircons of the leucosome in the Three Valley Gap paragneiss (cf. samples s298-92 and YK-TVG-97) around 1.3 Ga. These cores may be detrital in origin, in which case deposition occurred after ~1.3 Ga. However, if the ~1.6–1.5 Ga upper intercept of the amphibolite boudin in the paragneiss, dated by Parkinson (1992), is a crystallisation age, then the paragneiss must be older than that. The ~1.3 Ga age of the paragneiss may then represent a younger event. Taking all data together, no convincing evidence exists that metasedimentary rocks of the Monashee cover sequence are younger than ~1.75 Ga, and therefore they may all predate the deposition of the Purcell Supergroup.

A problem in the literature is that deposition of the basal quartzite occurred between ~1.99 and ~1.85 Ga (Crowley, 1997), concurrent with migmatisation at all levels of the basement (~1.85 Ga, Crowley, 1999; ~1.8 Ga, cf. Vanderhaeghe et al., 1999; ~1.8 Ga, Chapter 5) including a location only several metres away from the cover sequence (sample s298-65; Chapter 5), and concurrent with intrusion of the Bourne granite and the Pettipiece pegmatite suite as little as ~250 m away from the cover sequence (Crowley, 1999; Crowley et al., 2001). Therefore, the entire cover is either older or younger than ~1.85–1.8 Ga. Metasedimentary rocks of the cover cannot be partly older and partly younger, unless an unrecognised unconformity exists within the cover sequence. If the

cover was deposited before ~1.85–1.8 Ga, then the younger $^{207}Pb/^{206}Pb$ ages of detrital zircons (which are all discordant; cf. Ross and Parrish, 1991; Crowley, 1997) are a result of modification by younger events. If the cover metasediments were pre-~1.85–1.8 Ga, then the cover may have been deformed in the Palaeoproterozoic, together with the basement, which would explain the Proterozoic upper intercept ages of monazites in cover pelitic schists (this study). However, Cordilleran deformation and metamorphism was after ~740 Ma (see below) and Palaeoproterozoic deformation was presumably a separate event. If the entire cover is younger than ~1.85–1.8 Ga (post-basement metamorphism), the 1852 Ma lower age constraint of the basal quartzite (crosscutting pegmatite; Crowley 1997) is wrong (see above).

The youngest intrusive rock that experienced the transposition that affected the entire Monashee Complex is the Mount Copeland syenite gneiss (Fyles, 1970; Currie, 1976), dated at 740 ± 36 Ma (U–Pb zircon; Okulitch, et al., 1981; Parrish and Scammell, 1988). Transposition and metamorphism (Cordilleran deformation and metamorphism) was therefore younger than 740 ± 36 Ma. The 724 ± 5 Ma Mount Grace syenite gneiss is thought to have experienced the same deformation events (U–Pb zircon; Crowley, 1997).

If the cover sequence is younger than ~1.85–1.8 Ga, and all deformation and metamorphism is younger than ~740 Ma, then Palaeoproterozoic upper intercept ages of possible monazite discordia chords (samples s298-30, s298-54, s298-70, s298-92 and YK-TVG-97, Table 6.3) indicate the presence of detrital cores.

Summarising, if non-magmatic monazite ages younger than ~75–70 Ma in Thor–Odin represent growth (or recrystallisation/Pb loss) during extension and retrograde metamorphism in the presence of fluids (Section 6.5.1; cf. Chapter 3), then Cordilleran

transposition deformation and metamorphism must have occurred between ~740 and ~75–70 Ma.

6.5.4. Indications of Mesozoic deformation and metamorphism

In the Monashee Complex, no evidence exists for deformation and metamorphism between ~740 and ~75–70 Ma, but some indications are presented in this section. Evidence for the age of deformation and metamorphism may be absent if (partial) dissolution, rather than growth, occurred of minerals used for U–Pb dating (see Chapter 5), and/or if Pb loss in older minerals was not complete. Deformation and metamorphism could possibly have occurred in the Middle Jurassic and/or mid-Cretaceous, as has been proposed for the Cariboo Mountains to the north of, and the Selkirk Mountains to the east of, (and both structurally above,) the Monashee Complex (Pigage, 1977; Archibald et al., 1983, 1984; Gerasimoff, 1988; Ferguson and Simony, 1991; Crowley and Brown, 1994; Colpron et al., 1996; Reid, 1999), and as has been inferred by earlier workers for the Monashee Complex (Brown et al., 1986; Journeay, 1986; Section 6.2).

Several indications of Mesozoic (and/or Palaeozoic) metamorphism exist in the Monashee Complex. Gibson (1997) reports a slightly discordant 78 Ma monazite in northern Frenchman Cap. Foster et al. (2002) report LA-MC-ICPMS $^{208}Pb/^{232}Th$ ages of one sample (DG136) in northern Frenchman Cap older than 100 Ma. However, the $^{207}Pb/^{206}Pb$ ages of these spots are older than the $^{208}Pb/^{232}Th$ ages and therefore the data are discordant. One grain in another sample (DG127mon10#4; Fig. 8f of Foster et al., 2002) yielded time-resolved data, which show that the oldest age component in the sample could be as old as 100 Ma. The Three Valley Gap paragneiss may indicate zircon

growth or Pb loss at ~89 Ma (Wasteneys, 1998, unpublished data) and 79.5 ± 2.0 Ma (sample YK-TVG-97 of this study; Section 6.4). No other concordant Middle Jurassic or mid-Cretaceous–Early Tertiary ages, that are not interpreted as being related to extension related fluids (i.e. older than ~75–70 Ma, cf. Chapter 3), are present in the Monashee Complex. However, Mesozoic or Palaeozoic ages are suggested by lower intercept ages of zircon and monazite discordia curves of Palaeoproterozoic intrusives (~300–100 Ma; Wanless and Reesor, 1974; Armstrong et al., 1991; Parkinson, 1991; Crowley, 1997, 1999) and by an upper intercept of a monazite discordia curve of a pelitic schist (118 +16/–8 Ma, Crowley and Parrish, 1999). Furthermore, ~89 Ma $^{40}Ar/^{39}Ar$ inverse isochron ages are recorded in Thor–Odin (Spark, 2001; Chapter 3). In this study, $^{207}Pb/^{206}Pb$ ages are up to ~300 Ma (Table 6.1). For these reasons, the possibility exists that deformation and metamorphism in the Monashee Complex took place in the Mesozoic, as in the Cariboo and Selkirk Mountains (or possibly in the Palaeozoic).

6.6. Conclusions

Monazite growth and/or recrystallisation in samples discussed in this chapter occurred between ~72 and ~50 Ma. Ages per sample are: s298-30: 54.2 ± 0.3 Ma; s298-54: 52.6 ± 6.3 Ma; s298-70: 60.7 ± 12.5 Ma (or continuous growth between ~70 and ~50 Ma); and s298-92+YK-TVG-97: 71.7 ± 1.5 Ma and 57.5 ± 5.0 Ma. All samples show evidence of older Pb. Therefore, monazite growth after ~72 Ma is secondary and may be related to extension. It should be noted that samples s298-92 and YK-TVG-97 record two ages of monazite growth, that may both be secondary. Older Pb may be from

Proterozoic detrital cores that may have lost most of their Pb, by e.g. recrystallisation, during one or more younger events. Penetrative deformation (transposition and folding) and metamorphism of the entire Monashee Complex may have taken place between ~740 Ma and ~75–70 Ma, although indications are sparse and inconclusive. The possibility exists that metamorphism took place between ~72 and ~50 Ma, an interpretation that is not preferred herein (cf. Chapter 3).

References

Aitken, J.D., McMechan, M.E., 1991. Middle Proterozoic assemblages. In: Gabrielse, H., Yorath, C.J. (Editors), Chapter 2 of Geology of the Cordilleran Orogen in Canada. Geological Survey of Canada, Geology of Canada no. 4, pp.97–124.

Archibald, D.A., Glover, J.K., Price, R.A., Farrar, E., Carmichael, D.M., 1983. Geochronology and tectonic implications of magmatism and metamorphism, southern Kootenay Arc and neighbouring regions, southeastern British Columbia. Part I: Jurassic to mid-Cretaceous. Canadian Journal of Earth Sciences 20: 1891–1913.

Archibald, D.A., Krogh, T.E., Armstrong, R.L., Farrar, E., 1984. Geochronology and tectonic implications of magmatism and metamorphism, southern Kootenay Arc and neighbouring regions, southeastern British Columbia. Part II: Mid-Cretaceous to Eocene. Canadian Journal of Earth Sciences 21: 567–583.

Armstrong, R.L., Parrish, R.R., van der Heyden, P., Scott, K., Runkle, D., 1991. Early Proterozoic basement exposures in the southern Canadian Cordillera: core gneiss of Frenchman Cap, Unit I of the Grand Forks Gneiss, and the Vaseaux Formation. Canadian Journal of Earth Sciences 28, 1169–1201.

Brown, R.L., Journeay, J.M., Lane, L.S., Murphy, D.C., Rees, C.J., 1986. Obduction, backfolding, and piggyback thrusting in the metamorphic hinterland of the southeastern Canadian Cordillera. Journal of Structural Geology 8, 255–268.

Carr, S.D., 1992. Tectonic setting and U–Pb geochronology of the early Tertiary Ladybird leucogranite suite, Thor–Odin – Pinnacles area, southern Omineca Belt, British Columbia. Tectonics 11, 258–278.

Colpron, M., Price, R.A., Archibald, D.A., Carmichael, D.M., 1996. Middle Jurassic exhumation along the western flank of the Selkirk fan structure: Thermobarometric and thermochronometric constraints from the Illecillewaet synclinorium, southeastern British Columbia. Geological Society of America Bulletin 108, 1372–1392.

Crowley, J.L., 1997. U–Pb geochronologic constraints on the cover sequence of the Monashee complex, Canadian Cordillera: Paleoproterozoic deposition on basement. Canadian Journal of Earth Sciences 34, 1008–1022.

Crowley, J.L., 1999. U–Pb geochronologic constraints on Paleoproterozoic tectonism in the Monashee complex, Canadian Cordillera: elucidating an overprinted geologic history. Geological Society of America Bulletin 111, 560–577.

Crowley, J.L., Brown, R.L., 1994. Tectonic links between the Clachnacudainn terrane and Selkirk allochthon, southern Omineca Belt, Canadian Cordillera. Tectonics 13, 1035–1051.

Crowley, J.L., Parrish, R.R., 1999. U–Pb isotopic constraints on diachronous metamorphism in the northern Monashee complex, southern Canadian Cordillera. Journal of Metamorphic Geology 17, 483–502.

Crowley, J.L., Brown, R.L., Parrish, R.R., 2001. Diachronous deformation and a strain gradient beneath the Selkirk allochthon, northern Monashee complex, southeastern Canadian Cordillera. Journal of Structural Geology 23, 1103–1121.

Currie, K.L., 1976. Notes and petrology of nepheline gneisses near Mount Copeland, British Columbia. Geological Survey of Canada, Bulletin 265.

Ferguson, C.A., Simony, P.S., 1991. Preliminary report on structural evolution and stratigraphic correlations, northern Cariboo Mountains, British Columbia. Geological Survey of Canada, Paper 91-1A, 103–110.

Foster, G., Gibson, H.D., Parrish, R.R., Horstwood, M., Fraser, J., Tindle, A., 2002. Textural, chemical and isotopic insights into the nature and behaviour of metamorphic monazite. Chemical Geology 191, 183–207.

Fyles, J.T., 1970. Jordan River area. British Columbia Department of Mines and Petroleum Resources, Bulletin 57.

Gerasimoff, M.D., 1988. The Hobson Lake pluton, Cariboo Mountains, British Columbia, and its significance to Mesozoic and early Cenozoic Cordilleran tectonics. MSc Thesis, Queen's University, Kingston, Ontario, Canada.

Gibson, H.D., 1997. Thermotectonic evolution of the northern Monashee complex, southern Omineca Belt, southeastern British Columbia. MSc Thesis, Carleton University, Ottawa, Ontario, Canada.

Gibson, H.D., Brown, R.L., Parrish, R.R., 1999. Deformation-induced inverted metamorphic field gradients: an example from the southeastern Canadian Cordillera. Journal of Structural Geology 21, 751–767.

Gilley, L.D., 1999. The nature and timing of partial melting in the Shuswap Metamorphic Core Complex: a SHRIMP U–Pb geochronologic investigation. BSc Thesis, Stanford University, Stanford, California, USA.

Höy, T., Godwin, C.I., 1988. Significance of a Cambrian date from galena lead-isotope data for the stratiform Cottonbelt deposit in the Monashee Complex, southeastern British Columbia. Canadian Journal of Earth Sciences 25, 1534–1541.

Johnson, B.J., 1994. Structure and tectonic setting of the Okanagan Valley fault system in the Shuswap Lake area, southern British Columbia. PhD Thesis, Carleton University, Ottawa, Ontario, Canada.

Johnston, D.H. 1997. Structural and thermal evolution of northwest Thor–Odin Dome, Monashee Complex, southeast British Columbia. PhD Thesis, University of New Brunswick, Fredericton, New Brunswick, Canada.

Johnston, D.H., Williams, P.F., Brown, R.L., Crowley, J.L., Carr, S.D., 2000. Northeastward extrusion and extensional exhumation of crystalline rocks of the Monashee Complex, southeastern Canadian Cordillera. Journal of Structural Geology 22, 603–625.

Journeay, J.M., 1986. Stratigraphy, internal strain, and thermo-tectonic evolution of northern Frenchman Cap dome, an exhumed basement duplex structure, Omineca hinterland, southeastern Canadian Cordillera. PhD Thesis, Queen's University, Kingston, Ontario, Canada.

Lane, L.S., 1984. Deformation history of the Monashee Decollement and Columbia River Fault zone. PhD Thesis, Carleton University, Ottawa, Ontario, Canada.

Monger, J.W.H., Price, R.A., Tempelman-Kluit, D.J., 1982. Tectonic accretion and the origin of the two major metamorphic and plutonic welts in the Canadian Cordillera. Geology 10, 70–75.

Montel, J.-M., Foret, S., Veschambre, M., Nicollet, C., Provost, A., 1996. Electron microprobe dating of monazite. Chemical Geology 131, 37–53.

Murphy, D.C., van der Heyden, P., Parrish, R.R., Klepacki, D.W., McMillan, W., Struik, L.C., Gabites, J., 1995. New geochronological constraints on Jurassic deformation of the western edge of North America, southeastern Canadian Cordillera. In: Miller, D.M., Busby, C. (Editors), Jurassic magmatism and tectonics of the North American

Cordillera. Boulder, Colorado, Geological Society of America Special Paper 299, 159–171.

Okulitch, A.V., Loveridge, W.D., Sullivan, R.W., 1981. Preliminary radiometric analyses of zircons from the Mount Copeland syenite gneiss, Shuswap Metamorphic Complex, British Columbia. Geological Survey of Canada, Paper 81-1A, 33–36.

Parkinson, D.L., 1991. Age and isotopic character of Early Proterozoic basement gneisses in the southern Monashee Complex, southeastern British Columbia. Canadian Journal of Earth Sciences 28, 1159–1168.

Parkinson, D.L., 1992. Age and tectonic evolution of the southern Monashee complex, southeastern British Columbia, a window into the deep crust. PhD Thesis, University of California in Santa Barbara, California, USA.

Parrish, R.R., 1990. U–Pb dating of monazite and its application to geological problems. Canadian Journal of Earth Sciences 27, 1431–1450.

Parrish, R.R., 1995. Thermal evolution of the southeastern Canadian Cordillera. Canadian Journal of Earth Sciences 32, 1618–1642.

Parrish, R.R., Scammell, R.J., 1988. The age of the Mount Copeland syenite gneiss and its metamorphic zircons, Monashee Complex, southeastern British Columbia. Geological Survey of Canada, Paper 88-2, 21–28.

Pigage, L.C., 1977. Rb–Sr dates for granodiorite intrusions on the northeast margin of the Shuswap Metamorphic Complex, Cariboo Mountains, British Columbia. Canadian Journal of Earth Sciences 14, 1690–1695.

Read, P.B., Klepacki, D.W., 1981. Stratigraphy and structure: northern half of Thor–Odin nappe, Vernon east-half map area, southern British Columbia. Geological Survey of Canada, Paper 81-1A, 169–173.

Reesor, J.E., Moore, J.M., 1971. Petrology and structure of the Thor–Odin gneiss dome, Shuswap metamorphic complex. Geological Survey of Canada, Bulletin 195.

Ross, G.M., Parrish, R.R., 1991. Detrital zircon geochronology of metasedimentary rocks in the southern Omineca Belt, Canadian Cordillera. Canadian Journal of Earth Sciences 28, 1254–1270.

Scammell, R.J., Brown, R.L., 1990. Cover gneisses of the Monashee Terrane: a record of synsedimentary rifting in the North American Cordillera. Canadian Journal of Earth Sciences 27, 712–726.

Scammell, R.J., Parrish, R.R., 1993. U–Pb zircon chronometry from a metamorphosed felsic volcaniclastic rocks in cover gneisses, Monashee terrane, southeastern British

Columbia. Geological Association of Canada - Mineralogical Association of Canada, Program with Abstracts 18, A93.

Spark, R.N., 2001. Crustal thickening and tectonic denudation within the Thor–Odin culmination, Monashee Complex, southern Canadian Cordillera. PhD Thesis, University of New Brunswick, Fredericton, New Brunswick, Canada.

Stern, R.A., 1997. The GSC Sensitive High Resolution Ion Microprobe (SHRIMP): analytical techniques of zircon U–Th–Pb age determination and performance evaluation. Geological Survey of Canada, Current Research 1997-F, Radiogenic Age and Isotopic Studies 10, 1–31.

Wanless, R.K., Reesor, J.E., 1974. Precambrian zircon age of orthogneiss in the Shuswap Metamorphic Complex, British Columbia. Canadian Journal of Earth Sciences 12, 326–332.

Wheeler, J.O., McFeely, P. (Compilers), 1991. Tectonic assemblage map of the Canadian Cordillera and adjacent parts of the United States of America: Geological Survey of Canada, Map 1712A, scale 1:2 000 000, 1 sheet.

Williams, M.L., Jercinovic, M.J., Terry, M.P., 1999. Age mapping and dating of monazite on the electron microprobe: Deconvoluting multistage tectonic histories. Geology 27, 1023–1026.

Williams, P.F., 1999. Fold Nappes and the problem of model driven interpretation. Specialist Group in Tectonics and Structural Geology Field Conference, Halls Gap, Victoria, Australia (February 14–19, 1999). Geological Society of Australia Abstracts Series #53, 267–268.

Table 6.1. ID-TIMS data for samples s298-30, s298-54, s298-70, s298-92 and YK-TVG-97.

Fraction size a	Wt. (µg) b	U (ppm) b	Pb* (ppm) b	$^{206}Pb/^{204}Pb$	Pb (pg) c	^{208}Pb (%)	Th/U d	$^{206}Pb/^{238}U$	$^{207}Pb/^{235}U$	$^{207}Pb/^{206}Pb$	$^{206}Pb/^{238}U$ Age (Ma)	$^{207}Pb/^{235}U$ Age (Ma)	Correlation coefficient	$^{207}Pb/^{206}Pb$ Age (Ma)	Discordance (%) e
S298-30 Blanket Mountain quartzite, UTM 412150E, 5625450N															
A (s,149–250)	20	105	73	8408	8	23.0	1.29	0.520220 ± .26%	13.7990 ± .27%	0.19238 ± .03%	2700.1 ± 11.6	2736.0 ± 5.1	0.9939	2762.6 ± 1.0	2.8
B (s,149–250)	30	142	50	915	91	17.4	0.80	0.302539 ± .47%	4.65449 ± .50%	0.11158 ± .15%	1703.9 ± 14.1	1759.1 ± 8.3	0.9559	1825.3 ± 5.3	7.6
C (s,149–250)	24	63	27	3692	10	11.6	0.55	0.384539 ± .24%	8.74166 ± .23%	0.16487 ± .09%	2097.4 ± 8.5	2311.4 ± 4.2	0.9185	2506.3 ± 3.2	19.1
M2 (s,149–250)	20	3806	97	1827	23	69.7	7.51	0.008556 ± .28%	0.05566 ± .41%	0.04718 ± .25%	54.9 ± 0.3	55.0 ± 0.4	0.8035	58.2 ± 12.0	5.7
M3 (s,149–250)	26	4643	142	5696	12	73.5	9.19	0.008918 ± .42%	0.06329 ± .35%	0.05147 ± .27%	57.2 ± 0.5	62.3 ± 0.4	0.7677	262.2 ± 12.5	78.5
M4 (s,149–250)	17	5952	138	5049	11	66.9	6.61	0.008476 ± .25%	0.05482 ± .25%	0.04691 ± .07%	54.4 ± 0.3	54.2 ± 0.3	0.9567	44.4 ± 3.5	–22.55
M5 (s,149–250)	*27*	*4287*	*80*	*5418*	*10*	*65.1*	*6.10*	*0.007214 ± 19.8%*	*0.04667 ± 19.8%*	*0.04692 ± .08%*	*46.3 ± 18.2*	*46.3 ± 17.9*	*1.0000*	*45.3 ± 4.0*	*–2.18*
S298-54 Blanket Mountain pelitic schist, UTM 410875E, 5623950N															
M1 (s,149–250)	45	2230	58	1190	46	70.3	7.75	0.008509 ± .25%	0.05530 ± .28%	0.04713 ± .20%	54.6 ± 0.3	54.7 ± 0.3	0.7323	56.0 ± 9.5	2.5
M2 (s,149–250)	31	2359	75	784	52	75.9	10.30	0.008502 ± 1.1%	0.05513 ± 1.1%	0.04703 ± .37%	54.6 ± 1.2	54.5 ± 1.2	0.9446	50.7 ± 17.5	–7.69
M3 (s,149–250)	22	2927	62	2069	17	63.1	5.65	0.008660 ± .57%	0.06029 ± .55%	0.05049 ± .44%	55.6 ± 0.6	59.4 ± 0.6	0.6924	217.7 ± 20.4	74.8
M4 (s,149–250)	19	2691	61	1828	15	65.4	6.25	0.008570 ± .17%	0.05913 ± .22%	0.05004 ± .15%	55.0 ± 0.2	58.3 ± 0.2	0.7394	196.9 ± 6.9	72.4
S298-70 Pelitic schist, ridge off NW side of Blanket Mountain, UTM 408700E, 5623175N															
M1 (s,149–250)	*14*	*6120*	*102*	*1341*	*33*	*55.6*	*4.16*	*0.008159 ± 10.2%*	*0.05852 ± 7.8%*	*0.05202 ± 10.0%*	*52.4 ± 10.6*	*57.7 ± 8.8*	*0.4103*	*286.2 +400.8/–533.2*	*82.0*
M2 (s,149–250)	14	2967	47	266	106	43.5	2.52	0.009907 ± .69%	0.06468 ± 2.0%	0.04735 ± 1.8%	63.6 ± 0.9	63.6 ± 2.5	0.5110	66.8 ± 84.1	4.9
M3 (s,149–250)	34	4044	99	1477	58	63.9	5.84	0.009725 ± .77%	0.06768 ± .84%	0.05047 ± .27%	62.4 ± 1.0	66.5 ± 1.1	0.9476	216.8 ± 12.6	71.6
M4 (s,149–250)	27	2132	47	2426	15	58.2	4.59	0.010174 ± .47%	0.06950 ± .51%	0.04954 ± .22%	65.3 ± 0.6	68.2 ± 0.7	0.9049	173.4 ± 10.1	62.7
M5 (s,149–250)	7	12905	325	2760	21	63.9	5.83	0.010038 ± .24%	0.06859 ± .26%	0.04955 ± .17%	64.4 ± 0.3	67.4 ± 0.3	0.7685	174.1 ± 8.0	63.3
S298-92 (small letters) + YK-TVG-97 (capitalised letters) Three Valley paragneiss, UTM 397675E, 5642775N															
A (s,149–250)	6	1773	21	542	16	0.9	0.029	0.013027 ± .12%	0.08751 ± .63%	0.04872 ± .57%	83.4 ± 0.2	85.2 ± 1.0	0.5626	134.4 ± 26.8	38.1
B (m,149–250)	18	1826	22	1185	23	1.1	0.037	0.013107 ± .11%	0.09161 ± .29%	0.05070 ± .25%	83.9 ± 0.2	89.0 ± 0.5	0.5517	227.0 ± 11.5	63.4
D (s,149–250)	15	1518	16	477	36	1.3	0.043	0.011612 ± .49%	0.07738 ± 1.2%	0.04833 ± .92%	74.4 ± 0.7	75.7 ± 1.7	0.6848	115.4 ± 43.5	35.7
F (m,149–250)	8	1904	21	416	30	0.8	0.027	0.012414 ± .26%	0.08145 ± .77%	0.04759 ± .69%	79.5 ± 0.4	79.5 ± 1.2	0.4408	78.7 ± 33.0	–1
G (m,149–250)	12	2241	26	719	29	1.4	0.047	0.012456 ± .86%	0.08413 ± 1.6%	0.04899 ± 1.3%	79.8 ± 1.4	82.0 ± 2.5	0.6171	147.1 ± 58.9	46.0
H (m, 105–149)	43	2126	24	1872	39	1	0.035	0.012580 ± .61%	0.08726 ± .64%	0.05031 ± .51%	80.6 ± 1.0	84.9 ± 1.0	0.6637	209.3 ± 23.7	61.9
a (s,149–250)	18	531	8	909	10	4.3	0.15	0.015362 ± .29%	0.10208 ± .51%	0.04820 ± .39%	98.3 ± 0.6	98.7 ± 1.0	0.6386	108.9 ± 18.5	9.8
b (m,149–250)	*55*	*1071*	*13*	*4800*	*10*	*3.4*	*0.11*	*0.012604 ± 9.3%*	*0.08498 ± 9.3%*	*0.04890 ± .76%*	*80.7 ± 15.0*	*82.8 ± 14.8*	*0.9967*	*143.1 ± 35.6*	*43.9*
c (s,149–250)	34	138	2	257	19	5	0.17	0.015138 ± .35%	0.10134 ± 1.2%	0.04855 ± 1.1%	96.9 ± 0.7	98.0 ± 2.3	0.5554	126.3 ± 50.1	23.5
d (s,149–250)	*21*	*329*	*4*	*134*	*44*	*9.5*	*0.35*	*0.011610 ± 14.5%*	*0.07868 ± 14.8%*	*0.04915 ± 2.5%*	*74.4 ± 21.5*	*76.9 ± 21.9*	*0.9851*	*155.0 ± 119.6*	*52.3*
e (s,149–250)	*18*	*235*	*3*	*787*	*5*	*7.6*	*0.27*	*0.014824 ± 6.3%*	*0.09773 ± 6.3%*	*0.04782 ± .91%*	*94.9 ± 11.8*	*94.7 ± 11.3*	*0.9895*	*90.2 ± 43.1*	*–5.2*
M1 (s,149–250)	15	3223	180	1099	32	81.5	14.36	0.011374 ± .50%	0.07277 ± .49%	0.04640 ± .38%	72.9 ± 0.7	71.3 ± 0.7	0.7064	18.6 ± 18.1	–293.6
M2 (s,149–250)	15	2526	205	1423	19	87	21.84	0.011620 ± .30%	0.07382 ± .62%	0.04608 ± .57%	74.5 ± 0.4	72.3 ± 0.9	0.4157	1.6 ± 27.3	–999
M4 (s,149–250)	8	1849	183	795	14	89.1	27.27	0.011769 ± 3.6%	0.08384 ± 5.1%	0.05167 ± 2.1%	75.4 ± 5.4	81.7 ± 8.0	0.9400	270.7 ± 97.3	72.6
M5 (s,149–250)	14	2140	188	783	23	90.2	30.17	0.009442 ± .99%	0.06051 ± 1.1%	0.04648 ± .45%	60.6 ± 1.2	59.7 ± 1.3	0.9115	22.5 ± 21.4	–169.5
M6 (s,149–250)	6	4785	239	549	30	84.3	17.49	0.008667 ± 3.0%	0.05586 ± 3.9%	0.04674 ± 1.4%	55.6 ± 3.4	55.2 ± 4.2	0.9530	36.0 ± 65.1	–54.9
m1 (s,149–250)	28	4019	115	3331	20	70.2	9.424	0.009396 ± 1.6%	0.05819 ± 1.6%	0.04492 ± .56%	60.3 ± 1.9	57.4 ± 1.7	0.9358	–59.9 ± 27.3	–999
m2 (s,149–250)	26	3032	147	3983	14	78.9	12.21	0.011312 ± .21%	0.07308 ± .48%	0.04686 ± .42%	72.5 ± 0.3	71.6 ± 0.7	0.4696	41.9 ± 20.3	–73.5
m3 (s,149–250)	45	3746	172	2497	51	76.6	10.75	0.011801 ± .16%	0.07737 ± .17%	0.04755 ± .10%	75.6 ± 0.2	75.7 ± 0.3	0.8268	77.0 ± 4.6	1.8
m4 (s,149–250)	22	5093	284	6347	17	75.8	10.35	0.014831 ± .28%	0.10284 ± .24%	0.05029 ± .18%	94.9 ± 0.5	99.4 ± 0.5	0.7849	208.4 ± 8.2	54.9

Errors are 1 std. error of mean in % except for age errors which are 2 std. errors in Ma

* = Radiogenic Pb

a = Single grain (s), multiple grains (m), single tip (st) or multiple tips (mt); sizes in micrometres

b = Include sample weight error of ± 0.001 mg in concentration uncertainty

c = Total common Pb in analysis

d = Th/U from 208*/206* and 207*/206* age

e = Discordance on chord to origin

Fractions dispayed in italics have large errors and are not shown in concordia plots

Table 6.2. SHRIMP data for samples s298-54 and s298-70.

Spot	U(ppm)	Th(ppm)	Th/U	± Th/U	Pb*(ppm)	204/206	± 204/206	f206	± f206	208/206	± 208/206	208/232	± 208/232	207/235	± 207/235	206/238	± 206/238	R	207/206	± 207/206
S298-54 Blanket Mountain pelitic schist, UTM 410875E, 5623950N																				
1.1	12832	27168	2.1172	0.0349	162	2.15E-04	2.98E-04	0.0040	0.0056	0.6697	0.0127	0.00280	0.00006	0.05807	0.00617	0.00851	0.00030	0.4422	0.04947	0.00475
1.2	6824	23740	3.4790	0.0158	110	1.08E-03	3.81E-04	0.0202	0.0072	1.1013	0.0201	0.00284	0.00005	0.07644	0.00780	0.00861	0.00016	0.2987	0.06442	0.00632
1.3	23074	31197	1.3520	0.0111	243	1.00E-05	1.00E-05	0.0002	0.0002	0.4355	0.0049	0.00276	0.00004	0.05621	0.00174	0.00822	0.00017	0.7524	0.04962	0.00102
2.1	15736	27867	1.7710	0.0253	171	3.09E-04	1.23E-04	0.0058	0.0023	0.5794	0.0101	0.00263	0.00005	0.05227	0.00304	0.00772	0.00026	0.6728	0.04911	0.00213
2.2	23982	176306	7.3516	0.0575	558	5.82E-04	1.20E-04	0.0109	0.0022	2.2685	0.0192	0.00258	0.00004	0.05401	0.00250	0.00811	0.00012	0.4476	0.04831	0.00202
3.1	20152	168114	8.3422	0.2102	502	5.35E-04	2.32E-04	0.0100	0.0044	2.6051	0.0240	0.00253	0.00006	0.05099	0.00459	0.00789	0.00026	0.4756	0.04687	0.00374
3.2	13039	200934	15.4102	0.1727	523	3.90E-04	2.86E-04	0.0073	0.0054	4.7632	0.0545	0.00252	0.00004	0.05191	0.00520	0.00797	0.00015	0.3026	0.04721	0.00454
3.3	20181	165170	8.1844	0.0121	524	1.39E-03	2.11E-04	0.0260	0.0040	2.6294	0.0203	0.00271	0.00003	0.04065	0.00403	0.00818	0.00011	0.2351	0.03603	0.00349
4.1	17170	179133	10.4328	0.1679	554	7.91E-04	3.35E-04	0.0148	0.0063	3.4089	0.0477	0.00281	0.00005	0.05403	0.00648	0.00836	0.00017	0.2844	0.04689	0.00543
4.2	10536	243691	23.1302	0.5441	588	7.20E-04	8.26E-04	0.0135	0.0155	7.3242	0.1313	0.00249	0.00006	0.05115	0.01414	0.00769	0.00020	0.2175	0.04824	0.01312
5.1	11657	130280	11.1761	0.1251	399	9.28E-04	2.62E-04	0.0174	0.0049	3.6365	0.0298	0.00285	0.00004	0.05201	0.00510	0.00846	0.00012	0.2661	0.04461	0.00425
6.1	15237	136907	8.9851	0.0293	423	2.22E-04	2.31E-04	0.0042	0.0043	2.8760	0.0260	0.00274	0.00003	0.06290	0.00484	0.00815	0.00012	0.3058	0.05597	0.00413
S298-70 Pelitic schist, ridge off NW side of Blanket Mountain, UTM 408700E, 5623175N																				
1.1	52985	26758	0.5050	0.0082	558	1.05E-04	2.01E-05	0.0020	0.0004	0.1592	0.0015	0.00330	0.00006	0.06750	0.00388	0.01014	0.00057	0.9898	0.04827	0.00040
1.2	*40900*	*192834*	*4.7148*	*7.0012*	*949*	*8.56E-04*	*2.24E-04*	*0.0160*	*0.0042*	*1.5709*	*0.3740*	*0.00345*	*0.00427*	*0.05986*	*0.12526*	*0.01028*	*0.02087*	*0.9890*	*0.04224*	*0.01320*
2.1	57112	215024	3.7650	0.0493	1092	5.10E-04	1.03E-04	0.0096	0.0019	1.1687	0.0070	0.00319	0.00005	0.06386	0.00340	0.00999	0.00034	0.7350	0.04635	0.00169
2.2	20998	100611	4.7915	0.0649	486	3.13E-04	1.31E-04	0.0059	0.0024	1.5118	0.0129	0.00343	0.00006	0.06713	0.00340	0.01046	0.00020	0.5021	0.04655	0.00206
3.1	21333	21805	1.0221	0.0089	257	2.25E-04	9.99E-05	0.0042	0.0019	0.3018	0.0060	0.00317	0.00007	0.06627	0.00276	0.01037	0.00015	0.4575	0.04636	0.00173
4.1	31573	61724	1.9550	0.0365	463	2.32E-04	5.77E-05	0.0044	0.0011	0.6057	0.0046	0.00329	0.00006	0.06490	0.00307	0.01029	0.00040	0.8868	0.04575	0.00101
4.2	27448	68878	2.5094	0.0691	449	1.42E-04	5.03E-05	0.0027	0.0009	0.8078	0.0129	0.00337	0.00008	0.06742	0.00430	0.01022	0.00059	0.9526	0.04785	0.00094
4.3	32823	217237	6.6184	0.1075	883	4.06E-04	1.37E-04	0.0076	0.0026	2.1065	0.0167	0.00319	0.00006	0.06930	0.00397	0.00985	0.00032	0.6522	0.05103	0.00223
5.1	30057	81955	2.7267	0.0493	409	2.54E-04	5.80E-05	0.0048	0.0011	0.8706	0.0059	0.00271	0.00005	0.05618	0.00194	0.00822	0.00020	0.7798	0.04960	0.00108
5.2	25829	23926	0.9263	0.0139	284	2.73E-04	1.05E-04	0.0051	0.0020	0.2945	0.0076	0.00314	0.00008	0.05902	0.00320	0.00955	0.00028	0.6303	0.04484	0.00190
6.1	79663	195577	2.4551	0.0165	1058	3.73E-04	2.44E-05	0.0070	0.0005	0.7664	0.0088	0.00271	0.00004	0.05297	0.00127	0.00849	0.00014	0.7680	0.04523	0.00070
6.2	32623	182752	5.6020	0.1088	700	6.10E-04	1.11E-04	0.0114	0.0021	1.7689	0.0095	0.00284	0.00005	0.05297	0.00312	0.00883	0.00034	0.7310	0.04351	0.00176
7.1	23694	175209	7.3948	0.1455	666	8.06E-04	6.46E-05	0.0151	0.0012	2.3207	0.0143	0.00315	0.00007	0.06188	0.00320	0.00965	0.00020	0.5063	0.04652	0.00209

Table 6.2. (continued)

Spot	204 corrected ages (Ma) 208/232	±	206/238	±	207/235	±	207/206	±	% conc	207 corrected ages 206/238	±
S298-54 Blanket Mountain pelitic schist, UTM 410875E, 5623950N											
1.1	56.48	1.21	54.64	1.90	57.31	5.94	170.32	210.09	32.1	54.48	1.87
1.2	57.39	1.06	55.24	1.00	74.79	7.38	755.32	221.98	7.3	54.04	0.91
1.3	55.74	0.83	52.74	1.09	55.53	1.67	177.36	48.52	29.7	52.57	1.09
2.1	53.19	0.95	49.57	1.66	51.74	2.94	153.07	105.07	32.4	49.44	1.65
2.2	52.13	0.72	52.05	0.79	53.41	2.41	114.61	100.23	45.4	51.97	0.78
3.1	51.03	1.24	50.67	1.66	50.50	4.45	42.69	180.53	118.7	50.68	1.65
3.2	50.85	0.76	51.20	0.95	51.39	5.03	59.92	214.42	85.5	51.19	0.91
3.3	54.71	0.59	52.53	0.68	40.46	3.94	0.00	0.00	0.0	53.27	0.65
4.1	56.73	1.10	53.65	1.08	53.43	6.26	43.59	255.55	123.1	53.67	1.03
4.2	50.24	1.26	49.39	1.29	50.65	13.76	110.95	810.51	44.5	49.31	1.03
5.1	57.44	0.90	54.28	0.75	51.48	4.93	0.00	0.00	0.0	54.45	0.70
6.1	55.22	0.61	52.32	0.77	61.94	4.64	451.24	172.78	11.6	51.74	0.74
S298-70 Pelitic schist, ridge off NW side of Blanket Mountain, UTM 408700E, 5623175N											
1.1	66.61	1.17	65.06	3.62	66.33	3.70	112.37	19.56	57.9	64.98	3.61
1.2	*69.59*	*85.85*	*65.92*	*131.80*	*59.03*	*113.43*	*0.00*	*0.00*	*0.0*	*66.34*	*132.64*
2.1	64.30	1.06	64.10	2.19	62.86	3.25	16.77	84.30	382.1	64.18	2.19
2.2	69.16	1.24	67.08	1.31	65.98	3.24	26.30	102.61	255.1	67.15	1.30
3.1	63.88	1.45	66.48	0.96	65.15	2.63	17.55	86.18	378.7	66.56	0.96
4.1	66.30	1.29	65.98	2.57	63.85	2.93	0.00	0.00	0.0	66.11	2.57
4.2	68.08	1.52	65.54	3.80	66.25	4.10	92.02	47.31	71.2	65.50	3.79
4.3	64.44	1.15	63.19	2.01	68.04	3.78	241.96	104.03	26.1	62.89	2.00
5.1	54.65	1.09	52.74	1.27	55.50	1.87	176.36	51.67	29.9	52.57	1.27
5.2	63.33	1.57	61.25	1.78	58.23	3.08	0.00	0.00	0.0	61.44	1.78
6.1	54.66	0.71	54.52	0.90	52.40	1.23	0.00	0.00	0.0	54.65	0.90
6.2	57.33	0.91	56.67	2.15	52.41	3.02	0.00	0.00	0.0	56.93	2.16
7.1	63.62	1.37	61.89	1.27	60.97	3.06	25.28	103.91	244.8	61.95	1.28

Errors are 1 std. error of mean

isotopes indicated by their masses: 204–208 = Pb; 232 = Th; 235 and 238 = U

* = Radiogenic Pb

f206 = fraction of 206Pb that is common Pb

%conc = concordance on chord from origin

Sample s298-70 spot 1.2 (dispayed in italics) has large errors and is not shown in concordia plots

Table 6.3. Regressions and average age calculations for samples s298-30, s298-54, s298-70, s298-92 and YK-TVG-97.

sample	fractions	upper intercept	error (Ma)	lower intercept	error (Ma)	average age (Ma)	error (Ma) *	MSWD	comments
s298-30	M2–4	2234	+504/–408	54.7	0.4			2.94	
s298-54	M1–4	3895	+1520/–777	54.6	0.4			1.11	
SHRIMP	**all**					**52.6**	**1.0[6.3]**	**2.5**	204Pb corr. (corrected) wtd. 206Pb/238U average
	all					53.0	1.0	2.9	207Pb corr. wtd. 206Pb/238U average
	3.1,3.3,4.1,5.1					47.6	9.8	1.7	204Pb corr. wtd. 207Pb/235U average of rev. disc. data
	all					54.3	1.5	7.5	204Pb corr. wtd. 208Pb/232Th average
s298-70	M2,M4	2079	+1370/–832	63.5	+1.1/–2.1			0	
SHRIMP	**all**					**60.7**	**3.6[12.4]**	**15**	204Pb corr. wtd. 206Pb/238U average
	all					60.8	3.6	15	207Pb corr. wtd. 206Pb/238U average
	all but 5.1,6.1,6.2					57.0	5.0	6.3	204Pb corr. wtd. 207Pb/235U average of rev. disc. data
	5.1,6.1,6.2					64.8	1.8[7.1]	2.0	204Pb corr. wtd. 206Pb/238U average - old
	2.1,2.2,3.1,4.1,5.2,6.1,6.2,7.1					54.2	3.5[6.8]	1.4	204Pb corr. wtd. 206Pb/238U average - young
	2.1,2.2,3.1,4.1,5.2,7.1					64.8	1.8	2.1	207Pb corr. wtd. 206Pb/238U average - old
	6.1,6.2					55.4	3.9	1.7	207Pb corr. wtd. 206Pb/238U average - young
	2.1,2.2,3.1,4.1,5.2,7.1					62.9	2.4	0.9	204Pb corr. wtd. 207Pb/235U average of rev. disc. data - old
	6.1,6.2					52.4	2.2	0	204Pb corr. wtd. 207Pb/235U average of rev. disc. data - young
	all but 5.1,6.1,6.2					65.5	1.6	2.5	204Pb corr. wtd. 208Pb/232Th average - old
	5.1,6.1,6.2					55.5	3.7	3	204Pb corr. wtd. 208Pb/232Th average - young
s298-92 +	M1,M2,m2					71.6	1.2	1.6	wtd. 207Pb/235U average
YK-TVG-97	**M1,M2,m2**					**71.7**	**1.5**		207Pb/235U average (error includes all errorbars)
	m1,M5,M6					58.6	4.2	3.7	wtd. 207Pb/235U average
	m1,M5,M6					**57.4**	**7.0**		207Pb/235U average (error includes all errorbars)
	m2,m4	590	55	76	2.1			0	
	m1,m4	528	50	72.9	2.9			0	
	M1,M4	2828	+2750/–1590	73.4	+1.8/–.9			0	

* errors between brackets include all errorbars

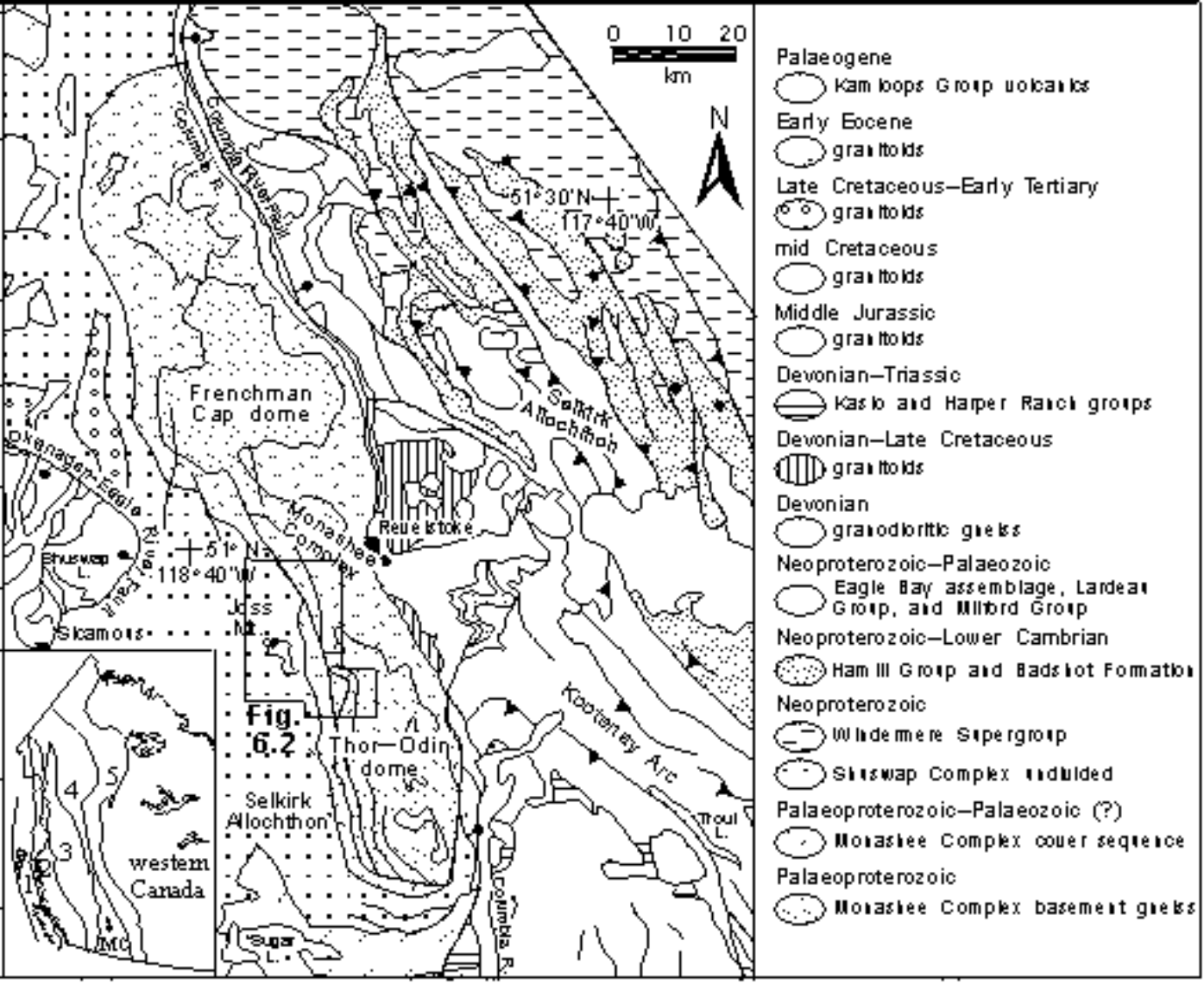

Fig. 6.1. Geological map of the Monashee Complex and surrounding geology. Modified after Wheeler and McFeely (1991). Inset: location of morphogeological belts of the Canadian Cordillera: 1. Insular Belt, 2. Coast Belt, 3. Intermontane Belt, 4. Omineca Belt, 5. Foreland Belt. MC indicates the location of the Monashee Complex.

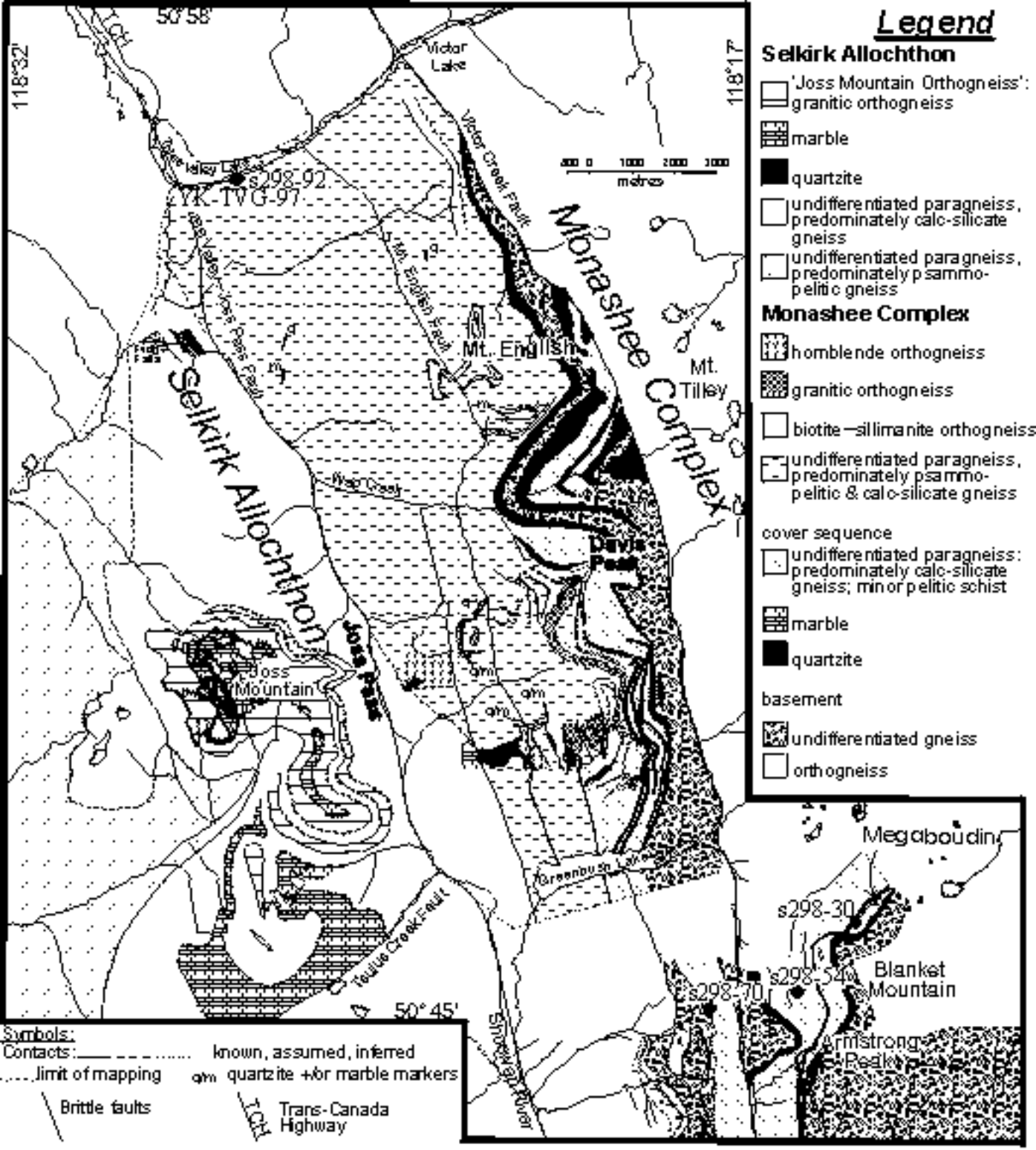

Fig. 6.2. Geological map of northwest Thor–Odin, after Johnston et al. (2000). Locations are shown for samples s298-30, s298-54, s298-70, s298-92 and YK-TVG-97.



Fig. 6.3. Dated quartzite (s298-30; ~10 m thick layers on the left part of the photograph) on N side of the Megaboudin, looking towards the N. Person on other side of pond for scale.

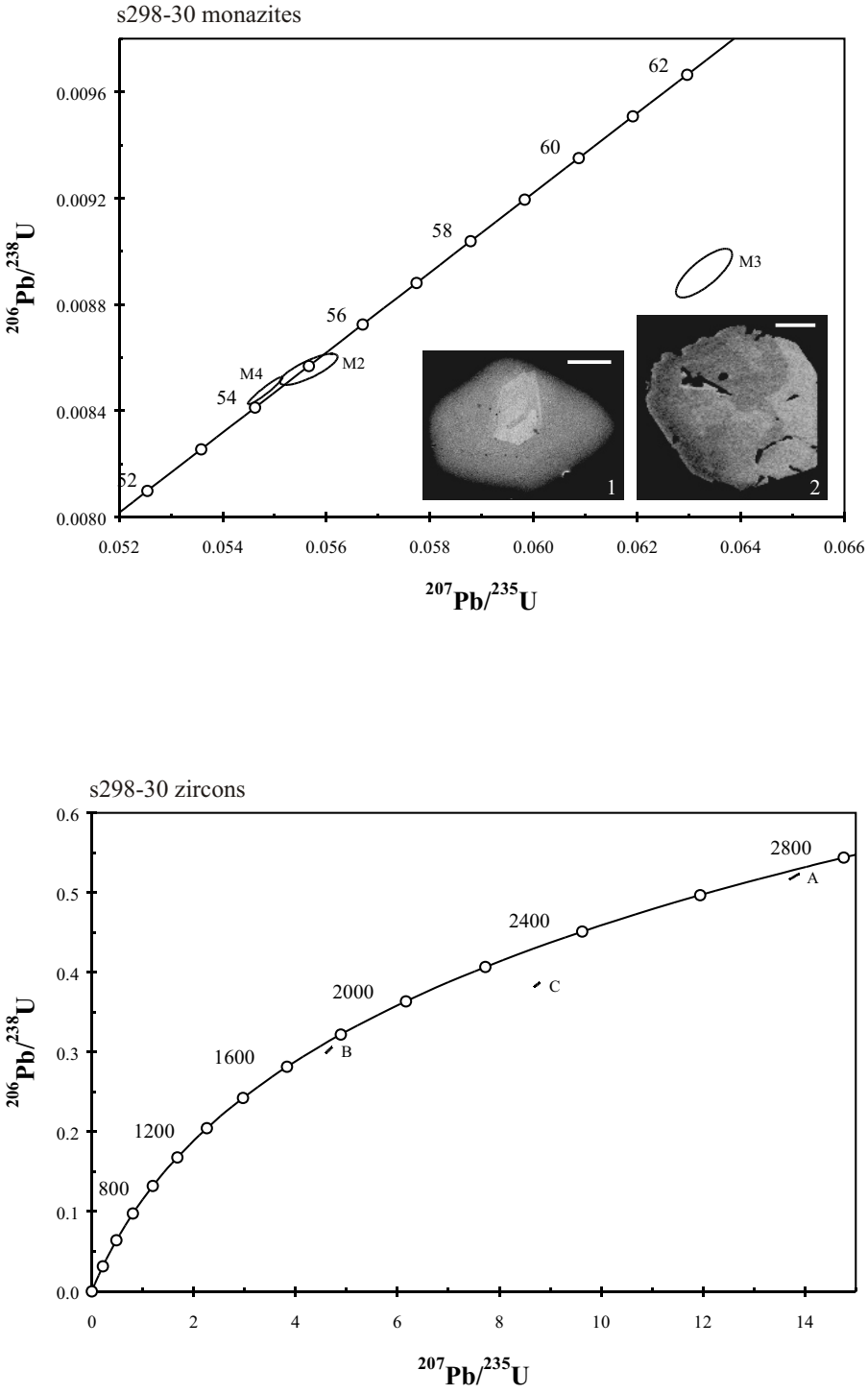

Fig. 6.4. Concordia diagrams for monazites (a) and detrital zircons (b) for the quartzite (s298-30). BSE images in (a) show representative examples of monazites. Scale bars are 50 μm. See text for discussion.

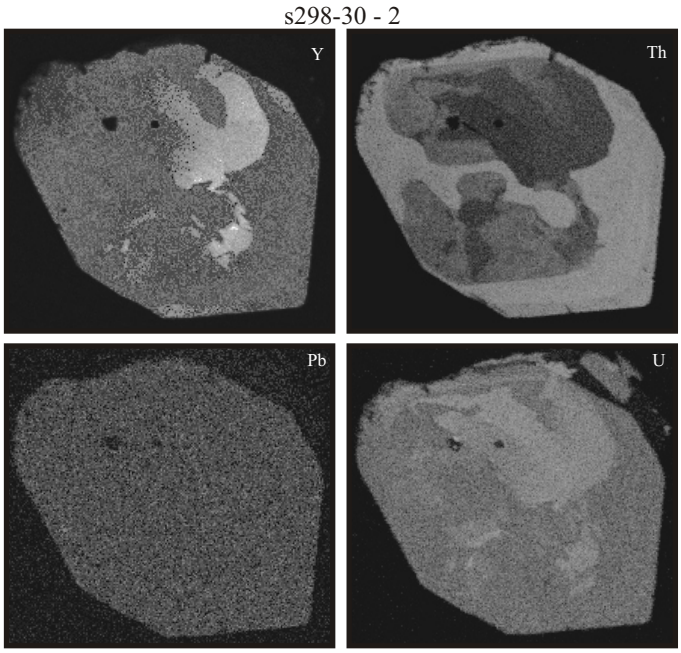

Fig. 6.5. Microprobe element maps (Y, Th, U and Pb) of monazite shown in BSE image 2 (sample s298-30, Fig. 6.4a), showing patchy domains. Scale shown in Fig. 6.4a.

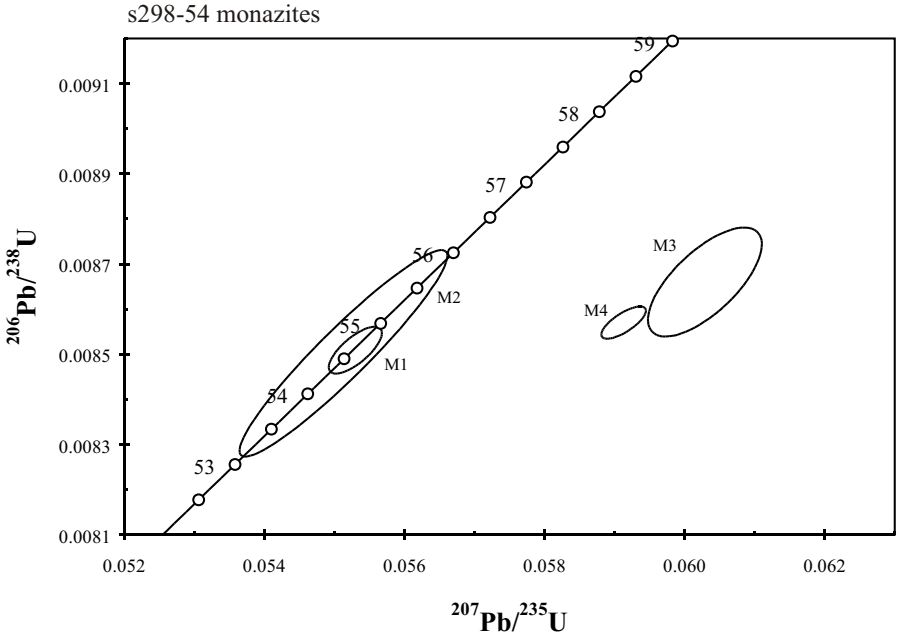

Fig. 6.6. Concordia plot of ID-TIMS data for pelitic schist s298-54.

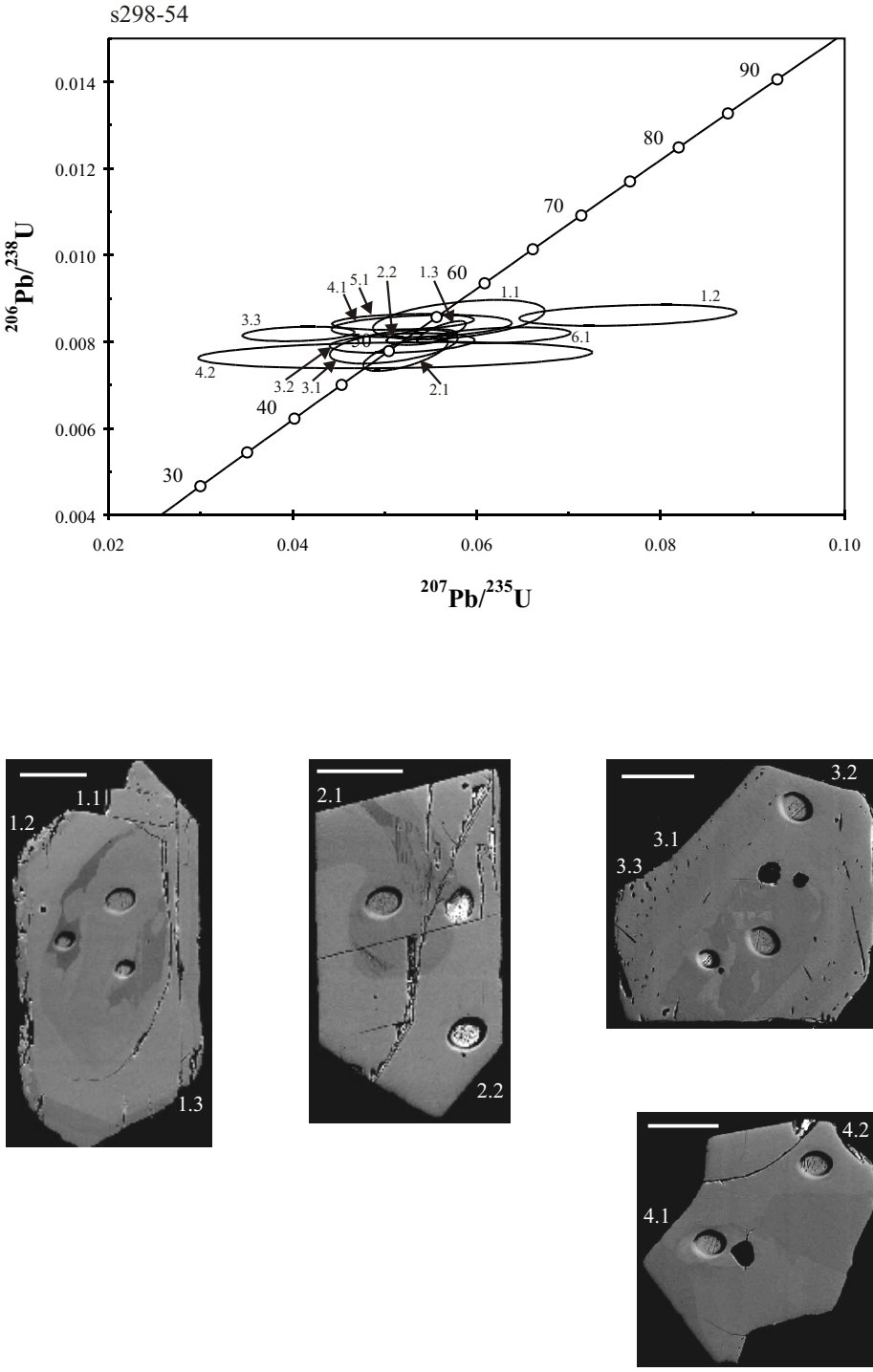

(a)

Fig. 6.7. Concordia diagrams showing SHRIMP data for sample s298-54. (a) $^{206}Pb/^{238}U$ versus $^{207}Pb/^{235}U$, also showing BSE images of representative monazites and analysed spots. Scale bars are 50 μm.

(b)

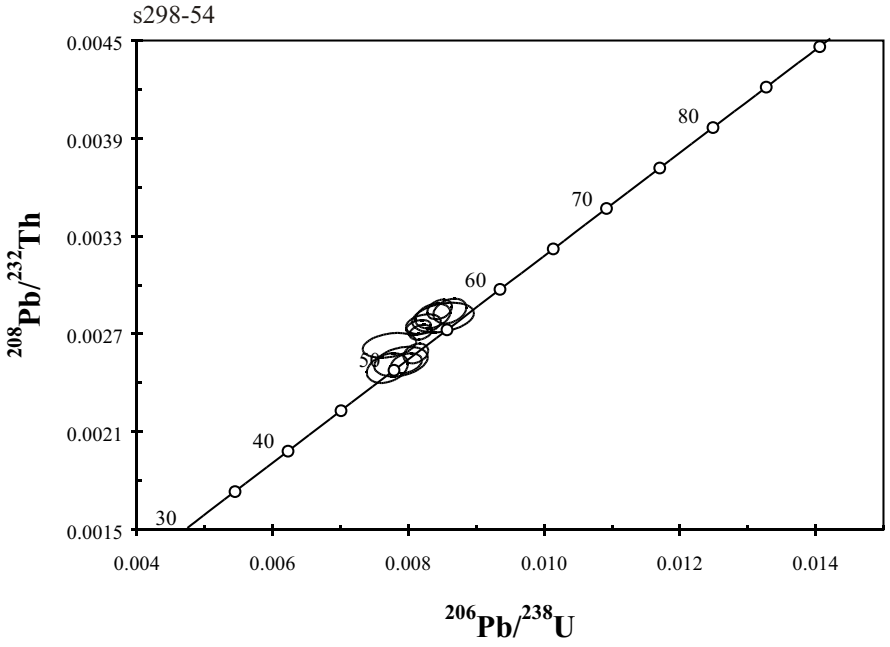

(c)

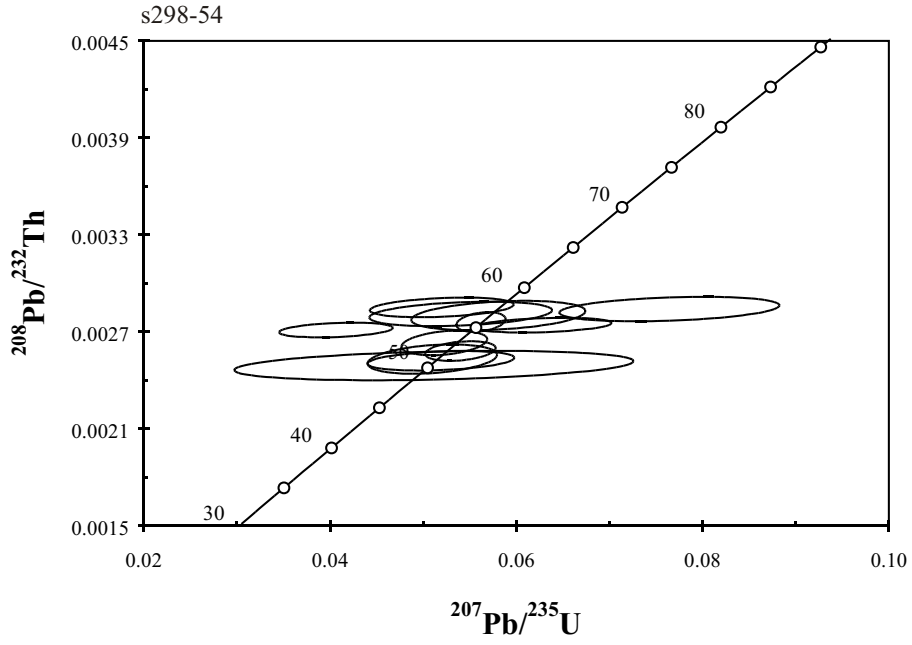

Fig. 6.7. (continued) (b) $^{208}Pb/^{232}Th$ versus $^{206}Pb/^{238}U$. (c) $^{208}Pb/^{232}Th$ versus $^{207}Pb/^{235}U$. Correlation coefficients between the errors of $^{208}Pb/^{232}Th$ and $^{206}Pb/^{238}U$, and between $^{208}Pb/^{232}Th$ and $^{207}Pb/^{235}U$, are taken to be 0.3.

(a)

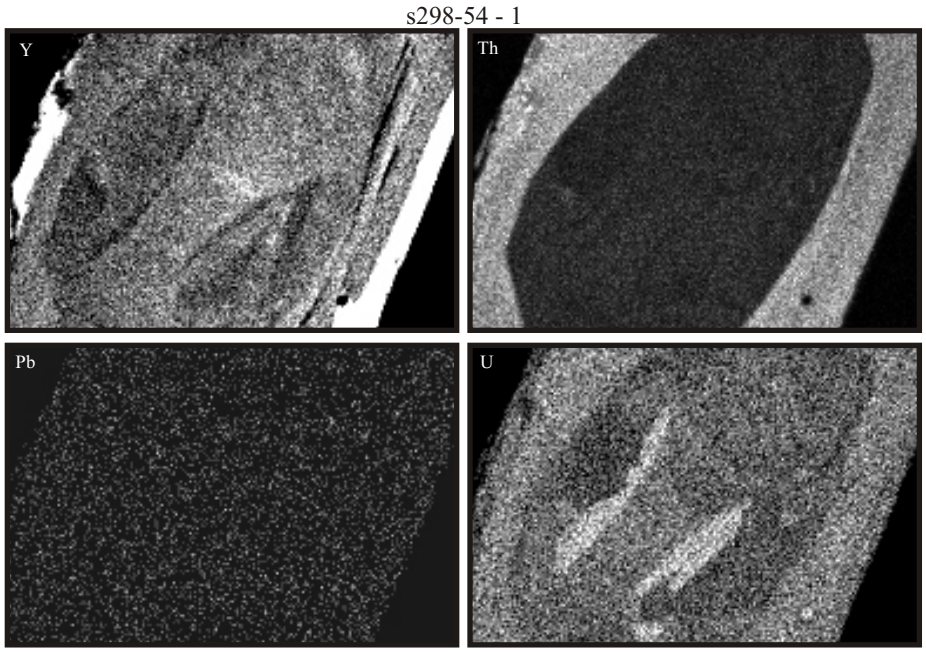

(b)

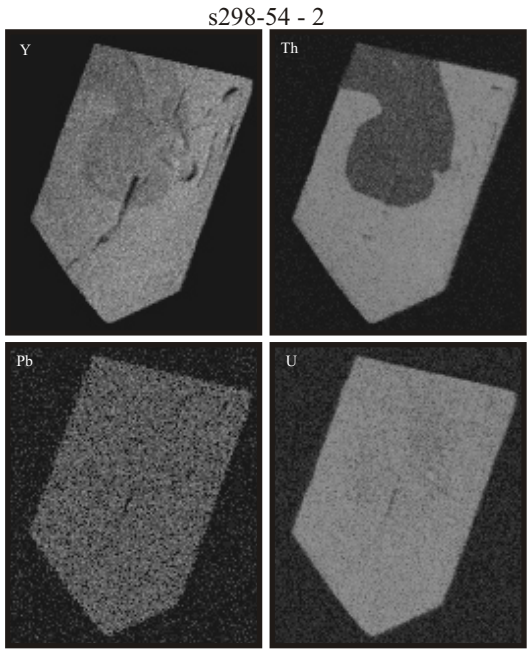

Fig. 6.8a–**d.** Microprobe element maps of monazites 1–4 shown in Fig. 6.7a (sample s298-54). See text for discussion.

(c)

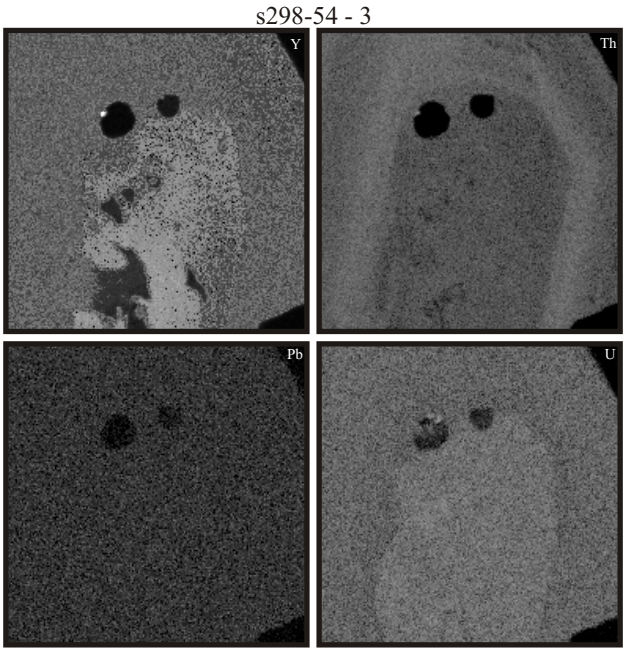

(d)

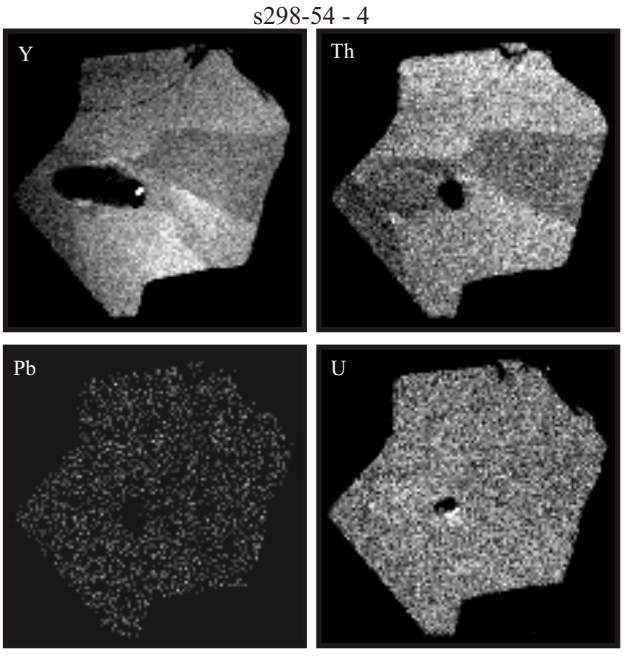

Fig. 6.8. (continued)



Fig. 6.9. Photograph of pelitic schist s298-70, looking E. Garnet and sillimanite are indicated. The hand lens is for scale.

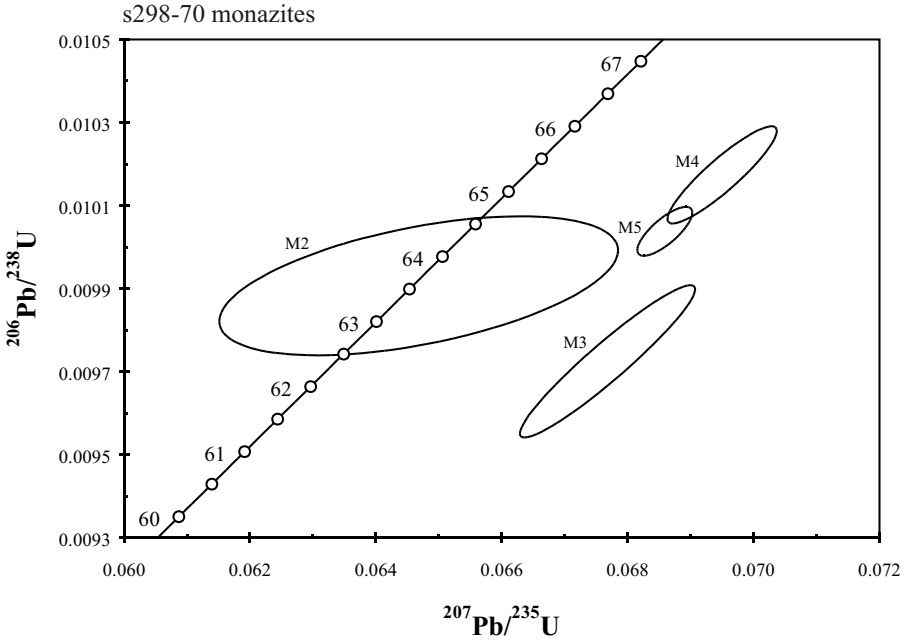

Fig. 6.10. Concordia diagram of ID-TIMS data for pelitic schist s298-70.

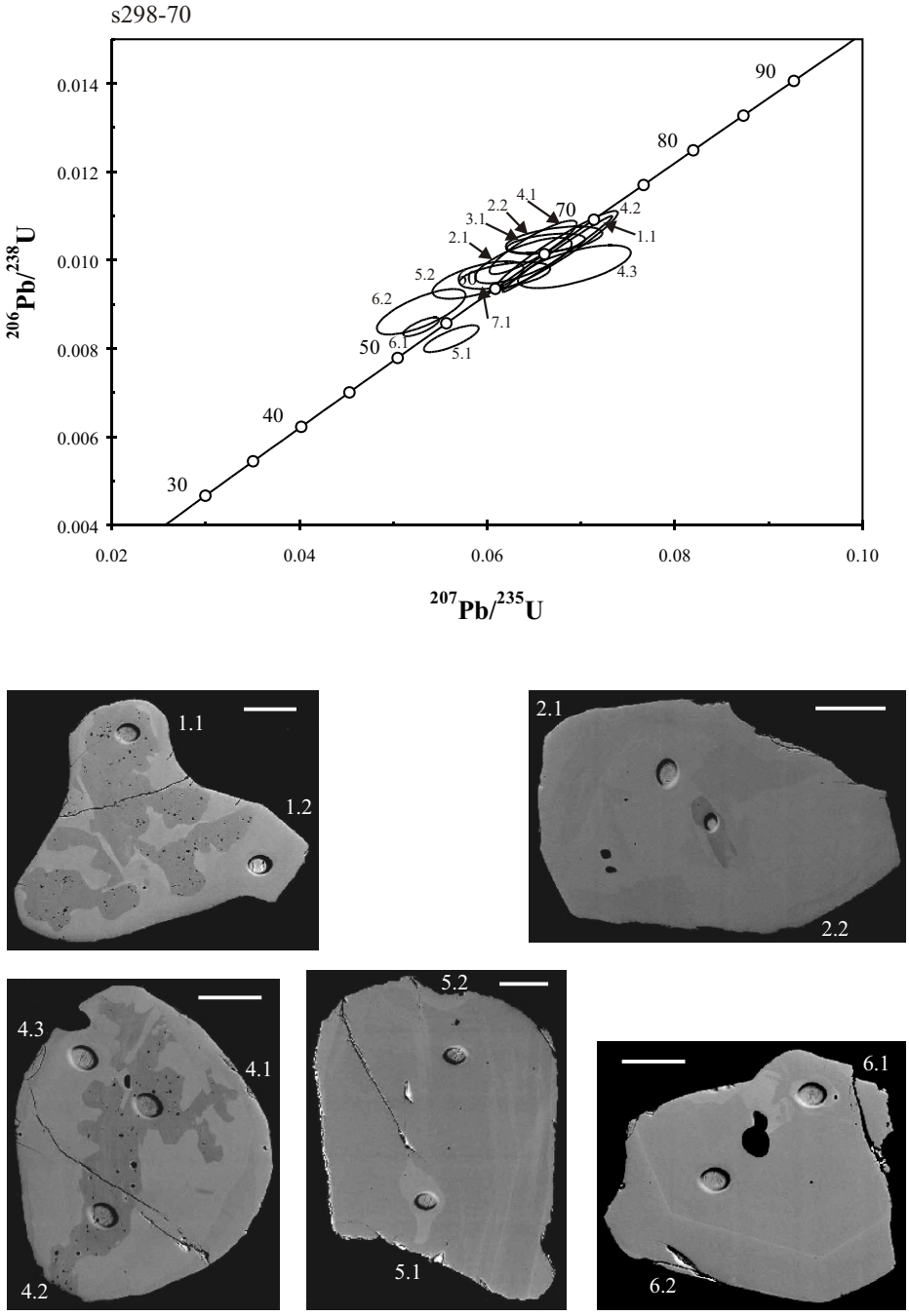

(a)

Fig. 6.11. Concordia plots showing SHRIMP data for sample s298-70. (a) $^{206}Pb/^{238}U$ versus $^{207}Pb/^{235}U$, also showing BSE images of representative monazites and analysed spots. Scale bars are 50 μm.

(b)

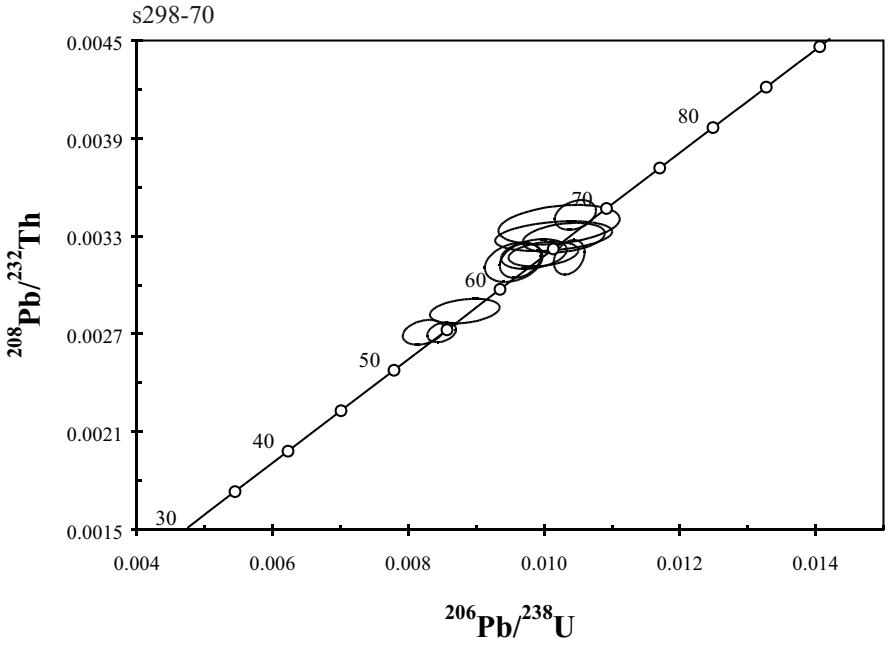

(c)

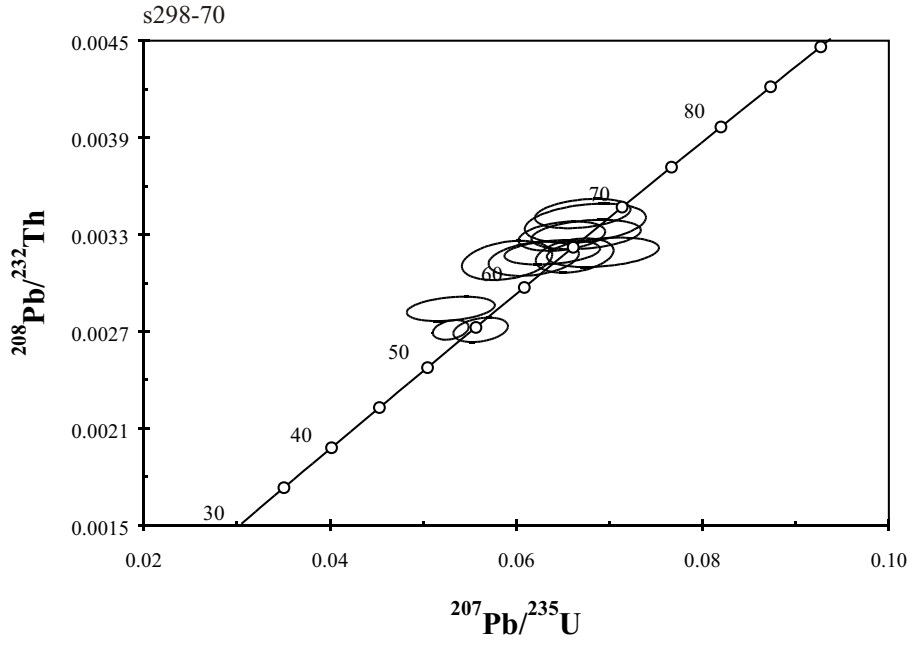

Fig. 6.11. (continued) (b) $^{208}Pb/^{232}Th$ versus $^{206}Pb/^{238}U$. (c) $^{208}Pb/^{232}Th$ versus $^{207}Pb/^{235}U$. Correlation coefficients between errors for plots (b) and (c) are taken to be 0.3.

(a)

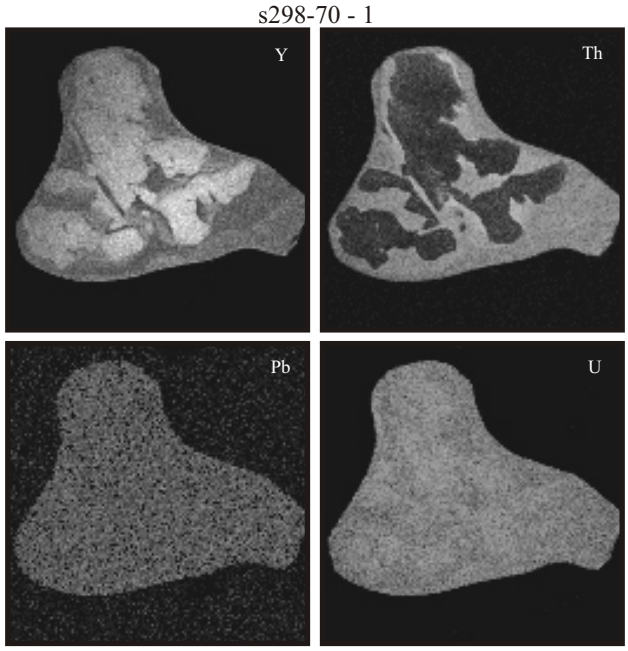

(b)

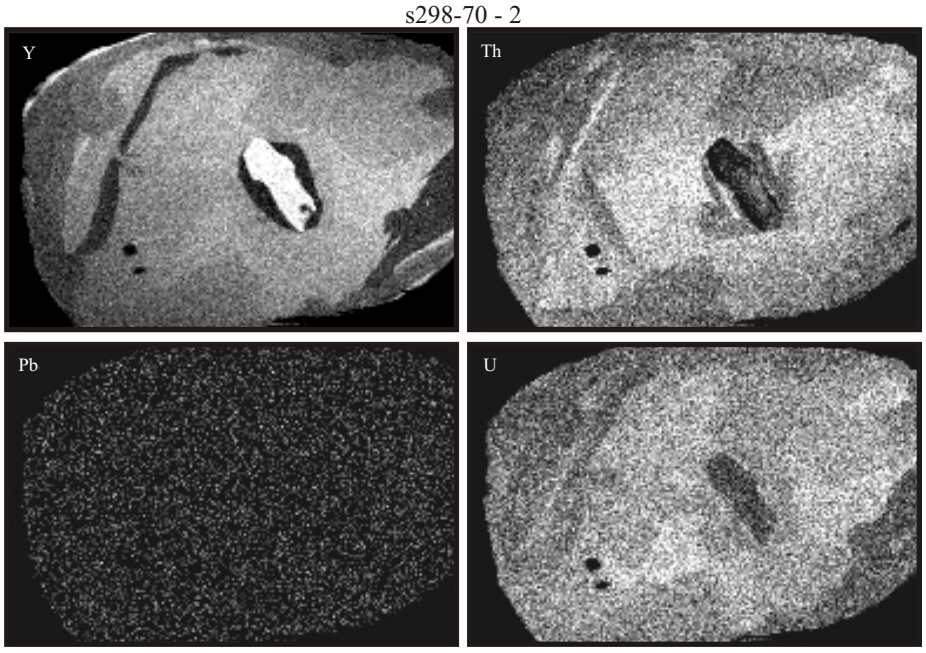

Fig. 6.12a–**c.** Microprobe element maps of monazites 1, 2 and 4 of sample s298-70 shown in Fig. 6.11a.

(c)

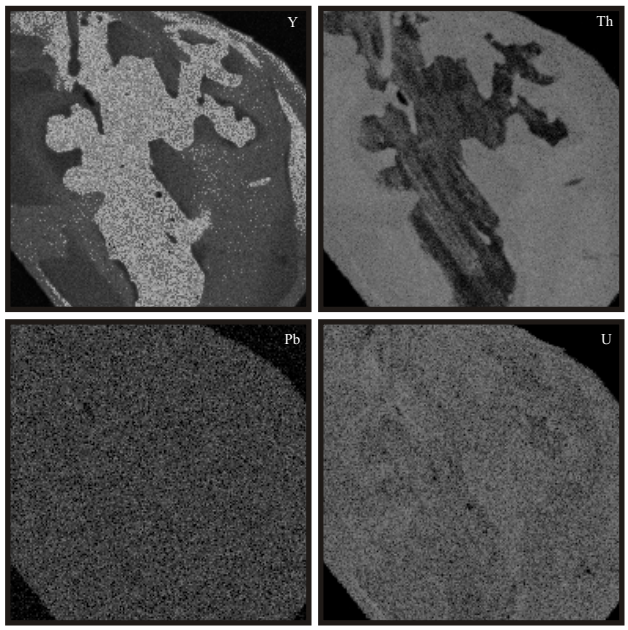

Fig. 6.12. (continued)

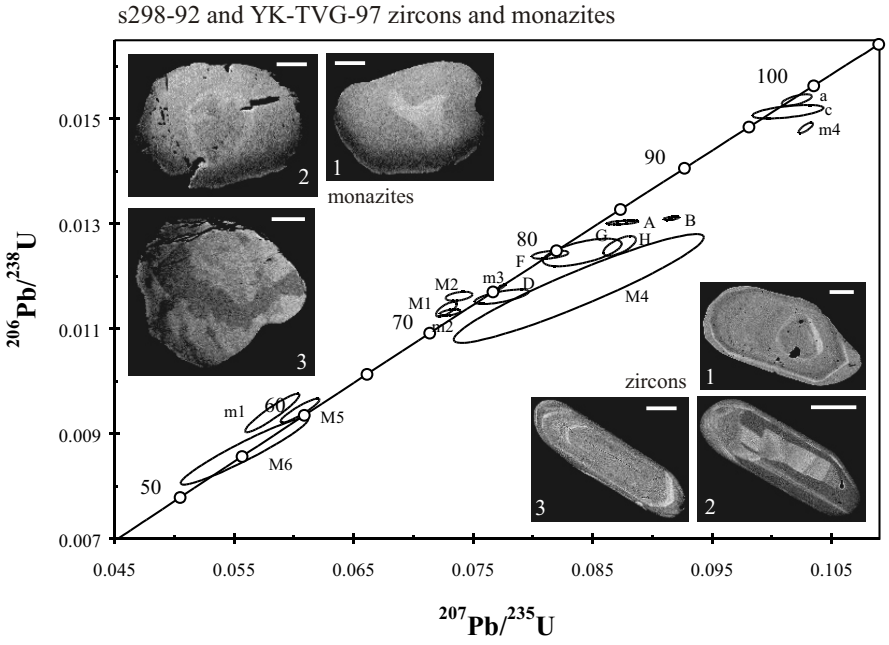

Fig. 6.13. Concordia plot and BSE images of zircons and monazites for the Three Valley Gap paragneiss (YK-TVG-97; labelled with capitalised letters) and its leucosome (s298-92; small letters). Monazite BSE images 1 and 2 and zircon image 1 are from YK-TVG-97 and the other images are from grains of s298-92. All scale bars are 50 μm.

(a)

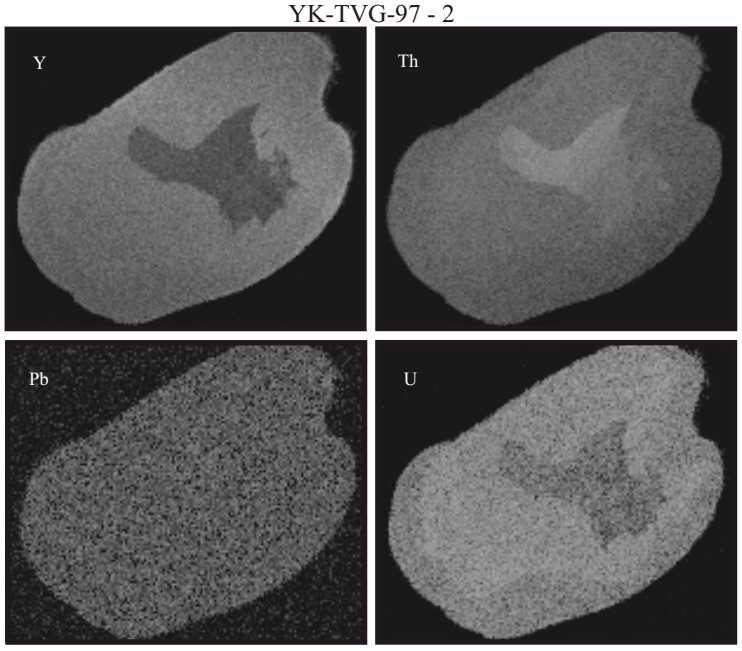

Fig. 6.14a–c. Microprobe element maps of monazites 1–3 of samples YK-TVG-97 and s298-92 (see Fig. 6.13).

(b)

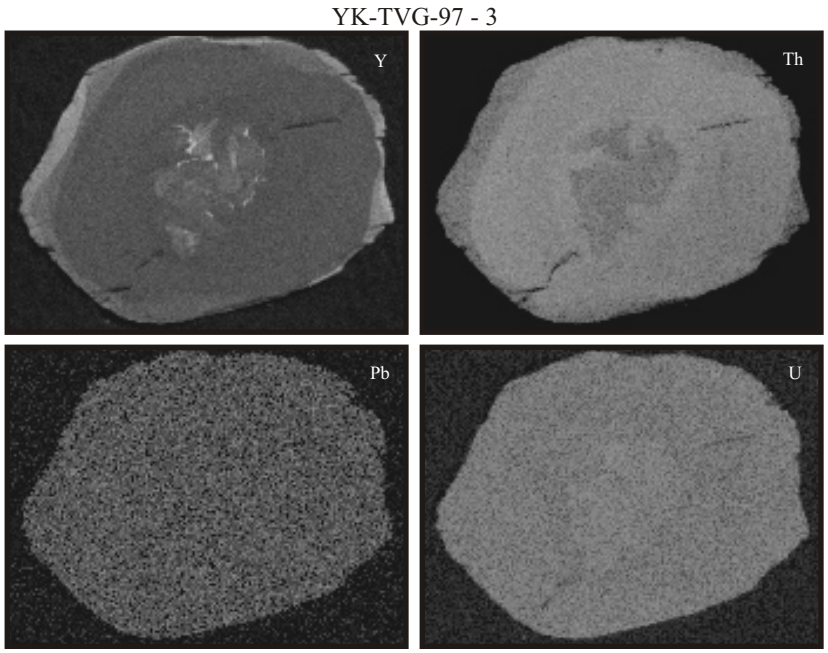

(c)

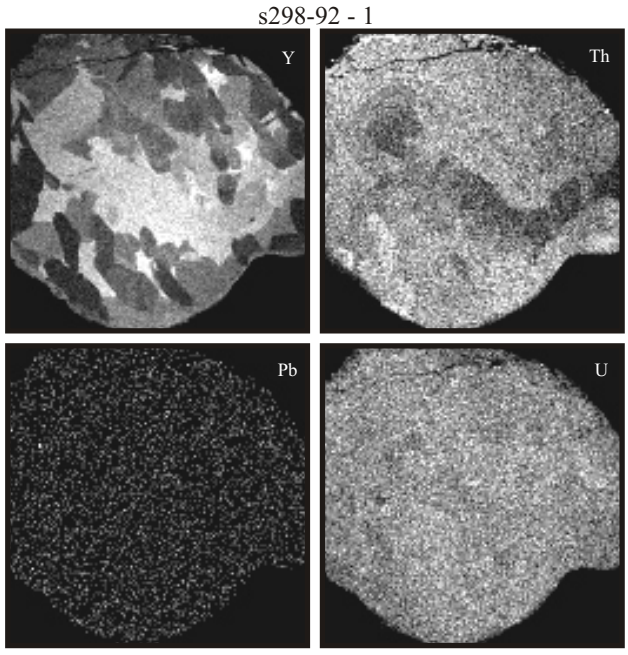

Fig. 6.14. (continued)

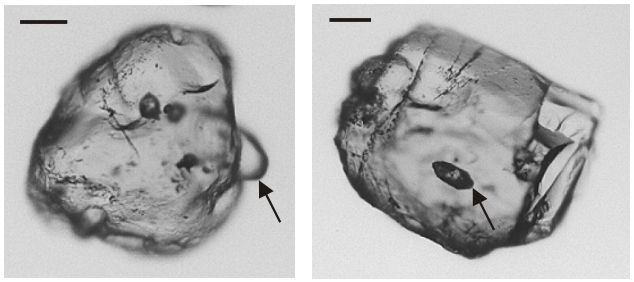

Fig. 6.15. Zircon inclusion (indicated by the arrows) in monazite. Scale bars are 50 μm. Although these examples are from sample s298-92, zircon inclusions in monazite have been recognised in most samples. However, no zircon inclusions were recognised in the monazites selected for dating.

Chapter 7

Age constraints on deformation and on deposition of (meta)sedimentary rocks of the Joss Mountain assemblage, west of the Monashee Complex, southeastern British Columbia

Abstract

U–Pb geochronology was carried out on two samples from Joss Mountain, in the Selkirk Allochthon, west of the Monashee Complex. The Joss Mountain orthogneiss is 362 ± 13 Ma. Intrusives of similar age have not been recognised in the Monashee Complex, which confirms the view that rocks of the Joss Mountain assemblage were at higher structural level than the Monashee Complex at the time of intrusion and/or deformation. One of two E–W-trending vertical undeformed pegmatites has a crystallisation age of 69.6 ± 2.5 Ma, which forms a lower age constraint on Cordilleran deformation at Joss Mountain. Johnston et al. (2000) dated a felsic dyke, folded by F_3, at 73.4 ± 1.5 Ma. F_3 at Joss Mountain is therefore constrained between ~73 and ~70 Ma.

7.1. Introduction

The Monashee Complex of southeastern British Columbia exposes ancestral North American basement rocks within the southern Omineca Belt (Fig. 7.1). Rocks of the Selkirk Allochthon overlie the Monashee Complex. Joss Mountain is situated west of the Monashee Complex, and has been mapped in detail by Johnston (1997) (Fig. 7.1).

The Joss Mountain assemblage was interpreted as being part of the Selkirk Allochthon (Johnston, 1997), but is lithologically very similar to the Monashee Complex.

U–Pb geochronology was carried out on two samples in order to make a better correlation of the Joss Mountain assemblage either with rocks of the Monashee Complex, or with rocks of the Selkirk Allochthon, and to constrain the age of deformation. The intrusive age of the Joss Mountain orthogneiss may be correlated with other intrusives in the region. A crosscutting pegmatite gives a lower age constraint on Cordilleran deformation at Joss Mountain. The ID-TIMS methods are the same as described in Section 5.3.1. Concordance and discordance are as defined in Section 5.3.3.

7.2. Geological background

The Monashee Complex consists of Palaeoproterozoic to Palaeozoic (?) orthogneisses and metasedimentary rocks (Armstrong et al., 1991, and references therein; Parkinson, 1991; Parrish, 1995, and references therein). It has two structural culminations: Frenchman Cap in the north and Thor–Odin in the south (Fig. 7.1). Rocks of the Selkirk Allochthon consist of Neoproterozoic and younger quartzite, marble, calc-silicate gneiss, paragneiss and orthogneiss (Parrish, 1995, and references therein). The Joss Mountain assemblage consists of the same lithologies as the Selkirk Allochthon and is described in detail in Johnston (1997). Metamorphism reached upper amphibolite facies conditions in the Monashee Complex, and lower to upper amphibolite facies conditions at higher structural levels including Joss Mountain (Johnston et al., 2000).

Peak of metamorphism at Joss Mountain is interpreted as having occurred at 93 ± 1.5 Ma, the age of monazites in pelitic schist (Johnston et al., 2000).

Rocks of the Monashee Complex and the Selkirk Allochthon have tight to isoclinal NE-verging F_1/F_2 folds, with generally SW-dipping axial planes. Overprinting relationships between F_1 and F_2 folds can rarely be seen, and therefore the folds are often referred to as F_1/F_2 folds. Rocks of the Monashee Complex and Selkirk Allochthon are strongly transposed (Williams, 1999; Spark, 2001), indicating that it is part of a regional NE-directed subhorizontal shear zone (Williams, 1999). Transposition caused dismembering of folds (e.g. Fig. 7.2) and lithological units, and therefore units cannot always be correlated on a regional scale. F_3 folds are isoclinal to open and verge predominantly to the NE within the Monashee Complex, and to the SW at Joss Mountain. They are overprinted by gentle upright F_4 folds. Shear bands in and around the Monashee Complex, a zone of concentrated extension along the NW flank of Thor–Odin (Johnston et al., 2000), and later brittle normal faults indicate crustal extension (D_5). Crustal extension occurred both by localised and generally large scale mechanisms (e.g. the Columbia River Fault; Fig. 7.1) and by penetrative and generally small scale mechanisms, such as shear bands and faults that occur throughout the Monashee Complex. Eocene (sub)vertical pegmatites (e.g. Johnston et al., 2000) and lamprophyres (e.g. Lane, 1984) intruded during extension and are undeformed.

7.3. Results

7.3.1. Joss Mountain orthogneiss (s279-123)

The Joss Mountain orthogneiss (Fig. 7.3; unit 25 of Johnston, 1997) occurs as two 50–150 m thick sheets, and some thinner lenses and layers above the upper sheet, in the metasedimentary rocks of the Joss Mountain assemblage (units 15–22 of Johnston, 1997; cf. rocks of the Selkirk Allochthon in Fig. 7.3). The upper sheet, sampled in 1995 by D.H. Johnston for geochronology (sample s279-123; see Fig. 7.3 for sample location), extends in outcrop over the Joss Mountain alpine area. The medium-grained grey homogeneous gneiss is a biotite-bearing leucocratic monzonite. It contains feldspar, quartz and biotite, with minor crystals of subhedral garnet (minerals given in order of decreasing content), accessory zircon and retrograde sericite, muscovite and chlorite .

The Joss Mountain orthogneiss has a SSW-dipping gneissosity/foliation, which is interpreted as being equivalent to the regional S_2 transposition foliation. Alternatively, the foliation may be the result of crustal extension. The foliation is not always parallel to the contact between the orthogneiss and the host rock. The gneiss has a weak shallow E–W-trending biotite lineation, which may well be related to, or have been reorientated by, Late Cretaceous–Eocene extension. The contact between the orthogneiss and the host rock is not well exposed, and crosscutting relationships between the orthogneiss and folds in the host rock could not be determined. Lenses of orthogneiss, up to several metres thick, exist in the host rocks close to the contact with the orthogneiss. The sheets of orthogneiss have broad warps, but tight F_1/F_2 folds, which are present in the surrounding metasedimentary rocks, have not been observed. The orthogneiss is therefore likely to have intruded after, or during, a late stage of F_1/F_2 folding, although it is possible that the orthogneiss intruded before F_1/F_2 folding and behaved as rigid sheets during folding.

Alternatively, the possibility exists that the contact between the orthogneiss and the host rocks is tectonic.

The lower orthogneiss sheet outcrops on the NE side of Joss Mountain. It contains more quartz and less biotite than the upper sheet, and the foliation is less well developed (cf. samples s279-123, s298-5, 235, 236 from the upper sheet and s298-225 from the lower sheet; Appendix IIb, c). It may be classified as a strongly foliated granite (Johnston, 1997) and it may not be the same unit as the orthogneiss in the upper sheet. It is possibly a later intrusion of the same suite, which would explain its more felsic composition, and its weaker foliation if intrusion occurred during deformation.

A ca. 100 m wide exposure of leucogranite (unit 26 of Johnston, 1997; sample s298-227) is exposed within the upper sheet, on the east side of Joss Mountain (Fig. 7.3). It is more felsic and more weakly foliated than the lower sheet of the Joss Mountain orthogneiss, and could also be a later intrusion of the same suite. The contact between the leucogranite and the Joss Mountain orthogneiss is sharp and curved, and the foliations in both units are parallel to each other, but not to their contact. The leucogranite does not have chilled margins.

Four single zircon crystals, fractions B, C, I and J, two multiple tip fractions E and K, two single tips, F and G, and fraction H consisting of six crystals, have been dated to constrain the protolith age of the Joss Mountain orthogneiss (Fig. 7.4, Table 7.1). Grains in fractions B, C and H are 149–250 μm, and in fractions E, F, G, I, J and K 105–149 μm. Zircons are euhedral bipyramidal prisms with aspect ratios of 1:3 to 1:4. All have excellent clarity, and all have inclusions. Cores are not visible, either optically or on the BSE pictures. BSE images show concentric zonations, and in some crystals

overgrowths (Fig. 7.4, grains 1 and 2 respectively). Based on morphology and concentric zonations, the crystals are interpreted as having an igneous origin. Fractions F and G (Table 7.1) gave very large errors because they were too small and yielded too low amounts of radiogenic Pb, and are therefore not shown on the concordia plot (Fig. 7.4). Fraction J is considered concordant, despite its slight reverse discordance (–1.1%), because its error ellipse overlaps concordia and because reverse discordance is not common for zircon fractions (Section 5.3.3). Reverse discordance of this fraction is therefore attributed to a small analytical error. The protolith age of the Joss Mountain orthogneiss is 362 ± 13 Ma, the weighted average of $^{207}Pb/^{206}Pb$ ages of fractions B, C, E, I, J and K and its 2σ error, and supported by the upper intercept age of a discordia chord through the same fractions (361 ± 27 Ma; Table 7.2). Fraction H is discordant, probably because one or more of the crystals contain a component of older inherited Pb. The old Pb component may be Proterozoic, because a discordia chord through fractions H and concordant fraction J has an upper intercept in the Archaean (2903 ± 960 Ma; Table 7.2). Discordance in other fractions may be a result of a younger (Eocene?) event or recent Pb loss.

7.3.2. Joss Mountain pegmatite (s298-4)

Sample s298-4 is from one of two ca. 4 m wide 090°-trending vertical granitic pegmatites from Joss Mountain, that can be traced for about 150 m along strike (Fig. 7.5). The sample location is shown in Fig. 7.3. The white pegmatite crosscuts the foliation (Fig. 7.6) and SW-verging F_3 folds in a semi-pelitic paragneiss of the Joss Mountain assemblage (lithology no. 16 of Johnston, 1997), and also intrudes the Joss Mountain

orthogneiss. Locally, in thin section, 1 mm wide fine-grained rims are present on the pegmatite, which may be thin chilled margins (samples s298-215a, b; Appendix IIb, c). However, clear evidence for a chilled margin is absent. The pegmatite contains subhedral feldspar, quartz, muscovite and garnet, accessory zircon, monazite, titanite and ilmenite, and retrograde epidote and sericite and late scapolite. Slight deformation of the pegmatite can be recognised in thin section only. Quartz grains are flattened and indented, and cracks in the grains are bent. Muscovite is recrystallised along its edges, and crystals are slightly bent. Quartz, feldspar and muscovite show undulose extinction. This slight deformation is considered post-F_3, because F_3 folds are clearly crosscut by the pegmatite, and the pegmatite is otherwise undeformed. The crystallisation age of the pegmatite would therefore give an upper age constraint on F_3 folding.

Three zircon fractions and five single monazite grains were analysed (Fig. 7.7, Table 7.1). All grains are 149–250 μm, except for zircon fraction D (74–105 μm). Based on their euhedral shapes, perfect igneous (concentric and sector) zonations in BSE images (Fig. 7.7), and the absence of cores, the monazite crystals in this sample could be interpreted as having an igneous origin. However, this will be disputed below. Some crystals have thin overgrowths. The BSE images show sector and concentric zonation, although one grain shows patchy domains (not shown). The dated crystals are all pale yellow and have an excellent clarity. Fraction M2 is subrounded and has an indentation. All others are euhedral. A small inclusion is visible in M3. Two monazite growth ages can be distinguished. Fractions M1–M4 are reversely discordant whereas M5 is normally discordant. The average $^{207}Pb/^{235}U$ age from fractions M2, M3 and M4, which yield a cluster of data, is 69.6 ± 2.5 Ma (error includes the range of ages of the three fractions

and their errors). The normal average is preferred over an average weighted according to the errors of the fractions, because $^{207}Pb/^{235}U$ ages with larger errors are not considered to be less meaningful than those with smaller errors. The $^{207}Pb/^{235}U$ age of M1 is 55.4 ± 0.6 Ma. Possibly, the two monazite ages do not reflect separate growth events, but a mixing line. The discordance of M5 may indicate the presence either of different age domains within the monazite, or of older radiogenic Pb in a young (e.g. 69.6 ± 2.5 or 55.4 ± 0.6 Ma) monazite.

Zircon crystals are euhedral bipyramidal prisms and have aspect ratios of 1:1.5–1:4. Especially the larger, 149–250 μm, crystals of fractions A and B, have many inclusions and fractures, are yellow, and are strongly altered and high in uranium (Table 7.1). The smaller, 74–105 μm, crystals of fraction D are clear, colourless, and have fewer inclusions. Fraction A consists of eight tips, B of one tip and D of fifteen small clear zircons. All zircon fractions give discordant data, which can be explained by inheritance, overgrowth, Pb loss, or a combination. No meaningful age can be derived from these data. BSE images of zircon crystals from the same sample that were not dated show strong alteration and metamictisation, presumably as a result of high U (Fig. 7.7, grain 1). This supports Pb loss as a main cause for discordance. Thin overgrowths and vague concentric zonations are also visible on the BSE images are, but no cores were observed (Fig. 7.7, grain 2).

The crystallisation age of the pegmatite is interpreted as being 69.6 ± 2.5 Ma, based on the average $^{207}Pb/^{235}U$ age of monazites M2, M3 and M4. Alternatively, 69.6 ± 2.5 Ma could represent a post-crystallisation event, e.g. metamorphic or fluid related, in which case the crystallisation age of the pegmatite (and F_3) would be older. However,

this is considered unlikely, because a felsic dyke at Joss Mountain, folded by F_3, is 73.4 ± 1.5 Ma (Johnston et al., 2000). The felsic dyke contains the F_3 axial planar foliation. The ages of the crosscutting pegmatite and the folded felsic dyke constrain F_3 at Joss Mountain between ~70 and ~73 Ma. The 55.4 ± 0.6 Ma single monazite age in the crosscutting pegmatite is interpreted as reflecting later growth, perhaps in the presence of meteoric fluids during extension (cf. Chapter 3), or of igneous fluids related to Eocene intrusions, e.g. the Ladybird granite suite (Carr, 1992). The fact that this 55.4 ± 0.6 Ma perfectly euhedral monazite (M1, Fig. 7.7) could grow after the crystallisation of the pegmatite shows that morphology does not always provide a unique solution for the origin of a crystal. Here, a euhedral monazite does not automatically imply an igneous origin.

7.4. Discussion

7.4.1. Late Devonian–Early Mississippian granitoids

Igneous activity was extensive during the Late Devonian and Early Mississippian in the Kootenay Terrane (cf. Fritz et al., 1991), which is part of the Selkirk Allochthon, now structurally overlying the Monashee Complex. The 358 ± 6 Ma Clachnacudainn orthogneiss (Reesor and Moore, 1971; Okulitch, 1985; Parrish, 1992) occurs in the part of the Kootenay Terrane that is now east of the Columbia River Fault, and the Griffin gneisses, the Seymour gneiss and the Mt. Fowler gneiss occurs in the Kootenay Terrane, geographically west of the Monashee Complex (Johnson, 1994). The Griffin gneisses are

interpreted as having the same age as a gneiss of the same type near Mara Lake, which has a U–Pb zircon age of 366 +10/–3 Ma (Johnson, 1994; H.A. Wasteneys, unpublished data, 1993). The Seymour gneiss is 359 ± 3 Ma (Parrish, 1992) and the Mt. Fowler gneiss 372 ± 6 Ma (Okulitch et al., 1975). Also, a felsic tuff in the Shuswap Lake area (Fig. 7.1) has been dated at 387 ± 4 Ma (R.L. Armstrong, unpublished data, 1981; in Okulitch, 1985). Since ~360 Ma intrusives are not recognised in the Monashee Complex, the Joss Mountain assemblage, is confirmed to be part of the Kootenay Terrane or Selkirk Allochthon and not of the Monashee Complex (cf. Johnson, 1994; Johnston et al., 2000), if the contact between the Joss Mountain orthogneiss and the metasedimentary rocks of the Joss Mountain assemblage is intrusive. Referring to Chapter 8, the presence of a ~360 Ma orthogneiss, and of Late Cretaceous SW-verging F_3 folds in other rocks of the Joss Mountain assemblage, would be consistent with this area being part of the top half of a mid- to Late Cretaceous NE-directed channel flow zone (Domain 2 of Chapter 8). Because it is unclear how the intrusion of the Joss Mountain orthogneiss relates to F_1/F_2 folding, the time of F_1/F_2 folding at Joss Mountain remains unconstrained.

7.4.2. Constraints on F_3 folding

F_3 at Joss Mountain is constrained between ~70 and ~73 Ma (Section 7.3). A 93 ± 1.5 Ma monazite age from a pelitic schist in the same area is interpreted as representing peak of metamorphism (Johnston et al., 2000). F_3 at Joss Mountain therefore occurred after the peak of metamorphism.

Previous workers have attempted to constrain F_3 folding in the Monashee Complex and it could be argued that F_3 folding is younger towards lower structural level.

However, the constraints in the Monashee Complex are not conclusive. Johnston et al. (2000) tried to constrain F_3 at Blanket Mountain, at a deeper structural level within Thor–Odin. They proposed that F_3 occurred there between ~54.5 and ~50 Ma, based on monazite ages in pegmatites (samples RB-1-93 and a suite of late tourmaline-bearing pegmatites respectively). However, sample RB-1-93 was redated using U–Pb zircon geochronology in this study (see Section 7.3). Its crystallisation age may be 1939 ± 6 Ma, and the 54.5 ± 1.0 Ma monazite age of Johnston et al. (2000) may be a result of a later event, e.g. extension (cf. Chapter 3). Using that interpretation, F_3 at Blanket Mountain may have occurred at any time after 1939 ± 6 Ma (and probably before ~75–70 Ma; Chapter 3).

Crowley et al. (2001) tried to constrain F_3 (and F_2) folding by dating folded and crosscutting pegmatites at different structural levels in Frenchman Cap by U–Pb methods. However, their age constraints are not conclusive, and to illustrate how ages of deformation can be interpreted as being older, their lower age constraints on deformation are discussed here. Crowley et al. (2001) interpreted a 51.0 ± 1.0 Ma pegmatite (sample 12 at their middle structural level) as being boudinaged by D_2 deformation. Two pegmatites at lower structural levels, with interpreted ages of 55.4 ± 3.0 Ma (sample 292B) and 51.8 ± 1.0 Ma (sample 60A), were interpreted as being folded by F_3 (Crowley et al., 2001). However, all dated fractions of all three samples are discordant. For sample 12, the 51.0 ± 1.0 Ma age of six discordant zircon fractions, which lie slightly below concordia between 52 and 50 Ma and have $^{207}Pb/^{206}Pb$ ages between 58.2 and 73.1 Ma, is taken as the crystallisation age. Discordance may be a result of mixing between ~51 Ma and an older age, which may be the crystallisation age. For samples 292B and 60A,

Crowley et al. (2001) interpreted the ages of lower intercepts of discordia chords through discordant zircon fractions as the crystallisation ages of the pegmatites. However, the crystallisation ages may be as old as their Palaeoproterozoic upper intercept ages, and the lower intercept ages could indicate a separate process, such as fluid-related growth, recrystallisation and/or Pb loss during extension (cf. Chapter 3). For these reasons, Crowley et al.'s (2001) age constraints are not conclusive and F_2 and F_3 in Frenchman Cap may well have ended before 51.0 ± 1.0 Ma at the middle structural level and before 55.4 ± 3.0 Ma at the lower level.

Furthermore, the structural relationships of the three pegmatites are inconclusive. Even if the crystallisation ages as interpreted by Crowley et al. (2001) are correct, F_3 and F_2 folding may still be older than they proposed. Crowley et al. (2001) interpreted sample 12 as being boudinaged by D_2 deformation, but this may actually have been caused by D_5 extension. They do not prove that the dated pegmatite layers are folded by F_3. Instead they use indirect evidence that "similar layers that are near the sampled layers (within 100 m) are deformed around fold hinges that are, based on style and orientation, correlated with F_3 structures" (Crowley et al., 2001, p. 1113). Similarly, sample 60A is not shown to be folded, but is correlated with a nearby folded pegmatite. The foliation in the pegmatite is unlikely to be related to transposition (S_2), because in the case of NE directed shear, a 1.85 Ga granite (in Fig. 11a–c of Crowley et al., 2001) would have been folded due to its orientation within the shortening field of simple shear (Paul F. Williams, 1999, personal communication). The foliation in the pegmatite is probably a result of D_5 extension. Sample 292B is not shown to be folded and its foliation may be a result of extension.

Deformation at the highest structural levels of Frenchman Cap dome was interpreted as being, at least partly, younger than a leucosome layer with lineated kyanite (sample 191 of Crowley and Parrish, 1999 and Crowley et al., 2001). Sample 191 was interpreted as being 57.8 ± 1.5 Ma, based on five reversely discordant monazite fractions and the lower intercept ages of two discordia chords through discordant zircons (Crowley and Parrish, 1999; Crowley et al., 2001). However, the discordia chords have Palaeoproterozoic upper intercept ages, and therefore the leucosome may be as old as that. Therefore, 57.8 ± 1.5 Ma could represent a post-crystallisation event, and crystallisation of the leucosome may have occurred earlier.

For the reasons outlined above, no conclusive age constraints exist for F_3 folding in the Monashee Complex. Therefore, an interpretation that F_3 folding is younger towards lower structural level cannot be justified.

7.5. Conclusions

(1) The protolith age of the Joss Mountain orthogneiss (s279-123) is 362 ± 13 Ma. Granitoids of similar age have not been recognised in the Monashee Complex. The presence of a ~360 Ma orthogneiss in the Joss Mountain assemblage suggests that the Joss Mountain assemblage was at higher structural level than the Monashee Complex at the time of intrusion and/or deformation.

(2) The age of F_3 folding at Joss Mountain is bracketed by a ~73 Ma folded pegmatite (Johnston et al., 2000) and a ~70 Ma crosscutting pegmatite (s298-4).

(3) Morphology of a crystal does not always provide definitive evidence of its origin. The 55.4 ± 0.6 Ma perfectly euhedral monazite (M1, Fig. 7.7) is younger than the age of the pegmatite (s298-4) and therefore can not represent the age of crystallisation of the pegmatite.

References

Armstrong, R.L., Parrish, R.R., van der Heyden, P., Scott, K., Runkle, D., 1991. Early Proterozoic basement exposures in the southern Canadian Cordillera: core gneiss of Frenchman Cap, Unit I of the Grand Forks Gneiss, and the Vaseaux Formation. Canadian Journal of Earth Sciences 28, 1169–1201.

Carr, S.D., 1992. Tectonic setting and U–Pb geochronology of the early Tertiary Ladybird leucogranite suite, Thor–Odin – Pinnacles area, southern Omineca Belt, British Columbia. Tectonics 11, 258–278.

Crowley, J.L., Parrish, R.R., 1999. U–Pb isotopic constraints on diachronous metamorphism in the northern Monashee complex, southern Canadian Cordillera. Journal of Metamorphic Geology 17, 483–502.

Crowley, J.L., Brown, R.L., Parrish, R.R., 2001. Diachronous deformation and a strain gradient beneath the Selkirk allochthon, northern Monashee complex, southeastern Canadian Cordillera. Journal of Structural Geology 23, 1103–1121.

Fritz, W.H., Cecile, M.P., Norford, B.S., Morrow, D., Geldetzer, H.H.J., 1991. Cambrian to Middle Devonian assemblages. In: Gabrielse, H., Yorath, C.J. (Editors), Chapter 7 of Geology of the Cordilleran Orogen in Canada. Geological Survey of Canada, Geology of Canada no. 4, pp.151–218.

Johnson, B.J., 1994. Structure and tectonic setting of the Okanagan Valley fault system in the Shuswap Lake area, southern British Columbia. PhD Thesis, Carleton University, Ottawa, Ontario, Canada.

Johnston, D.H. 1997. Structural and thermal evolution of northwest Thor–Odin Dome, Monashee Complex, southeast British Columbia. PhD Thesis, University of New Brunswick, Fredericton, New Brunswick, Canada.

Johnston, D.H., Williams, P.F., Brown, R.L., Crowley, J.L., Carr, S.D., 2000. Northeastward extrusion and extensional exhumation of crystalline rocks of the

Monashee Complex, southeastern Canadian Cordillera. Journal of Structural Geology 22, 603–625.

Lane, L.S., 1984. Deformation history of the Monashee Decollement and Columbia River Fault zone. PhD Thesis, Carleton University, Ottawa, Ontario, Canada.

Okulitch, A.V., Wanless, R.K., Loveridge, W.D., 1975. Devonian plutonism in south–central British Columbia. Canadian Journal of Earth Sciences 12, 1760–1769.

Okulitch, A.V., 1985. Paleozoic plutonism in southeastern British Columbia. Canadian Journal of Earth Sciences 22, 1409–1424.

Parkinson, D.L., 1991. Age and isotopic character of Early Proterozoic basement gneisses in the southern Monashee Complex, southeastern British Columbia. Canadian Journal of Earth Sciences 28, 1159–1168.

Parrish, R.R., 1992. Miscellaneous U–Pb zircon dates from southeast British Columbia. Geological Survey of Canada, Paper 91-2, 143–153.

Parrish, R.R., 1995. Thermal evolution of the southeastern Canadian Cordillera. Canadian Journal of Earth Sciences 32, 1618–1642.

Reesor, J.E., Moore, J.M., 1971. Petrology and structure of the Thor–Odin gneiss dome, Shuswap metamorphic complex. Geological Survey of Canada, Bulletin 195.

Spark, R.N., 2001. Crustal thickening and tectonic denudation within the Thor–Odin culmination, Monashee Complex, southern Canadian Cordillera. PhD Thesis, University of New Brunswick, Fredericton, New Brunswick, Canada.

Wheeler, J.O., McFeely, P. (Compilers), 1991. Tectonic assemblage map of the Canadian Cordillera and adjacent parts of the United States of America: Geological Survey of Canada, Map 1712A, scale 1:2 000 000, 1 sheet.

Williams, P.F., 1999. Fold Nappes and the problem of model driven interpretation. Specialist Group in Tectonics and Structural Geology Field Conference, Halls Gap, Victoria, Australia (February 14–19, 1999). Geological Society of Australia Abstracts Series #53, 267–268.

Table 7.1. ID-TIMS data for samples s279-123 and s298-4.

Fraction size a	Wt. (µg) b	U (ppm) b	Pb* (ppm) b	$^{206}Pb/^{204}Pb$	Pb (pg) c	^{208}Pb (%)	Th/U d	$^{206}Pb/^{238}U$	$^{207}Pb/^{235}U$	$^{207}Pb/^{206}Pb$	$^{206}Pb/^{238}U$ Age (Ma)	$^{207}Pb/^{235}U$ Age (Ma)	Correlation coefficient	$^{207}Pb/^{206}Pb$ Age (Ma)	Discordance (%) e
Sample S279-123 Joss Mountain orthogneiss, UTM 399478E, 5630383N															
B (s,149–250)	2	1229	61	190	43	7.8	0.28	0.05080 ± .72%	0.3740 ± 2.6%	0.05339 ± 2.2%	319.5 ± 4.5	322.6 ± 14.2	0.5936	345.4 ± 100.2	7.7
C (s,149–250)	2	933	51	212	31	7.7	0.28	0.05586 ± .26%	0.4139 ± 1.6%	0.05375 ± 1.5%	350.4 ± 1.8	351.7 ± 9.7	0.6328	360.4 ± 66.7	2.9
E (mt, 105–149)	1	2250	125	297	28	9	0.33	0.05573 ± .46%	0.4134 ± 1.1%	0.05379 ± .89%	349.6 ± 3.1	351.3 ± 6.4	0.5906	362.4 ± 40.0	3.6
F (st, 105–149)	*0*	*726*	*39*	*55*	*31*	*6.8*	*0.24*	*0.05516 ± 1.2%*	*0.3857 ± 8.7%*	*0.05072 ± 7.9%*	*346.1 ± 8.2*	*331.3 ± 49.1*	*0.6676*	*228.0 +330.1/–414.4*	*–53.25*
G (st, 105–149)	*0*	*1290*	*71*	*53*	*27*	*11.7*	*0.44*	*0.05345 ± 1.1%*	*0.3926 ± 7.0%*	*0.05327 ± 6.4%*	*335.7 ± 7.4*	*336.3 ± 40.2*	*0.6365*	*340.5 +264.9/–317.0*	*1.5*
H (m,149–250)	17	390	24	742	35	10.2	0.39	0.05981 ± 1.8%	0.5021 ± 2.4%	0.06088 ± .83%	374.5 ± 13.2	413.1 ± 16.5	0.9634	635.1 ± 35.7	42.2
I (s, 105–149)	3	349	19	464	8	8.3	0.30	0.05549 ± .48%	0.4139 ± .84%	0.05410 ± .71%	348.1 ± 3.2	351.7 ± 5.0	0.5348	375.3 ± 32.1	7.4
J (s, 105–149)	3	246	14	388	7	7.8	0.28	0.05731 ± .33%	0.4238 ± .97%	0.05363 ± .83%	359.2 ± 2.3	358.7 ± 5.8	0.5472	355.5 ± 37.6	–1.07
K (mt, 105–149)	2	790	44	960	6	9	0.33	0.05581 ± .29%	0.4134 ± .48%	0.05373 ± .40%	350.1 ± 2.0	351.3 ± 2.8	0.5494	359.6 ± 18.0	2.7
S298-4 Joss Mountain pegmatite, crosscutting F_3 folds, UTM 397200E, 5629875N															
A (mt,149–250)	50	4102	40	572	250	0.7	0.025	0.010711 ± .18%	0.07087 ± .64%	0.04799 ± .56%	68.7 ± 0.3	69.5 ± 0.9	0.5223	98.6 ± 26.7	30.5
B (st,149–250)	21	5760	57	210	430	1.4	0.048	0.010818 ± .25%	0.07231 ± 1.7%	0.04848 ± 1.5%	69.4 ± 0.3	70.9 ± 2.3	0.6411	122.7 ± 73.1	43.7
D (m, 74–105)	25	671	7	1319	8	6.4	0.225	0.010067 ± .29%	0.06960 ± .34%	0.05014 ± .21%	64.6 ± 0.4	68.3 ± 0.5	0.7951	201.6 ± 9.7	68.3
M1 (s,149–250)	39	25430	434	8793	64	53.4	3.729	0.008815 ± .57%	0.05604 ± .57%	0.04611 ± .12%	56.6 ± 0.6	55.4 ± 0.6	0.9778	3.2 ± 5.8	–999
M2 (s,149–250)	36	18467	435	9665	50	56.5	4.235	0.011339 ± .78%	0.07247 ± .78%	0.04635 ± .12%	72.7 ± 1.1	71.0 ± 1.1	0.9879	16.1 ± 5.8	–353.9
M3 (s,149–250)	59	12739	277	6230	91	51.3	3.438	0.010987 ± .43%	0.06992 ± .40%	0.04616 ± .19%	70.4 ± 0.6	68.6 ± 0.5	0.8961	5.8 ± 9.3	–999
M4 (s,149–250)	24	30106	669	4882	105	54.9	3.963	0.011099 ± .24%	0.07065 ± .25%	0.04617 ± .06%	71.2 ± 0.3	69.3 ± 0.3	0.9707	6.4 ± 2.9	–999
M5 (s,149–250)	12	50633	1143	7645	59	53	3.715	0.011713 ± .39%	0.07999 ± .36%	0.04953 ± .20%	75.1 ± 0.6	78.1 ± 0.5	0.8679	173.0 ± 9.2	56.9

Errors are 1 std. error of mean in % except for age errors which are 2 std. errors in Ma

* = Radiogenic Pb

a = Single grain (s), multiple grains (m), single tip (st) or multiple tips (mt); sizes in micrometres

b = Include sample weight error of ± 0.001 mg in concentration uncertainty

c = Total common Pb in analysis

d = Th/U from 208*/206* and 207*/206* age

e = Discordance on chord to origin

Fractions dispayed in italics have large errors and are not shown in concordia plots

Table 7.2. Regressions and average age calculations for samples s279-123 and s298-4.

sample	fractions	upper intercept	error (Ma)	lower intercept	error (Ma)	average age (Ma)	error (Ma) *	MSWD	comments
s279-123	**B,C,E,I,J,K**					**362**	**13**	**0.2**	wtd. (weighted) 207Pb/206Pb average
	B,C,E,I,J,K	361	27	–25	460			0.24	
	H,J	2903	960	359.4	2.6			0	
s298-4	M2,M3,M4					69.2	1.6	8.5	wtd. 207Pb/235U average
	M2,M3,M4					**69.6**	**2.5**		207Pb/235U average (error includes all errorbars)
	M4,M5	1767	+215/–197	72.6	0.4				

* errors between brackets include all errorbars

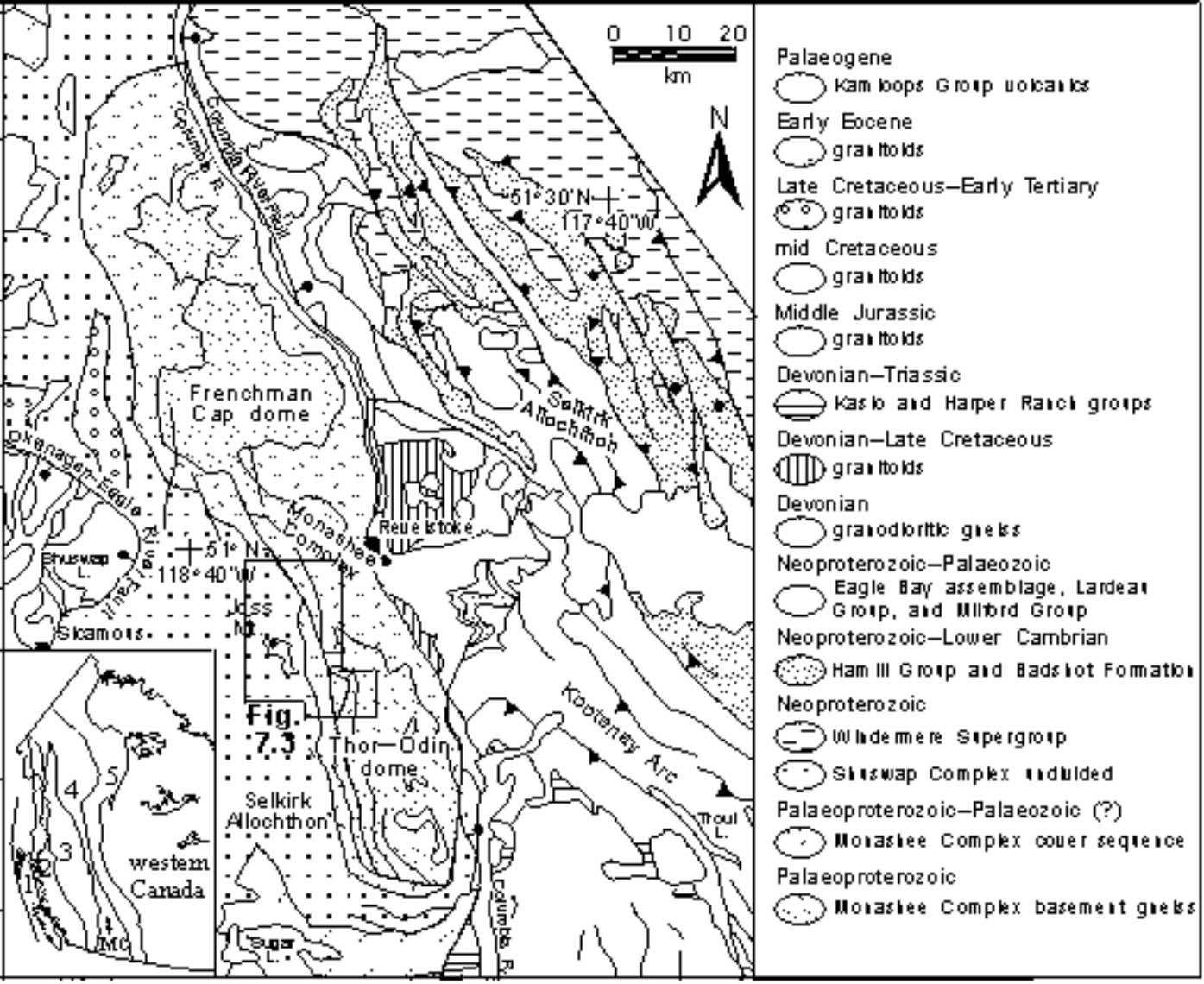

Fig. 7.1. Geological map of the Monashee Complex and surrounding geology. Modified after Wheeler and McFeely (1991). Inset: location of morphogeological belts of the Canadian Cordillera: 1. Insular Belt, 2. Coast Belt, 3. Intermontane Belt, 4. Omineca Belt, 5. Foreland Belt. MC indicates the location of the Monashee Complex.

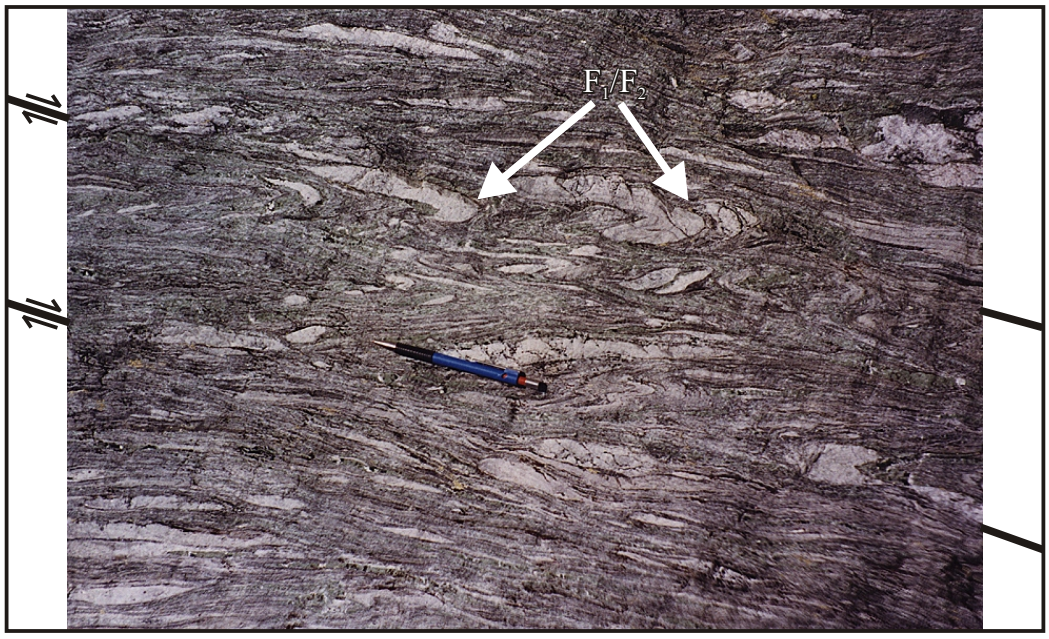

Fig. 7.2. Transposition foliation, in calc-silicate gneiss in the Megaboudin (Fig. 7.3), looking down towards the NW. F_1/F_2 folds are dismembered by local shears. Pencil for scale.

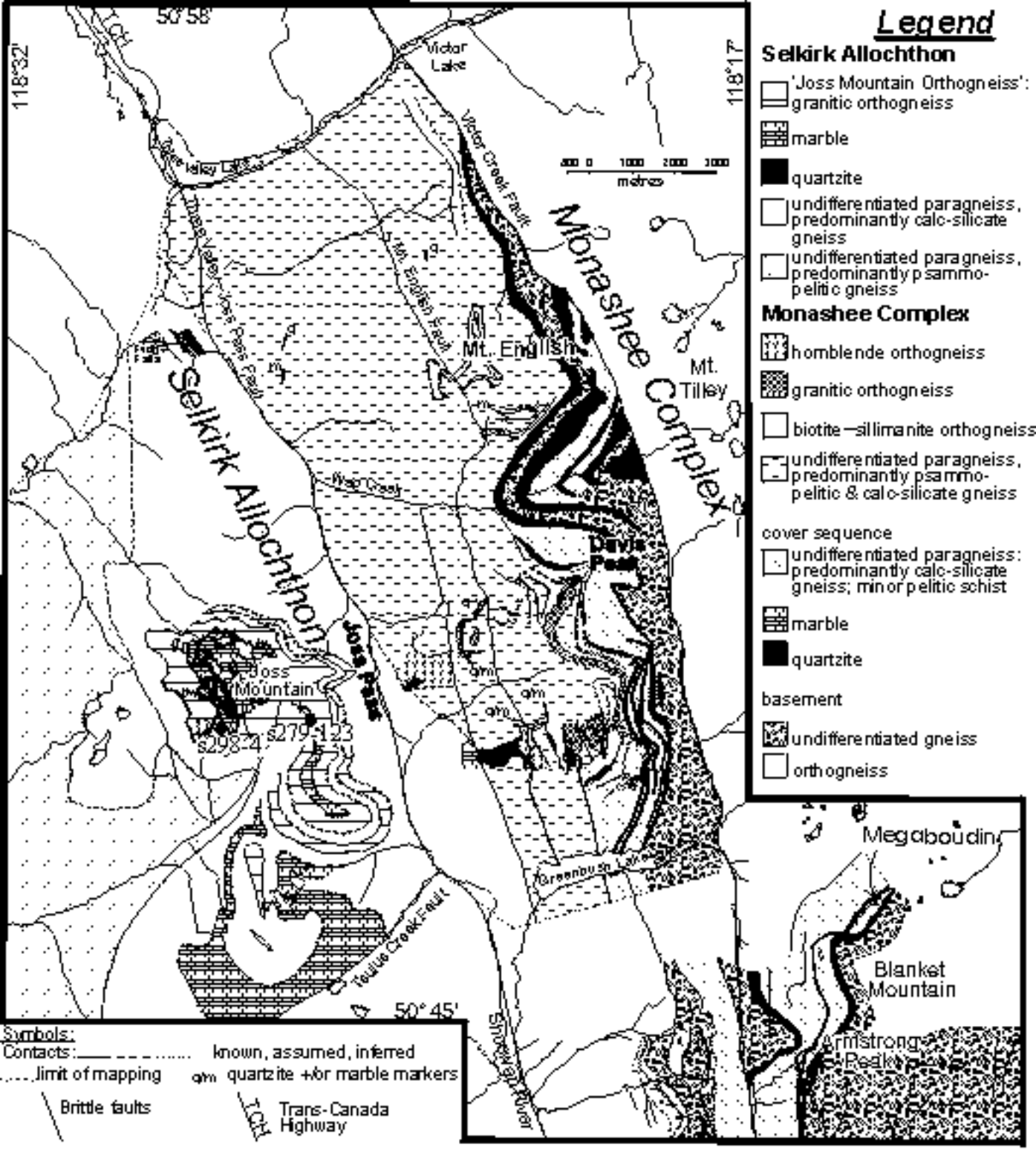

Fig. 7.3. Geological map of northwest Thor–Odin, after Johnston et al. (2000). Locations are shown for samples s298-4 and s279-123.

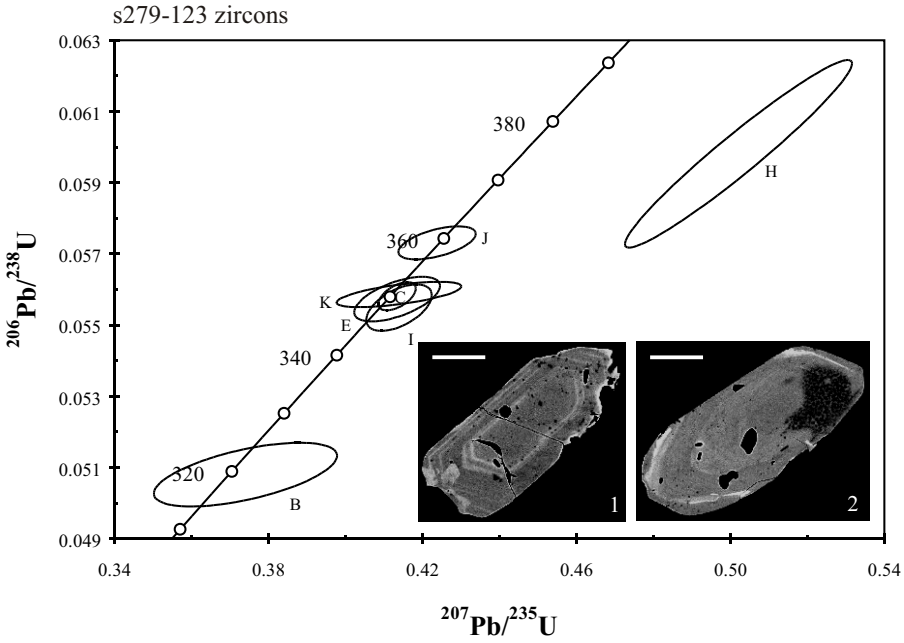

Fig. 7.4. Concordia plot for the Joss Mountain orthogneiss (s279-123) with two representative examples of zircon BSE images. See text for discussion. Dark part on the right side of zircon image 2 is dirt on the grain mount. Scale bars are 50 μm.

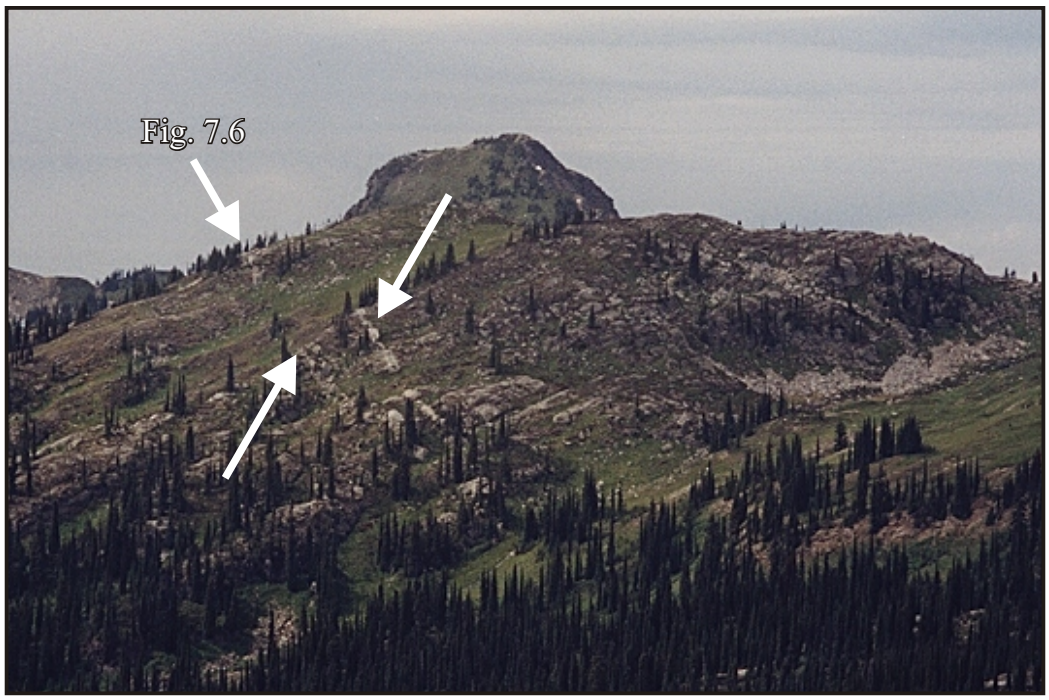

Fig. 7.5. Two E–W-trending pegmatite dykes (s298-4) crosscutting the Joss Mountain orthogneiss, marble and pelitic schists at Joss Mountain. Picture taken from the E side of Joss Mountain, looking to the WNW.



Fig. 7.6. Contact of the dated pegmatite (s298-4) at Joss Mountain, crosscutting the foliation in the host paragneiss. Viewing direction is down to the ENE. Compass for scale.

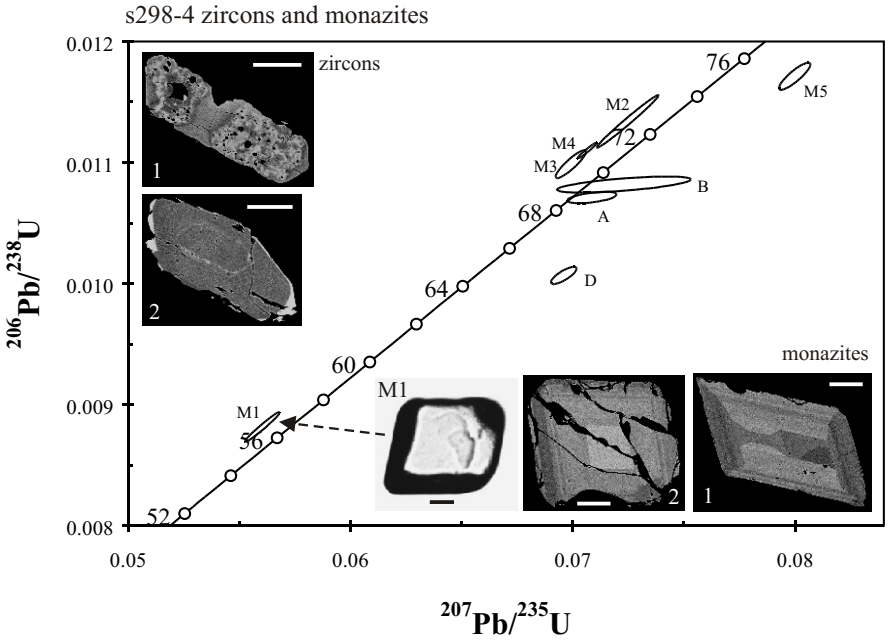

Fig. 7.7. Concordia plot and BSE images of zircons and monazites for the crosscutting pegmatite at Joss Mountain (s298-4). Numbering and grains of BSE images are not the same as the dated fractions. The photomicrograph of monazite M1 was taken in alcohol in a petri dish under a transmitting light microscope. All scale bars are 50 μm.

Chapter 8

Possibility of channel flow in the southern Canadian Cordillera; a new approach to explain existing data

Abstract

Existing structural, metamorphic and geochronological data in and close to the Shuswap Metamorphic Complex in the southern Canadian Cordillera are shown to be consistent with a channel flow model. Previously, ductile deformation was explained in terms of large scale thrusts or detachments, that were linked with brittle thrusts in the Rocky Mountains. These detachments required extensive displacement, and are incapable of explaining the penetrative ductile deformation throughout the Shuswap Metamorphic Complex. Ductile deformation involving large non-coaxial strain can explain the transposition that is characteristic of the high-grade rocks, and can transform discontinuities, such as unconformities and faults, into thrust-like structures, which do not necessarily have thrust-related displacement. The non-coaxial flow converts pre-existing folds, and coeval dragfolds, into isoclinal dismembered folds, as seen in the southern Omineca Belt. Up to three generations of such recumbent folds can be recognised (e.g. in the Monashee Complex). These recumbent folds are overprinted by one or more generations of late, upright to steeply inclined, generally post-metamorphic folds. All structures are modified by (Late Cretaceous?–)Early Tertiary crustal extension.

In the southern Omineca Belt, three general structural levels (domains) can be distinguished, based on the orientation and vergence of folds. In the lowest three levels

folds are mostly recumbent, whereas in the uppermost level they are upright. The lowest three levels may represent a channel flow zone (cf. Beaumont et al., 2001). NE-verging folds of the lowest level may have formed during top-to-the-NE detachment flow and/or in the lower part of a channel flow zone (the sense of shear would be the same in both; e.g. the Monashee Complex). When detachment flow changed to channel flow, the sense of shear changed in the upper part of the channel flow zone, causing overprinting of NE-verging folds by SW-verging folds (e.g. most parts of the Shuswap Metamorphic Complex). If temperature was increasing, it is conceivable that the channel flow zone widened. Therefore, in the highest structural levels within the channel flow zone, SW-verging folds developed in areas where no NE-verging folds exist (e.g. the Cariboo Mountains). Upright folds and the absence of recumbent folds in the highest structural level (the uppermost part of the Cariboo Mountains), above the channel flow zone, are a result of the crustal shortening that caused the non-coaxial strain at deeper structural levels.

The channel flow model as presented herein explains all ductile structures and accommodates existing metamorphic and geochronological data. Although this model may be inaccurate in detail, and may not be a unique solution, it demonstrates that there are different, and perhaps more reasonable ways, of explaining existing data. It is important that current interpretations are constantly reevaluated, and that new models are developed.

8.1. Introduction

Current tectonic models in the Canadian Cordillera involve large scale detachments near the base of the crust, beneath the Intermontane and Omineca Belts. In the Omineca Belt, a NE-directed detachment is drawn between the Monashee Complex (an exposure of ancestral North American rocks within the Omineca Belt; Fig. 8.1) and the overlying rocks of the Selkirk Allochthon. This detachment, the Monashee Décollement (e.g. Brown, 1980; Read and Brown, 1981; Journeay, 1986; and Brown et al., 1992, and references therein), was interpreted as outcropping along the west, north and south side of the Monashee Complex. It has been traced on seismic profiles and interpreted as being continuous with the basal décollement beneath the Rocky Mountain fold and thrust belt (e.g. Brown et al., 1992; Cook, 1995) (Fig. 8.1). Displacements on these large scale detachments is large. For example, Brown and Carr (1990, and references therein) inferred 100 km displacement on the Monashee Décollement and 100 km on the unexposed underlying basement thrusts, to accommodate the 200 km shortening in the Rocky Mountain Foreland Belt (Price and Mountjoy, 1970; Price, 1981).

Detailed field mapping by Johnston et al. (2000), Spark (2001), S. Kruse, P.D. McNeill and P.F. Williams (2003, unpublished data) failed to reveal any significant discontinuity that could be interpreted as a large scale detachment in the southern part of the Monashee Complex. Furthermore, models based on Rocky Mountain type thrusting do not explain isoclinal folds and transposition, which comprise the main deformation features (Kuiper and Williams, in preparation). Williams (1999) proposed that thrust-like structures may form by transposition of discontinuities, such as unconformities and faults. These structures have thrust geometry but do not necessarily have thrust-related

displacement (Williams, 1999). Williams and Jiang (in review) have proposed a model that is capable of explaining all ductile structures in the Monashee Complex, and is consistent with channel flow (see Section 8.2; cf. Beaumont et al., 2001). This model explains all early ductile structures in the Monashee Complex, and may require a smaller amount of crustal shortening for formation of these structures than previous models based on thrusting.

If channel flow can explain ductile structures and metamorphism in the Monashee Complex, it is expected to be applicable to the region surrounding the Monashee Complex in the southern Canadian Cordillera. This study, which is based on the literature as well as detailed research and mapping of the author and co-workers on the geology of Thor–Odin, tests the channel flow hypothesis for consistency with the geology of the studied areas in and close to the surrounding Shuswap Metamorphic Complex (Fig. 8.1). It is possible to fit the existing structural, metamorphic and geochronological data into a (channel flow) model that is different from currently accepted hypotheses, which are based on a Rocky Mountain type thrusting model. Furthermore, the channel flow model does not have the geometrical problems (see Kuiper and Williams, in preparation) that the earlier models have. The structural, metamorphic and geochronological data can be subject to interpretation, and the channel flow model presented herein needs to be tested in detail in specific areas by workers in those areas. The model may not be a unique solution for the studied part of the Shuswap Metamorphic Complex and surroundings, and it may be inaccurate in detail, but the fact that it applies to the existing data stresses the necessity to continuously reevaluate current hypotheses.

The theoretical model of channel flow as developed by Beaumont et al. (2001)

and the assignment of folding generations, as used in this study, are described in this section. Williams and Jiang's (in review) application of the model to the Monashee Complex is briefly reviewed in Section 8.2. The structural, metamorphic and geochronological data of the surrounding region (described by structural level in Section 8.3) are shown to be compatible with a general model for the southern Canadian Cordillera, based on channel flow (Section 8.6). In order to have a general idea of the model before reading about the detailed geology per structural level, the reader may wish to read Section 8.6 before Section 8.3.

8.1.1. Channel flow model

The channel flow model proposed by Beaumont et al. (2001) is based on coupled thermal-mechanical modelling of mid-crustal deformation. The model suggests that deformation in shortening crust, as a result of subduction, follows a predictable two stage evolution. After sufficient crustal thickening, involving upright folding (Fig. 8.2a), a thick detachment zone of non-coaxial flow develops within the weakest rocks of the middle crust (at amphibolite facies pressure, temperature, and fluid conditions) (Fig. 8.2b; Williams and Jiang, in review; cf. Beaumont et al., 2001). Fold vergence and sense of shear are expected to be towards the direction of transport. The crust continues to shorten, and the detachment zone evolves into a channel flow zone, which has a reverse sense of shear and fold vergence in its top part (Fig. 8.2c; Williams and Jiang, in review; Beaumont et al., 2001). At the centre of the channel, flow velocity is at a maximum. It is likely that the channel flow zone changes thickness, and that the rocks move with respect to the channel flow zone as the crust thickens and erodes. In that case, complicated

overprinting relationships may develop.

The timing of the transition from detachment to channel flow is controlled by the interplay between shortening rate and strength of the crust, which is essentially determined by temperature, pressure and the presence or absence of fluids including melts. During both detachment flow and channel flow, non-coaxial strain produces a horizontal transposition foliation, dragfolding, and shearing of inherited structures (Williams and Jiang, in review). Rocks above and in front of these zones of non-coaxial strain continue to shorten.

8.1.2. Fold generations

Thorough understanding of the formation of fold generations with time is essential in developing any model based on overprinting relationships of folds. By convention, fold generations are assigned on the basis of overprinting relationships (Hobbs et al., 1976). Commonly, it is implied that folds of one generation developed at the same time or as a result of one deformation event. However, several fold generations can develop at the same time or during one event (e.g. F_1, F_2, and F_3 folds form at T_3 at different locations; folds d_1, c_2 and a_3 in Fig. 8.3) and folds of one generation may have developed at different times in different places (e.g. F_1 folds form during T_1, T_2, and T_3 at different locations; folds a_1, c_1 and d_1 in Fig. 8.3). In the channel flow model (see below), different fold generations can develop at the same time (e.g. during detachment flow) and folds of the same generation can develop during different events (e.g. an F_1 fold can develop during detachment flow at one location, whereas an F_1 fold can form during channel flow in another location). To address this problem, in this chapter, detachment

flow folds (DFFs) and channel flow folds (CFFs) are referred to as the folds developed during detachment flow and channel flow respectively, irrespective of their generations. Where reference to previous literature is made, folds may be indicated by their generations as reported in literature, before they are assigned the terms DFF or CFF. Throughout this chapter different generations of folds, in various areas, correspond to either DFFs or CFFs (e.g. in one area F_2 folds are CFFs, whereas in another area F_3 folds are CFFs).

8.2. Deformation in the Monashee Complex explained by a channel flow model

Penetrative ductile deformation in the Monashee Complex, and a fold vergence reversal zone in northwest Thor–Odin (southern dome of the Monashee Complex; Fig. 8.1), have been explained by Johnston et al. (2000) by an extrusion model, and by Williams and Jiang (in review) in terms of the channel flow model. Furthermore, Williams and Jiang (in review) conclude that the Monashee Complex and the Selkirk Allochthon have been transposed penetratively, that the Monashee Décollement does not exist as a detachment, and that the original relationship between the Monashee Complex and Selkirk Allochthon is obscured by the transposition.

Tight to isoclinal F_1 folds in the Monashee Complex are interpreted both as folds predating detachment flow and as early dragfolds formed during detachment flow but predating channel flow. The isoclinal F_1 folds could have had any orientation initially, but were transposed during detachment and channel flow. Large scale fold nappes in the Monashee Complex (e.g. Reesor and Moore, 1971) are interpreted as pre-detachment F_1

folds (Williams and Jiang, in review).

NE-verging tight to isoclinal F_2 folds in the Monashee Complex and in overlying rocks that are part of the Shuswap Metamorphic Complex may be examples of DFFs, because their NE vergence is towards the flow direction (cf. Section 8.1.1). Alternatively, they could be CFFs in the lower part of the channel flow zone. The F_2 folds are interpreted as having formed as dragfolds during detachment or channel flow towards the NE, with fold axes rotating towards parallelism with the direction of non-coaxial flow (Williams and Jiang, in review).

Open to isoclinal F_3 folds show a vergence reversal along the west and SW side of the Monashee Complex (Figs. 8.2, 8.4). Vergence is NE on the NE side of this vergence reversal zone, and SW on the SW side, higher up in the structural sequence. This is consistent with channel flow being ongoing at the time of F_3 folding (cf. Section 8.1.1).

Metamorphism is upper amphibolite facies throughout most of the Monashee Complex (e.g. Journeay, 1986; Johnston et al., 2000). The high temperature metamorphic conditions would provide the low competency of the rocks required for channel flow (cf. Beaumont et al., 2001; Williams and Jiang, in review).

8.3. The channel flow model applied to the tectonic elements of the southern Omineca Belt

Part of establishing the validity of the channel flow model for the Monashee Complex is testing consistency of the model with the regional geology. The areas discussed are indicated in Fig. 8.1. The area east of the Southern Rocky Mountain

Trench (SRMT) is not discussed, because deformation occurred there at lower temperatures than in rocks west of the SRMT, and may not have been directly related to channel flow. The area west of the Okanagan–Eagle River Fault is not discussed; however, available information on that area is consistent with interpretations herein. The area surrounding the Valhalla Complex is not discussed in detail, because these rocks are Triassic–Jurassic low grade sedimentary and volcanic rocks, and intrusives, that were probably not involved in channel flow (perhaps comparable to Domain 4, see below).

In general, in all areas of amphibolite-facies metamorphism and transposition, NE-verging folds exist, which are interpreted here as DFFs or CFFs that formed in the lower part of the channel flow zone. Areas where these folds are overprinted by SW-verging CFF folds, or where only SW-verging folds are present (this is possible if the channel flow zone is thicker than the detachment flow zone), can be interpreted as having been originally at shallower structural levels (top half of the channel flow zone), than areas in which only NE-verging folds are present. Overprinting post-metamorphic upright or steeply inclined folds may have formed either at high structural levels, above the detachment zone or channel flow zone (in which case folds become less recumbent and formed under lower metamorphic conditions in going up the structural sequence), or after channel flow, during a separate event. Thus, where high grade rocks are present, isoclinal recumbent folds can be expected, and where low grade rocks are present, upright folds may have formed.

Within the area discussed in this chapter, four pre-extensional structural levels (or domains; Fig. 8.4) can be recognised, which are summarised in Section 8.6 and Fig. 8.5. In this section, structural, metamorphic and geochronological data are described and

discussed by domain. A summary of descriptions and interpretations is given in Table 8.1.

8.3.1. Domain 1: structures and metamorphism

In the Malton Gneiss, large scale SW-verging F_1 nappes are overprinted by NE-verging tight F_2 folds (Morrison, 1982). F_3 folds are tight and verge to the NE (Morrison, 1982). The Malton Gneiss has been interpreted as an imbricate stack of thrust slices of North American basement thrust towards the NE (Morrison, 1982; McDonough and Simony, 1988), similar to early interpretations of duplexing as part of the Monashee Décollement on the SW flank of the Monashee Complex (Brown et al., 1986; Coleman, 1989; McNicoll and Brown, 1995). These thrust slices were inferred from repetition of stratigraphy. The thrusts may actually be a result of transposition of earlier structures like the Monashee Décollement as proposed in Williams and Jiang (in review). Metamorphism reached kyanite–staurolite grade in the Malton Gneiss and sillimanite grade, up to 7.5 kbar and 700˚C, in the cover rocks above the Malton Gneiss (Morrison, 1982). NE vergence and high metamorphic facies conditions during F_2 and F_3 is consistent with the folds being DFFs, and/or CFFs developed in the lower part of the channel flow zone.

In the area south of Thor–Odin and north of the Pinnacles area (Carr, 1992), referred to herein as the Fosthall area (Fig. 8.1), D_1 and D_2 structures are equivalent to structures in the southern Monashee Complex. Geology of the Monashee Complex has been described and discussed in Section 8.2. The transposition foliation curves around the Monashee Complex, dipping to the south or SW, as does the vergence reversal zone

(Fig. 8.4). F_3 folds verge towards the north in the Fosthall area, north of Cusson Creek/Vidler Ridge (see Carr, 1991). Farther south, F_3 folds verge southwards (see Domain 2) and F_3 axes plunge shallowly west. Peak metamorphic amphibolite-facies conditions prevailed during F_2 and at least part of F_3 (Carr, 1991). The D_2 structures in the Fosthall area are interpreted herein as DFFs or early CFFs in the lower part of the channel flow zone. The F_3 folds are interpreted as CFFs in the lower part of the channel flow zone, based on their vergence reversal in Domain 2. D_1 structures could have formed during or before detachment and/or channel flow folding.

The Valhalla Complex, excluding the Palaeocene–Eocene granitoids that are present in it, is an exposure of deep structural levels, similar to the Monashee Complex. Metamorphism reached amphibolite facies within the Valhalla Complex, and metamorphism varies between chlorite, biotite and garnet grade in rocks above the Valkyr Shear Zone (VSZ) that structurally overlie the complex (Carr et al., 1987; Simony and Carr, 1997). In the Valhalla Complex, F_2 folds are overturned tight asymmetric folds. F_3 is coaxial with F_2 and plunges shallowly west to NW and verges E–NE at high structural levels in the paragneisses. F_3 axial planes dip west to SW (Schaubs and Carr, 1998; Schaubs et al., 2001). At lower levels, transposition is stronger and folds are rare (Schaubs and Carr, 1998). F_2 and F_3 folds postdate metamorphic mineral growth (Schaubs et al., 2001). The Gwillim Creek shear zone (e.g. Schaubs et al., 2001) is concordant with S_2. Movement on this shear zone was synchronous with F_2 and F_3 at higher structural levels in the complex, or outlasted folding (Schaubs et al., 2001). NE-verging F_3 folds overprint E–NE-verging F_2 folds. Therefore, F_2 and F_3 folds could be CFFs in the lower part of the channel flow zone. F_2 folds could also possibly be DFFs.

However, the interpretation that both folding events are post-metamorphic is not consistent with either interpretation.

8.3.2. Domain 1: timing of deformation

Brown et al. (1986) inferred deformation and deep burial of the Monashee Complex in the Jurassic, based on regional correlations and using balanced cross sections. Journeay (1986) recognised two pulses of deformation and metamorphism in Frenchman Cap. He related F_2 folds and 'related thrust faults' (transposition and DFFs or early CFFs in this study) to the first episode of upper plate to-the-east displacement (MD_1) on the Monashee Décollement. Metamorphism related to MD_1 (M_1) was upper amphibolite–lower granulite in the core of Frenchman Cap to middle amphibolite along the flanks of the dome. Journeay (1986) interpreted MD_1 and M_1 as being related to Middle Jurassic displacement between the Monashee Complex and the Selkirk Allochthon. He related F_3 folding (CFFs herein) to the second episode of upper plate to-the-east displacement on the Monashee Décollement (MD_2). M_2 (related to MD_2) was middle greenschist in the core of the complex, and upper amphibolite–lower granulite at higher structural levels. M_2 occurred at low pressure. MD_2, M_2 and F_3 are interpreted as being related to mid-Cretaceous regional deformation (Journeay, 1986). The inverted isograds during M_2 (Journeay, 1986) are consistent with channel flow being ongoing, because during channel flow isotherms are folded and become locally overturned (cf. Beaumont et al., 2001).

More recently, Cordilleran deformation and metamorphism in the Monashee Complex have been interpreted as occurring diachronously between 78 Ma at high

structural levels and 49 Ma at deep structural levels (Parrish, 1995, and references therein; Crowley and Parrish, 1999; Gibson et al., 1999). However, in Chapter 3, these ages are reinterpreted as representing extension; fluids infiltrating during extension caused resetting of $^{40}Ar/^{39}Ar$ hornblende ages and growth of monazite, titanite, xenotime and zircon. Peak of metamorphism and deformation must have been earlier. Detachment or channel flow (or in earlier models Cordilleran deformation) could well have started in the Middle Jurassic, an age previously proposed by Brown et al. (1986) and Journeay (1986) (see above), and an age of deformation east and north of the Shuswap Metamorphic Complex (Pigage, 1977; Archibald et al., 1983, 1984; Gerasimoff, 1988; Ferguson and Simony, 1991; Crowley and Brown, 1994; Colpron et al., 1996; Reid, 1999). Also during this time, the Intermontane Superterrane accreted to western North America (Monger et al., 1982; Murphy et al., 1995). NE-verging folds, related to transposition and to detachment flow folding, or to early channel flow folding, may have formed at this time. Channel flow probably continued until ~73 Ma, because F_3 folding at Joss Mountain (Fig. 8.1) is interpreted as occurring between ~73 and ~70 Ma (Kuiper et al., 2000; cf. Johnston et al., 2000), and because kyanite was still stable after 73 Ma in the Mica Creek area of the northern Shuswap Complex (Crowley et al., 2000; see below), except for the northernmost part, which was at slightly higher structural level (see below). The main stage of F_3 folding in the northern Shuswap Complex probably occurred in the mid-Cretaceous, when the Insular Superterrane accreted to western North America (Monger et al., 1982).

Middle Jurassic ages are not recorded within the Monashee Complex, and mid- to Late Cretaceous to Early Tertiary ages that are probably not related to extension-related

fluids (i.e. older than ~75–70 Ma, cf. Chapter 3) are rare. The only published ages are a 78 Ma monazite (Gibson, 1997), which is slightly discordant, and ~89 Ma $^{40}Ar/^{39}Ar$ inverse isochron ages (Spark, 2001; Chapter 3). Foster et al. (2002) report LA-MC-ICPMS $^{208}Pb/^{232}Th$ ages from one sample (DG136) in northern Frenchman Cap older than 100 Ma. However, the $^{207}Pb/^{206}Pb$ ages of each of the spots is older than the $^{208}Pb/^{232}Th$ ages and therefore the data are discordant. One grain in another sample (DG127mon10#4; Fig. 8f of Foster et al., 2002) yielded time-resolved data which show that the oldest age component in the sample could be as old as 100 Ma, but evidence is "sparsely documented" as "only 1 out of 15 in situ analyses was largely above 60 Ma" in that sample (Foster et al., 2002, p.196).

The reason for the lack of Middle Jurassic to ~75–70 Ma ages in the Monashee Complex is most likely that, over a long period of time, partial dissolution rather than growth occurred of the minerals used for U–Pb dating (cf. Chapter 5). Dissolved parts of the crystals migrated with the melts from the Monashee Complex (and also from unexposed rocks that were at a similar structural level as the Monashee Complex) and crystallized in the Middle Jurassic and mid-Cretaceous granitoids above the Monashee Complex, similar to the ones which are now present in rocks surrounding the complex (e.g. Archibald et al., 1983, 1984; Colpron et al., 1996). Because the different domains moved laterally with respect to each other (Section 8.6) melts from the Monashee Complex may have crystallised in areas that are now unexposed or eroded, and Middle Jurassic and mid-Cretaceous granitoids in the rocks that are now surrounding the Monashee Complex may have originated in Domain 1 levels that are currently unexposed. Dissolution in the Monashee Complex was not complete, because

Proterozoic zircon and monazite is present in the Monashee Complex (e.g. Armstrong et al., 1991; Parkinson, 1991; Crowley, 1997, 1999; Crowley and Ghent, 1999; Vanderhaeghe et al., 1999). This model will be discussed in more detail in Section 8.4. The absence of Devono-Mississippian plutons and mineral ages in the Monashee Complex may be explained in the same way.

The Gwillim Creek shear zones in the Valhalla Complex were active at some time between 110 and 51 Ma (Schaubs and Carr, 1998), and F_2 and F_3 are at least the same age (see above). Schaubs et al. (2002) interpret deformation as having taken place at ~70 Ma, based on ages of Spear and Parrish (1996) from monazite in a pelitic paragneiss and pelitic schists, zircon in anatectic leucosome, and monazite and zircon in a pegmatite that crystallised before the thermal peak of metamorphism. Although this may be a reasonable interpretation, the possibility that ~70 Ma zircon and monazite grew during extension (cf. Chapter 3) cannot be ruled out. Spear and Parrish (1996) argue, based on unpublished SHRIMP data, that Pb loss in monazite from the pelitic paragneiss gradually increases from the core to the rim of monazite grains, and that therefore diffusion was a main cause for discordance and not new growth. They argue "presuming that most of the Pb diffusion occurred at or close to the highest temperature, then the age of Pb loss must also be the age of the peak temperature" (Spear and Parrish, 1996, p.758). However, it is now known that Pb loss in monazite can take place by other mechanisms, e.g. (hydrothermal) alteration (Hawkins and Bowring, 1997; Braun et al., 1998; Poitrasson et al., 2000), for example during extension. Therefore, the movement on the Gwillim Creek shear zones and F_2 and F_3 deformation are not constrained to less than between 110 and 51 Ma (Schaubs and Carr, 1998) and could possibly be related to channel flow. The

rocks above the VSZ preserve Middle Jurassic and older structures (Carr et al., 1987). Also, they have been deformed and intruded by Middle Jurassic, mid-Cretaceous and Middle Eocene plutons (Carr et al., 1987; Simony and Carr, 1997, and references therein). They could be part of Domain 4. One distinctive aspect of the Valhalla Complex with respect to the Monashee Complex is the presence of Late Cretaceous and Palaeocene–Eocene plutons (e.g. Simony and Carr, 1997). This may indicate that the Valhalla Complex was at higher structural levels within Domain 1, during channel flow, and perhaps during detachment flow, than the Monashee Complex.

8.3.3. Domain 2: structures and metamorphism

The Shuswap Metamorphic Complex (Fig. 8.1) is defined herein as the area bounded by the Okanagan–Eagle River Fault (OERF), the Adams–North Thompson Fault (ANTF) and the SRMT, excluding the Monashee Complex and Malton Gneiss. It also includes the area south of the Malton Gneiss that is below the sillimanite isograd. The northern Shuswap Complex is defined herein as the area between the Monashee Complex and Malton Gneiss (Fig. 8.1). The southern Shuswap Complex is referred to as the part of the Shuswap Metamorphic Complex south of the northern Shuswap Complex, that is studied herein (Fig. 8.1) although the Shuswap Metamorphic Complex extends farther south than the studied area. In the northern Shuswap Complex, F_1 folds, such as the Scrip Nappe, are NW-trending SW-verging recumbent structures (Simony et al., 1980; Raeside and Simony, 1982; Sevigny and Simony, 1989). The interpretation of vergence and trend of these folds has been based on inverted stratigraphy, as the fold hinges are not exposed. The F_1 folds are folded by NE-verging tight F_2 folds with axial planes dipping

SW. F_3 axial surfaces are upright or steeply SW-dipping. The Mica Creek Antiform (and the Porcupine Creek Anticlinorium to the east) is interpreted as F_3 folds (Simony et al., 1980). Metamorphic facies in the northern Shuswap Complex varies from sillimanite–K-feldspar grade (~720°C and >7.34 kbar; Scammell, 1993) near the Monashee Complex to kyanite grade close to the Malton Gneiss (Digel et al., 1998; Crowley et al., 2000). F_3 folds deform the peak metamorphic isograds, whereas the F_2 folds are crosscut by these isograds (Simony et al., 1980; Raeside and Simony, 1982; Sevigny and Simony, 1989; Digel et al., 1998). F_2 folding was therefore pre-peak of metamorphism and F_3 largely post-peak of metamorphism. F_1 folding in the northern Shuswap Complex may have been pre-detachment flow. F_1 folds are completely transposed, which is consistent with high non-coaxial strain predicted by the channel flow model. F_2 folds are analogous to the F_2 folds in the Monashee Complex in their tightness and vergence (Table 8.1). Thus they could be DFFs, or CFFs in the lower half of the the channel flow zone. Post-metamorphic F_3 structures such as the Mica Creek Antiform (and the Porcupine Creek Anticlinorium and adjacent structures in the SRMT, see Simony et al., 1980), with upright or steeply dipping axial surfaces, indicate shortening at high structural levels during convergence and may be coeval with channel flow at lower levels. The F_3 structures probably formed above the channel flow zone (and/or possibly after channel flow during a separate event) because (1) there is no distinct vergence, (2) they formed after the peak of metamorphism (not during or before the peak of metamorphism as would expected if they were formed in the channel flow zone) and (3) the metamorphic facies during F_3 folding, was apparently not high enough for channel flow (cf. Beaumont et al., 2001; Williams and Jiang, in review). Thus, unlike F_3 folds in

the Monashee Complex, which are CFFs, F_3 structures in the northern Shuswap Complex are related to low-temperature shortening above the channel flow zone. Alternatively, the F_3 folds could have formed during a (later) separate event.

The area between Frenchman Cap, and the Okanagan–Eagle River Fault and the Adams–North Thompson Fault, was mapped in detail by Fyson (1970) and later by Johnson (1994). Rocks at deep structural levels, away from these faults and farther to the east, typically show tight NE-verging F_2 folds, consistent with detachment flow- or channel flow-related transposition structures, both in the Monashee Complex (cf. Williams and Jiang, in review) and in the northern Shuswap Complex. These folds are overprinted by moderately to steeply inclined, commonly overturned, W–SW-verging F_3 folds, which may have been CFFs, formed in the upper half of the channel flow zone. F_3 folds are overprinted by later discontinuous NW- and north-trending upright folds (late F_3 and F_4; Fyson, 1970). Upper amphibolite facies metamorphism was ongoing during NE-directed flow (Johnson, 1994; Johnson and Brown, 1996). Sillimanite grew before F_3 and was stable during F_3 (Johnson, 1994). The rocks in this area with SW-verging F_3 folds grade upward into rocks with upright to steeply SW-dipping F_3 axial surfaces, and lower metamorphic facies, in the northern Shuswap Complex (see above).

In the Pinnacles area, D_1 and D_2 structures, and metamorphic conditions, are the same as in the Fosthall area (see above). F_3 folds verge towards the south (south of Cusson Creek/Vidler Ridge; Carr, 1991; cf. Fig. 8.4).

8.3.4. Domain 2: timing of deformation

In the Mica Creek area the (latest) peak of metamorphism is interpreted as having

occurred at 100 Ma, based on zircon and monazite U–Pb ages from a foliated garnet–sillimanite-bearing peraluminous granite (Sevigny et al., 1990). This granite was generated by partial melting of a pelitic source at 700 ± 25°C and emplaced during F_2 at about 28 km depth (7.5 kbar, Sevigny et al., 1989). Emplacement during F_2 is based on the presence of a foliation coplanar with the regional metamorphic foliation. Scammell (1993) interprets compressional deformation, metamorphism and anatexis as occurring from ~135 until after ~97 Ma. In his model, based on thermochronology of monazite, titanite, hornblende, rutile, muscovite and apatite, thrust-parallel extension occurred between 100 and 94 Ma. Ca. 10 km of overburden was removed and cooling occurred around that time interval (during convergence). Subsequent extension occurred in the Eocene. Two-mica leucogranites formed at 135 ± 2 Ma, ~100–97 Ma, and 71–57 Ma. Sevigny et al. (1990) also report ages of metamorphism with errors overlapping ~75–70 Ma (e.g. oldest age is 77.1 ± 7.5 Ma). These are within the range of ages younger than ~75–70 Ma, which are herein interpreted as being related to extension-related fluids. However, ages could be older than ~75–70 Ma and not related to extension, based on Sevigny et al. (1990) alone.

Crowley et al. (2000) show ages between 175 and 50 Ma for the Mica Creek area, which is considered herein as part of the northern Shuswap Complex, which they interpret as indicating five different deformation events: 175–160, 140–120, 110, 100–90 and 75–50 Ma. However, the five deformation events as proposed in their paper are not really supported by the data (e.g. ages of between 160 and 140 Ma are present) and their data can be interpreted in many different ways, e.g. their data could fit a model of deformation and metamorphism in the Middle Jurassic (~175–160 Ma) and mid-

Cretaceous (100–90 Ma), and extension between ~75–70 and 50 Ma. Crowley et al. (2000) also report ages of deformation and metamorphism between 160 and 100 Ma, but if there was a gradual and continuous transition between Middle Jurassic F_2 deformation and Cretaceous F_3 deformation (see channel flow model, Williams and Jiang, in review), then it is not surprising that metamorphism and mineral growth occurred continuously. Monazite inclusions in kyanite are ~85–73 Ma, and therefore kyanite was probably still growing at 73 Ma (Crowley et al., 2000), consistent with F_3 and channel flow still being ongoing farther south at Joss Mountain and in the Monashee Complex.

Sevigny et al. (1989, 1990) interpret F_2 (rather than F_3) as being ongoing in the mid-Cretaceous. However, their interpretation is based on foliation in a 100 Ma granite parallel to the regional metamorphic foliation, which could perhaps have formed during later channel flow deformation. Also, in this chapter, F_3 folds in the northern Shuswap Complex are interpreted as having formed at high structural levels above the channel flow, which is inconsistent with temperatures still being high as proposed by Sevigny et al. (1989, 1990) and Scammell (1993) (see above). These contradictions remain unresolved.

West of the Monashee Complex, $^{40}Ar/^{39}Ar$ hornblende ages are interpreted as indicating cooling below the closure temperature for argon in hornblende between Late Palaeocene and Middle Eocene time (Johnson, 1994). Alternatively, these ages could be related to extension-related fluid activity.

8.3.5. Domain 3: structures and metamorphism

The Clachnacudainn Complex has predominantly SW-verging SE-plunging large

scale folds, interpreted by Crowley and Brown (1994) as F_2 folds. The axial planar S_2 foliation dips towards the NE. F_1 is inferred based on inclusion trails in garnets. F_3 folds are upright, open and ESE trending. F_4 is local and only represented by lineations. The polyphase structures continue to the east across the Standfast Creek Fault into the Illecillewaet Synclinorium (see Colpron et al., 1996). Metamorphism in the Clachnacudainn Complex was greenschist facies during D_1 and middle amphibolite during D_2 (and slightly lower along the Standfast Creek Fault). Five to ten km exhumation occurred between D_2 and D_3 (Crowley and Brown, 1994). Price (1986, 2000) interprets the Clachnacudainn terrane as being a tectonic wedge (also including rocks of the Selkirk Allochthon west of the Monashee Complex as well as the Quesnel terrane), which delaminated the overlying Kootenay Arc/Illecillewaet Synclinorium. This interpretation is based on a reversal in vergence of structures from NE in the east to SW in the west, farther west in the Selkirk Fan (see below), which Price (1986, 2000) attributes to extrusion at the tip of the wedge. In his model, the NE-verging thrust zone in the east eventually evolves into the basal décollement of the Rocky Mountain foreland fold and thrust belt. SW-verging thrusts, folds and fold nappes developed above the wedge (in the Illecillewaet Synclinorium and the Clachnacudainn Complex). In the model proposed herein, this wedge would be the channel flow zone. The wedge model requires a relatively rigid 'terrane' bounded by a top-to-the-west shear zone at the top, and a top-to-the-east shear zone at the bottom. The channel flow model explains the more ductile deformation that is evident in the rocks, and does not require two shear zones, but a zone of SW-verging folds representing the upper part of the channel flow zone and a zone of NE-verging folds representing the lower part (similar to structures on

the SW side of the Monashee Complex, see above). In the Clachnacudainn Complex, the SW-verging F_2 folds may be CFFs representing the higher part of channel flow. The centre of the channel flow would then have to be below the present day erosion surface, which seems consistent with the cross section drawn by Price (1986, p. 250). F_2 folds in the Clachnacudainn Complex would be analogous to F_3 folds in, and SW of, the Monashee Complex (in structural style, but not in timing, see Section 8.6). F_3 folding in the Clachnacudainn Complex occurred after cooling and exhumation. Thus, the F_3 folds would be a result of late compression, at a high structural level above the channel flow zone (during or after channel flow).

The Selkirk Fan is dominated by NE-dipping SW-verging F_2 folds in the SW, and SW-dipping NE-verging F_3 folds (Brown and Tippett, 1978), or F_2 and F_3 folds (Gibson et al., 2002), in the NE. A large scale recumbent F_1 nappe, the Goldstream Nappe, is believed to be east verging, based on reversals in stratigraphy (Brown and Tippett, 1978). More F_1 nappes are present both to the north (the Scrip Nappe, see above; F_1 fold nappes in the Cariboo Mountains, see below) and to the south in the Kootenay Arc (references in Brown and Tippett, 1978). In the Kootenay Arc, these F_1 nappes have been interpreted as being both east verging and west verging (Colpron et al., 1998, and references therein). Williams and Jiang (in review) explain that the original vergence of F_1 folds in the Monashee Complex cannot be determined, because they were transposed and therefore dismembered by subsequent F_2 folding and transposition. Therefore, units cannot be traced over long distances and vergence cannot be determined. Preservation of original F_1 fold vergence occurs only at higher structural levels, which were presumably less transposed (see also Murphy, 1987, and below). Regional metamorphism in the

Illecillewaet Synclinorium ranges from the chlorite zone at high structural levels to biotite and garnet zones at lower structural levels (Colpron et al., 1996), consistent with the Illecillewaet Synclinorium being at a higher structural level than the Monashee Complex during channel flow. Cooling and exhumation occurred during F_2 folding. F_2 folds probably formed in the upper part of channel flow (CFFs), similarly to F_2 in the Clachnacudainn Complex, but at a higher level. F_3 folds (and late F_2 folds on the east flank?; Gibson et al., 2002) may have resulted from compression at a high structural level above the channel flow zone, during and after extrusion of the rocks of the Selkirk Fan, and during or after channel flow.

The Cariboo Mountains are located NW of the northern Shuswap Complex. F_1 folds are E-verging metre-scale folds and F_2 folds verge SW (Reid et al., 2002). Murphy (1987) proposes a model to explain the transition from upright biotite-grade F_2 folds to near-recumbent kyanite–staurolite-grade NE-dipping SW-verging F_2 folds. Upright folds in this model result from boundary-parallel shortening at higher structural levels above the channel flow zone, whereas at lower structural levels, non-coaxial strain becomes important. The SW-verging folds in the Cariboo Mountains resulted from northeastward underthrusting of the North American continental plate margin, comparable to the wedge model of Price (1986, 2000). The highest grade of metamorphism in the Cariboo Mountains (at the deepest structural level) is in the garnet zone. SW-verging D_2 structures were pre-peak of metamorphism. F_3 folds are NW trending and NE verging, and were generally late or post-metamorphic (except for at the lowest structural levels, where a Cretaceous metamorphic overprint exists; Reid et al., 2003). F_3 folds can be interpreted as late compressional structures, formed either during channel flow at a level

above the channel flow zone, or after channel flow (similar to F_3 folds in the Selkirk Fan, see above). NE-trending F_4 warps and upright folds are also present. NW-trending F_1 nappe structures verge NE (Murphy 1987; Ferguson and Simony, 1991; Reid et al., 2002). Axial planar foliation (S_1) is apparent at shallow structural levels, but is almost completely transposed at deeper structural levels. These data are all consistent with the channel flow model, in a similar way to structures and metamorphism in the Clachnacudainn Complex and Selkirk Fan, described above. The deep structural levels, where the SW-verging near-recumbent folds are present, are at the same level as the Illecillewaet Synclinorium, and represent the top part of channel flow. Towards higher structural levels, SW-verging folds grade into upright folds, which are interpreted as a result of lateral compression above the channel flow zone. These highest structural levels did not experience detachment or channel flow and is referred to as Domain 4.

8.3.6. Domain 3: timing of deformation

Colpron et al. (1996) contend that the western flank of the Selkirk Fan was exhumed during development of SW-verging structures at deeper levels. The bulk of SW-verging structures in the Illecillewaet Synclinorium formed between ~173 and 168 Ma (based on the relationships between folding and the Fang and Tangier stocks; see Colpron et al., 1996), and cooling occurred around the same time (based on biotite and muscovite $^{40}Ar/^{39}Ar$ cooling ages). SW-verging fold nappe formation (F_2), and cooling, in the Clachnacudainn Complex are inferred to have occurred in the Middle Jurassic, based on correlations with the Illecillewaet Synclinorium (Crowley and Brown, 1994; Colpron et al., 1996). Metamorphism in the Clachnacudainn Complex in the middle and

Late Cretaceous was related to intrusion of granitoid plutons. $^{40}Ar/^{39}Ar$ ages are consistent with ages of Cretaceous plutonism and later extension (Colpron et al., 1999). For metamorphism to be at lower metamorphic facies than in the Monashee Complex, and for cooling/exhumation to occur in the Middle Jurassic, the Selkirk Fan including the Illecillewaet Synclinorium (and the Cariboo Mountains, see below), and the Clachnacudainn Complex at a deeper structural level, must have been exhumed or extruded during detachment or channel flow in the Monashee Complex. F_3 folds in the Clachnacudainn Complex and Illecillewaet Synclinorium (and in the Selkirk Fan) formed after the rocks were exhumed, during or after channel flow, and indicate compression at high structural level. However, Gibson et al.'s (2002) interpretation of the exhumation as not occurring until the mid-Cretaceous–Early Tertiary on the eastern flank of the Selkirk Fan is not consistent with this interpretation. Ages younger than ~75–70 Ma in the Clachnacudainn Complex are herein interpreted as being related to extension.

In the Cariboo Mountains, as in the Selkirk Fan, deformation occurred mainly in the Jurassic and not in the Cretaceous (Brown and Tippett, 1978; Murphy, 1987; Ferguson and Simony, 1991). F_2 folding in the Cariboo Mountains is older than 174 Ma, the age of the Hobson Lake Pluton (Gerasimoff, 1988; Ferguson and Simony, 1991; Reid, 1999; Reid et al., 2002). Pigage (1977) constrained F_2 folding to between the Upper Triassic and the Upper Jurassic by Rb–Sr dating of granodiorite intrusions. In the Illecillewaet Synclinorium (and Selkirk Fan), exhumation, fast cooling and SW-verging (F_2) folding took place in the Jurassic (Colpron et al. 1996; see above). Similarly, exhumation of the Cariboo Mountains (and also the Kootenay Arc) could have been related to Middle Jurassic F_2 folding.

F_2 folds in the northern Shuswap Complex predate metamorphism and F_3 folds postdate metamorphism, as in the Cariboo Mountains (and in the Selkirk Fan and Clachnacudainn Complex). However, in the northern Shuswap Complex, Middle Jurassic as well as Cretaceous ages of metamorphism and deformation, are preserved. Preservation of Cretaceous ages probably indicates that these rocks were at a deeper structural level for a longer time than the rocks in the Cariboo Mountains and underwent the middle to Late Cretaceous deformation (channel flow folding at deeper levels). This interpretation is consistent with this area being part of Domain 2.

In the Selkirk Fan and in the Cariboo Mountains, Cretaceous plutons are present, which suggests that Cretaceous deformation (channel flow) and melting occurred at lower levels (similar to the Monashee Complex) in those areas. Colpron et al. (1996) report that 110–90 Ma plutons crosscut all structures in the Illecillewaet Synclinorium. This interpretation is consistent with interpretations by Archibald et al. (1983, 1984). They conclude that in the Kootenay Arc, late-synkinematic to post-kinematic granodioritic plutons were emplaced in Middle Jurassic time (170–165 Ma) during amphibolite facies regional metamorphism. Mid-Cretaceous (~100 Ma) plutons were emplaced in a "tectonically dormant suprastructure" (Purcell Anticlinorium), accompanying renewed heating, deformation and metamorphism in the "deepest levels of an evolving infrastructure" (Kootenay Arc; Archibald et al., 1984, p. 567). The Kootenay Arc forms the western flank of the Selkirk Fan/Purcell Anticlinorium. The Porcupine Creek Anticlinorium farther to the east is separated from the Selkirk Fan/Purcell Anticlinorium by the Purcell Fault.

8.4. Granitoid migration

As noted in Section 8.3, the deepest structural levels (Domain 1), below the vergence reversal zone, are devoid of Devono-Mississippian, Middle Jurassic and mid-Cretaceous plutons (with the exception of the Valhalla Complex, which has mid- to Late Cretaceous plutons; Carr et al., 1987). The reason is probably that rocks of Domain 1 were still too deep at the times of deformation and/or granite formation for granitoid crystallisation. During channel flow, melts may have formed within (and below) these deep areas, but then migrated upward and crystallised in the overlying rocks (Domains 2, 3), leaving rocks of Domain 1 relatively dry but migmatitic (e.g. the Monashee Complex) (cf. Kuiper, 2002). Minerals (e.g. zircon, monazite, titanite, xenotime) used for U–Pb dating that grew at earlier times in Domain 1 (e.g. Proterozoic in the Monashee Complex; Armstrong et al., 1991; Parkinson, 1991; Crowley, 1997, 1999; Crowley and Ghent, 1999; Vanderhaeghe et al., 1999) dissolved partly or completely, and their dissolved parts migrated up with these melts to crystallise in the overlying rocks. Some undissolved parts are now present as old (e.g. Proterozoic) cores in minerals. During extension, granitoids (Ladybird and Coryell suites; Carr et al., 1987; Carr, 1992; Simony and Carr, 1997) probably formed by decompressional melting and crystallised at levels that are at the present day erosional surface.

The model of granitoid migration is consistent with models proposed for the Himalayas (e.g. Beaumont et al., 2001; Grujic et al., 2002). A channel flow model has been proposed by Beaumont et al. (2001) and Grujic et al. (2002), with channel flow and extrusion occurring towards the south, between the Main Central Thrust and the South

Tibetan Detachment, within the Greater Himalayan Sequence. Migmatites form within the channel flow zone, whereas leucogranites are more abundant in the top half of the channel flow zone or the upper Greater Himalayan Sequence, and above the channel flow zone boundary or South Tibetan Detachment (e.g. Coleman, 1998; Beaumont et al., 2001; Grujic et al., 2002). Coleman (1998) proposed that the leucogranites are related to the migmatites below, based on proximity and timing.

For the model of the southern Canadian Cordillera to be possible, the chemistry of Jurassic and Cretaceous (and perhaps Devono-Mississippian) granitoids needs to be consistent with an origin from rocks similar to those of the Monashee Complex (i.e. Proterozoic North American crustal rocks), with possibly some input from the mantle. Eocene granitoid suites may have a larger mantle component, and/or they may have a crustal source. Sr and Nd isotopes serve the purpose of tracing the origin of the granitoids well. Additional information can be derived from inherited material (e.g. zircon) and petrological composition of the granitoids. The origin of Devono-Mississippian granitoids has not been discussed in the literature. In this section the origins of Jurassic–Eocene granitoids is reviewed.

8.4.1. Origin of granitoids

8.4.1.1. Origin of Middle–Late Jurassic granitoids

In the Middle Jurassic, from west to east, the first crustally contaminated granitoids with negative ϵ_{Nd} values (–9.1 to –1.1) and initial $^{87}Sr/^{86}Sr$ ratios greater than

0.704 (alkalic and calc-alkalic intrusives) occur within the Omineca Belt east of Okanagan Lake (Fig. 8.1; Ghosh, 1995a; $^{87}Sr/^{86}Sr$ = 0.704–0.712, Armstrong, 1988). Furthermore, they show Early Proterozoic zircon inheritance, and some contain muscovite crystals (Armstrong, 1988; Ghosh, 1995a), both of which indicate (partial) derivation from the crust. Intrusive rocks around and west of Okanagan Lake did not show crustal contamination, suggesting absence of old crustal basement in that area. Based on geochemical and Nd isotopic data from Triassic metasedimentary rocks in southern Quesnellia (which lies within the Intermontane Superterrane; Monger et al., 1991; cf., Fig. 8.1), Unterschutz et al. (2002) concluded that crustal contamination from old North American continental rocks occurred earlier (Triassic), and farther west (west of Kootenay Lake).

8.4.1.2. Origin of Cretaceous granitoids

Cretaceous granites east of Okanagan Lake are mantle derived and have high to moderate degrees of crustal contamination (ϵ_{Nd} = –8.5 to 2.4 and $^{87}Sr/^{86}Sr$ = 0.704 to 0.7094; Brandon and Lambert, 1993; Ghosh, 1995a). $^{87}Sr/^{86}Sr$ is up to 0.730 in the Omineca Belt, which means that these magmas involved large percentages (approximating 100%) of older crust, and a mantle component may not be involved (Armstrong, 1988). Many show S-type characteristics and enrichment in Al and K (Armstrong, 1988). Furthermore, the presence of biotite, muscovite and garnet in the granites, and to a lesser extent hornblende, indicates crustal contamination of the granites (Ghosh, 1995a). Based on Sr and Nd isotopic data, Brandon and Lambert (1993) interpret mid-Cretaceous granitoids as having formed largely due to melting of

Precambrian crustal basement gneisses and Proterozoic metapelites in the Kootenay Arc. Peraluminous ~100 Ma granites in the northern Monashee Mountains have high $^{87}Sr/^{86}Sr$ ratios (0.71492–0.72786) and inherited Precambrian zircons (Sevigny et al., 1989; Kyser et al., 1994), further supporting evidence for a Precambrian crustal source. Rocks west of Okanagan Lake do not show crustal contamination.

8.4.1.3. Origin of Palaeocene–Eocene granitoids

The leucogranite Ladybird suite and Coryell syenites have very low negative ϵ_{Nd} values (–13.7 to –6.8) and high $^{87}Sr/^{86}Sr$ ratios (0.7071 to 0.7095), suggesting that these rocks were mainly a result of crustal melting of a model 1.8 Ga old sialic crust in the case of the Ladybird suite, or incorporation of old crustal materials in more primitive possibly mantle derived magma in the case of the Coryell syenites (Ghosh, 1995a, b). Alkalic magmatism and biotite–hornblende granite intrusion in the Palaeocene and Eocene suggest that more primitive magma was also present. Peraluminous ~63 Ma granites in the northern Monashee Mountains have high $^{87}Sr/^{86}Sr$ ratios (0.71533–0.74181) and inherited Precambrian zircons (Sevigny et al., 1989; Kyser et al., 1994), supporting a Precambrian crustal source.

8.4.2. Consistency with the model presented in this chapter

The incorporation of more and more crustal material and less primitive mantle material from the Early Jurassic until the Late Cretaceous supports thickening and melting of the crust (during detachment and/or channel flow). The zone of thickened

crust became wider from the Jurassic to the Cretaceous (cf. Armstrong, 1988; Ghosh, 1995a). Early Proterozoic crust (e.g. the Monashee Complex) being a source for Middle Jurassic and Cretaceous plutons in the Omineca Belt is consistent with the model presented herein, in which melts migrated up from the Monashee Complex at those times, while detachment/channel flow was ongoing. Renewed input of primitive melts in the Palaeocene and Eocene is consistent with extension (and erosion) being ongoing around that time. Continued thickening would have resulted in further increase in crustal contamination. Extension is a reasonable cause for decompressional melting of (Early Proterozoic) crust, with simultaneous input from the mantle.

8.5. Exposure of structural levels in the southern Canadian Cordillera

Domains 1 and 2 (Fig. 8.4) are now exposed within the Shuswap Metamorphic Complex, as a result of movement on late normal faults, late folding and erosion, which are thought to have occurred after channel flow. The lowest structural levels, coinciding with the highest levels of metamorphism, are exposed within the Malton Gneiss, the Valhalla Complex and the Monashee Complex, and within the area that lies SW of the Monashee Complex but NE of the fold vergence reversal zone (Fig. 8.4). They are exposed by normal faults such as the Columbia River Fault (CRF), the ANTF and the Slocan Lake Fault (SLF), and the extensional VSZ. Along the western flank of Frenchman Cap, normal faults have not been mapped. However, the presence of N–S trending lineaments, which are related to faulting along the western flank of Thor–Odin, suggest that faults may be present along the western flank of Frenchman Cap. The only

location where the transitional boundary between Domains 1 and 2 is exposed, is the fold vergence reversal zone, SW of the Monashee Complex (Fig. 8.4). It can be traced south of Thor–Odin in the Selkirk Allochthon, towards the western flank of Thor–Odin, east of Joss Mountain (Fig. 8.4, cf. Johnston et al., 2000), where it ends, probably because it is obscured by later extension.

Domain 2 is exposed by the CRF, OERF and ANTF. SW-verging F_3 folds grade northward into upright to steeply SW-dipping F_3 folds, and metamorphic conditions become lower, in the northern Shuswap Complex, indicating a gradation towards shallower structural levels to the north. This gradation is probably exposed by movement on the North Thompson and the Columbia River faults. Movement on the North Thompson Fault is interpreted as being mainly dip-slip and west-side-down, because there is no strike separation of metamorphic highs and lows across the fault, and the metamorphic conditions are lower west of the fault in the Cariboo Mountains than east of the fault in the northern Shuswap Complex (Digel et al., 1998). Similarly, movement on the CRF can be interpreted as being mainly dip-slip and east-side-down, because the northern Selkirk Mountains are at lower metamorphic facies than the northern Shuswap Complex to the west. However, in the north, the structural and metamorphic levels appear to be similar in the two areas, which can be explained by the ending of the CRF in that area (see regional geology maps by Digel et al., 1998; Crowley et al., 2000). The highest grade in the northern Shuswap Complex is sillimanite–K-feldspar, and in the Selkirk and Cariboo Mountains it is sillimanite. Towards the north, rocks in all three areas trend towards lower grades (kyanite ± staurolite, and garnet zones; see Digel et al., 1998; Crowley et al., 2000, and references therein), and therefore shallower structural

levels. Structural levels within Domain 2 are probably higher towards the south, away from the fold vergence reversal zone. The Cariboo and Selkirk Mountains (as well as the Porcupine Creek Anticlinorium) expose the highest structural levels (Domain 3, Fig. 8.4).

8.6. Geological model

Four pre-extensional structural levels can be recognised in the southern Omineca Belt (Fig. 8.4). The following description is general and may be inaccurate in detail for some areas. Domain 1: the deepest structural level below the F_3 vergence reversal zone in the Shuswap Metamorphic Complex, where both DFFs and CFFs are NE verging, and where the metamorphism was upper amphibolite facies during both folding events. Areas are the Monashee Complex, Valhalla Complex and Malton Gneiss (Figs. 8.4, 8.5). Domain 2: the structural level immediately above the F_3 vergence reversal zone within the Shuswap Metamorphic Complex (Figs. 8.4, 8.5), where DFFs or early CFFs are NE verging and later CFFs are SW verging and where both deformation events occurred during upper amphibolite facies metamorphism. Domain 3: the structural level that shows SW-verging channel flow structures at (lower) amphibolite facies (Selkirk Fan and related areas; the Illecillewaet Synclinorium, Clachnacudainn Complex and Cariboo Mountains; Figs. 8.4, 8.5). Domain 4: the highest structural level, with upright folds that developed above the channel flow zone (Fig. 8.4). All levels have post-metamorphic upright or steeply inclined folds. The northernmost part of the Shuswap Metamorphic Complex shows NE-verging DFFs or CFFs overprinted by post-metamorphic late upright folds (Fig. 8.5).

The earliest indications for channel flow are SW-verging folds in Domain 3, which formed in the Middle Jurassic. At that time, NE-verging folds may already have started forming in Domains 1 and 2, in the lower part of the channel flow zone, or (partly) in the earlier existing detachment flow zone. In the mid-Cretaceous, upright post-metamorphic folds formed in Domain 3. In Domain 2, SW-verging folds formed, while in Domain 1 NE-verging folds formed. This suggests that the domains moved upward with respect to the channel flow zone, with Domain 3 moving out of the channel flow zone and Domain 2 moving from the lower part of the zone to the upper part. Domain 1 remained in the lower part of the zone. Channel flow structures were overprinted by folds that formed above the channel flow zone in all domains. Rocks moving upward with respect to the channel flow zone can be achieved by erosion, or thinning or downward movement of the channel flow zone. Rocks moving up through different parts of the channel flow zone (possibly combined with thinning of the zone) is more likely than thinning of the zone alone, because high structural levels (Domain 3) were probably exhumed in the Middle Jurassic and moved from the SW-verging zone (upper part of channel flow) to levels above the channel flow zone (see above). Lower structural levels (Domains 1 and 2) continued flowing towards the NE. This implies that the parts of Domains 1 and 2 that are exposed now (e.g. the Monashee Complex) occurred farther west of the exposed parts of Domain 3 (e.g. the Selkirk Fan) in the Middle Jurassic than they do today or in the Cretaceous. The eastern-most indication for channel flow is the unexposed zone below the Clachnacudainn Complex and Illecillewaet Synclinorium (Section 8.3.5).

Fig. 8.3 summarises fold overprinting relationships that develop according to the

geological model presented in this chapter. During detachment flow (pre-Middle Jurassic?), NE-verging folds may have formed in Domains 1 and 2. During channel flow, (Middle Jurassic) SW-verging folds developed in Domain 3, while NE-verging folding started or continued in Domains 1 and 2. Later during channel flow, in the mid- to Late Cretaceous, NE-verging folds were overprinted by NE-verging folds in Domain 1, and by SW-verging folds in Domain 2. To explain SW-verging folds in Domain 3, and the absence of earlier NE-verging folds, the channel flow zone in the Middle Jurassic has been drawn thicker than the detachment zone before that time (Fig. 8.3). Thickening of the channel flow zone is consistent with an increase in temperature, as is expected during thickening of the tectonic pile. In the Cretaceous, rocks moved upward with respect to the channel flow zone, due to further thickening and erosion, explaining the development of upright or steeply inclined, post-metamorphic folds, overprinting SW-verging older folds, in Domain 3. The same effect can result from the channel flow zone either thinning, or moving downward, or a combination of both.

8.7. Conclusions

(1) Most of the structural, metamorphic, and geochronological data in the southern Omineca Belt are consistent with a channel flow model (Beaumont et al., 2001), as proposed by Williams and Jiang (in review) for the Monashee Complex.

(2) The channel flow model explains why: (a) the deepest structural level only shows NE-verging structures (possibly from detachment flow, and more certainly from subsequent deformation in the lower part of the channel flow zone), intermediate structural levels

show NE-verging structures (from detachment flow, and/or deformation in the lower part of the channel flow zone) overprinted by SW-verging structures (from deformation in the upper half of the channel flow zone), and the highest levels show only SW-verging structures, (b) SW-verging structures are never overprinted by NE-verging structures, (c) the highest metamorphic facies conditions are at the lowest structural levels, (d) high structural levels cooled before low structural levels.

(3) The Monashee Complex is the deeper basement to the Selkirk Allochthon, which is interpreted to be not allochthonous. The boundary between them is gradational and its original nature is obscured by transposition.

(4) Channel flow probably occurred mainly between the Middle Jurassic and the mid- to Late Cretaceous. It occurred probably at younger ages towards lower structural levels (from Middle Jurassic to mid-Cretaceous), because the boundary moved downward relative to the rocks through the time. Detachment flow, and possibly channel flow, may have started before the Middle Jurassic. (5) The absence of Devono-Mississippian, Middle Jurassic, and mid-Cretaceous granitoids at the deepest structural levels can be explained by melts originating in these zones and moving upward.

(6) Minerals used for U–Pb dating, which grew earlier (e.g. in the Proterozoic), may have been partly dissolved, and new mineral growth and overgrowth did not take place at the deepest structural levels, explaining the absence of Devono-Mississippian, Middle Jurassic, and mid-Cretaceous U–Pb ages at the deepest structural levels.

References

Archibald, D.A., Glover, J.K., Price, R.A., Farrar, E., Carmichael, D.M., 1983.

Geochronology and tectonic implications of magmatism and metamorphism, southern Kootenay Arc and neighbouring regions, southeastern British Columbia. Part I: Jurassic to mid-Cretaceous. Canadian Journal of Earth Sciences 20: 1891–1913.

Archibald, D.A., Krogh, T.E., Armstrong, R.L., Farrar, E., 1984. Geochronology and tectonic implications of magmatism and metamorphism, southern Kootenay Arc and neighbouring regions, southeastern British Columbia. Part II: Mid-Cretaceous to Eocene. Canadian Journal of Earth Sciences, 21: 567–583.

Armstrong, R.L., 1988. Mesozoic and early Cenozoic magmatic evolution of the Canadian Cordillera. Geological Society of America Special Paper 218, 55–91.

Armstrong, R.L., Parrish, R.R., van der Heyden, P., Scott, K., Runkle, D., 1991. Early Proterozoic basement exposures in the southern Canadian Cordillera: core gneiss of Frenchman Cap, Unit I of the Grand Forks Gneiss, and the Vaseaux Formation. Canadian Journal of Earth Sciences 28, 1169–1201.

Beaumont, C., Jamieson, R.A., Nguyen, M.H., Lee, B., 2001. Mid-crustal channel flow in large hot orogens: results from coupled thermal-mechanical models. In: Cook, F., Erdmer. P. (Compilers), 2001, Slave–Northern Cordillera Lithospheric Evolution (SNORCLE) Transect and Cordilleran Tectonics Workshop Meeting (February 22–25), Pacific Geoscience Centre, Lithoprobe Report No. 79, 112–170.

Brandon, A.D., Lambert, R.StJ., 1993. Geochemical characterization of mid-Cretaceous granitoids of the Kootenay Arc in the southern Canadian Cordillera. Canadian Journal of Earth Sciences 30, 1076–1090.

Braun, J., Montel, J.M., Nicollet, C., 1998. Electron microprobe dating of monazite from high-grade gneisses and pegmatites of the Kerala Khondalite Belt, southern India. Chemical Geology 146, 65–85.

Brown, R.L., 1980. Frenchman Cap dome, Shuswap complex, British Columbia: a progress report. In: Current Research, Part A, Geological Survey of Canada, Paper 80-1A, 47–51.

Brown, R.L., Carr, S.D., 1990. Lithospheric thickening and orogenic collapse within the Canadian Cordillera. Proceedings of the Pacific Rim ‘90 Congress, Brisbane, Australia, Australasian Institute of Mining and Metallurgy 2, 1–10.

Brown R.L., Tippett, C.R., 1978. The Selkirk fan structure of the southeastern Canadian Cordillera. Geological Society of America Bulletin 89, 548–558.

Brown, R.L., Carr, S.D., Johnson, B.J., Coleman, V.J., Cook, F.A., Varsek, J.L., 1992. The Monashee décollement of the southern Canadian Cordillera: a crustal-scale shear zone linking the Rocky Mountain foreland belt to lower crust beneath accreted terranes. In: McClay, K.R. (Editor), Thrust Tectonics. Chapman and Hall, London, UK, pp. 357–364.

Brown, R.L., Journeay, J.M., Lane, L.S., Murphy, D.C., Rees, C.J., 1986. Obduction, backfolding, and piggyback thrusting in the metamorphic hinterland of the southeastern Canadian Cordillera. Journal of Structural Geology 8, 255–268.

Carr, S.D., 1991. Three crustal zones in the Thor–Odin – Pinnacles area, southern Omineca Belt, British Columbia. Canadian Journal of Earth Sciences 28, 2003–2023.

Carr, S.D., 1992. Tectonic setting and U–Pb geochronology of the early Tertiary Ladybird leucogranite suite, Thor–Odin – Pinnacles area, southern Omineca Belt, British Columbia. Tectonics 11, 258–278.

Carr, S.D., Parrish, R.R.., Brown, R.L., 1987. Eocene structural development of the Valhalla complex, southeastern British Columbia. Tectonics 6, 175–196.

Coleman, M..E., 1998. U–Pb constraints on Oligocene–Miocene deformation and anatexis within the central Himalaya, Marsyandi Valley, Nepal. American Journal of Science 298, 553–571.

Coleman, V.J., 1990. The Monashee décollement at Cariboo Alp and regional kinematic indicators, southeastern British Columbia. MSc Thesis, Carleton University, Ottawa, Ontario, Canada.

Colpron, M., Price, R.A., Archibald, D.A., Carmichael, D.M., 1996. Middle Jurassic exhumation along the western flank of the Selkirk fan structure: Thermobarometric and thermochronometric constraints from the Illecillewaet synclinorium, southeastern British Columbia. Geological Society of America Bulletin 108, 1372–1392.

Colpron, M., Warren, M.J., Price, R.A., 1998. Selkirk fan structure, southeastern Canadian Cordillera: Tectonic wedging against an inherited basement ramp. Geological Society of America Bulletin 110, 1060–1074.

Colpron, M., Price, R.A., Archibald, D.A., 1999. $^{40}Ar/^{39}Ar$ thermochronometric constraints on the tectonic evolution of the Clachnacudainn complex, southeastern British Columbia. Canadian Journal of Earth Sciences 36, 1989–2006.

Cook, F.A., 1995. Lithospheric processes and products in the southern Canadian Cordillera: a Lithoprobe perspective. Canadian Journal of Earth Sciences 32, 1803–1824.

Crowley, J.L., 1997. U–Pb geochronologic constraints on the cover sequence of the Monashee complex, Canadian Cordillera: Paleoproterozoic deposition on basement. Canadian Journal of Earth Sciences 34, 1008–1022.

Crowley, J.L., 1999. U–Pb geochronologic constraints on Paleoproterozoic tectonism in the Monashee complex, Canadian Cordillera: elucidating an overprinted geologic

history. Geological Society of America Bulletin 111, 560–577.

Crowley, J.L., Brown, R.L., 1994. Tectonic links between the Clachnacudainn terrane and Selkirk allochthon, southern Omineca Belt, Canadian Cordillera. Tectonics 13, 1035–1051.

Crowley, J.L., Ghent, E.D., 1999. An electron microprobe study of the U–Th–Pb systematics of metamorphosed monazite: the role of Pb diffusion versus overgrowth and recrystallization. Chemical Geology 157, 285-302.

Crowley, J.L., Parrish, R.R., 1999. U–Pb isotopic constraints on diachronous metamorphism in the northern Monashee complex, southern Canadian Cordillera. Journal of Metamorphic Geology 17, 483–502.

Crowley, J.L., Ghent, E.D., Carr, S.D., Simony, P.S., Hamilton, M.A., 2000. Multiple thermotectonic events in a continuous metamorphic sequence, Mica Creek area, southeastern Canadian Cordillera. Geological Materials Research 2, 1–45.

Crowley, J.L., Brown, R.L., Parrish, R.R., 2001. Diachronous deformation and a strain gradient beneath the Selkirk allochthon, northern Monashee complex, southeastern Canadian Cordillera. Journal of Structural Geology 23, 1103–1121.

Digel, S.G., Ghent, E.D., Carr, S.D., Simony, P.S., 1998. Early Cretaceous kyanite–sillimanite metamorphism and Paleocene sillimanite overprint near Mount Cheadle, southeastern British Columbia: geometry, geochronology, and metamorphic implications. Canadian Journal of Earth Sciences 35, 1070–1087.

Ferguson, C.A., Simony, P.S., 1991. Preliminary report on structural evolution and stratigraphic correlations, northern Cariboo Mountains, British Columbia. Geological Survey of Canada, Paper 91-1A, 103–110.

Foster, G., Gibson, H.D., Parrish, R.R., Horstwood, M., Fraser, J., Tindle, A., 2002. Textural, chemical and isotopic insights into the nature and behaviour of metamorphic monazite. Chemical Geology 191, 183–207.

Fyson, W.K., 1970. Structural relations in metamorphic rocks, Shuswap Lake area, British Columbia. In: Wheeler, J.O. (Editor), Structure of the southern Canadian Cordillera. Geological Association of Canada Special Paper 6, 107–122.

Gerasimoff, M.D., 1988. The Hobson Lake pluton, Cariboo Mountains, British Columbia, and its significance to Mesozoic and early Cenozoic Cordilleran tectonics. MSc Thesis, Queen's University, Kingston, Ontario, Canada.

Ghosh, D.K., 1995a. Nd–Sr isotopic constraints on the interactions of the Intermontane Superterrane with the western edge of North America in the southern Canadian Cordillera. Canadian Journal of Earth Sciences 32, 1740–1758.

Ghosh, D.K., 1995b. U–Pb geochronology of Jurassic to early Tertiary granitic intrusives from the Nelson–Castlegar area, southeastern British Columbia, Canada. Canadian Journal of Earth Sciences 32, 1668–1680.

Gibson, H.D., 1997. Thermotectonic evolution of the northern Monashee complex, southern Omineca Belt, southeastern British Columbia. MSc Thesis, Carleton University, Ottawa, Ontario, Canada.

Gibson, H.D., Brown, R.L., Parrish, R.R., 1999. Deformation-induced inverted metamorphic field gradients: an example from the southeastern Canadian Cordillera. Journal of Structural Geology 21, 751–767.

Gibson, H.D., Brown, R.L., Carr, S.D., 2002. Tectonic Evolution of the Selkirk Fan: A Composite Middle Jurassic – Cretaceous Structure, Northern Selkirk Mountains, Southern British Columbia. In: Cook, F., Erdmer, P. (Compilers), 2002, Slave–Northern Cordillera Lithospheric Evolution (SNORCLE) Transect and Cordilleran Tectonics Workshop Meeting (February 21–24), Pacific Geoscience Centre, Lithoprobe Report No. 82, 127–128.

Grujic, D., Hollister, L.S., Parrish, R.R., 2002. Himalayan metamorphic sequence as an orogenic channel: insight from Bhutan. Earth and Planetary Science Letters 198, 177–191.

Hawkins, D.P., Bowring, S.A., 1997. U–Pb systematics of monazite and xenotime: case studies from the Paleoproterozoic of the Grand Canyon, Arizona. Contributions to Mineralogy and Petrology 127, 87–103.

Hobbs, B.E., Means W.D., Williams, P.F., 1976. An Outline of Structural Geology. Wiley, New York.

Johnson, B.J., 1994. Structure and tectonic setting of the Okanagan Valley fault system in the Shuswap Lake area, southern British Columbia. PhD Thesis, Carleton University, Ottawa, Ontario, Canada.

Johnson, B.J., Brown, R.L., 1996. Crustal structure and early Tertiary extensional tectonics of the Omineca belt at 51˚N latitude, southern Canadian Cordillera. Canadian Journal of Earth Sciences 33, 1596–1611.

Johnston, D.H., Williams, P.F., Brown, R.L., Crowley, J.L., Carr, S.D., 2000. Northeastward extrusion and extensional exhumation of crystalline rocks of the Monashee Complex, southeastern Canadian Cordillera. Journal of Structural Geology 22, 603–625.

Journeay, J.M., 1986. Stratigraphy, internal strain, and thermo-tectonic evolution of northern Frenchman Cap dome, an exhumed basement duplex structure, Omineca

hinterland, southeastern Canadian Cordillera. PhD Thesis, Queen's University, Kingston, Ontario, Canada.

Journeay, J.M., Williams, S.P., 1995. Geological Survey of Canada, Open File 2948 (v. 1.0).

Kuiper, Y.D., 2002. When did deformation and peak of metamorphism take place in the Monashee Complex? In: Cook, F., Erdmer, P. (Compilers), 2002, Slave–Northern Cordillera Lithospheric Evolution (SNORCLE) Transect and Cordilleran Tectonics Workshop Meeting (February 21–24), Pacific Geoscience Centre, Lithoprobe Report No. 82, 89–90.

Kuiper, Y.D., Carr, S.D., Williams, P.F., 2000. Age constraints on penetrative structures at Joss Mountain, in the Selkirk Allochthon, southern Canadian Cordillera. In: Cook, F., Erdmer, P. (Compilers), 2000, Slave–Northern Cordillera Lithospheric Evolution (SNORCLE) Transect and Cordilleran Tectonics Workshop Meeting (February 25–27), University of Calgary, Lithoprobe Report No. 72, 168.

Kuiper, Y.D., Williams, P.F., in preparation. Mechanisms and timing of Cordilleran deformation in the Monashee Complex, southern Canadian Cordillera.

Kyser, T.K., Ghent, E.D., Sevigny, J.H., 1994. Petrogenesis of two-mica granites, northern Monashee Mountains, British Columbia: Evidence from oxygen, hydrogen and strontium isotopic compositions. Geological Society of America Bulletin 106, 1531–1537.

McDonough, M.R., Simony, P.S., 1988. Structural evolution of basement gneisses and Hadrynian cover, Bulldog Creek area, Rocky Mountains, British Columbia. Canadian Journal of Earth Sciences 25, 1687–1702.

McNicoll, V.J., Brown, R.L., 1995. The Monashee décollement at Cariboo Alp, southern flank of the Monashee complex, southern British Columbia, Canada. Journal of Structural Geology 17, 17–30.

Monger, J.W.H., Price, R.A., Tempelman-Kluit, D.J., 1982. Tectonic accretion and the origin of the two major metamorphic and plutonic welts in the Canadian Cordillera. Geology 10, 70–75.

Monger, J.W.H., Wheeler, J.O., Tipper, H.W., Gabrielse, H., Harms, T., Struik, L.C., Campbell, R.B., Dodds, C.J., Gehrels, G.E., O'Brien, J., 1991. Part B. Cordilleran terranes. In: Gabrielse, H., Yorath, C.J. (Editors), Upper Devonian to Middle Jurassic assemblages, Chapter 8 of Geology of the Cordilleran Orogen in Canada. Geological Survey of Canada, Geology of Canada no. 4, pp. 281-327.

Morrison, M.L., 1982. Structure and petrology of the Malton gneiss complex. PhD Thesis, University of Calgary, Calgary, Alberta, Canada.

Murphy, D.C., 1987. Suprastructure/infrastructure transition, east–central Cariboo Mountains, British Columbia: geometry, kinematics and tectonic implications. Journal of Structural Geology 9, 13–29.

Murphy, D.C., van der Heyden, P., Parrish, R.R., Klepacki, D.W., McMillan, W., Struik, L.C., Gabites, J., 1995. New geochronological constraints on Jurassic deformation of the western edge of North America, southeastern Canadian Cordillera. In: Miller, D.M., Busby, C. (Editors), Jurassic magmatism and tectonics of the North American Cordillera. Boulder, Colorado, Geological Society of America Special Paper 299, 159–171.

Parkinson, D.L., 1991. Age and isotopic character of Early Proterozoic basement gneisses in the southern Monashee Complex, southeastern British Columbia. Canadian Journal of Earth Sciences 28, 1159–1168.

Parrish, R.R., 1995. Thermal evolution of the southeastern Canadian Cordillera. Canadian Journal of Earth Sciences 32, 1618–1642.

Pigage, L.C., 1977. Rb–Sr dates for granodiorite intrusions on the northeast margin of the Shuswap Metamorphic Complex, Cariboo Mountains, British Columbia. Canadian Journal of Earth Sciences 14, 1690–1695.

Poitrasson, F., Chenery, S., Shepherd, T.J., 2000. Electron microprobe and LA-ICP-MS study of monazite hydrothermal alteration: Implications for U–Th–Pb geochronology and nuclear ceramics. Geochimica et Cosmochimica Acta 64, 3283–3297.

Price, R.A., 1981. The Cordilleran Thrust and Fold Belt in the southern Canadian Rocky Mountains. In: K.R. McClay and N.J. Price (Editors), Thrust and nappe tectonics. Geological Society of London, Special Publication 9, 427–448.

Price, R.A., 1986. The southeastern Canadian Cordillera: thrust faulting, tectonic wedging, and delamination of the lithosphere. Journal of Structural Geology 8, 239–254.

Price, R.A., 2000. The evolution of the southern Cordilleran foreland thrust and fold belt and the kinematics of Cordilleran orogenesis. GeoCanada2000, Abstract 435.

Price, R.A., Mountjoy, E.W., 1970. Geologic structure of the Canadian Rocky Mountains between Bow and Athabasca rivers – a progress report. Geological Survey of Canada, Special Paper 6, 7–25.

Raeside, R.P., Simony, P.S., 1982. Stratigraphy and deformational history of the Scrip Nappe, Monashee Mountains, British Columbia. Canadian Journal of Earth Sciences. 20, 639–650.

Read, P.B., Brown, R.L., 1981. Columbia River fault zone: southeastern margin of the Shuswap and Monashee complexes, southern British Columbia. Canadian Journal of Earth Sciences 18, 1127–1145.

Reid, L.F., 1999. Mid-Jurassic Hobson Lake pluton of the central Cariboo Mountains, British Columbia: Re-examination of critical field relationships. In: Cook, F., Erdmer, P. (Compilers), 1999, Slave–Northern Cordillera Lithospheric Evolution (SNORCLE) Transect and Cordilleran Tectonics Workshop Meeting (March 5–7), University of Calgary, Lithoprobe Report No. 69, 296.

Reid, L.F., Simony, P.S., Ross, G.M., 2002. Dextral strike-slip faulting in the Cariboo Mountains, British Columbia: a natural example of wrench tectonics in relation to Cordilleran tectonics. Canadian Journal of Earth Sciences 39, 953–970.

Reid, L.F., Heaman, L.M., Simony, P.S., Pattison, D.R.M., 2003. Relationship between multiple phases of Mesozoic deformation and metamorphism in the Cariboo Mountains, Omineca Belt, central British Columbia. Cordilleran Tectonics Workshop Meeting (February 7–9, 2003), Carleton University, Ottawa, 29.

Reesor, J.E., Moore, J.M., 1971. Petrology and structure of the Thor–Odin gneiss dome, Shuswap metamorphic complex. Geological Survey of Canada, Bulletin 195.

Scammell, R.J., 1993. Mid-Cretaceous to Tertiary thermotectonic history of former mid-crustal rocks, southern Omineca Belt, Canadian Cordillera. PhD Thesis, Queen's University, Kingston, Ontario, Canada.

Schaubs, P.M., Carr, S.D., 1998. Geology of metasedimentary rocks and late Cretaceous deformation history, in the Northern Valhalla complex, British Columbia. Canadian Journal of Earth Sciences 38, 1018–1036.

Schaubs, P.M., Carr, S.D., Berman, R.G., 2002. Structural and metamorphic constraints on ca. 70 Ma deformation of the northern Valhalla complex, British Columbia: implications for the tectonic evolution of the southern Omineca belt. Journal of Structural Geology 24, 1195–1214.

Sevigny, J.H., Simony, P.S., 1989. Geometric relationship between the Scrip Nappe and metamorphic isograds in the northern Adams River area, Monashee Mountains, British Columbia. Canadian Journal of Earth Sciences 26, 606–610.

Sevigny, J.H., Parrish, R.R., Ghent, E.D., 1989. Petrogenesis of peraluminous granites, Monashee Mountains, southeastern Canadian Cordillera. Journal of Petrology 30, 557–581.

Sevigny, J.H., Parrish, R.R., Donelick, R.A., Ghent, E.D., 1990. Northern Monashee Mountains, Omineca Crystalline Belt, British Columbia: Timing of metamorphism, anatexis, and tectonic denudation. Geology 18, 103–106.

Simony, P.S., Ghent, E.D., Craw, D., Mitchell, W., Robbins, D.B., 1980. Structural and metamorphic evolution of northeast flank of Shuswap complex, southern Canoe River area, British Columbia. Geological Society of America Memoir 153, 445–460.

Simony, P.S., Carr, S.D., 1997. Large lateral ramps in the Eocene Valkyr shear zone: extensional ductile faulting controlled by plutonism in southern British Columbia. Journal of Structural Geology 19, 769–784.

Spark, R.N., 2001. Crustal thickening and tectonic denudation within the Thor–Odin culmination, Monashee Complex, southern Canadian Cordillera. PhD Thesis, University of New Brunswick, Fredericton, New Brunswick, Canada.

Spear, F.S., Parrish, R.R., 1996. Petrology and cooling rates of the Valhalla Complex, British Columbia, Canada. Journal of Petrology 37, 733–765.

Unterschutz, J.L.E., Creaser, R.A., Erdmer, P., Thompson, R.I., Daughtry, K.L., 2002. North American margin origin of Quesnel terrane strata in the southern Canadian Cordillera: Inferences from geochemical and Nd isotopic characteristics of Triassic metasedimentary rocks. Geological Society of America Bulletin 114, 462–475.

Vanderhaeghe, O., Teyssier, C., Wysoczanski, R., 1999. Structural and geochronological constraints on the role of partial melting during the formation of the Shuswap metamorphic core complex at the latitude of the Thor–Odin dome, British Columbia. Canadian Journal of Earth Sciences 36, 917–943.

Williams, P.F., 1999. Fold Nappes and the problem of model driven interpretation. Specialist Group in Tectonics and Structural Geology Field Conference, Halls Gap, Victoria, Australia (February 14–19, 1999). Geological Society of Australia Abstracts Series #53, 267–268.

Williams, P.F., Jiang, D., in review. The relationship between thrusting, nappe formation, and channel flow. An example from the Canadian Cordillera.

Table 8.1. Overview of deformation, metamorphism, and age constraints presented by previous workers. This table serves as a summary of the interpretations made herein, and therefore only references on which the interpretations are based are cited. Ages of Cordilleran deformation and metamorphism (F2 and F3) younger than ~75–70 Ma (e.g. Monashee Complex, Valhalla Complex, Pinnacles Area) are here reinterpreted as possibly representing extension-related fluids, and are therefore omitted from this overview. General descriptions per domain, and interpretations based on those, are shown in the last column. See text for further discussion and references.

deformation	relationship to metamorphism	peak metamorphic grade	age of deformation (Ma)	references (geochronology references are indented)	Domains: general descriptions and interpretations
Monashee Complex (and area S–SW of it, but N–NE of the F3 vergence reversal zone)					**Domain 1: Deepest structural levels, within the Shuswap Metamorphic Complex.**
F1 tight to isoclinal					NE-verging folds (referred to in the table as F1 and F2) are overprinted by NE-verging (F3) folds. Although these structures (F2, F3) have previously been interpreted as being ~78–49 Ma in age, they are interpret herein as being older, e.g. Middle Jurassic and/or mid to Late Cretaceous (Chapter 3; Kuiper, 2002). These structures are overprinted by gentle (F4) folds and extensional structures (F2, F3) have previously been interpreted as F2 and F3 folds formed during, and partly after, (upper) amphibolite facies metamorphism. **Interpretation:** NE-verging F2 folds formed during detachment flow, or in the lower part of the channel flow zone (during Middle Jurassic?). NE-verging F3 folds formed in the lower part of the channel flow zone (during mid- to Late Cretaceous?). Overprinting gentle upright folds may have formed during further shortening, after the rocks moved out of the channel flow zone (or during a later separate event).
F2 tight to isoclinal, NE-verging	syn-peak	upper amphibolite		Brown (1980), Read and Brown (1981), Journeay (1986), Carr (1991), Brown et al. (1992) and references therein, Johnston et al. (2000), Spark (2001), Williams and Jiang (in review)	
F3 isoclinal to open, NE-verging	syn/post-peak?		mid- to Late Cretaceous ?		
F4 gentle upright folds					
D5 extension			Late Cretaceous–Early Eocene (~75–70 – 50 Ma)	Kuiper et al. (2000, 2001), Chapter 3	
Malton Complex					
F1 SW-verging large scale nappes					
F2 NE-verging tight folds	pre-/syn-peak	amphibolite		Morrison (1982), McDonough and Simony (1988)	
F3 NE-verging tight folds	post-peak				
F4 open folds, SE trending extension					
Valhalla Complex					
F1 (as F2)					
F2 overturned tight asymmetric, E–NE-verging	post-peak	amphibolite		Carr et al. (1987), Simony and Carr (1997), Schaubs and Carr (1998), Schaubs et al. (2001)	
F3 verging E–NE	post-peak		110–51 Ma or older		
F4 open upright folds extension				Schaubs and Carr (1998), Schaubs et al. (2001)	
Northern Shuswap Complex					**Domain 2: Intermediate structural levels, within the Shuswap Metamorphic Complex.**
F1 SW-verging large scale nappes					NE-verging folds (referred to in the table as F1 and F2) are overprinted by SW-verging (F3) folds. These structures are overprinted by extensional structures. NE-verging folds formed during (upper) amphibolite metamorphism, and SW-verging folds during and after peak of metamorphism. **Interpretation:** NE-verging folds formed during detachment flow, or in the lower part of the channel flow zone. SW-verging folds formed in the top part of the channel flow zone. In the Northern Shuswap Complex, late upright or steeply dipping folds formed instead of SW-verging folds, which may have formed during further shortening, after the rocks moved out of the channel flow zone. The Northern Shuswap Complex was probably at a higher structural level, during late folding, than other areas in Domain 2.
F2 NE-verging tight folds	pre-peak	upper amphibolite	compression/metamorphism 135–<97 Ma	Simony et al. (1980), Raeside and Simony (1982), Sevigny and Simony (1989), Digel et al. (1998)	
F3 upright or steeply SW dipping folds	post-peak		Eocene	Scammell (1993), Crowley et al. (2000)	
extension					
Area west of Monashee Complex					
F1 (as F2)					
F2 NE-verging folds	syn-peak	upper amphibolite		Johnson (1994), Johnson and Brown (1996)	
F3 moderately to steeply inclined, commonly overturned, W–SW-verging	syn/post-peak		cooling in Late Palaeocene/ Early Eocene	Johnson (1994)	
extension					
Pinnacles area (S–SW of the F3 vergence reversal zone)					
F1 (as F2)					
F2 N–NE-verging	syn-peak	amphibolite		Carr (1991)	
F3 S–SW-verging	syn/post-peak				
extension					
Clachnacudainn Complex					**Domain 3: Highest structural levels, surrounding the Shuswap Metamorphic Complex.**
F1 inclusion trails in garnets	pre-peak				NE-verging folds do not seem to be preserved. SW-verging folds (F2) overprint F1 folds, which may have formed before Cordilleran deformation. The SW-verging folds formed during metamorphism, up to lower to middle amphibolite facies. Rocks cooled in the Middle Jurassic during late folding. Upright or steeply dipping folds (F3, F4) formed after peak of metamorphism. **Interpretation:** SW-verging folds formed in the top part of the channel flow zone, in the Middle Jurassic. Upright or steeply dipping folds, formed during further shortening, after the rocks moved out of the channel flow zone (in the mid-Cretaceous), while channel flow was still ongoing at lower structural levels (Domains 1 and 2).
F2 SW-verging, SE-plunging large scale folds	syn-peak	middle amphibolite	~173–168 Ma	Crowley and Brown (1994), Price (1986, 2000)	
F3 upright, open and ESE-trending	post-peak			Colpron et al. (1996)	
F4 local, lineations					
Selkirk Fan					
F1 E-verging, large scale, nappe					
F2 SW-verging (in the SW)	syn/post-peak	up to lower amphibolite		Brown and Tipett (1978), Colpron et al. (1996)	
F3 NE-verging (in the NE)	post-peak		>110–90 Ma	Colpron et al. (1996)	
Cariboo Mountains					
F1					
F2 upright to near-recumbent, SW-verging	pre-peak		Jurassic (>174 Ma)	Murphy (1987), Ferguson and Simony (1991)	
F3 NE-verging	late syn/post-peak	up to lower amphibolite		Ferguson and Simony (1991), Murphy (1987), Brown and Tippett (1978), Gerasimoff (1988)	
F4 gentle upright folds					

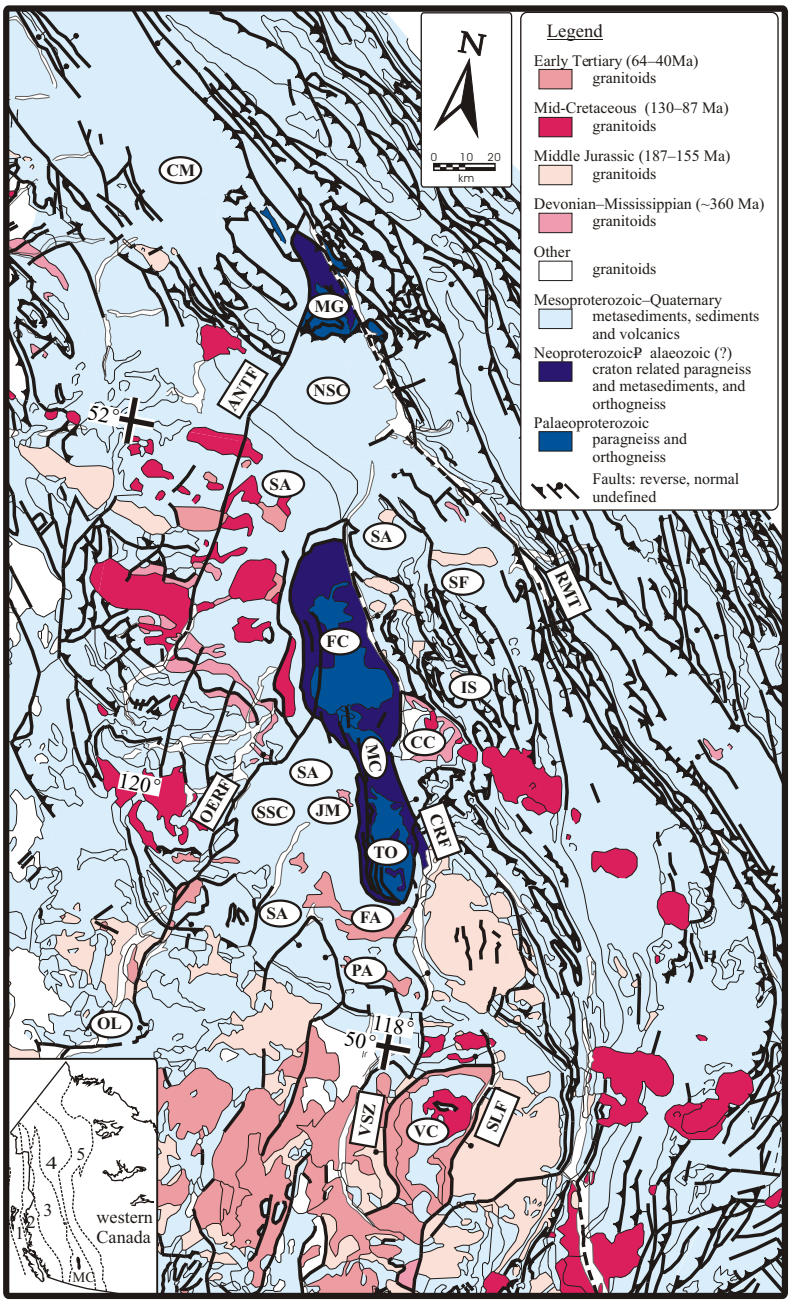

Fig. 8.1. Tectonic assemblage map (after Journeay and Williams, 1995). Areas referred to in the text are indicated in ellipses: CC = Clachnacudainn Complex, CM = Cariboo Mountains, FA = Fosthall Area, FC = Frenchman Cap Dome, IS = Illecillewaet Synclinorium, JM = Joss Mountain, MC = Monashee Complex, MG = Malton Gneiss, NSC = Northern Shuswap Metamorphic Complex, OL = Okanagan Lake, PA = Pinnacles Area, SA = Selkirk Allochthon, SF = Selkirk Fan, SSC = Southern Shuswap Metamorphic Complex, TO = Thor–Odin Dome, VC = Valhalla Complex, (SMC = Shuswap Metamorphic Complex; in text, not shown). Faults are indicated in rectangles: ANTF = Adams–North Thompson Fault, CRF = Columbia River Fault, OERF = Okanagan–Eagle River Fault, RMT = Rocky Mountain Trench, SLF = Slokan Lake Fault, VSZ = Valkyr Shear Zone. Inset: location of morphogeological belts of the Canadian Cordillera: 1. Insular Belt, 2. Coast Belt, 3. Intermontane Belt, 4. Omineca Belt, 5. Foreland Belt. MC indicates the location of the Monashee Complex.

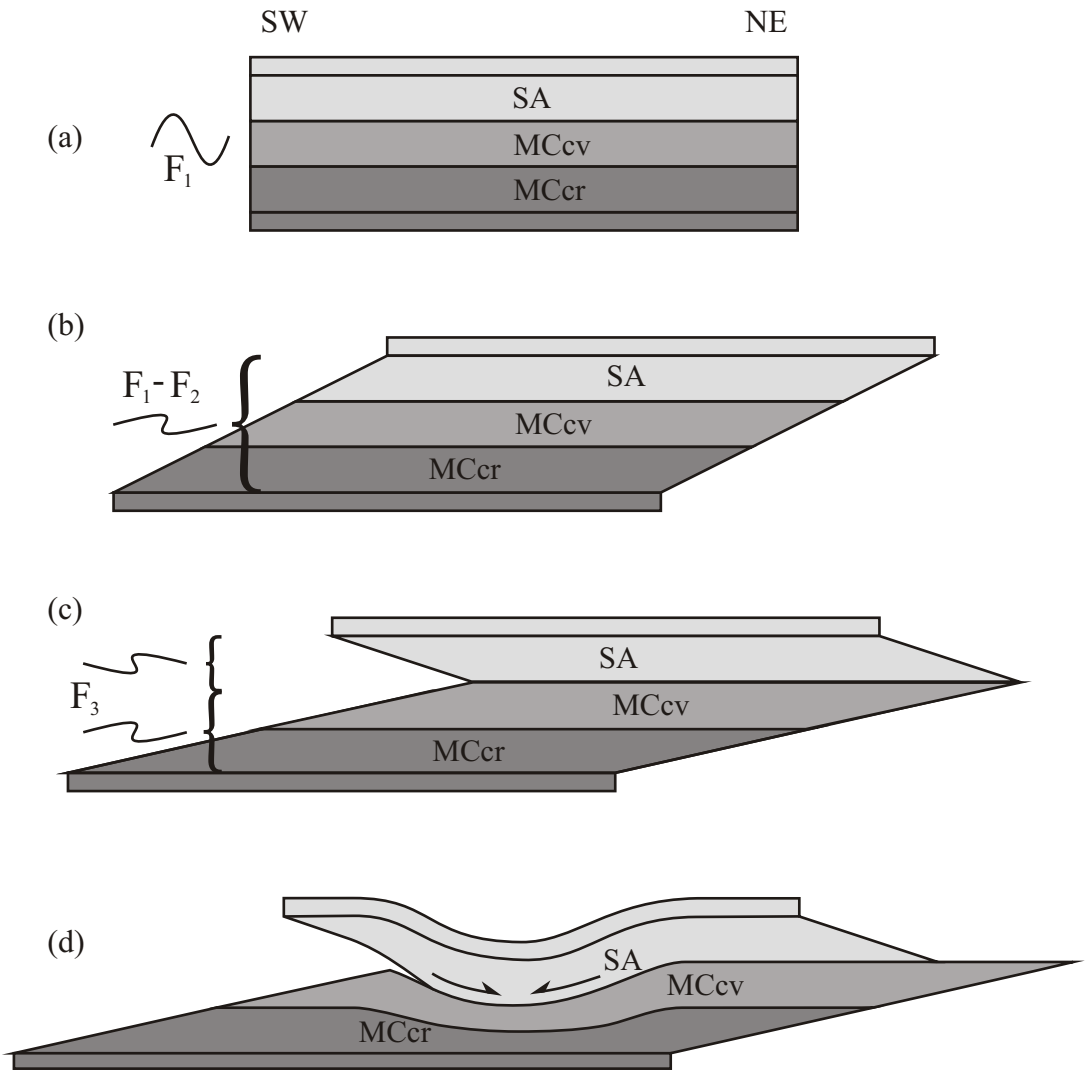

Fig. 8.2. Diagrammatic cross sections representing the history of the Monashee Complex (MC). (a) Three layers represent the Selkirk Allochthon (SA) and the MC cover (MCcv) and core (MCcr). The upright folds represent any folds that may have existed before development of the shear zone. (b) Detachment style shear zone with constant sense of shear across the zone. Asymmetry of modified F_1 and new F_2 is shown. These folds are referred to herein as detachment flow folds (DFFs). (c) Channel flow with sense of shear changing across the shear zone. New dragfolds (F_3) have different asymmetries depending on whether they lie in the upper sinistral or lower dextral part of the shear zone. These channel flow folds (CFFs) verge to the SW in the upper part (Domain 2 of Fig. 8.4) and to the NE in the lower part of the zone (Domain 1 of Fig. 8.4). (d) Crustal extension was accommodated by ductile deformation in all three units and by the development of a ductile shear zone at the top of the Monashee Compex cover sequence. (Modified after Williams and Jiang, in review.)

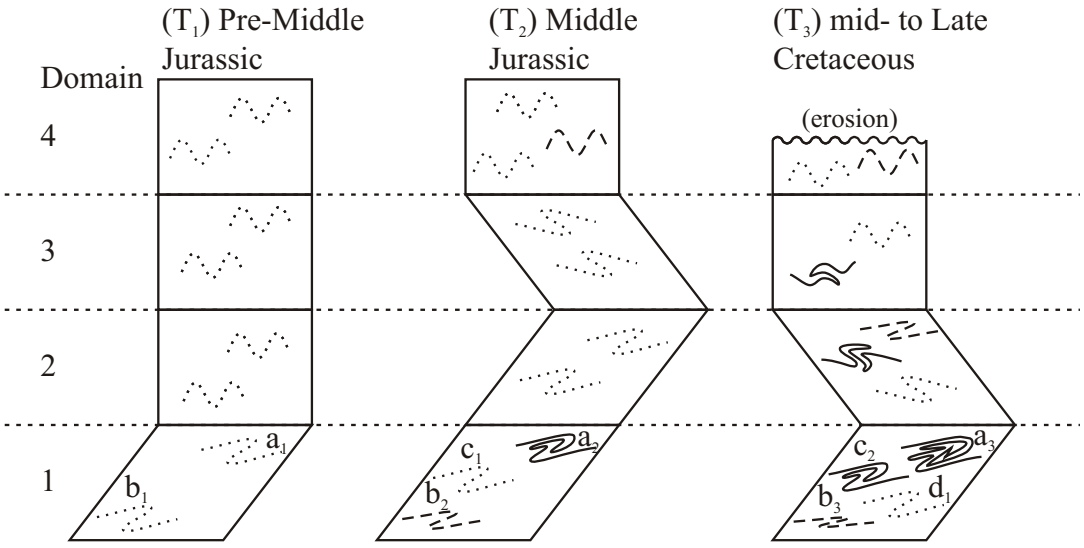

Fig. 8.3. Folds a–d illustrate different possible fold overprinting relationships. Dotted, dashed and solid lines are new, inherited and overprinted folds respectively. Folds may or may not be overprinted. Fold a is overprinted at T_2 and T_3, whereas fold b escapes overprinting, but becomes tighter. Folds of the same generation can form at different times (F_1 folds, e.g. a_1, c_1 and d_1, form at T_1, T_2 and T_3, respectively) and folds of different generations can form at the same time (F_1, F_2 and F_3 folds, e.g. d_1, c_2 and a_3, form at T_3) (see Section 8.1.2).

The model explains fold overprinting relationships as areas move upward with respect to the channel flow zone, in time (see Section 8.6). Before the Middle Jurassic, detachment flow causes NE-verging folds in Domains 1 (and possibly Domain 2). In the Middle Jurassic, channel flow is ongoing in Domains 1–3. The channel flow zone is thicker than the pre-Middle Jurassic detachment zone, in order to explain SW-verging folds in Domain 3 that are not overprinting earlier NE-verging folds. In the mid- to Late Cretaceous, rocks moved up with respect to the channel flow zone, due to further thickening and erosion. The same effect can be reached by the channel flow zone thinning or moving downward, or a combination of the two .

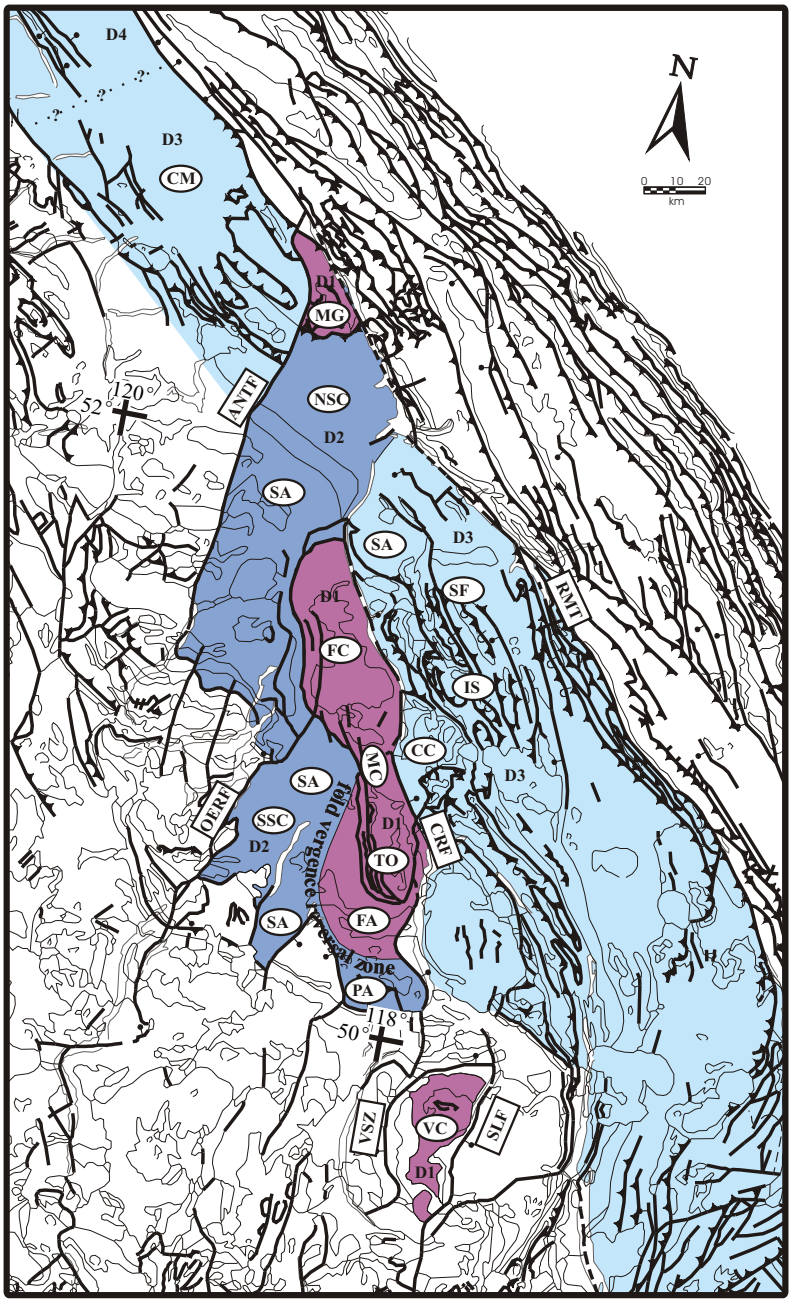

Fig. 8.4. Domain division: Domain 1 (purple) is the deepest structural level, where NE-verging channel flow folds (CFFs) and/or detachment flow folds (DFFs) exist; Domain 2 (dark blue) is an intermediate structural level, where NE-verging DFFs or CFFs are overprinted by SW-verging CFFs; Domain 3 (light blue) is a higher intermediate level, where SW-verging CFFs are present and NE-verging folds absent; Domain 4 (north of Domain 3) is the highest structural level where only upright folds are present. Overprinting post-metamorphic upright or steeply dipping folds are present in all domains. The boundaries between domains are mostly faults. The F_3 vergence reversal zone, which forms the centre of the channel flow zone, is exposed SW of Thor-Odin. The boundary between Domain 1 and 2 at that location is gradual. Areas that are not discussed are in white. Abbreviations as in Fig. 8.1.

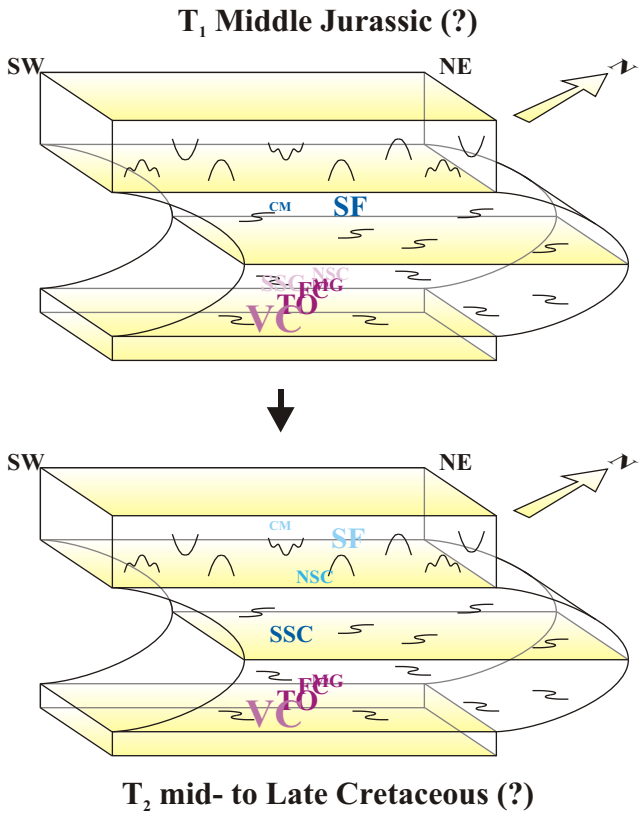

Fig. 8.5. Location of areas discussed in the text, with respect to the channel flow zone, changing with time. CM = Cariboo Mountains, FC = Frenchman Cap Dome, MG = Malton Gneiss, NSC = Northern Shuswap Metamorphic Complex, SF = Selkirk Fan, SSC = Southern Shuswap Metamorphic Complex, TO = Thor–Odin Dome, VC = Valhalla Complex. Structural domains are indicated by colours (purple = Domain 1, dark blue = Domain 2, light blue = Domain 3; cf. Fig. 8.4) and higher structural levels within the domains are indicated by lighter colours. Areas indicated in small letters are in the back of the diagram, and areas indicated in large letters in the front. Further geographical orientations, and orientation with respect to the channel flow direction, can be inferred from positions of areas relative to other areas in the same structural domain, and relative to the north (N-arrow). The relative geographical position of the various domains is uncertain (i.e. the Selkirk Fan may have been further west or east relative to Thor–Odin, than is shown). Folds are only indicated on the front faces of the diagrams. Structures that formed during T_1 are overprinted by structures that formed during T_2 (e.g. in the SSC, NE-verging folds that formed during T_1 are overprinted by SW-verging folds that formed during T_2; see also Fig. 8.3). T_1 and T_2 may correspond to the Middle Jurassic and mid- to Late Cretaceous (cf. Fig. 8.3).

Chapter 9

Conclusions

A strong indication exists for the resetting of $^{40}Ar/^{39}Ar$ hornblende ages in amphibolites by meteoric fluids during extension (Chapter 3). Hornblende samples from amphibolites in Thor–Odin younger than ~75–70 Ma, with plateau or near-plateau $^{40}Ar/^{39}Ar$ spectra, occur in rocks which underwent greater oxygen and hydrogen isotope exchange with infiltrating meteoric waters than hornblende samples yielding $^{40}Ar/^{39}Ar$ dates older than ~75–70 Ma. $^{40}Ar/^{39}Ar$ hornblende dates younger than ~75–70 Ma are reinterpreted as being a result of partial or complete Ar loss, due to interaction between hornblende and meteoric fluids. Infiltration of isotopically light meteoric fluids was probably related to normal faulting in Thor–Odin.

At present, one could argue that U–Pb data of Chapters 5, 6 and 7 are consistent with models of progressive younging of Cordilleran deformation and metamorphism, from ~170 Ma in the Selkirk and Cariboo Mountains to ~78 Ma at the highest structural levels in the Monashee Complex to 49 Ma at the deepest structural levels of the complex. However, these data and data of previous workers are also consistent with extension occurring between ~75–70 Ma and ~50 Ma in the Monashee Complex. Monazite, zircon, titanite and xenotime could have grown during extension, in the presence of meteoric fluids, possibly mixed with igneous fluids derived from pegmatites that intruded during extension. Cordilleran deformation and metamorphism then occurred earlier, perhaps in the Middle Jurassic and/or mid- to Late Cretaceous, as in the rocks overlying the Monashee Complex. In the Monashee Complex, it must have occurred after ~740 Ma,

the age of the Mt. Copeland syenite gneiss in Frenchman Cap, which experienced transposition and F_{1-3} folding. A period of zircon dissolution in a basement migmatitic orthogneiss sample in Thor–Odin (Chapter 5), at a time between ~1.8 Ga and 52 Ma, indicates that any event that occurred within this time period is not recorded by zircon in this sample. The same could be true for other zircon, monazite, titanite and xenotime crystals in the Monashee Complex. If U–Pb accessory phases did not grow and/or dissolved during a deformation or metamorphic event, then geological events may not be recorded by the minerals used for dating. These minerals may not have started growing until rocks started to cool down sufficiently, e.g. during extension.

Devono-Mississippian, Middle Jurassic and mid-Cretaceous granitoids that are present in the rocks overlying the Monashee Complex are absent in the Monashee Complex (Chapter 8). Melts may have originated in the deepest structural levels, e.g. the Monashee Complex, migrated upward and crystallised at higher structural levels (Domains 2 and 3 of Chapter 8). Pre-existing (e.g. Palaeoproterozoic) zircon and other minerals used for U–Pb dating may have (partly) dissolved and moved up with these melts and precipitated at higher structural levels, leaving the Monashee Complex free of Devono-Mississippian, Middle Jurassic, and mid-Cretaceous U–Pb accessory phases.

Late Cretaceous–Early Eocene monazite in metasedimentary rocks described in Chapter 6, shows evidence for the presence of older Pb. However, old age domains were not detected by electron microprobe and SHRIMP methods. The old Pb may be from Proterozoic detrital cores that may have lost most of their Pb, by e.g. recrystallisation, during one or more younger events. Late Cretaceous to Early Eocene monazite growth may be related to extension-related fluids.

Most of the structural, metamorphic, and geochronological data in the southern Canadian Omineca Belt are consistent with a channel flow model. This model explains the ductile deformation at all scales, in contrast to earlier models that were based on thrusting. The deepest structural level has only NE-verging structures, as a result of deformation in the lower part of the channel flow zone and possibly of earlier detachment flow. Intermediate levels have NE-verging structures, due to detachment flow and/or deformation in the lower part of the channel flow zone, overprinted by SW-verging structures formed in the upper half of the channel flow zone. The highest levels show only SW-verging structures that formed in the upper part of the channel flow zone. Furthermore, the channel flow model explains why SW-verging structures are never overprinted by NE-verging structures, why the highest metamorphic facies conditions are at the lowest structural levels, and why high levels cool before low levels.

Some ages derived during this study yield age constraints on local geological problems. (1) A migmatitic orthogneiss in the basement sequence of Thor–Odin has a protolith age of ~2.1 Ga or a composite age between ~2.4 and ~2.1 Ga, and a migmatisation age of ~1.8 Ga. Overgrowth occurred at 52 Ma. The migmatisation age confirms that deformation and metamorphism took place as early as the Palaeoproterozoic in the basement rocks of the Monashee Complex. The 52 Ma overgrowths may indicate extension or metamorphism. Dissolution occurred at a time between ~1.8 Ga and 52 Ma. Any geological events that may have occurred during this time interval are not recorded by zircon in this sample. (2) The Joss Mountain orthogneiss yields a protolith age of 362 ± 13 Ma. Because ~360 Ma granitoids do not occur in the Monashee Complex, the Joss Mountain assemblage is confirmed to be part of

the Kootenay Terrane or Selkirk Allochthon. (3) F_3 folding at Joss Mountain occurred between ~73 and ~70 Ma.

The main conclusion of this study is that Late Cretaceous to Early Eocene ages may represent extension and the presence of fluids, and not Cordilleran deformation and metamorphism. The actual age of Cordilleran deformation and metamorphism may not be recorded in the Monashee Complex. Although at present no concrete evidence exists, data presented in this study strongly support these interpretations, and therefore they need to be considered in future studies.

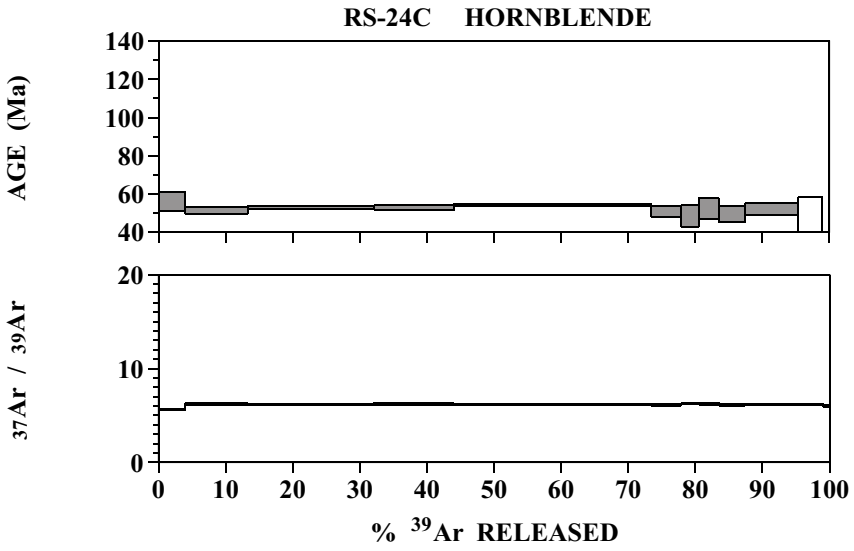

T°C	^{39}Ar(mV)	^{39}Ar(%)	AGE (Ma)±1σ	% ATM	^{37}Ar/^{39}Ar	^{36}Ar/^{40}Ar	^{39}Ar/^{40}Ar	% IIC
950	49.3	3.9	55.7 ± 4.8	79.5	5.64	0.002691	0.014964	3.47
975	117.5	9.3	51.2 ± 1.6	54.3	6.21	0.001839	0.03642	4.13
1000	237.9	18.8	52.7 ± .8	34.6	6.16	0.001175	0.050573	3.98
1025	150.7	11.9	52.6 ± 1.2	41.1	6.18	0.001394	0.045618	4
1050	371.9	29.4	54.2 ± .5	23.2	6.18	0.000787	0.057857	3.9
1075	55.8	4.4	50.6 ± 3	63.7	6.14	0.002156	0.029202	4.12
1100	32.7	2.5	48.3 ± 5.6	77.7	6.26	0.002628	0.018841	4.39
1125	39.2	3.1	52.1 ± 5.5	74.6	6.17	0.002524	0.019836	4.03
1175	48.6	3.8	49.3 ± 4.3	77.1	6.1	0.002609	0.018941	4.19
1250	98.9	7.8	51.8 ± 3.1	73.9	6.16	0.002502	0.020525	4.04
1350	46.3	3.6	45.9 ± 12.2	93.5	6.17	0.003164	0.005775	4.53
1400	13	1	-183.1 ±-85.6	105	6.01	0.003565	0.001284	0.68

TOTAL GAS AGE = 52.4 ± 1.4 Ma
J = .002302 ± 1.151E-05 (.5 %)
^{37}Ar/^{39}Ar, ^{36}Ar/^{40}Ar AND ^{39}Ar/^{40}Ar ARE CORRECTED FOR MASS SPECTROMET ER
DISCRIMINATION,INTERFERING ISOTOPES AND SYSTEM BLANKS
% IIC - INTERFERING ISOTOPE S CORRECTION

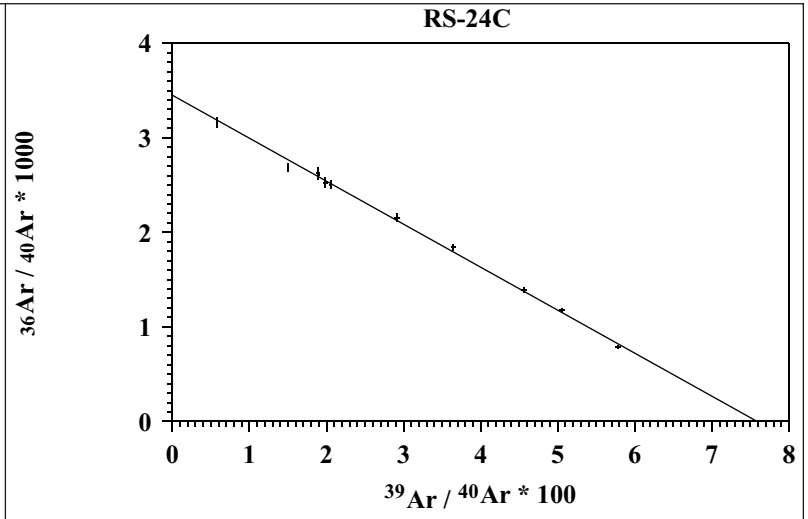

	T°C	(^{39}Ar/^{40}Ar)*100	(^{36}Ar/^{40}Ar)*1000
1	950	1.496 ± .012	2.691 ± .047
2	975	3.642 ± .028	1.839 ± .034
3	1000	5.057 ± .033	1.175 ± .022
4	1025	4.561 ± .035	1.394 ± .028
5	1050	5.785 ± .033	.787 ± .016
6	1075	2.92 ± .035	2.156 ± .043
7	1100	1.884 ± .025	2.628 ± .053
8	1125	1.983 ± .028	2.524 ± .055
9	1175	1.894 ± .019	2.609 ± .048
10	1250	2.052 ± .014	2.502 ± .044
11	1350	.577 ± .003	3.164 ± .052

# ITERATIONS = 3
XBAR = 3.919
YBAR = 1.667
SUM S = 9.095
SLOPE =-.455 ± .006 INCLUDING SUMS
Y = 3.056 ± .499 (^{40}Ar/^{36}Ar INITIAL= 327 ± 53)
(Y=0)
Y = 3.45 ± .028 (40Ar/36Ar INITIAL= 289 ± 2)
(X=0)
J = .002302 ± 1.151E-05
ISOCHRON AGE = 53.911 ± .65 Ma (2σ UNCERTAINTY INCLUDING ERROR IN J)

Appendix I. ^{40}Ar/^{39}Ar data, recalculated after Spark (2001). Spectrum plot and data (left) and inverse isochron plot and data (right). Steps used for inverse isochron calculations are shaded in the spectra.

RS-25C HORNBLENDE

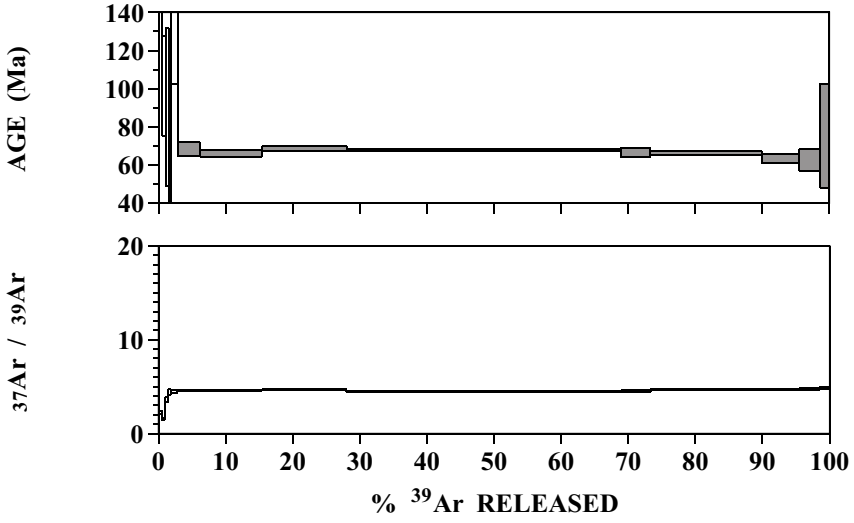

T°C	^{39}Ar(mV)	^{39}Ar(%)	AGE (Ma)±1σ	% ATM	^{37}Ar/^{39}Ar	^{36}Ar/^{40}Ar	^{39}Ar/^{40}Ar	% IIC
750	1.7	0.4	290.1 ± 62.3	57.9	2.25	0.001959	0.005372	0.36
900	1.8	0.5	101.3 ± 26.2	40.7	1.57	0.001374	0.022737	0.55
950	1.6	0.4	90.1 ± 41.4	53.5	3.62	0.001804	0.020096	1.42
975	1.5	0.4	36.6 ± 31.6	60.7	4.43	0.002042	0.041808	3.91
1000	3.3	0.9	320.3 ± 218	5.2	4.49	0.000186	0.01085	0.68
1025	12.4	3.3	68.1 ± 3.6	11.9	4.6	0.000432	0.050531	2.3
1050	34	9.2	65.9 ± 1.6	12.7	4.61	0.000449	0.052019	2.37
1075	46.5	12.5	68.4 ± 1.2	9	4.68	0.000322	0.05222	2.33
1100	151.1	40.9	67.7 ± .5	6.3	4.49	0.000223	0.054572	2.26
1125	16.3	4.4	66.5 ± 2.5	2.4	4.53	0.000134	0.057066	2.32
1200	61.4	16.6	66.4 ± .9	6.3	4.68	0.000233	0.055447	2.4
1275	20.4	5.5	63.3 ± 2.4	15.5	4.72	0.000545	0.052415	2.52
1350	11.5	3.1	62.5 ± 5.6	41.6	4.73	0.001414	0.03678	2.56
1450	5.1	1.3	75.3 ± 27.3	80.4	4.85	0.00272	0.010219	2.22

TOTAL GAS AGE = 70.8 ± 4.8 Ma

J = .002235 ± 1.1175E-05 (.5 %)

^{37}Ar/^{39}Ar, ^{36}Ar/^{40}Ar AND ^{39}Ar/^{40}Ar ARE CORRECTED FOR MASS SPECTROMETER DISCRIMINATION,INTERFERING ISOTOPES AND SYSTEM BLANKS

% IIC - INTERFERING ISOTOPE S CORRECTION

RS-25C

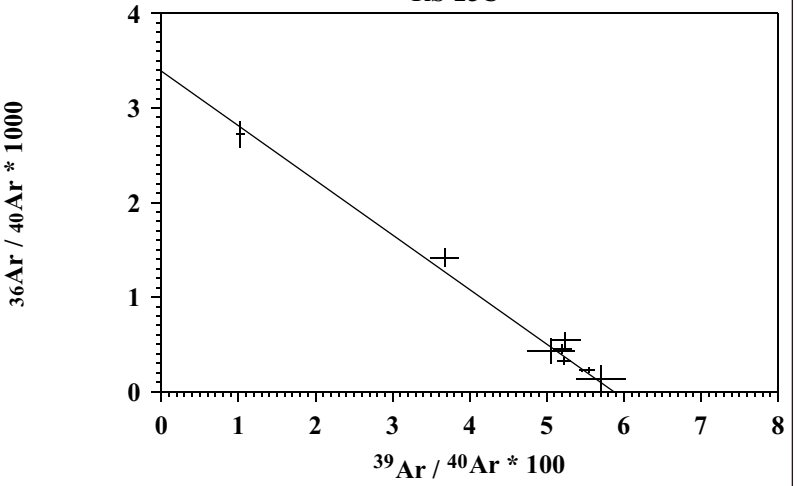

	T°C	(^{39}Ar/^{40}Ar)*100	(^{36}Ar/^{40}Ar)*1000
1	1025	5.053 ± .309	.432 ± .136
2	1050	5.201 ± .117	.449 ± .05
3	1075	5.222 ± .086	.322 ± .037
4	1100	5.457 ± .037	.223 ± .012
5	1125	5.706 ± .318	.134 ± .142
6	1200	5.544 ± .073	.233 ± .03
7	1275	5.241 ± .2	.545 ± .084
8	1350	3.678 ± .186	1.414 ± .097
9	1450	1.021 ± .053	2.72 ± .139

ITERATIONS =3

XBAR = 5.31

YBAR = .322

SUM S = 5.38

SLOPE =-.578 ± .026 INCLUDING SUMS

X = 5.869 ± .026

(Y=0)

Y = 3.056 ± .499 (^{40}Ar/^{36}Ar INITIAL= 327 ± 53)

Y = 3.389 ± .141 (40Ar/36Ar INITIAL= 295 ± 12)

(X=0)

J = .002235 ± 1.1175E-05

ISOCHRON AGE = 67.406 ± .63 Ma (2σ UNCERTAINTY INCLUDING ERROR IN J)

RS-51B HORNBLENDE

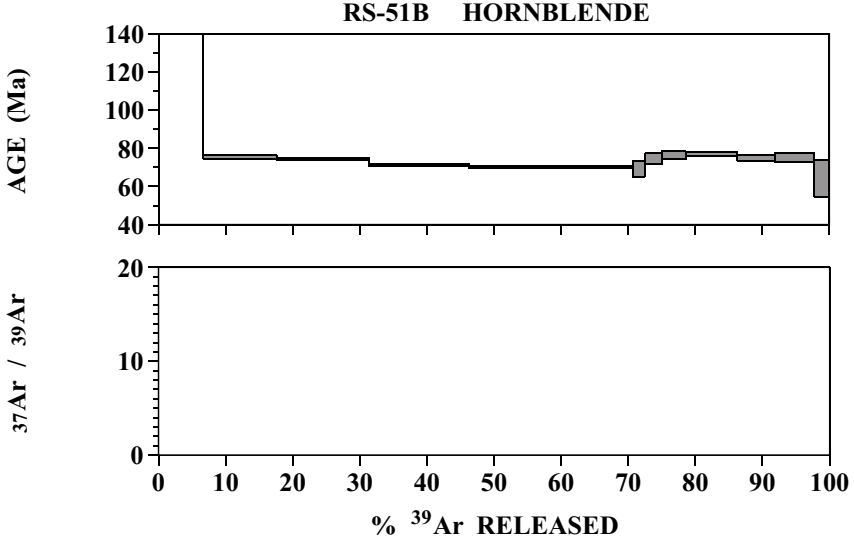

T°C	^{39}Ar(mV)	^{39}Ar(%)	AGE (Ma)±1σ	% ATM	^{37}Ar/^{39}Ar	^{36}Ar/^{40}Ar	^{39}Ar/^{40}Ar	% IIC
950	124.5	6.5	223.5 ± 2	22.5	3.84	0.000762	0.013543	0.72
975	206.8	10.9	75.4 ± .8	19.9	4.18	0.000677	0.043161	1.88
1000	259.3	13.7	74.2 ± .6	15.2	4.21	0.000517	0.046452	1.92
1025	282.5	14.9	71.2 ± .6	12.2	4.27	0.000419	0.050128	2.02
1050	462.9	24.4	70.1 ± .4	8.2	3.95	0.000282	0.053243	1.89
1075	34	1.8	69.1 ± 4.1	46.5	4.14	0.001573	0.031468	2.01
1100	48.2	2.5	74.6 ± 2.9	38.5	4.17	0.001304	0.033458	1.89
1125	66.3	3.5	76.4 ± 2.1	32.9	4.08	0.001115	0.035673	1.81
1175	145.6	7.7	76.9 ± 1.1	24.1	3.98	0.000818	0.040077	1.76
1250	107.5	5.6	74.9 ± 1.6	40.8	3.98	0.001382	0.032111	1.8
1350	109.7	5.8	75.1 ± 2.4	60.5	4	0.002047	0.021402	1.8
1400	42.3	2.2	64.1 ± 9.7	88.2	3.92	0.002985	0.007479	2.03

TOTAL GAS AGE = 83.2 ± .9 Ma

J = .002308 ± 1.154E-05 (.5 %)

^{37}Ar/^{39}Ar, ^{36}Ar/^{40}Ar AND ^{39}Ar/^{40}Ar ARE CORRECTED FOR MASS SPECTROMET ER DISCRIMINATION,INTERFERING ISOTOPES AND SYSTEM BLANKS

% IIC - INTERFERING ISOTOPE S CORRECTION

RS-51B

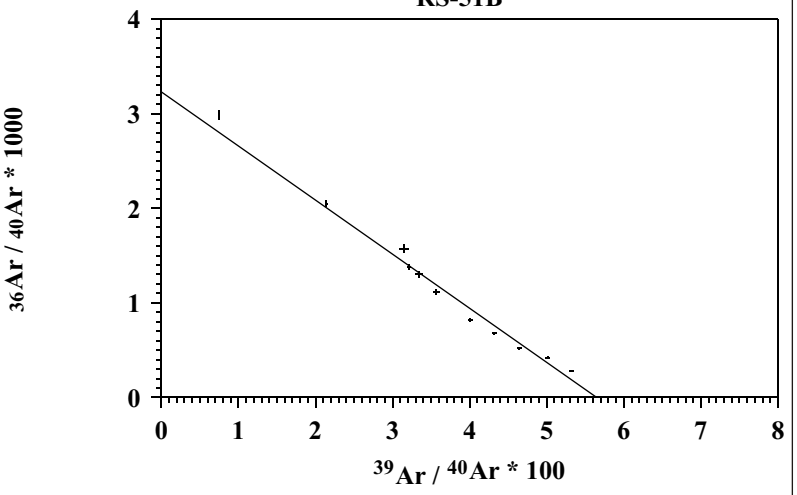

	T°C	(^{39}Ar/^{40}Ar)*100	(^{36}Ar/^{40}Ar)*1000
1	975	4.316 ± .028	.677 ± .014
2	1000	4.645 ± .028	.5170001 ± .011
3	1025	5.012 ± .029	.419 ± .011
4	1050	5.324 ± .028	.282 ± .007
5	1075	3.146 ± .063	1.573 ± .046
6	1100	3.345 ± .05	1.304 ± .036
7	1125	3.567 ± .043	1.115 ± .03
8	1175	4.007 ± .029	.818 ± .019
9	1250	3.211 ± .025	1.382 ± .027
10	1350	2.14 ± .014	2.047 ± .034
11	1400	.747 ± .006	2.985 ± .051

ITERATIONS =4

XBAR = 4.292

YBAR = .776

SUM S = 104.826

SLOPE =-.573 ± .027 INCLUDING SUMS

Y = 3.056 ± .499 (^{40}Ar/^{36}Ar INITIAL= 327 ± 53)
(Y=0)

Y = 3.232 ± .12 (40Ar/36Ar INITIAL= 309 ± 11)
(X=0)

J = .002308 ± 1.154E-05

ISOCHRON AGE = 72.236 ± 1.2 Ma (2σ UNCERTAINTY INCLUDING ERROR IN J)

RS-119B HORNBLENDE

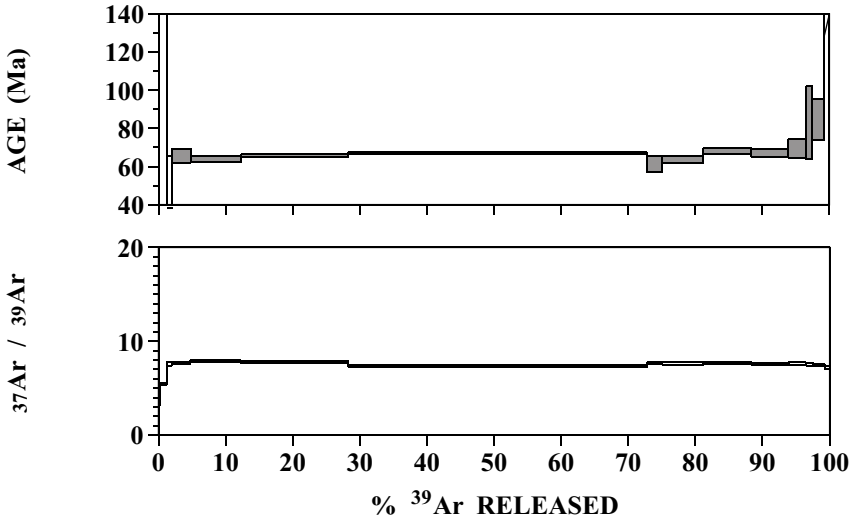

T°C	^{39}Ar(mV)	^{39}Ar(%)	AGE (Ma)±1σ	% ATM	^{37}Ar/^{39}Ar	^{36}Ar/^{40}Ar	^{39}Ar/^{40}Ar	% IIC
750	1.6	0.2	448.1 ± 66.3	43.5	3.33	0.001472	0.004467	0.41
950	5.5	0.9	300.8 ± 20.3	37.4	5.47	0.001266	0.007698	0.86
980	4.6	0.7	51.8 ± 13.6	68.4	7.56	0.002313	0.024087	4.84
1000	16.4	2.7	65.7 ± 3.6	36.7	7.7	0.00125	0.037913	3.98
1025	45	7.5	63.9 ± 1.4	23.3	7.86	0.000799	0.047256	4.16
1050	95.3	15.9	65.5 ± .7	10.9	7.75	0.000384	0.053509	4.01
1075	265.8	44.5	67.2 ± .4	5.6	7.4	0.000201	0.055329	3.75
1100	13.1	2.2	61.2 ± 4.3	29.6	7.71	0.00102	0.045127	4.24
1125	36.7	6.1	63.7 ± 1.6	16.3	7.62	0.000573	0.051615	4.05
1175	42.7	7.1	68.2 ± 1.5	15.1	7.67	0.000531	0.048803	3.83
1225	32.8	5.5	67.1 ± 2	23.6	7.52	0.000812	0.044777	3.82
1275	15.6	2.6	69.5 ± 4.7	47.9	7.63	0.001624	0.02952	3.75
1325	5.7	0.9	83 ± 19.2	71.4	7.56	0.002416	0.013518	3.18
1400	10.6	1.7	84.6 ± 10.7	76.1	7.46	0.002577	0.011062	3.08
1450	4.4	0.7	172.4 ± 43.8	80.6	7.2	0.002729	0.004299	1.67

TOTAL GAS AGE = 71.1 ± 1.3 Ma

J = .002235 ± 1.1175E-05 (.5 %)

^{37}Ar/^{39}Ar, ^{36}Ar/^{40}Ar AND ^{39}Ar/^{40}Ar ARE CORRECTED FOR MASS SPECTROMET ER DISCRIMINATION,INTERFERING ISOTOPES AND SYSTEM BLANKS

% IIC - INTERFERING ISOTOPE S CORRECTION

RS-119B

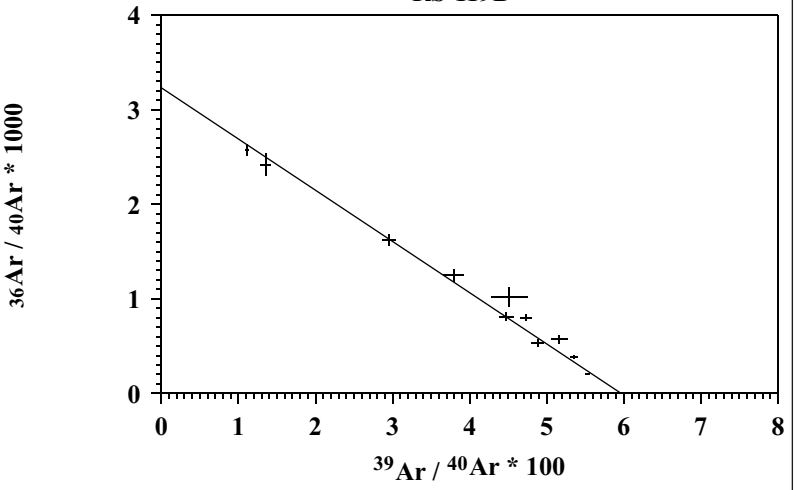

	T°C	(^{39}Ar/^{40}Ar)*100	(^{36}Ar/^{40}Ar)*1000
1	1000	3.791 ± .132	1.25 ± .068
2	1025	4.725 ± .074	.799 ± .033
3	1050	5.35 ± .046	.384 ± .019
4	1075	5.532 ± .03	.201 ± .007
5	1100	4.512 ± .236	1.02 ± .104
6	1125	5.161 ± .105	.573 ± .045
7	1175	4.88 ± .08	.531 ± .037
8	1225	4.477 ± .092	.812 ± .045
9	1275	2.952 ± .089	1.624 ± .061
10	1325	1.351 ± .068	2.416 ± .117
11	1400	1.106 ± .02	2.577 ± .06

ITERATIONS =3

XBAR = 5.007

YBAR = .519

SUM S = 20.239

SLOPE =-.542 ± .018 INCLUDING SUMS

Y = 3.056 ± .499 (^{40}Ar/^{36}Ar INITIAL= 327 ± 53)
(Y=0)

Y = 3.232 ± .093 (40Ar/36Ar INITIAL= 309 ± 8)
(X=0)

J = .002235 ± 1.1175E-05

ISOCHRON AGE = 66.342 ± .69 Ma (2σ UNCERTAINTY INCLUDING ERROR IN J)

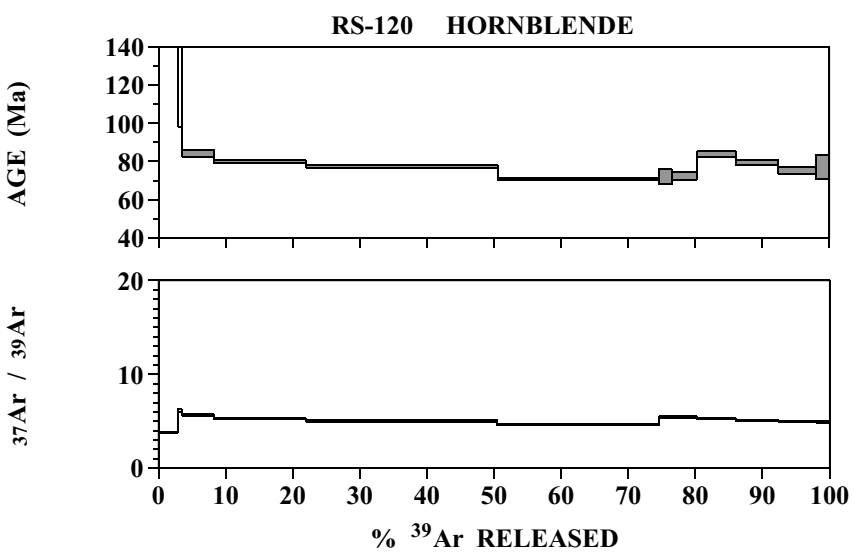

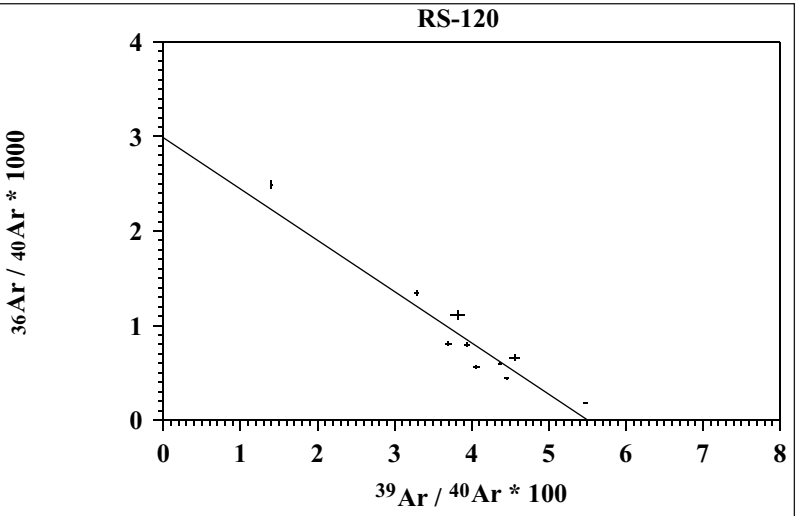

T°C	^{39}Ar(mV)	^{39}Ar(%)	AGE (Ma)±1σ	% ATM	^{37}Ar/^{39}Ar	^{36}Ar/^{40}Ar	^{39}Ar/^{40}Ar	% IIC
950	48.2	2.8	407.9 ± 4.6	18.5	3.79	0.000629	0.00745	0.49
975	8.9	0.5	119.1 ± 20.8	59.9	6.19	0.002024	0.01357	1.93
1000	79.3	4.7	84.2 ± 1.7	23.7	5.69	0.000805	0.03697	2.37
1025	228.6	13.7	79.9 ± .7	12.9	5.28	0.00044	0.044558	2.29
1050	476.4	28.5	77.3 ± .6	17.5	5.03	0.000594	0.043701	2.25
1075	401.3	24	70.7 ± .4	5.3	4.61	0.000186	0.054823	2.22
1100	32.5	1.9	71.9 ± 3.9	32.7	5.46	0.001112	0.038201	2.61
1125	61.5	3.6	72.3 ± 2	19.2	5.47	0.000659	0.045612	2.6
1175	96.9	5.8	83.9 ± 1.4	16.5	5.26	0.000563	0.040602	2.19
1250	105.1	6.3	79.5 ± 1.4	23.4	5.05	0.000795	0.03939	2.2
1350	93.2	5.5	75.2 ± 1.8	39.7	5	0.001344	0.032849	2.28
1400	34.1	2	76.9 ± 6.3	73.6	4.89	0.002492	0.014008	2.19

TOTAL GAS AGE = 87.2 ± .8 Ma
J = .002324 ± 1.162E-05 (.5 %)
^{37}Ar/^{39}Ar, ^{36}Ar/^{40}Ar AND ^{39}Ar/^{40}Ar ARE CORRECTED FOR MASS SPECTROMET ER
DISCRIMINATION,INTERFERING ISOTOPES AND SYSTEM BLANKS
% IIC - INTERFERING ISOTOPE S CORRECTION

	T°C	(^{39}Ar/^{40}Ar)*100	(^{36}Ar/^{40}Ar)*1000
1	1000	3.697 ± .039	.805 ± .025
2	1025	4.455 ± .027	.44 ± .012
3	1050	4.37 ± .023	.594 ± .011
4	1075	5.482 ± .029	.186 ± .006
5	1100	3.82 ± .093	1.112 ± .05
6	1125	4.561 ± .07	.659 ± .032
7	1175	4.06 ± .039	.563 ± .02
8	1250	3.939 ± .035	.795 ± .021
9	1350	3.284 ± .029	1.344 ± .027
10	1400	1.4 ± .015	2.492 ± .047

# ITERATIONS =5
XBAR = 4.363
YBAR = .62
SUM S = 294.693
SLOPE =-.543 ± .061 INCLUDING SUMS
X = 5.506 ± .146
Y = 3.056 ± .499 (^{40}Ar/^{36}Ar INITIAL= 327 ± 53)
Y = 2.987 ± .273 (40Ar/36Ar INITIAL= 334 ± 30)
(X=0)
J = .002324 ± 1.162E-05
ISOCHRON AGE = 74.565 ± 2.26 Ma (2σ UNCERTAINTY INCLUDING ERROR IN J)

RS-125B HORNBLENDE

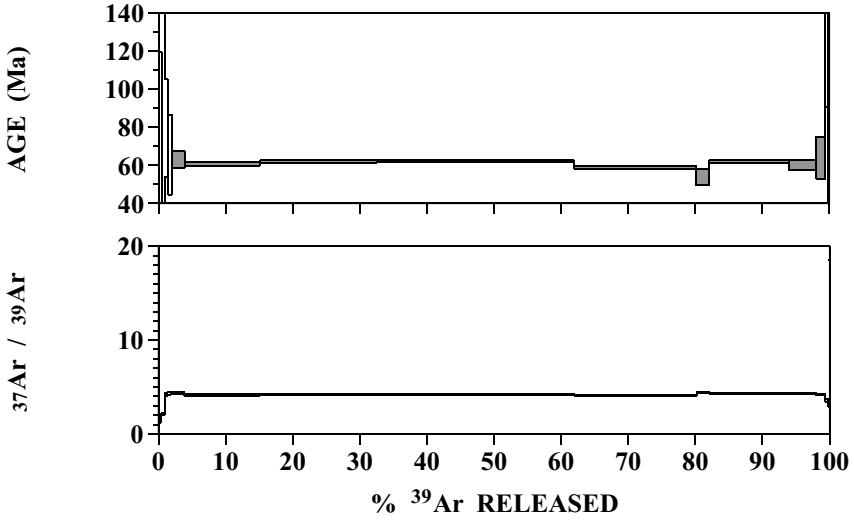

T°C	^{39}Ar(mV)	^{39}Ar(%)	AGE (Ma)±1σ	% ATM	^{37}Ar/^{39}Ar	^{36}Ar/^{40}Ar	^{39}Ar/^{40}Ar	% IIC
750	2.1	0.3	154.9 ± 35.3	49.1	1.28	0.00166	0.01262	0.32
900	2.9	0.5	-2640.5 ±-3799	7.5				
950	2.2	0.3	79.6 ± 25.4	42.7	4.2	0.001448	0.028053	1.83
975	3.3	0.5	65.5 ± 21	50.1	4.28	0.001698	0.029851	2.22
1000	11.1	1.9	62.9 ± 4.3	22.9	4.35	0.000793	0.048057	2.33
1025	64.2	11.2	60.6 ± .9	10.6	4.13	0.000373	0.058129	2.29
1050	99.5	17.4	62 ± .6	7.2	4.18	0.000257	0.059023	2.27
1075	167.6	29.3	62.3 ± .5	6	4.23	0.000213	0.059582	2.29
1100	104.5	18.3	58.9 ± .6	5	4.1	0.000187	0.063566	2.34
1125	11	1.9	53.6 ± 4.1	23.2	4.4	0.000807	0.056184	2.73
1200	68.1	11.9	61.8 ± .9	8.7	4.3	0.000311	0.058153	2.34
1275	22.7	3.9	60.1 ± 2.7	31.8	4.29	0.001083	0.044776	2.4
1350	7.2	1.2	63.8 ± 11.2	62.4	4.19	0.002111	0.023236	2.22
1400	3	0.5	136.3 ± 45.8	74.1	3.57	0.002507	0.007338	0.99
1450	0.9	0.1	350.1 ± 340	81.4	3.2	0.002754	0.00193	0.45

TOTAL GAS AGE = 62.5 ± 1.7 Ma

J = .002235 ± 1.1175E-05 (.5 %)

^{37}Ar/^{39}Ar, ^{36}Ar/^{40}Ar AND ^{39}Ar/^{40}Ar ARE CORRECTED FOR MASS SPECTROMETER DISCRIMINATION,INTERFERING ISOTOPES AND SYSTEM BLANKS

% IIC - INTERFERING ISOTOPE S CORRECTION

RS-125B

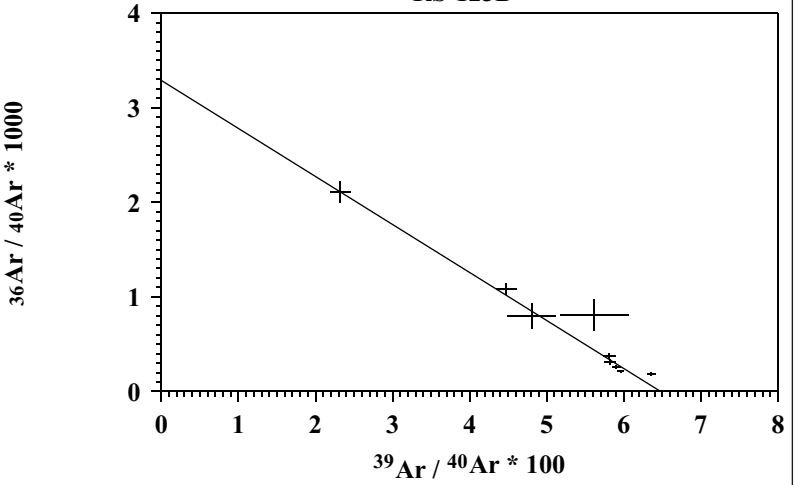

	T°C	(^{39}Ar/^{40}Ar)*100	(^{36}Ar/^{40}Ar)*1000
1	1000	4.805 ± .315	.793 ± .133
2	1025	5.812 ± .078	.373 ± .03
3	1050	5.902 ± .054	.257 ± .019
4	1075	5.958 ± .04	.213 ± .012
5	1100	6.356 ± .057	.187 ± .019
6	1125	5.618 ± .441	.807 ± .164
7	1200	5.815 ± .074	.311 ± .029
8	1275	4.477 ± .135	1.083 ± .061
9	1350	2.323 ± .13	2.111 ± .113

ITERATIONS = 3

XBAR = 5.9

YBAR = .292

SUM S = 21.693

SLOPE =-.5080001 ± .051 INCLUDING SUMS

X = 6.476 ± .064

(Y=0)

Y = 3.056 ± .499 (^{40}Ar/^{36}Ar INITIAL= 327 ± 53)

Y = 3.289 ± .303 (40Ar/36Ar INITIAL= 303 ± 28)

(X=0)

J = .002235 ± 1.1175E-05

ISOCHRON AGE = 61.193 ± .89 Ma (2σ UNCERTAINTY INCLUDING ERROR IN J)

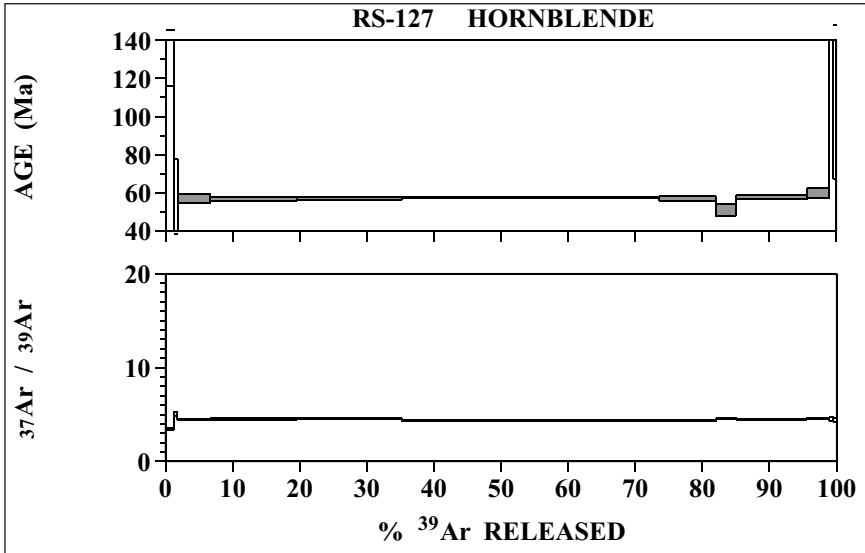

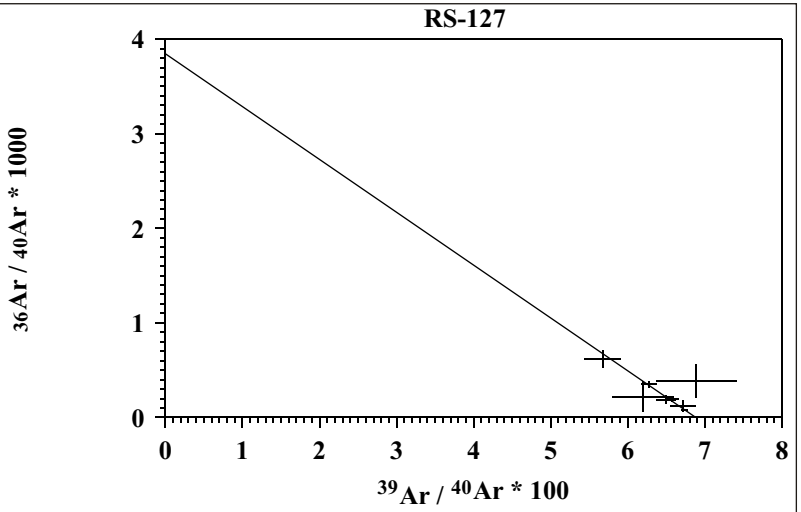

T°C	^{39}Ar(mV)	^{39}Ar(%)	AGE (Ma)±1σ	% ATM	^{37}Ar/^{39}Ar	^{36}Ar/^{40}Ar	^{39}Ar/^{40}Ar	% IIC
950	5.2	1.2	130.4 ± 14.6	43.4	3.44	0.001468	0.016821	0.99
975	2.4	0.5	58 ± 19.5	47.2	5.06	0.001601	0.035545	2.92
1000	21.2	4.8	57 ± 2.4	17.7	4.49	0.000619	0.056761	2.63
1025	56.5	12.9	56.7 ± 1	9.8	4.52	0.000351	0.0627	2.67
1050	68.3	15.6	56.9 ± .7	4.9	4.55	0.000194	0.065697	2.67
1075	167.4	38.2	57.5 ± .4	1.5	4.34	0.000076	0.067359	2.53
1100	37.1	8.4	56.9 ± 1.1	2.2	4.33	0.000122	0.067111	2.54
1125	13.4	3	51 ± 2.9	10.1	4.56	0.000387	0.068846	2.96
1200	46.1	10.5	57.6 ± 1.1	4.5	4.5	0.000187	0.064969	2.61
1275	14.3	3.2	59.7 ± 2.6	5	4.57	0.000218	0.06199	2.57
1350	2.7	0.6	3518 ± 1396	0.2	4.5	0.000007	0.000369	0.3
1400	2	0.4	107.5 ± 40.2	61.4	4.42	0.002075	0.013952	1.49

TOTAL GAS AGE = 123.3 ± 115.9 Ma

J = .002235 ± 1.1175E-05 (.5 %)

^{37}Ar/^{39}Ar, ^{36}Ar/^{40}Ar AND ^{39}Ar/^{40}Ar ARE CORRECTED FOR MASS SPECTROMETER DISCRIMINATION,INTERFERING ISOTOPES AND SYSTEM BLANKS

% IIC - INTERFERING ISOTOPES CORRECTION

	T°C	(^{39}Ar/^{40}Ar)*100	(^{36}Ar/^{40}Ar)*1000
1	1000	5.676 ± .233	.619 ± .090
2	1025	6.27 ± .1	.351 ± .036
3	1050	6.569 ± .087	.194 ± .03
4	1075	6.735 ± .042	.076 ± .01
5	1100	6.711 ± .163	.122 ± .059
6	1125	6.884 ± .52	.387 ± .176
7	1200	6.496 ± .124	.187 ± .045
8	1275	6.199 ± .4	.218 ± .159

ITERATIONS =3

XBAR = 6.633

YBAR = .138

SUM S = 2.13

SLOPE =-.56 ± .063 INCLUDING SUMS

X = 6.88 ± .031

(Y=0)

Y = 3.056 ± .499 (^{40}Ar/^{36}Ar INITIAL= 327 ± 53)

(X=0)

J = .002235 ± 1.1175E-05

ISOCHRON AGE = 57.66 ± .54 Ma (2σ UNCERTAINTY INCLUDING ERROR IN J)

RS-128 HORNBLENDE

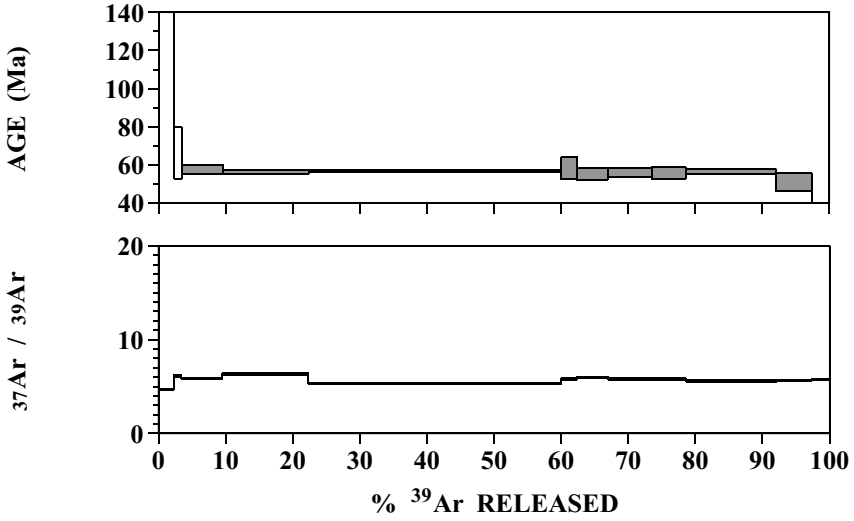

T°C	^{39}Ar(mV)	^{39}Ar(%)	AGE (Ma)±1σ	% ATM	^{37}Ar/^{39}Ar	^{36}Ar/^{40}Ar	^{39}Ar/^{40}Ar	% IIC
950	18.1	2.2	156 ± 9.9	57.1	4.67	0.00193	0.011005	1.16
975	9.1	1.1	66.1 ± 13.6	53	6.13	0.001788	0.028913	3.16
1000	48.6	6	57.5 ± 2.4	23.1	5.84	0.000795	0.054585	3.41
1025	102.5	12.8	56.3 ± 1.1	14.8	6.36	0.000516	0.06186	3.79
1050	300.4	37.6	56.9 ± .5	9.8	5.33	0.00034	0.065047	3.13
1075	19	2.3	58.3 ± 5.9	39	5.79	0.001323	0.042709	3.34
1100	37.3	4.6	55.2 ± 3.2	28	5.96	0.000958	0.053258	3.61
1125	51.9	6.5	55.9 ± 2.2	24.3	5.77	0.000833	0.055358	3.45
1175	40.8	5.1	55.6 ± 2.9	35	5.8	0.001189	0.047882	3.49
1250	107.4	13.4	56.5 ± 1.2	28.4	5.6	0.000967	0.051931	3.31
1350	42.7	5.3	50.8 ± 4.7	74.6	5.65	0.002524	0.020549	3.68
1400	20.7	2.5	27 ± 14.6	95	5.74	0.003215	0.007553	6.76

TOTAL GAS AGE = 58 ± 1.4 Ma

J = .002322 ± 1.161E-05 (.5 %)

^{37}Ar/^{39}Ar, ^{36}Ar/^{40}Ar AND ^{39}Ar/^{40}Ar ARE CORRECTED FOR MASS SPECTROMETER DISCRIMINATION,INTERFERING ISOTOPES AND SYSTEM BLANKS

% IIC - INTERFERING ISOTOPES CORRECTION

RS-128

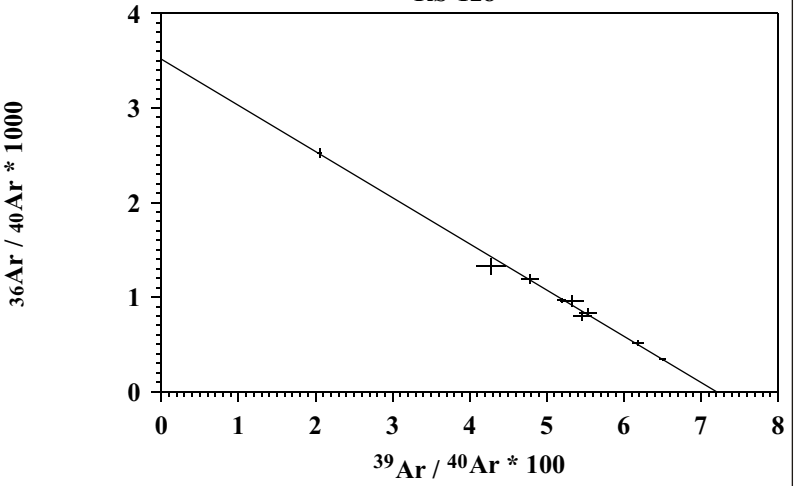

	T°C	(^{39}Ar/^{40}Ar)*100	(^{36}Ar/^{40}Ar)*1000
1	1000	5.458 ± .122	.795 ± .048
2	1025	6.186 ± .072	.516 ± .027
3	1050	6.504 ± .04	.34 ± .01
4	1075	4.27 ± .193	1.323 ± .089
5	1100	5.325 ± .153	.958 ± .061
6	1125	5.535 ± .116	.833 ± .046
7	1175	4.788 ± .112	1.189 ± .05
8	1250	5.193 ± .054	.967 ± .026
9	1350	2.054 ± .026	2.524 ± .05

ITERATIONS = 3

XBAR = 5.648

YBAR = .758

SUM S = 1.877

SLOPE =-.489 ± .006 INCLUDING SUMS

X = 7.2 ± .02

(Y=0)

Y = 3.056 ± .499 (^{40}Ar/^{36}Ar INITIAL= 327 ± 53)

Y = 3.516 ± .036 (40Ar/36Ar INITIAL= 284 ± 2)

(X=0)

J = .002322 ± 1.161E-05

ISOCHRON AGE = 57.246 ± .44 Ma (2σ UNCERTAINTY INCLUDING ERROR IN J)

RS-130 HORNBLENDE

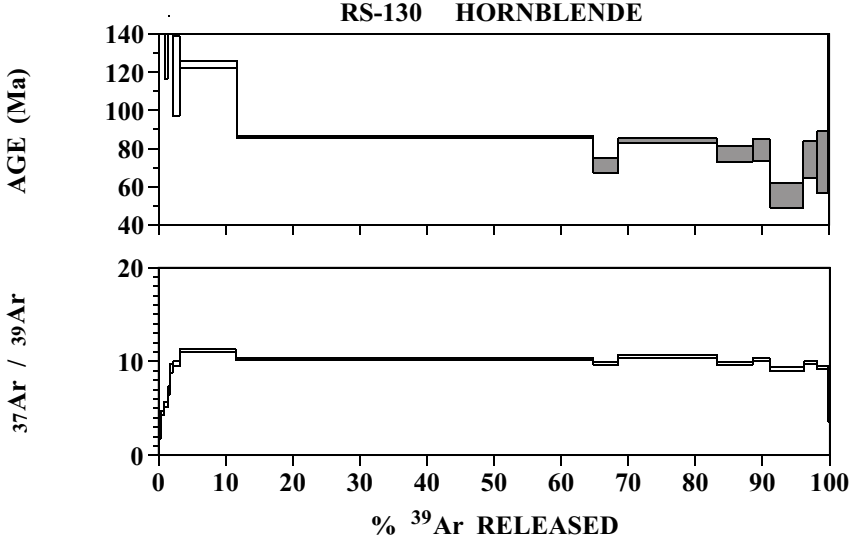

T°C	^{39}Ar(mV)	^{39}Ar(%)	AGE (Ma)±1σ	% ATM	^{37}Ar/^{39}Ar	^{36}Ar/^{40}Ar	^{39}Ar/^{40}Ar	% IIC
750	1.4	0.3	377.9 ± 79	34.3	1.91	0.001162	0.006275	0.26
900	1.8	0.4	564.7 ± 64.8	27.6	4.49	0.000934	0.004393	0.49
950	1.8	0.4	153.5 ± 37	40.5	5.4	0.001371	0.014868	1.37
975	1.1	0.2	223.7 ± 74.2	28.3	6.89	0.000962	0.012027	1.32
1000	1.7	0.4	278.8 ± 44	12.2	9.23	0.00043	0.011634	1.52
1025	3.9	1	117.9 ± 20.9	29.4	9.75	0.00101	0.023123	3.05
1050	32.4	8.4	124.2 ± 1.8	18.4	11.14	0.000623	0.025555	3.34
1075	203.9	53.1	86.1 ± .5	7.5	10.27	0.000262	0.042126	4.18
1100	14.4	3.7	71 ± 3.7	16.7	9.76	0.000605	0.045646	4.71
1175	56.2	14.6	84.2 ± 1.2	11.3	10.54	0.0004	0.04119	4.38
1225	20.5	5.3	77.1 ± 4.2	23.7	9.76	0.000819	0.038736	4.38
1275	9.9	2.5	78.9 ± 5.7	27.9	10.19	0.000967	0.03559	4.48
1350	19	4.9	55.2 ± 6.4	52.6	9.15	0.001785	0.033874	5.53
1400	7.9	2	74 ± 9.7	59.9	9.87	0.002028	0.021281	4.59
1450	6.1	1.6	72.8 ± 16.3	77.7	9.35	0.002628	0.012068	4.41
1475	0.7	0.2	1076.4 ± 352	61.1	4	0.002066	0.001064	0.34

TOTAL GAS AGE = 94.4 ± 3.1 Ma

J = .002235 ± 1.1175E-05 (.5 %)

^{37}Ar/^{39}Ar, ^{36}Ar/^{40}Ar AND ^{39}Ar/^{40}Ar ARE CORRECTED FOR MASS SPECTROMET ER DISCRIMINATION,INTERFERING ISOTOPES AND SYSTEM BLANKS

% IIC - INTERFERING ISOTOPE S CORRECTION

RS-130

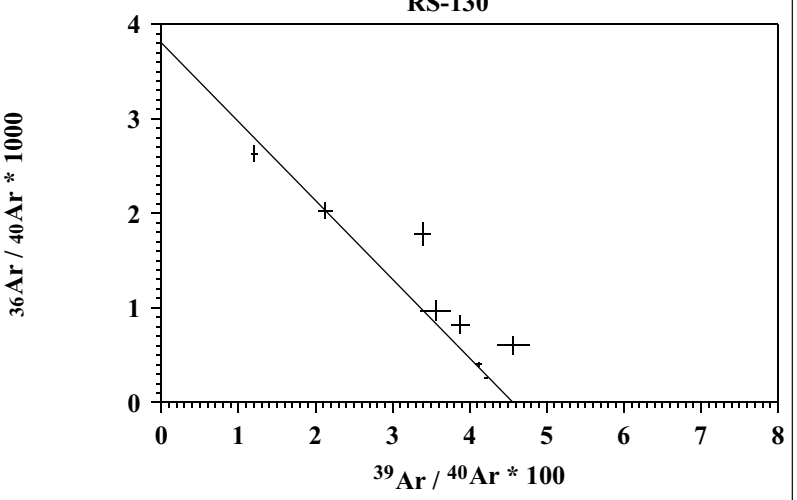

	T°C	(^{39}Ar/^{40}Ar)*100	(^{36}Ar/^{40}Ar)*1000
1	1075	4.212 ± .023	.262 ± .008
2	1100	4.564 ± .211	.605 ± .099
3	1175	4.119 ± .044	.4 ± .023
4	1225	3.873 ± .117	.819 ± .098
5	1275	3.559 ± .194	.967 ± .11
6	1350	3.387 ± .104	1.785 ± .125
7	1400	2.128 ± .095	2.028 ± .089
8	1450	1.206 ± .042	2.628 ± .089

ITERATIONS =3

XBAR = 4.022

YBAR = .45

SUM S = 45.716

SLOPE =-.834 ± .078 INCLUDING SUMS

X = 4.562 ± .056

(Y=0)

Y = 3.056 ± .499 (^{40}Ar/^{36}Ar INITIAL= 327 ± 53)

(X=0)

J = .002235 ± 1.1175E-05

ISOCHRON AGE = 86.267 ± 1.46 Ma (2σ UNCERTAINTY INCLUDING ERROR IN J)

RS-131 HORNBLENDE

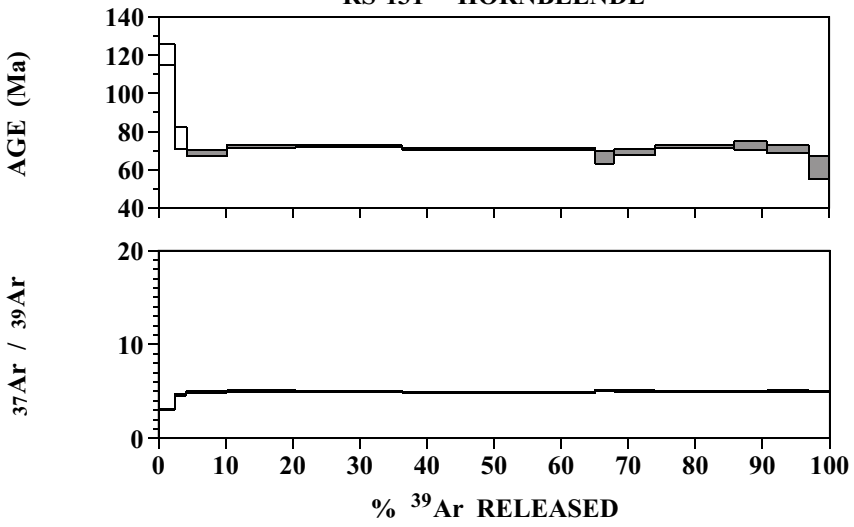

T°C	^{39}Ar(mV)	^{39}Ar(%)	AGE (Ma)±1σ	% ATM	^{37}Ar/^{39}Ar	^{36}Ar/^{40}Ar	^{39}Ar/^{40}Ar	% IIC
950	31.2	2.3	120.4 ± 5.3	48.7	3.09	0.001647	0.017118	0.92
975	22.8	1.7	76.5 ± 5.9	33.1	4.59	0.001125	0.035375	2.05
1000	79.3	6	68.5 ± 1.5	18.1	4.94	0.000622	0.048602	2.44
1025	132.8	10.1	72.1 ± 1	13.7	5.02	0.000471	0.048638	2.37
1050	207.7	15.8	72.4 ± .7	10.3	5.01	0.000355	0.050399	2.35
1075	376.8	28.8	71 ± .5	6.1	4.89	0.000214	0.053778	2.34
1100	36.1	2.7	66.3 ± 3.4	29.1	5.07	0.000991	0.043423	2.58
1125	79.8	6.1	69 ± 1.5	17.5	5.05	0.000602	0.048527	2.48
1175	155.1	11.8	72 ± .8	13.8	4.99	0.000473	0.048675	2.36
1250	63.3	4.8	72.7 ± 2.1	33.8	5	0.001146	0.037023	2.34
1350	81	6.2	70.8 ± 2.2	50	5.04	0.001693	0.028737	2.42
1400	40.4	3	60.9 ± 6.1	79.6	4.99	0.002693	0.013653	2.73

TOTAL GAS AGE = 72.1 ± .9 Ma

J = .00231 ± 1.155E-05 (.5 %)

^{37}Ar/^{39}Ar, ^{36}Ar/^{40}Ar AND ^{39}Ar/^{40}Ar ARE CORRECTED FOR MASS SPECTROMETER DISCRIMINATION,INTERFERING ISOTOPES AND SYSTEM BLANKS

% IIC - INTERFERING ISOTOPES CORRECTION

RS-131

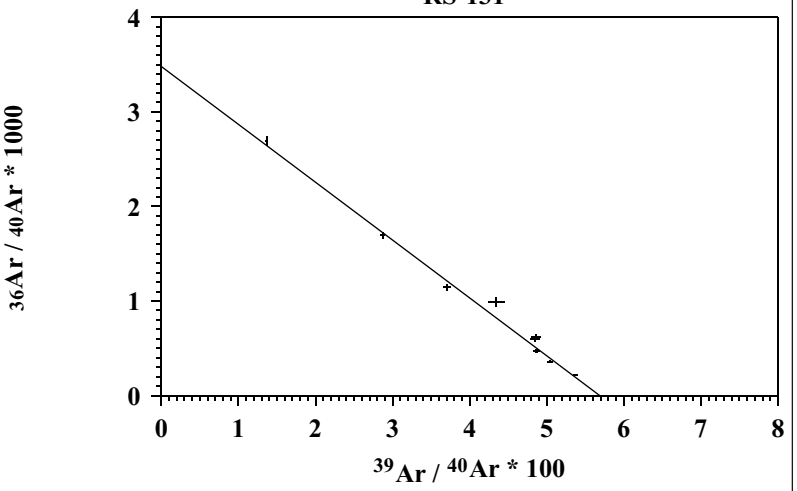

	T°C	(^{39}Ar/^{40}Ar)*100	(^{36}Ar/^{40}Ar)*1000
1	1000	4.86 ± .062	.622 ± .028
2	1025	4.863 ± .041	.471 ± .018
3	1050	5.039 ± .033	.355 ± .012
4	1075	5.377 ± .03	.214 ± .007
5	1100	4.342 ± .109	.991 ± .049
6	1125	4.852 ± .06	.602 ± .028
7	1175	4.867 ± .037	.473 ± .015
8	1250	3.702 ± .046	1.146 ± .032
9	1350	2.873 ± .026	1.693 ± .032
10	1400	1.365 ± .013	2.693 ± .049

ITERATIONS =3

XBAR = 4.653

YBAR = .632

SUM S = 24.428

SLOPE =-.612 ± .018 INCLUDING SUMS

X = 5.687 ± .032

Y = 3.056 ± .499 (^{40}Ar/^{36}Ar INITIAL= 327 ± 53)

Y = 3.48 ± .088 (40Ar/36Ar INITIAL= 287 ± 7)

(X=0)

J = .00231 ± 1.155E-05

ISOCHRON AGE = 71.81 ± .75 Ma (2σ UNCERTAINTY INCLUDING ERROR IN J)

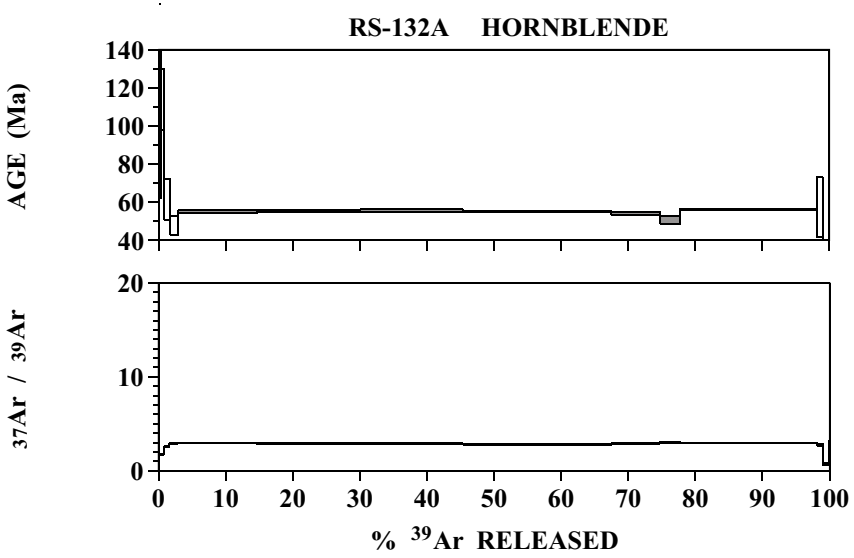

T°C	^{39}Ar(mV)	^{39}Ar(%)	AGE (Ma)±1σ	% ATM	^{37}Ar/^{39}Ar	^{36}Ar/^{40}Ar	^{39}Ar/^{40}Ar	% IIC
750	1.9	0.2	112.8 ± 50.8	64.8	1.69	0.002189	0.012121	0.55
900	4.1	0.5	113.8 ± 15.8	47	1.75	0.00159	0.018119	0.56
950	5.9	0.7	61.3 ± 10.9	43.6	2.57	0.001477	0.036191	1.41
975	9.9	1.3	47.7 ± 4.9	33.4	2.87	0.00114	0.055023	1.98
1000	88.6	11.6	54.8 ± .7	11.7	2.96	0.000405	0.063694	1.8
1025	117.7	15.4	55.1 ± .5	8.3	2.93	0.00029	0.065774	1.77
1050	116.3	15.3	55.5 ± .5	6.4	2.89	0.00023	0.066534	1.74
1075	168.2	22.1	55.1 ± .4	4.1	2.82	0.00015	0.068784	1.71
1100	54.9	7.2	54 ± .9	7.4	2.87	0.00027	0.067572	1.77
1125	23.4	3	50.8 ± 2.1	14.9	3.03	0.000522	0.066049	1.97
1200	154.6	20.3	56.1 ± .5	5.4	2.96	0.000195	0.06659	1.76
1250	7	0.9	57.3 ± 15.7	72.9	2.75	0.002464	0.018725	1.61
1350	6.4	0.8	-504.2 ±-138.8	-60.7	.72 -	.002055 -	0.014737	0
1450	0.7	0.1	209.3 ± 395	84.6	2.82	0.00286	0.00278	0.56

TOTAL GAS AGE = 55.8 ± 1.1 Ma

J = .002235 ± 1.1175E-05 (.5 %)

^{37}Ar/^{39}Ar, ^{36}Ar/^{40}Ar AND ^{39}Ar/^{40}Ar ARE CORRECTED FOR MASS SPECTROMET ER DISCRIMINATION,INTERFERING ISOTOPES AND SYSTEM BLANKS

% IIC - INTERFERING ISOTOPE S CORRECTION

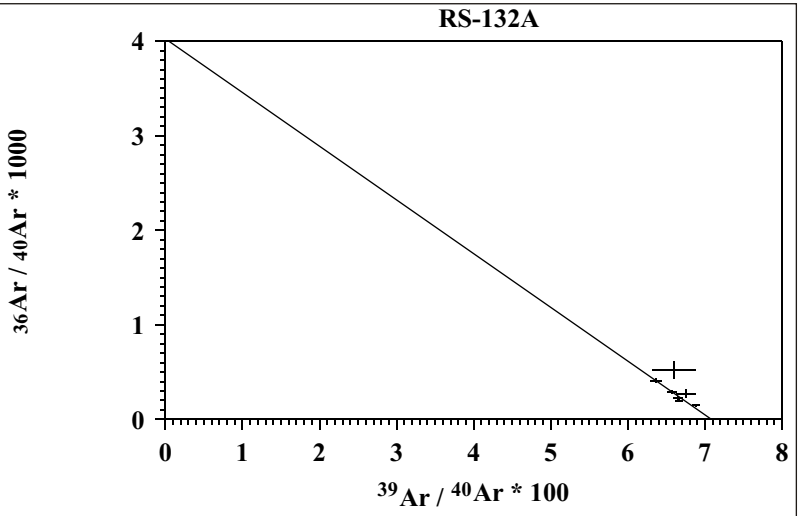

	T°C	(^{39}Ar/^{40}Ar)*100	(^{36}Ar/^{40}Ar)*1000
1	1000	6.369 ± .071	.405 ± .024
2	1025	6.577 ± .059	.29 ± .019
3	1050	6.653 ± .06	.23 ± .019
4	1075	6.878 ± .049	.15 ± .013
5	1100	6.757 ± .125	.27 ± .043
6	1125	6.604 ± .281	.522 ± .094
7	1200	6.659 ± .05	.195 ± .014

ITERATIONS =3

XBAR = 6.673

YBAR = .233

SUM S = 6.177

SLOPE =-.569 ± .115 INCLUDING SUMS

X = 7.085 ± .105

(Y=0)

Y = 4.025 ± .773 (40Ar/36Ar INITIAL= 248 ± 47)

Y = 3.056 ± .499 (^{40}Ar/^{36}Ar INITIAL= 327 ± 53)

J = .002235 ± 1.1175E-05

ISOCHRON AGE = 56.018 ± 1.08 Ma (2σ UNCERTAINTY INCLUDING ERROR IN J)

RS-132C HORNBLENDE

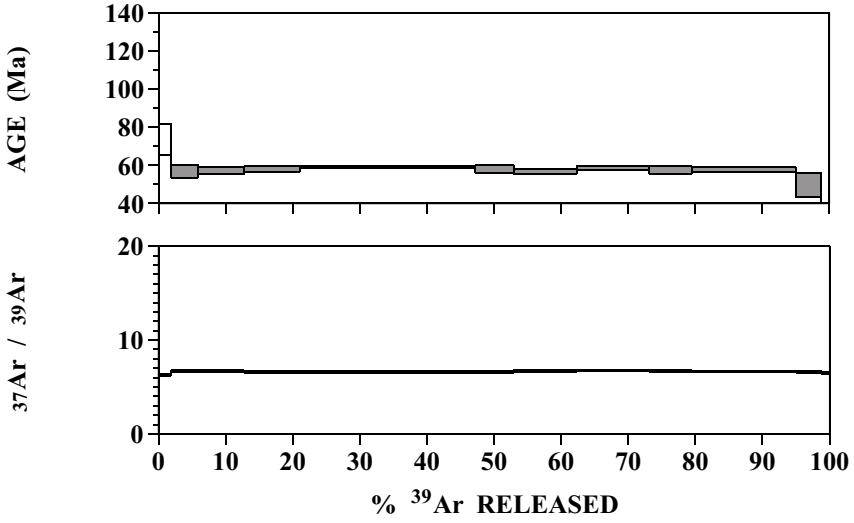

T°C	^{39}Ar(mV)	^{39}Ar(%)	AGE (Ma)±1σ	% ATM	^{37}Ar/^{39}Ar	^{36}Ar/^{40}Ar	^{39}Ar/^{40}Ar	% IIC
950	19.1	1.8	73.5 ± 8.3	70.3	6.31	0.002376	0.016411	2.95
975	40.3	3.9	56.9 ± 3.4	44.3	6.68	0.001503	0.039756	3.92
1000	72	6.9	57 ± 1.8	28.7	6.73	0.00098	0.050855	3.95
1025	85.3	8.2	58 ± 1.4	23	6.63	0.000788	0.053949	3.83
1050	269.6	26.1	59.2 ± .5	10.3	6.6	0.000359	0.061628	3.74
1075	59.1	5.7	57.9 ± 2.1	31.9	6.63	0.001084	0.047825	3.83
1100	97.5	9.4	56.8 ± 1.3	27.3	6.74	0.00093	0.052083	3.97
1125	110.3	10.7	58.6 ± 1.2	23.1	6.75	0.000787	0.053419	3.86
1175	65.9	6.3	57.5 ± 2.1	43.5	6.68	0.001476	0.039965	3.89
1250	160.9	15.6	57.9 ± 1.1	37.4	6.66	0.001269	0.04411	3.85
1350	38.7	3.7	49.5 ± 6.3	83.5	6.58	0.002826	0.0136	4.39
1400	12.1	1.1	7 ± 37.2	99	6.46	0.003364	0.003074	28.01

TOTAL GAS AGE = 57.5 ± 1.3 Ma

J = .002306 ± 1.153E-05 (.5 %)

^{37}Ar/^{39}Ar, ^{36}Ar/^{40}Ar AND ^{39}Ar/^{40}Ar ARE CORRECTED FOR MASS SPECTROMETER DISCRIMINATION,INTERFERING ISOTOPES AND SYSTEM BLANKS

% IIC - INTERFERING ISOTOPE S CORRECTION

RS-132C

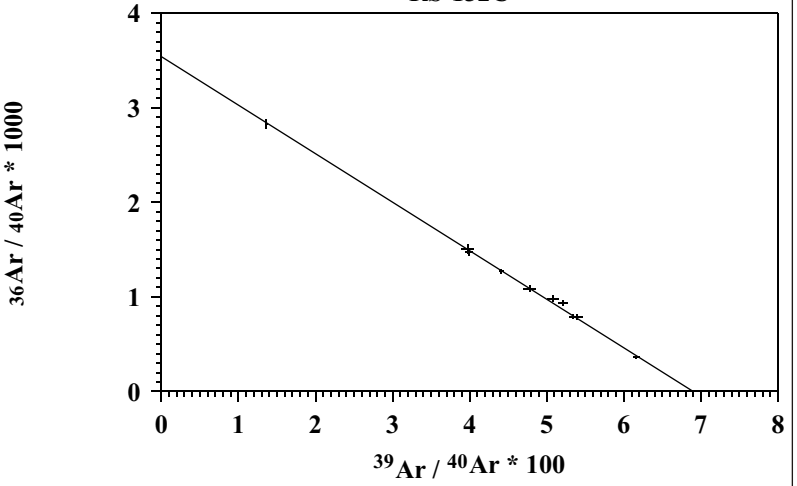

	T°C	(^{39}Ar/^{40}Ar)*100	(^{36}Ar/^{40}Ar)*1000
1	975	3.975 ± .082	1.503 ± .049
2	1000	5.085 ± .073	.98 ± .034
3	1025	5.394 ± 6.800001E-02	.788 ± .028
4	1050	6.162 ± .038	.359 ± .012
5	1075	4.782 ± 7.900001E-02	1.084 ± .036
6	1100	5.208 ± .058	.93 ± .028
7	1125	5.341 ± .055	.787 ± .024
8	1175	3.996 ± .051	1.476 ± .037
9	1250	4.411 ± .032	1.269 ± .025
10	1350	1.36 ± .013	2.826 ± .051

ITERATIONS =3

XBAR = 4.992

YBAR = .978

SUM S = 4.319

SLOPE =-.514 ± .007 INCLUDING SUMS

X = 6.899 ± .029

Y = 3.056 ± .499 (^{40}Ar/^{36}Ar INITIAL= 327 ± 53)

Y = 3.541 ± .04 (40Ar/36Ar INITIAL= 282 ± 3)

(X=0)

J = .002306 ± 1.153E-05

ISOCHRON AGE = 59.302 ± .54 Ma (2σ UNCERTAINTY INCLUDING ERROR IN J)

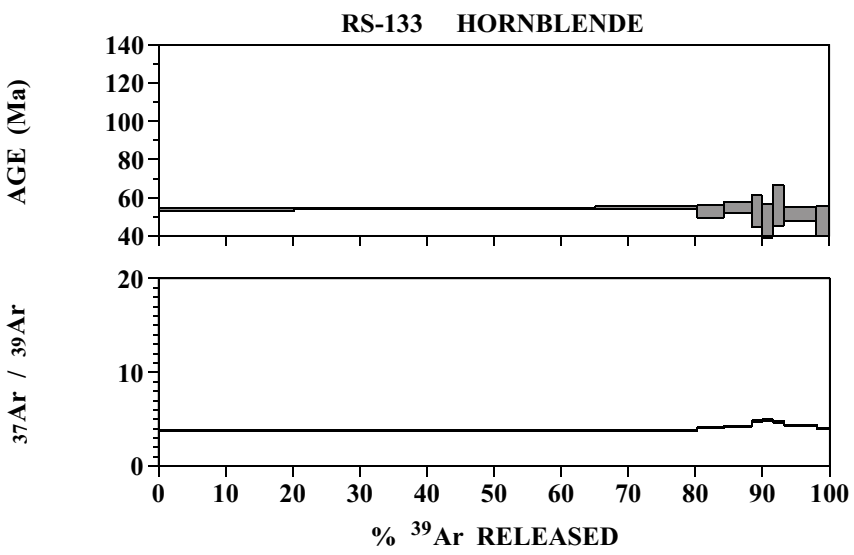

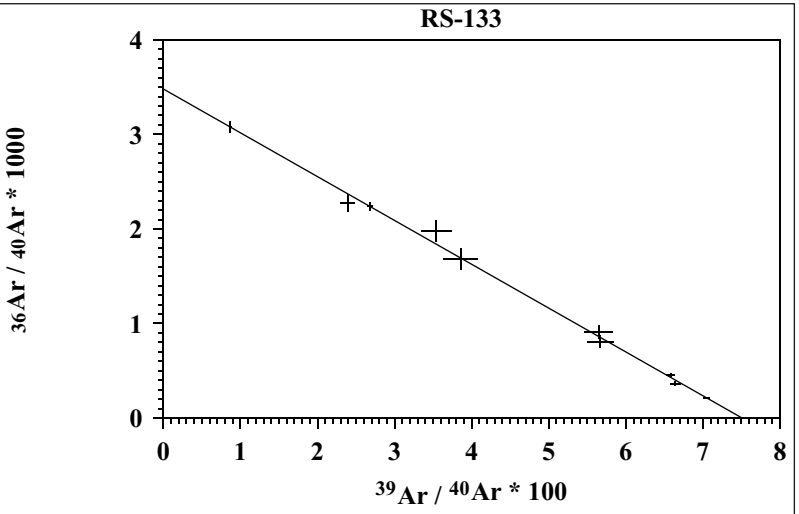

T°C	^{39}Ar(mV)	^{39}Ar(%)	AGE (Ma)±1σ	% ATM	^{37}Ar/^{39}Ar	^{36}Ar/^{40}Ar	^{39}Ar/^{40}Ar	% IIC
975	177.5	20.1	53.5 ± .7	13.3	3.81	0.000458	0.065836	2.31
1025	396	44.9	54.2 ± .4	5.9	3.76	0.000209	0.07052	2.25
1050	133.5	15.1	54.8 ± .8	10.3	3.78	0.000362	0.06644	2.24
1075	34.9	3.9	52.7 ± 3.3	26.5	4.09	0.000906	0.056502	2.53
1100	37	4.2	54.7 ± 2.9	23.4	4.23	0.000803	0.056694	2.53
1125	13.4	1.5	52.8 ± 8.2	49.7	4.79	0.001678	0.038546	2.97
1175	14.1	1.6	47.6 ± 9	58.4	4.86	0.001972	0.035408	3.32
1250	14.6	1.6	55.6 ± 10.6	67.2	4.71	0.00227	0.023905	2.79
1350	42.3	4.8	51.2 ± 3.6	66.3	4.33	0.002241	0.026846	2.75
1400	17.1	1.9	41.8 ± 13.4	91.1	4.03	0.003079	0.008712	3.07

TOTAL GAS AGE = 53.6 ± 1 Ma

J = .0023 ± .0000115 (.5 %)

^{37}Ar/^{39}Ar, ^{36}Ar/^{40}Ar AND ^{39}Ar/^{40}Ar ARE CORRECTED FOR MASS SPECTROMETER DISCRIMINATION,INTERFERING ISOTOPES AND SYSTEM BLANKS

% IIC - INTERFERING ISOTOPES CORRECTION

	T°C	(^{39}Ar/^{40}Ar)*100	(^{36}Ar/^{40}Ar)*1000
1	975	6.583 ± .055	.458 ± .017
2	1025	7.052 ± .04	.209 ± .008
3	1050	6.644 ± .067	.362 ± .022
4	1075	5.65 ± .187	.906 ± .071
5	1100	5.669 ± .171	.803 ± .064
6	1125	3.854 ± .227	1.678 ± .113
7	1175	3.54 ± .195	1.972 ± .111
8	1250	2.39 ± 9.399999E-02	2.27 ± .091
9	1350	2.684 ± .037	2.241 ± .046
10	1400	.871 ± .011	3.079 ± .062

ITERATIONS =2

XBAR = 6.045

YBAR = .677

SUM S = 4.207

SLOPE =-.464 ± .005 INCLUDING SUMS

X = 7.507 ± .018

Y = 3.056 ± .499 (^{40}Ar/^{36}Ar INITIAL= 327 ± 53)

Y = 3.479 ± .035 (40Ar/36Ar INITIAL= 287 ± 2)

(X=0)

J = .0023 ± .0000115

ISOCHRON AGE = 54.431 ± .4 Ma (2σ UNCERTAINTY INCLUDING ERROR IN J)

RS-134B HORNBLENDE

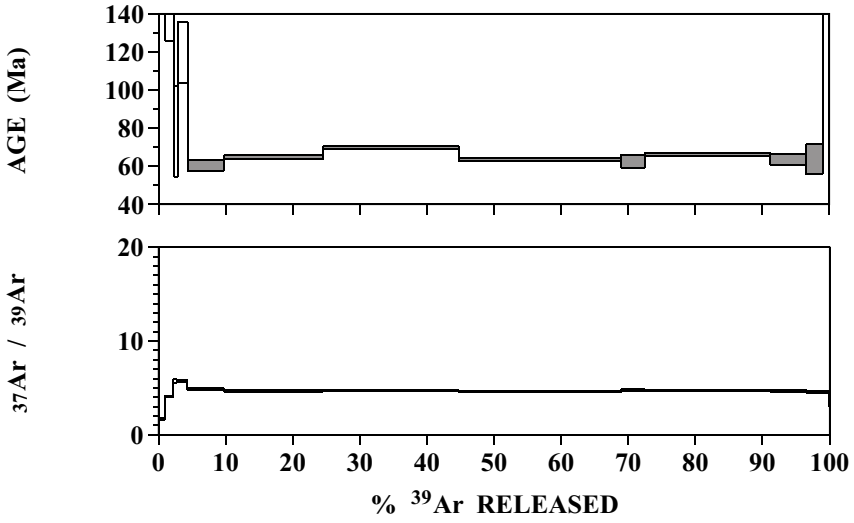

T°C	^{39}Ar(mV)	^{39}Ar(%)	AGE (Ma)±1σ	% ATM	^{37}Ar/^{39}Ar	^{36}Ar/^{40}Ar	^{39}Ar/^{40}Ar	% IIC
800	4	0.8	269.8 ± 25.2	36.7	1.68	0.001242	0.008746	0.28
950	5.8	1.2	140.8 ± 15.2	34.6	4.07	0.001174	0.017909	1.1
975	2.6	0.5	78.2 ± 23.9	43.9	5.69	0.001489	0.027927	2.52
1000	6.9	1.5	119.4 ± 15.9	22.1	5.76	0.000761	0.025229	1.78
1025	24.4	5.3	60.4 ± 2.7	17.6	4.89	0.000616	0.053513	2.72
1050	67	14.7	64.6 ± 1.1	12.9	4.67	0.000449	0.053057	2.45
1075	92.1	20.2	69.8 ± .8	11.6	4.69	0.000402	0.049819	2.29
1100	110.2	24.2	63.3 ± .7	7.1	4.58	0.000257	0.057758	2.45
1125	15.7	3.4	62.6 ± 3.4	15.8	4.76	0.000563	0.052639	2.57
1200	84.8	18.6	66.1 ± .9	11.7	4.68	0.000408	0.052584	2.4
1275	24.8	5.4	63.5 ± 2.8	21.9	4.68	0.000755	0.048371	2.49
1350	11.1	2.4	63.6 ± 7.7	53.9	4.57	0.001826	0.028532	2.43
1425	3.8	0.8	264.2 ± 50.9	66.9	4.55	0.002263	0.00468	0.78
1450	0.5	0.1	845.7 ± 640	78.2	3.51	0.002645	0.000812	0.32

TOTAL GAS AGE = 72.2 ± 3 Ma

J = .002235 ± 1.1175E-05 (.5 %)

^{37}Ar/^{39}Ar, ^{36}Ar/^{40}Ar AND ^{39}Ar/^{40}Ar ARE CORRECTED FOR MASS SPECTROMETER DISCRIMINATION,INTERFERING ISOTOPES AND SYSTEM BLANKS

% IIC - INTERFERING ISOTOPES CORRECTION

RS-134B

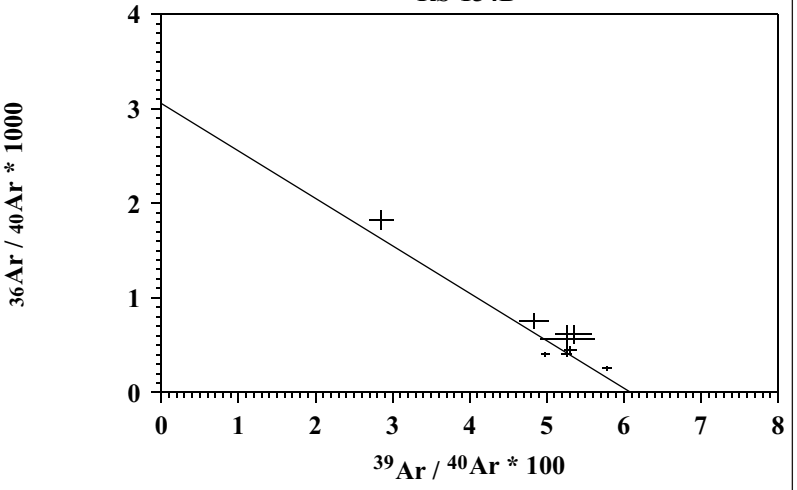

	T°C	(^{39}Ar/^{40}Ar)*100	(^{36}Ar/^{40}Ar)*1000
1	1025	5.351 ± .235	.616 ± .097
2	1050	5.305 ± .082	.449 ± .034
3	1075	4.981 ± .055	.402 ± .023
4	1100	5.775 ± .06	.257 ± .023
5	1125	5.263 ± .351	.563 ± .146
6	1200	5.258 ± .066	.408 ± .027
7	1275	4.837 ± .188	.755 ± .081
8	1350	2.853 ± .155	1.826 ± .103

ITERATIONS =4

XBAR = 5.257

YBAR = .418

SUM S = 32.041

SLOPE =-.502 ± 9.399999E-02 INCLUDING SUMS

X = 6.091 ± .193

(Y=0)

Y = 3.056 ± .499 (^{40}Ar/^{36}Ar INITIAL= 327 ± 53)

(X=0)

J = .002235 ± 1.1175E-05

ISOCHRON AGE = 64.995 ± 2.29 Ma (2σ UNCERTAINTY INCLUDING ERROR IN J)

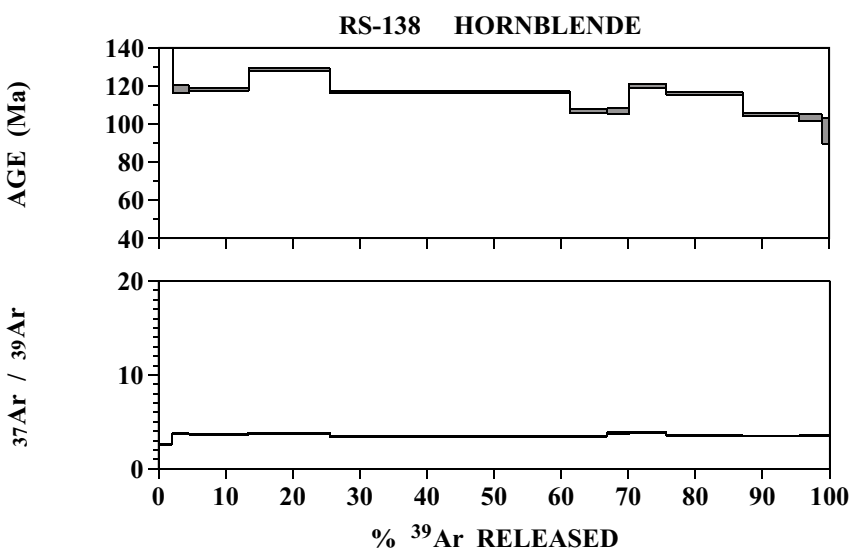

T°C	^{39}Ar(mV)	^{39}Ar(%)	AGE (Ma)±1σ	% ATM	^{37}Ar/^{39}Ar	^{36}Ar/^{40}Ar	^{39}Ar/^{40}Ar	% IIC
950	50.2	2	516.4 ± 4.4	10.5	2.62	0.000355	0.00629	0.3
975	60.8	2.4	118.2 ± 2.2	17.3	3.72	0.000589	0.028377	1.2
1000	220.3	8.9	117.9 ± .8	5.9	3.65	0.000205	0.032372	1.18
1025	299.8	12.1	128.7 ± .7	4	3.8	0.00014	0.030193	1.14
1050	885.4	35.7	116.5 ± .5	1.7	3.44	0.000062	0.034266	1.12
1075	136.6	5.5	106.5 ± 1	6	3.43	0.000209	0.0359	1.2
1100	83.7	3.3	106.9 ± 1.6	10	3.81	0.000343	0.034266	1.33
1125	135.1	5.4	120 ± 1	4.7	3.88	0.000164	0.0322	1.24
1175	283.1	11.4	115.9 ± .7	3.6	3.55	0.000127	0.033776	1.16
1250	206.3	8.3	104.8 ± .8	8	3.48	0.000274	0.035789	1.24
1350	85.4	3.4	103.2 ± 1.9	30.3	3.51	0.001027	0.027535	1.27
1400	27.8	1.1	96.3 ± 6.9	68.5	3.52	0.002316	0.013367	1.35

TOTAL GAS AGE = 124.8 ± .8 Ma

J = .002331 ± 1.1655E-05 (.5 %)

^{37}Ar/^{39}Ar, ^{36}Ar/^{40}Ar AND ^{39}Ar/^{40}Ar ARE CORRECTED FOR MASS SPECTROMETER DISCRIMINATION,INTERFERING ISOTOPES AND SYSTEM BLANKS

% IIC - INTERFERING ISOTOPES CORRECTION

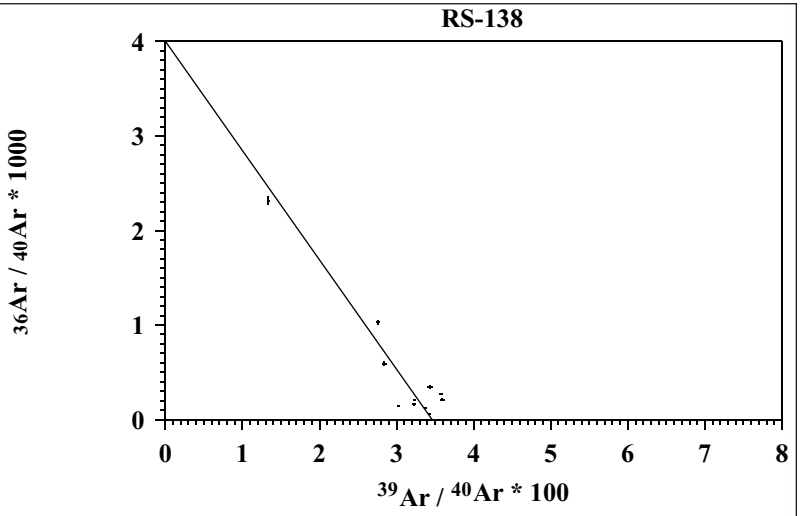

	T°C	(^{39}Ar/^{40}Ar)*100	(^{36}Ar/^{40}Ar)*1000
1	975	2.837 ± .031	.589 ± .022
2	1000	3.237 ± .018	.205 ± .007
3	1025	3.019 ± .016	.14 ± .005
4	1050	3.426 ± .017	.062 ± .002
5	1075	3.59 ± .025	.209 ± .012
6	1100	3.426 ± .032	.343 ± .019
7	1125	3.22 ± .021	.164 ± .011
8	1175	3.377 ± .018	.127 ± .006
9	1250	3.578 ± .021	.274 ±.009
10	1350	2.753 ± .022	1.027 ± .023
11	1400	1.336 ± .016	2.316 ± .045

ITERATIONS =3

XBAR = 3.216

YBAR = .282

SUM S = 850.787

SLOPE =-1.157 ± .203 INCLUDING SUMS

Y = 3.056 ± .499 (^{40}Ar/^{36}Ar INITIAL= 327 ± 53)
(Y=0)

Y = 4.003 ± .659 (40Ar/36Ar INITIAL= 249 ± 41)
(X=0)

J = .002331 ± 1.1655E-05

ISOCHRON AGE = 117.581 ± 2.28 Ma (2σ UNCERTAINTY INCLUDING ERROR IN J)

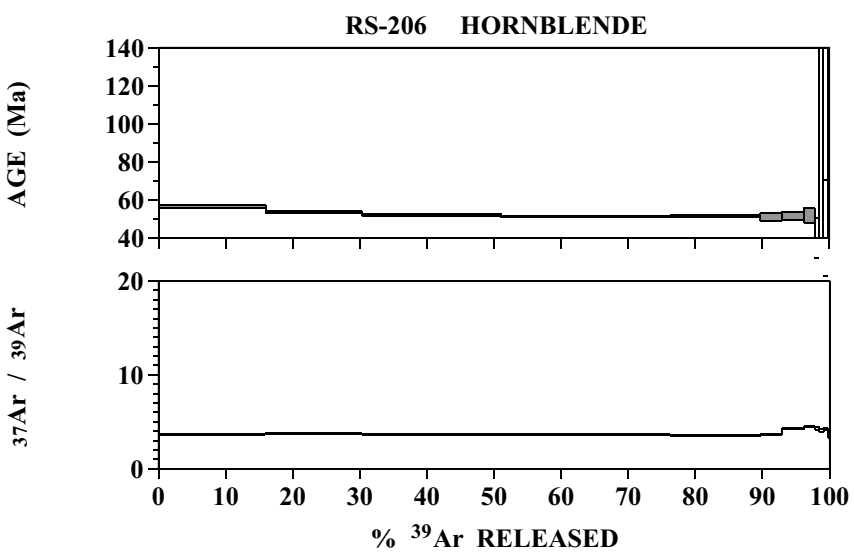

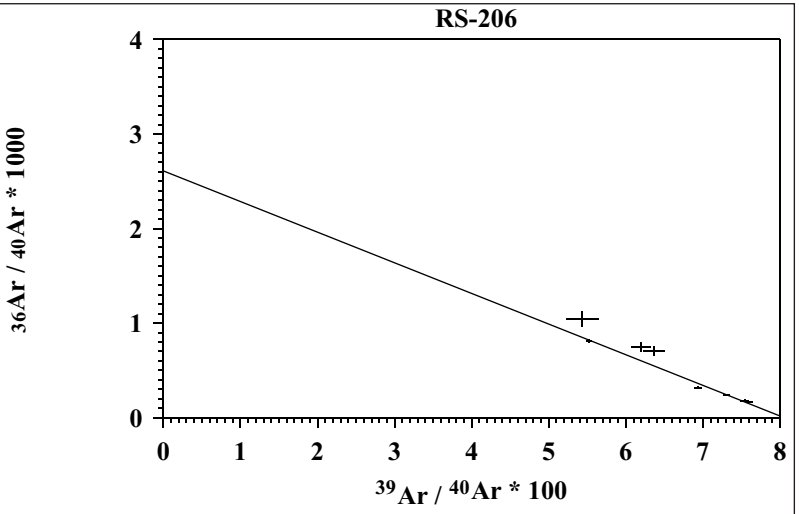

T°C	^{39}Ar(mV)	^{39}Ar(%)	AGE (Ma)±1σ	% ATM	^{37}Ar/^{39}Ar	^{36}Ar/^{40}Ar	^{39}Ar/^{40}Ar	% IIC
950	287.8	15.8	56.6 ± .6	23.8	3.66	0.000807	0.055179	2.23
975	260.6	14.3	53.7 ± .5	9	3.71	0.000313	0.069337	2.37
1000	376.8	20.8	52.3 ± .4	6.7	3.66	0.000235	0.073059	2.39
1025	455.5	25.1	51.4 ± .3	4.5	3.6	0.000161	0.076068	2.39
1050	243.6	13.4	51.5 ± .5	4.9	3.51	0.000179	0.075444	2.32
1075	57.6	3.1	51 ± 1.9	20.6	3.67	0.000706	0.063619	2.46
1100	60.8	3.3	51.5 ± 2	21.9	4.25	0.00075	0.061931	2.82
1125	28.5	1.5	51.9 ± 4	30.7	4.49	0.001046	0.054375	2.96
1175	11.9	0.6	40 ± 10.4	66.4	4.28	0.002237	0.034333	3.59
1250	10.9	0.6	45.4 ± 17.5	74.4	4.05	0.002508	0.023033	3.02
1350	11.7	0.6	45.3 ± 25.2	90.5	4.23	0.003061	0.008526	3.16
1400	4.7	0.2	752.6 ± 72.5	22	3.52	0.000744	0.003475	0.34

TOTAL GAS AGE = 54.9 ± .8 Ma

J = .002312 ± 1.156E-05 (.5 %)

^{37}Ar/^{39}Ar, ^{36}Ar/^{40}Ar AND ^{39}Ar/^{40}Ar ARE CORRECTED FOR MASS SPECTROMET ER DISCRIMINATION,INTERFERING ISOTOPES AND SYSTEM BLANKS

% IIC - INTERFERING ISOTOPE S CORRECTION

	T°C	(^{39}Ar/^{40}Ar)*100	(^{36}Ar/^{40}Ar)*1000
1	950	5.517 ± .034	.807 ± .016
2	975	6.933 ± .047	.313 ± .012
3	1000	7.305 ± .043	.235 ± .009
4	1025	7.606 ± .042	.161 ± .007
5	1050	7.544 ± .053	.179 ± .012
6	1075	6.361 ± .139	.706 ± .048
7	1100	6.193 ± .128	.75 ± .05
8	1125	5.437 ± .209	1.046 ±.079

ITERATIONS =3

XBAR = 7.011

YBAR = .337

SUM S = 22.699

SLOPE =-.325 ± .02 INCLUDING SUMS

X = 8.053001 ± .071

(Y=0)

Y = 3.056 ± .499 (^{40}Ar/^{36}Ar INITIAL= 327 ± 53)

(X=0)

J = .002312 ± 1.156E-05

ISOCHRON AGE = 51.052 ± .7 Ma (2σ UNCERTAINTY INCLUDING ERROR IN J)

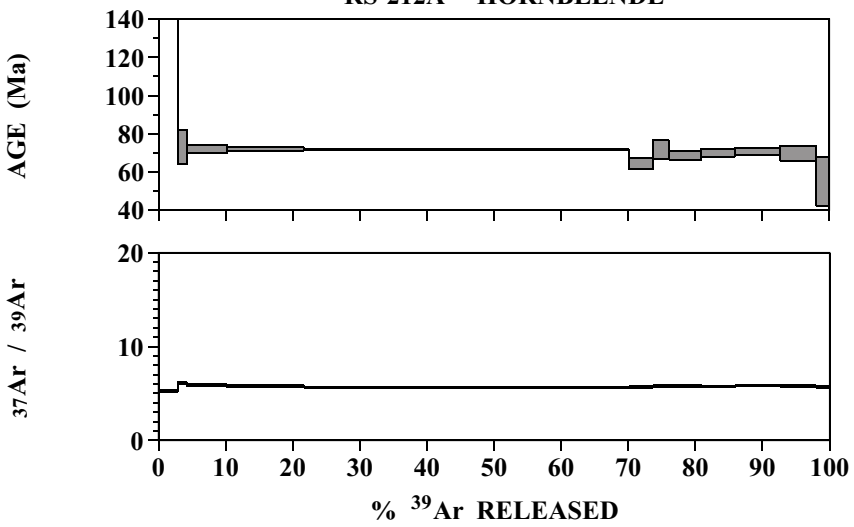

T°C	^{39}Ar(mV)	^{39}Ar(%)	AGE (Ma)±1σ	% ATM	^{37}Ar/^{39}Ar	^{36}Ar/^{40}Ar	^{39}Ar/^{40}Ar	% IIC
950	34.7	2.8	273.1 ± 6.1	45.4	5.24	0.001536	0.007634	0.87
975	17.1	1.3	72.7 ± 8.9	61	6.07	0.00206	0.021586	2.84
1000	73.5	5.9	71.9 ± 1.8	34.1	5.87	0.001158	0.036915	2.77
1025	141.2	11.4	72 ± 1	22.8	5.79	0.000776	0.043182	2.72
1050	596.1	48.4	71.6 ± .4	9.1	5.66	0.000311	0.051221	2.67
1075	43.6	3.5	64.2 ± 3	37.8	5.67	0.001281	0.039058	2.95
1100	30.5	2.4	71.6 ± 4.8	46.4	5.76	0.00157	0.030122	2.72
1125	58.8	4.7	68.5 ± 2.3	37.8	5.78	0.001282	0.036592	2.85
1175	61.9	5	69.9 ± 2.1	37.6	5.72	0.001275	0.035945	2.76
1250	82.5	6.7	70.7 ± 1.9	41	5.83	0.00139	0.033643	2.79
1350	65.7	5.3	69.5 ± 4	60.8	5.76	0.002056	0.022784	2.8
1400	24.8	2	54.9 ± 12.9	88.5	5.72	0.002995	0.008453	3.43

TOTAL GAS AGE = 76.7 ± 1.1 Ma

J = .002288 ± 1.144E-05 (.5 %)

^{37}Ar/^{39}Ar, ^{36}Ar/^{40}Ar AND ^{39}Ar/^{40}Ar ARE CORRECTED FOR MASS SPECTROMET ER DISCRIMINATION,INTERFERING ISOTOPES AND SYSTEM BLANKS

% IIC - INTERFERING ISOTOPE S CORRECTION

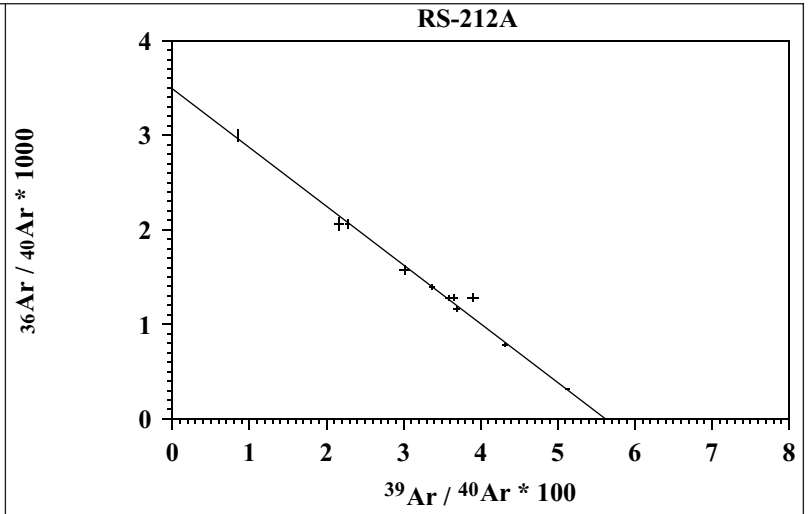

	T°C	(^{39}Ar/^{40}Ar)*100	(^{36}Ar/^{40}Ar)*1000
1	975	2.158 ± .062	2.06 ± .069
2	1000	3.691 ± .04	1.158 ± .029
3	1025	4.318 ± .033	.776 ± .017
4	1050	5.122 ± .026	.311 ± .007
5	1075	3.905 ± .073	1.281 ± .042
6	1100	3.012 ± .065	1.57 ± .049
7	1125	3.659 ± .049	1.282 ± .034
8	1175	3.594 ± .045	1.275 ± .03
9	1250	3.364 ± .033	1.39 ± .029
10	1350	2.278 ± .026	2.056 ± .051
11	1400	.845 ± .012	2.995 ± .064

ITERATIONS =2

XBAR = 4.101

YBAR = .943

SUM S = 18.681

SLOPE =-.622 ± .015 INCLUDING SUMS

Y = 3.056 ± .499 (^{40}Ar/^{36}Ar INITIAL= 327 ± 53)
(Y=0)

Y = 3.491 ± .065 (40Ar/36Ar INITIAL= 286 ± 5)
(X=0)

J = .002288 ± 1.144E-05

ISOCHRON AGE = 71.988 ± .84 Ma (2σ UNCERTAINTY INCLUDING ERROR IN J)

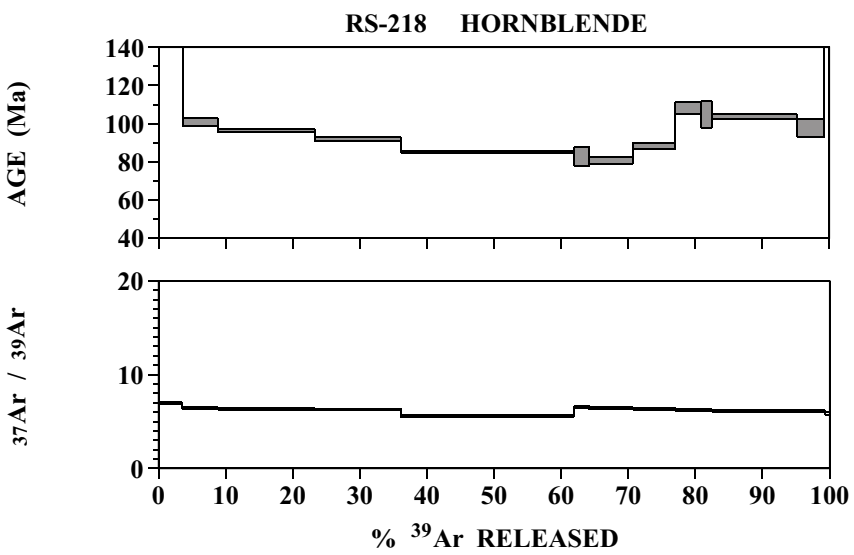

T°C	^{39}Ar(mV)	^{39}Ar(%)	AGE (Ma)±1σ	% ATM	^{37}Ar/^{39}Ar	^{36}Ar/^{40}Ar	^{39}Ar/^{40}Ar	% IIC
950	40.2	3.5	790.1 ± 6.6	22.6	7.01	0.000765	0.003233	0.66
975	60.7	5.3	100.7 ± 2.2	19.3	6.47	0.00066	0.032126	2.3
1000	163.9	14.3	96.3 ± .9	12.6	6.34	0.000433	0.036485	2.34
1025	146.8	12.8	91.8 ± 1	11.6	6.28	0.000398	0.038766	2.41
1050	295.2	25.8	85.1 ± .6	6.6	5.57	0.000229	0.044236	2.27
1075	25.8	2.2	82.6 ± 4.9	33.5	6.55	0.001139	0.032361	2.76
1100	74	6.4	80.5 ± 1.8	20	6.41	0.000683	0.04007	2.76
1125	72.3	6.3	88.2 ± 1.7	19.7	6.31	0.000672	0.036635	2.5
1175	43.8	3.8	108.2 ± 3.1	26.9	6.19	0.000913	0.027049	2.07
1200	18.5	1.6	104.8 ± 7	38.3	6.18	0.001299	0.023547	2.12
1250	144.3	12.6	103.7 ± 1	13.4	6.12	0.000456	0.03352	2.12
1350	47.1	4.1	97.8 ± 4.6	62.2	6.12	0.002106	0.015523	2.22
1400	8.3	0.7	361.1 ± 78.2	79.3	5.87	0.002685	0.002133	0.82

TOTAL GAS AGE = 124.5 ± 1.8 Ma

J = .002297 ± 1.1485E-05 (.5 %)

^{37}Ar/^{39}Ar, ^{36}Ar/^{40}Ar AND ^{39}Ar/^{40}Ar ARE CORRECTED FOR MASS SPECTROMET ER DISCRIMINATION,INTERFERING ISOTOPES AND SYSTEM BLANKS

% IIC - INTERFERING ISOTOPE S CORRECTION

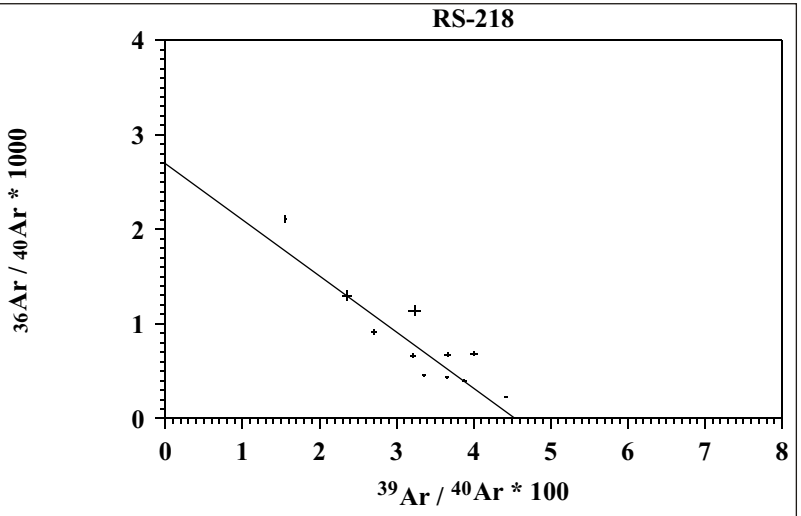

	T°C	(^{39}Ar/^{40}Ar)*100	(^{36}Ar/^{40}Ar)*1000
1	975	3.212 ± .038	.66 ± .025
2	1000	3.648 ± .023	.433 ± .012
3	1025	3.876 ± .027	.398 ± .013
4	1050	4.423 ± .024	.229 ± 9.000E-03
5	1075	3.236 ± .084	1.139 ± .054
6	1100	4.007 ± .047	.683 ± .025
7	1125	3.663 ± .04	.672 ± .023
8	1175	2.704 ± .037	.913 ± .029
9	1200	2.354 ± .064	1.299 ± .054
10	1250	3.352 ± .022	.456 ± .013
11	1350	1.552 ± .015	2.106 ± .039

ITERATIONS =6

XBAR = 3.633

YBAR = .536

SUM S = 520.872

SLOPE =-.594 ± .096 INCLUDING SUMS

Y = 3.056 ± .499 (^{40}Ar/^{36}Ar INITIAL= 327 ± 53)
(Y=0)

Y = 2.695 ± .354 (40Ar/36Ar INITIAL= 371 ± 48)
(X=0)

J = .002297 ± 1.1485E-05

ISOCHRON AGE = 89.069 ± 3.66 Ma (2σ UNCERTAINTY INCLUDING ERROR IN J)

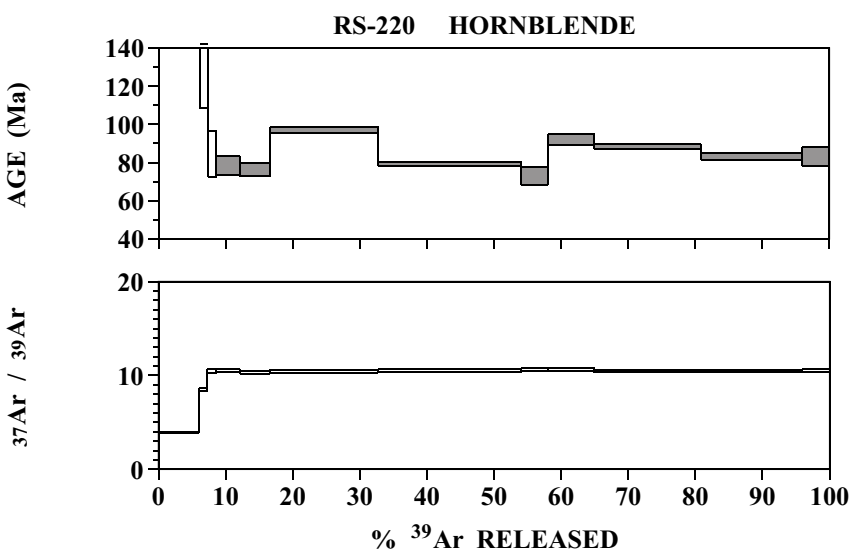

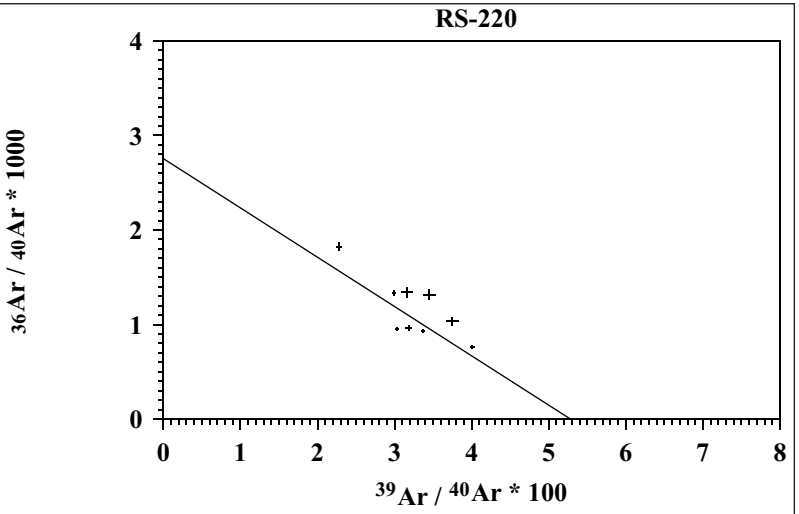

T°C	^{39}Ar(mV)	^{39}Ar(%)	AGE (Ma)±1σ	% ATM	^{37}Ar/^{39}Ar	^{36}Ar/^{40}Ar	^{39}Ar/^{40}Ar	% IIC
950	47.6	6	414.2 ± 4	8.1	3.93	0.000276	0.008295	0.52
975	9.1	1.1	125.2 ± 16.7	50.1	8.46	0.001693	0.016109	2.61
1000	10.3	1.3	84.5 ± 11.9	47	10.45	0.001592	0.025522	4.49
1025	27.7	3.5	78.4 ± 5.2	39.4	10.53	0.001339	0.03161	4.83
1050	34.9	4.4	76.2 ± 3.5	30.2	10.35	0.001032	0.037461	4.87
1075	126.2	16.1	97.1 ± 1.4	28	10.43	0.00095	0.030312	3.98
1100	167.1	21.3	79.3 ± 1	22.5	10.49	0.000765	0.040111	4.76
1125	31.2	3.9	72.9 ± 4.5	38.6	10.61	0.001314	0.034481	5.19
1175	54.2	6.9	92 ± 2.7	28.3	10.61	0.000963	0.031838	4.24
1250	124.9	15.9	88.3 ± 1.3	27.4	10.47	0.00093	0.03366	4.33
1350	117.7	15	83.3 ± 1.7	39.4	10.47	0.001335	0.029852	4.56
1400	31.7	4	83 ± 4.8	53.8	10.56	0.001822	0.022772	4.61

TOTAL GAS AGE = 107.6 ± 1.5 Ma
J = .002333 ± 1.1665E-05 (.5 %)
^{37}Ar/^{39}Ar, ^{36}Ar/^{40}Ar AND ^{39}Ar/^{40}Ar ARE CORRECTED FOR MASS SPECTROMET ER
DISCRIMINATION,INTERFERING ISOTOPES AND SYSTEM BLANKS
% IIC - INTERFERING ISOTOPE S CORRECTION

	T°C	(^{39}Ar/^{40}Ar)*100	(^{36}Ar/^{40}Ar)*1000
1	1025	3.161 ± .077	1.339 ± .056
2	1050	3.746 ± .079	1.032 ± .046
3	1075	3.031 ± .02	.95 ± .019
4	1100	4.011 ± .027	.765 ± .017
5	1125	3.448 ± .08	1.314 ± .055
6	1175	3.183 ± .041	.963 ± .03
7	1250	3.366 ± .024	.93 ± .019
8	1350	2.985 ± .021	1.335 ± .026
9	1400	2.277 ± .036	1.822 ± .043

# ITERATIONS =5
XBAR = 3.32
YBAR = 1.023
SUM S = 242.693
SLOPE =-.522 ± .139 INCLUDING SUMS
X = 5.282 ± .715
(Y=0)
Y = 3.056 ± .499 (^{40}Ar/^{36}Ar INITIAL= 327 ± 53)
Y = 2.755 ± .466 (40Ar/36Ar INITIAL= 362 ± 61)
(X=0)
J = .002333 ± 1.1665E-05
ISOCHRON AGE = 77.951 ± 9.5 Ma (2σ UNCERTAINTY INCLUDING ERROR IN J)

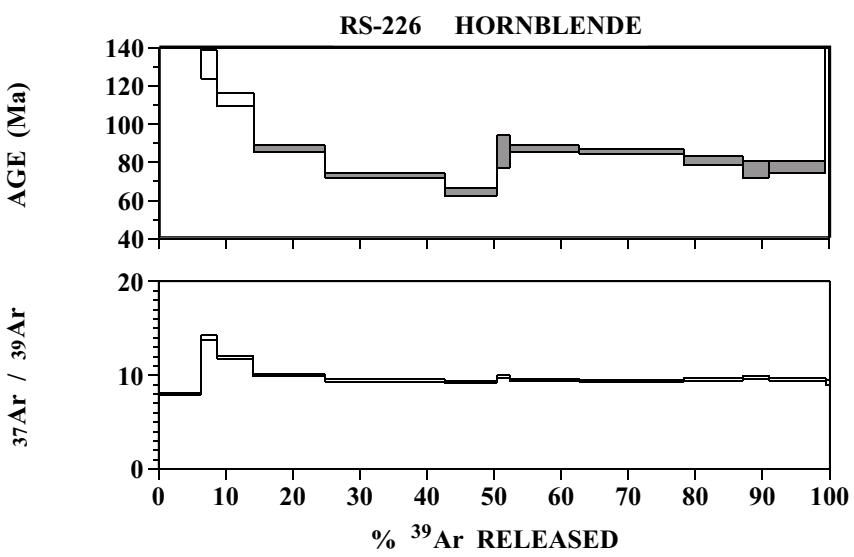

T°C	^{39}Ar(mV)	^{39}Ar(%)	AGE (Ma)±1σ	% ATM	^{37}Ar/^{39}Ar	^{36}Ar/^{40}Ar	^{39}Ar/^{40}Ar	% IIC
950	51.7	6.3	265.9 ± 5.3	45	8.02	0.001523	0.007938	1.39
975	19.1	2.3	131.4 ± 7.5	39.5	14.02	0.001339	0.01828	4.1
1000	44.8	5.4	112.7 ± 3.4	33.8	11.9	0.001147	0.02347	3.95
1025	87	10.6	87.1 ± 1.7	31.7	10.02	0.001077	0.031556	4.13
1050	146	17.8	73.1 ± 1.1	27.4	9.46	0.000931	0.040151	4.55
1075	63.8	7.8	64.4 ± 2	22.2	9.28	0.000765	0.048706	4.99
1100	15.5	1.8	85.7 ± 8.6	37.1	9.83	0.001262	0.029386	4.12
1150	84.6	10.3	87 ± 1.8	32	9.47	0.001086	0.031484	3.91
1200	127.7	15.6	85.7 ± 1.3	30.2	9.41	0.001026	0.0328	3.94
1250	72.3	8.8	80.9 ± 2.1	33.7	9.53	0.001143	0.033042	4.19
1300	32	3.9	76.3 ± 4.5	51.5	9.78	0.001744	0.025625	4.53
1400	68.5	8.3	77.4 ± 3	61.4	9.55	0.002078	0.020139	4.37
1450	4.9	0.6	833 ± 143	73.8	9.26	0.002499	0.00102	0.87

TOTAL GAS AGE = 100.8 ± 3 Ma

J = .002295 ± 1.1475E-05 (.5 %)

^{37}Ar/^{39}Ar, ^{36}Ar/^{40}Ar AND ^{39}Ar/^{40}Ar ARE CORRECTED FOR MASS SPECTROMET ER DISCRIMINATION,INTERFERING ISOTOPES AND SYSTEM BLANKS

% IIC - INTERFERING ISOTOPE S CORRECTION

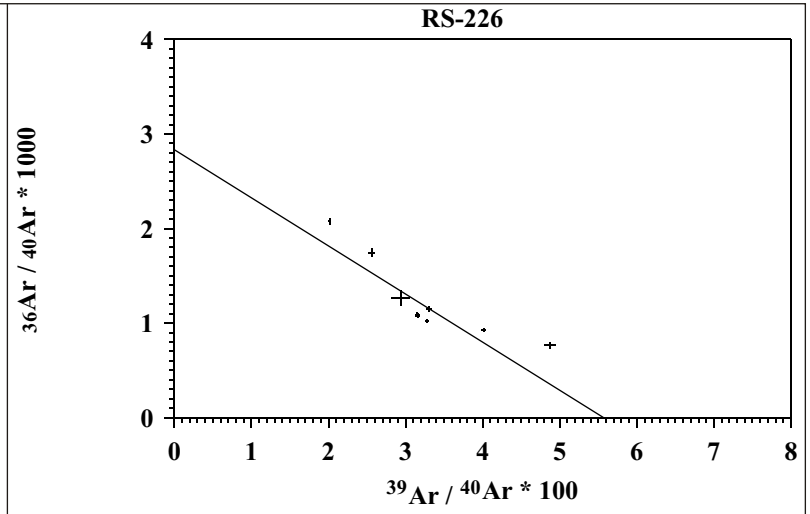

	T°C	(^{39}Ar/^{40}Ar)*100	(^{36}Ar/^{40}Ar)*1000
1	1025	3.155 ± .027	1.077 ± .023
2	1050	4.015 ± .029	.931 ± .02
3	1075	4.87 ± .076	.765 ± .035
4	1100	2.938 ± .119	1.262 ± .08
5	1150	3.148 ± .028	1.086 ± .024
6	1200	3.28 ± .023	1.026 ± .02
7	1250	3.304 ± .034	1.143 ± .029
8	1300	2.562 ± .044	1.744 ± .045
9	1400	2.013 ± .016	2.078 ± .036

ITERATIONS =6

XBAR = 3.303

YBAR = 1.152

SUM S = 250.468

SLOPE =-.509 ± .107 INCLUDING SUMS

X = 5.568 ± .603

(Y=0)

Y = 3.056 ± .499 (^{40}Ar/^{36}Ar INITIAL= 327 ± 53)

Y = 2.833 ± .359 (40Ar/36Ar INITIAL= 352 ± 44)

(X=0)

J = .002295 ± 1.1475E-05

ISOCHRON AGE = 72.843 ± 7.36 Ma (2σ UNCERTAINTY INCLUDING ERROR IN J)

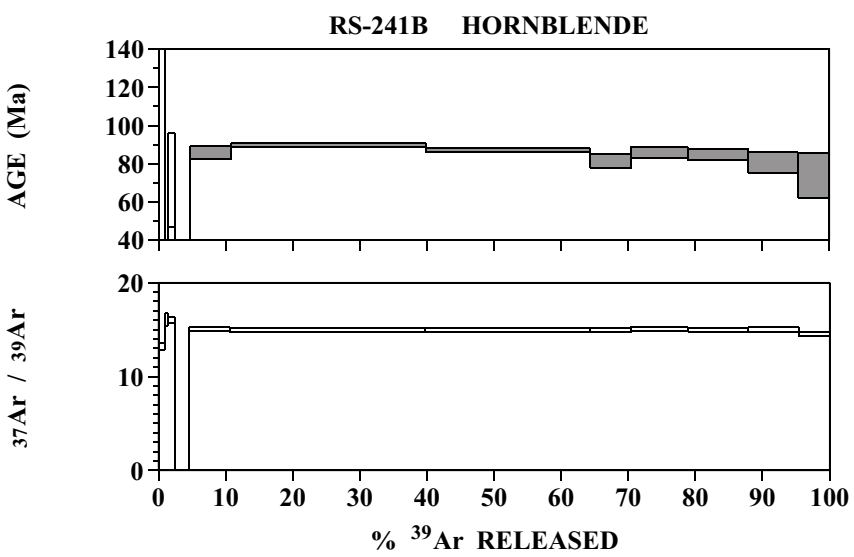

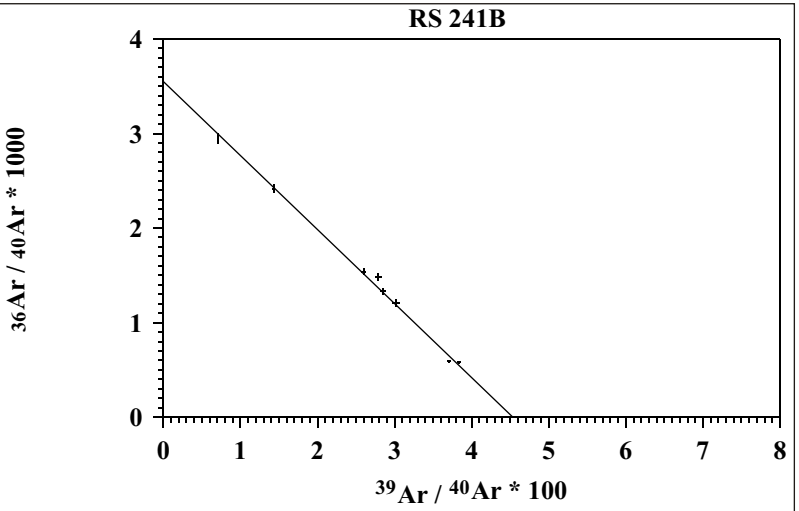

T°C	^{39}Ar(mV)	^{39}Ar(%)	AGE (Ma)±1σ	% ATM	^{37}Ar/^{39}Ar	^{36}Ar/^{40}Ar	^{39}Ar/^{40}Ar	% IIC
950	6	0.9	649.9 ± 56.7	45.7	13.2	0.001546	0.002862	1.38
975	2.4	0.3	-18.7 ±-74.6	104	16.08	0.003518	0.010716	25.87
1000	6.3	1	71.2 ± 24.6	70.5	15.99	0.00238	0.016586	7.86
1025	13.8	2.2	-	-	- -	-	-	
1050	38.1	6.1	85.6 ± 3.4	35.5	15.08	0.00121	0.030187	6.31
1075	181.2	29	89.6 ± 1	17.3	14.93	0.000591	0.037054	6
1100	153.5	24.6	86.9 ± 1	16.9	15	0.000582	0.038393	6.2
1125	37.5	6	81.3 ± 3.7	43.6	14.93	0.001478	0.027886	6.53
1175	53.3	8.5	85.8 ± 2.8	39.2	15.05	0.00133	0.028473	6.29
1250	56.1	8.9	84.5 ± 2.8	45.3	14.99	0.001536	0.026003	6.34
1350	46.5	7.4	80.4 ± 5.3	71.4	15.02	0.002418	0.014293	6.63
1400	28.8	4.6	73.7 ± 12	87.1	14.57	0.002948	0.00703	6.94

DISCRIMINATION,INTERFERING ISOTOPES AND SYSTEM BLANKS
J = .00229 ± 1.145E-05 (.5 %)
^{37}Ar/^{39}Ar, ^{36}Ar/^{40}Ar AND ^{39}Ar/^{40}Ar ARE CORRECTED FOR MASS SPECTROMET ER
DISCRIMINATION,INTERFERING ISOTOPES AND SYSTEM BLANKS
% IIC - INTERFERING ISOTOPE S CORRECTION

	T°C	(^{39}Ar/^{40}Ar)*100	(^{36}Ar/^{40}Ar)*1000
1	1050	3.018 ± .048	1.21 ± .037
2	1075	3.705 ± .023	.591 ± .014
3	1100	3.839 ± .025	.582 ± .015
4	1125	2.788 ± .043	1.478 ± .039
5	1175	2.847 ± .033	1.33 ± .033
6	1250	2.6 ± .028	1.536 ± .032
7	1350	1.429 ± .013	2.418 ± .045
8	1400	.703 ± .006	2.948 ± .054

# ITERATIONS =3
XBAR = 3.114
YBAR = 1.112
SUM S = 14.364
SLOPE =-.783 ± .022 INCLUDING SUMS
X = 4.534 ± .041
(Y=0)
Y = 3.056 ± .499 (^{40}Ar/^{36}Ar INITIAL= 327 ± 53)
(X=0)
J = .00229 ± 1.145E-05
ISOCHRON AGE = 88.858 ± 1.22 Ma (2σ UNCERTAINTY INCLUDING ERROR IN J)

RS-243 HORNBLENDE

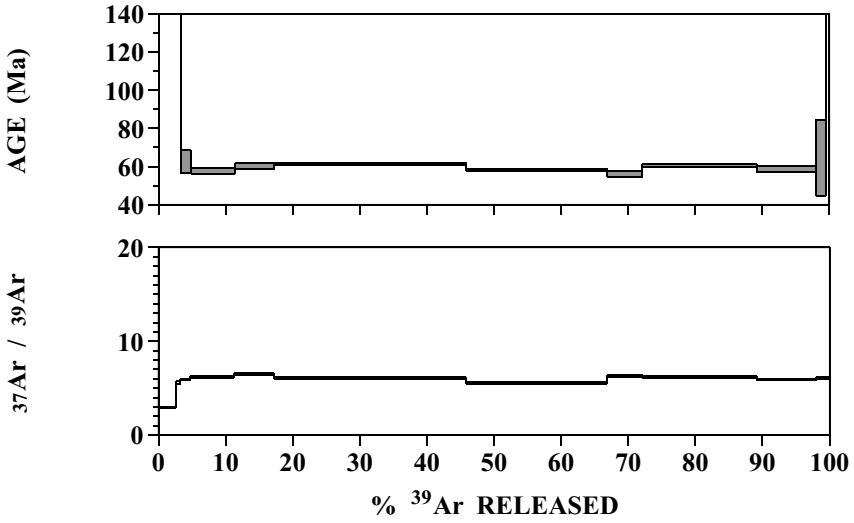

T°C	^{39}Ar(mV)	^{39}Ar(%)	AGE (Ma)±1σ	% ATM	^{37}Ar/^{39}Ar	^{36}Ar/^{40}Ar	^{39}Ar/^{40}Ar	% IIC
950	38.7	2.6	165.2 ± 7.3	62.5	2.98	0.002115	0.009092	0.73
975	8.9	0.6	205.5 ± 28.2	43.7	5.62	0.001478	0.010834	1.17
1000	22.3	1.5	62.5 ± 6.1	54.6	5.91	0.001848	0.029842	3.31
1025	96.8	6.5	57.7 ± 1.5	37.8	6.17	0.001281	0.044456	3.71
1050	87.5	5.9	60.2 ± 1.5	30.6	6.47	0.001042	0.047383	3.75
1075	422.6	28.6	61.5 ± .5	13.5	6.06	0.000463	0.057907	3.44
1100	309.8	20.9	58.3 ± .5	15.2	5.55	0.000521	0.059853	3.31
1125	77.8	5.2	56 ± 1.7	36.9	6.32	0.001254	0.046374	3.91
1200	251.9	17	60.4 ± .7	25.6	6.17	0.000869	0.050738	3.56
1275	131.1	8.8	58.6 ± 1.4	48.3	5.91	0.001638	0.036348	3.51
1350	21.1	1.4	64.6 ± 19.8	91.2	6.1	0.003085	0.005604	3.32
1400	8	0.5	5665.2 ± 883	6.2	6.08	0.000209	0.000098	0.4

TOTAL GAS AGE = 261.9 ± 192.7 Ma

J = .002328 ± 1.164E-05 (.5 %)

^{37}Ar/^{39}Ar, ^{36}Ar/^{40}Ar AND ^{39}Ar/^{40}Ar ARE CORRECTED FOR MASS SPECTROMET ER DISCRIMINATION,INTERFERING ISOTOPES AND SYSTEM BLANKS

% IIC - INTERFERING ISOTOPE S CORRECTION

RS-243

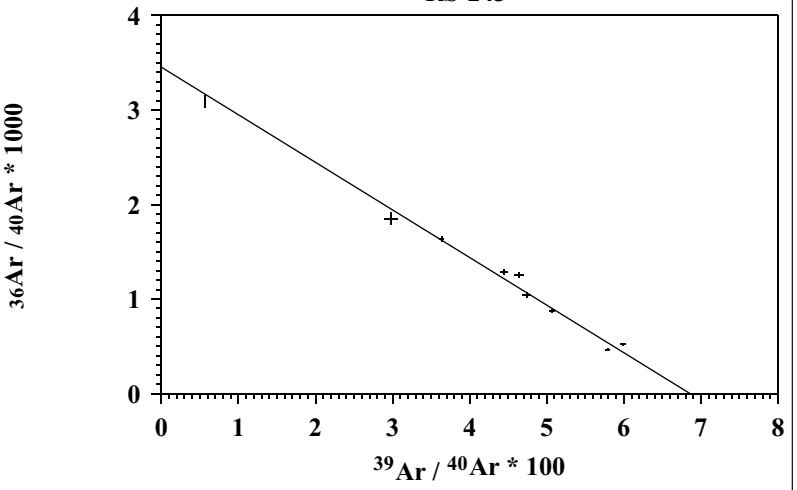

	T°C	(^{39}Ar/^{40}Ar)*100	(^{36}Ar/^{40}Ar)*1000
1	1000	2.984 ± .084	1.848 ± .064
2	1025	4.445 ± .047	1.281 ± .028
3	1050	4.738 ± .056	1.042 ± .028
4	1075	5.79 ± .032	.463 ± .011
5	1100	5.985 ± .036	.5210001 ± .013
6	1125	4.637 ± .059	1.254 ± .031
7	1200	5.073 ± .032	.869 ± .017
8	1275	3.634 ± .027	1.638 ± .029
9	1350	.56 ± .008	3.085 ± .067

ITERATIONS =3

XBAR = 5.077

YBAR = .897

SUM S = 45.253

SLOPE =-.504 ± .024 INCLUDING SUMS

X = 6.859 ± .092

(Y=0)

Y = 3.056 ± .499 (^{40}Ar/^{36}Ar INITIAL= 327 ± 53)

Y = 3.452 ± .129 (40Ar/36Ar INITIAL= 289 ± 10)

(X=0)

J = .002328 ± 1.164E-05

ISOCHRON AGE = 60.199 ± 1.09 Ma (2σ UNCERTAINTY INCLUDING ERROR IN J)

RS-244 HORNBLENDE

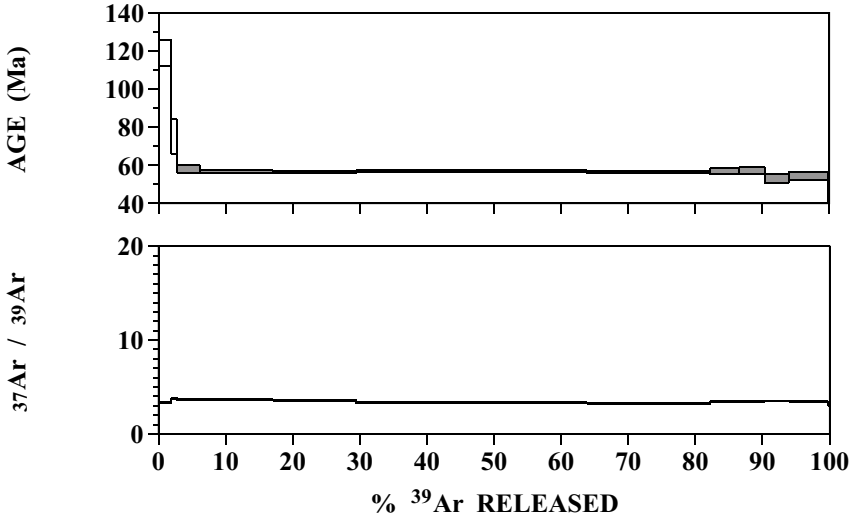

T°C	^{39}Ar(mV)	^{39}Ar(%)	AGE (Ma)±1σ	% ATM	^{37}Ar/^{39}Ar	^{36}Ar/^{40}Ar	^{39}Ar/^{40}Ar	% IIC
950	33.8	1.8	118.9 ± 6.8	67.9	3.31	0.002299	0.010862	1.06
975	15.1	0.8	75 ± 9	45.4	3.75	0.001538	0.029577	1.77
1000	62.2	3.4	58.1 ± 1.9	25.4	3.66	0.000865	0.052507	2.18
1025	197.6	10.8	56.8 ± .7	15.1	3.62	0.000516	0.061143	2.19
1050	224.7	12.3	56.4 ± .6	11	3.6	0.00038	0.064583	2.2
1075	626.2	34.4	57 ± .3	5.9	3.31	0.000205	0.067569	2
1100	335.4	18.4	56.3 ± .4	7.3	3.24	0.000255	0.067326	1.98
1125	78.6	4.3	56.8 ± 1.6	24.2	3.4	0.000823	0.054587	2.06
1175	70.1	3.8	57.1 ± 1.9	33.2	3.43	0.001128	0.047832	2.07
1250	64.7	3.5	52.9 ± 2.4	55.5	3.49	0.001878	0.034482	2.26
1350	104.5	5.7	54.4 ± 2.2	62.7	3.43	0.002121	0.028104	2.17
1400	4.7	0.2	-663.9 ±-288.8	117	3.12	0.003967	0.001295	0.02

TOTAL GAS AGE = 57.8 ± .6 Ma
J = .002312 ± 1.156E-05 (.5 %)
^{37}Ar/^{39}Ar, ^{36}Ar/^{40}Ar AND ^{39}Ar/^{40}Ar ARE CORRECTED FOR MASS SPECTROMETER DISCRIMINATION,INTERFERING ISOTOPES AND SYSTEM BLANKS
% IIC - INTERFERING ISOTOPES CORRECTION

RS-244

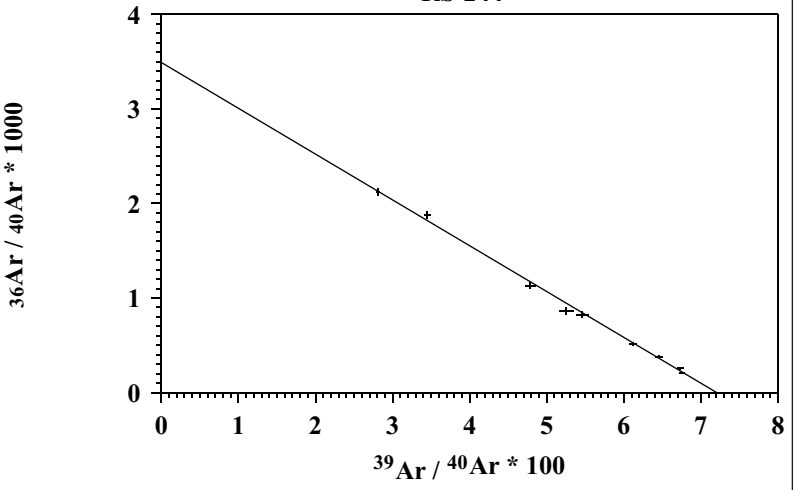

	T°C	(^{39}Ar/^{40}Ar)*100	(^{36}Ar/^{40}Ar)*1000
1	1000	5.25 ± .092	.865 ± .038
2	1025	6.114 ± .047	.516 ± .017
3	1050	6.458 ± .047	.38 ± .014
4	1075	6.756 ± .036	.205 ± .006
5	1100	6.732 ± .041	.255 ± .01
6	1125	5.458 ± .08	.823 ± .033
7	1175	4.783 ± .07	1.128 ± .034
8	1250	3.448 ± .042	1.878 ± .039
9	1350	2.81 ± .022	2.121 ± .037

# ITERATIONS = 3
XBAR = 6.004
YBAR = .581
SUM S = 7.186
SLOPE =-.485 ± 8.000001E-03 INCLUDING SUMS
X = 7.205 ± .021
(Y=0)
Y = 3.056 ± .499 (^{40}Ar/^{36}Ar INITIAL= 327 ± 53)
Y = 3.491 ± .052 (40Ar/36Ar INITIAL= 286 ± 4)
(X=0)
J = .002312 ± 1.156E-05
ISOCHRON AGE = 56.969 ± .45 Ma (2σ UNCERTAINTY INCLUDING ERROR IN J)

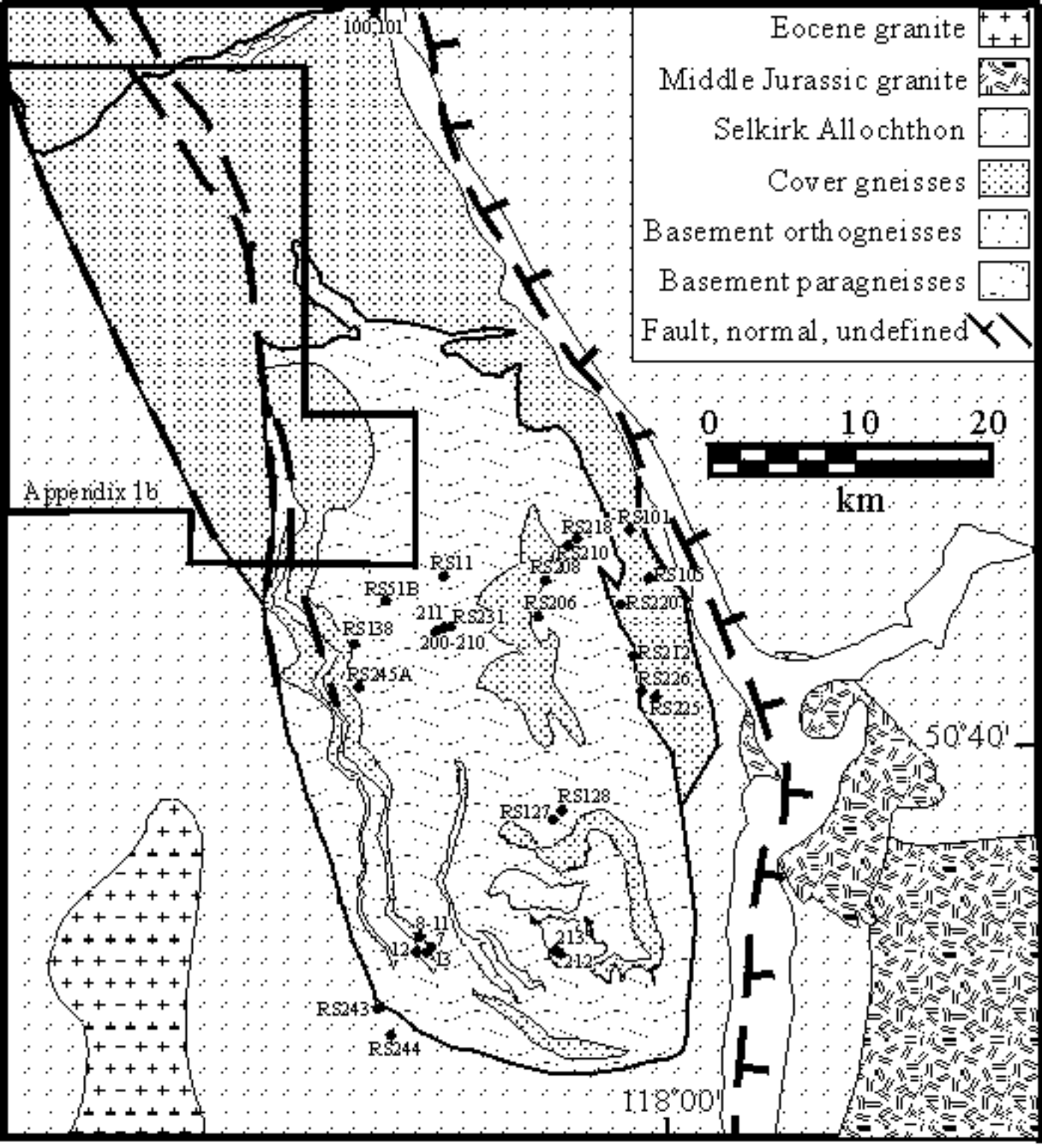

Appendix IIa. Sample location map. Map after Spark (2001). See Appendix IIc for UTM coordinates.

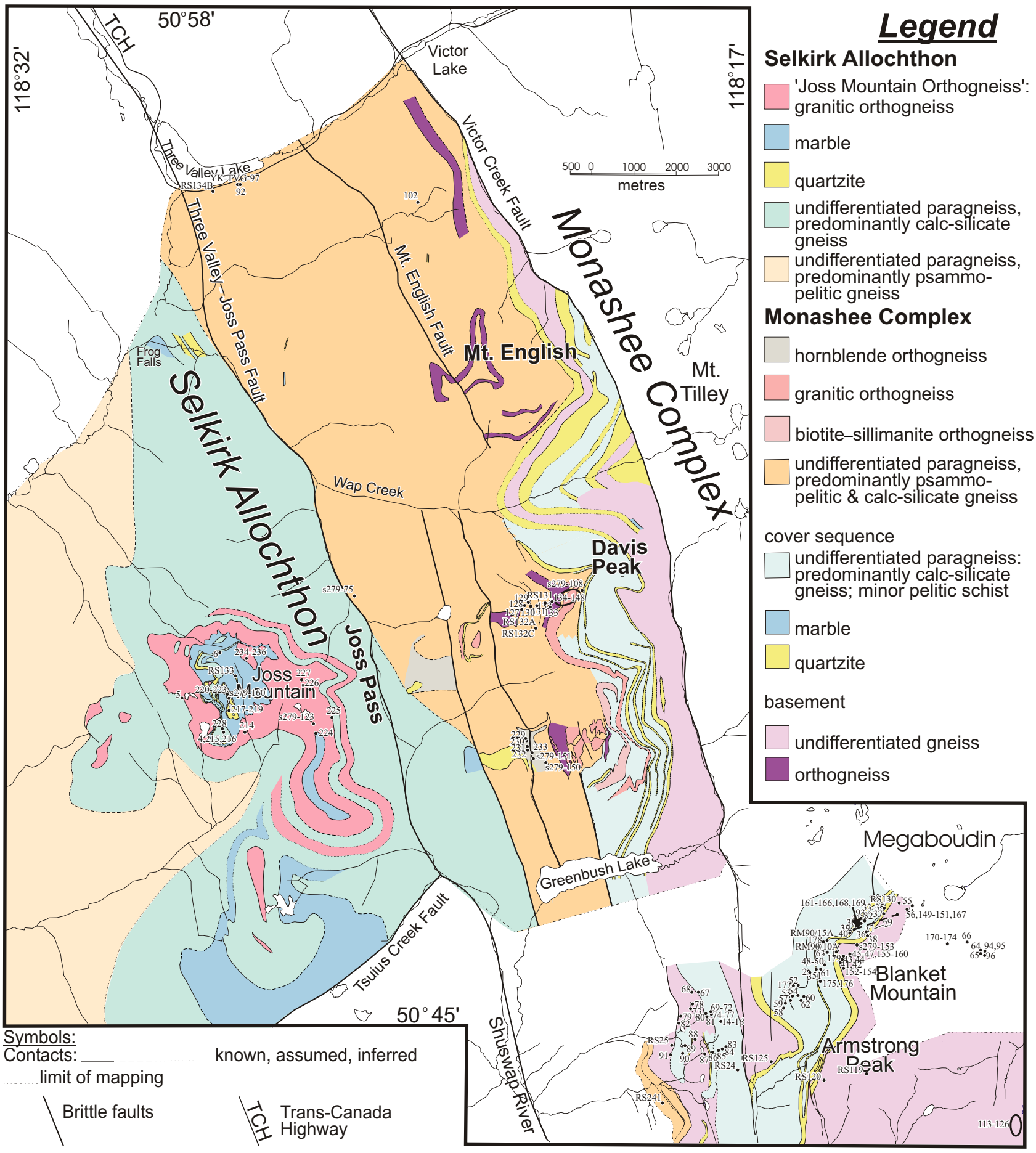

Appendix Ib. Sample location map. Map after Johnston et al. (2000). See Appendix Ic for UTM coordinates.

Appendix IIc. Sample UTM coordinates.

sample nr	rock type	easting (m)	northing (m)
s298-1	regolith	411680	5624675
s298-2	calc-silicate gneiss	411080	5624300
s298-3	calc-silicate gneiss	411120	5624200
s298-4	pegmatite	397150	5629850
s298-5	orthogneiss	396220	5630590
s298-6	mylonite	397120	5631610
s298-7	paragneiss	416740	5600000
s298-8	pelitic schist	416150	5600480
s298-9	quartzite	416150	5600480
s298-10	quartzite	416150	5600480
s298-11	regolith	416150	5600480
s298-12	pelitic schist	415900	5599790
s298-13	quartzite	416400	5599700
s298-14	pelitic schist	409050	5623100
s298-15	pelitic schist	409050	5622950
s298-16	pelitic schist	409050	5622850
s298-17	quartzite	412200	5625200
s298-18	pelitic schist	412275	5625235
s298-19	marble	312350	5625265
s298-20	quartzite	412425	5625300
s298-21	calc-silicate gneiss	412500	5625335
s298-22	calc-silicate gneiss	412575	5625365
s298-23	calc-silicate gneiss	412650	5625400
s298-24	calc-silicate gneiss	412725	2625435
s298-25	paragneiss	412800	5625465
s298-26	amphibolite	412875	5625500
s298-27	paragneiss	412950	5625535
s298-28	paragneiss	413025	5625565
s298-29	orthogneiss	413100	5625600
s298-30	quartzite	412150	5625450
s298-32	lamprophyre	412530	5625500
s298-33	calc-silicate gneiss	412850	5625700
s298-34	calc-silicate gneiss	412850	5625700
s298-35	calc-silicate gneiss	412850	5625700
s298-36	calc-silicate gneiss	412500	5625200
s298-37	calc-silicate gneiss	412850	5625600
s298-38	calc-silicate gneiss	412550	5625100
s298-39	pelitic schist	412140	5625250
s298-40	amphibolite	412140	5625250
s298-41	orthogneiss	411750	5624400
s298-42	amphibolite	411890	5624500
s298-43	quartzite	411900	5624620
s298-44	small vein	412050	5624610
s298-45	pelitic schist	412150	5624890
s298-46	pelitic schist	412150	5624890
s298-47	calc-silicate gneiss	412150	5624890
s298-48	amphibolite	411400	5624400
s298-49	amphibolite	411400	5624400

sample nr	rock type	easting (m)	northing (m)
s298-50	leucosome	411400	5624400
s298-51	paragneiss	411350	5624250
s298-52	leucosome	411020	5623950
s298-53	pelitic schist	410600	5623950
s298-54	pelitic schist	410850	5623950
s298-55	orthogneiss	413350	5625700
s298-56	orthogneiss	413250	5625600
s298-58	calc-silicate gneiss	410450	5623400
s298-59	calc-silicate gneiss	410450	5623470
s298-60	paragneiss	410980	5623950
s298-61	quartzite	411500	5624200
s298-62	quartzite	410930	5623480
s298-63	amphibolite	411470	5624750
s298-64	quartzite	415050	5624700
s298-65	orthogneiss	415050	5624650
s298-66	pelitic schist	414750	5624950
s298-67	pegmatite	408450	5623700
s298-68	pelitic schist	408250	5623700
s298-69	amphibolite	408650	5623250
s298-70	pelitic schist	408650	5623250
s298-71	pelitic schist	408650	5623250
s298-72	pegmatite	408650	5623250
s298-73	pelitic schist	408300	5623280
s298-74	calc-silicate gneiss	408650	5623250
s298-75	amphibolite	408650	5623250
s298-76	pelitic schist	408650	5623250
s298-77	marble	408650	5623250
s298-78	lamprophyre	408300	5623410
s298-79	paragneiss	408050	5623150
s298-80	orthogneiss	408590	5623250
s298-81	orthogneiss	408590	5623160
s298-82	pegmatite	408030	5623050
s298-83	orthogneiss	409080	5622500
s298-84	leucosome	408960	5622380
s298-85	amphibolite	408900	5622300
s298-86	lamprophyre	408770	5622250
s298-87	mylonite	408600	5622200
s298-88	pelitic schist	408310	5622550
s298-89	pelitic schist	408120	5622460
s298-90	amphibolite	408020	5622300
s298-91	orthogneiss	407800	5622240
s298-92	leucosome	397675	5642775
s298-93	lamprophyre	412240	5625550
s298-94	marble	415200	5624670
s298-95	marble	415200	5624670
s298-96	orthogneiss	415200	5624540
s298-97	paragneiss	394500	5645500

Appendix IIc. (continued)

sample nr	rock type	easting (m)	northing (m)
s298-100	carbonatite	413900	5650400
s298-101	calc-silicate gneiss	413900	5650400
s298-102	amphibolite	402450	5642550
s298-103	orthogneiss	393500	5647500
s298-104	pelitic schist	393500	5647500
s298-105	pegmatite	393500	5647500
s298-106	paragneiss	393500	5647500
s298-107	paragneiss	387500	5648300
s298-108	paragneiss	385250	5650000
s298-109	orthogneiss	385250	5650000
s298-110	lamprophyre	385250	5650000
s298-111	pelitic schist	385250	5650000
s298-112	lamprophyre	384400	5650400
s298-113	orthogneiss	415800	5620550
s298-114	vein	415790	5620700
s298-115	orthogneiss	415750	5620600
s298-116	amphibolite	415900	5620480
s298-117	aplite	415850	5620400
s298-118	orthogneiss	415900	5620480
s298-119	amphibolite	416000	5620450
s298-120	pegmatite	416000	5620450
s298-121	orthogneiss	415800	5620550
s298-122	pegmatite	415850	5620510
s298-123	orthogneiss	415770	5620500
s298-124	orthogneiss	415700	5620460
s298-125	pegmatite	415850	5620510
s298-126	orthogneiss	415850	5620510
s298-127	paragneiss	404230	5632850
s298-128	pelitic schist	404420	5632950
s298-129	amphibolite	404620	5632950
s298-130	paragneiss	404560	5632800
s298-131	amphibolite	404760	5632800
s298-132	paragneiss	404860	5632870
s298-133	orthogneiss	404940	5632730
s298-134	paragneiss	405450	5633000
s298-135	paragneiss	405450	5633000
s298-136	paragneiss	405450	5633000
s298-137	amphibolite	405350	5632650
s298-138	amphibolite	405350	5632550
s298-139	paragneiss	405530	5632950

sample nr	rock type	easting (m)	northing (m)
s298-140	paragneiss	405690	5632400
s298-141	amphibolite	405650	5632650
s298-142	orthogneiss	405600	5632800
s298-143	marble	405580	5632900
s298-144	amphibolite	405250	5632700
s298-145	leucosome	405160	5632690
s298-146	pelitic schist	405160	5632620
s298-147	amphibolite	405450	5633000
s298-148	calc-silicate gneiss	405450	5633000
s298-149	orthogneiss	413250	5625600
s298-150	orthogneiss	413250	5625600
s298-151	amphibolite	413250	5625600
s298-152	pelitic schist	411900	5624400
s298-153	paragneiss	411900	5624400
s298-154	pelitic schist	411900	5624400
s298-155	pelitic schist	412150	5624890
s298-156	pegmatite	412150	5624890
s298-157	vein	412150	5624890
s298-158	corundum	412150	5624890
s298-159	sillimanite	412150	5624890
s298-160	rotated garnet	412150	5624890
s298-161	marble	412240	5625370
s298-162	leucosome	412240	5625370
s298-163	leucosome	412240	5625370
s298-164	leucosome	412240	5625370
s298-165	leucosome	412240	5625370
s298-166	quartzite	412240	5625370
s298-167	orthogneiss	413250	5625600
s298-168	amphibolite	412240	5625370
s298-169	pelitic schist	412240	5625370
s298-170	corundum	414320	5624800
s298-171	garnet	414320	5624800
s298-172	green mineral	414320	5624800
s298-173	pelitic schist	414320	5624800
s298-174	amphibolite	414320	5624800
s298-175	pelitic schist	411320	5624100
s298-176	amphibolite	411320	5624100
s298-177	pelitic schist	410850	5623900
s298-178	pelitic schist	411450	424920
s298-179	amphibolite	412020	5624480

Appendix IIc. (continued)

sample nr	rock type	easting (m)	northing (m)
s298-200	marble	417350	5616560
s298-201	calc-silicate gneiss	417350	5616560
s298-202	calc-silicate gneiss	417350	5616560
s298-203	amphibolite	417350	5616560
s298-204	orthogneiss	417350	5616560
s298-205	arkose	417350	5616560
s298-206	pegmatite	417350	5616560
s298-207	quartzite	417350	5616560
s298-208	pegmatite	417350	5616560
s298-209	marble	417350	5616560
s298-210	pelitic schist	417350	5616560
s298-211	marble	417700	5616800
s298-212	orthogneiss	423750	5699880
s298-213	aplite	423625	5600025
s298-214	pegmatite	397650	5629850
s298-215	pegmatite	397150	5629850
s298-216	orthogneiss	397150	5629850
s298-217	quartzite	397310	5630420
s298-218	amphibolite	397310	5630420
s298-219	calc-silicate gneiss	397310	5630420
s298-220	amphibolite	397240	5630680
s298-221	pegmatite	397240	5630680
s298-222	pelitic schist	397240	5630680
s298-223	pelitic schist	397240	5630680
s298-224	marble	399410	5629770
s298-225	orthogneiss	399790	5630120
s298-226	lamprophyre	399290	5630800
s298-227	leucogranite	399190	5631050
s298-228	pelitic schist	387200	5629950
s298-229	pelitic schist	404310	5629580
s298-230	orthogneiss	404330	5629450
s298-231	quartzite	404400	5629600
s298-232	pelitic schist	404400	5629600
s298-233	amphibolite	404400	5629600
s298-234	pegmatite	397740	5631620
s298-235	orthogneiss	397740	5631620
s298-236	orthogneiss	397740	5631620

code	collector
s298	Yvette D. Kuiper
s279	Dennis H. Johnston
RS	Robert N. Spark
JC	James L. Crowley
RM, YK-TVG	Paul F. Williams

all sample locations
(except J.L. Crowley's) on map 1

J.L. Crowley's sample locations in:
Crowley, 1997 (CJES) (JC-335)
Crowley, 1999 (GSA) all others

sample nr	rock type	easting (m)	northing (m)
s279-75	orthogneiss	400325	5633145
s279-108	orthogneiss	405640	5633240
s279-123	orthogneiss	399478	5630383
s279-150	pegmatite	404610	5629610
s279-151	orthogneiss	404560	5629670
s279-153	pegmatite	412252	5624711
s279-160	pelitic schist	397400	5630690
YK-TVG-97	paragneiss	397675	5642775
Rm 90/10A	paragneiss	411680	5624700
Rm 90/15A	Fsp bearing quartzite	411450	5624890
RS-11A	orthogneiss	418120	5616850
RS-24C	amphibolite	409054	5612881
RS-25C	amphibolite	407939	5622363
RS-51B	amphibolite	414718	5618228
RS-101A	pegmatite	428100	5622225
RS-105	paragneiss	428750	5619250
RS-119B	amphibolite	412518	5621706
RS-120	amphibolite	411493	5621561
RS-125B	amphibolite	410059	5622182
RS-127	amphibolite	423585	5606561
RS-128	amphibolite	424051	5607004
RS-130	amphibolite	412426	5624632
RS-131	amphibolite	405132	5632890
RS-132A	amphibolite	404708	5632318
RS-132C	amphibolite	404680	5632244
RS-133	amphibolite	397334	5631304
RS-134B	amphibolite	397403	5642629
RS-138	amphibolite	413124	5615876
RS-206	amphibolite	422843	5617504
RS-208	arkose	423700	5618950
RS-210	orthogneiss	424250	5621200
RS-212A	amphibolite	427736	5615318
RS-218	amphibolite	424822	5621517
RS-220	amphibolite	427129	5617936
RS-225B	pegmatite	429850	5613150
RS-226	amphibolite	428333	5613553
RS-231	orthogneiss	417920	5616950
RS-241B	amphibolite	407602	5621088
RS-243	amphibolite	414329	5596427
RS-244	amphibolite	415016	5594957
RS-245A	orthogneiss	413200	5613200
JC-60B	orthogneiss	388920	5694190
JC-60C	orthogneiss	388920	5694190
JC-65	orthogneiss	388830	5692810
JC-79	gneiss amphibolite	389020	5692490
JC-84	pegmatite	389940	5687940
JC-85	pelitic schist	390130	5687830
JC-91	pegmatite	390220	5686730
JC-291	pegmatite	388290	5692520
JC-308	pegmatite	390300	5686680
JC-311	orthogneiss	391230	5686880
JC-335	quartzite	386930	5695690
JC-337	amphibolite	389070	5692230
PCA-305B-83	orthogneiss	389330	5688340

Appendix III. Unused stable isotope data. All other data in Chapter 3.

sample nr	rock type	oxygen whole rock	quartz	feldspar	hydrogen whole rock	hydrous and/or retrograde minerals in percentage	easting (m)	northing (m)
Thor–Odin								
Cranberry Mountain East								
s298-203	amphibolite	2.6				no thin section	417350	5616560
s298-204	pelitic schist	8.9				no thin section	417350	5616560
s298-205	aplite	11.1				no thin section	417350	5616560
s298-206	pegmatite	3.5	8.5	5.3		no thin section	417350	5616560
s298-207	quartzite	3.1	11.0	0.6		no thin section	417350	5616560
Other								
S279-75	orthogneiss	7.7	11.4	9.4		5 bt, <0.5 chl, <0.5 ser	400325	5633145
S279-108	orthogneiss	10.1	11.8	10.9		10 bt, <0.5 ser	405640	5633240
S279-123	orthogneiss	7.5				6 bt, <0.5 chl, <1 ser	399478	5630383
S279-151	hornbl. Orthogneiss	3.7			–156.4	no thin section	404560	5629670
s298-5	orthogneiss	7.5		7.4		5 bt, <0.5 chl, 1 ser	396220	5630590
S298-29	orthogneiss	9.3	10.8	9.5	–55	15 bt, <0.5 ser	413100	5625600
S298-80	orthogneiss	5.2	9.9	3.9		5 bt, <0.5 chl, <1 ser	408590	5623250
S298-126	orthogneiss	9.9	9.9	10.9		5 bt, 2 ms/ser	415850	5620510
S298-167	orthogneiss	9.5	12.9	9.3		15 bt, <1 chl, <1 ser	413250	5625600
RS-11A	orthogneiss	10.8			–94.1	5 bt, 1 chl, 2 ms/ser ser	418120	5616850
RS-210	orthogneiss	3.3	10.4	1.7	–142.7	4 bt, 3 chl, 1 ser	424250	5621200
RS-231	orthogneiss	9.5	10.8	8.1		1bt, <1 ser	417920	5616950
RS-245A	orthogneiss	10.8				7 bt, <0.5 chl, <1 ser	413200	5613200
S298-65L	leucos. in orthogneiss	8.5	11.6	8.6		3 bt, <0.5 chl, <1 ser	415050	5624650
S279-150	pegmatite	3.0	12.4	6.5		no thin section	404610	5629610
S279-153	pegmatite	9.2				no thin section	412252	5624711
S298-82	pegmatite	12.9				1 bt, <0.5 ser	408030	5623050
S298-120	pegmatite	9.4				5 bt, <1 chl, 1 ms, <1 ser	416000	5620450
RS-101A	pegmatite	10.3				<1 bt, <0.5 chl, <0.5 ms, <0.5 ser	428100	5622225
RS-225B	pegmatite	6.4				1 bt, <0.5 chl, 3 ser,	429850	5613150
S298-92	leucosome in paragneiss	8.9	10.5	7.6		5 bt, 1 chl, 1 ser	397675	5642775
S298-62	felsic paragneiss	10.6	10.5	11.2		2 bt, 1 ms, <0.5 ser	410930	5623480
S298-124	paragneiss	8.7				7 bt, 1 ms, <0.5 ser	415700	5620460
S298-127	felsic paragneiss	10.7	11.3	10.0		no thin section	404230	5632850
RS-105	paragneiss	8.9		8.0		7 bt, 1 ser, fractures	428750	5619250
Rm 90/10A	paragneiss	10.9				1 bt, 2 ser	411680	5624700
Rm 90/15A	Fsp bearing quartzite	9.8	11.1	9.8		<1 bt,	411450	5624890
S298-64	Fsp bearing quartzite	–0.5	8.6	–1.4		1 bt, 1 chl, 1 ms, 1 ser, filled/altered fractures	415050	5624700
S298-30	quartzite	11.8				1 bt	412150	5625450
S298-71	ky–grt rich part in pelitic schist		11.6	10.5		1 chl, filled/altered fractures	408650	5623250
S298-6	arkose	6.4		7.6		<1 chl, 1 ser, filled/altered fractures	397120	5631610
RS-208	arkose	6.8	10.6	5.4		5 ms, 1 ser	423700	5618950
S279-160	pelitic schist				–138.3	10 bt, <1 chl, <1 ser	397400	5630690
Frenchman Cap								
JC-311	orthogneiss	6.1	8.0	7.4	–51.3	10 bt, <1 ser, 3 hbl	391230	5686880
JC-60B	orthogneiss	6.7	7.7	7.2		no thin section	388920	5694190
JC-60C	orthogneiss	6.1				3 bt, <1 ser	388920	5694190
JC-65	orthogneiss	6.0				4 bt, <1 ser, 6 hbl	388830	5692810
JC-84	pegmatite	4.3	11.7	6.1		1 bt, 1 chl, 4 ser	389940	5687940
JC-91	pegmatite	6.1				3 bt, <0.5 chl, 4 ser	390220	5686730
JC-291	pegmatite	6.7				1 bt, 1 ser	388290	5692520
JC-308	pegmatite	7.6				<1 bt, <1 ser	390300	5686680
JC-79	gneiss amphibolite	3.3	5.9	4.7		25 bt, < 1 ser, 45 hbl	389020	5692490
JC-337	amphibolite	3.4		6.4		25 bt, < 1 ser, 40 hbl	389070	5692230
JC-335	quartzite	11.4				5 bt, 10 ms, <1 ser	386930	5695690

Mineral abbreviations after Kretz (1983), and ser = sericite
Most severe whole-rock depletion seems to be in rocks with alteration/retrograde minerals

Vita

Candidate's full name: Yvette Dominique Kuiper

Place and date of birth: Eemnes, the Netherlands
April 9, 1974

Universities attended: Utrecht University, Utrecht, the Netherlands
September 1992 - September 1997
M.Sc.

Publications:

Kuiper, Y.D., 2002. The interpretation of inverse isochron diagrams in $^{40}Ar/^{39}Ar$ geochronology. Earth and Planetary Science Letters 203, 499–506.

Kuiper, Y.D., Lin, S., Böhm, Ch.O., Corkery, M.T., 2003 (accepted). Structural geology of the Assean Lake and Aiken River shear zones, northern Manitoba (NTS 64A1, 2 and 8). In: Report of Activities 2003, Manitoba Industry, Trade and Mines, Manitoba Geological Survey.

Kuiper, Y.D., (in review). Isotopic age constraints from electron microprobe U–Th–Pb dates, using a three-dimensional concordia diagram. Geology.

Conference presentations:

Kuiper, Y.D., 1998. Microstructural, petrological and geochronological studies on the Thor–Odin dome, Monashee Complex, southern Canadian Cordillera; proposed Ph.D. research. In: Cook, F. and P. Erdmer (compilers), Slave–Northern Cordillera Lithospheric Evolution (SNORCLE) Transect and Cordilleran Tectonics Workshop Meeting (March 6–8, 1998), Simon Fraser University, Lithoprobe Report No. 64, 272–273.

Kuiper, Y.D., Carr, S.D., Williams, P.F., 1998. Microstructural, petrological and geochronological studies on the Thor–Odin dome, Monashee Complex, southern Canadian Cordillera. In: Lin, S., Bleeker, W., Elliott, C., van Staal, C.R. (compilers), Geological Association of Canada NUNA conference and Canadian Tectonics Group 18th Annual Meeting (September 26–28, 1998), Canmore, Alberta, Canada.

Kuiper, Y.D., Carr, S.D., Williams, P.F., 1999. Geochronological, petrological and microstructural studies on the Thor–Odin dome, Monashee Complex, southern Canadian Cordillera. In: Cook, F. and P. Erdmer (compilers), Slave–Northern Cordillera Lithospheric Evolution (SNORCLE) Transect and Cordilleran Tectonics

Workshop Meeting (March 5–7, 1999), University of Calgary, Lithoprobe Report No. 69, 296.

Kuiper, Y.D., Carr, S.D., Williams, P.F., 2000. Age constraints on penetrative structures at Joss Mountain, in the Selkirk Allochthon, southern Canadian Cordillera. In: Cook, F. and P. Erdmer (compilers), Slave–Northern Cordillera Lithospheric Evolution (SNORCLE) Transect and Cordilleran Tectonics Workshop Meeting (February 25–27, 2000), University of Calgary, Lithoprobe Report No. 72, 168.

Kuiper, Y.D., Taylor, B.E., Williams, P.F., Carr, S.D, 2001. Early Eocene extension-related fluids in the Monashee Complex, southeastern BC. In: Cook, F. and P. Erdmer (compilers), Slave–Northern Cordillera Lithospheric Evolution (SNORCLE) Transect and Cordilleran Tectonics Workshop Meeting (February 22–25, 2001), Pacific Geoscience Centre, Lithoprobe Report No. 79, 89–90.

Kuiper, Y.D., Williams, P.F., Taylor, B.E., Carr, S.D, 2001. Timing of deformation in the Monashee Complex re-interpreted: new constraints from oxygen and hydrogen isotope studies. In: Lafrance, B., Canadian Tectonics Group 21st Annual Meeting (October 26–28, 2001), Sudbury, Ontario, Canada.

Kuiper, Y.D., 2002. When did deformation and peak of metamorphism take place in the Monashee Complex? In: Cook, F. and P. Erdmer (compilers), Slave–Northern Cordillera Lithospheric Evolution (SNORCLE) Transect and Cordilleran Tectonics Workshop Meeting (February 21–24, 2002), Pacific Geoscience Centre, Lithoprobe Report No. 82, 89–90.

Kuiper, Y.D., Kruse, S. Williams, P.F., McNeill, P.D., 2002. Possibility of channel flow in the southern Canadian Cordillera; a new approach to explain existing data. In: Cook, F. and P. Erdmer (compilers), Slave–Northern Cordillera Lithospheric Evolution (SNORCLE) Transect and Cordilleran Tectonics Workshop Meeting (February 21–24, 2002), Pacific Geoscience Centre, Lithoprobe Report No. 82, 132–133.

Kuiper, Y.D., Williams, P.F., 2003. Proterozoic migmatisation in a basement orthogneiss, and Late Cretaceous to Early Eocene monazite ages in cover rocks of Thor–Odin dome of the Monashee Complex, southeastern British Columbia; a SHRIMP and ID–TIMS study. Cordilleran Tectonics Workshop Meeting (February 7–9, 2003), Carleton University, Ottawa, 18.

Kuiper, Y.D., 2003. U–Pb isotopic dating of multiple geological events; an example from the Monashee Complex, British Columbia. University of New Brunswick Graduate Student Association 11th Annual Conference on Student Research (February 14–15, 2003), University of New Brunswick, Fredericton, 11.

Kuiper, Y.D., 2003. Isotopic age constraints from electron microprobe U–Th–Pb dates, using a three-dimensional concordia diagram. Geological Association of Canada

Mineralogical Association of Canada and Society of Economic Geologists Annual Meeting (May 25–29, 2003), Vancouver.

Kuiper, Y.D., Williams, P.F., 2003. Constraining deformation and metamorphism in Thor–Odin dome of the Monashee Complex, southeastern British Columbia; how some events may be preserved in the U–Pb record and others may not. Geological Association of Canada and Mineralogical Association of Canada Annual Meeting (May 25–29, 2003), Vancouver.